CLIMATE AND OCEAN DYNAMICS AT THE BRAZILIAN MARGIN - PAST AND PRESENT

EDITED BY: Jacek Raddatz, Christoph Häggi, André Bahr and Cristiano M. Chiessi

PUBLISHED IN: Frontiers in Marine Science and Frontiers in Earth Science

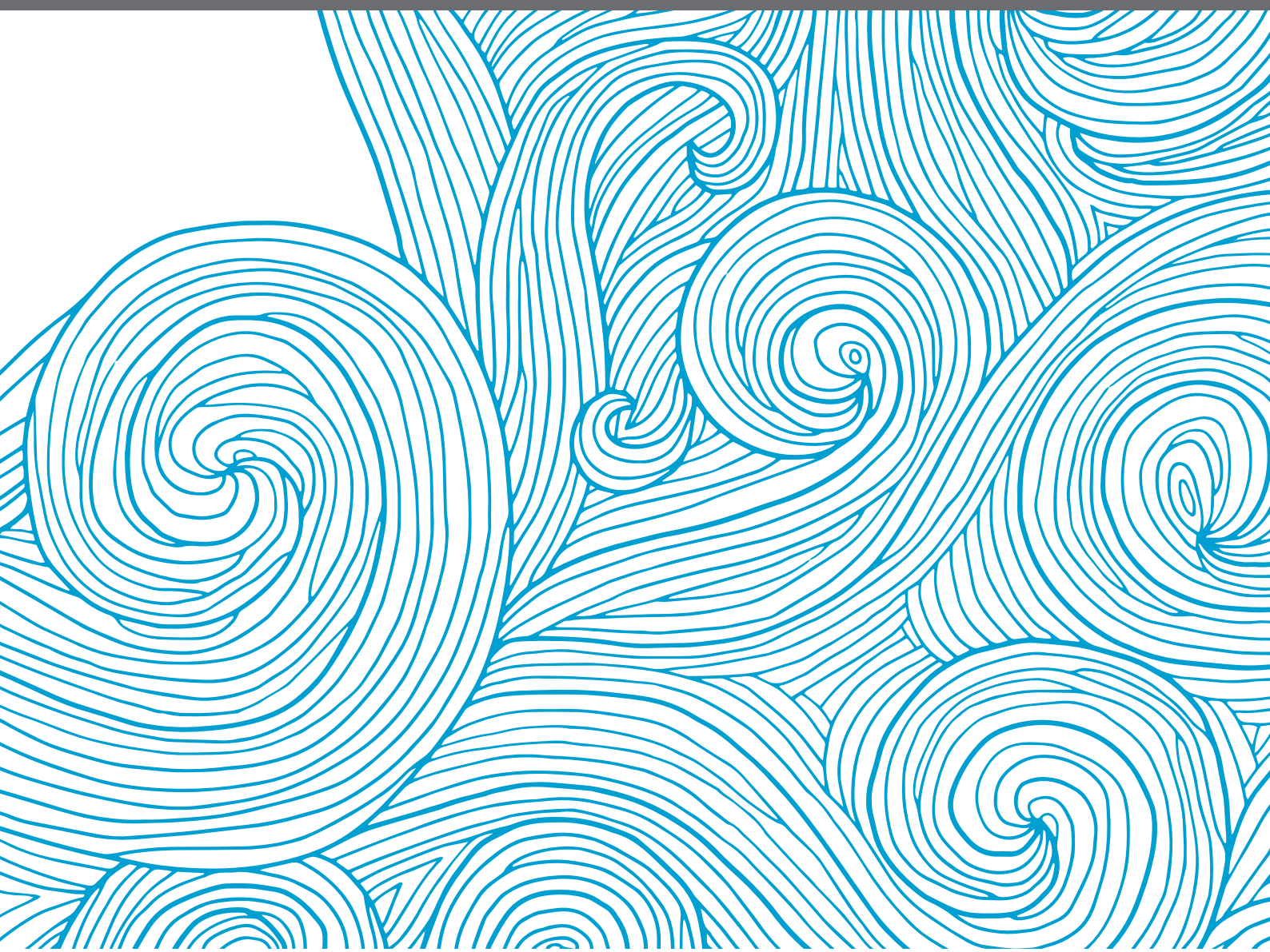

frontiers Research Topics

ISSN 1664-8714
ISBN 978-2-83250-416-1
DOI 10.3389/978-2-83250-416-1

About Frontiers

Frontiers is more than just an open-access publisher of scholarly articles: it is a pioneering approach to the world of academia, radically improving the way scholarly research is managed. The grand vision of Frontiers is a world where all people have an equal opportunity to seek, share and generate knowledge. Frontiers provides immediate and permanent online open access to all its publications, but this alone is not enough to realize our grand goals.

Frontiers Journal Series

The Frontiers Journal Series is a multi-tier and interdisciplinary set of open-access, online journals, promising a paradigm shift from the current review, selection and dissemination processes in academic publishing. All Frontiers journals are driven by researchers for researchers; therefore, they constitute a service to the scholarly community. At the same time, the Frontiers Journal Series operates on a revolutionary invention, the tiered publishing system, initially addressing specific communities of scholars, and gradually climbing up to broader public understanding, thus serving the interests of the lay society, too.

Dedication to Quality

Each Frontiers article is a landmark of the highest quality, thanks to genuinely collaborative interactions between authors and review editors, who include some of the world's best academicians. Research must be certified by peers before entering a stream of knowledge that may eventually reach the public - and shape society; therefore, Frontiers only applies the most rigorous and unbiased reviews.
Frontiers revolutionizes research publishing by freely delivering the most outstanding research, evaluated with no bias from both the academic and social point of view. By applying the most advanced information technologies, Frontiers is catapulting scholarly publishing into a new generation.

What are Frontiers Research Topics?

Frontiers Research Topics are very popular trademarks of the Frontiers Journals Series: they are collections of at least ten articles, all centered on a particular subject. With their unique mix of varied contributions from Original Research to Review Articles, Frontiers Research Topics unify the most influential researchers, the latest key findings and historical advances in a hot research area! Find out more on how to host your own Frontiers Research Topic or contribute to one as an author by contacting the Frontiers Editorial Office: frontiersin.org/about/contact

CLIMATE AND OCEAN DYNAMICS AT THE BRAZILIAN MARGIN - PAST AND PRESENT

Topic Editors:
Jacek Raddatz, Goethe University Frankfurt, Germany
Christoph Häggi, Department of Earth Sciences, ETH Zurich, Switzerland
André Bahr, Heidelberg University, Germany
Cristiano M. Chiessi, University of São Paulo, Brazil

Citation: Raddatz, J., Häggi, C., Bahr, A., Chiessi, C. M., eds. (2022). Climate and Ocean Dynamics at the Brazilian Margin - Past and Present.
Lausanne: Frontiers Media SA. doi: 10.3389/978-2-83250-416-1

Table of Contents

04 ***Editorial: Climate and Ocean Dynamics at the Brazilian Margin – Past and Present***
Jacek Raddatz, André Bahr, Cristiano M. Chiessi and Christoph Häggi

07 ***Tropical South American Rainfall Response to Dansgaard-Oeschger Stadials of Marine Isotope Stage 5***
Igor M. Venancio, Rodrigo A. Nascimento, Thiago P. Santos, Andre L. Belem, Douglas O. Lessa, Ralf Tiedemann, Cristiano M. Chiessi, Stefan Mulitza and Ana Luiza S. Albuquerque

17 ***Calcium Carbonate Dissolution Triggered by High Productivity During the Last Glacial–Interglacial Interval in the Deep Western South Atlantic***
Jaime Y. Suárez-Ibarra, Cristiane F. Frozza, Pâmela L. Palhano, Sandro M. Petró, Manuel F. G. Weinkauf and Maria A. G. Pivel

31 ***REE Anomalies Changes in Bottom Sediments Applied in the Western Equatorial Atlantic Since the Last Interglacial***
Thiago A. Sousa, Igor Martins Venancio, Eduardo Duarte Marques, Thiago S. Figueiredo, Rodrigo Azevedo Nascimento, Joseph M. Smoak, Ana Luiza S. Albuquerque, Claudio Morisson Valeriano and Emmanoel Vieira Silva-Filho

45 ***Spatiotemporal Discharge Variability of the Doce River in SE Brazil During MIS 6 and 5***
Iris Arndt, Silke Voigt, Rainer Petschick, Alicia Hou, Jacek Raddatz, Ana Luiza S. Albuquerque and André Bahr

59 ***Coupled Oceanic and Atmospheric Controls of Deglacial Southeastern South America Precipitation and Western South Atlantic Productivity***
Karl J. F. Meier, Andrea Jaeschke, Janet Rethemeyer, Cristiano M. Chiessi, Ana Luiza S. Albuquerque, Vincent Wall, Oliver Friedrich and André Bahr

79 ***Marine Paleoproductivity From the Last Glacial Maximum to the Holocene in the Southwestern Atlantic: A Coccolithophore Assemblage and Geochemical Proxy Perspective***
Guilherme A. Pedrão, Marcus V. Hirama, Mariana O. Tomazella, Ana Luiza S. Albuquerque, Cristiano M. Chiessi, Karen B. Costa and Felipe A. L. Toledo

95 ***Controlling Parameters of Benthic Deep-Sea Foraminiferal Biogeography at the Brazilian Continental Margin (11-22°S)***
Anna Saupe, Johanna Schmidt, Jassin Petersen, André Bahr, Bruna Borba Dias, Ana Luiza Spadano Albuquerque, Rut Amelia Díaz Ramos and Patrick Grunert

112 ***The Cold-water Coral* Solenosmilia Variabilis *as a Paleoceanographic Archive for the Reconstruction of Intermediate Water Mass Temperature Variability on the Brazilian Continental Margin***
S. Endress, N. Schleinkofer, A. Schmidt, D. Tracey, N. Frank and J. Raddatz

126 ***Late Pleistocene to Holocene Variations in Marine Productivity and Terrestrial Material Delivery to the Western South Atlantic***
Ana Lúcia Lindroth Dauner, Gesine Mollenhauer, Jens Hefter, Márcia Caruso Bícego, Michel Michaelovitch de Mahiques and César de Castro Martins

frontiers | Frontiers in Marine Science

TYPE Editorial
PUBLISHED 21 September 2022
DOI 10.3389/fmars.2022.1033387

OPEN ACCESS

EDITED AND REVIEWED BY
Charitha Bandula Pattiaratchi,
University of Western Australia,
Australia

*CORRESPONDENCE
Jacek Raddatz
raddatz@em.uni-frankfurt.de

SPECIALTY SECTION
This article was submitted to Coastal Ocean Processes, a section of the journal Frontiers in Marine Science

RECEIVED 31 August 2022
ACCEPTED 05 September 2022
PUBLISHED 21 September 2022

CITATION
Raddatz J, Bahr A, Chiessi CM and Häggi C (2022) Editorial: Climate and ocean dynamics at the Brazilian margin – Past and present. *Front. Mar. Sci.* 9:1033387. doi: 10.3389/fmars.2022.1033387

Editorial: Climate and ocean dynamics at the Brazilian margin – Past and present

Jacek Raddatz[1]*, André Bahr[2], Cristiano M. Chiessi[3] and Christoph Häggi[4]

[1]Institute of Geosciences, Goethe University Frankfurt, Frankfurt, Germany, [2]Institute of Earth Sciences, Heidelberg University, Heidelberg, Germany, [3]School of Arts, Sciences and Humanities, University of São Paulo, São Paulo, Brazil, [4]Department of Earth Sciences, ETH Zurich, Zürich, Switzerland

KEYWORDS

ITCZ, South Atlantic, Quaternary, millennial-scale climate change, SACZ, continental margins, marine productivity

Editorial on the Research Topic
Climate and ocean dynamics at the Brazilian margin - Past and present

Continental margins account for only about one-third of the surface covered by the oceans, but are responsible for more than 80% of the carbon sequestration in marine sediments. Tropical continental margins receive some of the largest terrestrial organic and inorganic fluxes to the marine realm. In particular, the Brazilian continental margin is located in a crucial region of the global oceanic conveyor belt and is central to the interaction between climate and ocean dynamics in low latitudes. Despite decades of research, it is not yet clear whether and how the highly vulnerable marine and terrestrial ecosystems in that region will respond to climate change. To better understand potential future climate scenarios and how they will alter the Brazilian margin, an important strategy is to reconstruct past climate and ocean dynamics. This research theme brings together synergistic research efforts from different Earth system disciplines to improve our understanding of the Brazilian margin as a key compartment of the (sub)tropical climate system and South Atlantic Ocean dynamics.

This Research Topic includes studies from the Brazilian margin that reconstruct past tropical climate and associated changes in precipitation patterns, land-sea interaction, changes in river discharge, changes in sea surface productivity, water mass properties, sediment diagenesis and geochemistry, and micropaleontological methods using foraminifera and coccolithophores.

In a very detailed investigation of marine isotope stage (MIS) 5, the study by Venancio et al. shows that foraminiferal Ba/Ca ratios can be used to to detect changes in fluvial discharge, which in turn can be linked to movements of the Intertropical Convergence Zone (ITCZ). Furthermore, the study shows that these precipitation changes were related to rapid Dansgaard/Oeschger (D/O) stadials.

Fluvial discharge from MIS 5 (and also MIS 6) is also reconstructed by Arndt et al. In this study, clay mineral compositions of deep-sea sediments are used to identify changes in the drainage basin of the Doce River caused by changes in the South Atlantic Convergence Zone (SACZ). The dominant temporal control on clay mineral composition (kaolinite and gibbsite versus illite, quartz, and albite) here appears not to be the short-term D/O cycles, but changes in Earth's orbit, particularly the precession cycle (21 ka), which causes variations in tropical seasonality.

The coupling of the terrestrial and marine domains during the late Pleistocene and Holocene is studied by Dauner et al. They show that organic matter (OM) composition (terrestrial versus marine) exhibited increased marine productivity between 50 and 39 ka BP and shifted to a more terrestrially dominated OM regime between 30 and 20 ka BP. Such changes may be associated with variations in upwelling and fluvial nutrient supply, as well as changes in surface water masses.

Sea surface paleoproductivity off the Brazilian margin is also reconstructed by Pedrão et al. They use a combination of coccolithopore assemblages and bulk sediment geochemistry showing that marine productivity was higher during the LGM and lower during the Holocene. The authors conclude that this was due to changes in sea level that under glacial conditions resulted in an exposed shelf and increased continental nutrient input to the ocean.

Interestingly, the feedback mechanism described above can also be observed during periods of Northern Hemisphere cooling, such as Heinrich Stadial 1 (HS1) (~18.5-15 ka). Meier et al. have collected several data sets based on biomarkers, foraminifer and sedimentary geochemistry. This very comprehensive approach clearly shows that HS1 can be considered an exceptional period during the last deglaciation. During HS1, they described pronounced hydroclimatic gradients leading to an extreme climate characterized by oceanic warming, extreme precipitation, and subsequent nutrient input.

The relation between terrestrial input and deep ocean properties during the last glacial on the Brazilian margin is shown by Suarez-Ibarra et al. They combined micropaleontological (benthic and planktonic foraminifera, ostracods), geochemical (stable carbon isotopes on benthic foraminifera), and sedimentological (carbonate and bulk sand content) data in order to link insolation to sea surface productivity and how the subsequent marine snow effects deep-sea carbonate dissolution. This study nicely shows that our knowledge in benthic-pelagic coupling is still somewhat limited.

The origin of deep-sea sediments on continental slopes is an important topic for the reconstruction of past climates. In their study, Sousa et al. use rare earth elements (REE) to identify the sources of deep-sea sediments. Their data clearly show that rivers can be the main source of REE in sediments of the western South Atlantic and that Fe minerals produced by continental weathering can be the major carriers of REE.

Deep-sea sediments on continental margins not only contain detrital material, but also calcareous organisms such as benthic foraminifera that have been investigated by Saupe et al. Along three subtropical transects the authors show that benthic foraminiferal assemblages are controlled by hydrodynamic conditions opening the opportunity to reconstruct current regimes with benthic foraminifera. In addition, benthic foraminifera are also influenced by the quantity and quality of organic matter flux as well as substrate properties.

Between the deep-sea and the surface, strong currents often prevent a continuous sedimentation and therefore paleoceanographic reconstructions are limited or even lacking. One possibility to circumvent this problem is to use cold-water corals (CWC). Endress et al. studies the scleractinian CWC *Solenosmilia variabilis* from the Bowie Mound as an archive for temperature reconstructions using Li/Mg ratios. They show that, especially during periods of Northern Hemisphere cooling such as HS4 and HS6, the intervening water masses warmed significantly, which may provide evidence for bipolar seesaw dynamics.

Overall, this set of studies improves our understanding on the interrelations between the terrestrial and marine realms on the Brazilian continental margin. They especially stress the importance of ITCZ and SACZ dynamics during Heinrich Stadials fostering new conceptual models while strengthening research synergies across various disciplines.

Author contributions

All listed authors have made a substantial contribution to the work and have approved it for publication.

Funding

CMC acknowledges the financial support from FAPESP (grants 2018/15123-4 and 2019/24349-9) and CNPq (grant 312458/2020-7).

Acknowledgments

The guest editors are thankful for the contributions made by the authors and co-authors. The editors would also like to thank the reviewers for their helpful comments and suggestions.

Conflict of interest

The authors declare that the research was conducted in the absence of any commercial or financial relationships that could be construed as a potential conflict of interest.

Publisher's note

frontiers in Earth Science

ORIGINAL RESEARCH
published: 16 February 2022
doi: 10.3389/feart.2022.826993

Tropical South American Rainfall Response to Dansgaard-Oeschger Stadials of Marine Isotope Stage 5

Igor M. Venancio[1,2], Rodrigo A. Nascimento[1], Thiago P. Santos[1], Andre L. Belem[3], Douglas O. Lessa[1], Ralf Tiedemann[4], Cristiano M. Chiessi[5], Stefan Mulitza[2] and Ana Luiza S. Albuquerque[1]*

[1]Programa de Geociências (Geoquímica), Universidade Federal Fluminense, Niterói, Brazil, [2]MARUM-Center for Marine Environmental Sciences, University of Bremen, Bremen, Germany, [3]Programa de Pós-Graduação Dinâmica dos Oceanos e da Terra, Universidade Federal Fluminense, Niterói, Brazil, [4]Alfred Wegener Institute for Polar and Marine Research, Bremerhaven, Germany, [5]School of Arts, Sciences and Humanities, University of São Paulo, São Paulo, Brazil

Tropical precipitation patterns will most likely be altered by future climate change, with major socioeconomic consequences for human populations that are highly reliant on water availability for subsistence like populations in northeastern (NE) Brazil. Socioeconomic consequences may be particularly disruptive in the occurrence of abrupt climate change. Understanding the response of tropical precipitation to abrupt climate change is a crucial task for improving future projections and devising adaptation policies. Past abrupt climate change events such as the Dansgaard-Oeschger (DO) cycles may provide relevant insights regarding the dynamics of the climate system under this type of climate change. Here we present a paleoceanographic reconstruction off NE Brazil based on geochemical analyses (stable oxygen isotopes, Mg/Ca and Ba/Ca) performed in planktonic foraminifera, that focus on DO stadials of Marine Isotope Stage 5 (MIS5, 130–71 ka). Our new Ba/Ca record shows increases in fluvial discharge linked to enhanced continental precipitation over NE Brazil during DO stadials of MIS5. Tropical precipitation patterns were altered with enhanced rainfall in NE Brazil during DO stadials as a consequence of a southward displacement of the Intertropical Convergence Zone, which, in turn, was likely a response to changes in ocean heat transport and sea ice cover, as highlighted by recent climate model simulations. The results presented here provide useful information on how abrupt climate change can impact tropical rainfall, which is crucial for tropical societies in order to delineate strategies to cope with future climate change.

Keywords: intertropical convergence zone, last interglacial, Dansgaard-Oeschger cycles, northeastern Brazil, sea surface temperature

OPEN ACCESS

Edited by:
David K. Wright,
University of Oslo, Norway

Reviewed by:
Peter Hopcroft,
University of Birmingham, United Kingdom
Guillaume Leduc,
UMR7330 Centre Européen de Recherche et d'enseignement de Géosciences de l'environnement (CEREGE), France

****Correspondence:***
Igor M. Venancio
imartins@uni-bremen.de

Specialty section:
This article was submitted to Quaternary Science, Geomorphology and Paleoenvironment, a section of the journal Frontiers in Earth Science

Received: *01 December 2021*
Accepted: *14 January 2022*
Published: *16 February 2022*

Citation:
Venancio IM, Nascimento RA, Santos TP, Belem AL, Lessa DO, Tiedemann R, Chiessi CM, Mulitza S and Albuquerque ALS (2022) Tropical South American Rainfall Response to Dansgaard-Oeschger Stadials of Marine Isotope Stage 5. Front. Earth Sci. 10:826993. doi: 10.3389/feart.2022.826993

INTRODUCTION

In the tropics, human populations are highly reliant on rainfall for socioeconomic development. Thus, appropriately projecting the response of tropical precipitation to future climate is crucial since it can have widespread socioeconomic impacts, especially in semiarid regions where water resources are scarce. The semiarid region of northeastern (NE) Brazil is one of the most vulnerable regions to climate change, and global and regional climate simulations suggest that this region will be impacted

by rainfall deficit by the end of the century (Marengo et al., 2017). Despite the importance of this topic, the projection of future tropical rainfall by numerical models is still challenging and requires improvement (Long et al., 2016). Tropical rainfall is mainly localized in a narrow band of deep convective clouds around the Equator known as the Intertropical Convergence Zone (ITCZ). It is paramount for model projections that the dynamics of ITCZ and its response to climate change is better constrained, since tropical rainfall is strongly controlled by its latitudinal migrations (Li and Xie, 2014). Thus, reconstructing precipitation changes during past abrupt climate events creates a deeper understanding on the response of the ITCZ to climate change, helping in the assessment of future impacts (McGee et al., 2014).

Dansgaard-Oeschger (DO) cycles can provide important insights regarding the response of the ITCZ to abrupt climate change (Zhang et al., 2017). DO cycles are characterized by an initial fast warming (interstadial) followed by a gradual cooling with an abrupt cooling at the end (stadial), as described by reconstructions from the high latitudes of the Northern Hemisphere (Wolff et al., 2010). Multiple triggers have been potentially linked to the occurrence of DO cycles such as changes in strength of the Atlantic meridional overturning circulation (AMOC) (Henry et al., 2016), sea ice dynamics (Li et al., 2010; Dokken et al., 2013), solar forcing (Braun et al., 2008), and even volcanism (Bay et al., 2004). Differences between DO cycles that occurred during Marine Isotope Stage 3 (MIS3) and Marine Isotope Stage 5 (MIS5) are also noteworthy. During MIS5, DO cycles lasted longer and the background climate conditions were different from MIS3, since global temperature was higher, the westerlies exhibited a more southerly position and AMOC was more stable (Buizert and Schmittner, 2015; Santos et al., 2020). These different climate backgrounds may have produced distinct responses in the tropics during MIS5, which still need to be more investigated in the literature, especially considering that abrupt events that occurred in past interglacials have the potential to occur in future warmer climates.

In the tropics, impacts of the DO cycles in rainfall patterns due to changes in the position of the ITCZ have been reported by several studies (Peterson et al., 2000; Itambi et al., 2009; Deplazes et al., 2013; Zhang et al., 2017). Weldeab et al. (2007) showed the impact of DO cycles in the West African Monsoon for the last 155 kyr, showing millennial-scale fluctuations in riverine freshwater input during the DO cycles of MIS5. However, the lack of appropriate records from the western margin of the equatorial Atlantic hinders the assessment of the hydrological impact of DO cycles of MIS5 to NE Brazilian precipitation.

In order to address this issue, we present new high-resolution stable oxygen isotopes ($\delta^{18}O$), Mg/Ca and Ba/Ca from planktonic foraminifera to reconstruct past changes in surface hydrography and in riverine discharge to the western equatorial Atlantic with focus on the DO cycles of MIS5. Our data show increases in fluvial discharge off NE Brazil linked to enhanced continental precipitation during DO stadials of MIS5. These results also allowed us to investigate the most probable factors responsible for such climate fluctuations.

REGIONAL SETTING

Marine sediment core GL-1248 (0°55.2′S, 43°24.1′W, 2264 m water depth) was collected in the western equatorial Atlantic (**Figure 1**). The upper ocean circulation in this region is mainly influenced by the northward-flowing North Brazil Current (NBC), which originates from the bifurcation of the South Equatorial Current (SEC) around 10°S (Peterson and Stramma, 1991; Stramma and England, 1999). In the upper-ocean (<100 m), the NBC transports Tropical Water (TW), which is a warm (>20°C) and saline (>36 psu) water mass (Stramma and England, 1999).

Seasonal changes in the trade wind system drive the variability of the NBC transport (Stramma et al., 1995). During austral summer and fall the ITCZ relocates southward, and the northeast (NE) trade winds strengthen (Hastenrath and Merle, 1987). This shifts the SEC bifurcation northward and weakens the NBC (Rodrigues et al., 2007). At the same time rainfall over northeastern Brazil increases, peaking from March to April. During austral winter and spring, the southeast (SE) trade winds strengthen and the ITCZ mean position is displaced northward, consequently decreasing precipitation over NE Brazil (Hastenrath and Merle, 1987).

The Parnaíba River is the main river discharging nearby our core site, and consequently the dominant source of fluvial waters and sediments to our study area under modern and past conditions (**Figure 1**) (e.g., Zhang et al., 2015; Sousa et al., 2021). Its main course has a length of approximately 1,400 km (Ramos et al., 2014), while the modern Parnaíba drainage basin area is approximately 344,000 km^2 (Marques et al., 2004), the latitudinal range covered by the Parnaíba basin is approximately 2–10°S.

MATERIALS AND METHODS

The age model of core GL-1248 is based on 12 AMS radiocarbon ages and the alignment of the Ti/Ca record of core GL-1248 to the ice $\delta^{18}O$ record of the North Greenland Ice Core Project (NGRIP) using the extended Greenland Ice Core Chronology (GICC05modelext) (Andersen et al., 2004; Wolff et al., 2010). Between 6.30 and 16.66 m core depth, the chronology of core GL-1248 was derived from the alignment of the Ti/Ca record of the core with NGRIP $\delta^{18}O$ (**Supplementary Figure S1**). Ti/Ca fluctuations of core GL-1248 were matched with the major changes in $\delta^{18}O$ from the NGRIP record, with tie-points being mostly located at the midpoint of abrupt excursions on both records. In addition, the onset of the Last Interglacial was defined by aligning the Ti/Ca record of core GL-1248 with the Antarctic methane record from EPICA Dome C (Loulergue et al., 2008) at approximately 129 ka on the AICC2012 time scale (Veres et al., 2013), similarly to previous studies (e.g., Govin et al., 2015). The complete age model was constructed using linear interpolation with the software clam 2.2 (Blaauw, 2010), where we used the median values of the calibrated age distributions (**Supplementary Figure S2**). The age model was supported by the U/Th-dated growth intervals of Brazilian speleothems during stadials (Wang

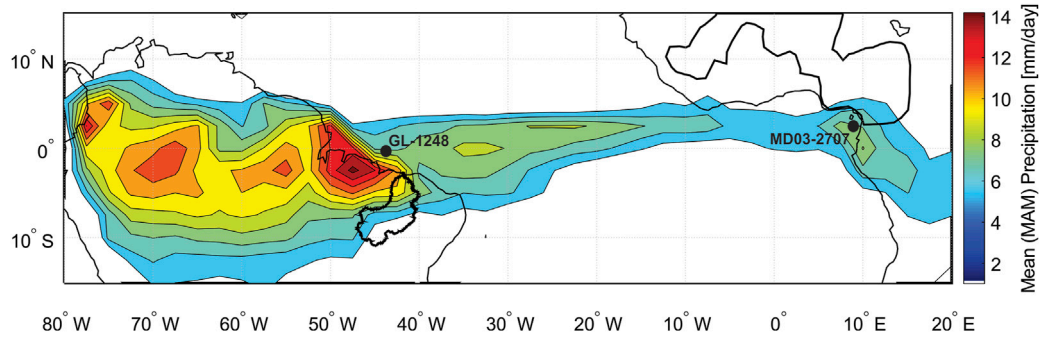

FIGURE 1 | Location of sediment cores GL-1248 (black dot) and core MD03-2707 (Weldeab et al., 2007) (black dot). Color-scale exhibits the mean precipitation (mm/day) between March and May extracted from GPCP dataset stored at NOAA/ESRL PSD (Adler et al., 2003) version 2.3. The Parnaíba River Basin and Sanaga/Niger River Basin (black contours) are displayed in the map.

et al., 2004). Since these growth intervals correspond to wet periods in northeastern Brazil, they should be coeval to the Ti/Ca peaks in our record. Radiocarbon ages and tie-points for core GL-1248 with their respective errors are summarized in **Supplementary Table S1**. Further details of the age model of core GL-1248 are described in Venancio et al. (2018).

Ten tests of *Globigerinoides ruber* (white) (250–355 μm) from core GL-1248 were analyzed for $\delta^{18}O$. All tests were handpicked under a binocular microscope. Oxygen isotope analyses were performed with a Finnigan MAT 252 mass spectrometer equipped with an automated carbonate preparation device Kiel III at MARUM, University of Bremen (Germany). Isotopic results were calibrated relative to the Vienna Pee Dee Belemnite (VPDB) using the NBS19. The standard deviation of the laboratory standard was lower than 0.07‰ for the measuring period. These results were previously reported in Venancio et al. (2018).

Mg/Ca and Ba/Ca were also analyzed in planktonic foraminifera *G. ruber* (white). For core GL-1248, Mg/Ca and Ba/Ca analyses were performed on samples comprising 30 shells of *G. ruber* (white, 250–300 μm). Samples were gently crushed and cleaned following the procedure described by Barker et al. (2003). Before dilution, samples were centrifuged for 10 min to exclude any remaining insoluble particles from the analyses (Groeneveld and Chiessi, 2011). The diluted solutions were analyzed with an ICP-OES Agilent Technologies 700 Series with an autosampler (ASX-520 Cetac) and a micro-nebulizer at MARUM. Each Mg/Ca and Ba/Ca value is averaged from three replicate runs. After every five samples one of two laboratory standards was measured to estimate the external reproducibility. Elements were measured at the following spectral lines: Mg (279.553 nm), Ca (315.887 nm), Ba (455.403 nm), Al (167.019 nm) and Fe (238.204 nm). The calibration series concentration for Ca ranged from 5 to 80 ppm. Each set of samples comprised four or five different dilutions, plus one blank. Only samples with Al/Ca <0.5 mmol/mol were used. Contamination was also monitored by analyzing the Fe/Ca ratios. The Fe/Ca ratio was higher than the cut off value (0.1 mmol/mol) proposed by Barker et al. (2003). However, no correlation was found between Ba/Ca and Mg/Ca on the one hand with Fe/Ca and Al/Ca (R^2 < 0.1) on the other hand (**Supplementary Figure S3**), providing no evidence for a link between the concentration of potential contamination-indicator elements (Fe and Al) and paleoenvironmental-indicator ratios (Mg/Ca and Ba/Ca). The Mg/Ca results were converted to temperatures using the Mg/Ca temperature equation of Gray and Evans (2019) for *G. ruber* (white). This equation iteratively corrects for seawater salinity and carbonate chemistry effects and we followed the method that uses pCO_2 to estimate seawater pH (Gray and Evans, 2019). Results of the Mg/Ca ratios and the SST estimations with their standard deviations are provided in the supplementary material.

The $\delta^{18}O$ of seawater ($\delta^{18}O_{sw}$) was estimated using Mg/Ca-SST and $\delta^{18}O$ from *G. ruber* (white) and by applying the paleotemperature equation of Mulitza et al. (2003). A conversion constant of 0.27‰ was applied to convert the values from VPDB to Vienna Standard Mean Ocean Water (VSMOW) (Hut, 1987). The effect of changes in global sea level was subtracted from the $\delta^{18}O_{sw}$ by considering the sea level reconstruction of Grant et al. (2012) and a glacial $\delta^{18}O$ increase of 0.008‰ m^{-1} sea level lowering (Schrag et al., 2002) to estimate an ice-volume corrected $\delta^{18}O_{sw}$ ($\delta^{18}O_{sw\text{-}ivc}$). $\delta^{18}O_{sw}$ estimation takes into account an uncertainty of 1.34°C for the Mg/Ca-SST estimations using the equation of Gray and Evans (2019), which is equivalent to 0.30‰ $\delta^{18}O$ change (Mulitza et al., 2003) and an analytical error for $\delta^{18}O$ of 0.07‰. Hence, the propagated error estimated for the $\delta^{18}O_{sw}$ is ±0.32‰. The $\delta^{18}O_{sw}$ results are provided in the supplementary material.

RESULTS

The $\delta^{18}O$ of *G. ruber* (white) ranged between −1.71 and −0.13‰ during MIS5 (**Figure 2B**). *G. ruber* (white) $\delta^{18}O$ values show marked millennial-scale increases (up to 0.6‰), which can be linked to the main DO stadials of MIS5 (**Figures 2A,B**). *G. ruber* (white) Mg/Ca values ranged from 3.36 to 4.77 mmol/mol, which is equivalent to SST estimates of 22.48–27.79°C (**Figure 2C**). In contrast with the $\delta^{18}O$ values, the Mg/Ca of *G. ruber* (white) do not exhibit a well-marked millennial-scale pattern during MIS5. The Ba/Ca values ranged from 1.25 to 4.86 μmol/mol

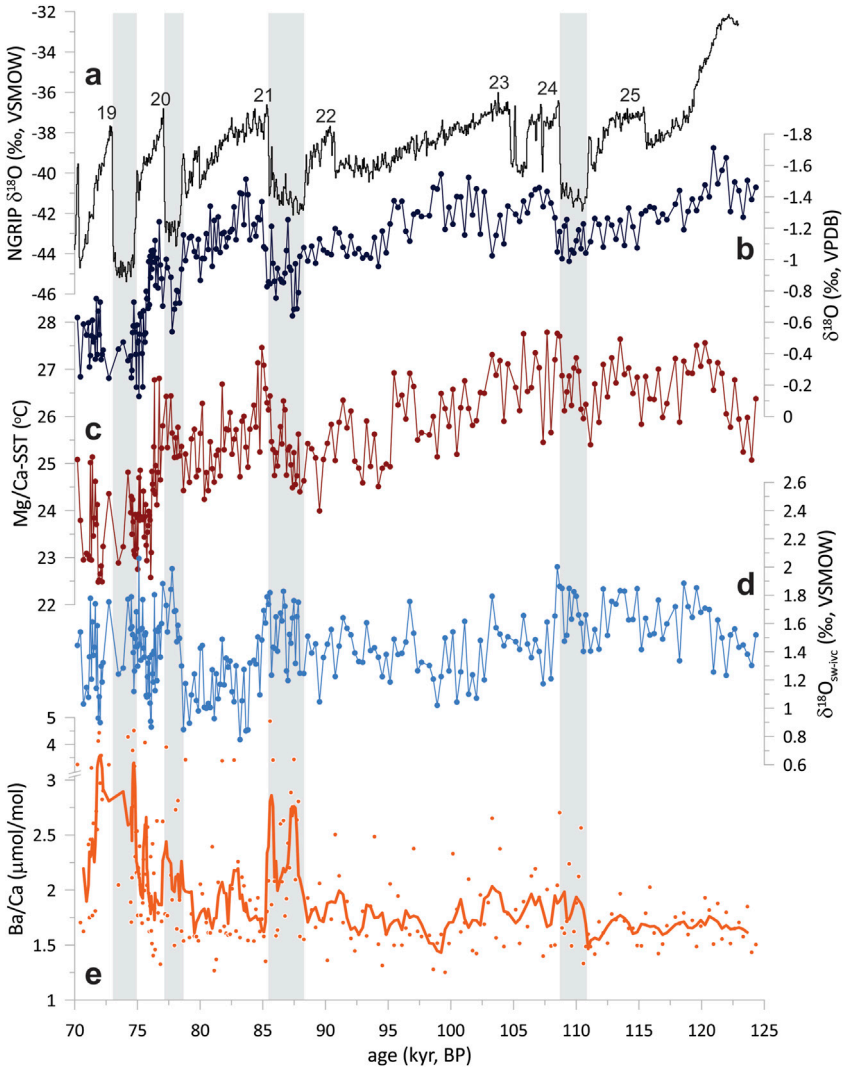

FIGURE 2 | Geochemical results from core GL-1248 compared to North Greenland Ice Core Project (NGRIP) ice stable oxygen isotope record ($\delta^{18}O_{ice}$). **(A)** $\delta^{18}O_{ice}$ from NGRIP on the GICC05modelext time scale (Andersen e al., 2004; Wolff et al., 2010; black line). **(B)** $\delta^{18}O$ of *Globigerinoides ruber* (white) from core GL-1248 (blue line). **(C)** Sea surface temperature (SST) derived from Mg/Ca of *Globigerinoides ruber* (white) from core GL-1248 (red line). **(D)** ice volume corrected $\delta^{18}O$ of seawater ($\delta^{18}O_{sw\text{-}ivc}$) of *Globigerinoides ruber* (white) from core GL-1248 (light blue line). **(E)** Ba/Ca ratios of *Globigerinoides ruber* (white) from core GL-1248 (orange line). Ba/Ca results are shown as 5-point running-average of the data points. Dansgaard-Oeschger (DO) stadials are marked by the grey bars, and the number of the DO cycles is exhibited in panel a.

(**Figure 2D**). Despite the more scattered data, Ba/Ca of *G. ruber* (white) values show millennial-scale increases (up to 3.3 µmol/mol) during most of the DO stadials of MIS5 (**Figure 2D**). The $\delta^{18}O_{sw\text{-}ivc}$ exhibited values ranging from 0.78 to 2.06‰ and similarly to the $\delta^{18}O$ values showed a well-marked millennial-scale pattern during MIS5 (**Figure 2E**), with increases in $\delta^{18}O_{sw\text{-}ivc}$ values (up to 1.2‰) during DO stadials. Besides the millennial-scale variations across MIS5, our results show a marked increase (decrease) in mean values of $\delta^{18}O$ (Mg/Ca-SST) of *G. ruber* (white) at 76 ka. Mean values of $\delta^{18}O$ and Mg/Ca-SST of *G. ruber* (white) subsequent to 76 ka were -0.51‰ and 23.66°C, respectively. Prior to 76 ka the $\delta^{18}O$ and Mg/Ca-SST of *G. ruber* (white) were −1.15‰ and 25.86°C, respectively.

DISCUSSION

Tropical MIS5 millennial-scale changes in sea surface salinity (SSS) linked to variations in riverine runoff were previously reported for the Gulf of Guinea (Weldeab et al., 2007). The authors showed well-marked decreases in Ba/Ca and increases in $\delta^{18}O_{sw}$ records from core MD03-2707 during DO stadials of MIS5, both proxies suggesting increase in SSS (**Figures 3D,E**). Their results indicate a reduction in precipitation over the catchments of the Niger and Sanaga rivers (3–25°N) during the DO stadials of MIS5, which was linked to reduced West African monsoonal rainfall (Weldeab et al., 2007). A comparison between our Ba/Ca record from GL-1248 with the Ba/Ca from

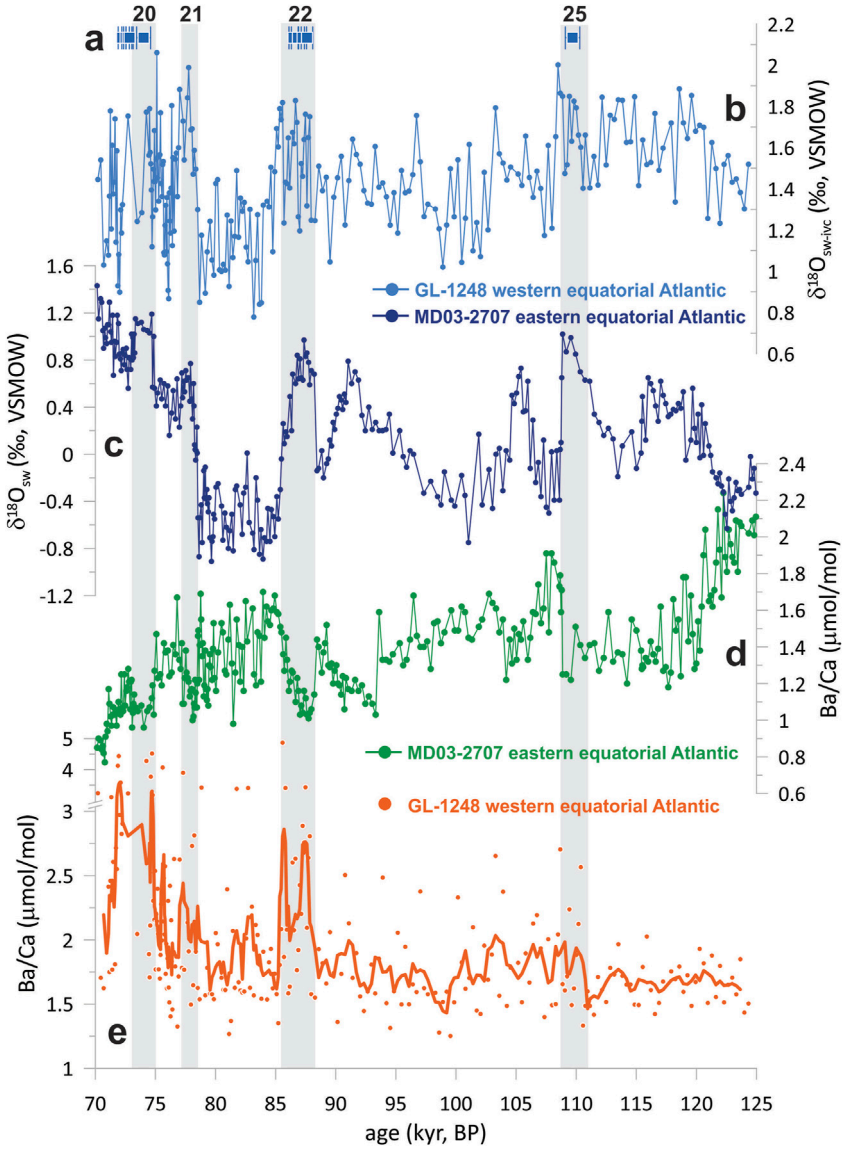

FIGURE 3 | Comparison of hydrological changes between eastern and western equatorial Atlantic. **(A)** Growth intervals of speleothem and travertine from northeastern Brazil with their respective dating errors (Wang et al., 2004, blue squares). **(B)** $\delta^{18}O_{sw\text{-}ivc}$ of *Globigerinoides ruber* (white) from core GL-1248 (light blue line). **(C)** $\delta^{18}O_{sw}$ of *Globigerinoides ruber* (pink) from core MD03-2707 (dark blue line, Weldeab et al., 2007). **(D)** Ba/Ca ratios of *Globigerinoides ruber* (pink) from core MD03-2707 (green line, Weldeab et al., 2007). **(E)** Ba/Ca ratios of *Globigerinoides ruber* (white) from core GL-1248 (orange line). Ba/Ca results are shown as 5-point running-average of the data points. Dansgaard-Oeschger stadials are marked by the grey bars.

core MD03-2707 (**Figure 3**) shows an opposite pattern of both records during DO stadials of MIS5, with core GL-1248 showing increases in Ba/Ca while core MD03-2707 shows decrease in Ba/Ca values. However, the $\delta^{18}O_{sw}$ record from core GL-1248 (**Figure 3**) shows increased values during DO stadials, similarly to the record of core MD03-2707.

The increases in Ba/Ca in core GL-1248 indicate enhanced riverine runoff during DO stadials of MIS5 (**Figure 3**). This suggestion agrees with data from Wang et al. (2004), which shows speleothem growth phases linked to high rainfall periods over northeastern Brazil (**Figure 3**). Thus, the enhanced runoff during DO stadials was probably due to enhanced continental precipitation over the Parnaiba catchment area. Fe/K and Fe/Ca ratios records from core GL-1248, as well as from a nearby core (CDH-86; Nace et al., 2014), confirm the occurrence of intense chemical weathering and terrestrial input, respectively (Fadina et al., 2019; Sousa et al., 2021; Piacsek et al., 2021) (**Supplementary Figure S4**). Concomitantly, Ti/Ca values from core MD99-2198 (Tobago Basin), as molybdenum (Mo) values from core MD03-2622 (Cariaco Basin), decrease during DO stadials, indicating a reduction in terrigenous contribution at those locations (Zhuravleva et al., 2021; Gibson and Peterson, 2014). The observed increases in $\delta^{18}O_{sw}$ in GL-1248 (**Figure 3**) were probably caused by distinct ocean-atmosphere processes

that influenced the $\delta^{18}O_{sw}$ signal, but not the Ba/Ca values. Bahr et al. (2013) explained this divergence between the Ba/Ca and $\delta^{18}O_{sw}$ by showing that these proxies have different mixing behaviors, it is conservative for $\delta^{18}O_{sw}$ and non-linear for Ba/Ca. This means that the signal of $\delta^{18}O_{sw}$ is more affected by the conservative mixing of different water end-members (e.g. freshwater or ocean water masses), while Ba can be removed or added into water by geochemical processes during mixing. For example, removal of adsorbed Ba by ion exchange during mixing of river and marine waters can introduce dissolved Ba into seawater (Hanor and Chan, 1977). Using core-top samples from the western tropical Atlantic, Bahr et al. (2013) showed that high Ba/Ca ratios in foraminiferal calcite can be recorded without any change in the $\delta^{18}O_{sw}$.

The intriguing divergence between Ba/Ca and $\delta^{18}O_{sw}$ signals in the western tropical Atlantic during MIS5 was also observed for the last termination. Venancio et al. (2020) showed that Ba/Ca of core GL-1248 increased during the Younger Dryas (YD), while several $\delta^{18}O_{sw}$ records for the western tropical Atlantic showed increases or no clear changes in the values, with the exception of the record from core CDH-86 (Nace et al., 2014) that showed a decrease in $\delta^{18}O_{sw}$ during the YD. The increases in $\delta^{18}O_{sw}$ in the western tropical Atlantic were attributed to a reduction of the cross-equatorial transport of saline waters due to a weakening of the NBC linked to slowdowns of the AMOC during the YD (Weldeab et al., 2006; Venancio et al., 2020). The results from our study and previous published works (Bahr et al., 2013; Venancio et al., 2020) show that Ba/Ca is a reliable proxy to track past changes fluvial discharge. $\delta^{18}O_{sw}$ gives a signal that is the result of freshwater discharge and ocean-atmosphere processes. The enhanced freshwater discharge during DO stadials of MIS5, as revealed by the Ba/Ca record, should have been translated into a decrease in $\delta^{18}O_{sw}$ at our site. However, we observe increases in $\delta^{18}O_{sw}$, which is probably due to oceanic processes that are driving the signal in an opposite direction. The most plausible explanation is that salinity increased off northeastern Brazil during DO stadials of MIS5 as a result of salt accumulation due to the weakening of the NBC, which is a coherent scenario considering slowdowns of the AMOC during these stadials (Böhm et al., 2015) and the coupling between AMOC and NBC dynamics (Weldeab et al., 2006). This explains the increases in $\delta^{18}O_{sw}$ in core GL-1248 during DO stadials of MIS5, and shows that freshwater discharge influence was surpassed by oceanic processes, which were recorded in the $\delta^{18}O_{sw}$ record at our site.

The antiphase rainfall responses to DO stadials of MIS5 between West Africa and northeastern Brazil suggests a common climatic mechanism. Since precipitation in both regions are influenced by the dynamics of the ITCZ, it is plausible that changes in ITCZ position caused changes in continental precipitation over the Parnaiba and Sanaga/Niger basins. Southward shifts of the ITCZ have been reported to occur during DO stadials, impacting rainfall patterns over the Cariaco Basin (Peterson et al., 2000; Deplazes et al., 2013; Gibson and Peterson, 2014), Tobago Basin (Zhuravleva et al., 2021), northeastern Brazil (Jaeschke et al., 2007; Zhang et al., 2017) and West Africa (Tjallingii et al., 2008; Itambi et al., 2009). Regarding the DO stadials of MIS5, the regional picture that emerges for tropical South America is a reduction in precipitation and runoff in Cariaco and Tobago Basins (Gibson and Peterson, 2014; Zhuravleva et al., 2021), with a concomitantly enhanced rainfall and fluvial discharge off northeastern Brazil, as shown by this study. Moreover, particularly in these regions located in South America, as in West Africa, local rainfall correlates with zonal mean ITCZ changes (Roberts et al., 2017) and might be used to evaluate large scale patterns of tropical rainfall. However, the main climatic forcing driving tropical rainfall changes linked to ITCZ shifts during DO cycles, especially during MIS5, remains elusive.

Wang et al. (2004) observed a strong correlation between speleothem growth phases and high austral autumn insolation at 10°S. This led the authors to conclude that additionally to the response of the ITCZ to the thermal bipolar seesaw (Crowley, 1992; Stocker and Johnsen, 2003), enhanced rainfall over northeastern Brazil was related to southward shifts of the ITCZ due to increased land/sea thermal contrast modulated by precessional forcing. However, although the precessional mechanism explains the enhanced rainfall during DO stadials 25 and 22, it does not explain DO stadials 21 and 20. During DO stadials 21 and 20, high Ba/Ca values off northeastern Brazil and low Ba/Ca off West Africa are observed (**Figures 3**, **4**). Thus, although precessional forcing may have modulated tropical rainfall related to the ITCZ dynamics during the past (e.g., Nascimento et al., 2021), it cannot be the sole factor that explains these proxy records during DO stadials of MIS5.

Utida et al. (2019) suggested that past ITCZ shifts were modulated by tropical South Atlantic (TSA) SST, where positive TSA-SST anomalies led to southward displacements of the annual-mean position of the ITCZ and enhanced precipitation over northeastern Brazil. This is consistent with previous interpretations which suggested a major role of the tropical forcing over ITCZ excursions (e.g., Xie and Carton, 2004). However, TSA-SST records from cores GL-1248 and MD03-2707 do not show well-marked increases during DO stadials (**Figure 4**). This indicates that TSA-SST probably played a secondary role regarding southward displacements of the annual-mean position of the ITCZ during DO stadials of MIS5. Thus, it is plausible to assume that extratropical forcing might be the dominant factor linked to ITCZ shifts, in line with recent studies (Schneider et al., 2014; Seo et al., 2014; Mulitza et al., 2017; Kang et al., 2018; Kang, 2020).

Recently, the study of Santos et al. (2020) suggested that the subtropical South Atlantic acted as a heat reservoir in periods of weakened AMOC during DO stadials of MIS 5. By using geochemical analyses performed in foraminifera recording the permanent thermocline from the western South Atlantic, the authors showed subsurface temperature and salinity increases during these events, which may also hold for the sea surface but can be hampered by local ocean-atmosphere feedbacks (Venancio et al., 2020). Such heat accumulation in the subtropics due to a weakened AMOC probably influenced the Hadley cell circulation and contributed to a southward ITCZ displacement (Frierson et al., 2013; Mulitza et al., 2017). Warming of one hemisphere leads to an ITCZ shift in order to balance the oceanic heating via cross-equatorial atmospheric energy transport (Donohoe et al., 2013; Marshall et al., 2014).

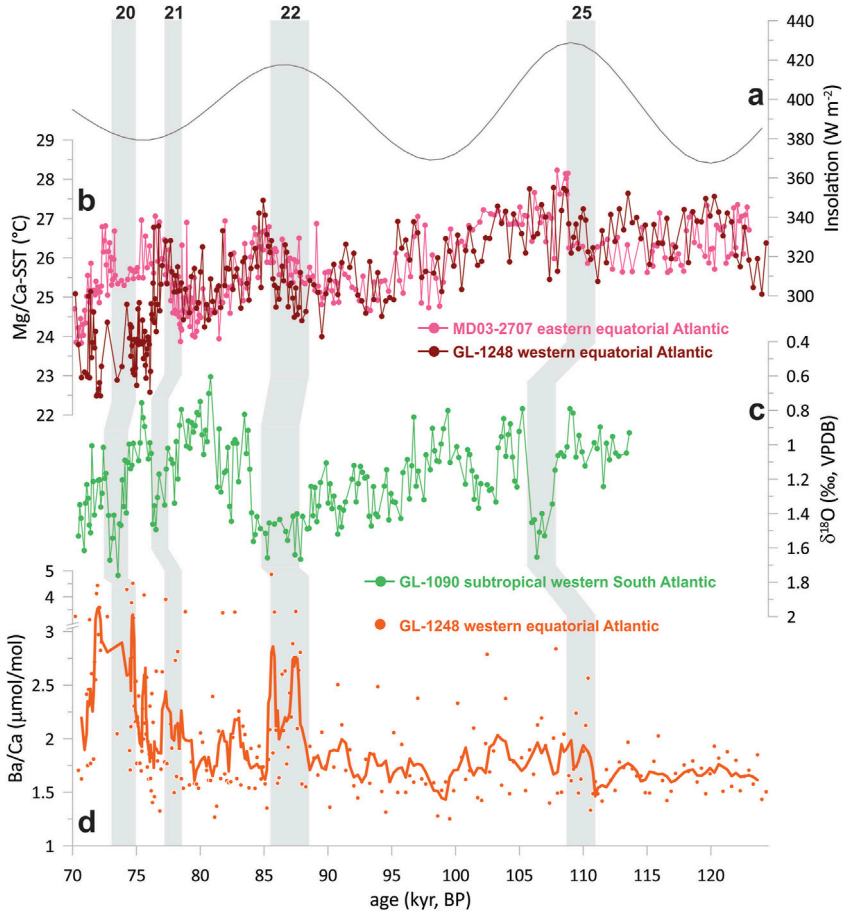

FIGURE 4 | Climatic forcings related to the tropical climate response to Dansgaard-Oeschger stadials. **(A)** Austral autumn insolation at 10°S (grey line, Berger and Loutre, 1991). **(B)** Sea surface temperature (SST) derived from Mg/Ca of *Globigerinoides ruber* (white) from core GL-1248 (red line) and from Mg/Ca of *Globigerinoides ruber* (pink) from core MD03-2707 (pink line). **(C)** $\delta^{18}O$ of *Globorotalia inflata* from core GL-1090 (light green line, Santos et al., 2020). **(D)** Ba/Ca ratios of *Globigerinoides ruber* (white) from core GL-1248 (orange line). Ba/Ca results are shown as running-average of the data points. Dansgaard-Oeschger stadials are marked by the grey bars.

Such ITCZ responses to cross-equatorial energy transport linked to AMOC changes were highlighted as the main factor that determines the magnitude of ITCZ shifts, especially if hemispherically asymmetric solar forcing is concentrated at higher latitudes (Yu and Pritchard, 2019). Except for DO stadial 25, periods with high Ba/Ca in core GL-1248 seem to coincide with the observed changes in South Atlantic subtropical heat content, exemplified by permanent thermocline $\delta^{18}O$ from core GL-1090 (**Figure 4**) (Santos et al., 2020). This indicates that such atmospheric adjustments due to variations in ocean heat transport contributes to the understanding of past changes in tropical precipitation.

Climate model simulations show that sea ice cover may also influence the position of the ITCZ (Chiang and Bitz, 2005). Advances in Northern Hemisphere sea ice cause cooling in high northern latitudes, which propagates towards the equator via ocean-atmosphere feedbacks and results in a southward shift of the ITCZ (Chiang and Bitz, 2005). Changes in Northern Hemisphere sea ice are also viewed as one of the main mechanisms linked to DO cycles (Li et al., 2010; Dokken et al., 2013). Thus, the southward displacements of ITCZ during DO stadials of MIS5 revealed by our proxy records may be caused by southward expansion of sea ice in high northern latitudes. Indeed, Rama-Corredor et al. (2015) show abrupt decreases in tropical North Atlantic SST during DO stadials of MIS5 as a consequence of rapid transmission of climate signals from high to low latitudes. This is also corroborated by the results from Deplazes et al. (2013), which show that the ITCZ system responds primarily to changes in Northern Hemisphere temperatures.

The SST reconstruction from core GL-1248, together with other tropical SST records, discarded a major role of TSA-SST as a trigger of rainfall changes during DO stadials of MIS5. Also, autumn insolation cannot be the sole factor controlling ITCZ displacements during MIS5, since our Ba/Ca record and XRF data for core GL-1248 do not display a precessional pace, and autumn insolation was low during DO stadials 21 and 20, while Ba/Ca exhibited high values. Therefore, our results indicate that

extratropical forcing related mainly to interhemispheric ocean heat transport and sea ice cover is probably the key factor influencing tropical rainfall changes due to ITCZ shifts during DO cycles of MIS5. Both processes impact ocean thermal gradients, which may be the main cause of the ITCZ displacements. This is in line with climate model simulations showing that tropical rainfall cannot be explained only by ocean heat transport or changes in sea ice extent (Roberts and Hopcroft, 2020). It is most probable that a combination of both factors is important in order to promote North Atlantic SST changes and consequently influence ITCZ position (Roberts and Hopcroft, 2020). Thus, tropical rainfall changes during DO stadials of MIS5 were mainly the result of meridional displacements of the ITCZ position due to extratropical perturbations. This might have been caused by ocean-atmosphere feedbacks (Chiang and Bitz, 2005) and/or changes in the energy budget (Marshall et al., 2014).

CONCLUSION

We reconstructed ocean surface conditions of the western equatorial Atlantic based on the $\delta^{18}O$, Mg/Ca and Ba/Ca ratios of planktonic foraminifera *G. ruber* (white) in order to investigate ocean-atmosphere changes during the DO stadials of MIS5. Our Ba/Ca record shows higher fluvial discharge during DO stadials, indicating enhanced rainfall over northeastern Brazil. The comparison with a Ba/Ca record from the eastern tropical Atlantic revealed opposite trends in rainfall between the West African monsoon domain and northern northeastern Brazil during DO stadials of MIS5. These opposite trends were probably caused by fluctuations in the latitudinal position of the ITCZ. We suggest that the main causes for these ITCZ displacements are changes in ocean heat transport and Northern Hemisphere sea ice cover. Our interpretations are in line with recent climate model simulations, which suggest that both factors influence the position of the ITCZ and tropical rainfall during abrupt climate events. In this sense, future changes in the meridional overturning circulation and sea ice cover, which are likely to occur under global warming, will probably alter tropical rainfall patterns, with major consequences to tropical societies. Our results provide an in-depth understanding of the dynamics of the climate system during abrupt climate change events, and highlight the need to improve strategies for mitigation and adaptation to future climate change, especially in semiarid regions which present high vulnerability to changes in the hydrological cycle.

DATA AVAILABILITY STATEMENT

The datasets presented in this study can be found in online repositories. The names of the repository/repositories and accession number(s) can be found below: Mendeley Data (http://dx.doi.org/10.17632/xdrpswbhnh.2).

AUTHOR CONTRIBUTIONS

IV designed the study, analyzed the data and wrote the manuscript with contribution from all authors. All authors contributed to the interpretation of results. All authors commented on and edited the manuscript.

FUNDING

This study was supported by the CAPES-ASpECTO project (grant 88887.091731/2014-01) CNPq-Aspecto (grant 429767/2018-8), CAPES-PRINT CLIMATE Project (grant 88887.310301/2018-00) and CNPq Project RAiN (grant 406322/2018-0). IMV acknowledges the scholarship from CAPES (grant 88881.512929/2020-01) and the Alexander von Humboldt Foundation. RAN acknowledges the scholarship from CAPES (grant 88887.176103/2018-00). CMC acknowledges the financial support from FAPESP (grants 2018/15123-4 and 2019/24349-9), CAPES (grants 564/2015 and 88881.313535/2019–01), CNPq (grant 312458/2020-7), and the Alexander von Humboldt Foundation. ALSA is a senior scholar CNPq (grant 302521/2017-8).

ACKNOWLEDGMENTS

We thank Petrobras for providing the sediment core used in this study. We also acknowledge the partial support from the Coordenação de Aperfeiçoamento de Pessoal de Nível Superior—Brasil (CAPES)—Finance Code 001.

SUPPLEMENTARY MATERIAL

The Supplementary Material for this article can be found online at: https://www.frontiersin.org/articles/10.3389/feart.2022.826993/full#supplementary-material

REFERENCES

Adler, R. F., Huffman, G. J., Chang, A., Ferraro, R., Xie, P.-P., Janowiak, J., et al. (2003). The Version-2 Global Precipitation Climatology Project (GPCP) Monthly Precipitation Analysis (1979–Present). *J. Hydrometeorol.* 4, 1147–1167. doi:10.1175/1525-7541(2003)004<1147:TVGPCP>2.0.CO;2

Andersen, K. K., Azuma, N., Barnola, J. M., Bigler, M., Biscaye, P., Caillon, N., et al. (2004). High-resolution Record of Northern Hemisphere Climate Extending into the Last Interglacial Period. *Nature* 431, 147–151. doi:10.1038/nature02805

Bahr, A., Schönfeld, J., Hoffmann, J., Voigt, S., Aurahs, R., Kucera, M., et al. (2013). Comparison of Ba/Ca and δOWATER18 as Freshwater Proxies: A Multi-Species Core-Top Study on Planktonic Foraminifera from the Vicinity of the Orinoco River Mouth. *Earth Planet. Sci. Lett.* 383, 45–57. doi:10.1016/j.epsl.2013.09.036

Barker, S., Greaves, M., and Elderfield, H. (2003). A Study of Cleaning Procedures Used for Foraminiferal Mg/Ca Paleothermometry. *Geochem. Geophys. Geosyst.* 4, a–n. doi:10.1029/2003GC000559

Bay, R. C., Bramall, N., and Price, P. B. (2004). Bipolar Correlation of Volcanism with Millennial Climate Change. *Proc. Natl. Acad. Sci.* 101, 6341–6345. doi:10.1073/pnas.0400323101

Berger, A., and Loutre, M. F. (1991). Insolation Values for the Climate of the Last 10 Million Years. *Quat. Sci. Rev.* 10, 297–317. doi:10.1016/0277-3791(91)90033-Q

Blaauw, M. (2010). Methods and Code for 'Classical' Age-Modelling of Radiocarbon Sequences. *Quat. Geochronol.* 5, 512–518. doi:10.1016/j.quageo.2010.01.002

Böhm, E., Lippold, J., Gutjahr, M., Frank, M., Blaser, P., Antz, B., et al. (2015). Strong and Deep Atlantic Meridional Overturning Circulation during the Last Glacial Cycle. *Nature* 517, 73–76. doi:10.1038/nature14059

Braun, H., Ditlevsen, P., and Chialvo, D. R. (2008). Solar Forced Dansgaard-Oeschger Events and Their Phase Relation with Solar Proxies. *Geophys. Res. Lett.* 35. doi:10.1029/2008GL033414

Buizert, C., and Schmittner, A. (2015). Southern Ocean Control of Glacial AMOC Stability and Dansgaard-Oeschger Interstadial Duration. *Paleoceanography* 30, 1595–1612. doi:10.1002/2015PA002795

Chiang, J. C. H., and Bitz, C. M. (2005). Influence of High Latitude Ice Cover on the marine Intertropical Convergence Zone. *Clim. Dyn.* 25, 477–496. doi:10.1007/s00382-005-0040-5

Crowley, T. J. (1992). North Atlantic Deep Water Cools the Southern Hemisphere. *Paleoceanography* 7, 489–497. doi:10.1029/92PA01058

de Sousa, T. A., Venancio, I. M., Valeriano, C. d. M., Heilbron, M., Weitzel Dias Carneiro, M. T., Mane, M. A., et al. (2021). Changes in Sedimentary Provenance and Climate off the Coast of Northeast Brazil since the Last Interglacial. *Mar. Geology.* 435, 106454. doi:10.1016/j.margeo.2021.106454

Deplazes, G., Lückge, A., Peterson, L. C., Timmermann, A., Hamann, Y., Hughen, K. A., et al. (2013). Links between Tropical Rainfall and North Atlantic Climate during the Last Glacial Period. *Nat. Geosci* 6, 213–217. doi:10.1038/ngeo1712

Dokken, T. M., Nisancioglu, K. H., Li, C., Battisti, D. S., and Kissel, C. (2013). Dansgaard-Oeschger Cycles: Interactions between Ocean and Sea Ice Intrinsic to the Nordic Seas. *Paleoceanography* 28, 491–502. doi:10.1002/palo.20042

Donohoe, A., Marshall, J., Ferreira, D., and Mcgee, D. (2013). The Relationship between ITCZ Location and Cross-Equatorial Atmospheric Heat Transport: From the Seasonal Cycle to the Last Glacial Maximum. *J. Clim.* 26, 3597–3618. doi:10.1175/JCLI-D-12-00467.1

Fadina, O. A., Venancio, I. M., Belem, A., Silveira, C. S., Bertagnolli, D. d. C., Silva-Filho, E. V., et al. (2019). Paleoclimatic Controls on Mercury Deposition in Northeast Brazil since the Last Interglacial. *Quat. Sci. Rev.* 221, 105869. doi:10.1016/j.quascirev.2019.105869

Frierson, D. M. W., Hwang, Y.-T., Fučkar, N. S., Seager, R., Kang, S. M., Donohoe, A., et al. (2013). Contribution of Ocean Overturning Circulation to Tropical Rainfall Peak in the Northern Hemisphere. *Nat. Geosci* 6, 940–944. doi:10.1038/ngeo1987

Gibson, K. A., and Peterson, L. C. (2014). A 0.6 Million Year Record of Millennial-Scale Climate Variability in the Tropics. *Geophys. Res. Lett.* 41, 969–975. doi:10.1002/2013GL058846

Govin, A., Capron, E., Tzedakis, P. C., Verheyden, S., Ghaleb, B., and Hillaire-Marcel, C. (2015). Sequence of Events From the Onset to the Demise of the Last Interglacial: Evaluating Strengths and Limitations of Chronologies used in Climatic Archives. *Quat. Sci. Rev.* 129, 1–36. doi:10.1016/j.quascirev.2015.09.018

Grant, K. M., Rohling, E. J., Bar-Matthews, M., Ayalon, A., Medina-Elizalde, M., Ramsey, C. B., et al. (2012). Rapid Coupling between Ice Volume and Polar Temperature over the Past 150,000 Years. *Nature* 491, 744–747. doi:10.1038/nature11593

Gray, W. R., and Evans, D. (2019). Nonthermal Influences on Mg/Ca in Planktonic Foraminifera: A Review of Culture Studies and Application to the Last Glacial Maximum. *Paleoceanography and Paleoclimatology* 34, 306–315. doi:10.1029/2018PA003517

Groeneveld, J., and Chiessi, C. M. (2011). Mg/Ca ofGloborotalia Inflataas a Recorder of Permanent Thermocline Temperatures in the South Atlantic. *Paleoceanography* 26, a–n. doi:10.1029/2010PA001940

Hanor, J. S., and Chan, L.-H. (1977). Non-conservative Behavior of Barium during Mixing of Mississippi River and Gulf of Mexico Waters. *Earth Planet. Sci. Lett.* 37, 242–250. doi:10.1016/0012-821X(77)90169-8

Hastenrath, S., and Merle, J. (1987). Annual Cycle of Subsurface Thermal Structure in the Tropical Atlantic Ocean. *J. Phys. Oceanogr.* 17, 1518–1538. doi:10.1175/1520-0485(1987)017<1518:acosts>2.0.co;2

Henry, L. G., McManus, J. F., Curry, W. B., Roberts, N. L., Piotrowski, A. M., and Keigwin, L. D. (2016). North Atlantic Ocean Circulation and Abrupt Climate Change during the Last Glaciation. *Science* 353, 470–474. doi:10.1126/science.aaf5529

Hut, G. (1987). "Consultants' Group Meeting on Stable Isotope Reference Samples for Geochemical and Hydrological Investigations," in *Consultants' Group Meeting on Stable Isotope Reference Samples for Geochemical and Hydrological Investigations* (Vienna, Austria: International Atomic Energy Agency). Available from: http://inis.iaea.org/search/search.aspx?orig_q=RN:18075746.

Itambi, A. C., von Dobeneck, T., Mulitza, S., Bickert, T., and Heslop, D. (2009). Millennial-scale Northwest African Droughts Related to Heinrich Events and Dansgaard-Oeschger Cycles: Evidence in marine Sediments from Offshore Senegal. *Paleoceanography* 24, a–n. doi:10.1029/2007PA001570

Jaeschke, A., Rühlemann, C., Arz, H., Heil, G., and Lohmann, G. (2007). Coupling of Millennial-Scale Changes in Sea Surface Temperature and Precipitation off Northeastern Brazil with High-Latitude Climate Shifts during the Last Glacial Period. *Paleoceanography* 22, a–n. doi:10.1029/2006PA001391

Kang, S. M. (2020). Extratropical Influence on the Tropical Rainfall Distribution. *Curr. Clim. Change Rep.* 6, 24–36. doi:10.1007/s40641-020-00154-y

Kang, S. M., Shin, Y., and Xie, S.-P. (2018). Extratropical Forcing and Tropical Rainfall Distribution: Energetics Framework and Ocean Ekman Advection. *Npj Clim. Atmos. Sci.* 1, 20172. doi:10.1038/s41612-017-0004-6

Li, C., Battisti, D. S., and Bitz, C. M. (2010). Can North Atlantic Sea Ice Anomalies Account for Dansgaard-Oeschger Climate Signals. *J. Clim.* 23, 5457–5475. doi:10.1175/2010JCLI3409.1

Li, G., and Xie, S.-P. (2014). Tropical Biases in CMIP5 Multimodel Ensemble: The Excessive Equatorial Pacific Cold Tongue and Double ITCZ Problems*. *J. Clim.* 27, 1765–1780. doi:10.1175/JCLI-D-13-00337.1

Long, S.-M., Xie, S.-P., and Liu, W. (2016). Uncertainty in Tropical Rainfall Projections: Atmospheric Circulation Effect and the Ocean Coupling. *J. Clim.* 29, 2671–2687. doi:10.1175/jcli-d-15-0601.1

Loulergue, L., Schilt, A., Spahni, R., Masson-Delmotte, V., Blunier, T., Lemieux, B., et al. (2008). Orbital and Millennial-Scale Features of Atmospheric CH4 Over the Past 800,000 Year. *Nature* 453, 383–386. doi:10.1038/nature06950

Marengo, J. A., Torres, R. R., and Alves, L. M. (2017). Drought in Northeast Brazil-past, Present, and Future. *Theor. Appl. Climatol.* 129, 1189–1200. doi:10.1007/s00704-016-1840-8

Marques, M., da Costa, M. F., Mayorga, M. I. d. O., and Pinheiro, P. R. C. (2004). Water Environments: Anthropogenic Pressures and Ecosystem Changes in the Atlantic Drainage Basins of Brazil. *AMBIO: A J. Hum. Environ.* 33, 68–77. doi:10.1579/0044-7447-33.1.68

Marshall, J., Donohoe, A., Ferreira, D., and McGee, D. (2014). The Ocean's Role in Setting the Mean Position of the Inter-tropical Convergence Zone. *Clim. Dyn.* 42, 1967–1979. doi:10.1007/s00382-013-1767-z

McGee, D., Donohoe, A., Marshall, J., and Ferreira, D. (2014). Changes in ITCZ Location and Cross-Equatorial Heat Transport at the Last Glacial Maximum, Heinrich Stadial 1, and the Mid-holocene. *Earth Planet. Sci. Lett.* 390, 69–79. doi:10.1016/j.epsl.2013.12.043

Mulitza, S., Boltovskoy, D., Donner, B., Meggers, H., Paul, A., and Wefer, G. (2003). Temperature:δ18O Relationships of Planktonic Foraminifera Collected from Surface Waters. *Palaeogeogr. Palaeoclimatol. Palaeoecol.* 202, 143–152. doi:10.1016/S0031-0182(03)00633-3

Mulitza, S., Chiessi, C. M., Schefuß, E., Lippold, J., Wichmann, D., Antz, B., et al. (2017). Synchronous and Proportional Deglacial Changes in Atlantic Meridional Overturning and Northeast Brazilian Precipitation. *Paleoceanography* 32, 622X–633. doi:10.1002/2017PA003084

Nace, T. E., Baker, P. A., Dwyer, G. S., Silva, C. G., Rigsby, C. A., Burns, S. J., et al. (2014). The Role of North Brazil Current Transport in the Paleoclimate of the Brazilian Nordeste Margin and Paleoceanography of the Western Tropical Atlantic during the Late Quaternary. *Palaeogeogr. Palaeoclimatol. Palaeoecol.* 415, 3–13. doi:10.1016/j.palaeo.2014.05.030

Nascimento, R. A., Venancio, I. M., Chiessi, C. M., Ballalai, J. M., Kuhnert, H., Johnstone, H., et al. (2021). Tropical Atlantic Stratification Response to Late Quaternary Precessional Forcing. *Earth Planet. Sci. Lett.* 568, 117030. doi:10.1016/j.epsl.2021.117030

Peterson, L. C., Haug, G. H., Hughen, K. A., and Röhl, U. (2000). Rapid Changes in the Hydrologic Cycle of the Tropical Atlantic during the Last Glacial. *Science* 290, 1947–1951. doi:10.1126/science.290.5498.1947

Peterson, R. G., and Stramma, L. (1991). Upper-level Circulation in the South Atlantic Ocean. *Prog. Oceanography* 26, 1–73. doi:10.1016/0079-6611(91)90006-8

Piacsek, P., Behling, H., Ballalai, J. M., Nogueira, J., Venancio, I. M., and Albuquerque, A. L. S. (2021). Reconstruction of Vegetation and Low Latitude Ocean-Atmosphere Dynamics of the Past 130 Kyr, Based on South American Montane Pollen Types. *Glob. Planet. Change* 201, 103477. doi:10.1016/j.gloplacha.2021.103477

Rama-Corredor, O., Martrat, B., Grimalt, J. O., López-Otalvaro, G. E., Flores, J. A., and Sierro, F. (2015). Parallelisms between Sea Surface Temperature Changes in the Western Tropical Atlantic (Guiana Basin) and High Latitude Climate Signals over the Last 140 000 Years. *Clim. Past* 11, 1297–1311. doi:10.5194/cp-11-1297-2015

Ramos, T. P. A., Ramos, R. T. d. C., and Ramos, S. A. Q. A. (2014). Ichthyofauna of the Parnaíba River Basin, Northeastern Brazil. *Biota Neotrop.* 14, 1–8. doi:10.1590/s1676-06020140039

Roberts, W. H. G., and Hopcroft, P. O. (2020). Controls on the Tropical Response to Abrupt Climate Changes. *Geophys. Res. Lett.* 47, e2020GL087518. doi:10.1029/2020GL087518

Roberts, W. H. G., Valdes, P. J., and Singarayer, J. S. (2017). Can Energy Fluxes Be Used to Interpret Glacial/interglacial Precipitation Changes in the Tropics. *Geophys. Res. Lett.* 44, 6373–6382. doi:10.1002/2017GL073103

Rodrigues, R. R., Rothstein, L. M., and Wimbush, M. (2007). Seasonal Variability of the South Equatorial Current Bifurcation in the Atlantic Ocean: A Numerical Study. *J. Phys. Oceanogr.* 37, 16–30. doi:10.1175/JPO2983.1

Santos, T. P., Ballalai, J. M., Franco, D. R., Oliveira, R. R., Lessa, D. O., Venancio, I. M., et al. (2020). Asymmetric Response of the Subtropical Western South Atlantic Thermocline to the Dansgaard-Oeschger Events of Marine Isotope Stages 5 and 3. *Quat. Sci. Rev.* 237, 106307. doi:10.1016/j.quascirev.2020.106307

Schneider, T., Bischoff, T., and Haug, G. H. (2014). Migrations and Dynamics of the Intertropical Convergence Zone. *Nature* 513, 45–53. doi:10.1038/nature13636

Schrag, D. P., Adkins, J. F., McIntyre, K., Alexander, J. L., Hodell, D. A., Charles, C. D., et al. (2002). The Oxygen Isotopic Composition of Seawater during the Last Glacial Maximum. *Quat. Sci. Rev.* 21, 331–342. doi:10.1016/S0277-3791(01)00110-X

Seo, J., Kang, S. M., and Frierson, D. M. W. (2014). Sensitivity of Intertropical Convergence Zone Movement to the Latitudinal Position of thermal Forcing. *J. Clim.* 27, 3035–3042. doi:10.1175/JCLI-D-13-00691.1

Stocker, T. F., and Johnsen, S. J. (2003). A Minimum Thermodynamic Model for the Bipolar Seesaw. *Paleoceanography* 18, a–n. doi:10.1029/2003PA000920

Stramma, L., and England, M. (1999). On the Water Masses and Mean Circulation of the South Atlantic Ocean. *J. Geophys. Res.* 104, 20863–20883. doi:10.1029/1999JC900139

Stramma, L., Fischer, J., and Reppin, J. (1995). The North Brazil Undercurrent. *Deep Sea Res. Oceanographic Res. Pap.* 42, 773–795. doi:10.1016/0967-0637(95)00014-W

Tjallingii, R., Claussen, M., Stuut, J.-B. W., Fohlmeister, J., Jahn, A., Bickert, T., et al. (2008). Coherent High- and Low-Latitude Control of the Northwest African Hydrological Balance. *Nat. Geosci* 1, 670–675. doi:10.1038/ngeo289

Utida, G., Cruz, F. W., Etourneau, J., Bouloubassi, I., Schefuß, E., Vuille, M., et al. (2019). Tropical South Atlantic Influence on Northeastern Brazil Precipitation and ITCZ Displacement during the Past 2300 Years. *Sci. Rep.* 9, 1698. doi:10.1038/s41598-018-38003-6

Venancio, I. M., Mulitza, S., Govin, A., Santos, T. P., Lessa, D. O., Albuquerque, A. L. S., et al. (2018). Millennial- to Orbital-Scale Responses of Western Equatorial Atlantic Thermocline Depth to Changes in the Trade Wind System since the Last Interglacial. *Paleoceanography and Paleoclimatology* 33, 1490–1507. doi:10.1029/2018PA003437

Venancio, I. M., Shimizu, M. H., Santos, T. P., Lessa, D. O., Portilho-Ramos, R. C., Chiessi, C. M., et al. (2020). Changes in Surface Hydrography at the Western Tropical Atlantic during the Younger Dryas. *Glob. Planet. Change* 184, 103047. doi:10.1016/j.gloplacha.2019.103047

Veres, D., Bazin, L., Landais, A., Toyé Mahamadou Kele, H., Lemieux-Dudon, B., Parrenin, F., et al. (2013). The Antarctic Ice Core Chronology (AICC2012): An Optimized Multi-Parameter and Multi-Site Dating Approach for the last 120 Thousand Years. *Clim. Past.* 9, 1738–1748. doi:10.5194/cp-9-1733-2013

Wang, X., Auler, A. S., Edwards, R. L., Cheng, H., Cristalli, P. S., Smart, P. L., et al. (2004). Wet Periods in Northeastern Brazil over the Past 210 Kyr Linked to Distant Climate Anomalies. *Nature* 432, 740–743. doi:10.1038/nature03067

Weldeab, S., Schneider, R. R., and Kölling, M. (2006). Deglacial Sea Surface Temperature and Salinity Increase in the Western Tropical Atlantic in Synchrony with High Latitude Climate Instabilities. *Earth Planet. Sci. Lett.* 241, 699–706. doi:10.1016/j.epsl.2005.11.012

Weldeab, S., Lea, D. W., Schneider, R. R., and Andersen, N. (2007). 155,000 Years of West African Monsoon and Ocean Thermal Evolution. *Science* 316, 1303–1307. LP – 1307. doi:10.1126/science.1140461

Wolff, E. W., Chappellaz, J., Blunier, T., Rasmussen, S. O., and Svensson, A. (2010). Millennial-scale Variability during the Last Glacial: The Ice Core Record. *Quat. Sci. Rev.* 29, 2828–2838. doi:10.1016/j.quascirev.2009.10.013

Xie, S.-P., and Carton, J. A. (2004). "Tropical Atlantic Variability: Patterns, Mechanisms, and Impacts," in *Earth's Climate* (American Geophysical Union), 121–142. doi:10.1029/147GM07

Yu, S., and Pritchard, M. S. (2019). A strong Role for the AMOC in Partitioning Global Energy Transport and Shifting ITCZ Position in Response to Latitudinally Discrete Solar Forcing in CESM1.2. *J. Clim.* 32, 2207–2226. doi:10.1175/JCLI-D-18-0360.1

Zhang, Y., Chiessi, C. M., Mulitza, S., Sawakuchi, A. O., Häggi, C., Zabel, M., et al. (2017). Different Precipitation Patterns across Tropical South America during Heinrich and Dansgaard-Oeschger Stadials. *Quat. Sci. Rev.* 177, 1–9. doi:10.1016/j.quascirev.2017.10.012

Zhang, Y., Chiessi, C. M., Mulitza, S., Zabel, M., Trindade, R. I. F., Hollanda, M. H. B. M., et al. (2015). Origin of increased terrigenous supply to the NE South American continental margin during Heinrich Stadial 1 and the Younger Dryas. *Earth Planet. Sci. Lett.* 432, 493–500. doi:10.1016/j.epsl.2015.09.054

Zhuravleva, A., Hüls, M., Tiedemann, R., Bauch, H. A., et al. (2021). A 125-ka Record of Northern South American Precipitation and the Role of High-to-Low Latitude Teleconnections. *Quat. Sci. Rev.* 270, 107159. doi:10.1016/j.quascirev.2021.107159

Conflict of Interest: The authors declare that the research was conducted in the absence of any commercial or financial relationships that could be construed as a potential conflict of interest.

Publisher's Note: All claims expressed in this article are solely those of the authors and do not necessarily represent those of their affiliated organizations, or those of the publisher, the editors, and the reviewers. Any product that may be evaluated in this article, or claim that may be made by its manufacturer, is not guaranteed or endorsed by the publisher.

frontiers in Earth Science

ORIGINAL RESEARCH
published: 23 March 2022
doi: 10.3389/feart.2022.830984

Calcium Carbonate Dissolution Triggered by High Productivity During the Last Glacial–Interglacial Interval in the Deep Western South Atlantic

Jaime Y. Suárez-Ibarra[1,2], Cristiane F. Frozza[1], Pâmela L. Palhano[1], Sandro M. Petró[3], Manuel F. G. Weinkauf[2] and Maria A. G. Pivel[4]*

[1]Programa de Pós-Graduação Em Geociências, Instituto de Geociências, Universidade Federal Do Rio Grande do Sul, Porto Alegre, Brazil, [2]Ústav Geologie a Paleontologie, Přírodovědecká Fakulta, Univerzita Karlova, Prague, Czech Republic, [3]itt OCEANEON, Instituto Tecnológico de Paleoceanografia e Mudanças Climáticas, Universidade Do Vale Do Rio Dos Sinos, São Leopoldo, Brazil, [4]Instituto de Geociências, Universidade Federal do Rio Grande do Sul, Porto Alegre, Brazil

OPEN ACCESS

Edited by:
Jacek Raddatz,
Goethe University Frankfurt, Germany

Reviewed by:
Selvaraj Kandasamy,
Xiamen University, China
Patrick Grunert,
University of Cologne, Germany

***Correspondence:**
Jaime Y. Suárez-Ibarra
jysuarezibarra@gmail.com
suarezij@natur.cuni.cz

Specialty section:
This article was submitted to Quaternary Science, Geomorphology and Paleoenvironment, a section of the journal Frontiers in Earth Science

Received: *07 December 2021*
Accepted: *17 February 2022*
Published: *23 March 2022*

Citation:
Suárez-Ibarra JY, Frozza CF, Palhano PL, Petró SM, Weinkauf MFG and Pivel MAG (2022) Calcium Carbonate Dissolution Triggered by High Productivity During the Last Glacial–Interglacial Interval in the Deep Western South Atlantic. Front. Earth Sci. 10:830984. doi: 10.3389/feart.2022.830984

Studies reconstructing surface paleoproductivity and benthic environmental conditions allow us to measure the effectiveness of the biological pump, an important mechanism in the global climate system. In order to assess surface productivity changes and their effect on the seafloor, we studied the sediment core SAT-048A, spanning 43–5 ka, recovered from the continental slope (1,542 m water depth) of the southernmost Brazilian continental margin, deep western South Atlantic. We assessed the sea surface productivity, the organic matter flux to the seafloor, and calcite dissolution effects, based on micropaleontological (benthic and planktonic foraminifers, ostracods), geochemical (benthic $\delta^{13}C$ isotopes), and sedimentological data (carbonate and bulk sand content). Superimposed on the induced changes related to the last glacial–interglacial transition, the reconstruction indicates a significant and positive correlation between the paleoproductivity proxies and the summer insolation. From the reconstructed data, it was possible to identify high (low) surface productivity, high (low) organic matter flux to the seafloor, and high (low) dissolution rates of planktonic Foraminifera tests during the glacial (postglacial). Furthermore, within the glacial, enhanced productivity was associated with higher insolation values, explained by increased northeasterly summer winds that promoted meandering and upwelling of the nutrient-rich South Atlantic Central Water. Statistical analyses support the idea that productivity is the main cause for seafloor calcium carbonate dissolution, as opposed to changes in the Atlantic Meridional Overturning Circulation (at least for the 25–4 ka period). Further efforts must be invested in the comprehension and quantification of the total organic matter and biogenic carbonate burial during time intervals with an enhanced biological pump, aiming to better understand their individual roles.

Keywords: planktonic Foraminifera, stable isotopes, Atlantic meridional overturning circulation, upper circumpolar deep water, North Atlantic deep water

INTRODUCTION

The oceanic biological pump is a primary mechanism to exchange CO_2 between the atmosphere and the oceans, and is therefore critically important for the acidity of the sea water and associated carbonate dissolution (Riebesell, 2004). An intensified biological pump in the oceans leads to an increase of exported biogenic carbon and carbonate burial in the sediments (Brummer and van Eijden, 1992). Since planktonic Foraminifera are important contributors to the pelagic calcium carbonate flux (Milliman et al., 1999; Schiebel, 2002; Kučera, 2007) they represent an important component of the global climate system through their role in the oceanic carbon and carbonate pump. The connection between strong changes in the oceanic biological pump and calcite dissolution is difficult to study in modern oceans, as sample areas with sufficient differences in bioproductivity also differ in several other environmental factors, thus confounding the results. In contrast, Pleistocene climate scenarios offer the possibility to investigate a relatively stable ecosystem under intensely changing bioproductivity scenarios.

The Late Quaternary climate is characterized by orbit-related glacial–interglacial fluctuations (EPICA Community Members, 2004; Jouzel et al., 2007) associated with CO_2 variations (Petit et al., 1999; Shakun et al., 2012). Nevertheless, the orbital forcing alone is not strong enough to induce the observed temperature changes and, thus, feedback mechanisms in the Earth's climate system are expected to have amplified (or reduced) the primary signal (Lorius et al., 1990; Shackleton, 2000). The oceanic carbonate pump system is critically influenced by changes in bioproductivity. High biological surface productivity can boost population densities and biomass of benthic communities, increasing the respiration processes and leading to the remineralization of higher percentages of organic matter (OM), resulting in the release of CO_2 and a reduction of the biologic carbon burial (Cronin et al., 1999; Hales, 2003). Besides, higher CO_2 release at the seafloor can lead to increased dissolution of biogenic carbonate, (e.g., planktonic Foraminifera tests; Schiebel, 2002). Therefore, an enhanced biological pump can have an unexpected effect, both decreasing the OM burial and dissolving biogenic carbonates, inhibiting higher quantities of C to be stored in the seafloor sediments (e.g., Zamelczyk et al., 2012; Naik et al., 2014).

Supra-lysoclinal pelagic carbonate dissolution has been described from the western South Atlantic in the past, being related to changes in bottom water masses (Petró et al., 2018a; Petró and Burone, 2018; Petró et al., 2021). Nevertheless, the relation between calcium carbonate dissolution and sea surface productivity has not yet been approached in the studied area. In this paper, we 1) reconstruct past changes in primary and export productivity during the last glacial–interglacial interval, 2) determine mechanisms that triggered calcium carbonate dissolution, and 3) investigate the role of productivity changes on carbonate corrosion from a core retrieved above the lysocline.

Oceanographic Setting

The studied sediment core was recovered off Santa Marta Cape in the western South Atlantic (**Figure 1A,B**). The proximal portion of the continental shelf of the Pelotas Basin represents a submerged coastal plain (Martins, 1984) that was exposed during the last Pleistocene regression (Marine Isotope Stage 2) and dissected by drainage networks from fluvial systems (Weschenfelder et al., 2014), which contributed to larger nutrient inputs from continental outflows compared to the Holocene.

Surface circulation in the shelf portion of the study area is dominated by the northward flowing Brazil Coastal Current, which carries the Coastal Water (CW), a mixture of oceanic and continental drainage waters. Offshore, the Brazil Current (BC) transports the warm (temperature, $T > 20^{\circ}C$) and salty (salinity, $S > 36$) Tropical Water (TW) southwards within the surface layer. The BC flows along the South American margin slope until it converges with the Malvinas Current (MC), a northward flowing surface current carrying the cold ($T < 15^{\circ}C$) and fresher ($S < 34.2$) Subantarctic Water, forming the Brazil/Malvinas Confluence (BMC) close to 38°S (Gordon and Greengrove, 1986). The BMC forms a large meander, which separates southward of the continental margin (Peterson and Stramma, 1991; Piola and Matano, 2017), and varies seasonally and interannually, moving to the north in austral autumn and winter, and to the south in spring and summer. This variation influences the nutrient distribution along the continental shelf of the Argentinian, Uruguayan, and south Brazilian coasts (Gonzalez-Silvera et al., 2006). Presently, two main continental sources of nutrients and freshwater for the area are the Río de la Plata Estuary (RdlPE) and the Patos-Mirim Lagoon System (PMLS). Although the configuration of continental drainage certainly changed under the varying sea-level conditions of the late Quaternary, they both represent sources of continental drainage and, thus, nutrients to the study area.

The water masses that circulate in the subsurface (**Figure 1C**) immediately below the TW are: the South Atlantic Central Water (SACW), the Antarctic Intermediate Water (AAIW), the Upper Circumpolar Deep Water (UCDW), the North Atlantic Deep Water (NADW), and the Antarctic Bottom Water (AABW) (Reid et al., 1976; Campos et al., 1995; Hogg et al., 1996; Stramma and England, 1999). The NADW promotes the preservation of carbonate, due to its oversaturation with carbonate ion (CO_3^{2-}) when compared to the overlying UCDW and the underlying AABW. Both, the UCDW and AABW, are undersaturated in CO_3^{2-} and, therefore, may lead to the dissolution of carbonate (Frenz et al., 2003). Indeed, Frenz and Henrich (2007) have shown that the depth of the interface between the NADW and the AABW defines the lysocline, below which carbonate dissolution occurs.

MATERIALS AND METHODS

The piston core SAT-048A was collected by *FUGRO Brasil–Serviços Submarinos e Levantamentos Ltda* for the *Agência Nacional do Petróleo* (ANP, Brazilian National Agency of Petroleum, Natural Gas and Biofuels) at 29°11′ S and 47°15′ W at 1,542 m water depth (**Figure 1**). The core, with a total recovery of 315 cm, was sampled at intervals of about 6 cm, for a total of 54

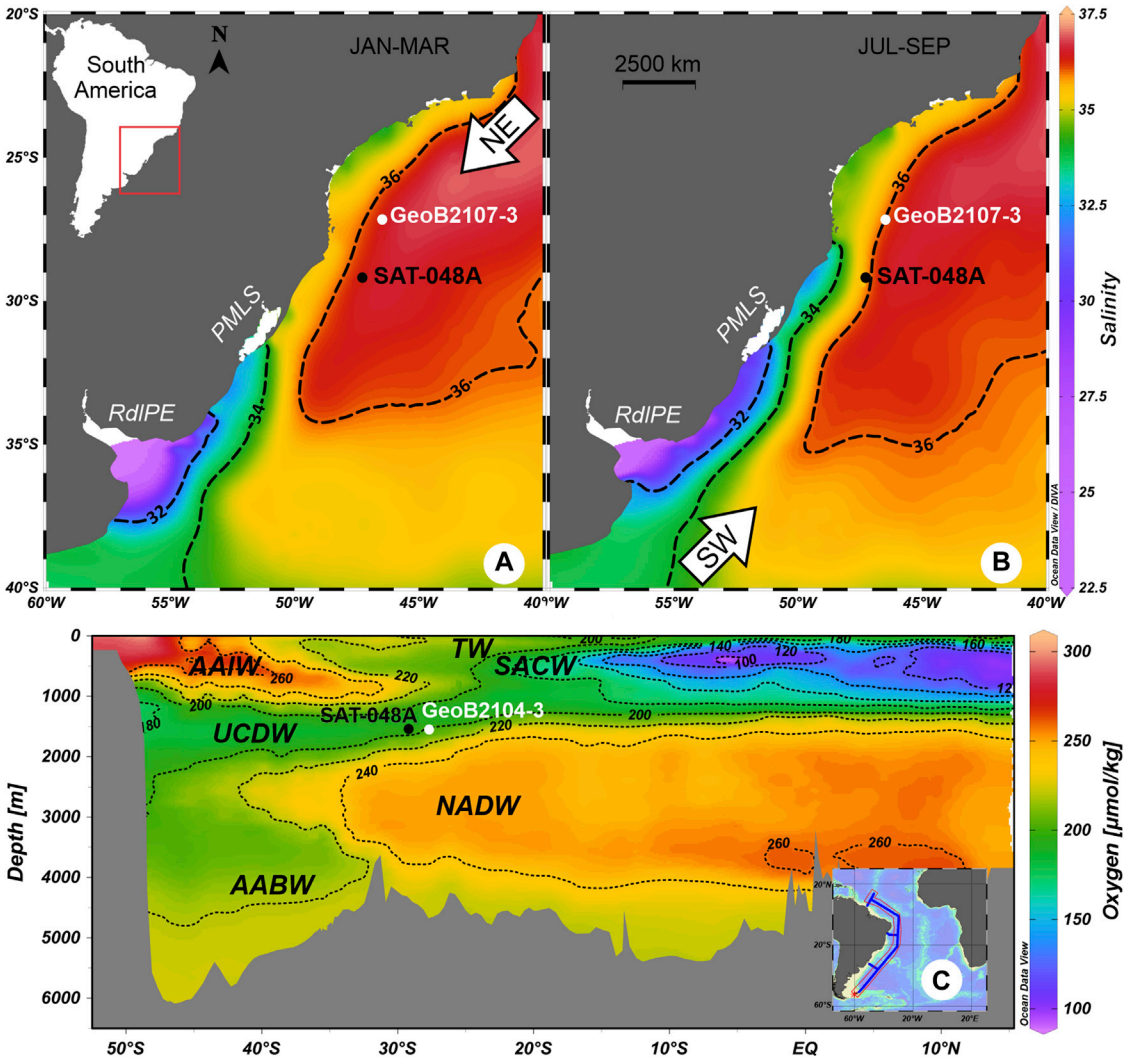

FIGURE 1 | Location of sediment core SAT-048A and other mentioned cores (GeoB2107-3, Gu et al., 2017, Pereira et al., 2018; GeoB2104-3, Howe J. N. W. et al., 2016) in the studied area, in map view **(A,B)** and as latitudinal cross section (C). Seasonal variation of average sea surface salinity (measured on the psu scale) for the months of (a) January–March (austral summer) and (b) July–September (winter) are based on data from the World Ocean Atlas 2013 (WOA13, Zweng et al., 2013). The isohalines 32, 34, and 36 (dashed lines) highlight the northward intrusion of less saline water from the south during winter (b) when compared to summer (a) conditions. This is related to seasonally predominating wind regimes, indicated as white arrows. The present Río de la Plata Estuary (RdlPE) and Patos-Mirim Lagoon System (PMLS) represent important continental nutrient sources in the study area. Dissolved oxygen concentrations (c; µmol/kg) in a transect along the South American continental margin show the South Atlantic water masses that circulate in the region: Tropical Water (TW), South Atlantic Central Water (SACW), Antarctic Intermediate Water (AAIW), Upper Circumpolar Deep Water (UCDW), North Atlantic Deep Water (NADW), and Antarctic Bottom Water (AABW).

samples. The core was missing the top 20 cm and the 196–217 cm interval. Each sample was washed over a 63 µm sieve and oven dried at temperatures below 60°C. The taxonomical identification of the planktonic Foraminifera species, from subsamples of at least 300 specimens larger than 150 µm split with a microsplitter, followed Bé (1967), Bé et al. (1977), Bolli and Saunders (1989), Hemleben et al. (1989), Kemle-von Mücke and Hemleben (1999), Schiebel and Hemleben (2017), and Morard et al. (2019).

We used a revised version of the Frozza et al. (2020) age model, based on the *rbacon* package (Blaauw and Christen, 2011; version 2.4.2) for the R software (R Core Team, 2019). The age model (**Supplementary Material**) used the ten AMS radiocarbon dates presented by Frozza et al. (2020), carried out on monospecific samples of planktonic Foraminifera, and the Laschamp geomagnetic excursion (J. Savian, personal communication, June 5, 2020) as an additional control point.

Past sea surface temperatures (SST) at 100 m water depth (SST_{100m}) were estimated using the modern analogue technique (MAT; Hutson, 1980) in the software PAST (version 4.05; Hammer et al., 2001). The paleo-SST_{100m} were calibrated with a dataset composed of: 1) relative abundances of planktonic Foraminifera of surface sediments from the South Atlantic Ocean extracted from the ForCenS database (Siccha and Kučera, 2017) as training data and 2) modern mean annual

temperature estimates for 100 m below sea level, obtained from the World Ocean Atlas 2013 (Locarnini et al., 2013) and extracted with the software Ocean Data View (Schlitzer, 2020). For the weighting parameter, we used the inverse dissimilarity based on the squared Chord dissimilarity index with a threshold of 0.28 and five analogues.

Sea surface paleo-productivity was assessed from the relative abundances of the species *Globigerinita glutinata* (Conan and Brummer, 2000; Souto et al., 2011) and the ratio between *Globigerina bulloides* and *Globigerinoides ruber* (*albus* and *ruber*) (*G.bull*:*G.rub*; Conan et al., 2002; Toledo et al., 2008). The OM flux to the seafloor, as a response to sea surface productivity, was estimated based on the benthic:planktonic Foraminifera ratio (B:P; Berger and Diester-Haass, 1988; Loubere, 1991; Gooday, 2002). While this parameter was applied on different size fractions in the past, with no clearly defined standard, it was shown that small size fraction differences do not impact analyses considerably (Schönfeld 2012; Weinkauf. 2018). As long as data for benthic and planktonic communities, as in our case, were extracted from the same sieve size fraction. The resulting B:P ratios will be comparable, indeed, being used in the literature (e.g., de Almeida et al., 2022). The ostracod valves abundances (number of valves in the >150 μm fraction per gram of sediment), and the $\delta^{13}C$ record of *Uvigerina* spp. ($\delta^{13}C_{Uvi}$; Mackensen, 2008) were also used to infer the OM flux to the seafloor. Part of these data (relative abundances of *G. bulloides* and *G. ruber*, $\delta^{13}C_{Uvi}$) were previously published by Frozza et al. (2020). For the $\delta^{13}C_{Uvi}$ measurements, approximately seven specimens of the benthic foraminiferal genus *Uvigerina* were selected from the 250 μm sediment fraction from each sample. The geochemical analyses were performed with a Thermo Scientific MAT-253 mass spectrometer, coupled to a Kiel IV carbonate device, by the Laboratory of Stable Isotopes of the University of California–Santa Cruz (SIL-UCSC). All results are expressed in δ-notation relative to the Vienna Pee-Dee Belemnite (VPDB) standard.

Dissolution effect proxies for this core were published by Suárez-Ibarra et al. (2021) and were based on the 1) the planktonic Foraminifera fragmentation intensity, which follows Berger (1970)'s fragments and broken shells counting, 2) the bulk sand fraction (%; Berger et al., 1982; Gonzales et al., 2017), 3) the number of whole planktonic Foraminifera tests per Gram of sediment (PF/g, Le and Shackleton, 1992), and 4) the relative $CaCO_3$ content of the sediment. Bulk sand contents were determined using a laser diffraction particle size analyzer Horiba Partica-LA-950 at the Climate Studies Center Centro de Estudo de Geologia Costeira e Oceânica (CECO) of the Universidade Federal do Rio Grande do Sul (UFRGS). The calcium carbonate content for the samples was determined by weight loss after reaction with 10% hydrochloric acid (HCl) at the Calcareous Microfossils Laboratory of the UFRGS.

All statistical analyses were conducted in the software PAST (version 4.05; Hammer et al., 2001). An overall relation between productivity and dissolution proxies was quantified using Spearman rank-order correlation. To objectively define phases of changing conditions through the analyzed time interval, a principal component analysis (PCA) on the correlation matrix including all the correlatable paleo-productivity proxies (PCA_P) and all dissolution proxies (PCA_D), respectively, was carried out. Using the first principal component of PCA_P ($PC1_P$), we objectively defined the borders between the three phases using a piecewise ordinary least-squares regression (OLS; Weinkauf et al., 2013): 1) We subdivided the $PC1_P$ vs age date into three subsets. The age-borders for each subset varied over a range of reasonable values (25.11–31.46 ka for the phase 1–Phase 2 border, 18.274–15.515 ka for the phase 2–Phase 3 border); 2) for each possible combination of phase borders, we calculated three independent OLS regression lines and their associated R^2-value; 3) we calculated the overall fit of the solution as the product of the three individual R^2-values; 4) the best phase border solution was the one that showed the highest overall R^2-value. The relationship between summer insolation and paleo-productivity, represented by the score of $PC1_P$, was analyzed using a reduced major axis regression. To study the interaction between productivity ($PC1_P$), bottom water intensity (reconstructed by the $^{231}Pa/^{230}Th$ ratio; McManus et al., 2004; Böhm et al., 2015), and dissolution ($PC1_D$), a multiple linear regression was carried out.

RESULTS

Sediments from core SAT-048A represent hemipelagic muds rich in carbonate. The average grain size of the samples is slightly sandy mud, and in general, ranges from slightly clayey mud to muddy sand in some cases. The recovered sediments correspond to the latest Pleistocene and early/middle Holocene muds of the Imbé formation. The age model (**Supplementary Material**) indicates sample ages ranging from 43 to 5 ka.

Planktonic Foraminifera species indicate two contrasting temporal distribution patterns: 1) species with higher abundances during the Late Pleistocene that decreased in abundance towards the Holocene, *Globigerinita glutinata* (**Figure 2C**), *Globigerina bulloides*, *Globoconella inflata*, and *Neogloboquadrina incompta* (**Supplementary Material**); 2) species with lower abundance values during the Late Pleistocene and higher abundances in the Holocene, *Globigerinoides ruber albus* and *G. ruber ruber*, *Trilobatus sacculifer*, *Globorotalia menardii*, *Globigerinella calida*, *Orbulina universa*, *Globorotalia tumida*, and *Globigerinoides conglobatus* (**Supplementary Material**).

The performance of the MAT (shown in the **Supplementary Material**) was generally very good, with an R^2 of 0.993. The annual mean paleo-SST_{100m} estimates for core SAT-048A are shown in **Figure 2E** (residuals shown in **Supplementary Material**). The annual mean reconstructions show lower values from the bottom of the core until 37 ka (on average 16°C), although the lowest value occurred at 25 ka (15.2°C). For the 37–15 ka period, the observed temperature variation was larger and fluctuated faster than during the rest of the record, spanning from 15 to 19°C. A warming trend is indicated to have occurred before the Last Glacial Maximum (LGM) at 25 ka, with values between 19 and 23°C and the warmest SST_{100m} value (22.5°C) observed at 7 ka.

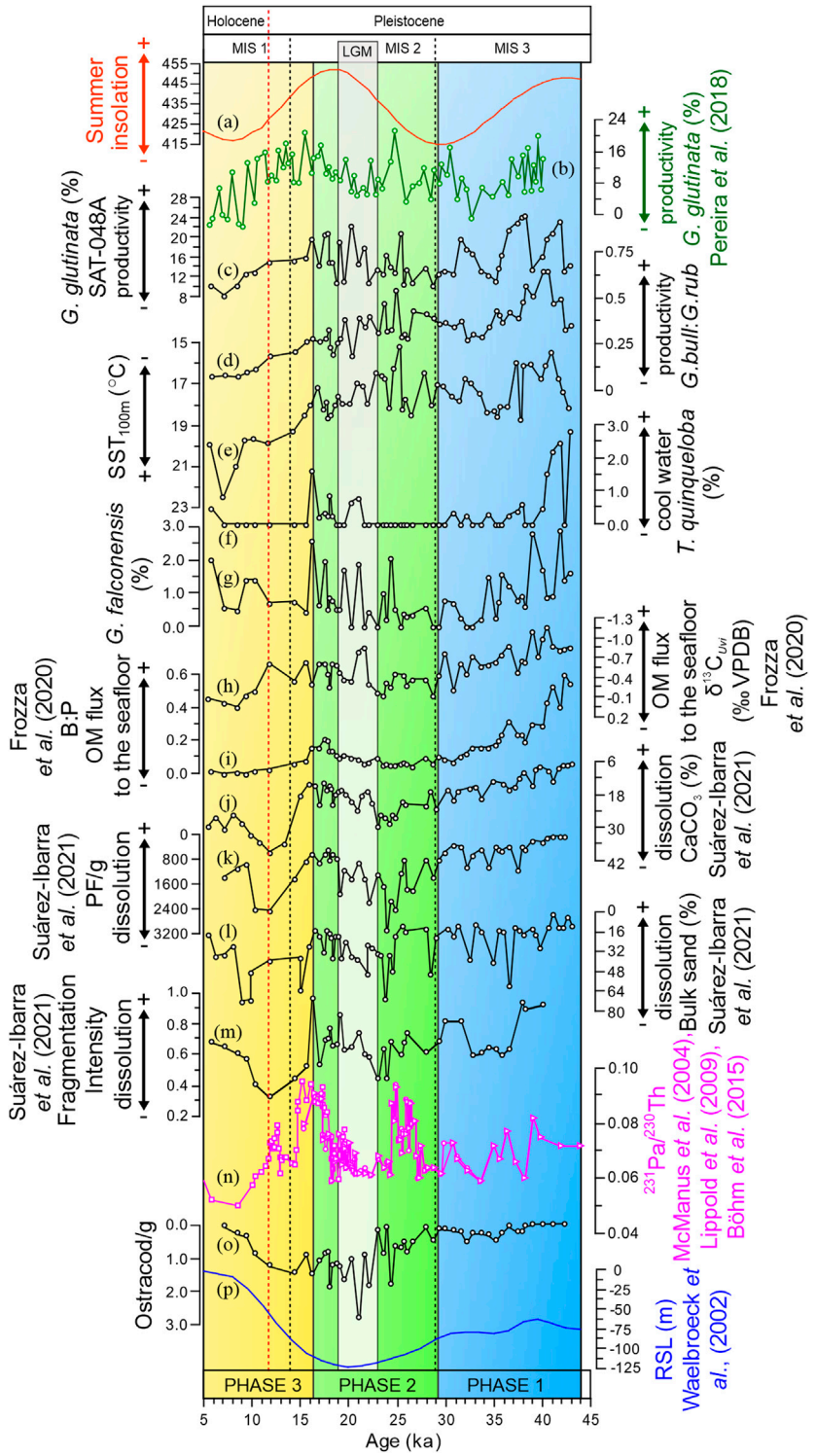

FIGURE 2 | Fluctuations in summer insolation, paleoenvironmental proxies for surface productivity, organic matter (OM) flux to the seafloor, $CaCO_3$ dissolution, Atlantic Meridional Overturning Circulation (AMOC) speed, and relative sea level. **(A)** Austral summer (February) insolation at 31° S (Laskar et al., 2004) **(B–C)** relative abundance of *G. glutinata* in cores GeoB2107-3 (b; Pereira et al., 2018) and SAT-048A (c; this study); **(D)** *G. bulloides*/*G. ruber* ratio (*G.bull*:*G.rub*); **(E)** SST_{100m} (°C) **(F–G)** relative abundance of *T. quinqueloba* (f) and *G. falconensis* (g); **(H)** $\delta^{13}C_{Uvi}$ (‰); **(I)** Benthic/Planktonic Foraminifera ratio (B:P) **(J)** $CaCO_3$ content of the sediment **(K)** number of planktonic Foraminifera tests per gram of sediment (PF/g) **(L)** sand bulk content (%) **(M)** fragmentation intensity **(N)** $^{231}Pa/^{230}Th$ values from McManus et al. (2004; squares), Lippold et al. (2009; circles), and Böhm et al. (2015; triangles) **(O)** Ostracods per gram of sediment (valves/g) **(P)** relative sea level (RSL; Waelbroeck et al., 2002). Note the inverted *y*-axes in (f), (g), and (i–k) to aid visualization. Proxies printed in black belong to sediment core SAT-048A. The three phases indicated in the plot are based on a principal component analysis of all productivity values, as shown in **Figure 3**.

All reconstructed paleoenvironmental proxies are shown in **Figure 2**. Paleo-productivity shows highest values in the 43–32/34 ka interval (superimposed on a decreasing trend), when reconstructed from *G. glutinata* abundances (**Figure 2C**) and the *G. bull*:*G.rub* ratios (**Figure 2D**), respectively. A relative plateau is witnessed for both proxies from 32/34 to 25 ka. The following time interval (25–17 ka) is characterized by an increasing trend. From 17 to 5 ka, *G. glutinata* and the *G. bull*:*G.rub* ratio show a decreasing trend with some of the lowest values of the entire record. The abundance of ostracods valves (**Figure 2**) is low during the 43–27 ka interval, then increases until 10 ka, and decreases afterward.

We ran a Spearman rank-order correlation to test the relationship between different productivity and dissolution proxies (**Table 1**). When the correlation was significant at the α = 0.05-level, the correlation coefficients ρ were categorized as either weak ($|\rho|$ = 0–0.33), medium ($|\rho|$ = 0.34–0.66), or strong ($|\rho|$ = 0.67–1). The paleo-productivity proxies *G. bull*/*G.rub* and *G. glutinata* (%) are not significantly correlated (p = 0.556), nevertheless, the correlations between productivity and OM flux proxies are all significant, ranging from medium to strong correlations. All the dissolution proxies are significantly correlated, also ranging from medium to strong. The correlation between productivity, OM flux and dissolution proxies are all significant, ranging from weak to strong relations, except for the FI vs *G. glutinata* (%) and the bulk sand (%) vs *G. glutinata* (%) proxies. The OM flux proxy Ostracod valves only showed a medium correlation with the *G. bull*/*G.rub* proxy and was also weakly–moderately correlated to three dissolution proxies.

These results indicate that all these proxies are also influenced by other environmental parameters, not just productivity and dissolution, respectively. Therefore, not any single proxy is suitable to provide an unbiased picture of the past environment. We, thus, aimed to develop synthetic productivity and dissolution proxies by combining all information in a PCA, which on its first axis amplifies the direction of largest variation in both parameters. PCAs were run both for productivity/OM flux (*G.bull*/*G.rub*, *G. glutinata* (%), $\delta^{13}C_{Uvi}$, and B:P; PCA_P) and dissolution proxies ($CaCO_3$, FI, PF/g, and bulk sand (%), PCA_D) on the data centered at zero and scaled to unit variance (**Supplementary Material**). The first principal component of the productivity/OM flux analysis ($PC1_P$) explains 62.14% of the variance in the data, while the first principal component for the dissolution proxies ($PC1_D$) captures 74.88% of data variance. The trends of $PC1_P$ and $PC1_D$ are shown in **Figure 3**, where the borders between three phases are based on the best solution of a set of piecewise OLS regressions with combinations of 70 feasible phase border scenarios. The loadings of the components on the principal component axes and the individual R^2-values from the piecewise regressions on which the phase borders are based are shown in the **Supplementary Material**. The optimal phase borders were determined by the R^2-product of 0.251 as follows: phase 1 (42.32–29.12 ka), where $PC1_p$ values decreased, indicating a reduction in productivity; phase 2 (28.56–16.15 ka), with stable to slightly increasing paleo-productivities; and phase 3 (15.51–5.77 ka), where productivity decreased again during the Holocene.

A reduced major axis regression between summer insolation and $PC1_P$ (**Supplementary Material**) yielded a significant (p < 0.001) correlation value of 0.476. A multiple linear regression between the independent variable $PC1_P$ and bottom water velocity ($^{231}Pa/^{230}Th$) and $PC1_D$ as dependent variable was carried out and results are shown in **Table 2**. Only $PC1_P$ is

TABLE 1 | Correlation coefficient (ρ) and statistical significance (p) for productivity and dissolution indices in sediment core SAT-048A from the western South Atlantic. *G. glutinata* (%): Relative abundance of *Globigerinita glutinata*; $\delta^{13}C_{Uvi}$: VPDB $\delta^{13}C$-values of shells of the benthic foraminifer genus *Uvigerina*; B:P: Ratio between benthic and planktonic Foraminifera; $CaCO_3$ (%): Relative $CaCO_3$ content of the sediment; FI: Planktonic foraminifera fragmentation intensity; PF/g: Number of Planktonic foraminiferal tests per gram of sediment; bulk sand (%): Relative sand content of the sediment; Ostracod valves: Number of Ostracod valves per Gram of sediment. Significant p-values (at α = 0.05) are highlighted in bold; for these, the correlation coefficient was marked as weak (italics), medium (bold), or strong (bold-italics).

	—	*G.bull/ G.rub*	*G. glutinata* (%)	$\delta^{13}C_{Uvi}$	B:P	$CaCO_3$ (%)	FI	PF/g	Sand bulk (%)
G. glutinata (%)	ρ	0.086	—	—	—	—	—	—	—
	p	0.556	—	—	—	—	—	—	—
$\delta^{13}C_{Uvi}$	ρ	**–0.441**	**–0.508**	—	—	—	—	—	—
	p	**0.002**	**<0.001**	—	—	—	—	—	—
B:P	ρ	**0.458**	**0.511**	***–0.795***	—	—	—	—	—
	p	**0.001**	**<0.001**	**<0.001**	—	—	—	—	—
$CaCO_3$ (%)	ρ	**–0.518**	**–0.430**	0.777	***–0.914***	—	—	—	—
	p	**<0.001**	**0.002**	**<0.001**	**<0.001**	—	—	—	—
FI	ρ	*0.329*	0.287	*–0.304*	**0.452**	**–0.567**	—	—	—
	p	**0.024**	**0.05**	**0.038**	**0.001**	**<0.001**	—	—	—
PF/g	ρ	**–0.371**	*–0.302*	***0.703***	***–0.811***	***0.831***	**–0.53**	—	—
	p	**0.009**	**0.035**	**<0.001**	**<0.001**	**<0.001**	**<0.001**	—	—
Sand bulk (%)	ρ	**–0.389**	–0.204	**0.473**	**–0.579**	**0.629**	**–0.606**	**0.576**	—
	p	**0.006**	0.16	**0.001**	**<0.001**	**<0.001**	**<0.001**	**<0.001**	—
Ostracod valves	ρ	**–0.354**	0.129	0.187	–0.229	0.24	**–0.334**	**0.479**	**0.304**
	p	**0.015**	0.387	0.207	0.121	0.104	**0.022**	**0.001**	**0.038**

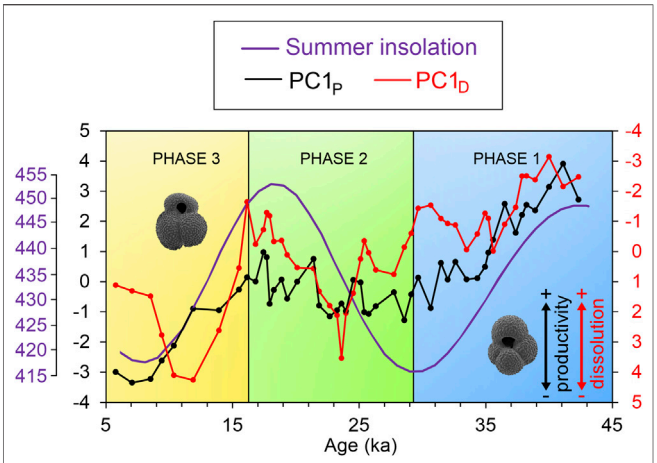

FIGURE 3 | Mean average for the first principal components of principal component analyses on all productivity proxies ($PC1_P$, black line) and all dissolution proxies ($PC1_D$, red line) in samples from sediment core SAT-048A in the South Atlantic. The purple line represents the Austral summer (February) insolation at 31° S (Laskar et al., 2004). The three phases defined by productivity trends (decreasing in phases 1 and 3, increasing in phase 2) are indicated. Dominant species of planktonic Foraminifera (*Globigerina bulloides* in phase 1, *Globigerinoides ruber* in phase 3) are indicated.

significantly influencing dissolution, and explains around 51% of the observed dissolution signal.

DISCUSSION

Radiocarbon Reversals

The occurrence of reversals in planktonic Foraminifera radiocarbon dates are not rare in the studies of the south Brazilian continental margin (SBCM, e.g., Sortor and Lund, 2011; Hoffman and Lund, 2012; Portilho-Ramos et al., 2019), being related either to: 1) morphological features of the sea bottom that remobilize sediments (such as turbidity or contour currents), or to 2) post-depositional chemical processes that affect the ^{14}C concentrations. The age model of core SAT-048A here presented (**Supplementary Figure S3**) indicates three intervals where samples yielded mean older ages (**Supplementary Table S3**). Nevertheless, the only significant difference is shown in the sample at 183.5 cm depth (31.1 ka before calibration), between 217 and 149 cm (27.8–22.7 ka), an interval constituted by hemipelagic mud rich in carbonate. According to Kowsmann et al. (2014), features of geological instability for the SBCM usually occurred between 28 and 15 ka, during relative low sea levels. Nevertheless, reversals of AMS ^{14}C planktonic Foraminifera dates from core SAT-048A are not associated to abrupt changes on the grain size record (**Supplementary Figure S4**). Moreover, the action of contour currents in the proximities of the study area (Viana, 2001; Duarte and Viana, 2007; Hernández-Molina et al., 2016) could, have gradually remobilized older particles (such as planktonic Foraminifera shells), masking the ^{14}C ages and increasing the temporal mixing.

Regarding the chemical processes, Rodrigues et al. (2020) reported older radiocarbon dates likely due to the upward migration of ^{14}C-depleted methane fluids from gas chimneys, as already reported for the south portion of the SBCM (Portilho-Ramos et al., 2018; Ketzer et al., 2020), which can precipitate in shell interstitial pores (Wycech et al., 2016), producing an alteration in the radiocarbon dates. Given the above, we tried to diminish the impact of radiocarbon reversals by using 1) a high number of correlation points (10 radiocarbon dates and one geomagnetic correlation point) and, 2) the *rbacon* package for software R, which implements Bayesian statistics that calculate mean ages for age model constructions, and has the capacity to deal with ^{14}C reversals.

Sea Surface Productivity

Three phases were defined from the $PC1_P$ trends (**Figure 3**). Phases 3 and 1 fall into time intervals with decreasing summer insolation values, while phase 2 is characterized by increasing summer insolation. The correlation between $PC1_P$ and summer insolation values is supported by the significant ($p < 0.001$) values of a reduced major axis regression ($r = 0.476$). This is supported by mechanisms, reported in the literature, that drove the paleo-productivity changes in the western South Atlantic. Portilho-Ramos et al. (2019) explained the high glacial productivity by a combination of short – but highly productive – austral summer upwelling periods and prolonged winter conditions favorable to the intrusion of RdlPE.

The short summer upwelling periods resulted from the enhanced northeasterly (NE) winds blowing along the shore during intervals with high summer insolation, both directly, by pushing surface waters offshore due to the Ekman transport (Chen et al., 2019), and indirectly by strengthening the BC meandering and, therefore, enhancing shelf break upwelling (Portilho-Ramos et al., 2015; Pereira et al., 2018). This interpretation is supported by the observed changes in the relative abundances of: 1) *Globigerinita glutinata* (Conan and Brummer, 2000; Souto et al., 2011), a species that feeds on

TABLE 2 | Results from a multiple linear regression between summarized paleo-productivity ($PC1_P$; first axis of a principal component analysis including all correlatable productivity proxies) and bottom water velocity $^{231}Pa/^{230}Th$ and summarized dissolution (first axis of a principal component analysis including all dissolution proxies) as dependent variable for sediment core SAT-048A from the South Atlantic. *p*-values significant at $\alpha = 0.05$ are indicated in bold.

	Coefficient	Standard error	*t*	*p*	R^2	*r*
Constant	0.286	1.425	0.201	0.842	–	–
$PC1_P$	–0.781	0.122	–6.402	**<0.001**	0.519	0.720
$^{231}Pa/^{230}Th$	–4.141	20.458	–0.202	0.840	0.091	0.302

diatoms (Schiebel and Hemleben, 2017) and therefore benefits from the glacial silicic acid-rich SACW intrusions in the area (Portilho-Ramos et al., 2019) (**Figure 2B,C**); 2) *Turborotalita quinqueloba*, which is associated with stronger intrusions of cooler SACW into the photic zone (Souto, et al., 2011; Lessa et al., 2014, 2016) (**Figure 2F**); and 3) *Globigerina falconensis*, which is associated with eutrophic conditions (Sousa et al., 2014) (**Figure 2G**). Additionally, a reconstructed SST_{100m} cooler than 20°C (Campos et al., 2000; Silveira et al., 2000; Castelão et al., 2004) along with a *G. bull*:*G.rub* ratio higher than 0.25 (Lessa et al., 2014) for the Pleistocene portion of the record indicates a constant presence of the SACW in the subsurface during the short austral upwelling of the late glacial.

Prolonged winter conditions involved prevalent southwesterly (SW) winds year-round which carried outflows from the Río de La Plata (RdlPE) (Pimenta et al., 2005; Piola et al., 2005) and other continental sources (Camaquã, Jaguarão, and Jacuí rivers)—presently converging in the PMLS–closer to the study area (Piola et al., 2000; Nagai et al., 2014). Strengthened SW winds would also displace the BMC to a location closer to the area (Gonzalez-Silvera et al., 2006), which is supported by the higher relative abundances of *Globoconella inflata* and *Neogloboquadrina incompta* (**Supplementary Material**). The abundances of these two species can be interpreted as an indicator for a BMC closer to the study area (Boltovskoy et al., 1996), induced by the enhanced SW winds during the late last glacial.

Several authors suggest that during low relative sea levels (glacial times), periods of higher nutrient availability and increased terrigenous sediment input were favored due to the more offshore position of the BC and the exposure of the continental shelf (Mahiques et al., 2007; Gu et al., 2017; Pereira et al., 2018, Portilho-Ramos et al., 2019). Moreover, the Río de la Plata (Lantzsch et al., 2014) and Jacuí and Camaquã river paleo-drainages (Weschenfelder et al., 2014) were closer to the study area during this interval (higher influence of the PMLS). Higher Fe/Ca values (Heil, 2006), higher relative abundances of eutrophile dinoflagellate cysts species (Gu et al., 2017), and high terrestrial palynomorph proportions (Bottezini et al., 2022), are all evidence of the greater influence of continental outflow in the study area under lower relative sea levels during the late last glacial (which approximately corresponds to our phases 1 and 2). Medium paleo-productivity estimates during the LGM (relative sea level approximately 120 m lower; **Figure 3**) stand in contrast to the higher sea levels during phase 1 (relative sea level approximately 75 m below, Waelbroeck et al., 2002), where higher (terrigenous-related) fertilization was expected due the lower eustatic sea level. This suggests a different influence for the continental terrigenous fertilization for mid-depth cores retrieved from the continental slope. In contrast, for the Holocene, the higher relative sea level and onshore displacement of the BC, as well as the absence of the SACW, inhibited the photic zone fertilization, leading to oligotrophic conditions (Mahiques et al., 2007), witnessed in the phase 3.

Organic Matter Flux to the Seafloor and Carbonate Dissolution

Orbital to suborbital climate cycles can influence the abundance of deep-sea benthic communities (Cronin et al., 1999). Since abundance fluctuations of benthic Foraminifera and ostracods are related to variations in particulate organic carbon fluxes to the seafloor (Smith et al., 1997; Rex et al., 2006; Rex and Etter, 2010), their use as surface paleo-productivity indicators is widespread (Nees et al., 1999; Herguera, 2000; Rasmussen et al., 2002; Gooday, 2003; Yasuhara et al., 2012). The surface productivity fluctuations, indicated by the *G. glutinata* abundance and *G. bull*:*G.rub*, are significantly correlated to those of the OM flux recorded by the B:P ratio and the $\delta^{13}C_{Uvi}$ (**Table 1**). This effective OM export from the surface to the seafloor revealed a high benthic–pelagic coupling (Toledo et al., 2007). The B:P changes are accompanied by a similar trend in inverse $\delta^{13}C_{Uvi}$ (**Figure 2H,I**), which are expected to decrease when higher OM fluxes, rich in ^{12}C due to the preferential incorporation of the light isotope during photosynthesis (Wefer et al., 1999), reach the seabed (Ravello and Hillaire-Marcel, 2007). Nevertheless, the abundance of ostracod valves (**Figure 2**) was only significantly correlated with *G. bull*:*G. rub* ratio values. Intriguingly, ostracod valves showed a hump-shaped relation with productivity (Yasuhara et al., 2012), where values increased under moderate OM supply and declined under very low and very high productive conditions. This is because under high-productivity scenarios, oxygen levels at the sea floor tend to decrease and deep-sea ostracods, which are mostly epifaunal (Jöst et al., 2017), would not respond well to such an environment. On the other hand, ostracods valves had a significant ($p > 0.001$) strong correlation ($\rho = -0.701$) with paleo-bathymetric variations, where abundances decreased exponentially with water depth increase (Rex et al., 2006; Rex and Etter, 2010).

Dissolution indicators suggest higher calcium carbonate dissolution during the beginning of Phases 1 and the transition of phases 2 and 3 (**Figure 2**, **3**), related to the OM flux. Enhanced dissolution could theoretically be triggered by two different processes: 1) increase in CO_2 concentrations (decreasing the water pH) due to the remineralization of OM at the seafloor (Jahnke et al., 1997; Schiebel, 2002) or 2) changes in the bottom water mass configuration related to AMOC dynamics (speed or geometry). Although the B:P ratios are also used as a dissolution indicator (Berger and Diester-Haass, 1988; Conan et al., 2002), Kučera (2007) states that this is only applicable for abyssal depths. We also have evidence from regional studies (Petró et al., 2018b) that benthic foraminifera are more prone to dissolution in this setting than planktonic foraminifers. This means that our observed B:P ratios are, in the worst case, an underestimate of the real situation because dissolution would attenuate it.

In the SBCM basins, the $\delta^{13}C_{Uvi}$ values have been used to infer oscillations of OM input (Toledo et al., 2007; Dias et al., 2018; Rodrigues et al., 2018; Frozza et al., 2020). Nevertheless, $\delta^{13}C_{Uvi}$ values are influenced by several factors, such as

accumulation rates of organic carbon, regional changes of water masses, the global carbon cycle, photosynthesis respiration processes, temperature, and pH (Ravelo and Hillaire-Marcel, 2007; Hesse et al., 2014). Calcite dissolution has, in contrast, no influence on the foraminiferal $\delta^{13}C$ (Petró et al., 2018b). Lund et al. (2015) suggested that lower values of benthic $\delta^{13}C$ during glacial times are associated with a weak AMOC. Nevertheless, the fluctuations of $\delta^{13}C_{Uvi}$ and the carbonate preservation could be the result of the interplay between the OM flux and water masses changes.

Based on εNd in planktonic Foraminifera at mid-depths in the western South Atlantic, Howe et al. (2016, 2018) showed variations of water masses at intermediate depths of 1,000–1,200 m (cores GeoB2107-3 and KNR159-3-36GGC) during the Holocene, and at 2,200 m (core GL-1090) since Heinrich Stadial 1. After the Heinrich Stadial 1, core GL-1090s εNd values decreased, becoming less radiogenic and more related to modern upper NADW values, while cores GeoB2107-3's and KNR159-3-36GGC's εNd values increased after about 10 ka, becoming more radiogenic and showing more affinity with modern AAIW. Sediment core GeoB2104-3 (1,500 m) is located between these aforementioned cores, at the same depth as sediment core SAT-048A on which the present study is based, at its εNd values remained stable during the 25–4 ka interval (Howe J. N. W. et al., 2016). This indicates that SAT048A's $\delta^{13}C_{Uvi}$ fluctuations were produced by the OM bottom flux rather than water masses reconfigurations–at least throughout the studied time interval.

In addition, the $^{231}Pa/^{230}Th$ ratio (**Figure 2N**) has been used to track the intensity of the AMOC (McManus et al., 2004; Lippold et al., 2009; Böhm et al., 2015), where lower values indicate a strengthened AMOC. During periods of high $^{231}Pa/^{230}Th$ values and indicating AMOC slowdown (like Heinrich Stadials), a higher concentration of respired CO_2 is accumulated in seafloor water masses. As proposed by Howe JN. et al. (2016), this is a possible explanation for the intervals of increased calcium carbonate dissolution. Nevertheless, the results from the multiple linear regression (**Table 2**) point to paleo-productivity as the main factor to influence dissolution. The multiple linear regression designates the sea surface productivity and OM flux to the seafloor as the principal agents of the calcium carbonate dissolution (**Figure 4**), at least for the 25–4 ka interval, which is related to changes in the summer insolation. This is true, even including the decoupling between productivity and dissolution visible in our data during the last ca. 5 kyrs (**Figure 3**). We hypothesize that the increasing dissolution at constantly low productivity, high AMOC rates (**Figure 2N**) and stable water mass configuration during this last segment of the record is related to the rising temperatures in this period, which increased the Mg/Ca values of the biogenic carbonate. Since higher Mg content facilitates dissolution of calcite, shells produced during this time would be more prone to dissolution, so that other environmental parameters were no longer the major factors that affected calcite dissolution. Future studies should investigate possible changes in bottom water mass configuration through εNd isotopes for the entire

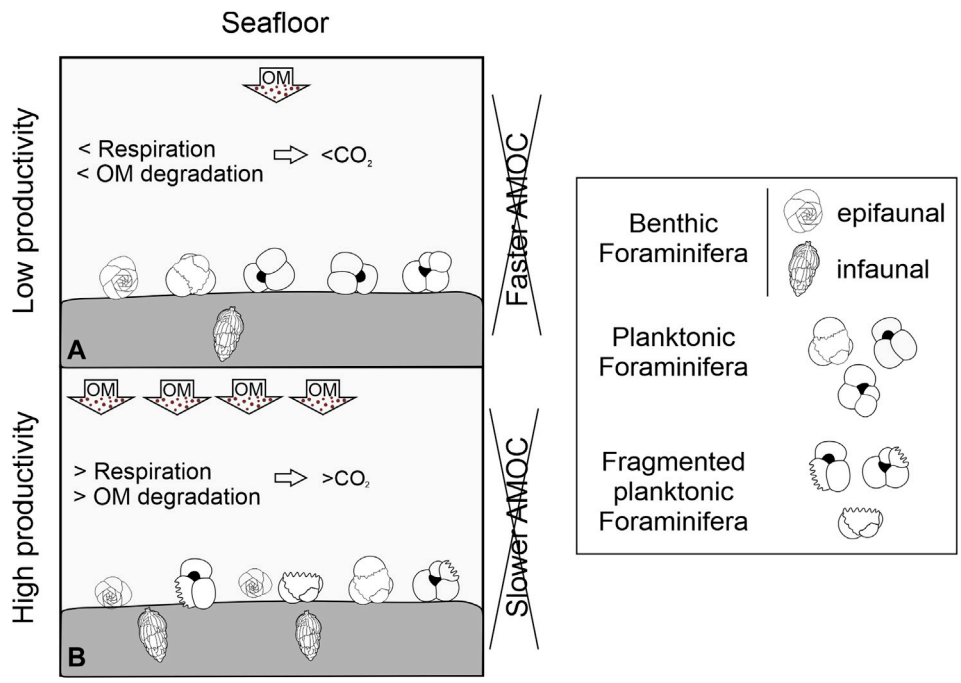

FIGURE 4 | Schematic representation of two possible end-member scenarios affecting carbonate dissolution on deep-water assemblages of sediment core SAT-048A (South Atlantic). The paleoceanographic changes could be triggered by: **(A)** Low organic matter (OM) inputs to the seafloor, which results in lower benthic abundances and better preservation of $CaCO_3$, or **(B)** high OM input that increases benthic abundances and CO_2 concentrations, decreases the seawater pH, and dissolves the planktonic Foraminifera tests (fragmentation on benthic Foraminifera was not assessed).

studied section to 1) increase our understanding of productivity-related carbon dissolution at the sea floor and 2) quantify the impact of changes of the biological pump on the total organic carbon and biogenic carbonates burial. This will considerably aid the understanding of the glacial inorganic carbon sequestration.

CONCLUSION

Planktonic Foraminifera assemblages from sediment core SAT-048A, along with geochemical analyses and sedimentological data, enabled us to reconstruct the surface and bottom water conditions that occurred during the last 43 kyrs in the western South Atlantic, and to contextualize the related production-dissolution processes in the area. The Pleistocene–Holocene transition was characterized by a shift from a glacial eutrophic environment to more oligotrophic post-glacial conditions, as suggested by the *G. bull*:*G.rub* ratio and the SST_{100m}, where intrusions of the nutrient-rich SACW were inhibited and the RdlPE and local river discharges (nowadays PMLS) were placed further away from the core site. The orbital-scale fluctuations of the upwelling dynamics (indicated by the relative abundances of *G. glutinata* and *T. quinqueloba*), modulated by insolation and NE wind changes, directly influenced the surface productivity and the OM fluxes to the seafloor (as shown by the B:P ratio and $\delta^{13}C_{Uvi}$). Imposed on the mechanisms behind the glacial–interglacial changes, stronger NE winds, generated by higher summer insolation, fertilized the photic zone, strengthened the BC, increased meandering, and enhanced intrusion of cooler and nutrient-richer waters into the subsurface layers. The enhanced upwelling conditions were also registered at the sea floor, where the bacterial decomposition of OM and the respiration of higher abundances of benthic communities increased the CO_2 concentration, which created more acidic conditions that caused different levels of carbonate dissolution, evidenced in the fragmentation of the planktonic Foraminifera tests. While changes in the bottom water masses could hypothetically cause the calcium carbonate dissolution, εNd analyses in a nearby sediment core at the same depth suggest no changes in the bottom water mass influence for the 25–4 ka interval, pointing to sea surface productivity and the intensity of the AMOC as possible causes of the carbonate dissolution. A multiple linear regression between summarized productivity and $^{231}Pa/^{230}Th$ (proxy for AMOC intensity), indicates that productivity is the main controlling factor of calcium carbonate dissolution. The continental influence (i.e., terrigenous input) must be better assessed in future studies, since, in contrast to expectations, no increased productivity was registered during the lowest relative sea level (LGM), when terrestrial input should have been highest. The dissolution of planktonic Foraminifera tests, induced by an enhanced biological pump (evidenced in the high glacial surface productivity and the high OM fluxes to the sea floor), must call the attention to future research, since a strong biological pump influences biogenic carbonate burial and CO_2 sequestration and burial at the seafloor.

DATA AVAILABILITY STATEMENT

The original contributions presented in the study are included in the article/**Supplementary Material**, further inquiries can be directed to the corresponding author.

AUTHOR CONTRIBUTIONS

JYSI and MAGP conceptualized the study; JYSI curated the data; JYSI conducted the formal analyses; MAGP and MFGW acquired funding; JYSI, CFF and PLP investigated the samples; JYSI, CFF, MFGW, MAGP developed the methods; MAGP provided the resources; MFGW and MAGP supervised the project; MFGW and MAGP validated the results; JYSI visualized the results; JYSI wrote the original draft; JYSI, CFF, PLP, SMP, MFGW, and MAGP reviewed and edited the manuscript.

FUNDING

This work was supported by the Brazilian Coordination of Higher Education Staff Improvement (CAPES) (grant number 88887.091729/2014-01), the Brazilian National Council for Scientific and Technological Development (CNPq) (grant number 407922/2016-4) and the PRIMUS program (grant number PRIMUS/20/SCI/019) and PROGRES Q45 grants, Charles University. JS-I was supported by the CNPq (MSc) and the STARS programs (PhD) from the Charles University, respectively. CF was supported by the CAPES (PhD).

ACKNOWLEDGMENTS

The authors are grateful to Gilberto Griep (*in memoriam*) for his commitment to making sediment cores retrieved for the industry available to the scientific community. We thank Dr. Igor Venâncio (Instituto Nacional de Pesquisas Espaciais, Brazil), Dr. João Coimbra (Universidade Federal do Rio Grande do Sul, Brazil), Dr. Geise dos Anjos Zerfass (Petróleo Brasileiro S.A., Brazil), Editor Dr. Jacek Raddatz and two reviewers, Dr. Selvaraj and Dr. Patrick Grunert for comments and suggestions that helped to improve this manuscript.

SUPPLEMENTARY MATERIAL

The Supplementary Material for this article can be found online at: https://www.frontiersin.org/articles/10.3389/feart.2022.830984/full#supplementary-material

REFERENCES

Bé, A. W. H. (1967). Foraminifera Families: Globigerinidae and Globorotaliidae, Conseil Permanent International Pour L'exploration De La Mer, Zooplankton. *Charlottenlund, Denmark: Conseil Int. pour l'Exploration*

Bé, A. W. H., Hemleben, C., Anderson, O. R., Spindler, M., Hacunda, J., Tuntivate-Choy, S., et al. (1977). Laboratory and Field Observations of Living Planktonic Foraminifera. *Micropaleontology* 23 (2), 155–179. doi:10.2307/1485330

Berger, W. H., Bonneau, M. C., and Parker, F. L. (1982). Foraminifera on the Deep-Sea Floor: Lysocline and Dissolution Rate. *Oceanologica acta* 5 (2), 249.

Berger, W. H., and Diester-Haass, L. (1988). Paleoproductivity: the Benthic/planktonic Ratio in Foraminifera as a Productivity index. *Mar. Geology.* 81, 15–25. doi:10.1016/00254813227(88)90014-X

Berger, W. H. (1970). Planktonic Foraminifera: Selective Solution and the Lysocline. *Mar. Geology.* 8, 111–138. doi:10.1016/0025-3227(70)90001-0

Blaauw, M., and Christen, J. A. (2011). Flexible Paleoclimate Age-Depth Models Using an Autoregressive Gamma Process. *Bayesian Anal.* 6 (3), 457–474. doi:10.1214/1148410.1214/ba/1339616472

Böhm, E., Lippold, J., Gutjahr, M., Frank, M., Blaser, P., Antz, B., et al. (2015). Strong and Deep Atlantic Meridional Overturning Circulation during the Last Glacial Cycle. *Nature* 517, 73–76. doi:10.1038/nature14059

Bolli, H. M., and Saunders, J. B. (1989). "Oligocene to Holocene Low Latitude Planktic Foraminifera," in *Plankton Stratigraphy* (K. Cambridge Earth Sciences SeriesCambridge University Press), 1, 155

Boltovskoy, E., Boltovskoy, D., Correa, N., and Brandini, F. (1996). Planktic Foraminifera from the Southwestern Atlantic (30 °-60 °S): Species-specific Patterns in the Upper 50 M. *Mar. Micropaleontology* 28, 53–72. doi:10.1016/0377-8398(95)00076-3

Bottezini, S. R., Leonhardt, A., Diniz, D., and Gonçalves, J. F. (2022). Climatic and Vegetational Dynamics in Southern Brazil between 47.8 and 7.4 Cal Ka BP: a Palynological Analysis. *Revista Brasileira de Paleontologia* 24 (4), 345–356. doi:10.4072/rbp.2021.4.05

Brummer, G. J. A., and van Eijden, A. J. M. (1992). "Blue-ocean" Paleoproductivity Estimates from Pelagic Carbonate Mass Accumulation Rates. *Mar. Micropaleontology* 19, 99–117. doi:10.1016/0377-8398(92)90023-D

Campos, E. J. D., Gonçalves, J. E., and Ikeda, Y. (1995). Water Mass Characteristics and Geostrophic Circulation in the South Brazil Bight: Summer of 1991. *J. Geophys. Res.* 100 (9), 18537–18550. doi:10.1029/95jc01724

Campos, E. J. D., Velhote, D., and da Silveira, I. C. A. (2000). Shelf Break Upwelling Driven by Brazil Current Cyclonic Meanders. *Geophys. Res. Lett.* 27, 751–754. doi:10.1029/1999GL010502

Castelão, R. M., Campos, E. J. D., and Miller, J. L. (2004). A Modelling Study of Coastal Upwelling Driven by Wind and Meanders of the Brazil Current. *J. Coastal Res.* 203, 662–671. doi:10.2112/1551-5036(2004)20662AMSOCU2.0.CO;2

Chen, H.-H., Qi, Y., Wang, Y., and Chai, F. (2019). Seasonal Variability of SST Fronts and Winds on the southeastern continental Shelf of Brazil. *Ocean Dyn.* 69, 1387–1399. doi:10.1007/s10236-019-01310-1

Conan, S. M.-H., and Brummer, G. J. A. (2000). Fluxes of Planktic Foraminifera in Response to Monsoonal Upwelling on the Somalia Basin Margin. *Deep Sea Res. Part Topical Stud. Oceanography* 47 (9-11), 2207–2227. doi:10.1016/s09670645(00)00022-99

Conan, S. M.-H., Ivanova, E., and Brummer, G. J. (2002). Quantifying Carbonate Dissolution and Calibration of Foraminiferal Dissolution Indices in the Somali Basin. *Mar. Geology.* 182 (3-4), 325–349. doi:10.1016/s0025-3227(01)00238-9

Cronin, T. M., De Martino, D. M., Dwyer, G. S., and Rodriguez-Lazaro, J. (1999). Deepsea Ostracode Species Diversity: Response to Late Quaternary Climate Change. *Mar. Micropaleontology* 37 (3-4), 231–249. doi:10.1016/S0377-8398(99)00026-2

de Almeida, F. K., de Mello, R. M., Rodrigues, A. R., and Bastos, A. C. (2022). Bathymetric and Regional Benthic Foraminiferal Distribution on the Espírito Santo Basin Slope, Brazil (SW Atlantic). *Deep Sea Res. Oceanographic Res. Pap.* 181, 103688. doi:10.1016/j.dsr.2022.103688

de Oliveira Lessa, D. V., Ramos, R. P., Barbosa, C. F., Da Silva, A. R., Belem, A., Turcq, B., et al. (2014). Planktonic Foraminifera in the Sediment of a Western Boundary Upwelling System off Cabo Frio, Brazil. *Mar. Micropaleontology* 106, 55–68. doi:10.1016/j.marmicro.2013.12.003

Dias, B. B., Barbosa, C. F., Faria, G. R., Seoane, J. C. S., and Albuquerque, A. L. S. (2018). The Effects of Multidecadal-Scale Phytodetritus Disturbances on the Benthic Foraminiferal Community of a Western Boundary Upwelling System, Brazil. *Mar. Micropaleontology* 139, 102–112. doi:10.1016/j.marmicro.2017.12.003

Duarte, C. S. L., and Viana, A. R. (2007). Santos Drift System: Stratigraphic Organization and Implications for Late Cenozoic Palaeocirculation in the Santos Basin, SW Atlantic Ocean. *Geol. Soc.* 276, 171–198. doi:10.1144/GSL.SP.2007.276.01.09

EPICA Community Members. (2004). Eight Glacial Cycles from an Antarctic Icecore. *Nature* 429, 623–628. doi:10.1038/nature02599

Frenz, M., Höppner, R., Stuut, J.-B. W., Wagner, T., and Henrich, R. (2003). Surface Sediment Bulk Geochemistry and Grain-Size Composition Related to the Oceanic Circulation along the South American Continental Margin in the Southwest Atlantic. In: *The South Atlantic in the Late Quaternary*, *Wefer, G., Mulitza, S., Ratmeyer. V.*, Springer-Verlag, Berlin, Heidelberg, New York, Tokyo, v. (eds), pp. 347–373.doi:10.1007/978-3-642-18917-3_17

Frenz, M., and Henrich, R. (2007). Carbonate Dissolution Revealed by silt Grain-Size Distribution: Comparison of Holocene and Last Glacial Maximum Sediments from the Pelagic South Atlantic. *Sedimentology* 54, 391–404. doi:10.1111/j.1365-3091.2006.00841.x

Frozza, C. F., Pivel, M. A. G., Suaáez-Ibarra, J. Y., Ritter, M. N., and Coimbra, J. C. (2020). Bioerosion on Late Quaternary Planktonic Foraminifera Related to Paleoproductivity in the Western South Atlantic. *Paleoceanography and Paleoclimatology*, e2020PA003865. doi:10.1029/2020pa003865

Gonzales, M. V., de Almeida, F. K., Costa, K. B., Santarosa, A. C. A., Camillo, E., de Quadros, J. P., et al. (2017). Help Index: Hoeglundina Elegans Preservation Index for Marine Sediments in the Western South Atlantic. *J. Foraminiferal Res.* 47, 56–69. doi:10.2113/gsjfr.47.1.56

Gonzalez-Silvera, A., Santamaría-del-Angel, E., and Millán-Núñez, R. (2006). Spatial and Temporal Variability of the Brazil-Malvinas Confluence and the La Plata Plume as Seen by SeaWIFS and AVHRR Imagery. *J. Geophys. Res.* 111, C06010. doi:10.1029/2004JC002745

Gooday, A. J. (2003). Benthic Foraminifera (Protista) as Tools in Deep-Water Palaeoceanography: Environmental Influences on Faunal Characteristics. *Adv. Mar. Biol.* 46, 1–90. doi:10.1016/S0065-28810(03)46002-110.1016/s0065-2881(03)46002-1

Gooday, A. J. (2002). Biological Responses to Seasonally Varying Fluxes of Organic Matter to the Ocean Floor: A Review. *J. oceanography* 58, 305–332. doi:10.1023/A:1015865826379

Gordon, A. L., and Greengrove, C. L. (1986). Geostrophic Circulation of the Brazil-Falkland confluence. *Deep Sea Res. A. Oceanographic Res. Pap.* 33 (5), 573–585. doi:10.1016/0198-0149(86)90054-3

Gu, F., Zonneveld, K. A. F., Chiessi, C. M., Arz, H. W., Pätzold, J., and Behling, H. (2017). Long-term Vegetation, Climate and Ocean Dynamics Inferred from a 73,500 Years Old marine Sediment Core (GeoB2107-3) off Southern Brazil. *Quat. Sci. Rev.* 172, 55–71. doi:10.1016/j.quascirev.2017.06.028

Hales, B. (2003). Respiration, Dissolution and the Lysocline. *Paleoceanography* 18 (4), 1–14. doi:10.1029/2003PA000915

Hammer, O., David, A. T., and Paul, D. (2001). Past: Paleontological Statistics Software Package for Education and Data Analysis. *Palaeontol. Electronica* 4 (1), 1–9

Heil, G. M. N. (2006). Abrupt Climate Shifts in the Western Tropical to Subtropical Atlantic Region during the Last Glacial. PhD Thesis. *Universtity of Bremen* 121.

Hemleben, C., Spindler, M., and Anderson, O. R. (1989). New York: Estados Unidos de América: Springer. doi:10.1007/978-1-4612-3544-6Modern Planktonic Foraminifera

Herguera, J. C. (2000). Last Glacial Paleoproductivity Patterns in the Eastern Equatorial Pacific: Benthic Foraminifera Records. *Mar. Micropaleontology* 40 (3), 259–275. doi:10.1016/S0377-8398(00)00041-4

Hernández-Molina, F. J., Soto, M., Piola, A. R., Tomasini, J., Preu, B., Thompson, P., et al. (2016). A Contourite Depositional System along the Uruguayan continental Margin: Sedimentary, Oceanographic and Paleoceanographic Implications. *Mar. Geology.* 378, 333–349. doi:10.1016/j.margeo.2015.10.008

Hesse, T., Wolf-Gladrow, D., Lohmann, G., Bijma, J., Mackensen, A., and Zeebe, R. E. (2014). Modelling $\delta^{13}C$ in Benthic Foraminifera: Insights from Model Sensitivity Experiments. *Mar. Micropaleontology* 112, 50–61. doi:10.1016/j.marmicro.2014.08.001

Hoffman, J. L., and Lund, D. C. (2012). Refining the Stable Isotope Budget for Antarctic Bottom Water: New Foraminiferal Data from the Abyssal Southwest Atlantic. *Paleoceanography* 27, PA1213. doi:10.1029/2011PA002216

Hogg, N. G., Owens, W. B., Siedler, G., and Zenk, W. (1996). Circulation in the Deep Brazil BasinThe South Atlantic: Present and Past Circulation. in *Berlin Heidelberg*. Editors G. Wefer, W. H. Berger, G. Siedler, and D. J. Webb (Springer-Verlag), 13–44.

Howe, J. N., Piotrowski, A. M., Noble, T. L., Mulitza, S., Chiessi, C. M., and Bayon, G. (2016a). North Atlantic Deep Water Production during the Last Glacial Maximum. *Nat. Commun.* 7, 11765. doi:10.1038/ncomms11765

Howe, J. N. W., Huang, K.-F., Oppo, D. W., Chiessi, C. M., Mulitza, S., Blusztajn, J., et al. (2018). Similar Mid-depth Atlantic Water Mass Provenance during the Last Glacial Maximum and Heinrich Stadial 1. *Earth Planet. Sci. Lett.* 490, 51–61. doi:10.1016/j.epsl.2018.03.006

Howe, J. N. W., Piotrowski, A. M., Oppo, D. W., Huang, K. F., Mulitza, S., Chiessi, C. M., et al. (2016b). Antarctic Intermediate Water Circulation in the South Atlantic over the Past 25,000 Years. *Paleoceanography* 31, 1302–1314. doi:10.1002/2016PA002975

Hutson, W. H. (1980). The Agulhas Current during the Late Pleistocene: Analysis of Modern Faunal Analogs. *Science* 207, 64–66. doi:10.1126/science.207.4426.64

Jahnke, R. A., Craven, D. B., McCorkle, D. C., and Reimers, C. E. (1997). $CaCO_3$ Dissolution in California continental Margin Sediments: The Influence of Organic Matter Remineralization. *Geochimica et Cosmochimica Acta* 61 (17), 3587–3604. doi:10.1016/S00167037(97)00184-110.1016/s0016-7037(97)00184-1

Jöst, A. B., Yasuhara, M., Okahashi, H., Ostmann, A., Arbizu, P. M., and Brix, S. (2017). Vertical Distribution of Living Ostracods in Deep-Sea Sediments, North Atlantic Ocean. *Deep Sea Res. Part Oceanographic Res. Pap.* 122, 113–121. doi:10.1016/j.dsr.2017.01.012

Jouzel, J., Masson-Delmotte, V., Cattani, O., Dreyfus, G., Falourd, S., Hoffmann, G., et al. (2007). Orbital and Millennial Antarctic Climate Variability over the Past 800,000 Years. *Science* 317, 793–796. doi:10.1126/science.1141038

Kemle-von Mücke, S., and Hemleben, C. (1999). *Foraminifera*. Editors D. Boltovskoy (Leiden: Backhuys Publishers), 43–73

Ketzer, M., Praeg, D., Rodrigues, L. F., Augustin, A., Pivel, M. A. G., Rahmati-Abkenar, M., et al. (2020). Gas Hydrate Dissociation Linked to Contemporary Ocean Warming in the Southern Hemisphere. *Nat. Commun.* 11, 3788. doi:10.1038/s41467-020-17289-z

Kowsmann, R. O., Lima, A. C., and Vicalvi, M. A. (2014). Feições indicadoras de instabilidade geológica no talude continental e no Platô de São Paulo. in *Geologia e Geomorfologia*. Editor R. O. Kowsmann (Rio de Janeiro: Elsevier), 71–98. doi:10.1016/B978-85-352-6937-6.50012-4

Kucera, M. (2007). "Chapter Six Planktonic Foraminifera as Tracers of Past Oceanic Environments," in *Proxies in Late Cenozoic Paleoceanography of Developments in Marine Geology*. Editors C. Hillaire-Marcel, A. de Vernal, and H. Chamley (Amsterdam: Elsevier), 1, 213–262. doi:10.1016/s1572-5480(07)01011-1

Lantzsch, H., Hanebuth, T. J. J., Chiessi, C. M., Schwenk, T., and Violante, R. A. (2014). The High-Supply, Current-Dominated continental Margin of southeastern South America during the Late Quaternary. *Quat. Res.* 81 (2), 339–354. doi:10.1016/j.yqres.2014.01.003

Laskar, J., Robutel, P., Joutel, F., Gastineau, M., Correia, A. C. M., and Levrard, B. (2004). A Long-Term Numerical Solution for the Insolation Quantities of the Earth. *A&A* 428 (1), 261–285. doi:10.1051/0004-6361:20041335

Le, J., and Shackleton, N. J. (1992). Carbonate Dissolution Fluctuations in the Western Equatorial Pacific during the Late Quaternary. *Paleoceanography* 7, 21–42. doi:10.1029/91PA02854

Lessa, D. V., Venancio, I. M., dos Santos, T. P., Belem, A. L., Turcq, B. J., Sifeddine, A., et al. (2016). Holocene Oscillations of Southwest Atlantic Shelf Circulation Based on Planktonic Foraminifera from an Upwelling System (Off Cabo Frio, Southeastern Brazil). *The Holocene* 26 (8), 1175–1187. doi:10.1177/0959683616638433

Lippold, J., Gruetzner, J., Winter, D., Lahaye, Y., Mangini, A., and Christl, M. (2009). Does Sedimentary $^{231}Pa/^{230}Th$ from the Bermuda Rise Monitor Past Atlantic Meridional Overturning Circulation. *Geophysical Research Letters*. 36. L12601. doi:10.1029/2009GL038068

Locarnini, R. A., Mishonov, A. V., Antonov, J. I., Boyer, T. P., Garcia, H. E., Baranova, O. K., et al. (2013). *World Ocean Atlas*. Editor A. Mishonov 2013.

Lorius, C., Jouzel, J., Raynaud, D., Hansen, J., and Treut, H. L. (1990). The Ice-Core Record: Climate Sensitivity and Future Greenhouse Warming. *Nature* 347, 139–145. doi:10.1038/347139a0

Loubere, P. (1991). Deep-sea Benthic Foraminiferal Assemblage Response to a Surface Ocean Productivity Gradient: a Test. *Paleoceanography* 6, 193–204. doi:10.1029/90PA02612

Lund, D. C., Tessin, A. C., Hoffman, J. L., and Schmittner, A. (2015). Southwest Atlantic Water Mass Evolution during the Last Deglaciation. *Paleoceanography* 30 (5), 477–494. doi:10.1002/2014pa002657

Mackensen, A. (2008). On the Use of Benthic Foraminiferal $\delta^{13}C$ in Palaeoceanography: Constraints from Primary Proxy Relationships. *Geol. Soc. Lond. Spec. Publications* 303, 121–133. doi:10.1144/SP303.9

Mahiques, M. M., Fukumoto, M. M., Silveira, I. C. A., Figueira, R. C. L., Bícego, M. C., Lourenço, R. A., et al. (2007). Sedimentary Changes on the Southeastern Brazilian Upper Slope during the Last 35,000 Years. *Acad. Bras. Ciênc.* 79 (1), 171–181. doi:10.1590/S0001-37652007000100018

McManus, J. F., Francois, R., Gherardi, J.-M., Keigwin, L. D., and Brown-Leger, S. (2004). Collapse and Rapid Resumption of Atlantic Meridional Circulation Linked to Deglacial Climate Changes. *Nature* 428 (6985), 834–837. doi:10.1038/nature02494

Milliman, J. D., Troy, P. J., Balch, W. M., Adams, A. K., Li, Y.-H., and Mackenzie, F. T. (1999). Biologically Mediated Dissolution of Calcium Carbonate above the Chemical Lysocline? *Deep Sea Res. Part Oceanographic Res. Pap.* 46 (10), 1653–1669. doi:10.1016/s0967-0637(99)00034-5

Morard, R., Füllberg, A., Brummer, G. A., Greco, M., Jonkers, L., Wizemann, A., et al. (2019). Genetic and Morphological Divergence in the Warm-Water Planktonic Foraminifera Genus *Globigerinoides*. *PLoS One* 14 (12), e0225246–30. doi:10.1371/journal.pone.0225246

Nagai, R. H., Ferreira, P. A. L., Mulkherjee, S., Martins, M. V., Figueira, R. C. L., Sousa, S. H. M., et al. (2014). Hydrodynamic Controls on the Distribution of Surface Sediments from the Southeast South American continental Shelf between 23°S and 38°S. *Continental Shelf Res.* 89, 51–60. doi:10.1016/j.csr.2013.09.016

Naik, S. S., Godad, S. P., Naidu, P. D., Tiwari, M., and Paropkari, A. L. (2014). Early- to Late-Holocene Contrast in Productivity, OMZ Intensity and Calcite Dissolution in the Eastern Arabian Sea. *The Holocene* 24 (6), 749–755. doi:10.1177/0959683614526936

Nees, S., Armand, L., De Deckker, P., Labracherie, M., and Passlow, V. (1999). A Diatom and Benthic Foraminiferal Record from the South Tasman Rise (southeastern Indian Ocean): Implications for Palaeoceanographic Changes for the Last 200,000 Years. *Mar. Micropaleontology* 38 (1), 69–89. doi:10.1016/S0377-8398(99)00039-0

Pereira, L. S., Arz, H. W., Pätzold, J., and Portilho-Ramos, R. C. (2018). Productivity Evolution in the South Brazilian Bight during the Last 40,000 Years. *Paleoceanography and Paleoclimatology* 33, 1339–1356. doi:10.1029/2018pa003406

Peterson, R. G., and Stramma, L. (1991). Upper-level Circulation in the South Atlantic Ocean. *Prog. Oceanography* 26 (1), 1–73. doi:10.1016/0079-6611(91)90006810.1016/0079-6611(91)90006-8

Petit, J. R., Jouzel, J., Raynaud, D., Barkov, N. I., Barnola, J.-M., Basile, I., et al. (1999). Climate and Atmospheric History of the Past 420,000 Years from the Vostok Ice Core, Antarctica. *Nature* 399, 429–436. doi:10.1038/20859

Petró, S. M., and Burone, L. (2018). Changes in Water Masses in the Late Quaternary Recorded at Uruguayan Continental Slope (South Atlantic Ocean)/Mudanças Nas Massas De Água Durante O Quaternário Tardio Registadas No Talude Continental Uruguaio (Oceano Atlântico Sul). *J. Sed. Env.* 3 (4), 280–289. doi:10.12957/jse.201810.12957/jse.2018.39156

Petró, S. M., Costa, E. O., Pivel, M. A. G., and Coimbra, J. C. (2018a). Lysocline and CCD Fluctuations Record in Pelotas Basin during the Late Quaternary. *Anuário IGEO UFRJ* 41 (2), 710–719. doi:10.11137/201810.11137/2018_2_710_719

Petró, S. M., Pivel, M. A. G., and Coimbra, J. C. (2021). Evidence of Supra-lysoclinal Dissolution of Pelagic Calcium Carbonate in the Late Quaternary in the Western South Atlantic. *Mar. Micropaleontology* 166. doi:10.1016/j.marmicro.2021.102013

Petró, S. M., Pivel, M. A. G., and Coimbra, J. C. (2018b). Foraminiferal Solubility Rankings: a Contribution to the Search for Consensus. *J. Foraminiferal Res.* 48 (4), 301–313. doi:10.2113/gsjfr.48.4.301

Pimenta, F. M., Campos, E. J. D., Miller, J. L., and Piola, A. R. (2005). A Numerical Study of the Plata River Plume along the Southeastern South American Continental Shelf. *Braz. J. oceanography* 53 (3/4), 129–146. doi:10.1590/S1679-87592005000200004

Piola, A. R., Campos, E. J. D., Moller, O. O., Charo, M., and Martinez, C. (2000). Subtropical Shelf Front off Eastern South America. *J. Geophys. Res.* 105(C3) (726), 6565–6578. doi:10.1029/1999jc000300

Piola, A. R., and Matano, R. P. Ocean Currents: Atlantic Western Boundary|Brazil Current/Falkland (Malvinas) Current, in Encyclopedia of Ocean Sciences, (2017), pp. 422–430. doi:10.1016/B978-0-12-409548-9.10541-X

Piola, A. R., Matano, R. P., Palma, E. D., Möller, O. O., and Campos, E. J. D. (2005). The Influence of the Plata River Discharge on the Western South Atlantic Shelf. *Geophys. Res. Lett.* 32, L01603. doi:10.1029/2004GL021638

Portilho-Ramos, R. C., Cruz, A. P. S., Barbosa, C. F., Rathburn, A. E., Mulitza, S., Venancio, I. M., et al. (2018). Methane Release from the Southern Brazilian Margin during the Last Glacial. *Sci. Rep.* 8, 5948. doi:10.1038/s41598-018-24420-0

Portilho-Ramos, R. d. C., Ferreira, F., Calado, L., Frontalini, F., and de Toledo, M. B. (2015). Variability of the Upwelling System in the southeastern Brazilian Margin for the Last 110,000years. *Glob. Planet. Change* 135, 179–189. doi:10.1016/j.gloplacha.2015.11.003

Portilho-Ramos, R. d. C., Pinho, T. M. L., Chiessi, C. M., and Barbosa, C. F. (2019). Understanding the Mechanisms behind High Glacial Productivity in the Southern Brazilian Margin. *Clim. Past* 15 (3), 943–955. doi:10.5194/cp-15-943-2019

R Core Team. (2019). *R: A Language and Environment for Statistical Computing*. Vienna: Austria. http://www.R-project.org/.

Rasmussen, T. L., Thomsen, E., Troelstra, S. R., Kuijpers, A., and Prins, M. A. (2002). Millennial-scale Glacial Variability versus Holocene Stability: Changes in Planktic and Benthic Foraminifera Faunas and Ocean Circulation in the North Atlantic during the Last 60,000 Years. *Mar. Micropaleontology* 47 (1-2), 143–176. doi:10.1016/S0377-8398(02)001159

Ravello, A. C., and Hillaire-Marcel, C. (2007). "The Use of Oxygen and Carbon Isotopes of Foraminifera in Paleoceanography," in *Proxies in Late Cenozoic Paleoceanography*. Editors C. Hillaire-Marcel and A. De Vernal (Amsterdam: Developments in Marine Geology, Elsevier).

Reid, J. L., Nowlin, W. D., Jr., and Patzert, W. C. (1976). On the Characteristics and Circulation of the Southwestern Atlanitc Ocean. *J. Phys. oceanography* 7, 62–91. doi:10.1175/1520-0485(1977)007<0062OTCACO>2.0.CO;2

Rex, M. A., and Etter, R. J. (2010). *Deep-sea Biodiversity: Pattern and Scale*. Cambridge: Harvard University Press, 354

Rex, M., Etter, R., Morris, J., Crouse, J., McClain, C., Johnson, N., et al. (2006). Global Bathymetric Patterns of Standing Stock and Body Size in the Deep-Sea Benthos. *Mar. Ecol. Prog. Ser.* 317, 1–8. doi:10.3354/meps317001

Riebesell, U. (2004). Effects of CO2 Enrichment on Marine Phytoplankton. *J. Oceanography* 60, 719–729. doi:10.1007/s10872-004-5764-z

Rodrigues, A. R., Pivel, M. A. G., Schmitt, P., de Almeida, F. K., and Bonetti, C. (2018). Infaunal and Epifaunal Benthic Foraminifera Species as Proxies of Organic Matter Paleofluxes in the Pelotas Basin, South-Western Atlantic Ocean. *Mar. Micropaleontology* 144, 38–49. doi:10.1016/j.marmicro.2018.05.007

Rodrigues, L. F., Macario, K. D., Anjos, R. M., Ketzer, J. M. M., Maraschin, A. J., Augustin, A. H., et al. (2020). Origin and Alteration of Organic Matter in Hydrate-Bearing Sediments of the Rio Grande Cone, Brazil: Evidence from Biological, Physical, and Chemical Factors. *Radiocarbon*, 62, 197–206. doi:10.1017/RDC.2019.109

Schiebel, R. (2002). Planktic Foraminiferal Sedimentation and the marine Calcite Budget. *Glob. Biogeochem. Cycles* 16 (4), 1–21. doi:10.1029/2001GB001459

Schiebel, R., and Hemleben, C. (2017). *Planktic Foraminifers in the Modern Ocean, Pp. 358*. Berlin, Germany: Springer. doi:10.1007/978-3-662-50297-6

Schlitzer, R. (2020). Ocean Data View. Available at: https://odv.awi.de.

Schönfeld, J. (2012). History and Development of Methods in Recent Benthic Foraminiferal Studies. *J. Micropalaeontol.* 31, 53–72. doi:10.1144/0262-821X11-008

Shackleton, N. J. (2000). The 100,000-year Ice-Age Cycle Identified and Found to Lag Temperature, Carbon Dioxide, and Orbital Eccentricity. *Science* 289, 1897–1902. doi:10.1126/science.289.5486.1897

Shakun, J. D., Clark, P. U., He, F., Marcott, S. A., Mix, A. C., Liu, Z., et al. (2012). Global Warming Preceded by Increasing Carbon Dioxide Concentrations during the Last Deglaciation. *Nature* 484, 49–54. doi:10.1038/nature10915

Siccha, M., and Kucera, M. (2017). ForCenS, a Curated Database of Planktonic Foraminifera Census Counts in marine Surface Sediment Samples. *Sci. Data* 4, 170109. doi:10.1038/sdata.2017.109

Silveira, I. C. A. d., Schmidt, A. C. K., Campos, E. J. D., Godoi, S. S. d., and Ikeda, Y. (2000). A corrente Do Brasil ao Largo da Costa Leste Brasileira. *Rev. Bras. Oceanogr.* 48 (2), 171–183. doi:10.1590/S1413-77392000000200008

Smith, C. R., Berelson, W., Demaster, D. J., Dobbs, F. C., Hammond, D., Hoover, D. J., et al. (1997). Latitudinal Variations in Benthic Processes in the Abyssal Equatorial Pacific: Control by Biogenic Particle Flux. *Deep Sea Res. Part Topical Stud. Oceanography* 44 (9-10), 2295–2317. doi:10.1016/S09670645(97)00022-210.1016/s0967-0645(97)00022-2

Sortor, R. N., and Lund, D. C. (2011). No Evidence for a Deglacial Intermediate Water $\Delta^{14}C$ Anomaly in the SW Atlantic. *Earth Planet. Sci. Lett.* 310 (1–2), 65–72. doi:10.1016/j.epsl.2011.07.017

Sousa, S. H. M., de Godoi, S. S., Amaral, P. G. C., Vicente, T. M., Martins, M. V. A., Sorano, M. R. G. S., et al. (2014). Distribution of Living Planktonic Foraminifera in Relation to Oceanic Processes on the southeastern continental Brazilian Margin (23°S-25°S and 40°W-44°W). *Continental Shelf Res.* 89, 76–87. doi:10.1016/j.csr.2013.11.027

Souto, D. D., de Oliveira Lessa, D. V., Albuquerque, A. L. S., Sifeddine, A., Turcq, B. J., and Barbosa, C. F. (2011). Marine Sediments from southeastern Brazilian continental Shelf: A 1200year Record of Upwelling Productivity. *Palaeogeogr. Palaeoclimatol. Palaeoecol.* 299, 49–55. doi:10.1016/j.palaeo.2010.10.032

Stramma, L., and England, M. (1999). On the Water Masses and Mean Circulation of the South Atlantic Ocean. *J. Geophys. Res.* 104 (C9), 20863–20883. doi:10.1029/1999JC900139

Suárez-Ibarra, J. Y., Frozza, C. F., Petró, S. M., and Pivel, M. A. G. (2021). Fragment or Broken? Improving the Planktonic Foraminifera Fragmentation Assessment. *PALAIOS* 36, 165–172. doi:10.2110/palo.2020.062

Toledo, F. A. L., Cachao, M., Costa, K. B., and Pivel, M. A. G. (2007). Planktonic Foraminifera, Calcareous Nannoplankton and Ascidian Variations during the Last 25 Kyr in the Southwestern Atlantic: A Paleoproductivity Signature? *Mar. Micropaleontology* 64 (1-2), 67–79. doi:10.1016/j.marmicro.2007.03.001

Toledo, F., Costa, K. B., Pivel, M. A. G., and Campos, E. J. D. (2008). Tracing Past Circulation Changes in the Western South Atlantic Based on Planktonic Foraminifera. *Rbp* 11 (3), 169–178. doi:10.4072/rbp.2008.3.03

Viana, A. R. (2001). Seismic Expression of Shallow-To Deep-Water Contourites along the South-Eastern Brazilian Margin. *Mar. Geophys. Researches* 22, 509–521. doi:10.1023/A:1016307918182

Waelbroeck, C., Labeyrie, L., Michel, E., Duplessy, J. C., McManus, J. F., Lambeck, K., et al. (2002). Sea-level and Deep Water Temperature Changes Derived from Benthic Foraminifera Isotopic Records. *Quat. Sci. Rev.* 21, 295–305. doi:10.1016/S0277-3791(01)00101-9

Wefer, G., Berger, W. H., Bijma, J., and Fischer, G. (1999). "Clues to Ocean History: A Brief Overview of Proxies," in *Use of Proxies in Paleoceanography: Examples from the South Atlantic*. Editors G. Fischer and G. Wefer (Berlin Heidelberg: Springer-Verlag), 68. doi:10.1007/978-3-642-58646-0_1

Weinkauf, M. F. G., and Milker, Y. (2018). The Effect of Size Fraction in Analyses of Benthic Foraminiferal Assemblages: A Case Study Comparing Assemblages from the >125 and >150 μm Size Fractions. *Front. Earth Sci.* 6, 37. doi:10.3389/feart.2018.00037

Weinkauf, M. F. G., Moller, T., Koch, M. C., and Kučera, M. (2013). Calcification Intensity in Planktonic Foraminifera Reflects Ambient Conditions Irrespective of Environmental Stress. *Biogeosciences*, 10, 6639–6655. doi:10.5194/bg-10-6639-2013

Weschenfelder, J., Baitelli, R., Corrêa, I. C. S., Bortolin, E. C., and dos Santos, C. B. (2014). Quaternary Incised Valleys in Southern Brazil Coastal Zone. *J. South Am. Earth Sci.* 55, 83–93. doi:10.1016/j.jsames.2014.07.004

Wycech, J., Kelly, D. C., and Marcott, S. (2016). Effects of Seafloor Diagenesis on Planktic Foraminiferal Radiocarbon Ages. *Geology* 44 (7), 551–554. doi:10.1130/G37864.1

Yasuhara, M., Hunt, G., Cronin, T. M., Hokanishi, N., Kawahata, H., Tsujimoto, A., et al. (2012). Climatic Forcing of Quaternary Deep-Sea Benthic Communities in the North Pacific Ocean. *Paleobiology* 38 (1), 162–179. doi:10.1666/10068.1

Zamelczyk, K., Rasmussen, T. L., Husum, K., Haflidason, H., de Vernal, A., Ravna, E. K., et al. (2012). Paleoceanographic Changes and Calcium Carbonate Dissolution in the central Fram Strait during the Last 20 Ka. *Quat. Res.* 78, 405–416. doi:10.1016/j.yqres.2012.07.006

Zweng, M. M., Reagan, J. R., Antonov, J. I., Locarnini, R. A., Mishonov, A. V., Boyer, T. P., et al. (2013). *World Ocean Atlas.* Editor A. Mishonov Technical, 2013.

Conflict of Interest: The authors declare that the research was conducted in the absence of any commercial or financial relationships that could be construed as a potential conflict of interest.

Publisher's Note: All claims expressed in this article are solely those of the authors and do not necessarily represent those of their affiliated organizations, or those of the publisher, the editors and the reviewers. Any product that may be evaluated in this article, or claim that may be made by its manufacturer, is not guaranteed or endorsed by the publisher.

frontiers | Frontiers in Marine Science

ORIGINAL RESEARCH
published: 31 May 2022
doi: 10.3389/fmars.2022.846976

REE Anomalies Changes in Bottom Sediments Applied in the Western Equatorial Atlantic Since the Last Interglacial

*Thiago A. Sousa[1], Igor Martins Venancio[1], Eduardo Duarte Marques[2], Thiago S. Figueiredo[1], Rodrigo Azevedo Nascimento[1], Joseph M. Smoak[3], Ana Luiza S. Albuquerque[1], Claudio Morisson Valeriano[3,4] and Emmanoel Vieira Silva-Filho[1]**

[1] Geoscience (Geochemistry) Graduate Program (Environmental Geochemistry), Fluminense Federal University, Niterói, Brazil, [2] Geological Survey of Brazil (SGB/CPRM), Belo Horizonte Regional Office, Belo Horizonte, Brazil, [3] School of Geosciences, University of South Florida, St. Petersburg, FL, United States, [4] Tektos - Geotectonic Research Group of the Faculty of Geology, State University of Rio de Janeiro (UERJ), Rio de Janeiro, Brazil

OPEN ACCESS

Edited by:
Miguel Angel Huerta-Diaz, Autonomous University of Baja California, Mexico

Reviewed by:
Yuan-Pin Chang, National Sun Yat-sen University, Taiwan
Daniel Smrzka, University of Vienna, Austria

***Correspondence:**
Emmanoel Vieira Silva-Filho
emmanoelvieirasilvafilho@id.uff.br

Specialty section:
This article was submitted to Marine Biogeochemistry, a section of the journal Frontiers in Marine Science

Received: 31 December 2021
Accepted: 19 April 2022
Published: 31 May 2022

Citation:
Sousa TA, Venancio IM, Marques ED, Figueiredo TS, Nascimento RA, Smoak JM, Albuquerque ALS, Valeriano CM and Silva-Filho EV (2022) REE Anomalies Changes in Bottom Sediments Applied in the Western Equatorial Atlantic Since the Last Interglacial. Front. Mar. Sci. 9:846976. doi: 10.3389/fmars.2022.846976

We reconstruct paleoredox conditions in the Western Equatorial Atlantic (WEA) over the glacial-interglacial cycle (~130 ka) by using new high-resolution REEs data and their anomalies from a marine sediment core (GL-1248) collected from the equatorial margin off the continental shelf of NE Brazil. This approach aims to improve the understanding of the dynamics of paleoclimatic and sedimentary inputs on the coast of northeastern Brazil. Marine sediments were analyzed *via* Mass Spectrometry (ICP-MS) after total digestion with HF/HNO_3. REEs proxies are a useful tool in understanding the transport and origin of sediments due to their physicochemical properties. Our data showed the Parnaíba River was the main source of REEs content in the western South Atlantic. Fe minerals (Fe-oxyhydroxides) produced *via* weathering of continental and tropical soils were the principal REE-carrier phase during transportation and ultimate deposition at core site GL-1248. Several regional climatic factors mainly rainfall changes contributed significantly to continental-REEs erosion of sedimentary layers of the Parnaíba Basin, and transport and deposition of the mobilized REEs from the continent to the study site. Furthermore, changes in the negative Ce-anomaly showed low variation along the core indicating a reduction in deep ocean oxygenation during the interglacial relative to the last glacial period. That variation, probably, was associated with glacial-interglacial variations in sea level with the exposure of the continental shelf. The origin of positive Eu anomalies in siliciclastic sediment, also observed in the core, was explained by preferential retention by feldspars such as plagioclases and potassium feldspars mostly from the assimilation of felspar during fractionation crystallization of felsic magma in the Parnaíba basin since the Last Interglacial.

Keywords: Rare Earth Elements, glacial-interglacial, weathering, Parnaíba Basin, sea level, Northeast Brazil

INTRODUCTION

The pattern of abundance in rare earth elements (REEs) has been applied as a reliable geochemical tool in paleoenvironmental and paleoclimatic studies to trace weathering, provenance, and climate changes that have occurred on the continent during the past (Taylor and McLennan, 1985). This is possible due to the physical and chemical characteristics of the REEs due to their electron configuration (+3), poor solubility, and the low concentrations in the waters of rivers and oceans. The REEs utility is further enhanced by its strong binding capability with sediments, low natural background levels, chemical stability, and low mobility (Antonina et al., 2013). Furthermore, REEs has a specific chemical behavior along the sedimentary column and differences in atomic weight strongly allows fractionation during geochemical processes that can be observed *via* normalization (Yusof et al., 2001). The exception to this rule is Ce and Eu, which, unlike the other REEs, can be subjected to the effects of redox processes, alternating their trivalent valences to Ce^{4+} and Eu^{2+} (De Baar et al., 1983; German and Elderfield, 1990).

Over the last few decades, much attention has been given to the application of Ce anomalies in paleoceanographic studies examining bottom water redox conditions (Wright-Clark and Holser, 1981; Elderfield and Pagett, 1986; Wang et al., 1986; Liu et al., 1988; Liu and Schmitt, 1990; Pattan et al., 2005; Tostevin et al., 2016), tectonic and stratigraphic reconstruction (Murray et al., 1990a; Murray et al., 1990b), diagenetic process (German and Elderfield, 1990; Murray et al., 1991) and as a potential indicator of eustatic sea-level changes (Wilde et al., 1996). Moreover, Ce-anomalies may help identify systematic variations in the sedimentary column, and the evolution of the environment by natural processes of continental erosion and autochthonous supply by continental shelf environments (Tostevin et al., 2016). Thus, it is also possible to investigate past climatic events and their consequences for the sedimentary dynamics (Xu et al., 2011). However, studies focusing on using REEs proxies for understanding paleoredox conditions in the western equatorial Atlantic (WEA) are still scarce. A wide approach on the topic is limited by the fact that in tropical/equatorial regions, the chemical and mineralogical composition of the sediment transported by rivers is strongly dependent on parent rock in the drainage basin, the intensity of weathering, and various grain sizes effects (Bouchez et al., 2011; Rousseau et al., 2019).

A recent study by Bohm et al. (2015) indicated a strong rate of ventilation in the deep Atlantic during interglacial periods. In the middle to deep Atlantic, a higher oxygenation rate was observed during the same period concerning glacial periods (Jaccard and Galbraith, 2012; Hoogakker et al., 2015). Moreover, millennial variations in redox conditions in the deep Atlantic are widely observed during the last glacial period (Hoogakker et al., 2015; Gottschalk et al., 2016). The reduction in glacial ocean oxygenation was possibly caused by increases in the biological pump, due to the remineralization of organic matter, and by the decrease in the rate of deep ocean ventilation associated with the reorganization of ocean circulation. Meanwhile, the Atlantic meridional overturning circulation (AMOC) in its warm mode during interglacial periods ventilates the mid-to-deep Atlantic Ocean (Rahmstorf, 2002). Many studies support the accumulation of remineralized carbon in the deep ocean during glacial periods (Curry and Oppo, 2005; Chalk et al., 2019). Given the depth of the GL-1248 sediment core (2264 m), it is expected to record changes in mid-depth Atlantic redox conditions over the last glacial-interglacial variation cycle.

Here, we present high-resolution data for the reconstruction of paleoredox conditions in the WEA over the glacial-interglacial cycle using REEs content and their anomalies from marine sediment core (GL-1248) collected along the equatorial Brazil margin off the continental shelf of NE Brazil. In addition, we compare our data with other relevant geochemical proxies and mineralogical information, to better constrain the causes behind the observed paleoredox changes, related to both drivers on the continent and Brazilian equatorial margin.

MATERIALS AND METHODS

Location, Lithology, and Sampling

A 19.29-m long marine sediment core (GL-1248) was collected at a water depth of 2264-m by Petróleo Brasileiro S.A. (Petrobrás) on the continental slope off the coast of northeastern Brazil (0°55.2'S; 43°24.1'W). The core location was 170 km off the coastline and 280 km to the north of the mouth of the Parnaiba River (**Figure 1**).

Venancio et al. (2018) previously described the lithological composition of GL-1248. It consists of greenish to olive sediments rich in silty clay between 1.00-12.99 m and 16.60-19.29 m. The sedimentary interval between 0-1.00 m and 12.99 to 16.60 m contains carbonate-rich sediments represented by more reddish and whitish clays.

The sub-sampling from core GL-1248 was conducted at the Operational Oceanography Laboratory (LOOP- UFF) by slicing at a resolution of 1 sample for every 4 centimeters. These samples were identified with core ID (GL-1248) followed by layer number, packed in an ultra-freezer, and subsequently freeze-dried. The lyophilized samples were ground using an agate mortar to homogenize particle size. The dry powder was weighed on a high precision analytical balance with 150 mg per sample and posteriorly inserted into porcelain crucibles. After that, the vessel was left in a muffle oven heated to 500°C for about 4 hours to eliminate the organic matter.

Sediment Core Chronology

The depth-age model of GL-1248 indicated the core covers the last 130 thousand years (details of the depth-age model can be seen at Venancio et al., 2018). The age model is based on 12 Accelerator Mass Spectrometry (AMS) radiocarbon ages for the upper 6.30-m core depth (~ 43.670 ka). For the lower part of core GL-1248 (6.30 to 16.66 m core depth; ~ 44-128 ka), ages were obtained through the alignment of the Ti/Ca ratio to the ice $\delta^{18}O$ record of the North Greenland Ice Core Project (Members, 2004; Wolff et al., 2010). They were established as MIS 1 (starts at 14 ka before present), MIS 3 (29–57 ka), MIS 4 (57–71 ka), MIS 5a (peak at 82 ka), MIS 5b (peak at 87 ka), MIS 5c (peak at 96 ka), MIS 5d (peak at 109 ka), MIS 5e (peak at 123 ka).

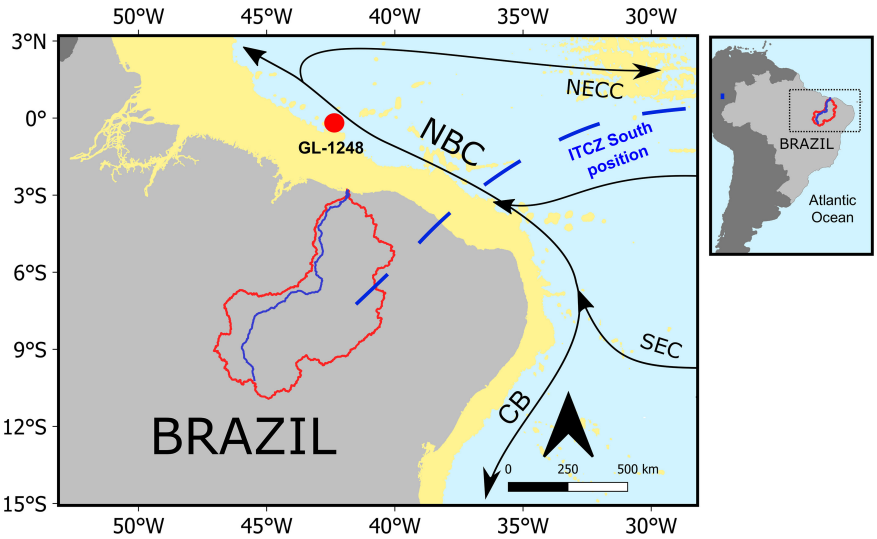

FIGURE 1 | The regional map shows the location of marine core GL-1248 from the western equatorial Atlantic (WEA) with the southmost position of the Intertropical Convergence Zone (ITCZ) during the end of austral summer (March-April). The core is represented by the red dot in geographic coordinates 0°55.2'S, 43°24.1'W; 2.264 m. The map also shows relevant surface currents such as the South Equatorial Current (SEC), North Equatorial Countercurrent (NECC), Brazilian Current (BC), and the North Brazil Current (NBC) in black arrows. The dashed blue line displays the approximate southern position of the Intertropical Convergence Zone (ITCZ) during austral summer (December–March). Source: References of Paleorecords according to Wang et al. (2004); Nace et al. (2014), Dupont et al. (2010), Zhang et al. (2015), figure adapted by Piacsek, 2020.

Geochemical Analysis

As described by Fadina et al. (2019), core GL-1248 was sampled every 4 cm (323 total samples) for bulk analyses, as Total Organic Carbon (TOC, in %) and stable isotopes ($\delta^{13}C$ and $\delta^{15}N$) analyses. Each sample was encapsulated in a tin (Sn) capsule after carbonate removal *via* acidification with 1 M HCl, 60 mg of dried and pulverized sediment. The bulk analysis was performed using a PDZ Europa ANCA-GSL elemental analyzer at the Stable Isotope Facility of the University of California, Davis (USA) with an analytical precision of ± 0.09%.

Elemental intensities of core GL-1248 (Fe, Ti, Ca, K, Al, and Mn) were obtained by scanning the split core surfaces of the archive halves with X-ray fluorescence Core Scanner II (AVAATECH Serial number 2), which is a semi-quantitative method for stepwise geochemical characterization of sediment cores at MARUM, University of Bremen (Germany). The XRF measurements were made downcore every 0.5 cm by irradiating 10 mm to 12 mm of the surface for the 20s at 10 kV. For a detailed description of the method, see Venancio et al. (2018).

REE Preparation

The approximately 0.150 g of the marine sediments samples (a total of 310) were roasted in muffle furnace for 2 hours at 450°C. After roasting time was achieved, samples were unloaded immediately from muffle furnace and were kept in desiccator to cool down. Each roasted samples were reweighed on a high precision analytical balance (± 0.0001g precision) to a total weight of about 0.1 g and added in the vessel to be digested in a Microwave (Speedwave®four - Berghof) with 4.0 mL mono-distilled nitric acid (HNO_3 65%) and 1.0 mL hydrofluoric acid (HF 70%) using the established US EPA method (Environmental Protection Agency 3052 Method). The goal of this method is total samples decomposition with judicious choice of acid combinations to give the highest recoveries for the target analytes. The mono-distilled nitric acid (HNO_3 65%) was used to effect sample digestion in microwave, while hydrofluoric acid (HF 70%) is capable of dissolving silicates contained in the sample. At the end of the process, the resulting solution was filtered with chemical analysis qualitative filter paper into a second acid-cleaned container and added the volume up to 15 mL with dilute solutions of boric acid (H_3BO_3) to avoid problems with HF permitting the complexation of fluoride to protect the quartz plasma torch. REEs and some trace elements (U and Th) of core GL-1248 were measured by ICP-MS (NexION 300D, Perkin Elmer, USA) at the LEA (Atomic Spectrometry Laboratory) at the Federal University of Espirito Santo (UFES). De Sousa et al. (2021) described the analytical standard procedures in detail. REEs patterns for selected samples from the core were normalized according to Post-Archean Australian Shale (PAAS) (Taylor and McLennan, 1985; Pourmand et al., 2012). The analytical precision and accuracy were better than ± 8% for the investigated elements. This was assessed with reference material (PACS-2 - Marine Sediment Reference Materials for Trace Metals and other Constituents) and by the results of the duplicate measurements of eight sediment samples, as well as duplicate measurements of reference material samples. Rare earth elements were divided into light REEs (LREEs, from La to Nd), middle REEs (MREEs, from Sm to Ho), and heavy

REEs (HREEs, from Er to Lu) according to Henderson (1984) and their ratios were calculated.

Cerium Anomaly

The extent of the Cerium anomaly is defined by the δCe [Ce]/[Ce*] ratio, where [Ce] is the cerium concentration and [Ce*] is the theoretical non-anomalous value interpolated from La and Nd values, according to the following equation below:

$$Ce/Ce* = 3Ce_N/(2La_N + Nd_N) \quad \text{Equation 1}$$

Where "**N**" refers to REEs normalized by Post Archean Average Australian Shale (PAAS; (Taylor and McLennan, 1985).

When Ce is relatively depleted compared to other REEs (Ce/Ce* < 1) a negative Ce-anomaly is observed suggesting an oxic environment condition (German and Elderfield, 1990; Pattan et al., 2005). Conversely, a positive Ce-anomaly results when Ce is enriched relative to its neighbors (Ce/Ce* > 1), suggesting anoxic/suboxic environment condition (German and Elderfield, 1990; Pattan et al., 2005).

Europium Anomaly

Another similar REEs anomaly that is occasionally recorded by Europium, represented by the δEu [Eu/Eu*] ratio, where [Eu] is the europium concentration and [Eu*] is the value obtained at the europium position by straight-line interpolation between the plotted points for Sm and Gd, according to the following equation below:

$$Eu/Eu* = Eu_N/(Sm_N + Gd_N)^{1/2} \quad \text{Equation 2}$$

where N refers to PAAS-normalized values developed by Pourmand et al. (2012).

Where "**N**" refers to REEs normalized by Post Archean Average Australian Shale (PAAS; (Taylor and McLennan, 1985).

When Eu is relatively enriched compared to other REEs (Eu/Eu* > 1) a positive Eu-anomaly suggests sediments and some sedimentary rocks containing a high amount of feldspar minerals, while negative Eu-anomaly indicate depletion or fractionation of the same mineral (Absar and Sreenivas, 2015; Liu et al., 2015).

Mineralogical Analysis

Mineralogical characterization was performed on 40 pulverized representative samples distributed within each marine oxygen isotope stage (MIS) of core GL-1248, using an X´PERT PRO MPD (PW 3040/60) X-ray powder diffractometer (XRD) with CuKα1 radiation (λ = 1,5406 Å) at the Mineral Analysis Laboratory (LAMIN), Mineral Resources Research Company (CPRM), Manaus, Amazonas, Brazil. Diffractograms were collected using Voltage 40kv, Current 40A, 2⊖ between 5° to 70° with a step size of 0.02° and 50s scanning time. For mineral identification, generated patterns were compared with a database from the International Center for *Diffraction Data – Powder Diffraction File* (ICDD-PDF). The patterns are specific to each mineral (i.e. quartz, 46-1045), and there may be different patterns for the same mineral, especially when there are variations in the chemical composition, solid solutions, etc.

RESULTS

Age Model and Sedimentation Rates

The depth-age model of core GL-1248 based on the AMS radiocarbon ages for the upper 6.3-m depth yielded an age of 44.0 ± 0.7 ka. For the lower part of the core (6.30 to 16.66 m core depth) ages were obtained through the alignment of the Ti/Ca ratio and the $\delta^{18}O$ record from the North Greenland Ice Core Project (Members, 2004; Wolff et al., 2010) with ages ranging from 44.0-129.0 ka. The sedimentary record includes a sedimentary hiatus between 2.18 m and 1.70 m (29.1 and 14.8 ka, respectively).

The sedimentary core profile comprises 4 marine isotope stages (MIS 1 to 5, excluding 2) according to changes in temperature derived from deep-sea core sample data (Lisiecki and Raymo, 2005). Diverse sedimentation rates (SR) are observed over MIS indicating a large fluctuation within the record (**Figure 2**). During MIS 5 (from ~ 128.0 ka to 71.0 ka), SR varies with the highest occurring within the MIS 5a (25.7 cm/kyr), whereas rates during MIS 5e are relatively constant at 6.93 cm/kyr. The glacial period MIS 4 (from ~ 71.0 ka to 57.0 ka) started with low SR (an average value of 13.0 cm/kyr) and increased notably during MIS 3 (from ~ 57.0 ka to 29.0 ka) reaching an average value of 32.1 cm/kyr.

An unusually low SR (3 cm/kyr) between 2.18 and 1.70-m core depth (from ~ 14.0 and 29.0 ka) is due to the hiatus, as reported for the region and period, although no significant lithological changes were observed. The hiatus covers every Henrich Stadials 1 (HS 1), where is characterized by abrupt records, on a millennial-scale, of precipitation in northeastern Brazil (Arz et al., 1998; Cruz et al., 2006; Zhang et al., 2015). This increase in the frequency of rainfall intensity also occurred within the Parnaíba River Basin and increased the discharge of terrestrial material to the ocean. Continuously, the entry of more continental debris favored greater kinetic and drag energy to the mouth of the Parnaíba River and the steep continental slope. The core GL-1248 was collected in a region with a high slope and under the influence of these phenomena on a millennial-scale. The origin of the hiatus comes from the high-energy input of the detrital material and the steep angle of the continental slope, which caused a collapse in the sedimentary record during sedimentation. Finally, the SR values during MIS 1 (starts at 14 ka before present) are irregular. Variations between 5.42 and 24.23 cm/kyr, with the highest values, reached within the interval of occurrence of abrupt events on a millennial-scale recorded (i.e. Younger Dryas) in the intervals 1.26 and 0.69 cm in the depth of core GL-1248.

Total REE and Trace Elements Distribution

The REE concentration vertical distributions of core GL-1248 are plotted in (**Figure 2**). The total REE concentrations (sum of La to Yb, excluding Tb, Ho, Tm, and Lu) of the sediment samples varied between 42.93 and 231.06 μg/g (with an average value of 152.44 μg/g). The highest ΣREE concentration values (231.06 μg/g) were recorded at 78 ka (1258-cm depth) within MIS 5. ΣREE concentrations were particularly high in glacial phases (MIS 4 and MIS 3), as well as in MIS 5a (MIS 5 interglacial sub-stage). In

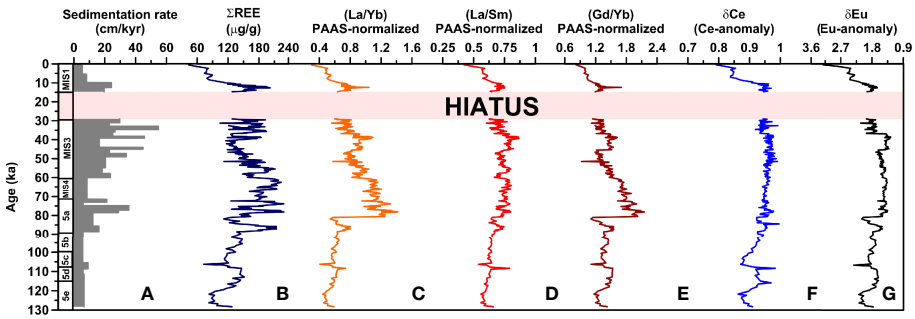

FIGURE 2 | Core GL-1248 profiles of **(A)** Sedimentation rate (cm/kyr) (Venancio et al., 2018), **(B)** ΣREE (μg/g), **(C)** $(La/Yb)_N$, **(D)** $(La/Sm)_N$, **(E)** $(Gd/Yb)_N$, **(F)** δCe (Ce-anomaly), and **(G)** δEu (Eu-anomaly). The dashed light red line marks a hiatus between 14.7 and 29.1 ka. **"N"** is representing the chondrite-normalization by PAAS (Post Archean Australian Shale) (Taylor and McLennan, 1985). Marine isotope stages (MIS) boundaries in this studied time interval are numbered from 1 to 5 (MIS 1, 3, and 5).

comparison, the lowest ΣREE concentration values (42.93 and 55.84 μg/g) were recorded on top-core (0.49 and 1.22 ka, respectively) within the MIS 1. ΣLREE (sum from La to Nd) varied between 30.12 and 198.92 μg/g (with an average of 127.00 μg/g), while ΣMREE and ΣHREE varied between 9.08 and 28.37 μg/g (with an average of 19.57 μg/g), and between 3.73 and 8.46 μg/g (with an average of 5.86 μg/g), respectively. Hence, ΣLREE is more abundant in nature than ΣMREE and ΣHREE. Both the ΣLREE/HREE ratios (8.08-21.84) and the ΣLREE/MREE ratios (3.32-7.97) are lower values than PAAS (28.31 and 10.05, respectively) (**Table S1**) (Taylor and McLennan, 1985). $(La/Yb)_N$ ratios PAAS-normalized varied between 0.30 and 1.42 μg/g (with average of 0.82 μg/g). The $(La/Gd)_N$ and $(Gd/Yb)_N$ PAAS-normalized ratios varied between 0.37 and 0.68 μg/g (with an average of 0.57 μg/g), and between 0.82 and 2.15 μg/g (with an average of 1.43 μg/g), respectively. The REEs profile distributions for their normalized ratios [$(La/Yb)_N$, $(La/Sm)_N$, and $(Gd/Yb)_N$] show a similar value with a marked increase of about 80 ka and a strong decrease of about 14 ka in core GL-1248. This maximum value obtained for REEs profile distribution coincides with the highest SR occurring within MIS 5a (25.7 cm/kyr), as well as a strong decrease in the SR right after abrupt Younger Dryas events (from 16.28 cm/kyr to 8.13 cm/kyr).

Anomalies in δCe and δEu

The negative δCe (Ce/Ce* < 1) values varied from 0.79 to 0.99 (with a mean value of 0.94) over the last 128 ka with a clear abrupt drop from the glacial period (near to 13 ka) to the top core (Interglacial period) (**Table S2**). The highest negative δCe of 0.99 occurs at the bottom core (near to 84 ka; 1341-cm depth), while the lowest negative δCe of 0.79 occur in modern conditions over the interglacial period (0.49 ka near to the top of core). The Interglacial periods (MIS 1 and MIS 5e), and the warm sub-stage of MIS 5 (MIS 5c) with opposing climatic conditions show a relatively large variability with minimum values of 0.79 (top core), 0.86 (~106 ka), 0.871 (~122 ka), respectively. The negative δCe during MIS 4 and MIS 3 has a relatively low variability with mean values ranging between 0.95 and 0.96, respectively.

The positive δEu (Eu/Eu* > 1) values varied from 1.28 to 3.22 (with a mean value of 1.68) with a strong decrease from the top core towards glacial periods (**Table S2**). Hence, the highest positive δEu of 3.22 occurs in the bottom core (near the top core of 0.49 ka), while the lowest positive δEu of 1.28 occurs proximate in the glacial condition around 38.59 ka (523-cm depth). Both modern condition and bottom core with interglacial period show variability with mean values ranging between 2.09 and 1.71, respectively, followed by MIS 3 mean values of 1.59. The highest δEu values coincide with the increase in RSL (relative sea level), and vice-versa (**Figure 2**).

Mineralogy

The mineralogical spectrum obtained through XRD of core GL-1248 revealed a moderate range array of minerals assembly over the last 130 ka. Forty samples were identified in the marine sediment predominantly quartz, calcite, and kaolinite. Other secondary minerals include biotite, feldspars potassium, smectite, calcite magnesium, and halite. The occurrence of iron oxide minerals as goethite was described by Fadina et al. (2019) of core GL-1248. In general, continent-sourced minerals such as quartz and kaolinite were observed during the interglacial and glacial periods (both cold and warm substages). Marine sourced minerals such as calcite were observed also over the core. Smectite clay mineral was identified in small proportions during MIS 4 and MIS 5. (See more in **Table S3**).

DISCUSSION

Glacial-Interglacial Controls on REE-Carrier Phases

Along with geochemical processes, the terrigenous material is transferred to the oceans as suspended sediments in rivers (Milliman and Maede et al., 1983) carrying information about the characteristics of the source areas and past climate changes over the continent (Bentahila et al., 2008; Revel et al., 2010; Revel et al., 2014; Revel et al., 2015; Walter et al., 2000). Weathering,

erosion, transport, deposition, and burial processes control the final composition of the deep-sea sediments (Johnsson et al., 1991; Johnsson, 1993; Morton and Hallsworth, 1999). The geological substrate under the action of weathering and climatic agents reflects a signature characteristic of the adjacent continent to the drainage basins (Depetris et al., 2003). Marine sediment cores have a high capacity to preserve valuable information about changes in sedimentary provenance and continental climate changes (De Sousa et al., 2021). Specifically, REEs are useful, as they do not fractionate during sedimentary processes, which widely distributed in continental rocks. As shown in **Figure 2**, high ΣREE records during glacial periods are coincident with elevated terrigenous depositions recorded in core GL-1248 (Venancio et al., 2018) linked to low relative sea level (Waelbroeck et al., 2002) during glacial periods and millennial-scale changes recorded in Ti/Ca ratios from sediment cores in the WEA (Arz et al., 1998; Wang et al., 2004; Jaeschke et al., 2007; Govin et al., 2012; Nace et al., 2014). These terrigenous loads are characteristic of glacial periods linked to low relative sea levels (Arz et al., 1999; Jaeschke et al., 2007). A combination of regional climatic factors, such as amplified wet deposition with enhanced precipitation and erosion, might be responsible for an increase of REEsconcentration reported in core GL-1248. Overall, REE concentration reported in core GL-1248 mixed in response to glacial-interglacial changes by, providing a high material transport combined with a low sea level. In opposite climatic conditions to glacial periods, as MIS 1 and 5e, beyond the warm sub-stage, MIS 5c exhibited less REE concentration and high sea-level recorded in core GL-1248, because of low regional precipitation and erosion, featuring the warm periods. Hence, REEs peaks that occurred at the end of MIS 5a (230.88 μg/g; ~74 ka) are incompatible with these trends observed in our data over interglacial periods. However, these peaks are coincident with Ti/Ca and Ti/Ca peaks and may be linked to Dansgaard-Oeschger (DO) stadials (**Figure 2**). In opposite, the average REE concentrations were appreciably low over both MIS 1 (125.78 μg/g) and 5e (109.15 μg/g) interglacial periods, when the RSL reached –17.46 m and –13.85 m, respectively. According to Rama-Corredor et al. (2015), over the MIS 5e (SST = 28.9°C) interglacial experienced higher temperatures than MIS 1 (SST = 28.3°C), which are attributed to processional modulation (Martrat et al., 2014). Higher SST observed in interglacial periods are reported in numerous studies as ice sheet reduction and consequently sea level increased by up to 5 m more than modern sea level (Hodgson et al., 2006; Rohling et al., 2007). The increase in sea level has most likely repositioned the mouth of the Parnaiba River farther from the core, reducing the supply of continental material. Therefore, the lower REEs average concentrations displayed in MIS 5e concerning MIS 1 justify the retention of a supply of continental material in the area site of core GL-1248.

Iron oxyhydroxides have an important role in controlling the REEs profile in core GL-1248 and from the correlation between ΣREE composition and $Fe_{(XRF)}$, there were three potential reservoirs (lithogenic, carbonates, and Fe-Mn oxides). A positive correlation with $Fe_{(XRF)}$ can be explained by tropical soil characteristics in the study region (**Figure 3**). In a recent study using the same core, Fadina et al. (2019) observed the presence of iron oxides (and oxyhydroxides) minerals, such as goethite in all samples. In addition, geochemical analysis in the $\delta^{13}C_{org}$ and $\delta^{15}N_{org}$ variations in GL-1248 support the earlier hypothesis that higher amounts of continent-derived materials were deposited on the continental slope of NE Brazil in the glacial periods as opposed to interglacial periods. Thus, these results are consistent with our XRD mineralogy results which follow the same glacial-interglacial alteration in the origin marine sediment GL-1248. In tropical Fe-rich oxide soils, as occur in northeastern Brazil, Fe-oxyhydroxides are important cementing agents and as such play an important role in the metal adsorption processes in this region (Seaman, 2013). According to Bigham et al. (2002) the tropical soil profile of northeastern Brazil was described as having a notable high content of iron oxides mainly goethite and ferrihydrite; an amorphous Fe-oxyhydroxide precursor of hematite formation (Bigham et al., 2002). Hence, REEs content bearing Fe particles derived from the weathering and erosion from the Parnaíba Basin increased in the supply of magnetic material (i.e. magnetite and/or hematite), that was transported by Parnaíba River until they are immobilized on the continental slope. These correlations coincide with an increase in precipitation on the continent in NE Brazil during the wetter conditions related to MIS 4 (De Sousa et al., 2021). Therefore, our results suggests that Fe-oxides may be a principal REE-carrier phase from a marine sediment core GL-1248.

Origin of the Negative Ce-Anomaly in WEA

Studies suggest that the Ce anomaly can be used as a proxy for oxygenation conditions in paleoceanography (German et al., 1990; Schijf et al., 1994; Tostevin et al., 2016). In this study, we presented a sub-millennial resolution record of Ce anomaly since the Last Interglacial. Given the water depth of the sediment core GL-1248 (2.264 m), we expect to observe changes in redox conditions of the mid-depth Atlantic over the last glacial-interglacial cycle. Indeed, our results show a remarkable glacial-interglacial variation (**Figure 4**). A negative Ce anomaly is observed during warm interglacial periods. Conversely, during the end of MIS 5 and over the glacial period, Ce presents no depletion relative to compared to other REEs (Ce anomaly = ~1). Meanwhile, no outstanding millennial variations in the Ce anomaly were observed through the record.

Curiously, our results indicate a reduction in deep ocean oxygenation during the interglacial relative to the last glacial period. These results contradict the well-known notion of a strong deep Atlantic ventilation rate during warm interglacial periods (Böhm et al., 2014). Indeed, previous studies show a higher mid to deep Atlantic oxygenation during interglacial relative to glacial periods (Jaccard and Galbraith, 2012; Hoogakker et al., 2015). Besides, millennial variations in deep Atlantic oxygenation conditions are widely observed during the last glacial period (Hoogakker et al., 2015; Gottschalk et al., 2016), which, despite the sub-millennial resolution, was not found in our Ce anomaly record. The reduced glacial deep ocean oxygenation was caused by an increase in the biological pump, due to the organic matter remineralization, and the decreasing of deep ocean ventilation rate associated with the reorganization of ocean circulation (Hoogakker et al., 2015;

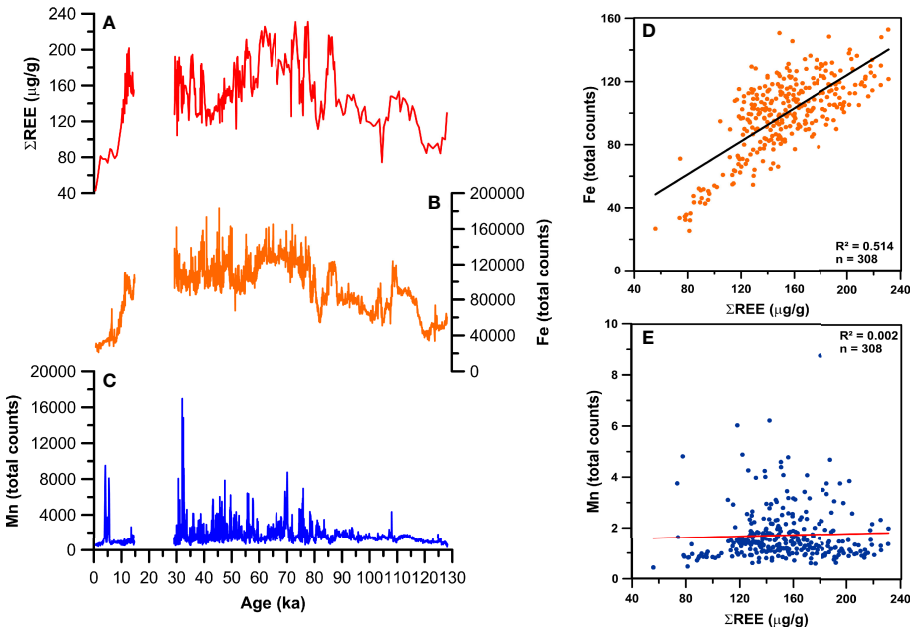

FIGURE 3 | Fe and Mn-REE relationship across the marine sediment studied with; **(A)** Plot of ΣREE concentration (red line) in GL-1248; **(B)** Plot of Fe total counts (orange line) in GL-1248; **(C)** Plot of Mn total counts (dark blue line) in GL-1248; **(D)** positive linear regression between Fe total counts (XRF) and ΣREE indicated by trendline (black line), equation correlation coefficient (R^2 = 0.514); and **(E)** weakly linear regression between Mn total counts (XRF) and ΣREE indicated by trendline (red line), equation correlation coefficient (R^2 = 0.002). ΣREE is shown in µg/g.

Jaccard et al., 2016). Meanwhile, the AMOC in its 'warm' mode during interglacial periods ventilates the mid to deep Atlantic Ocean (Rahmstorf, 2002). Many studies support the accumulation of remineralized carbon in the deep ocean during glacial periods (Curry and Oppo, 2005; Chalk et al., 2019). Together, these results indicate that the Ce anomaly in sediment core GL-1248 was not recording changes in paleoredox conditions of the mid-depth Atlantic in the Brazilian equatorial margin region. This poses the question; what does control the observed glacial-interglacial variation in Ce anomaly? Here we suggest that changes in Ce anomaly were caused by glacial-interglacial variations in sea level through its control on the exposure of the continental shelf. Given its flat morphology, eustatic changes in sea level during glacial-interglacial cycles may result in rapid exposure or drowning of the continental shelf in the Brazilian equatorial margin. Sediment core GL-1248 shows a higher sedimentation rate during the glacial relative to interglacial MIS 5 and MIS 1 (Venancio et al., 2018). This was caused by the lower sea level during glacial periods, allowing terrigenous material, with no Ce anomaly to be discharged directly onto the continental slope, near-site GL-1248. Conversely, during high sea-level periods, the terrigenous input was reduced due to the drowning of the continental shelf, which increased the percentage of biogenic $CaCO_3$ in bulk sediment. Studies indicate that biogenic $CaCO_3$ shows Ce depletion relative to the other REEs, resulting in a negative Ce anomaly in $CaCO_3$-rich sediments (Pattan et al., 2005). Therefore, we argue that a higher proportion of $CaCO_3$ relative to continental material caused the negative Ce anomaly during interglacial periods in GL-1248. Indeed, the reduction in terrigenous input to site GL-1248, as can be exemplified by reduced ΣREE, and enhanced accumulation of biogenic $CaCO_3$ during warm periods in the western equatorial Atlantic (Rühlemann et al., 1996) corroborate our hypothesis.

Given that the continental shelf break starts at about 40 m water depth in the Brazilian equatorial margin, our Ce anomaly only responded to changes in sea level above this isobath. This explains fast changes in Ce anomaly late during termination 1 (~10.5 ka) and no changes during the end of MIS 5 and the over the glacial period when the sea level was near or below the continental shelf break. Furthermore, the similar geochemical behavior of sensitive redox elements such as the Uranium element along the curve of cerium anomalies reinforces the argument that what modulates the conditions discussed within the sediment is not the presence of oxygen in the water column, but the depth of oxygen penetration (**Figure 5**). Additionally, the sedimentation rate can play a key role as they allow more time for the diffusion of uranyl ions from the water column into the sediment (Crusius and Thomson, 2000; Tribovillard et al., 2006).

The Continental Response of Europium Anomalies to Paleoclimate Changes in NE Brazil

Several studies in marine sediments suggest that the positive Eu anomaly is inherited from the content of feldspar in the source bedrock. This is possible due to the easy incorporation of Eu in the structure of felspar during the petrogenetic process. Hence, Eu content in the marine sediments is higher than other REEs

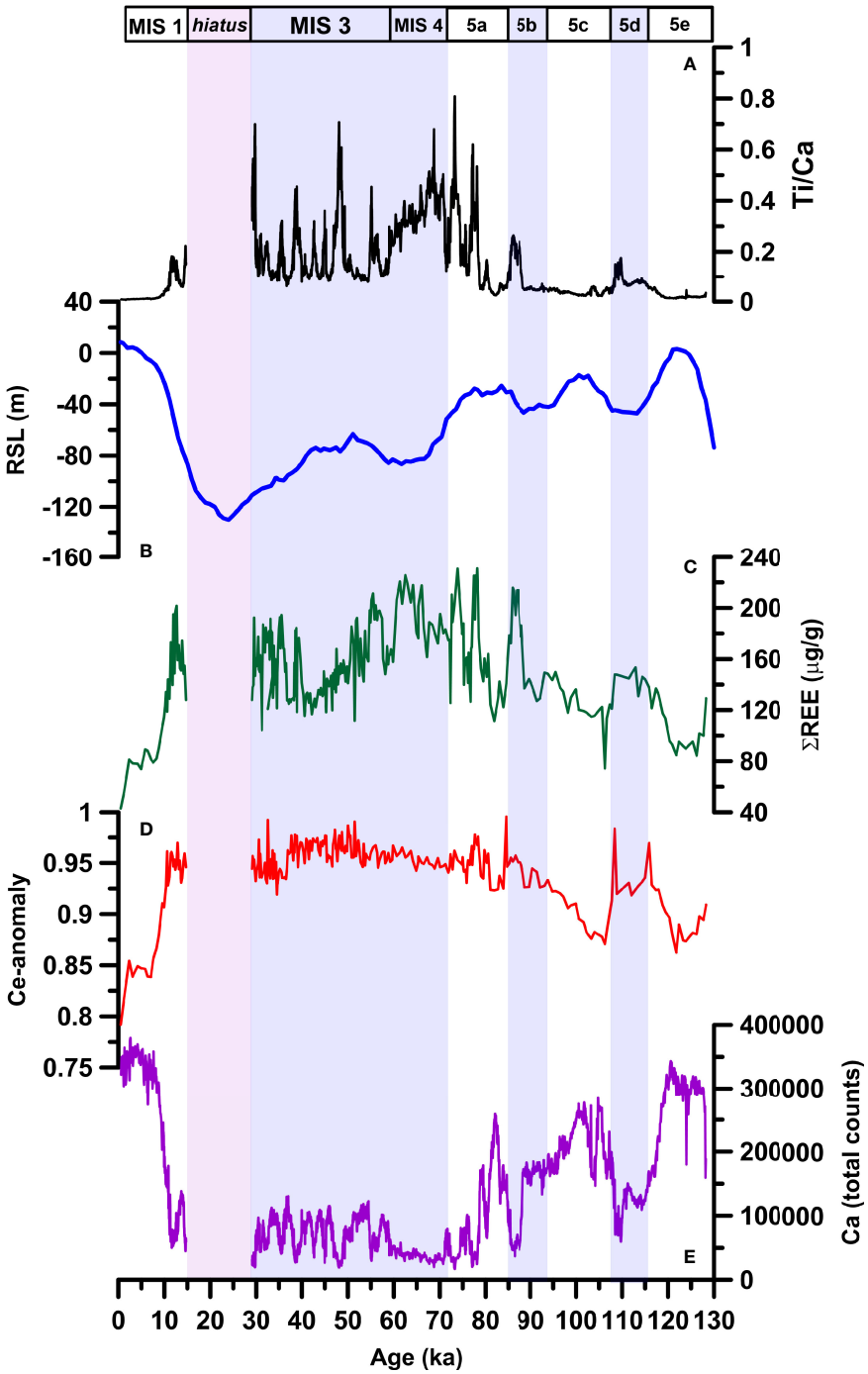

FIGURE 4 | Glacial-Interglacial variability as shown by the comparison between periods of high and low terrigenous sediment delivery to the study site with: **(A)** Ti/Ca ratio from GL-1248 (Venancio et al., 2018) (black line); **(B)** Relative sea level (m) from GL-1248 (Waelbroeck et al., 2002) (dark blue line); **(C)** ∑REE concentration (this study) from GL-1248 (dark green line); **(D)** Ce-anomaly (this study) from GL-1248 (red line); and **(E)** Ca total counts (XRF). MIS boundaries in the studied time interval are numbered from 1 to 5, as well as in the cold substages of MIS 5 (5d and 5b). These cold periods are highlighted in blue bars.

breaking the straight-line shape of the REEs pattern curve (Henderson, 1984; Liu et al., 2015). Positive Eu anomalies and abundances of REEs were reported in sediments and some sedimentary rocks containing feldspar, whereas Eu-depleted felsic igneous rocks and high LREE/HREE ratios, and most basalt does not present Eu anomalies and low LREE/HREE ratios (Absar and Sreenivas, 2015; Liu et al., 2015). The distribution of positive Eu anomaly values observed of core

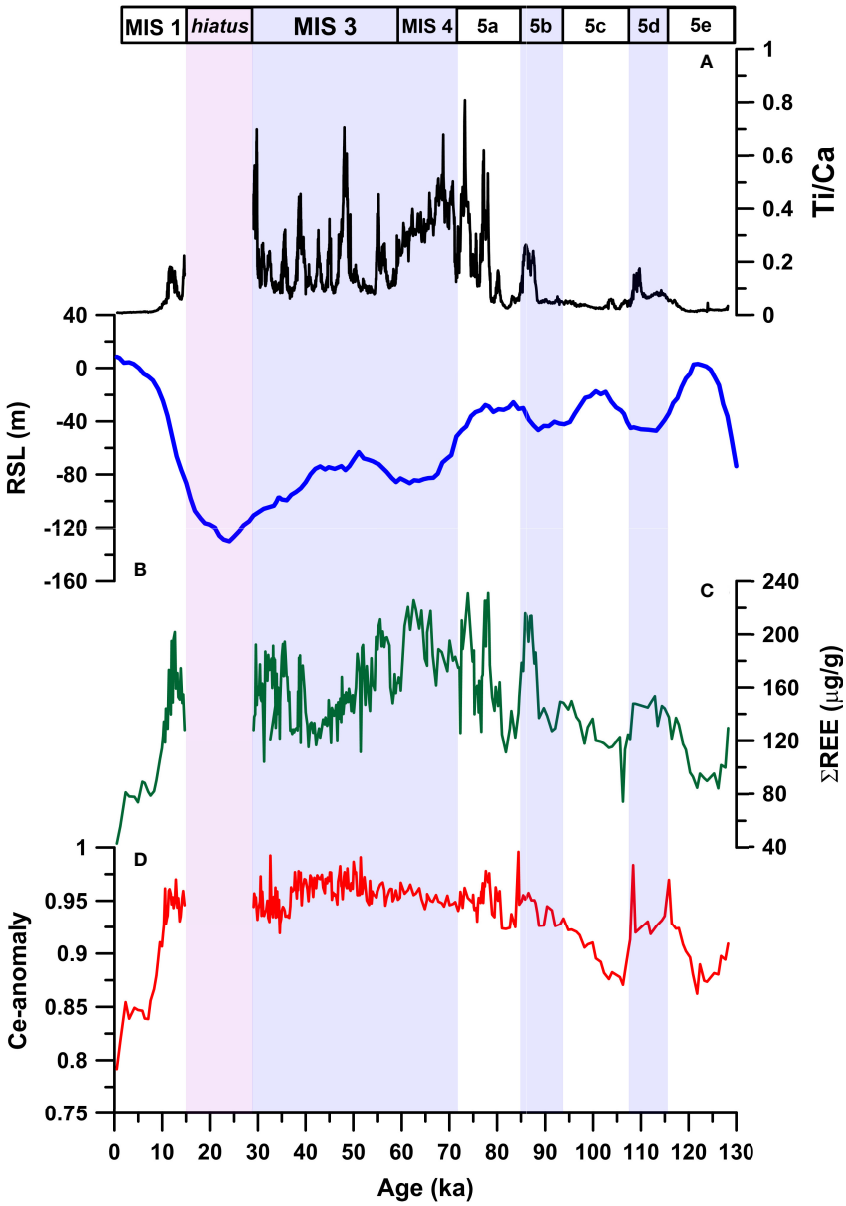

FIGURE 5 | Glacial-Interglacial variability as shown by the comparison between periods of high and low terrigenous sediment delivery to the study site with: **(A)** Ti/Ca ratio from GL-1248 (Venancio et al., 2018) (black line); **(B)** Relative sea level (m) from GL-1248 (Waelbroeck et al., 2002) (dark blue line); **(C)** ΣREE concentration (this study) from GL-1248 (dark green line); and **(D)** Ce-anomaly (this study) from GL-1248 (red line). MIS boundaries in the studied time interval are numbered from 1 to 5, as well as in the cold substages of MIS 5 (5d and 5b). These cold periods are highlighted in blue bars.

GL-1248 was more expressive up to 3.21 and 1.27, respectively (**Figure 6**). This suggests that parental rock from the sediments belongs to the felsic rock, or that there is a lack of deep-sourced mafic and ultramafic components (Liu et al., 2015). Thus, the Eu anomaly can be used to study the sources of sedimentary rocks (Taylor and McLennan, 1985; Liu et al., 2015).

As mentioned in the previous topic, the detritic end-members are an effective REE-carrier phase in the sediments of core GL-1248. In the detritic phase carrying REEs, the most common was occurrence was no anomaly unless it is inherited from the continental source (some minerals may have an anomaly). In this work, strong positive Eu anomalies are observed in modern values during the interglacial period, following a sharp decline towards the glacial period registered in the core GL-1248 (**Figure 2**). During the process of partial intracrustal fusion, Eu^{+3} reduces to Eu^{+2} and replaces with Ca^{+2}-bearing minerals, as of feldspar. Hence, the lower crustal has a feldspar-rich, and upper crustal rocks depleted of Eu relative to other REEs. This anomaly is usually propagated into the oceans by weathering and river transported delivery of continental rocks (Abdalla, 2012).

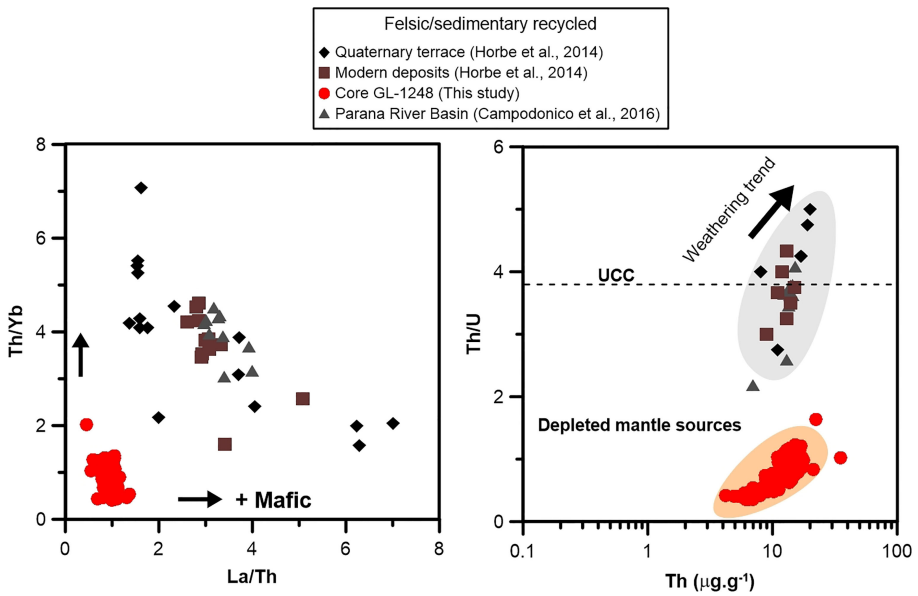

FIGURE 6 | Diagrams of the classification of the sediments by McLennan et al. (1993). Red symbols indicate samples of core GL-1248; Black symbols indicates quaternary terrace samples from the Amazon basin (Horbe et al., 2014); Brown symbols indicates modern deposits samples from the Amazon basin (Horbe et al., 2014); and grey symbols indicate samples of the Parana River basin (Campodonico et al., 2016).

Therefore, positive Eu anomalies are usually a particular factor inherited from specific source rocks since this signal is recorded from the magmatic process until its deposition. The slight positive Eu anomalies were observed in the Amazon basin, where the Amazon River at Óbidos varied between 1.16 and 1.39 (Rousseau et al., 2019), Solimões River varied between 0.98 and 1.36, and Madeira River varied between 1.01 and 1.31 (values calculated by Viers et al. (2008). As well as for fluvial sediment from the Orinoco basin and Maroni Basin that varied between 1.08 and 1.23, and 1.40 and 1.64, respectively (Rousseau et al., 2019). Marine sediments located in Santos Basin (southern Atlantic) had a slightly positive Eu anomaly varied between 0.978 and 1.33 (this study). Picouet et al. (2002) observed strong Eu anomalies in the Niger River (Africa) associated with granitic rocks present in the drainage basin that had this characteristic.

In the igneous systems, positive Eu anomalies found in siliciclastic sediment are also explained by preferential retention by feldspars such as plagioclases and potassium feldspars, particularly in felsic melts (Terekhov and Shcherbakova, 2006; Campodonico et al., 2016). This can be observed in **Figure 6** showing the origin of sediment source according to Taylor and McLennan (1985), which indicates that core GL-1248 derived from a more felsic and/or recycled sedimentary source, as described by others (Absar and Sreenivas, 2015; Liu et al., 2015; Campodonico et al., 2016). In addition, our Sm/Nd data compared with data from the Eu/Eu* (this study) and Sr isotopes (Sousa et al., 2021), illustrated in **Figure 7**, also suggest more felsic end members, as the more differentiated the igneous rock, that is, the more felsic it is, the lower the Sm/Nd ratio will be. It is 0.325 in the chondritic mantle and 0.173 in the PAAS, which represents the upper continental crust. The $^{87}Sr/^{86}Sr$ can be interpreted as the lower, the more basic end member, the higher, and the more felsic. Therefore in this case, when the Sr isotope ratio goes up and Sm/Nd goes down (coinciding peaks in the diagram), they indicate felsic sources entering. This indicates the origin of positive Eu anomalies in marine sediment was from a felsic magma in the Parnaíba basin with assimilation of feldspar during fractionation crystallization over the Last Interglacial.

CONCLUSION

Rare Earth Elements concentration records in core GL-1248 collected from the continental slope off northeastern Brazil had a wide range over the Last Interglacial. The Parnaíba River was the main source of REEs content to the western South Atlantic. Fe elements (Fe-oxyhydroxides) produced *via* weathering of continental and tropical soils were the principal REE-carrier phase in the soils, during transportation until immobilization at core site GL-1248. Regional factors, such as climate, rainfall regime, runoff events, and relative sea-level changes contributed significantly to continental-REEs erosion of sedimentary layers of the Parnaíba Basin, and transport and deposition of mobilized REE from the continent to the study site.

Peaks in REEs were correlated with peaks of Ti/Ca ratios from NE Brazil verifying that REEs content delivered at our site was transported with fluvial materials during continental runoff events corresponding to millennial-scale variability. Furthermore,

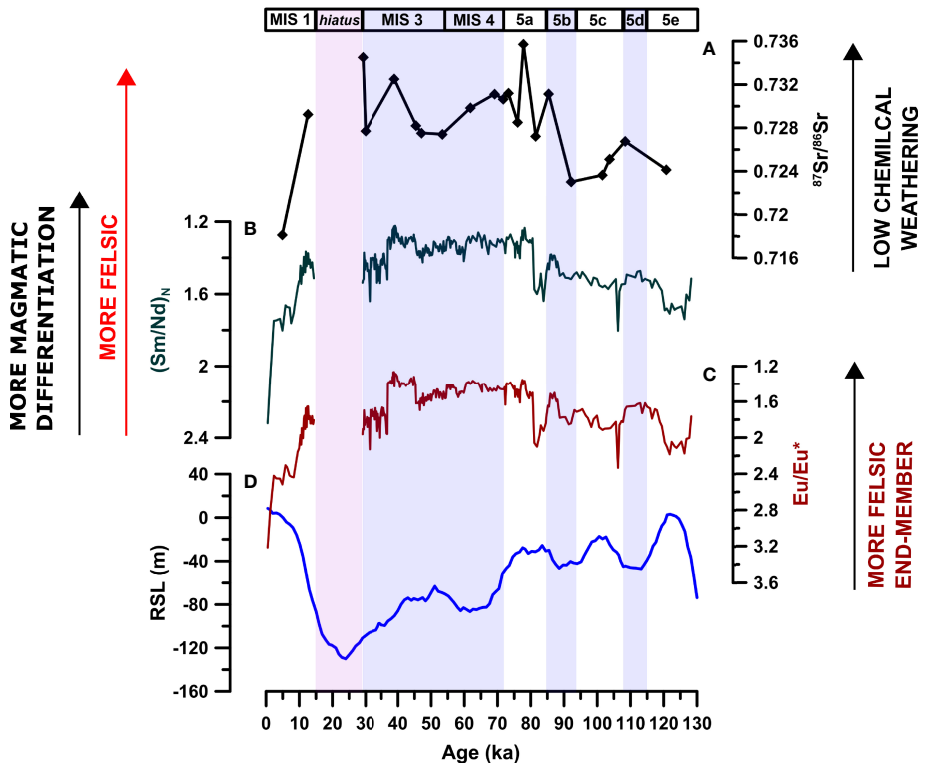

FIGURE 7 | Glacial-Interglacial variability as shown by the comparison diagram between felsic sources in core GL-1248: **(A)** $^{87}Sr/^{86}Sr$ isotopes ratios (Sousa et al., 2021) (black line); **(B)** Sm/Nd ratios normalized by PAAS (this study) (dark green line); **(C)** Eu/Eu* anomalies (this study) (dark red line); and **(D)** Relative sea-level from (Waelbroeck et al., 2002) (blue line). MIS boundaries in the studied time interval are numbered from 1 to 5, except 2 (hiatus), as well as in the cold substages of MIS 5 (5d and 5b). These cold periods are highlighted in blue bars.

variation in sea-level changes and precipitation patterns influence its deposition as well as transportation.

Changes in the negative Ce-anomaly obtained in sediment showed not behave as a proxy for changes in deep ocean oxygenation during the interglacial relative to the last glacial period. Here, we observed that variation was caused by glacial-interglacial variations in sea level through its control over the exposure of the continental shelf. Given its flat morphology, eustatic changes in sea level during glacial-interglacial cycles can result in rapid exposure or drowning of the continental shelf on the Brazilian equatorial margin.

The origin of positive Eu anomalies in siliciclastic sediment was explained by preferential retention by feldspars such as plagioclases and potassium feldspars, particularly in felsic melts. In core GL-1248, this anomaly was caused by a felsic magma from the Parnaíba Basin with assimilation of felspar during fractionation crystallization since the Last Interglacial.

DATA AVAILABILITY STATEMENT

The original contributions presented in the study are included in the article/**Supplementary Material**. Further inquiries can be directed to the corresponding author.

AUTHOR CONTRIBUTIONS

TS: conceptualization and writing - original draft. IV: writing and review and editing. EM: writing and review. TF: writing and review. RN: writing and review. JS: writing and review. AA: review and funding acquisition. CV: supervision, review, editing. ES-F: supervision, conceptualization writing, review editing, and funding acquisition. All authors contributed to the article and approved the submitted version.

FUNDING

This study was financed in part by the Coordenação de Aperfeiçoamento de Pessoal de Nível Superior – Brasil (CAPES) – Finance Code 001. Currently, The Fundação de Amparo a Pesquisa do Estado do Rio de Janeiro – FAPERJ is responsible for funding TS research. CAPES financially supported IV with a scholarship (grant 88887.156152/2017-00). This study was financed in part by CNPq Project RAiN (grant 406322/2018-0).

ACKNOWLEDGMENTS

We appreciate the support of CAPES-ASPECTO project (Grant 88887.091731/2014-01). We thank R. Kowsman (CENPES/

Petrobras) and Petrobras Core Repository staff (Macaé/Petrobras) for providing sediment core GL-1248. This study was financed in part by CNPq Project RAiN (grant 406322/2018-0) and INCT-TMCOcean (INCT-Continent-Ocean Material Transfer – II CNPq, process No. 465.290/2014-0).

SUPPLEMENTARY MATERIAL

The Supplementary Material for this article can be found online at: https://www.frontiersin.org/articles/10.3389/fmars.2022.846976/full#supplementary-material

Supplementary Table 1 | Summary of the total REE concentrations, REE-sum, and their ratio of the marine sediments from the Coast of Northeast Brazil (GL-1248) since the Last Interglacial. MIS is Marine Isotope Stage; LREE is light rare earth elements; HREE is heavy rare earth elements.

Supplementary Table 2 | Distribution of Trace elements, ratios PAAS-normalized (Post-Archean Australian Shale), and occurrence anomalies of the marine sediments from the Coast of Northeast Brazil (GL-1248) since the Last Interglacial. MIS is Marine Isotope Stage.

Supplementary Table 3 | Mineral array in selected samples of marine sediment GL-1248 with corresponding to ages (ka), Marine Oxygen Isotope Stage (MIS), radiogenic isotopes, main mineral source, minerals abundances. Minerals are differentiated into main minerals, other minerals, and trace minerals by red, green, and black text colors, respectively.

REFERENCES

Abdalla, N. R. (2012). *Rare Earth Elements as a Paleo-Ocean Redox Proxy Within the Union Springs Member of the Marcellus Formation. Pennsylvania 2012. 41 F. Thesis (Bachelor of Science) - Department of Geosciences* (Pennsylvania: College of Earth and Mineral Sciences, The Pennsylvania State University).

Absar, N., and Sreenivas, B. (2015). Petrology and Geochemistry of Greywackes of the ~1.6 Ga Middle Aravalli Supergroup, Northwest India: Evidence for Active Margin Processes. *Int. Geol. Rev.* 57 (2), 134–158. doi: 10.1080/00206814.2014.999355

Antonina, N., Shazili, M., Yunus, K., Chuan, O. M., Yaacob, R., and Sharifah, F. N. (2013). Geochemistry of the Rare Earth Elements (Ree) Distribution in Terengganu Coastal Waters: A Study Case From Redang Island Marine Sediment. *Open J. Mar. Sci.* 03, 154–159. doi: 10.4236/ojms.2013.33017

Arz, H. W., Pätzold, J., and Wefer, G. (1998). Correlated Millennial-Scale Changes in Surface Hydrography and Terrigenous Sediment Yield Inferred From Last-Glacial Marine Deposits Off Northeastern Brazil. *Quat. Res.* 50 (2), 157–166. doi: 10.1006/qres.1998.1992

Arz, H. W., Pätzold, J., and Wefer, G. (1999). Climatic Changes During the Last Deglaciation Were Recorded in Sediment Cores From the Northeastern Brazilian Continental Margin. *Geo-Mar. Lett.* 19 (3), 209–218. doi: 10.1007/s003670050111

Bentahila, Y., Othman, D. B., and Luck, J. M. (2008). Strontium, Lead and Zinc Isotopes in Marine Cores as Tracers of Sedimentary Provenance: A Case Study Around Taiwan Orogen. *Chem. Geol.* 248 (1), 62–82. doi: 10.1016/j.chemgeo.2007.10.024

Bigham, J. M., Fitzpatrick, R. W., and Schulze, D. (2002). Soil Mineralogy With Environmental Applications. Madison. *Soil Sci. Soc Am. J.*, 7 323–366. doi: 10.2136/sssabookser7. Iron oxides. In: Dixon, J.B. Schulze, D.G.

Bohm, E., Lippold, J., Gutjahr, M., Frank, M., Blaser, P., Antz, B., et al. (2014). Strong and Deep Atlantic Meridional Overturning Circulation During the Last Glacial Cycle. *Nature.* 517 (7532), 73–76. doi: 10.1038/nature14059

Bouchez, J., Gaillardet, J., France-Lanord, C., Maurice, L., and Dutra-Maia, P. (2011). Grain Size Control of River Suspended Sediment Geochemistry: Clues From Amazon River Depth Profiles. *Geochem. Geophys. Geosyst.* 12 (3), 1–24. doi: 10.1029/2010GC003380

Campodonico, V. A., García, M. G., and Pasquini, A. I. (2016). The Geochemical Signature of Suspended Sediments in the Parana River Basin: Implications for Provenance, Weathering, and Sedimentary Recycling. *Catena.* 143, 201–214. doi: 10.1016/j.catena.2016.04.008

Chalk, T. B., Foster, G. L., and Wilson, P. A. (2019). Dynamic Storage of Glacial CO_2 in the Atlantic Ocean Revealed by Boron [$CO_3$2-] and Ph Records From ODP Hole 162-980A, 162-980B and 162-908C. *Pangaea*. 510, 1–11. doi: 10.1594/PANGAEA.898075

Crusius, J., and Thomson, J. (2000). Comparative Behavior of Authigenic Re, Mo and U During Reoxidation and Subsequent Long-Term Burial in Marine Sediments. *Geochim. Cosmochim. Acta* 64, 2233–2243. doi: 10.1016/S0016-7037(99)00433-0

Cruz, F. W., Burns, S. J., Karmann, I., Sharp, W. D., and Vuille, M. (2006). Reconstruction of Regional Atmospheric Circulation Features During the Late Pleistocene in Subtropical Brazil From Oxygen Isotope Composition of Speleothems. *Earth Planet. Sci. Lett.* 248 (1–2), 494–506. doi: 10.1016/j.epsl.2006.06.019

Curry, W. B., and Oppo, D. W. (2005). Glacial Water Mass Geometry and the Distribution of δ 13C of ΣCO_2 in the Western Atlantic Ocean. *Paleoceanography.* 20 (1), 1–12. doi: 10.1029/2004PA001021

De Baar, H. J. W., Bacon, M. P., and Brewer, P. G. (1983). Rare-Earth Distributions With a Positive Ce Anomaly in the Western North Atlantic Ocean. *Nature.* 301 (5898), 324–327. doi: 10.1038/301324a0

Depetris, P. J., Probst, J.-L., Pasquini, A. I., and Gaiero, D. M. (2003). The Geochemical Characteristics of the Paraná River Suspended Sediment Load: An Initial Assessment. *Hydrol. Process.* 17 (7), 1267–77. doi: 10.1002/hyp.1283

De Sousa, T. A., Venancio, I. M., Valeriano, C. M., Heilbron, M., Dias Carneiro Weitzel,M. T., Mane, M. A., et al (2021). Changes in Sedimentary Provenance and Climate Off the Coast of Northeast Brazil Since the Last Interglacial. *Mar. Geol.* 435, 106454. doi: 10.1016/j.margeo.2021.10

Dupont, L. M., Schlütz, F., Ewah, C. T., Jennerjahn, T. C., Paul, A., and Behling, H. (2010). Two-Step Vegetation Response to Enhanced Precipitation in Northeast Brazil During Heinrich Event 1. *Glob. Chang. Biol.* 16, 1647–60. doi: 10.1111/j.1365-2486.2009.02023.x

Elderfield, H., and Pagett, R. (1986). Rare Earth Elements in Ichthyolites: Variations With Redox Conditions and Depositional Environment. *Sci. Total Environ.* 49, 175–197. doi: 10.1016/0048-9697(86)90239-1

Fadina, O. A., Venancio, I. M., Belem, A., Silveira, C. S., de Castro Bertagnolli, ,. D., Silva-Filho, E. V., et al. (2019). Paleoclimatic Controls on Mercury Deposition in Northeast Brazil Since the Last Interglacial. *Quat. Sci. Rev.* 221, 105869. doi: 10.1016/j.quascirev.2019.105869

German, C. R., and Elderfield, H. (1990). Application of the Ce Anomaly as a Paleoredox Indicator: The Ground Rules. *Paleoceanography* 5 (5), 823–833. doi: 10.1029/PA005i005p00823

Gottschalk, S., Fehm, T. F., Deán-Ben, X. L., Tsytsarev, V., and Razansky, D. (2016). Correlation Between Volumetric Oxygenation Responses and Electrophysiology Identifies Deep Thalamocortical Activity During Epileptic Seizures. *Neurophotonics* 4 (1), 011007. doi: 10.1117/1.nph.4.1.011007

Govin, A., Holzwarth, U., Heslop, D., Ford Keeling, L., Zabel, M., Mulitza, S., et al. (2012). Distribution of Major Elements in Atlantic Surface Sediments (36°N-49°s): Imprint of Terrigenous Input and Continental Weathering. *Geochem. Geophys. Geosyst.* 13 (1), 1–23. doi: 10.1029/2011GC003785

Henderson, P. (1984). *Rare Earth Elements Geochemistry* (Amsterdam -Oxford -New York -Tokyo: Elsevier), 1984.

Hodgson, D. A., Verleyen, E., Squier, A. H., Sabbe, K., Keely, B. J., Saunders, K. M., et al. (2006). Interglacial Environments of Coastal East Antarctica: Comparison of MIS 1 (Holocene) and MIS 5e (Last Interglacial) Lake-Sediment Records. *Quat. Sci. Rev.* 25 (1-2), 179–197. doi: 10.1016/j.quascirev.2005.03.004

Hoogakker, B. A. A., Elderfield, H., Schmiedl, G., McCave, I. N., Rickaby, R. E. M., and Shackleton, N. J. (2015). Bottom Water Oxygen Reconstructions Iberian Margin Sediment Core MD95-2042 Between 0 and 150,000 Years BP. *Pangaea* 8 (1), 40–3. doi: 10.1594/PANGAEA.856564

Horbe, A. M.C., da Trindade, I. R., Dantas, E. L., Santos, R. V., and Roddaz, M. (2014). Provenance of Quaternary and Modern Alluvial Deposits of the Amazonian Floodplain (Brazil) Inferred From Major and Trace Elements

and Pb–Nd–Sr Isotopes. *Palaeogeogr. Palaeoclimatol. Palaeoecol.*, 411, 144–54. doi: 10.1016/j.palaeo.2014.06.019

Jaccard, S., and Galbraith, E. (2012). Large Climate-Driven Changes of Oceanic Oxygen Concentrations During the Last Deglaciation. *Nat. Geosci.* 5, 151–156. doi: 10.1038/NGEO1352

Jaccard, S., Galbraith, E., Martínez-García, A., and Anderson, R. (2016). Covariation of Deep Southern Ocean Oxygenation and Atmospheric CO_2 Through the Last Ice Age. *Nature.* 530, 207–210. doi: 10.1038/nature16514

Jaeschke, A., Rühlemann, C., Arz, H., Heil, G., and Lohmann, G. (2007). Coupling of Millennial-Scale Changes in Sea Surface Temperature and Precipitation Off Northeastern Brazil With High-Latitude Climate Shifts During the Last Glacial Period. *Paleoceanography* 22 (4), 1–10. doi: 10.1029/2006PA001391

Johnsson, M. J., Stallard, R.F., and Lundberg, N. (1991). Controls on the Composition of Fluvial Sands From a Tropical Weathering Environment: Sands of the Orinoco Drainage Basin, Venezuela and Colombia. *Bull. Geol. Soc. Am.*, 103:1622–647.

Johnsson, M. J. (1993). The System Controlling the Composition of Clastic Sediments. *Geol. Soc. Am. Spec. Pap.*, 1–20. doi: 10.1130/spe284-p1

Lisiecki, L. E., and Raymo, M. E. (2005). A Pliocene-Pleistocene Stack of 57 Globally Distributed Benthic δ^{18}o Records. *Paleoceanography* 20 (1). doi: 10.1029/2004pa001071

Liu, Y., Cheng, Y., Liu, J., Zhang, L., Zhang, C., and Zheng, C. (2015). Provenance Discrimination of Surface Sediments Using Rare Earth Elements in the Yalu River Estuary, China. *Environ. Earth Sci.* 74 (4), 3507–3517. doi: 10.1007/s12665-015-4391-x

Liu, Y.-G., Miah, M. R. U., and Schmitt, R. A. (1988). Cerium: A Chemical Tracer for Paleo-Oceanic Redox Conditions. *Geochim. Cosmochim. Acta* 52 (6), 1361–1371. doi: 10.1016/0016-7037(88)90207-4

Liu, Y.-G., and Schmitt, R. A. (1990). Elemental Abundances in Marine Carbonates From ODP Leg 115 Holes (Table 1). *Pangaea* 115, 709–14,. doi: 10.1594/PANGAEA.755473

Liu, Y. G., and Schmitt, R. A. (1990). "Cerium Anomalies in Western Indian Ocean Cenozoic Carbonates, Leg 115," in *Proc. of the Ocean Drilling Program. Scientific Results*, vol. Vol. I IS . Ed. R. A. Duncan (TX, USA: Ocean Drilling Program, College Station), 709–7 14, pp.

Cerium Anomalies in WesternMartrat, B., Jimenez-Amat, P., Zahn, R., and Grimalt, J. O. (2014). Similarities and Dissimilarities Between the Last Two Deglaciations and Interglaciations in the North Atlantic Region. *Quat. Sci. Rev.* 99, 122–134. doi: 10.1016/j.quascirev.2014.06.016

McLennan, S. M., Hemming, S., McDaniel, D. K., and Hanson, G. N. (1993). Geochemical Approaches to Sedimentation, Provenance, and Tectonics. *Geol. Soc. Am. Spec. Pap.* 284, 21–40. doi: 10.1130/spe284-p21

Milliman, J. M., and Meade, R. H. (1983). Worldwide Delivery of River Sediment to the Oceans. *J Geol.*, 91, 1–21.

Members, N. (2004). High-Resolution Record of Northern Hemisphere Climate Extending Into the Last Interglacial Period. *Nature.* 431 (7005), 147–151. doi: 10.1038/nature02805

Morton, A. C., and Hallsworth, C. R. (1999). Processes Controlling the Composition of Detrital Heavy Mineral Assemblages in Sandstones. *Sedimentary Geology* 124, 3–29. doi: 10.1016/S0037-0738(98)00118-3

Murray, R. W., Brink, M. R. B., Brumsack, H. J, Gerlach, D. C., and Russ, G. P.III (1991). Rare Earth Elements in Japan Sea Sediments and Diagenetic Behavior of Ce/Ce∗: Results From ODP Leg 127. *Geochim. Cosmochim. Acta* 55 (9), 2453–2466. doi: 10.1016/0016-7037(91)90365-C

Murray, R. W., Buchholtz Ten Brink, M. R., Jones, D. L., Gerlach, D. C., and Russ, G. P. III. (1990a). Rare Earth Elements as Indicators of Different Marine Depositional Environments in Chert and Shale. *Geology* 18 (3), 268. doi: 10.1130/0091-7613(1990)018<0268:reeaio>2.3.co;2

Nace, T. E., Baker, P. A., Dwyer, G. S., Silva, C. G., Rigsby, C. A., Burns, S. J., et al. (2014). The Role of North Brazil Current Transport in the Paleoclimate of the Brazilian Nordeste Margin and Paleoceanography of the Western Tropical Atlantic During the Late Quaternary. *Paleogeogr. Palaeoclimatol. Palaeoecol.* 415, 3–13. doi: 10.1016/j.palaeo.2014.05.030

Pattan, J. N., Pearce, N. J. G., and Mislankar, P. G. (2005). Constraints in Using Cerium-anomaly of Bulk Sediments as an Indicator of Paleo Bottom Water Redox Environment: A Case Study From the Central Indian Ocean Basin. *Chem. Geol.* 221 (3–4), 260–278. doi: 10.1016/j.chemgeo.2005.06.009

Picouet, C., Dupré, B., Orange, D., and Valladon, M. (2002). Major and Trace Element Geochemistry in the Upper Niger River (Mali): Physical and Chemical Weathering Rates and CO_2 Consumption. *Chem. Geol.* 185 (1-2), 93–124. doi: 10.1016/s0009-2541(01)00398-9

Piacsek, P., Behling, H., Gu, F., Venancio, I., Lessa, D., Belem, A., et al (2021). Changes in Sea Surface Hydrography and Productivity in the Western Equatorial Atlantic Since the Last Interglacial *Palaeogeogr. Palaeoclimatol. Palaeoecol.* 562. 10.1016/j.palaeo.2020.109952.

Pourmand, A., Dauphas, N., and Ireland, T. J. (2012). A Novel Extraction Chromatography and MC-ICP-MS Technique for Rapid Analysis of REE, Sc, and Y: Revising CI-chondrite and Post-Archean Australian Shale (PAAS) Abundances. *Chem. Geol.* 291, 38–54. doi: 10.1016/j.chemgeo.2011.08.011

Rahmstorf, S. (2002). Ocean Circulation and Climate During the Past 120,000 Years. *Nature.* 419, 207–214. doi: 10.1038/nature01090

Rama-Corredor, O., Martrat, B., Grimalt, J. O., Lopez Otalvaro, G. E., Flores, J. A., and Sierro, F. (2015). Parallelisms Between Sea Surface Temperature Changes in the Western Tropical Atlantic (Guiana Basin) and High Latitude Climate Signals Over the Last 140 000 Years. *Clim. Past.* 11, 1297–1311. doi: 10.5194/cp-11-1297-2015

Revel, M., Ducassou, E., Grousset, F. E., Bernasconi, S. M., Migeon, S., Revillon, S., et al (2010). 100,000 Years of African Monsoon Variability Recorded in Sediments of the Nile Margin *Quat. Sci. Rev.* 29 (11), 1342–1362. doi: 10.1016/j.quascirev.2010.02.006

Revel, M., Colin, C., Bernasconi, S., Combourieu-Nebout, N., Ducassou, E., Grousset, F.E., et al (2014). 21,000 Years of Ethiopian African Monsoon Variability Recorded in Sediments of the Western Nile Deep-Sea Fan. *Reg. Environ. Change* 14 (5), 1685–1696. doi: 10.1007/s10113-014-0588-x

Revel, M., Ducassou, E., Skonieczny, C., Colin, C., Bastian, L., Bosch, D., et al (2015). 20,000 Years of Nile River Dynamics and Environmental Changes in the Nile Catchment Area as Inferred From Nile Upper Continental Slope Sediments *Quat. Sci. Rev.* 130, 200–221. doi: 10.1016/j.quascirev.2015.10.030

Rohling, E. J., Grant, K., Hemleben, C., Siddall, M., Hoogakker, B. A. A., Bolshaw, M., et al. (2007). High Rates of Sea-Level Rise During the Last Interglacial Period. *Nat. Geosci.* 1 (1), 38–42. doi: 10.1038/ngeo.2007.28

Rousseau, T. C. C., Roddaz, M., Moquet, J. S., Handt Delgado, H., Calves, G., and Bayon, G. (2019). Controls on the Geochemistry of Suspended Sediments From Large Tropical South American Rivers (Amazon, Orinoco, and Maroni). *Chem. Geol.* 522, 38–54. doi: 10.1016/j.chemgeo.2019.05.027

Rühlemann, C., Frank, M., Hale, W., Mangini, A., Mulitza, S., Müller, P. J., et al. (1996). Late Quaternary Productivity Changes in the Western Equatorial Atlantic: Evidence From ^{230}Th-Normalized Carbonate and Organic Carbon Accumulation Rates. *Mar. Geol.* 135 (1–4), 127–152. doi: 10.1016/S0025-3227(96)00048-5

Schijf, J., de Baar, H. J. W., and Millero, F. J. (1994). Kinetics of Ce and Nd Scavenging in Black Sea Waters. *Mar. Chem.* 46 (4), 345–359. doi: 10.1016/0304-4203(94)90031-0

Seaman, J. C. (2013). Competitive Sorption and Transport of Heavy Metals in Soils and Geological Media. *Soil Sci. Soc Am. J.* 77 (6), 2216. doi: 10.2136/sssaj2013.0004br

Taylor, S. R., and McLennan, S. M. (1985). The Continental Crust: Its Composition and Evolution. *Phys. Earth Planet. Inter.* 42 (3), 196–197. doi: 10.1016/0031-9201(86)90093-2

Terekhov, E. N., and Shcherbakova, T. F. (2006). Genesis of Positive Eu Anomalies in Acid Rocks From the Eastern Baltic Shield. *Geochem. Int.* 44, 439–455. doi: 10.1134/S0016702906050028

Tostevin, R., Shields, G. A., Tarbuck, G. M., He, T., Clarkson, M. O., and Wood, R. A. (2016). Effective Use of Cerium Anomalies as a Redox Proxy in Carbonate-Dominated Marine Settings. *Chem. Geol.* 438, 146–162. doi: 10.1016/j.chemgeo.2016.06.027

Tribovillard, N., Algeo, T. J., Lyons, T., and Riboulleau, A. (2006). Trace Metals as Paleoredox and Paleoproductivity Proxies: An Update. *Chem. Geol.* 232 (1–2), 12–32,0009-2541. doi: 10.1016/j.chemgeo.2006.02.012

Venancio, I. M., Mulitza, S., Govin, A., Santos, T. P., Lessa, D. O., Albuquerque, A., et al. (2018). Millennial-to Orbital-Scale Responses of Western Equatorial Atlantic Thermocline Depth to Changes in the Trade Wind System Since the

Last Interglacial. *Paleoceanogr. Paleoclimatol.* 33 (12), 1490–1507. doi: 10.1029/2018PA003437

Viers, J., Roddaz, M., Filizola, N., Guyot, J.-L., Sondag, F., Brunet, P., et al. (2008). Seasonal and Provenance Controls on Nd–Sr Isotopic Compositions of Amazon Rivers Suspended Sediments and Implications for Nd and Sr Fluxes Exported to the Atlantic Ocean. *Earth Planet. Sci. Lett.* 274 (3-4), 511–523. doi: 10.1016/j.epsl.2008.08.011

Waelbroeck, C., Labeyrie, L., Michel, E., Duplessy, J. C., Mcmanus, J. F., Lambeck, K., et al. (2002). Sea-level and Deep-Water Temperature Changes Derived From Benthic Foraminifera Isotopic Records. *Quat. Sci. Rev.* 21 (1-3), 295–305. doi: 10.1016/s0277-3791(01)00101-9

Walter, H.J., Hegner, E., Diekmann, B., and Kuhn, G. (2000). Provenance and Transport of Terrigenous Sediment in the South Atlantic Ocean and Their Relations to Glacial and Interglacial Cycles: Nd and Sr Isotopic Evidence. *Geochim, Cosmochim Acta.* 64 (22), 3813–3827. doi: 10.1016/S0016-7037(00)00476-2

Wang, X., Auler, A. S., Edwards, R. L., Cheng, H., Cristalli, P. S., Smart, P. L., et al. (2004). Wet Periods in Northeastern Brazil Over the Past 210 Kyr Linked to Distant Climate Anomalies. *Nature.* 432, 740. doi: 10.1038/nature03067

Wang, Y.-L., Liu, Y.-G., and Schmitt, R. A. (1986). Rare Earth Element Geochemistry of South Atlantic Deep-Sea Sediments: Ce Anomaly Change at ~54 My. *Geochim. Cosmochim. Acta* 50 (7), 1337–1355. doi: 10.1016/0016-7037(86)90310-8

Wilde, P., Quinby-Hunt, M. S., and Erdtmann, B.-D. (1996). The Whole-Rock Cerium Anomaly: A Potential Indicator of Eustatic Sea-Level Changes in Shales of the Anoxic Facies. *Sediment. Geol.* 101 (1-2), 43–53. doi: 10.1016/0037-0738(95)00020-8

Wolff, E. W., Chappellaz, J., Blunier, T., Rasmussen, S. O., and Svensson, A. (2010). Millennial-scale Variability During the Last Glacial: The Ice Core Record. *Quat. Sci. Rev.* 29 (21–22), 2828–2838. doi: 10.1016/j.quascirev.2009.10.013

Wright-Clark, J., and Holser, W. T. (1981). Rare-Earth Elements in Conodont Apatite as a Measure of Redox Conditions in Ancient Seas. *Geol. Soc Am.* 13, 586.

Xu, F., Li, A., Li, T., Xu, K., Chen, S., Qiu, L., et al. (2011). Rare Earth Element Geochemistry in the Inner Shelf of the East China Sea and Its Implication to Sediment Provenances. *J. Rare. Earths.* 29 (7), 702–709. doi: 10.1016/s1002-0721(10)60526-1

Yusof, A. M., Akyil, S., and Wood, A. K. H. (2001). Rare Earth Elements Determination and Distribution Patterns in Sediments of a Polluted Marine Environment by Instrumental Neutron Activation Analysis. *J. Radioanal. Nucl. Chem.* 249 (2), 333–341. doi: 10.1023/a:1013297932536

Zhang, Y., Chiessi, C. M., Mulitza, S., Zabel, M., Trindade, R. I. F., Hollanda, M. H., et al. (2015). Origin of Increased Terrigenous Supply to the NE South American Continental Margin During Heinrich Stadial 1 and the Younger Dryas. *Earth Planet. Sci. Lett.* 432, 493–500. doi: 10.1016/j.epsl.2015.09.054

Conflict of Interest: The authors declare that the research was conducted in the absence of any commercial or financial relationships that could be construed as a potential conflict of interest.

Publisher's Note: All claims expressed in this article are solely those of the authors and do not necessarily represent those of their affiliated organizations, or those of the publisher, the editors and the reviewers. Any product that may be evaluated in this article, or claim that may be made by its manufacturer, is not guaranteed or endorsed by the publisher.

frontiers | Frontiers in Earth Science

ORIGINAL RESEARCH
published: 06 June 2022
doi: 10.3389/feart.2022.864381

Spatiotemporal Discharge Variability of the Doce River in SE Brazil During MIS 6 and 5

Iris Arndt[1], Silke Voigt[1], Rainer Petschick[1], Alicia Hou[2], Jacek Raddatz[1], Ana Luiza S. Albuquerque[3] and André Bahr[2]*

[1]Institute of Geosciences, Goethe University Frankfurt, Frankfurt, Germany, [2]Institute of Earth Sciences, Heidelberg University, Heidelberg, Germany, [3]Departamento de Geoquímica, Universidade Federal Fluminense, Rio de Janeiro, Brazil

The modern precipitation balance in southeastern (SE) Brazil is regulated by the South American summer Monsoon and threatened by global climate change. On glacial-interglacial timescales, monsoon intensity was strongly controlled by precession-forced changes in insolation. To date, relatively little is known about the spatiotemporal distribution of tropical precipitation in SE Brazil and the resulting variability of fluvial discharge on glacial-interglacial timescales. Here, we present X-ray diffraction-derived mineralogical data for the 150–70 ka period (marine isotope stage (MIS) 6 to MIS 5) from the Doce River basin. This area was sensitive to changes in monsoonal precipitation intensity due to its proximity to the South Atlantic Convergence Zone. The data, obtained from a marine sediment core (M125-55–7) close to the Doce river mouth (20°S), show pronounced changes in the Doce River suspension load's mineralogical composition on glacial-interglacial and precessional timescales. While the ratio of silicates to carbonates displays precession-paced changes, the mineralogical composition of the carbonate-free fraction discriminates between two assemblages which strongly vary between glacial and interglacial time scales, with precession-forced variability only visible in MIS 5. The first assemblage, dominated by high contents of kaolinite and gibbsite, indicates intensified lowland erosion of mature tropical soils. The second one, characterized by higher contents of the well-ordered illite, quartz and albite, points to intensified erosion of immature soils in the upper Doce Basin. High kaolinite contents in the silicate fraction prevailed in late MIS 6 and indicate pronounced lowland soil erosion along a steepened topographic gradient. The illite-rich mineral assemblage was more abundant in MIS 5, particularly during times of high austral summer insolation, indicating strong monsoonal rainfall and intense physical erosion in the upper catchment. When the summer monsoon weakened in times of lower insolation, the mineral assemblage was dominated by kaolinite again, indicative of lower precipitation and runoff in the upper catchment and dominant lowland erosion.

Keywords: fluvial discharge, summer monsoon, Marine Isotope Stage 6 (MIS 6), Marine Isotope Stage 5 (MIS 5), X-ray diffractometry (XRD), southeastern Brazil, western tropical Atlantic

OPEN ACCESS

Edited by:
Joyanto Routh, Linköping University, Sweden

Reviewed by:
Sanjeev Kumar, Physical Research Laboratory, India
Sophia Hines, Woods Hole Oceanographic Institution, United States

****Correspondence:***
Iris Arndt
iris.arndt@stud.uni-frankfurt.de

Specialty section:
This article was submitted to Quaternary Science, Geomorphology and Paleoenvironment, a section of the journal Frontiers in Earth Science

Received: *28 January 2022*
Accepted: *05 May 2022*
Published: *06 June 2022*

Citation:
Arndt I, Voigt S, Petschick R, Hou A, Raddatz J, Albuquerque ALS and Bahr A (2022) Spatiotemporal Discharge Variability of the Doce River in SE Brazil During MIS 6 and 5. Front. Earth Sci. 10:864381. doi: 10.3389/feart.2022.864381

INTRODUCTION

The Doce River watershed, situated in southeastern Brazil, is considered a region strongly sensitive to climate variability and especially vulnerable to the socio-economic and environmental impacts of climate change (May et al., 2020). This region is expected to suffer from long-term droughts, flooding through heavy rainfalls, coastal erosion, which will lead to a decline in silviculture viability, reduced croplands, a loss of biodiversity, a decrease in hydroelectric generating capacity and accompanying risks to human health (May et al., 2020). Dry winters and rainy summers in the region are caused by the South American Summer Monsoon (SASM) (Carvalho, 2020; **Figure 1**). Future climate models indicate that this pattern will strengthen over eastern Brazil, leading to a further decrease in precipitation during the dry season (June, July and August) and an increase in precipitation during the rainy season (December, January and February) (FEAM, 2011; IPCC, 2021). Models for different future climate scenarios display complex, at times contradictory, spatial patterns of summer precipitation increases and decreases for the Doce Basin (FEAM, 2011). While climate model projections are constantly improving, they are still subject to uncertainties, of which some are being narrowed down and others are irreducible (Knutti & Sedláček, 2013). Uncertainties regarding regional precipitation development make regional and seasonal paleoclimate data highly valuable for estimating future precipitation patterns (Tierney et al., 2020), which is particularly important for vulnerable regions like the Doce watershed.

Paleoclimate studies from the last glacial period and the Holocene indicate that solar irradiation and high latitude temperature changes affect South American monsoonal precipitation patterns by impacting atmospheric as well as ocean circulation and SST distribution in the tropical South Atlantic (e.g., Bahr et al., 2021; Cruz et al., 2009, 2005; Jaeschke et al., 2007; Kanner et al., 2012; Stríkis et al., 2018, 2015). In eastern Brazil, monsoon intensity over the past 300 ka was primarily controlled by precession-forced changes in insolation but also indirectly affected by changing atmospheric greenhouse gas concentrations, which can modify both the inter- and intrahemispheric temperature gradients (Rind, 1998; Hou et al., 2020a) and thereby intensity of the Hadley circulation and southeast trade winds (Seo et al., 2014). The magnitude of interhemispheric SST gradients can also play a role in determining the strength and position of the South Atlantic Convergence Zone (SACZ) (Stríkis et al., 2015), a convective band which spans from the Amazon Basin to the western South Atlantic releasing moisture provided by low level winds (Kodama, 1992). The convective activity in the SACZ and the Amazon Basin are the main components regulating the SASM (Jones & Carvalho, 2002). Therefore, changes in the strength and/or position of the SACZ impact SASM related precipitation distribution. The pattern is complicated by an additional insolation-driven east-west antiphased precipitation dipole

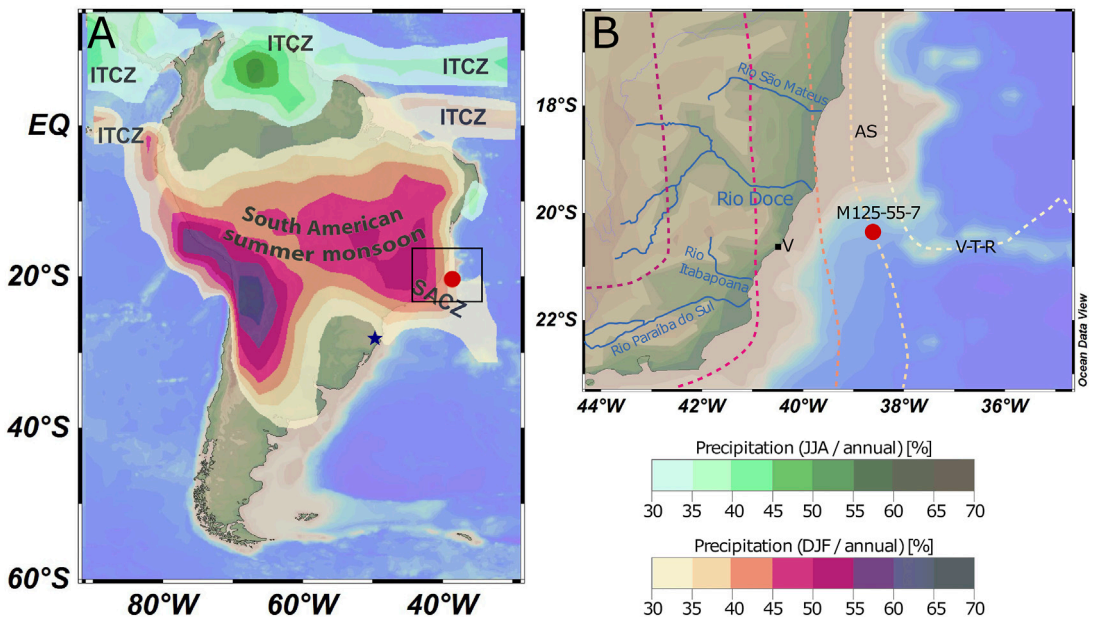

FIGURE 1 | (A) Distribution of austral summer and winter rain belts related to the position of the Intertropical Convergence Zone (ITCZ) and the South Atlantic Convergence Zone (SACZ) over a topographic and bathymetric Ocean Data View map of South America and surrounding oceans (Schlitzer, 2021), adapted from Flantua et al. (2016) and Vuille and Garreaud (2011). The location of Core M125-55-7 (this study) is marked with a red dot and is situated at the northern margin of the SACZ. The continental area in proximity to the core location is influenced by the South American Summer Monsoon (SASM). The overlain color schemes show how much of the annual precipitation occurs during the austral summer months (orange to blue) and winter months (green scale) in percent. The blue star marks the location of the Botuverá Cave, situated at the southern margin of the SACZ, from where MIS five $\delta^{18}O$ stalagmite data are available (Cruz et al., 2005). **(B)** Close up of the study area showing the location of Core M125-55-7 (red dot) close to the Doce river mouth at 20°S. The colored dashed lines indicate the percentages of summer precipitation in the total annual precipitation. For reference the City of Vitória is indicated (V), as well as the Vitória-Trinidade-Rise (V-T-R) and the Abrolhos Shelf (AS).

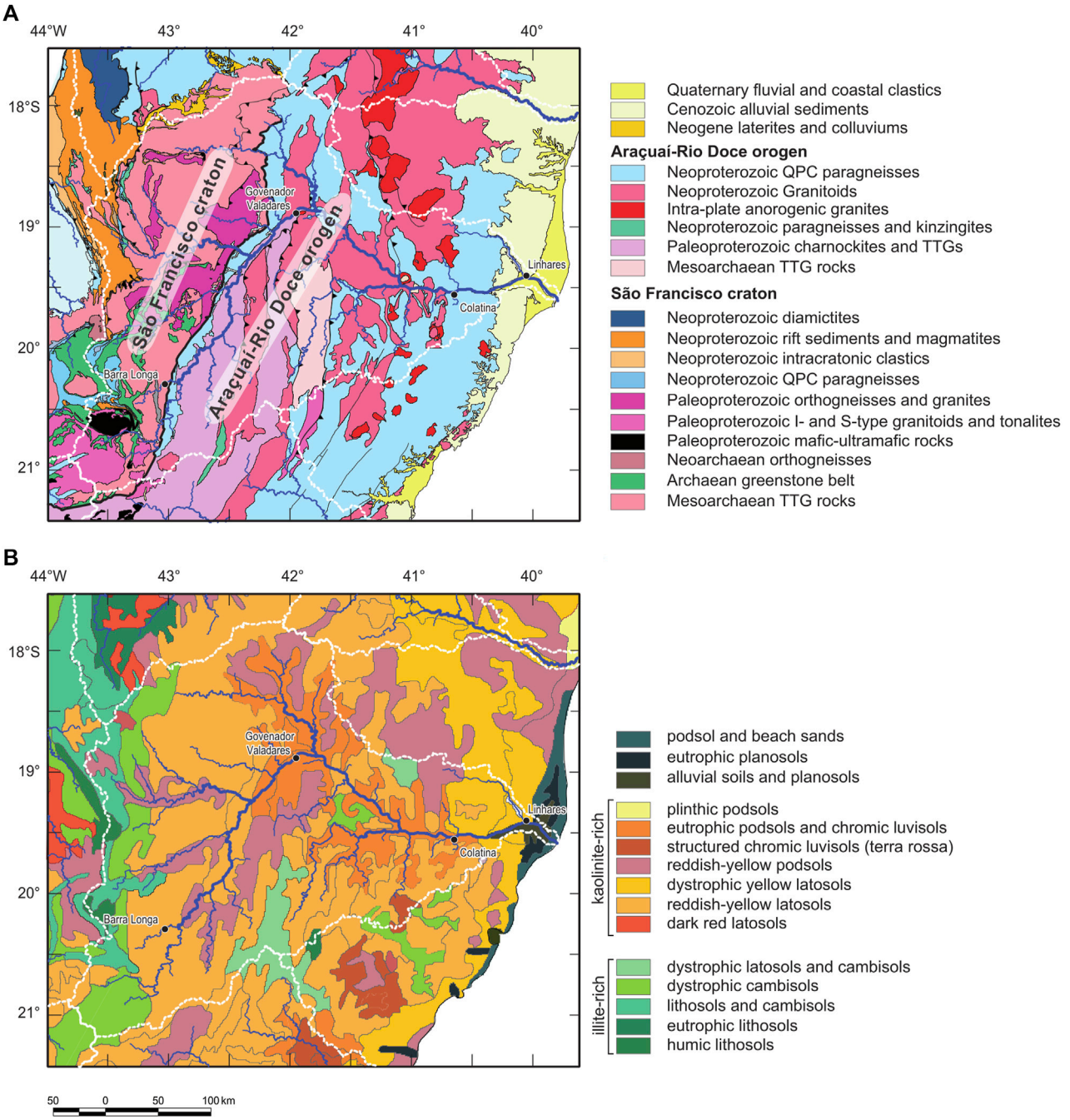

FIGURE 2 | Geologic **(A)** and soil **(B)** map of the Doce river discharge area. White stippled lines mark the boundaries of discharge areas. Geology is compiled from the tectonic map inset of the geological map of Brazil, 1:1.000.000, sheets Belo Horizonte, Rio Doce, Rio de Janeiro and Vitoria (CPRM–Serviço Geológico do Brasil, 2004). Soil data are digital versions of the Mapa de Solos do Brasil 1:5.000.000 (Embrapa-SNLCS, 1981; Bliss, 2013), and drainage and discharge data are from GRDC (2020).

occurring over tropical South America, which weakened during glacial phases (Cruz et al., 2009).

To assess the complex paleoprecipitation patterns, regional paleoclimate records are needed. Here, we provide a record of the past spatiotemporal precipitation variability in the Doce Basin, based on changes in the mineral composition of the discharged sediment analyzed via X-ray diffraction (XRD). The Doce Basin encompasses both the SACZ domain as well as the (south)eastern coastal lowlands of Brazil and thus is ideally suited to track past spatial precipitation variability. We investigated an 80 kyr time interval from late Marine Isotope Stage (MIS) 6 to the end of MIS 5, which spans over glacial, transitional and interglacial climate phases, covers a large range of CO_2 conditions (185–290 ppm V (Petit et al., 1999)) and includes several precession cycles.

CLIMATE AND GEOLOGICAL SETTING

The Doce watershed covers an area of 86,715 km^2. Fluvial discharge flows from elevations of over 1,500 m for roughly 850 km until reaching the Doce delta at around 19.7°S (May et al., 2020). The Caparaó mountains confine the basin to the south and the Espinhaço mountains to the west and northwest. The westernmost portion of the Doce Basin is part of the Archaean São-Francisco craton, whereas most of the basin is geologically assigned to the Proterozoic Araçuai orogen (de Almeida et al., 2000; **Figure 2**). Lithologically the basin consists predominantly of migmatites, granitoids, gneisses, schists and quartzites of Precambrian age with a few Late Proterozoic to Cambrian granitoid intrusion in the upper to middle catchment. Neogene sandstones, claystones and conglomerates cover the coastal area near the Doce river mouth (Schobbenhaus et al., 1981; **Figure 2**). In the middle to lower catchment, the rocks are overlain by thick soil layers, mainly latosols (= ferralsols, after Food and Agriculture Organization of the United Nations (FAO) classification) (**Figure 2**). In the upper mountainous regions, soils are thin and immature (FAO-UNESCO, 1971). The present-day climate in the basin is humid subtropical to tropical with dry winters and temperate to hot summers (Alvares et al., 2013), with maximum precipitation occurring in the austral summer months (December, January and February) due to the SASM. The seasonal precipitation variability leads to seasonal differences in the magnitude of water and suspended sediment discharge from the Doce River, which reach maximum values in January (Oliveira & Quaresma, 2017). Today, sediment discharge from the Doce River amounts to approximately 10 million tons per year (Lima et al., 2005; Souza & Knoppers, 2011).

While the large amounts of tropical soils in the source region make this area particularly suitable for palaeoclimate reconstructions via clay mineral analyses (Thiry, 2000), the position of the basin at the northeastern extension of the SACZ (**Figure 1**) makes its catchment sensitive to small changes in the positioning and strength of the SASM. Furthermore, the soil distribution in the Doce Basin allows for discrimination between head- and lowland-sourced sediments (**Figure 2**).

MATERIALS AND METHODS

The analyzed sediments are derived from piston gravity core M125-55–7, recovered during research cruise M125 with the German research vessel METEOR in March and April 2016. The core was taken at 20° 21.807′ S and 38° 37.387' W, 165 km from the Brazilian coast, from a water depth of 1960 m (Bahr et al., 2016). The total length of the core is 11.75 m of which a section from 2.2 to 5.2 m was sampled in steps of 2.5 cm. 119 samples with 3–9 ml of sediment material were taken from the core with open syringes. The sediment consists of greyish, greenish silty clays which are partly bioturbated and contain bioclasts. No structures within the core sediments point towards a disturbance of sedimentation by contour currents or turbidites. Furthermore, the core location chosen is situated on a submarine hill structure identified via multibeam sounders. PARASOUND data from the uppermost 40 m of sediment show continuous parallel strata at the coring site, indicating undisturbed hemipelagic sedimentation (Hou et al., 2020a Supporting Information Figure 4S).

The age model for this core was developed by Hou et al. (2020b). The ages are based on tuning of the benthic $\delta^{18}O$ record (*Uvigerina* spp.) to the LR04 benthic $\delta^{18}O$ stack (Lisiecki & Raymo, 2005) and ^{14}C dating in the upper 120 cm (Hou et al., 2020b). Based on this age model, our data set spans from roughly 70 to 150 ka, covering the late MIS 6, termination II (T II) and MIS 5.

Sample Preparation

Approximately 2 ml (~3 g) of each sample were dried, ground by hand and filled into sample holders from the rear side to gain texture-free bulk sediment samples. The rest of each sample was dissolved in 20% formic acid and rinsed with deionized water after decarbonization. The clay-sized fraction, < 2 µm, was separated through the Atterberg method (4 cm settling height) with sodium phosphate to avoid flocculation. After retrieving the clay-sized fraction, 0.1 ml of magnesium chloride solution was added to each sample suspension. Texture-free clay samples were created by inserting the clay powder from the rear side into the sample holder. The texture-free sample XRD measurement provides data for semi-quantitative mineral phase analysis. Textured clay samples were obtained by dissolving 20 mg of the clay powder in 2 ml deionized water, pipetting the suspension on circular glass slides and letting them dry at room temperature. Data from textured samples indicate the variability in clay mineral quantity more precisely and are used for the structural analysis of illites. After being exposed to an ethylene glycol atmosphere, the textured clay samples were remeasured to expand clay minerals such as smectites. This procedure makes the illite and smectite peaks more easily distinguishable from mixed layer mineral peaks (**Figure 3**).

Optical Analysis

We analyzed the sieving residuals of sizes greater than 250 µm under a stereo microscope, identifying the main calcifying organisms and their superficially visible preservation state. Additionally, we prepared smear slides of the bulk sediment from equivalent core depths. The smear slides were analyzed under a Zeiss Axio Imager A2 Microscope at up to 1,250 times magnification, to evaluate the microscopic content of the samples.

X-Ray Diffractometry (XRD)

All samples were measured with a PANalytical X'Pert PRO diffractometer, equipped with a copper X-ray tube, a Ni-filter, an automatic divergence aperture, a sample spinner, a sample changer with a capacity of 15 samples and a X'Celerator detector. The measuring voltage was 40 kV and the electric current was 30 mA. Measurements were performed in steps below 0.01° 2Θ with 30–50 s per step.

Four types of XRD measurements were performed. Firstly, the whole sediment was analyzed in a texture-free manner in the bulk

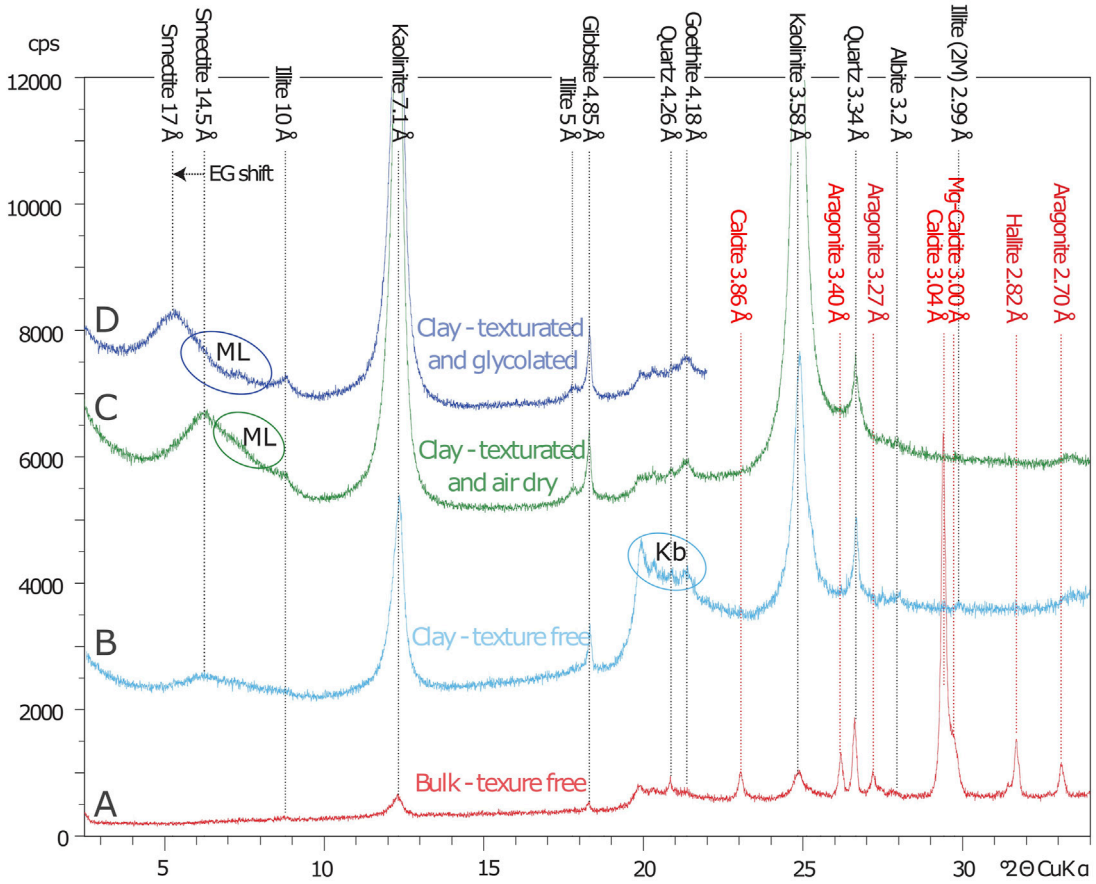

FIGURE 3 | Diffractogram showing the result of the four different preparation methods at one sample (Nr. 480). The y scale is to be viewed relatively within each measurement and does not indicate absolute values or relative intensities between different measurement types. **(A)** The bulk texture-free samples indicate the carbonate peaks, some halite, as well as quartz and low albite content. **(B)** Peaks from other phases, such as goethite and clay minerals are more distinctly seen in the texture-free measurements conducted on the decarbonized clay fraction. In curve B several high peaks at 20–21.5° 2Θ are reflections from kaolinites with b-axis variabilities (Kb). **(C)** Due to the sheet like crystal habit of clay minerals, their diffraction peaks are most intense, and thus best measurable, in the textured preparation. At around 7° 2Θ reflections from mixed layer minerals (ML) are detectable between the smectite and illite peak. **(D)** To minimize the possible interference of these mixed layer minerals with the illite and smectite peaks and to reliably identify the expandable smectite phase, the textured clay fraction samples are remeasured after exposure to an ethylene glycol (EG) atmosphere.

sediment analysis. Secondly, the clay fraction only was analyzed in a texture-free manner. Thirdly, the clay fraction was analyzed with orientated particles in the textured analysis. And lastly, the textured clay samples were remeasured after exposure to an ethylene glycol atmosphere (**Figure 3**). The XRD datasets are available in the **Supplementary Material**.

XRD Data Evaluation

The XRD data is visualized in a diffractogram displaying the measured reflexes in relative counts per second (cps) over the measurement angle 2Θ for each sample (see **Figure 3**). The changes in abundance of a mineral phase were evaluated by measuring the peak intensity (texture-free samples) or the peak area (textured samples). The software used for data evaluation is MacDiff 4.2.6 (Petschick, 2010). Peak intensity measurements were applied to gain semi-quantitative sediment composition data from the texture-free samples. For the necessary peak intensity correction, we used Reference Intensity Ratios (RIRs) from Powder Diffraction File™ 4 (PDF-4). Peak area measurements were applied to determine the relative abundance of clay mineral phases within the textured samples. For the peak area correction, Biscaye factors were used (Biscaye, 1965).

The values of the peak heights or areas of all measured phases were summed for each sample and defined as 100% of the sediment (e.g., for the bulk sediment in **Figure 4I**). The relative percentages of the phases are calculated thereafter. Aragonite, Mg-calcite and calcite are additionally evaluated separately as percentages of the sum of all carbonate phases from the bulk sediment.

RESULTS

The carbonate to silicate ratio indicates an insolation-paced relative increase in terrestrial material within the sediment

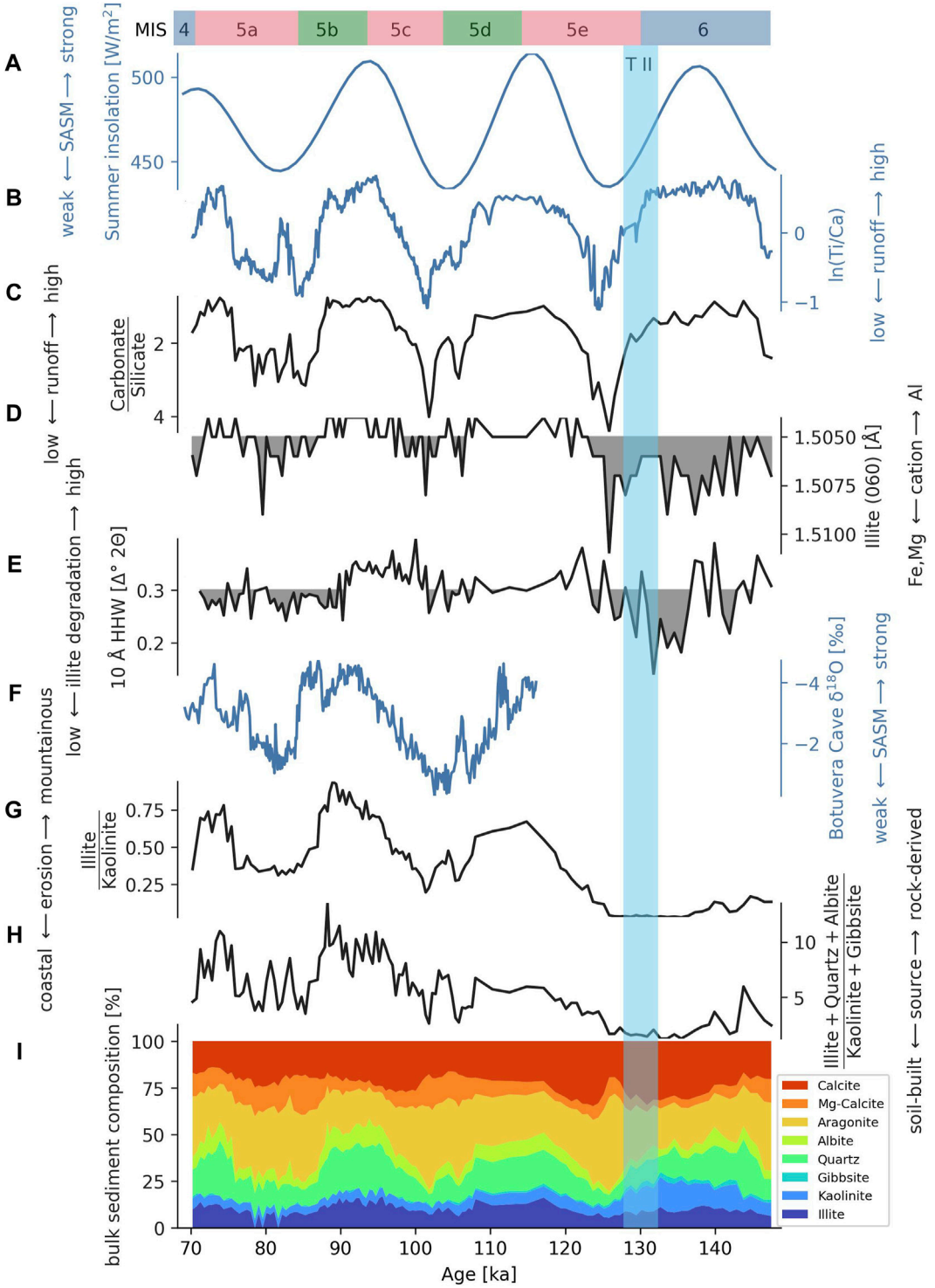

FIGURE 4 | Bulk sediment and river derived fraction XRD data compared to **(A)** the summer insolation curve at 20°S (Laskar et al., 2004), **(B)** ln (Ti/Ca) ratios based on x-ray fluorescence scanning of Core M125-55-7 (Hou et al., 2020a). **(C)** The carbonate to silicate ratio is calculated from the bulk sediment measurements and indicates the relative discharge of terrestrial material through runoff. During high insolation phases, discharge is enhanced. **(D)** The (060) peak around 1.50 Å (texture free clay fraction) indicates the proportion of different elements occupying the octahedra cation position in illite, with Fe^{2+} and Mg^{2+} indicating wider spacing and Al^{3+} lower spacing. Values above 1.505 Å are shaded. Al-rich illites are more abundant in phases of high discharge in MIS 5. **(E)** The width of the of the 10 Å illite peak at half of its maximum height is expressed as the half height width (HHW) within the textured clay fractions. Values below 0.3 Δ° 2Θ are shaded. Brought 10 Å peaks indicate higher degradation or lower crystallinity, occurring predominantly in high insolation phases. **(F)** $\delta^{18}O$ values from the Botuverá Cave (cave location see **Figure 1**) from Cruz et al.

(*Continued*)

FIGURE 4 | (2005). **(G)** The Illite to kaolinite ratio is calculated from the textured clay fraction measurements. It represents the discharge proportion from the mountainous region, with immature, illite rich soils to the mature kaolinite rich soils of the lowlands and coastal areas where soils are particularly low in illite. Erosion in mountainous areas seems to be enhanced during interglacial high insolation phases. **(H)** Quartz, albite and illite are mainly derived from disintegrated parent rock grains within immature soils while kaolinite and gibbsite are newly built in mature soils. Their ratio is calculated from texture-free clay fraction measurements and indicates the proportion of parent rock to soil sourced discharge. **(I)** Proportion of all mineral phases determined from the bulk sediment measurements.

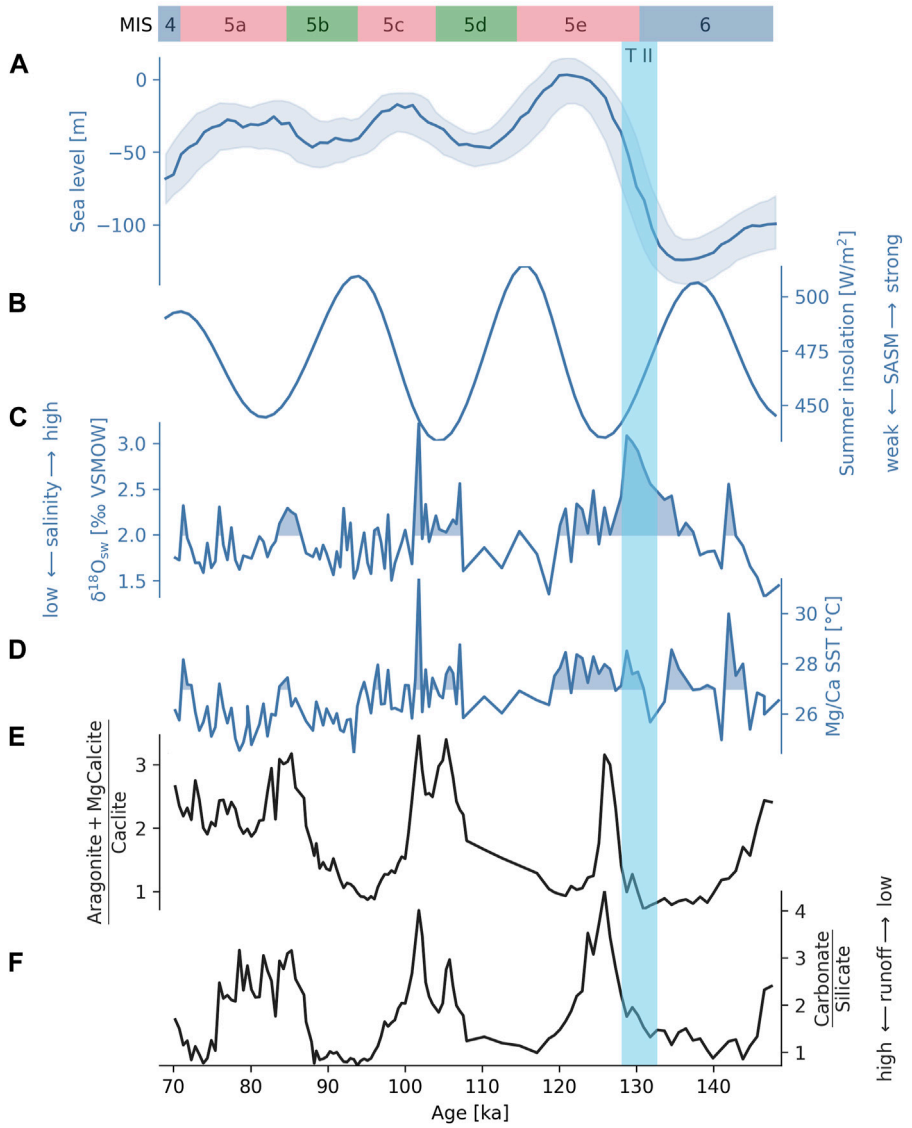

FIGURE 5 | Proportion of calcite phases compared to environmental proxies. **(A)** Sea level curve relative to today from Spratt and Lisiecki (2016). **(B)** Austral summer insolation curve at 20°S (Laskar et al., 2004). **(C)** Ice-volume-free seawater $\delta^{18}O$ curve from Core M125-55–7 (Hou et al., 2020a). **(D)** *Globigerinoides ruber* (pink) Mg/Ca SST from Core M125-55–7 (Hou et al., 2020b). **(E)** Relation of the carbonate phases aragonite and Mg-calcite to calcite. The ratio is intensifying the carbonate trends seen in the bulk sediment record (**Figure 4I**), with aragonite and Mg-calcite being decreased and calcite being increased in high insolation phases. **(F)** The carbonate to silicate ratio indicates the discharge intensity of the Doce River. The remarkable co-variability of carbonate phase proportions and discharge indicates that the riverine influx impacts the marine environmental conditions. High discharge seemed to be more profitable for calcitic organisms while in times of higher evaporation, indicated by high temperatures and salinities, aragonitic and Mg-calcitic organisms dominate the carbonate production.

(**Figures 4A–C**). The ratio of illite, quartz and albite to kaolinite and gibbsite within the bulk sediment was low during MIS six but increased during MIS 5 (**Figure 4H**). During MIS 6, illite to kaolinite is very low, while MIS 5 has a higher background illite to kaolinite ratio (**Figure 4G**). During MIS 5, the illite to kaolinite ratio increases and decreases in phase with insolation. Similarly, the mineral phases illite, quartz and albite are dominant in the bulk sediment during MIS 5 in times of high insolation, while

kaolinite and gibbsite are relatively reduced. Furthermore, the illite to kaolinite ratio displays an asymmetric pattern with a gradual increase followed by a rather abrupt decline, as seen at 108 ka and 87 ka. A similar pattern is visible in the illite, albite and quartz to kaolinite and gibbsite ratio.

Further investigations on the half height width of the 10 Å illite peak of the textured clay fraction indicated that all illites are relatively well crystallized, with half height widths of below 0.4 Δ° 2Θ (**Figure 4E**). Using the illite polytype quantification approach after Grathoff and Moore (1996) on the texture-free clay samples, indicates that most illites (>90%) are of the 2M type, indicating growth as micas under high temperatures, whereas roughly 8% are 1M illites, typically formed in soils. The 5 Å to 10 Å illite ratios fluctuate around a value of 0.5, pointing to illites with mainly Al^{3+} as octahedral cation. Values greater than 0.4 indicate aluminum-rich illites while decreasing values signify an increasing magnesium and iron content (Esquevin, 1969). Similarly, the position of the (060) illite peak indicates the dominance of aluminum-rich illites, especially during high discharge phases (**Figure 4D**).

Aragonite, present at 35–63%, is the most abundant within the carbonate phases. Aragonite suppliers present in the samples are pteropod shells and a few other gastropod and bivalve shells. The shells are well preserved and did not show superficially visible signs of dissolution. Mg-calcite, mainly supplied by echinoderms and some miliolid foraminifera, makes up 5–28% of the carbonates. Calcite is delivered by benthic and planktonic foraminifera as well as coccolithophores and accounts for 22–58% of the carbonate fraction. In times of lower insolation, aragonite and Mg-calcite are the dominant carbonate phases, while in times of higher insolation, aragonite and Mg-calcite contents decrease, and calcite is relatively more abundant. This variability is well observed in the aragonite plus Mg-calcite to calcite ratio (**Figure 5E**). The sharp peak at 126 ka is especially rich in aragonite and is followed by a peak in calcite at around 123 ka (**Figure 4I**). This pattern is repeated less intensely during later intervals of carbonate phase development, wherein aragonite and Mg-calcite peaks at 106 and 88 ka are followed by calcite increases at 100 and 82 ka, respectively.

DISCUSSION

Mineral Phase Origins

To determine the relationship between mineralogical changes in the sediments and precipitation changes in the hinterland, it is necessary to evaluate the main origins of the mineral phases. Possible mineral sources can be categorized into terrestrial sources and marine sources. Marine sources are mainly skeletal remains of marine organisms. Terrestrial sources are more diverse; they include terrestrial material delivered from distal sources via marine currents and material from the Doce watershed and adjacent regions. The majority of the Doce watershed area is covered by thick mature soils, mainly latosols and podzols (**Figure 2**). In these mature soils, weatherable parent rock minerals are dissolved, and kaolinite and gibbsite are built (WRB, 2015). The formation of illites within the soil could be a result of orthoclase weathering (Meunier and Velde, 2004). In the mountainous regions of the upper catchment, soils are less mature (FAO-UNESCO, 1971). Due to the less intense petrogenesis the present lithosols and cambisols contain a higher percentage of parent rock fragments. A large percentage of the Doce watersheds lithology are felsic rocks like granitoids and gneisses (**Figure 2**). Therefore, we consider muscovite, quartz and albite as likely parent rock fragments. Below we will discuss the main origins of the mineral phases measured in our samples and categorize them into four groups of origin: 1. marine built: aragonite, Mg-calcite and calcite; 2. distal sources: smectite and chlorite; 3. immature soil derived material: illite, albite and quartz; 4. mature soil derived material: kaolinite and gibbsite.

1. Marine built: The measured carbonate phases in the samples are aragonite, Mg-calcite and calcite. Noticeable terrestrial input is unlikely, as there are no significant amounts of limestone outcropping in the Doce watershed (Schobbenhaus et al., 1981). Moreover, the amount of visible clastic, non-biogenous carbonate grains in the samples was below 1%. The main mature soils present (ferralsol and acrisol) are acidic (WRB, 2015; FAO-UNESCO, 1971), prohibiting intense soil carbonate formation. Typical regional soils have low pH values of four–six and are often limed to make them suitable for agriculture (Abreu Jr et al., 2003; Santos et al., 2014). Thus, soil carbonates are not considered a significant contributor to carbonate preserved in the marine sediments. Bacterial carbonate precipitation is possible (e.g., Kranz et al., 2010) but scarce in Cenozoic open marine environments (Riding, 2000). We do not expect it to be a substantial carbonate contributor but cannot exclude a contribution to the micritic carbonate ooze. We analyzed the bulk sediment samples microscopically, and they consisted of both planktic (coccolithophores, foraminifera, gastropods) and benthic (foraminifera, echinoderms, gastropods, bivalves) calcifying organisms. Overall, the carbonate phases contained in the sediment seem to be mainly built by calcifying organisms.

2. Distal sources: Smectite and chlorite are detectable in the clay samples. They are, however, not present in the clay fraction transported by the Doce River (Tintelnot, 1995) nor are they typically built in tropical soils, but rather indicative for dryer and cooler climates (Velde, 1995). They likely originated from soils in south Brazil and Argentina (smectite) and the Patagonian region (chlorite) from where they were transported northward to the core site *via* marine currents (Jones, 1984; Petschick et al., 1996; Warratz et al., 2017). As they are not discharged from the Doce Basin and thus not indicative of regional climate variability, they are not further discussed.

3. Immature soil derived: Illite polytype quantification after Grathoff and Moore (1996) indicates that over 90% of the illites in the analyzed sediments originate from ground muscovite (M2 type), while only 8% are newly formed in soils (M1 type). The illite crystallinity, measured *via* the half-height widths of the 10 Å illite peak, provides another indicator for their origin. Low half height widths, below 0.4 Δ° 2Θ, point towards an illite development from fine-grained mica (Velde & Meunier, 2008). All samples have illite crystallinity values below 0.4 Δ° 2Θ and even decrease below 0.2 Δ° 2Θ during late MIS 6. High 5 Å to 10 Å illite peak ratios, around 0.5, indicate aluminum-rich illites

(Esquevin, 1969), also pointing towards a muscovite origin. The mineralogical illite parameters suggest the parent rocks provided for most of the illite contained in the sediment, while soil-built illites were a minor contributor. Most mature soils in the Doce watershed contain only approximately 3% mica. The soils on the coastal, Neogene clastic sediments have even lower mica concentrations of around 0.1% (Melo et al., 2001). However, the percentage of illite relative to all clay minerals transported in the Doce River is approximately 20% (Tintelnot, 1995). The discrepancy between the illite content of the mature soil and the detrital river discharge underlines that another significant source of illite must be present, in this case, the thin and immature soils of the upper catchment. Quartz and albite, like illite, originate from weathered parent rock and are present in regional soils. Higher quartz and albite concentrations are however expected in the immature soils of the upper catchment, due to lower rates of chemical weathering. Weatherable minerals, like feldspars, are usually scarce or absent in the mature ferralsols, while quartz can sustain this intense weathering (WRB, 2015). The covarying behavior of quartz, illite and albite indicates that these phases are delivered *via* a similar process. It is expected that through enhanced erosivity during heavy precipitation events, more parent rock derived mineral phases from the immature soils of the mountainous hinterland are transported to the ocean. Overall, we assume that the major proportion of the parent rock derived grains (illite, quartz, and albite) are delivered from erosion in mountainous areas with shallow soils while only a small proportion comes from the mature soils in the lowlands, making these mineral phases indicative of input from immature soils.

4. Mature soil derived: Kaolinite is newly built during ferralsol formation (WRB, 2015), and ferralsols/latosols are the most abundant mature soils in the Doce Basin (FAO-UNESCO, 1971; **Figure 2**). Gibbsite is typically formed under high weathering regimes and is also a common phase in ferralsols (Mohr et al., 1972; Sanchez, 2019). The regional mature soils have kaolinite contents of 50–80% (Melfi et al., 1983; Cunha et al., 2019), while in the sediment load of the Doce River, close to the river mouth, kaolinites make up approximately 80% of the transported clay minerals (Tintelnot, 1995). Kaolinite and gibbsite are thus indicative of material derived from regional mature lowland soils.

On the eastern and southeastern Brazilian coast, the Doce River is associated with the highest suspended sediment discharge into the Atlantic Ocean (Lima et al., 2005; Souza & Knoppers, 2011) and is the river mouth closest to the core site. Additionally, the ratio of illite to kaolinite at the coring depth of ~2,000 m, matches that of the shelf and the Doce River itself. The smaller São Mateus River, adjacent to the north (**Figure 1**), shares a similar illite to kaolinite ratio (Tintelnot, 1995). The nearest river with a similarly large catchment area and sediment discharge to the Doce River is the Jequitinhonha River mouthing into the South Atlantic at around 16°S (Souza and Knoppers, 2011). This river has an illite to kaolinite signature twice as high and the illite to kaolinite ratio of the even larger São Francisco River, mouthing at ~ 10°S, is over four times higher than that of the Doce River (Tintelnot, 1995). At present, it appears that the Doce River is the main regional supplier of terrestrial sediment deposited at the continental slope at 20°S. The satellite analysis of regional riverine turbidity plumes underlines this assumption, as the suspended material of smaller rivers to the north of the Doce River is contained on the inner shelf while the Doce River delivers material to the offshore region (Oliveira et al., 2012). In times of low sea levels, however, more input from the coastal areas adjacent to the Doce watershed can be expected. A deposition of small amounts of sediment from smaller catchments with similar mineral compositions transported by the southward flowing Brazil Current cannot be ruled out. However, adjacent catchments are significantly smaller and supply less sediment. Therefore, we argue that the Doce catchment is the main supplier of regional terrestrial sediment to the coring site and changes in the terrestrial mineral assemblage of the core sediment are caused by changes in the Doce River discharge composition.

Within the Doce watershed, a regional distribution of different mineral sources allows for the discrimination between three areas: the mountainous regions with thin immature soils in the upper catchment as the source for most of the illite, quartz and albite; the mature, thick soil plains of the middle and lower catchment, being low in illite and rich in kaolinite; and the almost illite-free coastal lowland soils (Melo et al., 2001) supplying mainly kaolinite. A distinction between the two endmembers (i.e., mountainous vs. coastal erosion) can be seen in the illite to kaolinite ratio (**Figure 4G**).

Carbonate Variability

Within the carbonate phases, a distinct insolation-related pattern is visible (**Figure 5**). Aragonite and Mg-calcite proportions are higher in times of low summer insolation and low fluvial discharge. In contrast, calcite is increased in times of high summer insolation and higher fluvial discharge. The rise of aragonite and Mg-calcite productivity in MIS five corresponds to some degree with elevated SST and salinity ($\delta^{18}O$ ice-free seawater) data from the same core (Hou et al., 2020a; **Figures 5C–E**).

At the core site, the lowest water mass is the Upper North Atlantic Deep Water (UNADW), which is present from the ocean floor (1,960 m) to depths of roughly 1,100 m (Bahr et al., 2016). The lower boarder of the UNADW lies around 2,500 m in this region (Henrich et al., 2003). Antarctic Intermediate Water (AAIW) flows at depths of 600–1,100 m (Bahr et al., 2016). Carbonate deposition at the core location occurred at a depth of ca. 2,000 m, which is well above both the tropical West Atlantic aragonite compensation depth (3,400 m) and the lower aragonite lysocline (2,500 m) (Gerhardt & Henrich, 2001). It has been reported that due to high fluvial nutrient input at around 19 to 23°S, primary productivity is elevated and metabolic CO_2, formed by respiration of the organic matter, can acidify the already slightly carbonate undersaturated AAIW. Therefore, aragonite dissolution can occur at above 1,330 m water depth in that area (Gerhardt & Henrich, 2001). Presently, aragonite is well preserved at water depths around 2,000 m in the western South Atlantic. During the last glacial maximum, preservation at this depth was very good to moderate (Henrich et al., 2003). The

shells we recovered through sieving appeared macroscopically well preserved and further dissolution analysis was not performed. At roughly 30°S, Petró et al. (2021) analyzed supra-lysoclinal carbonate dissolution from MIS 5 to MIS 1, by analyzing foraminifera fragmentation. They report good preservation at roughly 1,500–2,000 m water depths for MIS 5. Furthermore, (aragonitic) scleractinian cold water corals are presently growing at around 900 m water depth. These corals even profited from strong runoff and higher nutrient availability during glacial periods (Bahr et al., 2020; Raddatz et al., 2020). We therefore assume a low aragonite solubility at the deposition site during both glacial and interglacial periods as well as low dissolution in the water column. Although, it cannot be excluded that some aragonite dissolution took place as aragonitic shells sank through the carbonate under-saturated AAIW, we argue that dissolution is not the driver for changes in the carbonate composition nor the carbonate to silicate ratio.

Since aragonite dissolution at the deposition site was probably low to moderate, the aragonite and Mg-calcite to calcite ratio likely reflects the relative productivity changes of the different calcifiers. Aragonite and Mg-calcite calcifiers could have been better adapted to elevated temperatures and salinities and less tolerant to increased nutrient levels and turbidity induced by high fluvial discharge. By contrast, calcitic organisms could have thrived in times of high summer insolation and higher fluvial discharge. The calcareous nannofossil assemblage from a nearby core (KF-12, taken at ~21°S) consists of over 60% opportunistic coccolithophores (*Emiliania huxlei* and *Gephyrocapsa* spp.) (Costa et al., 2016). In times of high fluvial discharge, Costa et al. (2016) saw an increase in these species, indicating higher surface water productivity due to a shallowing nutricline. The relatively high calcite proportion seen in our samples during enhanced fluvial discharge phases could similarly be caused by an increase in opportunistic coccolithophore species due to their ability to adapt better to nutrient enrichment in the surface water.

Monsoon Driven Discharge Variability During MIS 5

The carbonate to silicate ratio can be driven by carbonate productivity, carbonate dissolution, and terrestrial input variability. In times of high fluvial nutrient influx, an increase in primary productivity and respiration is expected, which could lead to acidification of the water masses and carbonate dissolution (Jahnke et al., 1994; Suárez-Ibarra et al., 2022). Runoff-dependent aragonite dissolution would drive the carbonate to silicate ratio in the same direction as increased fluvial sediment influx. Thus, carbonate dissolution, if present, enhances the relative silicate content. Runoff enhanced primary productivity could also increase the overall carbonate production and sedimentation rates. As such the impact of carbonate productivity could have a major impact on the carbonate to silicate ratio. Costa et al. (2016), however, observed a negative correlation between calcareous nannofossil productivity and the carbonate content in the fine fraction in their data, indicating dilution by terrestrial input in times of increased runoff. The core from Costa et al. (2016) was collected from less than 200 km south of M125-55-7 and includes sediments from 50 to 140 ka. Their core position is further from the Doce river mouth and closer to the mouth of the Paraiba do Sul, a river that nowadays has less than half of the Doce River's yearly fluvial discharge (Lima et al., 2005). We assume that our core's sediments are similarly or even more strongly controlled by fluvial sediment influx than the core studied by Costa et al. (2016). Therefore, we argue that the carbonate to silicate ratio can be used to indicate the fluvial discharge intensity of the Doce River.

The carbonate to silicate ratio indicates an increased overall fluvial discharge during intervals of high austral summer insolation and confirms the previously measured ln (Ti/Ca) (Hou et al., 2020a). Its insolation dependence appears to be more robust during MIS 5 (**Figure 4**). A strengthening of the monsoon system during high insolation periods of the MIS 5 interglacial would have caused heavy seasonal precipitation in the Doce watershed. Intense summer monsoon precipitation may have increased the erosivity of the Doce River, especially in the Espinaço and Caparaó mountains in the western and southern upper and middle catchment. Increased transport of disintegrated parent rock material from immature soils would be expected in this scenario and is confirmed by the mineral composition of the discharge in high insolation phases of MIS 5. While carbonate to silicate ratios decrease, the immature soil derived phases albite, quartz and illite are relatively increased (**Figure 4H**). The high illite to kaolinite ratio and illite mineral parameter development during high insolation intervals (**Figures 4D,G**) underline the notion that erosion in the mountainous hinterland is enhanced in MIS 5 high insolation periods.

The illite crystallinity, indicated by the half-height width of the 10 Å illite peak, refers to the amount of consecutively stacked illite crystal layers. Illite crystallinity is generally high in Core M125-55-7 sediments, indicating that illites are mostly crushed mica particles (Velde & Meunier, 2008). Still, a slight decrease can be seen during high insolation phases of MIS 5. A reduced crystallinity could indicate an increased supply of soil-built illites in times of high insolation or stronger weathering of the parent rock in immature soils, delivering more degraded illites. Illite polytype quantification indicates that only a low proportion of illites (8%) could be soil-built (1M type). Therefore, we assume that a decrease in crystallinity mainly indicates increased muscovite comminution due to intensified weathering in mountainous regions. High insolation phases in MIS 5 co-occur with an increase in aluminum at the octahedral cation position, as indicated by a lower illite (060) peak position (**Figure 4D**). This could be a sign of stronger illite degradation, promoting a reduction of Fe in illite through leaching in times of high insolation and increased monsoonal precipitation. High illite degradation, the increased proportion of aluminum-rich illites and the overall increase in illites in the discharged sediment indicate increased erosion from mountainous regions, suggesting an increase in heavy precipitation events in these regions. It is thus likely that a strong summer monsoon, similar to the present-day SASM, developed during the high insolation phases of MIS 5. As insolation maxima were higher during MIS 5 than they are

nowadays in MIS 1 (Laskar et al., 2004), the summer monsoon during MIS 5 was likely more intense than the present-day SASM.

During the low austral summer insolation phases of MIS 5, discharge from the Doce River decreased as indicated by the carbonate to silicate ratio increase. High illite crystallinity also points to lower illite degradation in low insolation phases. Furthermore, there was a reduction in the proportion of parent rock derived fraction to soil-built fraction. A decrease in erosivity and weathering indicates reduced water availability, which we interpret as a weakening of the summer monsoon system during the low insolation phases of MIS 5. The low illite to kaolinite ratio supports our interpretation that, due to a weakened summer monsoon, erosion in the upper river course is reduced, making mature lowland soils the primary supplier for the fluvial sediment load. At the same time, SE trade winds and with them austral winter precipitation could have increased in MIS 5 low insolation phases similar to the situation in MIS 6 proposed by Hou et al. (2020b). An intensification in coastal precipitation would further support the erosion of illite depleted, kaolinite rich coastal soils.

The asymmetry of the illite to kaolinite curve indicates a slow increase in mountainous erosion, driven by a gradually intensifying monsoon, followed by a rapid decrease in the ratio of illite to kaolinite as monsoonal precipitation weakened. A similar pattern is visible in the ratio of parent rock derived minerals to soil-built minerals (**Figure 3H**). It is to be noted that a continuation of the heavy monsoon signal during already decreasing insolation takes place at the beginning of the cooler substages MIS 5d and MIS 5b. This could be an indicator of higher moisture availability in the Doce Basin during global cooling. The overall tendency of the system for a slow moisture increase followed by a rapid decrease in moisture availability, as shown in our data, highlights the region's potential vulnerability to increasing droughts in a changing climate (May et al., 2020).

To assess the spatial variability in monsoonal rainfall intensity, we compared our data to a $\delta^{18}O$ stalagmite record from the Botuverá Cave (Cruz et al., 2005), which is located around 28°S, near the coast of southern Brazil and at the south margin of the SACZ (see **Figure 1**). The effect of the insolation driven strength of monsoonal precipitation on the $\delta^{18}O$ values from the Botuverá Cave and the illite to kaolinite ratio from the Doce watershed are in phase (**Figures 4F,G**). As these two sites are located on the opposite margins of the SACZ, we assume that the monsoonal system weakened and strengthened with insolation variability during MIS five rather than being displaced latitudinal.

Lowland Discharge During Late MIS 6

Like during MIS 5, an increase in sediment discharge during phases of high summer insolation is visible during MIS 6. However, the dominance of parent rock derived material from immature soils over mature soil-built mineral phases during the high insolation period is missing. Also, the illite to kaolinite ratios, which showed a clear covariation with insolation in MIS 5, stay continuously low throughout MIS 6 and are well below the values from low insolation phases during MIS 5. This could be an indicator of stronger erosion in the illite-depleted present-day coastal areas and the widely exposed Brazilian shelf area during MIS 6 (Maia et al., 2010; Bastos et al., 2016), due to sea levels of more than 100 m below present (Spratt & Lisiecki, 2016). At low sea levels the Doce catchment would expand to include more of the present coastal and shelf areas. During the period of reduced illite input in MIS 6, illites show more variable but overall higher iron and/or magnesium contents and higher crystallinities (**Figures 4D,E**). This indicates that the delivered illites derive mainly from crushed muscovite in lower soil layers close to the parent rock. A steeper topographic gradient at an exposed shelf could have induced erosion of low soil layers at times exhibiting some better-preserved parent rock derived material, like illites with higher crystallinities. The increased variability underlines a more diverse, lower soil origin of the few illites eroded during MIS 6, in contrast to the more stable and abundant supply of illites from the immature soils in the upper catchment in MIS 5. Overall, we assume that erosivity in the mountainous regions was reduced while coastal erosion was increased during MIS 6. Hou et al. (2020b) proposed that very strong trade winds caused prolonged SST warming in the western tropical South Atlantic during late MIS 6. The presence of strong trade winds and high SSTs, which increase coastal precipitation, could reinforce the enhanced mature lowland soil erosion indicated by the low parent rock derived to soil-built phase ratio, the illite to kaolinite ratio and the illite mineral parameters (**Figure 4**).

As the overall sediment discharge remained insolation dependent, it is likely that moisture availability was also increased in the Doce watershed during the high insolation phases of MIS 6. The lack of immature soil derived mineral phases during periods of high moisture availability indicates a difference in the distribution and short-term precipitation intensity between MIS 5 and MIS 6. Precipitation anomalies related to the modern SASM are more intense in the upper catchment of the Doce River (**Figure 1**). The sediment load discharged during December and January is roughly twice as much as the combined load during the rest of the year (Oliveira & Quaresma, 2017). Thus, monsoon-related heavy precipitation events in the upper catchment contribute largely to today's sediment discharge. A similar discharge pattern can explain the mineral assemblage of the high insolation phases in MIS 5 but not in MIS 6. The insolation-dependent increase in sediment influx to the ocean during MIS 6 comprised mostly soil-built phases. This points towards low precipitation intensity and erosivity in the upper river course in favor of more evenly distributed precipitation over the kaolinite-rich, mature soil layers of the Doce Basin and increased lowland erosion. We propose that during MIS 6 precipitation in the mountainous areas was reduced and fewer heavy precipitation events occurred, compared to MIS 5. Therefore, it is likely that the summer monsoon system along the SACZ was poorly developed throughout MIS 6, even during periods of high insolation.

High Northern Latitude Temperatures and Local Precipitation

The difference in discharge composition between glacial (MIS 6) and interglacial (MIS 5) seen in our data agrees with previous studies indicating that the mainly insolation driven precipitation patterns over SE Brazil are affected by high northern latitude temperature changes and global pCO_2 (Cruz et al., 2005, 2009; Hou et al., 2020a). We assume that during MIS 6, lowland winter

precipitation in the Doce Basin was higher and the region experienced less intense but more frequent precipitation all year round, eroding more mature lowland soils and less immature mountainous soils. Moreover, our data show reduced summer monsoon precipitation during MIS 6. A driver of reduced summer precipitation in the Doce Basin could be a weakened SACZ caused by reduced AMOC during MIS 6, leading to higher temperatures at the SW Atlantic and shifting the sea-land interaction and thus the strength of the convection belts, as previously described for eastern Brazil during reduced AMOC phases of the Holocene (Bahr et al., 2021).

From our data, we can infer that the predominant rainfall regime in the Doce Basin shifted from well-developed lowland and coastal precipitation in MIS 6 to insolation-dependent heavy summer monsoon precipitation in the mountainous regions during MIS 5. Similarly, precipitation models propose that by 2080 global warming will have induced a slight increase in summer precipitation in the Doce watershed while winter precipitation will be decreased (FEAM, 2011; IPCC, 2021). Flooding associated with particularly heavy monsoonal summer precipitation and accurate flood forecasts are already a problem in the Doce watershed (Tomasella et al., 2019); an increase in heavy precipitation events would exacerbate this issue. Our data further indicate that riverine discharge was mostly insolation-dependent during interglacial periods. However, the observed shift in the precipitation pattern from glacial to interglacial conditions suggest that the likelihood of heavy precipitation events in the mountainous areas could increase and SE trade wind induced precipitation in the coastal areas could decrease with global warming. The trends seen in our paleoenvironmental data are in line with climate model precipitation predictions, underlining the need to prepare the region for increasing monsoonal heavy precipitation events and lowland droughts. We suggest further investigations on the spatial distribution of paleoprecipitation in the region, to test this hypothesis and to expand upon the understanding of climate-related precipitation changes in the Doce watershed area.

CONCLUSION

The availability in terrestrial sediment input from the Doce River to the marine sediment core M125-55-7 shows that insolation changes primarily paced fluvial discharge during the interval from 150 to 70 ka before present. Changes in the mineralogical composition of the discharge indicate that a strong summer monsoon system developed during the high austral summer insolation phases of the interglacial MIS 5, wherein heavy precipitation events increased erosion in the mountainous regions. During the low summer insolation phases of MIS 5, the monsoonal system was weakened, and lowland erosion became the main supplier of detrital fluvial discharge. During the glacial interval MIS 6, lowland and coastal erosion dominated the discharged sediment. A strong monsoonal precipitation pattern, increasing erosion in mountainous regions, was not developed. We propose that during MIS 5, the austral summer monsoon system strengthened and weakened in phase with insolation along a stationary SACZ. In contrast, the summer monsoon system throughout (late) MIS 6 was poorly developed, even in times of high insolation. Therefore, the impact of lowland precipitation on the riverine discharge was dominant throughout MIS 6. In this study, we interpret relative changes in riverine discharge. For a quantitative comparison with present and future climate scenarios, further research is needed. From the qualitative assessment of our paleoenvironmental data, we can infer that global warming may lead to more erosive SASM-related heavy precipitation events in summer and reduced mean annual precipitation in the lowland. This inference corresponds to recent climate models (IPCC, 2021), indicating that with ongoing anthropogenic global warming, the region of the Doce watershed will become more vulnerable to both flooding and droughts.

DATA AVAILABILITY STATEMENT

The original contributions presented in the study are included in the article/**Supplementary Material**, further inquiries can be directed to the corresponding author.

AUTHOR CONTRIBUTIONS

IA: Conceptual model development, XRD data analysis and interpretation, manuscript writing and illustration. SV: Project design, supported manuscript writing, contributed illustration, cruise participation. RP: Supervision of sample preparation and XRD data analyses, exchange of scientific ideas, illustration refinement. AH: Exchange of scientific ideas, manuscript corrections. JR: Exchange of scientific ideas, manuscript corrections, cruise participation. AA: Cruise participation. AB: Exchange of scientific ideas, manuscript corrections, cruise chief scientist. All authors revised and approved the manuscript.

FUNDING

The METEOR expedition M125 was funded by the Deutsche Forschungsgemeinschaft (DFG) and the Bundesministerium für Bildung und Forschung (BMBF). AB was supported by DFG grant BA3809/9, AA is a CNPq senior researcher (grant 302521/2017-8).

ACKNOWLEDGMENTS

The authors kindly acknowledge the support by captain, crew members and the scientific party of R/V Meteor during the M125 expedition. We thank Jens O. Herrle for his support in the preparation of smear-slides and the identification of calcifying organisms and Lisa Preussner for helping with the clay sample preparation.

SUPPLEMENTARY MATERIAL

The Supplementary Material for this article can be found online at: https://www.frontiersin.org/articles/10.3389/feart.2022.864381/full#supplementary-material

Data Sheet 1 | bulk sediment texture free XRD data

Data Sheet 2 | clay fraction texture free XRD data

Data Sheet 3 | clay fraction textured XRD data

Data Sheet 4 | mineralogical parameters of illite

REFERENCES

Abreu Jr., C. H., Jr., Muraoka, T., and Lavorante, A. F. (2003). Relationship between Acidity and Chemical Properties of Brazilian Soils. *Sci. Agric. (Piracicaba, Braz.)* 60, 337–343. doi:10.1590/S0103-90162003000200019

Almeida, F. F. M. d., Brito Neves, B. B. d., and Dal Ré Carneiro, C. (2000). The Origin and Evolution of the South American Platform. *Earth-Science Rev.* 50, 77–111. doi:10.1016/S0012-8252(99)00072-0

Alvares, C. A., Stape, J. L., Sentelhas, P. C., de Moraes Gonçalves, J. L., Sparovek, G., Arp, G., et al. (2013). Köppen's Climate Classification Map for BrazilPhotosynthesis-Induced Biofilm Calcification and Calcium Concentrations in Phanerozoic Oceans. *metzScience* 22292, 7111701–7281704. doi:10.1126/science.105720410.1127/0941-2948/2013/0507

Bahr, A., Doubrawa, M., Titschack, J., Austermann, G., Nürnberg, D., Albuquerque, A. L., et al. (2020). Monsoonal Forcing Controlled Cold Water Coral Growth off South-Eastern Brazil during the Past 160 Kyrs. *Paleobiogeoscience Clim. Connect.* doi:10.5194/bg-2020-206

Bahr, A., Kaboth-Bahr, S., Jaeschke, A., Chiessi, C., Cruz, F., Carvalho, L., et al. (2021). Late Holocene Precipitation Fluctuations in South America Triggered by Variability of the North Atlantic Overturning Circulation. *Paleoceanogr. Paleoclimatol* 36, e2021PA004223. doi:10.1029/2021PA004223

Bahr, A., Spadano Albuquerque, A. L., Ardenghi, N., Batenburg, S. J., Bayer, M., Catunda, M. C., et al. (2016). South American Hydrological Balance and Paleoceanography during the Late Pleistocene and Holocene (SAMBA)-Cruise No. M125, *March 21-April 15, 2016 – Rio J. (Brazil)-Fortaleza Braz.* (Bremen (Germany): METEOR-Berichte M125), 54, 34. doi:10.2312/cr_m125

Bastos, A. C., Amado-Filho, G. M., Moura, R. L., Sampaio, F. M., Bassi, D., and Braga, J. C. (2016). Origin and Sedimentary Evolution of Sinkholes (Buracas) in the Abrolhos Continental Shelf, Brazil. *Palaeogeogr. Palaeoclimatol. Palaeoecol.* 462, 101–111. doi:10.1016/j.palaeo.2016.09.009

Biscaye, P. E. (1965). Mineralogy and Sedimentation of Recent Deep-Sea Clay in the Atlantic Ocean and Adjacent Seas and Oceans. *Geol. Soc. Am. Bull.* 76, 803–832. doi:10.1130/0016-7606(1965)76[803

Bliss, N. (2013). *LBA-ECO LC-08 Soil, Vegetation, and Land Cover Maps for Brazil and South America. Data Set*. Oak Ridge, Tennessee, U.S.A. Available on-line (from Oak Ridge National Laboratory Distributed Active Archive Center Available at: http://daac.ornl.gov.

Carvalho, L. M. V. (2020). Assessing Precipitation Trends in the Americas with Historical Data: A Review. *WIREs Clim. Change* 11, e627. doi:10.1002/wcc.627

Costa, K. B., Cabarcos, E., Santarosa, A. C. A., Battaglin, B. B. F., and Toledo, F. A. L. (2016). A Multiproxy Approach to the Climate and Marine Productivity Variations along MIS 5 in SE Brazil: A Comparison between Major Components of Calcareous Nannofossil Assemblages and Geochemical Records. *Palaeogeogr. Palaeoclimatol. Palaeoecol.* 449, 275–288. doi:10.1016/j.palaeo.2016.02.032

CPRM – Serviço Geológico do Brasil (2004). *Geological Map of Brazil 1:1.000.000 Scale: Geographic Information System-GIS*. Brasília: CPRM.

Cruz, F. W., Burns, S. J., Karmann, I., Sharp, W. D., Vuille, M., Cardoso, A. O., et al. (2005). Insolation-driven Changes in Atmospheric Circulation over the Past 116,000 Years in Subtropical Brazil. *Nature* 434, 63–66. doi:10.1038/nature03365

Cruz, F. W., Vuille, M., Burns, S. J., Wang, X., Cheng, H., Werner, M., et al. (2009). Orbitally Driven East-West Antiphasing of South American Precipitation. *Nat. Geosci.* 2, 210–214. doi:10.1038/ngeo444

Cunha, A. d. M., Fontes, M. P. F., and Lani, J. L. (2019). Mineralogical and Chemical Attributes of Soils from the Brazilian Atlantic Forest Domain. *Sci. Agric. (Piracicaba, Braz.)* 76, 82–92. doi:10.1590/1678-992x-2017-0109

Embrapa-SNLCS (1981). *Mapa des Solos do Brasil, 1:5.000.000*. Rio de Janeiro (Brazil): Empresa Brasileira de Pesquisa Agropecuária - Serviço National de Levantamento e Conservação de solos.

Esquevin, J. (1969). Influence de la composition chimique des illites sur leur cristallinité. *Bull. Cent. Researches Pau-SNPA* 3, 147–153.

FAO-UNESCO (1971). *Soil Map of the World, 1:5.000.000*. Paris (France): South America.

FEAM (2011). *Avaliação de impactos de mudanças climáticas sobre a economia mineira: relatório resumo*.

Flantua, S. G. A., Hooghiemstra, H., Vuille, M., Behling, H., Carson, J. F., Gosling, W. D., et al. (2016). Climate Variability and Human Impact in South America during the Last 2000 years: Synthesis and Perspectives from Pollen Records. *Clim. Past.* 12, 483–523. doi:10.5194/cp-12-483-2016

Gerhardt, S., and Henrich, R. (2001). Shell Preservation of Limacina Inflata (Pteropoda) in Surface Sediments from the Central and South Atlantic Ocean: A New Proxy to Determine the Aragonite Saturation State of Water Masses. *Deep Sea Res. Part I Oceanogr. Res. Pap.* 48, 2051–2071. doi:10.1016/S0967-0637(01)00005-X

Grathoff, G. H., and Moore, D. M. (1996). Illite Polytype Quantification Using WILDFIRE Calculated X-Ray Diffraction Patterns. *Clays Clay Minerals* 44, 835–842. doi:10.1346/CCMN.1996.0440615

GRDC (2020). *Major River Basins of the World/Global Runoff Data Centre, GRDC. 2nd, Rev. Ext*. Koblenz, Germany: Federal Institute of Hydrology BfG.

Henrich, R., Baumann, K.-H., Gerhardt, S., Gröger, M., and Volbers, A. (2003). Carbonate Preservation in Deep and Intermediate Water Masses in the South Atlantic: Evaluation and Geological Record (A Review), 645, 670. doi:10.1007/978-3-642-18917-3_28

Hou, A., Bahr, A., Raddatz, J., Voigt, S., Greule, M., Albuquerque, A. L., et al. (2020a). Insolation and Greenhouse Gas Forcing of the South American Monsoon System across Three Glacial-Interglacial Cycles. *Geophys. Res. Lett.* 47, e2020GL087948. doi:10.1029/2020GL087948

Hou, A., Bahr, A., Schmidt, S., Strebl, C., Albuquerque, A. L., Chiessi, C. M., et al. (2020b). Forcing of Western Tropical South Atlantic Sea Surface Temperature across Three Glacial-Interglacial Cycles. *Glob. Planet. Change* 188, 103150. doi:10.1016/j.gloplacha.2020.103150

IPCC (2021). *Climate Change 2021: The Physical Science Basis. Contribution of Working Group I to the Sixth Assessment Report of the Intergovernmental Panel on Climate Change*.

Jaeschke, A., Rühlemann, C., Arz, H., Heil, G., and Lohmann, G. (2007). Coupling of Millennial-Scale Changes in Sea Surface Temperature and Precipitation off Northeastern Brazil with High-Latitude Climate Shifts during the Last Glacial Period. *Paleoceanography* 22, a–n. doi:10.1029/2006PA001391

Jahnke, R. A., Craven, D. B., and Gaillard, J.-F. (1994). The Influence of Organic Matter Diagenesis on CaCO3 Dissolution at the Deep-Sea Floor. *Geochimica Cosmochimica Acta* 58, 2799–2809. doi:10.1016/0016-7037(94)90115-5

Jones, C., and Carvalho, L. M. V. (2002). Active and Break Phases in the South American Monsoon System. *J. Clim.* 15, 905–914. doi:10.1175/1520-0442(2002)015<0905:AABPIT>2.0

Jones, G. A. (1984). Advective Transport of Clay Minerals in the Region of the Rio Grande Rise. *Mar. Geol.* 58, 187–212. doi:10.1016/0025-3227(84)90123-3

Kanner, L. C., Burns, S. J., Cheng, H., and Edwards, R. L. (2012). High-Latitude Forcing of the South American Summer Monsoon during the Last Glacial. *Science* 335, 570–573. doi:10.1126/science.1213397

Knutti, R., and Sedláček, J. (2013). Robustness and Uncertainties in the New CMIP5 Climate Model Projections. *Nat. Clim. Change* 3, 369–373. doi:10.1038/nclimate1716

Kodama, Y. (1992). Large-Scale Common Features of Subtropical Precipitation Zones (The Baiu Frontal Zone, the SPCZ, and the SACZ) Part I: Characteristics of Subtropical Frontal Zones. *J. Meteorological Soc. Jpn.* 70, 813–836. doi:10.2151/jmsj1965.70.4_813

Kranz, S. A., Gladrow, D. W., Nehrke, G., Langer, G., and Rosta, B. (2010). Calcium Carbonate Precipitation Induced by the Growth of the Marine Cyanobacteria Trichodesmium. *Limnol. Oceanogr.* 55, 2563–2569. doi:10.4319/lo.2010.55.6.2563

Laskar, J., Robutel, P., Joutel, F., Gastineau, M., Correia, A. C. M., and Levrard, B. (2004). A Long-Term Numerical Solution for the Insolation Quantities of the Earth. *A&A* 428, 261–285. doi:10.1051/0004-6361:20041335

Lima, J. E. F. W., Lopes, W. T. A., Carvalho, N. O., Vieira, M. R., and Silva, E. M. (2005). "Suspended Sediment Fluxes in the Large River Basins of Brazil," in *Sediment Budgets 1, Proceedings of the Foz Do Iguaçu Symposium, IAHS Scientific Assembly* (Foz do Iguaçu (Brazil): IAHS Publ.), 355–363.

Lisiecki, L. E., and Raymo, M. E. (2005). A Pliocene-Pleistocene Stack of 57 Globally Distributed Benthic δ18O Records. *Paleoceanography* 20, a–n. doi:10.1029/2004PA001071

Maiada, R. M. d. C. C., Reisdos, A. T. d., Alvesda, E. d. C. C., Silva, C. G., Guerra, J. V., Gorini, C., et al. (2010). Architecture and stratigraphic framework of shelf sedimentary systems off Rio de Janeiro state, Northern Santos Basin-Brazil. *Braz. J. Oceanogr.* 58, 15–29. doi:10.1590/S1679-87592010000500003

May, P., Alonso, L., Barbosa, F., Brito, M. C., Laureano, F., Maroun, C., et al. (2020). Mainstreaming Climate Change in the Rio Doce Watershed Restoration. Available at: https://portals.iucn.org/library/node/49066 (Accessed November 22, 2021). doi:10.2305/iucn.ch.2020.06.en

Melfi, A. J., Cerri, C. C., Kronberg, B. I., Fyfe, W. S., and McKinnon, B. (1983). Granitic Weathering: a Brazilian Study. *J. Soil Sci.* 34, 841–851. doi:10.1111/j.1365-2389.1983.tb01076.x

Melo, V. F., Singh, B., Schaefer, C. E. G. R., Novais, R. F., and Fontes, M. P. F. (2001). Chemical and Mineralogical Properties of Kaolinite-Rich Brazilian Soils. *Soil Sci. Soc. Am. J.* 65, 1324–1333. doi:10.2136/sssaj2001.6541324x

Meunier, A., and Velde, B. (2004). "The Geology of Illite," in *Illite: Origins, Evolution and Metamorphism*. Editors A. Meunier and B. Velde (Berlin, Heidelberg: Springer), 63–143. doi:10.1007/978-3-662-07850-1_3

Mohr, E. C. J., Van Baren, F. A., and Van Schuylenborgh, J. (1972). *Tropical Soils – A Comprehensive Study of Their Genesis*. 3rd ed. The Hague (Netherlands): Mouton - Ichtiar Baru - Van Hoeve.

Oliveira, E. N. d., Knoppers, B. A., Lorenzzetti, J. A., Medeiros, P. R. P., Carneiro, M. E., and Souza, W. F. L. d. (2012). A Satellite View of Riverine Turbidity Plumes on the NE-E Brazilian Coastal Zone. *Braz. J. Oceanogr.* 60, 283–298. doi:10.1590/S1679-87592012000300002

Oliveira, K. S. S., and Quaresma, V. d. S. (2017). Temporal Variability in the Suspended Sediment Load and Streamflow of the Doce River. *J. S. Am. Earth Sci.* 78, 101–115. doi:10.1016/j.jsames.2017.06.009

Petit, J. R., Jouzel, J., Raynaud, D., Barkov, N. I., Barnola, J.-M., Basile, I., et al. (1999). Climate and Atmospheric History of the Past 420,000 Years from the Vostok Ice Core, Antarctica. *Nature* 399, 429–436. doi:10.1038/20859

Petró, S. M., Pivel, M. A. G., and Coimbra, J. C. (2021). Evidence of Supra-lysoclinal Dissolution of Pelagic Calcium Carbonate in the Late Quaternary in the Western South Atlantic. *Mar. Micropaleontol.* 166, 102013. doi:10.1016/j.marmicro.2021.102013

Petschick, R., Kuhn, G., and Gingele, F. (1996). Clay Mineral Distribution in Surface Sediments of the South Atlantic: Sources, Transport, and Relation to Oceanography. *Mar. Geol.* 130, 203–229. doi:10.1016/0025-3227(95)00148-4

Petschick, R. (2010). *MacDiff 4.2.6 Manual*. Available at: http://www.uni-frankfurt.de/69528130/Petschick___MacOS_Software.

Raddatz, J., Titschack, J., Frank, N., Freiwald, A., Conforti, A., Osborne, A., et al. (2020). Solenosmilia Variabilis-Bearing Cold-Water Coral Mounds off Brazil. *Coral Reefs* 39, 69–83. doi:10.1007/s00338-019-01882-w

Riding, R. (2000). Microbial Carbonates: the Geological Record of Calcified Bacterial-Algal Mats and Biofilms. *Sedimentology* 47, 179–214. doi:10.1046/j.1365-3091.2000.00003.x

Rind, D. (1998). Latitudinal Temperature Gradients and Climate Change. *J. Geophys. Res.* 103, 5943–5971. doi:10.1029/97JD03649

P. A. Sanchez (Editor) (2019). "Mineralogy," *Properties and Management of Soils in the Tropics* (Cambridge: Cambridge University Press), 196–209. doi:10.1017/9781316809785.010

Santos, E. O. de. J., Gontijo, I., and Silva, M. B. da. (2014). Spatial Variability of Soil Acidity Attributes and Liming Requirement for Conilon Coffee. *Coffee Sci.* 9, 275–283. Available at: http://www.sbicafe.ufv.br/handle/123456789/8052. (Accessed April 22, 2022).

Schlitzer, R. (2021). Ocean Data View (ODV). Available at: https://odv.awi.de/ (Accessed April 22, 2022).

Schobbenhaus, C., Campos, D. de. A., Derze, G. R., and Asmus, H. E. (1981). *Geologic Map of Brazil and Adjoining Ocean Floor Including Mineral Deposits, Scale 1: 1500 000*. Brasilia: Departamento Nacional da Producao Mineral.

Seo, K.-H., Frierson, D. M. W., and Son, J.-H. (2014). A Mechanism for Future Changes in Hadley Circulation Strength in CMIP5 Climate Change Simulations. *Geophys. Res. Lett.* 41, 5251–5258. doi:10.1002/2014GL060868

Souza, W. F. L., and Knoppers, B. (2011). Fluxos de água e sedimentos a costa leste Do Brasil: relações entre a tipologia e as pressões antrópicas. *Geochim. Bras.* 17, 57–74.

Spratt, R. M., and Lisiecki, L. E. (2016). A Late Pleistocene Sea Level Stack. *Clim. Past.* 12, 1079–1092. doi:10.5194/cp-12-1079-2016

Stríkis, N. M., Chiessi, C. M., Cruz, F. W., Vuille, M., Cheng, H., Souza Barreto, E. A., et al. (2015). Timing and Structure of Mega-SACZ Events during Heinrich Stadial 1. *Geophys. Res. Lett.* 42, 5477–5484A. doi:10.1002/2015GL064048

Stríkis, N. M., Cruz, F. W., Barreto, E. A. S., Naughton, F., Vuille, M., Cheng, H., et al. (2018). South American Monsoon Response to Iceberg Discharge in the North Atlantic. *Proc. Natl. Acad. Sci. U.S.A.* 115, 3788–3793. doi:10.1073/pnas.1717784115

Suárez-Ibarra, J. Y., Frozza, C. F., Palhano, P. L., Petró, S. M., Weinkauf, M. F. G., and Pivel, M. A. G. (2022). Calcium Carbonate Dissolution Triggered by High Productivity during the Last Glacial-Interglacial Interval in the Deep Western South Atlantic. *Front. Earth Sci.* 10. doi:10.3389/feart.2022.830984

Thiry, M. (2000). Palaeoclimatic Interpretation of Clay Minerals in Marine Deposits: an Outlook from the Continental Origin. *Earth-Science Rev.* 49, 201–221. doi:10.1016/S0012-8252(99)00054-9

Tierney, J. E., Poulsen, C. J., Montañez, I. P., Bhattacharya, T., Feng, R., Ford, H. L., et al. (2020). Past Climates Inform Our Future. *Science* 370. doi:10.1126/science.aay3701

Tintelnot, M. (1995). *Transport and Deposition of Fine-Grained Sediments on the Brazilian Continental Shelf as Revealed by Clay Mineral Distribution*.

Tomasella, J., Sene Gonçalves, A., Schneider Falck, A., Oliveira Caram, R., Rodrigues Diniz, F. l., Rodriguez, D. a., et al. (2019). Probabilistic Flood Forecasting in the Doce Basin in Brazil: Effects of the Basin Scale and Orientation and the Spatial Distribution of Rainfall. *J. Flood Risk Manag.* 12, e12452. doi:10.1111/jfr3.12452

B. Velde (Editor) (1995). *Origin and Mineralogy of Clays: Clays and the Environment* (Berlin, Heidelberg: Springer). doi:10.1007/978-3-662-12648-6

Velde, B., and Meunier, A. (2008). "Fundamentals of Clay Mineral Crystal Structure and Physicochemical Properties," in *The Origin of Clay Minerals in Soils and Weathered Rocks*. Editors B. Velde and A. Meunier (Berlin, Heidelberg: Springer), 3–73. doi:10.1007/978-3-540-75634-7_1

Vuille, M., and Garreaud, R. D. (2011). "Ocean-atmosphere Interactions on Interannual to Decadal Timescales," in *Handbook of Environmental Change* (Los Angeles, New Delhi, Singapore: Sage Publications London), 471–496.

Warratz, G., Henrich, R., Voigt, I., Chiessi, C. M., Kuhn, G., and Lantzsch, H. (2017). Deglacial Changes in the Strength of Deep Southern Component Water and Sediment Supply at the Argentine Continental Margin. *Paleoceanography* 32, 796–812. doi:10.1002/2016PA003079

WRB, IUSS Working Group (2015). World Reference Base for Soil Resources 2014, Update 2015 International Soil Classification System for Naming Soils and Creating Legends for Soil Maps. *World Soil Resour. Rep. No.* 106, 192.

Conflict of Interest: The authors declare that the research was conducted in the absence of any commercial or financial relationships that could be construed as a potential conflict of interest.

Publisher's Note: All claims expressed in this article are solely those of the authors and do not necessarily represent those of their affiliated organizations, or those of the publisher, the editors and the reviewers. Any product that may be evaluated in this article, or claim that may be made by its manufacturer, is not guaranteed or endorsed by the publisher.

frontiers | Frontiers in Marine Science

ORIGINAL RESEARCH
published: 30 June 2022
doi: 10.3389/fmars.2022.878116

Coupled Oceanic and Atmospheric Controls of Deglacial Southeastern South America Precipitation and Western South Atlantic Productivity

Karl J. F. Meier[1], Andrea Jaeschke[2], Janet Rethemeyer[2], Cristiano M. Chiessi[3], Ana Luiza S. Albuquerque[4], Vincent Wall[2], Oliver Friedrich[1] and André Bahr[1]*

[1] Institute of Earth Sciences, Heidelberg University, Heidelberg, Germany, [2] Institute of Geology and Mineralogy, University of Cologne, Cologne, Germany, [3] School of Arts, Sciences and Humanities, University of São Paulo, São Paulo, Brazil, [4] Programa de Geociências (Geoquímica), Universidade Federal Fluminense, Niterói, Brazil

OPEN ACCESS

Edited by:
Ed Hathorne, Helmholtz Association of German Research Centres (HZ), Germany

Reviewed by:
Li Lo, National Taiwan University, Taiwan
Pepijn Bakker, VU Amsterdam, Netherlands
Daniel Gebregiorgis, Georgia State University, United States

***Correspondence:**
Karl J. F. Meier
karl.meier@geow.uni-heidelberg.de

Specialty section:
This article was submitted to Marine Biogeochemistry, a section of the journal Frontiers in Marine Science

Received: *17 February 2022*
Accepted: *26 May 2022*
Published: *30 June 2022*

Citation:
Meier KJF, Jaeschke A, Rethemeyer J, Chiessi CM, Albuquerque ALS, Wall V, Friedrich O and Bahr A (2022) Coupled Oceanic and Atmospheric Controls of Deglacial Southeastern South America Precipitation and Western South Atlantic Productivity. Front. Mar. Sci. 9:878116. doi: 10.3389/fmars.2022.878116

Various mechanisms were proposed as substantial drivers of (sub)tropical South American hydroclimate changes during the last deglaciation. However, the interpretation of past precipitation records from the regions affected by the South American Summer Monsoon, the dominant hydroclimatic system in (sub)tropical South America, still insufficiently consider feedbacks between oceanic and atmospheric processes evident in modern observational data. Here, we evaluate ocean-atmosphere feedbacks active in the region from 19 to 4 ka based on a multi-proxy record comprising lipid biomarker, bulk sediment elemental composition and foraminiferal geochemistry from a sediment core retrieved from the tropical western South Atlantic offshore eastern Brazil at ~22°S. Our proxy data together with existing paleoclimate records show that the consideration of large scale synoptic climatic features across South America is crucial for understanding the past spatio-temporal rainfall variability, especially during the last deglaciation. While the paleohydrological data from our study site show relatively stable precipitation across the deglaciation in the core region of the South Atlantic Convergence Zone, distinct hydroclimatic gradients developed across the continent during Heinrich Stadial 1, which climaxed at ~16 ka. By then, the prevalent atmospheric and oceanic configuration caused more frequent extreme climatic events associated with positive rainfall in the northern portion of eastern South America and in the southeastern portion of the continent. These climatic extremes resulted from substantial warming of the sub (tropical) western South Atlantic sea surface that fostered oceanic moisture transport towards the continent and the reconfiguration of quasi-stationary atmospheric patterns. We further find that enhanced continental precipitation in combination with low glacial sea level strongly impacted marine ecosystems *via* enhanced terrigenous organic matter input in line with augmented nutrient release to the ocean. Extreme rainfall events similar to those that occurred during Heinrich Stadial 1 are likely to recur in South America as a

consequence of global warming, because the projected reduction of the intra-hemispheric temperature gradient may lead to the development of atmospheric patterns similar to those in force during Heinrich Stadial 1.

Keywords: organic/inorganic geochemistry, South American Monsoon System, land-ocean teleconnection, South Atlantic Convergence Zone, last deglacial and holocene, South American Low Level Jet

INTRODUCTION

Past precipitation records from (sub)tropical South America highlighted that on orbital timescales, precipitation associated to the South American Monsoon System (SAMS) and South Atlantic Convergence Zone (SACZ), which is a particular feature of the SAMS, was mainly controlled by austral summer insolation. High (low) insolation lead to increased (decreased) moisture convection across the Amazon basin, which in turn increases (decreases) moisture export towards the southeast, seasonally feeding the SACZ and resulting in increased (decreased) SAMS rainfall over most parts of South America (Cruz et al., 2005; Hou et al., 2020). However, millennial-scale variations in South American precipitation during the last deglacial, such as Heinrich Stadial 1 (HS1) were driven by a different global climate forcing: induced by high-latitude forcing, the reorganization of cross-equatorial heat transport resulted from a marked slowdown of the AMOC leading to diminished oceanic heat export into the Northern Hemisphere. In turn, the distinct bi-polar distribution of heat in the Atlantic Ocean was expressed by simultaneous cooling of the northern and warming of the southern hemispheric sectors of the Atlantic Ocean. This global redistribution of heat had a determining influence on the latitudinal position and strength of atmospheric convection belts over the tropical Atlantic and affected the latitudinal position of the Intertropical Convergence Zone (ITZC). The southward shift of the ITCZ results from increased northward atmospheric heat transport into the colder hemisphere during phases of weak AMOC that is necessary to compensate the interhemispheric heat imbalance, and is in line with an intensification and a cross-equatorial extension of the Northern Hemisphere Hadley-Cell (Donohoe et al., 2012; McGee et al., 2014; Mulitza et al., 2017). Past studies indeed show a direct influence on moisture availability across South America by southward shifts of the ITCZ during periods of weak AMOC, which are, however, confined to the SAMS region in northern South America (Zhang and Delworth, 2005; Deplazes et al., 2013; Zhang et al., 2017; Bahr et al., 2018).

Southward shifts of the ITCZ and the associated adjustment of moisture flux pathways across tropical South America were further invoked to indirectly affect precipitation in the realm of the SACZ (Wang et al., 2007; Kanner et al., 2012; Stríkis et al., 2015; Stríkis et al., 2018). The latter studies implied that the deglacial high-latitude forced climatic perturbations and concomitant southward ITCZ shifts further boosted SACZ strength, thereby favoring moisture transport towards tropical and subtropical South America. However, Campos et al. (2019) revealed that precipitation anomalies in E and SE Brazil during phases of rapid climatic perturbations during the last deglaciation, i.e. HS1, were related to enhanced moisture flux from the tropical South Atlantic rather than SACZ intensification as suggested by prior studies. Further, variability in strength and extension of the SACZ, which determines precipitation in SE Brazil, is independent of a direct influence by the ITCZ. Instead, the SACZ strength appears to rather depend on synoptic climatic features across the Southern Hemisphere (Vera et al., 2002; Liebmann et al., 2004; Marengo et al., 2004; Silva and Berbery, 2006; Gelbrecht et al., 2018). Gelbrecht et al. (2018), for instance, found that eastward propagating atmospheric Rossby waves were the main driver of SACZ variability. The Rossby wave train determines the position of cyclonic and anticyclonic circulation across South America and the South Atlantic, which dominates the moisture flux towards the realm of the SACZ and subtropical South America. Yet, the ITCZ was found to play an indirect role in the synoptic atmospheric configuration in the Southern Hemisphere as southward shifts of the ITCZ weaken (invigorate) the strength of the subtropical (mid-latitude) jet, hence affecting the Southern Hemisphere Rossby wave train (Lee et al., 2011; Ceppi et al., 2013).

Since such synoptic climatic features were not considered in past paleo-precipitation studies from South America, the variability of SACZ-related precipitation and its controlling mechanisms during phases of rapid climatic perturbations during the last deglaciation such as during HS1 are not well constrained yet. Further, existing high-resolution SACZ reconstructions covering the last deglaciation are primarily based on terrestrial climate archives such as speleothems (Cruz et al., 2006; Cruz et al., 2007; Stríkis et al., 2015; Stríkis et al., 2018), while climate reconstructions from the core region of the SACZ based on marine sediment archives are still sparse (Campos et al., 2019).

Here we present a multiproxy record of marine sediment Core M125-35-3 collected off SE Brazil close to the Paraíba do Sul River mouth, whose catchment drains the core region of the modern SACZ (**Figure 1**). Thus, Core M125-35-3 is ideally located to reconstruct changes in the extension and intensity of the SACZ, its impact on the regional environment and the connectivity between SACZ and oceanographic changes during the last deglaciation. Our focus lies on the most intense phase of the interhemispheric seesaw during HS1 at ~16 ka which is captured by a high, sub-centennial-scale temporal resolution (in average ~57 yr). We first evaluate the capacity of the utilized inorganic and organic geochemical proxies to capture continental hydroclimate changes and their impact on terrestrial and marine environments. Then we discuss our

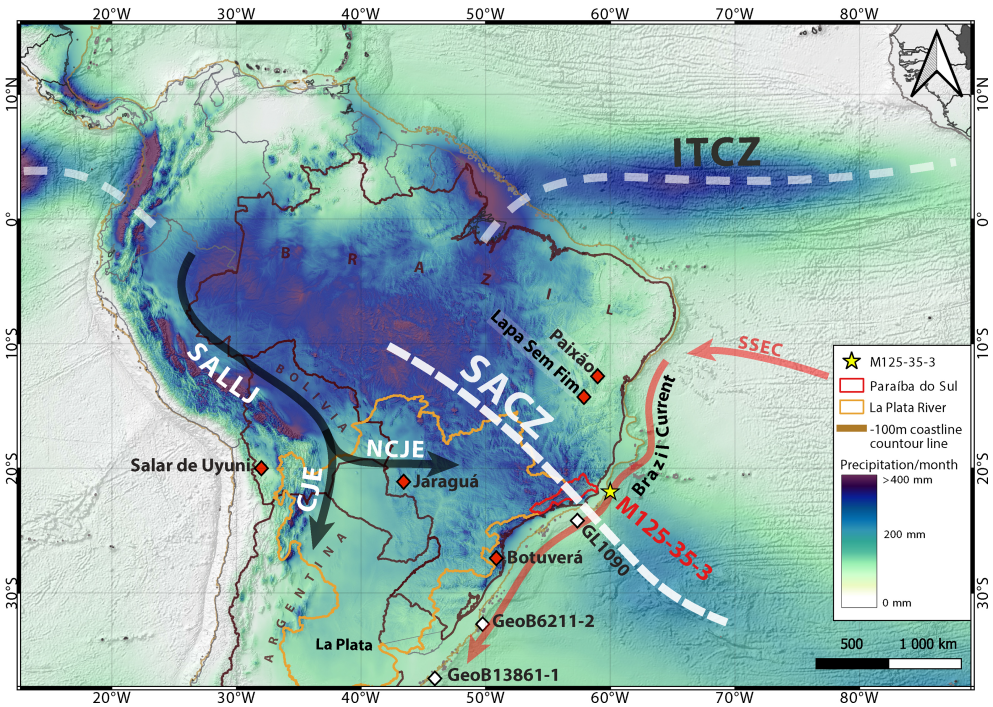

FIGURE 1 | Map of monthly average austral summer precipitation (December-February) across (sub)tropical South America (Karger et al., 2021). The precipitation pattern illustrates a fully established South American Monsoonal System. Note enhanced precipitation along the South Atlantic Convergence Zone (SACZ) indicated by NW-SE oriented white dashed line. The yellow asterisk marks Core M125-35-3 (this study). White diamonds indicate marine sedimentary climate archives mentioned in the text. Red diamonds reflect terrestrial paleo-rainfall reconstructions mentioned in the text. Black arrows indicate the South American Low Level Jet (SALLJ) in two different modes: the southward oriented Chaco Jet Event (CJE) and the eastward oriented No Chaco Jet Event (NCJE). The red and orange outlines indicate the drainage basins of the Paraíba do Sul located in the core region of the SACZ and the La Plata River. Countries mentioned in the main text (i.e. Brazil, Bolivia and Argentina) were outlined. The thick orange arrows represent major oceanic surface currents in the western sub(tropical) South Atlantic, namely the southward flowing Brazil Current which is fed by the southern South Equatorial Current (SSEC). ITCZ, Intertropical Convergence Zone.

findings in the context of large-scale atmospheric and oceanic fluctuations. We highlight that past precipitation variability and associated river run-off had a great influence on nutrient availability and marine productivity in the western tropical South Atlantic. Yet, the quantity of terrestrial influx to our study site is largely determined by the shelf extension and only subordinately controlled by precipitation intensity. Further we find that deglacial variability in the SAMS/SACZ system depends on a complex interplay of atmospheric and oceanographic processes on hemispheric scales. Unexpectedly, the spatial precipitation pattern reconstructed for glacial background conditions during HS 1 resembles modern observations and numerical model scenarios of future anthropogenic climate change under rising greenhouse gas concentrations (Gonzalez et al., 2013; Vera and Díaz, 2015; Saurral et al., 2017; Masson-Delmotte et al., 2021). Thus, improving our understanding of the response of the SAMS to climatic perturbations is instrumental in order to more reliably project how the spatial distribution and intensity of rainfall events might develop in response to global warming. This does not only relate to the socio-economic impacts of water shortage or flooding on the continent but must also consider the potential impact of marked changes in the hydrological cycle on coastal marine ecosystems.

OCEANOGRAPHIC AND CONTINENTAL SETTING

The Brazilian margin in the western tropical South Atlantic is dominated by the southward flowing Brazil Current (BC), which is the western boundary current of the South Atlantic subtropical gyre carrying warm tropical and oligotrophic waters of the Southern South Equatorial Current (SSEC) (Peterson and Stramma, 1991) (**Figure 1**). The BC flows southwards along the Brazilian margin from ~10°S as far as ~38°S where it converges with the northward-flowing cold Malvinas Current (MC) (Stramma and England, 1999) (**Figure 1**).

For the discussion of continental climate variability, we define the following geographic regions (**Figure 1**): (i) eastern South America (ESA) is defined as the region between ~10 and 20°S along the coastal realm of Brazil; (ii) southeastern South America (SESA) describes the region of Brazil south of 20°S including the Paraíba do Sul catchment; (iii) southern southeastern South America (SSESA), i.e. the region south of 30°S downstream the Paraná River and comprising the La Plata catchment (**Figure 1**).

Since we defined SESA as the region between ~20° and ~30°S it represents a transitional zone between tropical and subtropical climate features. During austral summer, modern precipitation

over SESA is dominated by the seasonal expansion and intensification of the SAMS/SACZ, which influence is greatest in the northern part of SESA in the core region of the SACZ including the Paraíba do Sul catchment (**Figure 1**). During austral winter, rainfall is related to mid-latitude cyclonic activity over the South Atlantic (Vera et al., 2002), affecting the Paraíba do Sul catchment less intensively than the southern part of SESA. With the onset of SAMS activity during austral summer, increased summer insolation enhances convection over tropical South America which induces increased moisture flux towards the continent in line with prevailing NE trade winds. The moist air is transported southward resulting in strong precipitation in the SACZ (Gan et al., 2004). The SACZ is a convective belt that extends from the Amazon basin southeastward into the western South Atlantic (Marengo et al., 2004).

Precipitation across ESA gradually decreases northward. In the southern part of ESA, which is closer to the NW-SE axis of the SACZ, precipitation seasonally increases in line with SAMS activity. Although SE trade winds continuously bring moisture towards the eastern headlands of Brazil, the hinterland region is characterized by a marked dry season during austral winter (Rao et al., 1993; Garreaud et al., 2009). The dry season becomes more extreme towards the semi-arid northeastern Brazil where an intensification of the Hadley Cell and descending convective motion of the Walker circulation results in increased aridity (Moura and Shukla, 1981; Ambrizzi et al., 2004; Garreaud et al., 2009; Marengo et al., 2017).

Seasonal variability in rainfall amounts across SSESA is weak. During austral summer, the coastal realms of SSESA receive increased rainfall when the SACZ is connected with the area of convection over the Amazon basin (Liebmann et al., 1999). During the SAMS season, the La Plata basin (including the Paraná catchment) receives large amounts of tropical moisture, when a northerly low-level flow is channeled east of the Andes and feeds convective storms over the subtropical plains (Saulo et al., 2000; Saulo et al., 2004; Marengo et al., 2004; Garreaud et al., 2009). This flow is known as the South American Low Level Jet (SALLJ), which we describe in more detail in section 5.3 (**Figure 1**). During austral winter, the main source of precipitation is frontal rainfall caused by incursions of sub-Antarctic cold fronts meeting tropical air masses (Vera et al., 2002; Garreaud et al., 2009).

The above described average precipitation pattern across South America may be disrupted by annual to multi-decadal climate phenomena (for a recent summary cf. Zanin and Satyamurty (2020)). Most importantly, a consistently described climate phenomenon is the occurrence of a tropical to subtropical precipitation dipole between the SAMS region influenced by the SACZ comprising the Paraíba do Sul catchment in SESA on the one hand and SSESA in the exit region of the SALLJ on the other hand (Nogués-Paegle and Mo, 1997; Robertson and Mechoso, 2000; Doyle and Barros, 2002; Díaz and Aceituno, 2003; Liebmann et al., 2004; Grimm, 2011; Boers et al., 2014; Grimm and Saboia, 2015; Jones and Carvalho, 2018; Zanin and Satyamurty, 2020). It is noteworthy that the SALLJ appears in two different configurations (**Figures 1**, **2**) (Salio and Nicolini, 2006): (i) the Chaco Jet Event (CJE); and (ii) the No Chaco Jet Event (NCJE). A main difference between those jet events is the meridional extension of the jet. Both jet events are channeled towards the southeastern portion of South America. The CJE, however, shows a maximum southward wind component above central Bolivia and continues northern Argentina. Instead, the NCJE protrudes eastward around 25°S, fostering moisture transport towards the SACZ at similar latitudes (Salio et al., 2002; Salio and Nicolini, 2006; Ramos et al., 2019) (**Figure 2**). This dipole pattern arises from the midlatitude Rossby wave train progressing eastward from the South Pacific Ocean and turns equatorward as it crosses the Andes Mountains. The prevalent mode of the SALLJ seems to be determined by the phase of the Rossby wave as it crosses the Andes Mountains and strongly modulates the upper and lower atmospheric circulation pattern across South America, in particular the circulation pattern and intensity of the SALLJ (**Figures 1**, **2**) (Vera et al., 2002; Liebmann et al., 2004; Vera et al., 2006; Silva and Berbery, 2006). Accordingly, a dipole pattern is determined by moisture flux carried during CJE (NCJE), leading to enhanced (decreased) precipitation over SSESA and dryer (wetter) conditions in the core region of the SACZ in SESA. Further, the negative dipole pattern has been linked to teleconnections associated with cooling of the North Atlantic, which leads to a southward shift of the ITCZ and enhanced cross-equatorial moisture flux over northwestern South America, finally feeding the northerly SALLJ in its CJE configuration during a negative SACZ/SALLJ dipole mode (Jones and Carvalho, 2018; Zanin and Satyamurty, 2020) (**Figure 2**). A positive SACZ/SALLJ dipole configuration operates the opposite way. The SACZ/SALLJ dipole appears to evolve as a feedback to changes in the spatial configuration of sea-surface temperatures (SST) in the western South Atlantic: a negative (positive) SACZ/SALLJ dipole is associated with warming (cooling) north (south) of 30°S (Venegas et al., 1997; Robertson and Mechoso, 2000; Doyle and Barros, 2002; Chaves and Nobre, 2004; Marengo et al., 2004; Garreaud et al., 2009). The spatial SST pattern, in particular warming of the western (sub)tropical South Atlantic north of 30°S, is fostered by radiative forcing after strengthening of the South Atlantic subtropical high above SESA induced by a stationary Rossby wave (**Figure 2**) (Robertson and Mechoso, 2000; Grimm and Ambrizzi, 2009; Grimm, 2011; Zanin and Satyamurty, 2020). This atmospheric configuration determines the exit region of the SALLJ, which corresponds to the CJE configuration: Atmospheric blocking by the persistent anticyclone diminishes easterly moisture flux during NCJE and reinforces northerly moisture flux towards SSESA *via* the CJE (**Figures 1**, **2**). This configuration could cause extreme weather events with marked droughts in the SACZ domain and floods in SSESA such as during the year 2014 as the SALLJ provides significant Amazon moisture export towards SSESA (Coelho et al., 2016) (**Figure 2**).

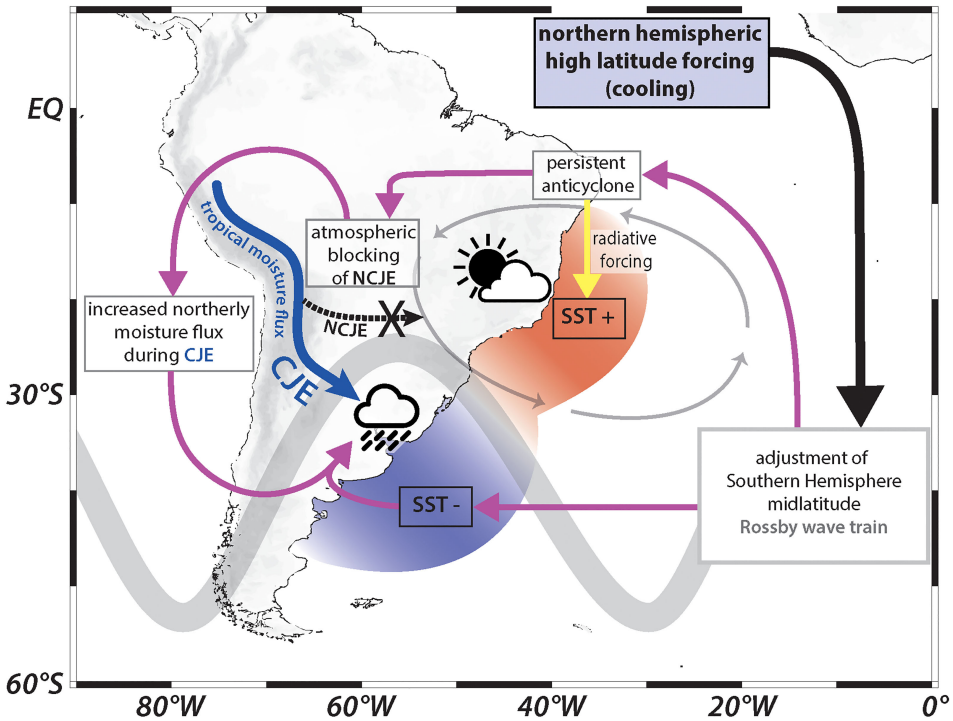

FIGURE 2 | Schematic representation of the mechanism active during the negative SALLJ/SACZ dipole phase in South America and the western South. Northern hemispheric cooling (in line with a southward shift of the ITCZ into the warmer Southern Hemisphere) triggers the adjustment of the Southern Hemisphere mid-latitude Rossby wave train (thick grey line). In turn, a persistent anticyclone (grey ellipse) establishes over eastern and southeastern Brazil. Increased radiative forcing (yellow arrow) leads to increased sea surface temperatures (SST) in the tropical western South Atlantic. The persistent anticyclone blocks the easterly flow of the SALLJ during its "non Chaco Jet Event" (NCJE) configuration (black dotted arrow) and prohibits tropical moisture flux towards southeastern South America (SESA). This results in dryer conditions across SESA. Tropical moisture is rather channeled by the SALLJ towards subtropical southern Southeastern South America during the "Chaco Jet Event" (CJE) (thick blue arrow), wich significantly increases rainfall in its exit region.

MATERIALS AND METHODS

Gravity core M125-35-3 was retrieved from the upper continental slope (21°53.606'S, 040°00.279'W, 428.6 m water depth), ~100 km off the Paraíba do Sul River mouth in SE Brazil during R/V Meteor cruise M125 in 2016 (Bahr et al., 2016). A total of 4.25 m of sediment was recovered. For lipid biomarker and bulk sediment elemental composition analyses, 89 sediment samples were taken downcore along the study interval between 25 and 170 cm covering the interval between 4 and 19 ka. Sample spacing for lipid biomarker and elemental analyses was not equidistant (in average ~1.5 cm) and adjusted to changing sedimentation rates in Core M125-35-3 to generate a temporally evenly resolved record. For foraminiferal geochemical analyses, the core was sampled between 25 and 170 cm at 1 cm spacing. Sampling was performed on the split-core working half of Core M125-35-3 using 10 cm^3 syringes at Universidade Federal Fluminense in Niterói, Brazil.

Lipid Biomarker Analysis

For biomarker analysis, sediment samples from Core M125-35-3 were freeze-dried and homogenized using an agate mortar. Samples (ca. 7 g) were ultrasonically extracted using a 2:1 mixture of dichloromethane (DCM) and methanol (MeOH), repeated 3 times. The extracts were combined and the solvent was subsequently removed by rotary evaporation under vacuum. The resulting total lipid extracts (TLE) were separated into polarity fractions using silica gel column chromatography. The apolar, ketone and polar fractions containing *n*-alkanes, alkenones, and glycerol dialkyl glycerol tetraethers (GDGTs) were eluted using *n*-hexane, DCM, and a 1:1 mixture of DCM and MeOH, respectively. After drying, the apolar and ketone fractions were dissolved in 50 µl *n*-hexane. The polar fractions were dissolved in *n*-hexane:isopropanol (95:5, v:v) and filtered through a 0.45 µm Polytetrafluoroethylene (PTFE) filter prior to analysis.

Alkenone and *n*-alkane measurements were carried out on an Agilent 7890 series II gas chromatograph equipped with an on-column injector and a Flame Ionization Detector (GC-FID) at the Institute of Geology and Mineralogy, University of Cologne. A fused silica capillary column (DB-5MS; 50 m x 0.2 mm, film thickness: 0.33 µm) was used with He as carrier gas. The samples were injected at 70°C, and the consecutive GC oven temperature was raised to 150°C at a rate of 20°C/min. By 150°C the temperature increase was reduced to 6°C/min to 320°C, which was held for 40 min. Both alkenones and *n*-alkanes were determined and quantified by authentic external standards.

Analytical precision for alkenone and *n*-alkane measurements was < 5% based on replicate standard analyses.

GDGTs were analyzed using ultra-high performance liquid chromatography (UHPLC; Agilent 1290 Infinity II) coupled to an Agilent 6460 Triple Quadrupole Atmospheric Pressure Chemical Ionization Mass Spectrometer (QQQ APCI MS) after the method from (Hopmans et al., 2016) at the Institute of Geology and Mineralogy, University of Cologne. Improved separation of 5- and 6-methyl branched GDGTs (brGDGTs) was augmented by using two coupled UHPLC silica columns (BEH HILIC columns, 2.1 x 150 mm, 1.7 µm; Waters™) connected with a guard column maintained at 30°C at a flowrate of 0.2 ml/min. Determination of specific GDGTs was accomplished by single ion monitoring and quantified using an internal C_{46} standard (Huguet et al., 2006), presuming a congruent response between the standard and measured GDGTs. Reproducibility of GDGT concentrations was < 9 %.

Concentrations of alkenones, *n*-alkanes, brGDGTs and crenarchaeol were converted to Mass Accumulation Rates (MAR) to ensure their independency of other sedimentary components. MARs were calculated as follows:

$$MAR_{bio}\left[\frac{\mu g}{ka\ \ cm^2}\right] = DBD\ \left[\frac{g}{cm^3}\right] \times SR\ \left[\frac{cm}{ka}\right] \times C_{bio}\left[\frac{\mu g}{g}\right]$$

where DBD is Dry Bulk Density calculated from sample volume and its dry weight, SR is the sedimentation rate and C_{bio} correspond to concentrations of alkenones, *n*-alkanes, brGDGTs or crenarchaeol (**Supplementary Material Figure S2**).

The Branched and Isoprenoid Tetraether (BIT) index was calculated as defined by (Hopmans et al., 2004):

$$\mathrm{BIT}_{index} = \frac{[I + II + III]}{[I + II + III] + [IV]}$$

where the roman numerals I, II and III refer to the non-isoprenoidal brGDGTs originating from terrestrial anaerobic soil bacteria. The group IV refers to the characteristic isoprenoidal GDGT "crenarchaeol" of aquatic Thaumarchaeota (formerly named Crenarchaeota) from marine environments. The BIT index is used to assess the relative fluvial input of terrestrial organic matter to marine environments and ranges from 0 (exclusively marine organic matter) and 1 (exclusively terrestrial organic matter) (Hopmans et al., 2004; Huguet et al., 2007).

Alkenones in marine sediments originate from haptophyte algae (i.e., coccolithophorides, dominated by *Emiliania huxleyi*) and high flux rates may therefore reflect higher surface oceanic productivity (Prahl et al., 1993; Rostek et al., 1997; Kirst et al., 1999; Herbert, 2014; Jaeschke et al., 2017). Long-chain *n*-alkanes are components of leaf-waxes from vascular plants and can be used as tracer for terrestrial input of organic matter to marine sediments (Freeman and Pancost, 2014; Jaeschke et al., 2017). Yet, *n*-alkanes may also source from bacterial degradation or matured contaminants. However, the calculated carbon preference index (CPI) from Core M125-35-3 is at average 3.2 (not shown), thus relatively high and comparable to modern soils, pointing to a predominance of well preserved terrestrial *n*-alkanes (Freeman and Pancost, 2014). GDGTs are membrane lipids synthesized by both aquatic archaea and terrestrial bacteria. We present MARs of crenarchaeol, a unique isoprenoidal GDGT, which is assumed to be specific to nitrifying marine mesophilic Thaumarchaeota, which are the most abundant single group of prokaryotes in the oceans, thus reflecting secondary production in the upper ocean (Karner et al., 2001; Sinninghe Damsté et al., 2002b; Sinninghe Damsté et al., 2002a). Mass accumulation rates of crenarchaeol are assigned to reflect secondary production by nitrifying Thaumarchaeota in the upper ocean. Further, we focus on accumulation rates of brGDGTs, which were attributed to terrestrial soil bacteria (Schouten et al., 2000; Weijers et al., 2006) and indicate changes in surface erosion and discharge towards our core location.

Bulk Sediment Elemental Analysis

X-Ray Fluorescence (XRF) analysis was performed on an ITRAX XRF Core Scanner (Cox Analytical Systems, Sweden) at the Institute of Geology and Mineralogy, University of Cologne. The freeze dried and homogenized aliquots of Core M125-35-3 were pressed into sample cups and covered with Ultralene® foil. The samples were placed into the core scanner in series enabling continuous measurement sequences. The XRF Scanner was equipped with a chromium (Cr) X-ray tube set to a voltage of 30 kV and a current of 55 mA. All 89 measurements were carried out at 1 mm resolution along the sample cup surface and a counting time of 60 s per sample. The multiple measurements per sample were averaged to determine most representative elemental quantities. The measured XRF spectra were quantified by external in-house standard measurements. Samples of Core M125-35-3 were quantified by using a set of 30 in-house standards from DSDP Site 511. For each element presented in this study, the standard calibration curves reveal a strong correlation ($r^2 > 0.8$).

XRF-derived geochemical data from Core M125-35-3 were grouped into elements which were associated with terrigenous run-off (i.e. Al, Si, K, Fe, Ti) and Ca, reflecting marine biogenic carbonate. In addition, we utilize ln(K/Al) and ln(Al/Si) ratios, which have been used to infer changes in continental moisture availability favoring chemical weathering in monsoonal dominated realms (Chiessi et al., 2010; Govin et al., 2012; Clift et al., 2014; Croudace and Rothwell, 2015; Bahr et al., 2021). Here, ln(K/Al) represents a measure of the intensification of chemical weathering as K is indicative for minerals (i.e. illite, potassium feldspar) which are predominant in dry regions with increased rates of mechanical over chemical weathering (Yarincik et al., 2000; Zabel et al., 2001; Burnett et al., 2011). Al is associated in products of intensive chemical weathering, being especially enriched in kaolinite, which is characteristic for tropical humid conditions (Bonatti and Gartner, 1973; Govin et al., 2012). Modern clay mineral compositions along the eastern and southeastern South American continental shelf clearly reflect the weathering regime of the hinterland as kaolinite is

predominant in the southeast and illite increase northward as more arid conditions prevail in ESA (Tintelnot, 1995). Thus, downcore ln(K/Al) of Core M125-35-2 is a pertinent proxy reflecting changes in the clay mineral composition which is strongly dependent on hinterland chemical weathering intensity and hence, moisture availability (Bahr et al., 2021). As related to past hydroclimate, low (high) ln(K/Al) reflect wetter (drier) conditions within the catchment area. We further compare the ln(K/Al) record with the ln(Al/Si) ratio, which has previously been used as proxy for chemical weathering intensity in South America (Chiessi et al., 2010). Decreased ln (Al/Si) are due to increased fluvial input of fine-grained quartz-rich material caused by higher rates of physical erosion in line with less humid conditions, while higher Al indicates stronger chemical weathering during wetter conditions (Biscaye, 1965; Govin et al., 2012).

Foraminiferal Geochemistry

For stable carbon isotope ($\delta^{13}C$) analysis, all samples were wet-sieved over a 63 μm mesh and oven-dried at 40°C. To avoid size-related ontogenetic effects (Elderfield et al., 2002), foraminiferal tests were sampled from the 355-400 μm size fraction (Friedrich et al., 2012) of the dried sediment. At minimum 50-60 individual foraminiferal tests of the surface-dwelling foraminifera *Globigerinoides ruber* (pink variety) (Chiessi et al., 2007) were handpicked under a stereo microscope. Subsequently, foraminiferal tests were gently crushed between two glass plates and residual detrital sediments from the exposed test chambers was removed. The crushed foraminiferal tests were rinsed three times with ultrapure methanol and ultrasonicated between each rinsing step. Stable isotope measurements were carried out on a Thermo Fisher MAT 253plus mass spectrometer equipped with an automatic Kiel IV carbonate preparation system at the Institute for Earth Sciences, Heidelberg University (Germany). Isotope values were calibrated to an in-house carbonate standard (Solnhofen limestone) and are reported in per mil (‰) relative to Vienna Peedee belemnite [VPDB]. Analytic precision based on repeated measurements of the in-house standard is < 0.03 ‰ for $\delta^{13}C$.

Venancio et al. (2017) inferred from sediment-trap studies located off SE Brazil at 23.6°S, that *G. ruber* (p) is the best-suited planktonic foraminiferal species to reconstruct surface-ocean conditions in the western South Atlantic. The sediment trap study revealed no significant seasonal changes in the occurrence of *G. ruber* (p), thus likely reflecting annual mean conditions. The calcification depth of *G. ruber* (p) at this study site was determined by (Venancio et al., 2017) as the mixed layer between 30 and 40 m water depth, which is comparable to the estimated calcification depth of *G. ruber* in the Pacific Ocean (Rippert et al., 2016).

The $\delta^{13}C$ of planktonic foraminifera shells are used to reconstruct the carbon isotopic composition of dissolved inorganic carbon (DIC) in seawater during calcification. The ambient seawater $\delta^{13}C_{DIC}$ during foraminiferal calcification is influenced by numerous processes, which may be distinguished into biotic and non-biotic processes. With respect to biotic effects, $\delta^{13}C_{DIC}$ of seawater reflects local changes in the balance between photosynthesis (increasing in $\delta^{13}C$) and respiration (decreasing $\delta^{13}C$). In the surface ocean (i.e. habitat of *G. ruber* (p)*)*, however, photosynthesis dominates over respiration (Ravelo and Hillaire-Marcel, 2007). Thus, $\delta^{13}C_{plank}$ of Core M125-35-3 likely reflects the rate of photosynthesis and amount of exported ^{12}C enriched particulate organic matter from the reservoir. Non-biotic effects may comprise advection or upwelling of water masses with different $\delta^{13}C_{DIC}$ signatures. Since *G. ruber* (p) occurs throughout the entire record of Core M125-35-3 and this species is associated to the oligotrophic waters carried by the Brazil Current one would not expect a substitution of different water-masses. Additionally, foraminiferal respiration and symbiont activity may bias $\delta^{13}C$ in foraminiferal tests. However, as we analyze a single species within a narrow size range, our record should be uniformly affected by these influences. Thus, next to other productivity-proxies shown in this study, $\delta^{13}C_{plank}$ may give supporting evidence in the interpretation of oceanic paleo-productivity.

Age Model

The initial age model of Core M125-35-3 was published in (Meier et al., 2021). For this study, we modified the initial model as we added one additional AMS ^{14}C age to improve the accuracy of the late deglacial shift from the Bølling-Allerød (B/A) interstadial to the Younger Dryas (YD) stadial (**Table 1**). The AMS ^{14}C dating was performed by BETA Analytics Limited in Miami (USA). All AMS ^{14}C ages (**Table 1**) were recalibrated with the most recent MARINE20 calibration curve (Heaton et al., 2020) and as recent findings on the marine radiocarbon reservoir effect off the Brazilian coast were published by Alves et al. (2021), we considered a $\Delta R = -84 \pm 125$. As done in (Meier et al., 2021) we used the CRAN R package Bacon (version 2.5.7) (Blaauw and Christen, 2011) to constrain the chronostratigraphy of Core M125-35-3. AMS ^{14}C were calibrated within the Bacon software using a student-t-distribution (Christen and Pérez, 2009) The improved age model covers the interval from ~19.3 ka to the late Holocene around ~4.0 ka comprising the last deglaciation, which we define as the period between the Last Glacial Maximum (LGM) and the beginning of the Holocene (H) including HS1, the B/A, and the YD. Sedimentation increase from ~10 cm/kyr during the latest LGM to maximum values of ~18.0 cm/kyr during the early deglaciation along HS1. After ~14.2 ka, sedimentation rates decrease rapidly to minimum values of ~4.0 cm/kyr. From the onset of the Holocene at ~11.7 ka, sedimentation rates slightly increase to 8 cm/kyr at the youngest part of the record at 4.0 ka (**Figure S1** in **Supplementary Material**).

RESULTS

The elemental ratios ($\Sigma_{Fe, Al, Ti, K}$)/Ca and biomarker proxies (MARs of brGDGTs and the BIT index) which are typically associated with continental runoff, reveal a steady deceasing trend during HS1 (**Figures 3H–J**). In contrast, mass accumulation rates of *n*-alkanes show increasing values and higher variability during HS1 (**Figure 3G**). Plant input, as inferred from long-chain *n*-alkanes, show an increased input of

TABLE 1 | Calibrated AMS ^{14}C ages measured on the planktonic foraminifera *Globigerinoides ruber* (pink) using the software Calib (version 8.2) and the MARINE20 calibration curve with ΔR = -81 ± 124.

Depth (cm)	Lab code	^{14}C age (yr BP)	Error of ^{14}C ages (yr)	2σ calibrated age range (cal yr BP)	Calibrated Median Age Probability (cal yr BP)	Remarks
25.5	BE-7261.1.1	3743	± 42	3261 - 3971	3610	
44.5	Beta-530016	6800	± 30	6878 - 7468	7189	
60.5	BE-7267.1.1	9414	± 43	9760 - 10535	10178	
67.5	Beta-606506	11200	± 30	12313 - 12927	12633	This study
75.5	Beta-530017	12890	± 40	14161 - 15104	14660	
90.5	BE-7268.1.1	12781	± 52	14027 - 14968	14492	
120.5	BE-7269.1.1	13516	± 54	15153 - 15970	15552	
150.5	BE-72701.1	14254	± 59	16118 - 16930	16518	
159.5	Beta530018	15780	± 40	18019 - 18685	18357	

If not specified, data are from Meier et al. (2021).

plant-derived organic matter at Core M125-35-3 from the end of LGM towards the late HS1 with maximum values around 3200 ng cm^{-2} ka^{-1} at ~15.0 ka. Remarkably, all biomarker-based proxies of Core M125-35-3 (alkenones, *n*-alkanes, brGDGTs and crenarchaeol) reveal a rapid decrease in coincidence with the onset of the B/A at ~14.6 ka (**Figures 3D, E, G, H**). Subsequently, the BIT index, *n*-alkane MARs and ($\Sigma_{Fe, Al, Ti, K}$)/Ca remain stable at very low values throughout the rest of the study interval. MARs of brGDGTs, crenarchaeol and alkenones of Core M125-35-3 mimic this pattern, but show an increase after ~7.0 ka during the mid-Holocene, which is of much higher amplitude in crenarchaeol and alkenone MARs (**Figures 3D, E, H**).

$\delta^{13}C_{plank}$ remains relatively constant during HS1 and increases steadily by ~0.5 ‰ during the Holocene (**Figure 3C**). In contrast, alkenone and crenarchaeol MARs reveal distinctly higher oceanic productivity during HS1, approach minimum values during the early Holocene, and show a subsequent continuous increase that accelerates after ~7 ka.

Both, ln(Al/Si) and ln(K/Al) ratios indicate slightly wetter conditions across the catchment of the Paraíba do Sul during HS1 compared to the LGM (**Figures 3A, B**). Drier conditions prevail during the B/A followed by a slight increase in moisture availability across the Paraíba do Sul catchment during the YD stadial. During the Holocene, a long-term decrease of ln(K/Al) and an increase of ln(Al/Si) reveals successively wetter conditions. Overall, precipitation variability in the Paraíba do Sul catchment during the deglacial is comparable or even slightly smaller than that of the Holocene (**Figures 3A, B**).

DISCUSSION

Effects of Enhanced Deglacial and Holocene Fluvial Run-Off on the Marine Environment

On longer time scales, spanning the entire record, our results reveal that a number of proxies from Core M125-35-3, which are commonly used to reconstruct terrestrial related environmental changes reveal a distinct correlation with the deglacial sea level rise defining the extension of the exposed continental shelf (**Figures 1**, **3**). Namely, elemental ratios typically associated with continental runoff ($\Sigma_{Fe, Al, Ti, K}$)/Ca, MARs of brGDGTs and the BIT index are clearly anti-correlated with the deglacial rising sea level (**Figures 3H–K**) and reveal a steady decreasing trend from the LGM towards the B/A. Yet an exception are *n*-alkane MARs, which display increasing values during HS1 prior to their rapid decrease at the onset of the B/A (**Figure 3G**). A secondary source of *n*-alkanes, which may bias the *n*-alkane MARs can be excluded, as the calculated carbon preference index (CPI) from Core M125-35-3 is at average 3.2 (not shown), thus relatively high and comparable to modern soils, pointing to a predominance of well preserved terrestrial *n*-alkanes (Huang et al., 1996; Freeman and Colarusso, 2001; Freeman and Pancost, 2014). The HS1 pattern of *n*-alkane concentrations corresponds well to the evolution of speleothem $\delta^{13}C$ values of Botuverá Cave located in SE Brazil (27°S) (Cruz et al., 2005) (**Figures 3F, G**). Amongst others, speleothem derived $\delta^{13}C$ provides information of biogenic activity above the cave and/or changes in the relative proportion of C_3 (trees and shrubs) to C_4 (drought-adapted grasses) vegetation, with C_3-plants having a lighter $\delta^{13}C$ signature than C_4 plants (Fleitmann et al., 2008; Novello et al., 2019). Here, we ascribe increasing *n*-alkane concentrations occurring parallel to decreasing $\delta^{13}C$ values of Botuverá Cave to the expansion of C_3-dominated Atlantic rainforest (tropical evergreen forest) onto the exposed shelf and the presence of subtropical gallery forests along the Paraíba do Sul during HS1 both substituting the tropical seasonal forest, savanna and grassland-dominated flora prevalent during the LGM. This is in line with late Pleistocene pollen-based reconstructions from Southern and SE Brazil suggesting an expansion of Atlantic rainforests and gallery forests after 17.0 ka (Behling, 1997; Behling, 2002; Gu et al., 2018) and somewhat later starting at 15 ka in SESA (Gu et al., 2017; Gu et al., 2018). The numerical modelling experiments from Maksic et al. (2022) further corroborate the described changes in biomes. Simultaneously, soil run-off decreased as observed from brGDGTs mass accumulation rates during HS1, which may indicate suppressed top-soil erosion induced by forest expansion (**Figure 3H**). The successive decrease in organic matter of terrestrial origin and especially the sudden decrease in both *n*-alkanes and brGDGTs during the B/A and Holocene point at a significantly reduced input of terrigenous organic matter to the upper slope likely amplified by other mechanisms (see *Discussion* below).

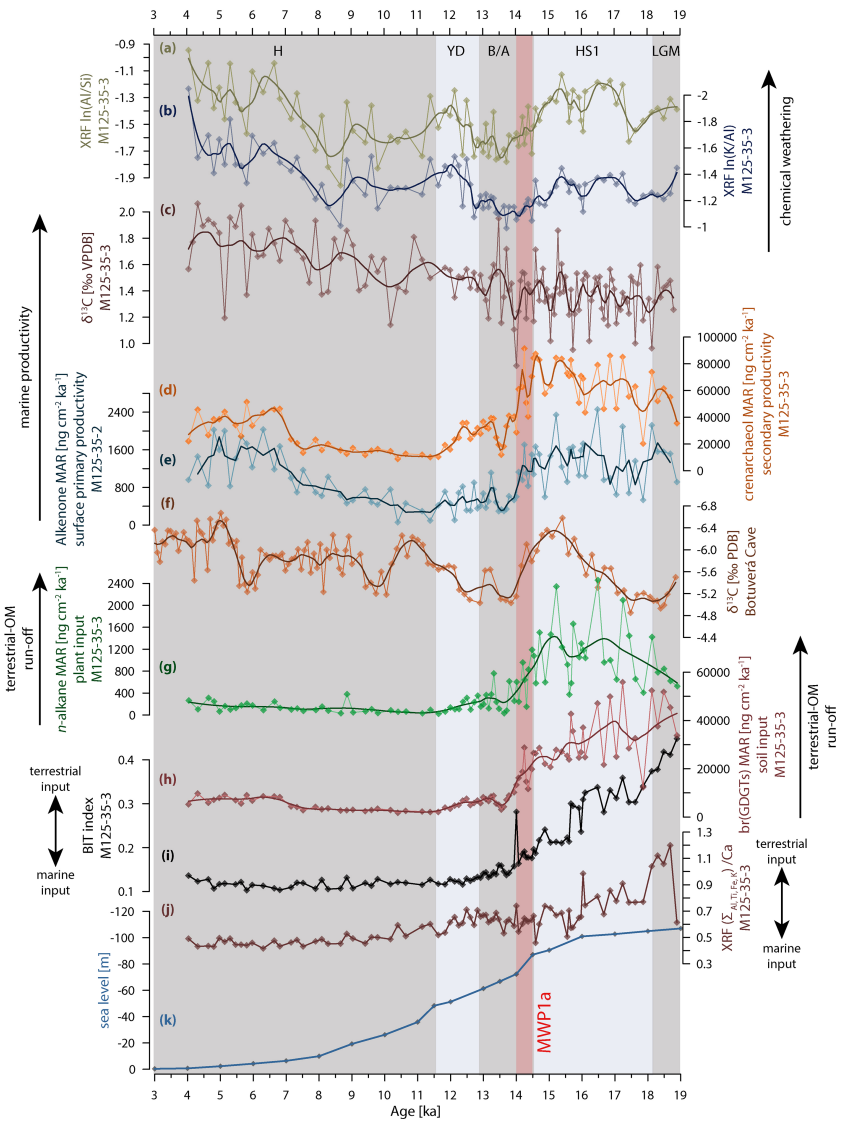

FIGURE 3 | Time series of lipid biomarker **(D, E, G, H, I)**, bulk sediment elemental composition **(A, B, J)** and foraminiferal geochemistry **(C)** data of Core M125-35-3 (this study) compared to a deglacial sea level **(K)** sea level reconstruction (Austermann et al., 2013) and terrestrial speleothem $\delta^{13}C$ **(F)** of Botuverá Cave (Cruz et al., 2005). Thick lines in panels a-h indicate 3-point running average. Bulk sediment elemental composition from Core M125-35-3: **(A)** ln(Al/Si), **(B)** ln(K/Al), j) ($\Sigma_{Fe, Al, Ti, K}$)/Ca. Lipid biomarker of Core M125-35-3): **(D)** Mass accumulation rate (MAR) of crenarchaeol, e) alkenone MAR, g) *n*-alkane MAR, **(H)** brGDGTs MAR, i) BIT index. **(C)** Stable carbon isotopes ($\delta^{13}C$) composition of *Globigerinoides ruber* (p). Arrows indicate direction of increases. Red shaded area marks the timing of Meltwater Pulse 1a (Brendryen et al., 2020). LGM, Last Glacial Maximum; HS1, Heinrich Stadial 1; B/A, Bølling-Allerød interstadial; YD, Younger Dryas; H, Holocene; MWP1a, Meltwater Pulse 1a.

Terrestrial input into oligotrophic waters carried by the Brazil Current alongshore southeastern Brazil would provide an important nutrient source for oceanic biota. In fact, high marine productivity at Core M125-35-3 during HS1, reflected by the increase in alkenone and crenarchaeol accumulation rates (**Figures 3D, E**) aligns with elevated accumulation rates of terrigenous elements (Fe, Al, Ti, K) (**Figure S3** in **Supplementary Material**), *n*-alkanes and brGDGTs (**Figures 3G, H**) pointing at high siliciclastic and organic matter input of terrestrial origin. Notably, the accumulation rates of Fe, Al, Ti, and K as well as Ca are high during HS1, which agrees with the presumption that enhanced marine productivity during higher terrestrial run-off increases deposition of carbonate and the relative content of Ca in the sediment (Govin et al., 2012). Thus, it is consistent to assume that a slightly invigorated continental hydrological cycle and particularly a marked low sea level enhanced nutrient and organic matter flux into the western tropical South Atlantic during HS1, boosting oceanic productivity. This proposed link between river run-off and marine productivity further fits to the suggestion that cold-water coral mounds in the vicinity of Core M125-35-3 flourished during times of enhanced organic-matter input from the continent due to enhanced nutrient and organic-matter availability (Bahr et al., 2020). To summarize,

we infer that terrestrial siliciclastic sediment and organic-matter flux to the upper slope off the Paraíba do Sul was maximal during HS1 and subsequently declined during the late deglacial and Holocene, largely owing to the rising eustatic sea level and ensuing coastline retreat.

Against the above discussed scenario, one might argue that $\delta^{13}C_{plank}$ values remain constantly low during HS1, instead of the expected more enriched values in response to high surface productivity. However, the isotopic fractionation of DIC due to enhanced marine productivity during HS1 may have been compensated by the enhanced input of terrestrial organic matter which is considerably depleted in ^{13}C. The $\delta^{13}C$ in the western subtropical South Atlantic must be considered an open system, where the reservoir and fixation of light ^{12}C by oceanic productivity is constantly compensated by run-off of terrestrial organic matter resulting in no notable fractionation in our $\delta^{13}C_{plank}$ record during HS1.

Interestingly, the rapid decrease in MARs of crenarchaeol, alkenones, *n*-alkanes and brGDGTs at ~14.6 ka at the onset of the B/A coincides with meltwater pulse 1a (Weaver et al., 2003; Brendryen et al., 2020), a phase of rapid sea level rise in which sea level rose by ~20 m within ~500 years (Liu et al., 2016) (**Figures 3D, E, G, H**). We note, that the rapid decrease in *n*-alkanes and brGDGTs might be intensified by a shift to slightly dryer conditions during the B/A onset as reflected by our ln(K/Al) and ln(Al/Si) records leading to decreased terrestrial run-off (**Figures 3A, B**). However, as existing pollen-based vegetation records of the Atlantic rainforest do not reveal a marked decrease or retreat (Gu et al., 2017; Gu et al., 2018), we infer that changes in the hydroclimate were rather small. Thus, we argue that meltwater pulse 1a marks a threshold, facilitated by the broad shelf off SE Brazil, when transgression suddenly flooded a wide area (**Figure 1**), which functions as a sediment trap during interglacial high sea level stands. Indeed, a similar situation was previously described for southern Brazil and Uruguay (Chiessi et al., 2008; Lantzsch et al., 2014). After flooding the shelf, the influx of terrestrial (organic) matter to the continental slope was substantially reduced and became rather insensitive to continental climatic variability compared to the period before the B/A that is characterized by high sediment input to the slope. Yet, during the Holocene, high $\delta^{13}C_{plank}$ as well as high accumulation rates of alkenone and crenarchaeol synthesizing Coccolithophorides and Thaumarchaeota, respectively (**Figures 3C–E**), point at increased oceanic productivity. Further, the BIT index remains low during the Holocene, although a slight increase of terrestrial-derived brGDGTs is observed (**Figures 3H, I**). This slight enhanced input of brGDGTs is apparently compensated by the increase of crenarchaeol in Core M125-35-3 due to higher marine productivity, which in sum leads to a low BIT index (**Figures 3D, H, I**). The dominance of marine organic matter during the Holocene is in line with the more distant shore line, especially after MWP 1a flooded the shelf (**Figure 3**), when terrestrial sediment and organic matter input to the upper slope were significantly reduced. However, as increasing ln(Al/Si) and decreasing ln(K/Al) ratios indicate successively wetter conditions after 8.5 ka, we argue that increased oceanic productivity during the Holocene was caused by increased terrestrial runoff fostered by successively wetter conditions across the Paraíba do Sul catchment eventually providing nutrients to the sub(tropical) South Atlantic. Nonetheless, increased river runoff in line with higher precipitation during the Holocene was less efficient in affecting the oceanic nutrient inventory than the sea-level fluctuations during the deglacial. This is also supported by the lower Holocene MARs of alkenones and crenarchaeol when compared to HS1. In addition, the isotopic fractionation displayed by $\delta^{13}C_{plank}$ may point to limited influx of ^{13}C-depleted terrestrial organic matter and diminished deposition in terrestrial derived sediments.

Deglacial and Holocene SAMS/SACZ Precipitation Variability Across South America

Previous studies have emphasized the role of an intensification and/or expansion of the SACZ for providing enhanced moisture for ESA and SESA during HS1 (Stríkis et al., 2015; Novello et al., 2017; Stríkis et al., 2018; Venancio et al., 2020). As the Paraíba do Sul catchment is within the core region of the SACZ, our record from Core M125-35-3 is, when combined with available paleo-hydrological records from its northern and southern boundaries, ideally suited to track both the strength and area of the SACZ. For this purpose, we compare our results with published trace metal data from speleothems from Botuverá Cave (27°S), which is located just south of the modern domain of the SACZ (Cruz et al., 2007) and $\delta^{18}O$ records of Lapa Sem Fim (16.1°S) and Paixão Caves (12.6°S) located to the north of the SACZ (**Figures 1**, **4C, D, I, J**).

Based on the ln(K/Al) and ln(Al/Si) data from Core M125-35-3 (**Figures 4A, B**), we suggest that precipitation intensity in the core domain of the SACZ (at least over the Paraíba do Sul catchment) did not vary markedly over the deglaciation, with slightly more precipitation during HS1 and the YD compared to the drier B/A. Indeed, neither of these intervals stick out as a climatic extreme in Core M125-35-3.

Trace metal data from Botuverá Cave (Sr/Ca and Mg/Ca) (Cruz et al., 2007) indicate an overall decreasing trend during HS1 pointing to progressively drier conditions (**Figures 4C, D**). Today, Botuverá Cave receives precipitation all year round with no pronounced dry season (during austral summer moisture derives from the SACZ/SAMS, during austral winter moisture is related to extra tropical cyclones (Gan and Rao, 1991; Vera et al., 2002). During HS1, however, a greater seasonal contrast in rainfall probably characterized the region, with a dry season during austral winter and wet austral summer season induced by the SAMS/SACZ. This is supported by palynological studies from southern and southeastern Brazil indicating the dominance of *Poaceae* reflecting rather cold and dry conditions, while modern-like *Araucaria* forests, which are intolerant to long dry seasons, were absent (Behling, 2002; Gu et al., 2017; Gu et al., 2020). A greater seasonal contrast is also supported by low $\delta^{18}O$ values in Botuverá Cave speleothems that point at the Amazon basin as the dominant moisture source

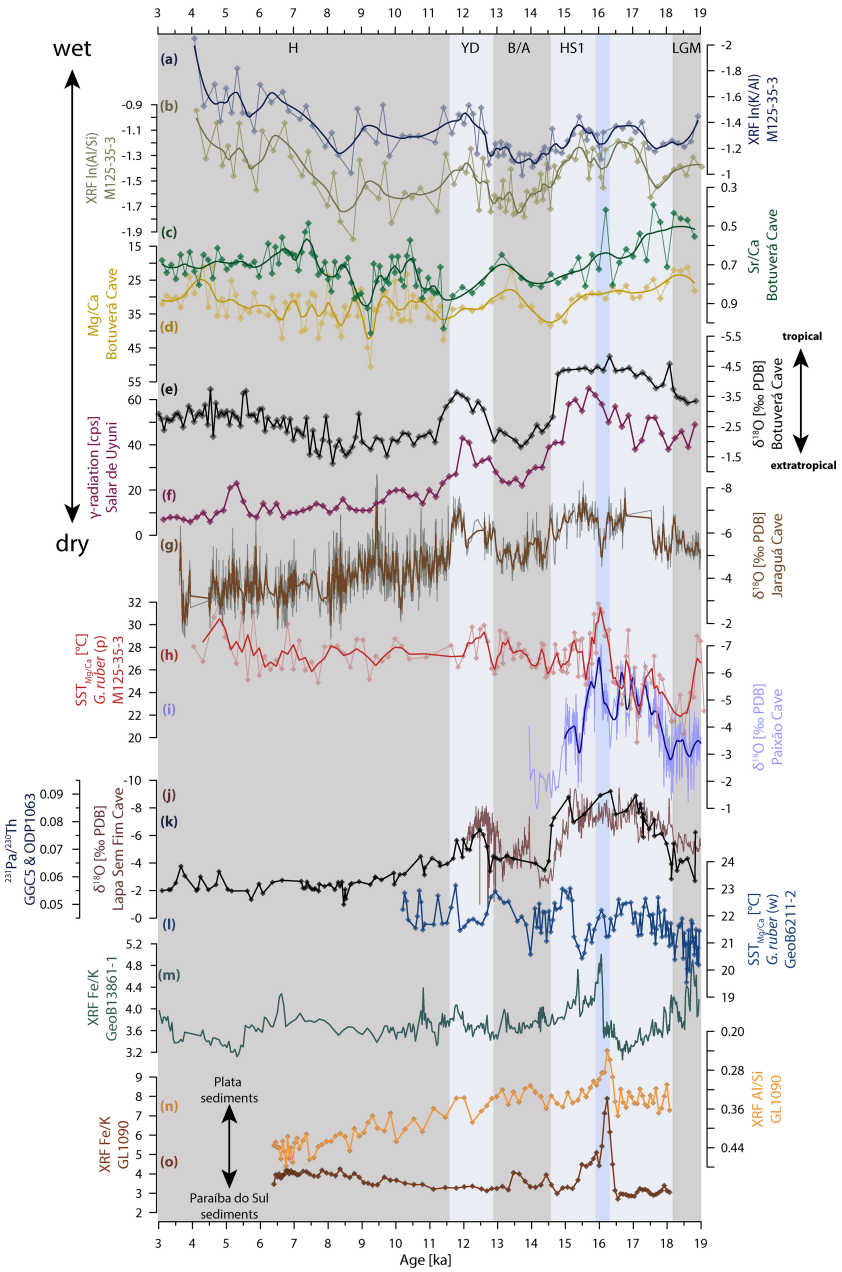

FIGURE 4 | Compilation of paleo precipitation records from South America together with sea-surface temperature (SST) reconstructions from the sub(tropical) South Atlantic. The blue shaded area marks the timing of the atmospheric adjustment to a negative like SALLJ/SACZ dipole pattern across South America at ~16.0 ka as explained in the main text (SALLJ: South American Low Level Jet, SACZ: South Atlantic Convergence Zone). **(A)** ln(Al/Si)) and **(B)** ln(K/Al) of Core M125-35-3 (this study). **(C)** Speleothem-based Sr/Ca, **(D)** Mg/Ca and **(E)** $\delta^{18}O$ of Botuverá Cave located in southeastern South America (Cruz et al., 2005, 2007). **(F)** γ-radiation based precipitation record from Salar de Uyuni located in the central Andes (Baker et al., 2001). **(G)** Speleothem-based $\delta^{18}O$ of Jaraguá Cave in central South America (Brazil) (Novello et al., 2017). **(H)** Mg/Ca-based SST reconstruction from Core M125-35-3 (Meier et al., 2021), **(I)** Paixão Cave speleothem based $\delta^{18}O$ ‰ records and **(J)** Lapa Sem Fim Cave speleothem based $\delta^{18}O$ compilation (Strikis et al., 2015, 2018) from eastern South America, **(K)** $^{231}Pa/^{230}Th$ compilation from Core GGC5 and ODP Site 1063 representing Atlantic Meridional Overturning Circulation strength (McManus et al., 2004; Böhm et al., 2015; Lippold et al., 2019), **(L)** $SST_{Mg/Ca}$ record of Core GeoB6211-2 (Chiessi et al., 2015) collected off southern Brazil, **(M)** XRF-derived Fe/K from Core GeoB13861-1 close to the La Plata River mouth (Warratz et al., 2017). **(N)** and **(O)** XRF derived ln(K/Al) and Fe/K from Core GL-1090 from the La Plata River mouth (Mathias et al., 2021). Thick lines in panels a-d and g-i indicate 3-point running average. LGM, Last Glacial Maximum; HS1, Heinrich Stadial 1; B/A, Bølling-Allerød interstadial; YD, Younger Dryas; H, Holocene; MWP1a, Meltwater Pulse 1a.

during HS1 (Bernal et al., 2016), which today fuels the SACZ. Hence, based on available data from Botuverá Cave, a reduction in winter-time precipitation can be inferred, while the SACZ-related precipitation appeared to have been relatively stable.

Intensification of SAMS/SACZ activity over ESA during HS1 was previously suggested by Stríkis et al. (2015) based on speleothem precipitation records from Lapa Sem Fim and Paixão Caves (**Figures 1**, **4I, J**). The positive precipitation anomalies in Lapa Sem Fim and Paixão Caves were related to so-called "Mega-SACZ-Events" that were presumed to be a consequence of enhanced convection of tropical-sourced moisture towards ESA and SESA (Stríkis et al., 2015). However, the new ln(K/Al) and ln(Al/Si) records of Core M125-35-3 do not support a strong intensification of the SACZ during HS1 (**Figures 3A, B**). The more frequent $\delta^{18}O$ minima in both cave records may be explained by northward expansions of the SACZ leading to increased precipitation above the cave sites. The core region of the SACZ, on the other hand, seems unaffected by potential northward expansions as the Paraíba do Sul catchment remains within the SACZ influence as inferred from ln(K/Al) and ln(Al/Si) of Core M125-35-3. An exception occurred around ~16 ka, when a minimum in $\delta^{18}O$ indicate the wettest phase in the Paixão record. Minimum $\delta^{18}O$ occurs synchronously with slightly dryer conditions across the Paraíba do Sul catchment area suggesting a northward displacement of the SACZ.

Interestingly, the Paixão Cave $\delta^{18}O$ record closely follows the Mg/Ca-based SST reconstruction of Core M125-35-3 (Meier et al., 2021) (**Figures 3H, I**). Further, the compiled $\delta^{18}O$ records of Lapa Sem Fim Cave (Stríkis et al., 2015; Stríkis et al., 2018) match remarkably well with the $^{231}Pa/^{230}Th$ compilation record of cores GGC5 and ODP Site 1063 from the North Atlantic (McManus et al., 2004; Böhm et al., 2015; Lippold et al., 2019), indicating a sluggish AMOC during HS1 (**Figures 3J, K**). These correlations may imply a connection between large-scale oceanographic changes in the western South Atlantic and precipitation pattern across ESA during HS1. Campos et al. (2019) showed that precipitation variability in ESA and SESA was driven by a mechanism independent of SAMS/SACZ activity. Campos et al. (2019) proposed that precipitation availability in ESA and to a lesser degree in SESA depended on atmospheric and oceanographic changes that resulted from the diminished interhemispheric heat transfer caused by a weakened AMOC. Based on model and proxy data, Campos et al. (2019) inferred that increased (decreased) moisture sourced from the warmer (colder) tropical South (North) Atlantic was transported with the SE (NE) trade winds during austral summer (winter). In fact, the good correlation of high SSTs at Core M125-35-3 and increased precipitation above Paixão Cave indicate that SSTs from the sub(tropical) South Atlantic played a crucial role in determining the amount of moisture advected by the SE winds towards ESA and SESA. High (low) SSTs in the sub(tropical) western South Atlantic probably contributed to warm and moist (cool and dry) air towards the continent. In contrast, the southerly located Botuverá Cave in SESA seems to be unaffected by this oceanic sub(tropical) moisture source as its precipitation record reveals continuously dryer conditions, especially during austral winter. It thus appears that during HS1 SE trade winds delivering oceanic-sourced moisture were primarily responsible for enhanced precipitation in tropical ESA (e.g., at Paixão and Lapa Sem Fim Caves) and to a lesser degree in the south where they contributed to the slightly wetter conditions across the Paraíba do Sul catchment. A gradual trend towards increasing precipitation in the northern portions of ESA may imply a relative increase in convective rainfall associated with a marked southward shift of the ITCZ during HS1. However, reconstructions of deglacial migrations of the ITCZ during northern hemispheric cooling suggest southward shifts of no more than 7° from its modern position (Arbuszewski et al., 2013; Schneider et al., 2014; Portilho-Ramos et al., 2017). A significant contribution of ITCZ rainfall to ESA is hence unlikely.

In addition, Chaves and Nobre (2004) showed that, based on observational data, positive SST anomalies in the western subtropical and tropical South Atlantic lead to a northward shift of the SACZ. This corroborates the interpretation that not a substantial intensification of the SACZ increased precipitation during HS1, but northward shifts/expansions of the SACZ additionally amplified precipitation in SESA as illustrated by the synchronous SST maximum at Core M125-35-3 and peak precipitation at the Paixão Cave record at ~16.0 ka (**Figures 4H, I**, **5**). Our findings lead us to recede from the previously suggested "Mega-SACZ-Event" and suggest that the slight increased precipitation in ESA and SESA during HS1 was primarily due to enhanced moisture advection from the tropical western South Atlantic. However, northward expansion or potential shifts of the SACZ might have additionally reinforced precipitation in ESA. Hence, our findings corroborate the mechanism proposed by Campos et al. (2019) for positive precipitation anomalies over tropical South America.

South American Low Level Jet Dynamics During the Deglaciation

While the deglacial hydroclimate variability in ESA and partially in SESA might be well explained by changes in trade wind intensity and SACZ dynamics, precipitation patterns across SSESA are strongly influenced by synoptic-scale climate features, that are usually insufficiently considered in paleoclimatic studies

The XRF-derived Fe/K record from Core GeoB13861-1 (38.0° S) (Warratz et al., 2017) collected off the La Plata River mouth (**Figures 1**, **4M**), as well as the Fe/K and Al/Si records from Core GL-1090 (24.92°S) (Mathias et al., 2021) retrieved off SE Brazil potentially show precipitation changes over SSESA, the southern part of the dipole. We updated the age model of Core GL-1090 applying the new MARINE20 calibration curve (Heaton et al., 2020) to enable a robust correlation with Core M125-35-3.

From the LGM towards ~16 ka, the Al/Si record of Core GL-1090 reveals relatively high values indicating smaller amounts of sediments from the La Plata River (**Figure 4N**) in SSESA. The Fe/K record of Core GeoB13861-1 displays decreasing values from the LGM to 16 ka, indicating a decreasing runoff of deeply

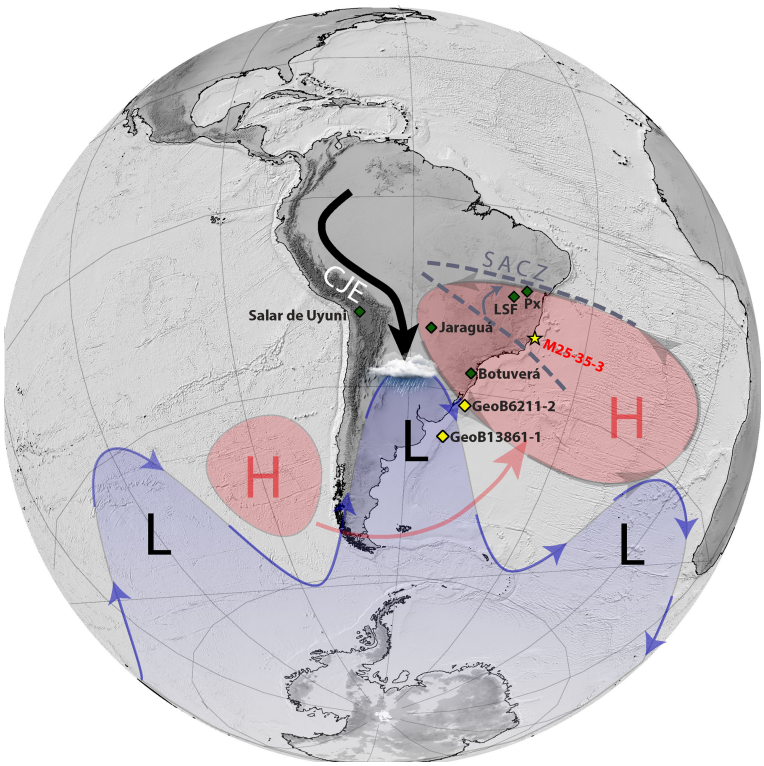

FIGURE 5 | Schematic illustration of atmospheric circulation patterns and rainfall anomalies in South America during Heinrich Stadial at ~16 ka. The blue shaded area marks the low-pressure system related to the steady eastward propagating Rossby wave train. High-pressure systems propagate northward as they pass the Andes (indicated by the red arrow). The quasi-stationary system that occurred at ~16 ka during HS1 foster a subtropical high-pressure system across South America (red area above South America). Substantial moisture transport *via* the Chaco Jet Event (CJE) configuration (black arrow) enhances rainfall in southern southeastern South America. Under this situation, the South Atlantic Convergence Zone (SACZ) was likely displaced northward relative to its modern position. Green and yellow diamonds indicate terrestrial and marine previously published precipitation records respectively. Px, Paixão Cave; LSF, Lapa Sem Fim Cave The yellow star marks Core M125-35-3 (this study).

weathered material from the Paraná catchment and the La Plata basin (**Figure 4M**). However, these values need to be interpreted with caution since decreased bottom current activity favors the deposition of fine grained clays of Al-rich illite and chlorite (which may contain significant amounts of Fe) from the circumantarctic area, potentially increasing Fe/K values during the late LGM and early HS1 (Warratz et al., 2017). However, the Fe/K record from Core GL-1090, collected ca. 10° to the north and ca. 1500 m shallower than GeoB13861-1, constantly displays low values from the LGM towards ~16.0 ka (**Figure 4O**) which is unlikely an effect of the northward dispersal of clays from the Southern Ocean [cf. **Figure 4** in (Warratz et al., 2017)]. Overall, we infer that hinterland runoff *via* the La Plata River and associated precipitation across the Paraná catchment in SSESA was relatively low between ca. 18 and 16 ka. As discussed above, ln(K/Al) and ln(Al/Si) ratios from Core M125-35-3 reveal slightly elevated precipitation during this interval (**Figures 4A, B**). Silva and Berbery (2006) observed a strong thermal front in the vicinity of southern Brazil during positive precipitation anomalies in SSESA. If this thermal front is not or only weakly established, precipitation in the SACZ region is enhanced. Indeed, SST from Core M125-35-3 are rather low and show an increasing trend from ca. 18 until 16 ka, comparable to the southerly located Mg/Ca-based SST record of Core GeoB6211-2 (32.5°S) collected off southern Brazil (Chiessi et al., 2015) (**Figure 4L**) pointing at a weak meridional SST gradient. Thus, we suggest that more moisture was transported towards the SACZ realm in SESA *via* the NCJE configuration. The dipole precipitation pattern was thus rather adjusted to a positive (increased) precipitation in SESA at the expense of dryer conditions in SSESA (**Figures 1**, **5**).

At ~16.0 ka a distinct change in the SACZ-SALLJ dipole configuration occurs, as displayed by the signal and spatial distribution of ensemble of precipitation records across South America presented in **Figure 4**. Noteworthy, the interval around 16 ka was associated to the most intense phase of Heinrich Event 1 (HE1) during HS1 and was characterized by the strongest thermal imbalance according to the interhemispheric seesaw (Meier et al., 2021). This pronounced phase of the interhemispheric thermal seesaw led to warming in the high-latitude southern South Atlantic, implying a markedly reduced equator to pole thermal gradient (Barker et al., 2009). These boundary conditions were also invoked to explain the vigorous warming in the western South Atlantic as observed in Mg/Ca-

based SSTs of Core M125-35-3 (**Figure 4H**) (Meier et al., 2021). During this interval at ~16.0 ka, the Jaraguá Cave speleothem record from central South America marks a distinct drying event (**Figures 1**, **3G**). Simultaneously, a distinct increase in Fe/K from Core GeoB13861-1 (Warratz et al., 2017) argues for marked wet events over the La Plata basin in SSESA (**Figure 3M**). Noteworthy, the Fe/K peak at ~16 ka at Core GeoB13861-1 coincides with a marked decrease in Al/Si of Core GL-1090 (**Figure 4N**), minimizing a potential imprint of allochthonous Al-enriched circumantarctic clays during times of relatively weak northward-flowing bottom currents (Warratz et al., 2017). We also infer that early diagenetic effects (e.g. by changing redox conditions) (Riedinger et al., 2005) are not the main cause for the Fe/K peak in Core GeoB13861-1 at ~ 16 ka as it coincides remarkably well with moist conditions over SSESA implied by the sudden decrease (increase) in Al/Si (Fe/K) of Core GL-1090 which during the deglacial was situated in a more proximal location relative to the La Plata River mouth due to the low sea level (Lantzsch et al., 2014; Mathias et al., 2021). At the same time, our ln(K/Al) and ln(Al/Si) record reveals a short intermittent dry period at 16.0 ka at the Paraíba do Sul catchment (**Figures 4A, B**). We note that ln(K/Al) and Si/Al from Core M125-35-3 as well as trace metal data from Botuverá Cave display rather moderate drying across the SACZ realm (**Figures 4A–D**). Missing tropical moisture export towards the SACZ domain in SESA *via* the NCJE would cause severely dry conditions which were, however, likely compensated by enhanced oceanic moisture flux in line with a vigorous warming in the western tropical South Atlantic (**Figure 4H**) at 16.0 ka. Thus, the precipitation pattern changed rapidly across South America at 16.0 ka towards a negative dipole configuration, where central South America (i.e. Jaraguá Cave) and SESA represented by Core M125-35-3 are characterized by drying and SSESA (i.e. the Paraná and Uruguay catchment) experienced distinct wet events. Notably, this precipitation dipole between SESA and SSESA coincided with the development of a distinct oceanographic front at around 16.0 ka in the western (sub)tropical South Atlantic as suggested by SST cooling at mid-latitude Core GeoB6211-2 (32.5°S) (Chiessi et al., 2015) parallel to pronounced warming at Core M125-35-3 (21.9°S) (Meier et al., 2021) (**Figures 4H, L**). As mentioned above, this thermal front is in line with increased precipitation in SSESA and drying in SESA, as observed by (Silva and Berbery, 2006). This pattern suggests that a strong and persistent CJE enhanced the flow of Amazon moisture towards the La Plata basin around 16.0 ka leading to anomalously high rainfall in SSESA. In this context, the concomitant dry phase at Jaraguá Cave is in line with the majority of Amazon moisture being transported southwards along the eastern margin of the Andes and to a lesser extend southeastward towards Jaraguá Cave and the Paraíba do Sul catchment area (**Figure 5**). Increased southward advection of Amazon moisture is also corroborated by a precipitation record from Salar de Uyuni on the Bolivian Altiplano in the central Andes showing increased rainfall throughout HS1 (**Figure 4F**) (Baker et al., 2001).

Although the negative precipitation dipole observed at ~16 ka fits to observational data such as the thermal front arising near SE Brazil (**Figures 4H, I**) (Silva and Berbery, 2006), there is still lack of a sufficient mechanism explaining the substantial reconfiguration of the lower atmospheric circulation and consecutive moisture transport across South America. Modern observations revealed that vast flooding and rainfall events may be strongly related to the behavior of Rossby wave propagation patterns. Extreme climate phases may be explained by high amplitude quasi-stationary Rossby waves resulting from a decreased atmospheric circulation caused by a reduction of the temperature difference between polar and mid-latitudes (Andreoli and Kayano, 2005; Coumou et al., 2014; Coumou et al., 2015; Coelho et al., 2016; Mann et al., 2017; Wolf et al., 2018). It is well documented that moisture flux by the SALLJ is largely dependent on the dynamics of synoptic-scale Rossby wave propagation (e.g. Salio et al., 2002; Carvalho et al., 2004; Liebmann et al., 2004; Marengo et al., 2004). We therefore suggest that around 16.0 ka, a time of maximum warming of the southern hemisphere due to the interhemispheric seesaw (Broecker, 1998; Stocker, 1998; Pedro et al., 2011; Barker and Diz, 2014; Meier et al., 2021), the overall decreased thermal gradient across the Southern Hemisphere led to a slowdown of the atmospheric circulation. Thus, the Rossby wave propagation became more stationary, leading to extreme and sustained climatic conditions in SSESA and SESA. The pattern suggests, that a strong subtropical high developed, which spread far across SESA, forcing the SALLJ to a NCJE-like configuration with an exit region above subtropical South America. Consequently, subsiding airmasses associated with a strong and stable subtropical high inhibited cloud cover leading to persistent radiative forcing, which likely fostered anomalously high SSTs as observed in Core M125-35-3 at 16 ka. This atmospheric and oceanic configuration in turn, led to vast increases in precipitation across SSESA. This pattern might be indirectly enhanced by a significantly southward shifted ITCZ at 16 ka. Climate models reveal a similar precipitation pattern across South America after significant weakening of the Southern Hemisphere Hadley cell affecting the subtropical and mid-latitude jets (**Figure 1** in Lee et al., 2011; Ceppi et al., 2013). Contrary, during the early and late phases of HS1, the atmospheric circulation and Rossby wave propagation was enhanced, leading to less pronounced and ephemeral extreme conditions similar to modern-like conditions. The dipole reconfiguration at 16 ka hence marks an anomalously persistent negative dipole mode lasting at least ~500 yrs (cf. blue shading in **Figure 4**). As discussed in Section 2, the occurrence of the negative dipole configuration such as at ~16 ka resembles hydroclimatic extremes of decadal- to interdecadal scales occurring under present-day conditions. However, modern trends and future projections of precipitation suggest an increase in the occurrence of the negative dipole pattern under quasi-stationary Rossby waves with hazardously increased rainfall across subtropical South America in SSESA due to global warming (Gonzalez et al., 2013; Junquas et al., 2013; Vera and Díaz, 2015; Saurral et al., 2017; Masson-Delmotte et al., 2021). It is astonishing that a similar climatic configuration could occur under considerably different boundary conditions. We hypothesize that both the future and the SACZ/SALLJ dipole evolution at ~16 ka respond to a common pattern, i.e., a reduced

hemispheric equator to pole thermal gradient as it is typical for both global warming scenarios (Masson-Delmotte et al., 2021) and HS1 (Barker et al., 2009).

Evolution of SAMS Dynamics After HS1

After HS1 (i.e., the late deglacial), ln(Al/Si) and ln(K/Al) of Core M125-35-3 suggest drier conditions during the B/A interstadial pointing to a weaker SAMS/SACZ which lasted until the beginning of the YD, when precipitation increased towards the onset of the Holocene (**Figures 4A, B**). This late deglacial pattern is consistent with the precipitation record from Jaraguá Cave (Novello et al., 2017) from the central domain of the SAMS/SACZ in central South America (Brazil) (**Figure 4G**). The strong late deglacial coupling of precipitation in the Paraíba do Sul catchment and Jaraguá Cave indicates that rainfall associated with the SAMS/SACZ intensity similarly determined precipitation in SESA and above Jaraguá Cave. If oceanic moisture would have dominated precipitation across the Paraíba do Sul catchment, one would a expect no clear correlation with the Jaraguá Cave speleothem record, located in central South America, distant from the coast (**Figure 5**). Indeed, SST cooling after 16 ka at the site of Core M125-35-3 implies less moisture export towards South America provided by evaporation over the sub(tropical) South Atlantic. Hence, we infer that during the late deglacial after HS1, oceanic moisture sourced from the (sub)tropical South Atlantic did not substantially contribute to moisture budget across SESA and a more modern-like precipitation pattern was established. Further, during the late deglacial the Fe/K and Al/Si of cores GeoB13861-1 and GL-1090 do not show any marked abrupt shift in precipitation across SSESA (**Figures 4M–O**). Thus, we assume, that late deglacial precipitation pattern associated with SACZ/SAMS variability was stabilized by the configuration of perpetually propagating non-stationary Rossby waves inhibiting sustained phases of extreme rainfall in SSESA such as during ~16 ka.

Drier conditions above the Paraíba do Sul catchment (**Figures 4A, B**) during the B/A can be assigned to the stabilization of temperatures in South America in coincidence with the Antarctic Cold Reversal indicating overall cooler and likely dryer conditions at the southern margins of the SAMS (Blunier et al., 1997; Chiessi et al., 2015; Pedro et al., 2016). Similarly to HS1, during the YD our records reflect a slight increase in SAMS/SACZ activity as recorded in Jaraguá Cave. This precipitation increase was likely related to warming of the Southern Hemisphere and enhanced moisture influx into South America due to Northern Hemisphere cooling leading to a southward shift of the ITCZ (Cruz et al., 2006; Novello et al., 2017). This is in contrast to the HS1, where the (sub)tropical western South Atlantic was involved as an important moisture source. SSTs of Core M125-35-3 indeed show a parallel warming trend during the YD, however, we assume that the quantity of oceanic-sourced moisture feeding SESA was greatly reduced because warming of the western tropical South Atlantic was much weaker compared to HS1.

From the mid Holocene (~8.5 ka) to the top of Core M125-35-3 our ln(K/Al) and ln(Al/Si) records reveal an increase in precipitation across the Paraíba do Sul catchment (**Figures 4A, B**). Simultaneously, the SST record from Core M125-35-3 shows an increase in temperatures towards ~30°C, which is somewhat lower as the SST peak at 16 ka (**Figure 4H**). At the same time, $\delta^{18}O$ from Jaraguá Cave shows decreased rainfall across central South America (**Figure 4G**). Supported by a slight decrease in the $\delta^{18}O$ Botuverá Cave record (**Figure 4E**), which shows an increased portion of oceanic moisture, we infer that during the mid- and late Holocene precipitation across SESA was enhanced by increased moisture flux from the sub(tropical) South Atlantic in line with higher SSTs.

CONCLUSIONS

Our deglacial multiproxy dataset of Core M125-35-3 reveals a strong impact of riverine run-off on marine biota in the western tropical South Atlantic and discloses new insights in the dynamics of the SAMS/SACZ. First, our data show that enhanced terrigenous nutrient and organic matter input fueled marine productivity in the realm of Core M125-35-3 during HS1, a consequence of low sea level and slightly enhanced continental precipitation. Second, vigorous warming of the (sub)tropical South Atlantic and substantial alteration of the atmospheric circulation during HS1 enhanced oceanic moisture flux towards eastern South America. Consequently, our findings imply that SAMS variability in SESA cannot be explained by changes in the intensity and geographic extent of the SACZ alone. Last, we demonstrate that reconstructions of rainfall patterns across SESA and SSESA need to consider the dynamics of Rossby wave trains and their influence on the SALLJ dynamics. Interestingly, numerical models imply that extreme climate conditions, as reflected by the persistent negative SALLJ/SACZ dipole pattern around ~16 ka during HS1, will likely recur under decisively different boundary conditions in the future as a consequence of global warming.

DATA AVAILABILITY STATEMENT

The datasets presented in this study can be found in online repositories. The names of the repository/repositories and accession number(s) can be found below: https://doi.pangaea.de/10.1594/PANGAEA.942656.

AUTHOR CONTRIBUTIONS

KM designed and conceptualized the study, took the lead in writing the manuscript, realized visualizations and conducted analytical work. AJ and JR conducted analytical work, aided in interpreting the results and worked on the manuscript. CC and OF contributed to the interpretation of the results and provided critical feedback and helped shape the manuscript. ALA contributed resources and contributed manuscript writing. VW conducted analytical work. AB contributed to the design of the study and implementation of

the research and contributed to the analysis interpretation of the results and writing of the manuscript. All authors contributed to the article and approved the submitted version.

FUNDING

AB acknowledges funding by the German Research Foundation (DFG; projects HO 5927/1-1 and BA 3809/14-1). AJ acknowledges financial support from DFG (grant 268236062 – SFB1211). CMC acknowledges financial support from FAPESP (grants 2018/15123-4 and 2019/24349-9), CAPES (grant 88881.313535/201901), CNPq (grant 312458/2020-7), and the Alexander von Humboldt Foundation. For the publication fee we acknowledge financial support by Deutsche Forschungsgemeinschaft (DFG) within the funding programme, Open Access Publikationskosten"as well as by Heidelberg University.

ACKNOWLEDGMENTS

We kindly acknowledge the captain and crew of R/V METEOR during research cruise M125. Further, we thank Bernd Knape for assistance in ICP-MS measurements, Oliver A. Kern, Laurin S. Kolb and Maria Wierzbicka-Wieczorek for scientific discussion, Julia Hoffmann and Barbara Hennrich for laboratory assistance. Nicole Mantke and Volker Wennrich are thanked for help with XRF analysis, Daniela Warok and Bianca Stapper for assistance in lipid biomarker analysis. We thank Ed Hathorne (editor) and three reviewers for constructive comments on our manuscript.

SUPPLEMENTARY MATERIAL

The Supplementary Material for this article can be found online at: https://www.frontiersin.org/articles/10.3389/fmars.2022.878116/full#supplementary-material

REFERENCES

Alves, E. Q., Macario, K. D., Spotorno, P., Oliveira, F. M., Muniz, M. C., Fallon, S., et al. (2021). Nineteenth-Century Expeditions and the Radiocarbon Marine Reservoir Effect on the Brazilian Coast. *Geochim. Cosmochim. Acta* 297, 276–287. doi: 10.1016/j.gca.2020.11.021

Ambrizzi, T., de Souza, E. B., and Pulwarty, R. S. (2004). "The Hadley and Walker Regional Circulations and Associated ENSO Impacts on South American Seasonal Rainfall," in *The Hadley Circulation: Present, Past and Future Advances in Global Change Research*. Eds. H. F. Diaz and R. S. Bradley (Dordrecht: Springer Netherlands), 203–235. doi: 10.1007/978-1-4020-2944-8_8

Andreoli, R. V., and Kayano, M. T. (2005). ENSO-Related Rainfall Anomalies in South America and Associated Circulation Features During Warm and Cold Pacific Decadal Oscillation Regimes. *Int. J. Climatol.* 25, 2017–2030. doi: 10.1002/joc.1222

Arbuszewski, J. A., deMenocal, P. B., Cléroux, C., Bradtmiller, L., and Mix, A. (2013). Meridional Shifts of the Atlantic Intertropical Convergence Zone Since the Last Glacial Maximum. *Nat. Geosci.* 6, 959–962. doi: 10.1038/ngeo1961

Austermann, J., Mitrovica, J. X., Latychev, K., and Milne, G. A. (2013). Barbados-Based Estimate of Ice Volume at Last Glacial Maximum Affected by Subducted Plate. *Nat. Geosci.* 6, 553–557. doi: 10.1038/ngeo1859

Bahr, A., Doubrawa, M., Titschack, J., Austermann, G., Koutsodendris, A., Nürnberg, D., et al. (2020). Monsoonal Forcing of Cold-Water Coral Growth Off Southeastern Brazil During the Past 160 Kyr. *Biogeosciences* 17, 5883–5908. doi: 10.5194/bg-17-5883-2020

Bahr, A., Hoffmann, J., Schönfeld, J., Schmidt, M. W., Nürnberg, D., Batenburg, S. J., et al. (2018). Low-Latitude Expressions of High-Latitude Forcing During Heinrich Stadial 1 and the Younger Dryas in Northern South America. *Global Planet. Change* 160, 1–9. doi: 10.1016/j.gloplacha.2017.11.008

Bahr, A., Kaboth-Bahr, S., Jaeschke, A., Chiessi, C., Cruz, F., Carvalho, L., et al. (2021). Late Holocene Precipitation Fluctuations in South America Triggered by Variability of the North Atlantic Overturning Circulation. *Paleoceanogr. Paleoclimatol.* 36, e2021PA004223. doi: 10.1029/2021PA004223

Bahr, A., Spadano Albuquerque, A. L., Ardenghi, N., Batenburg, S., Bayer, M., Catunda, M. C., et al. (2016). *South American Hydrological Balance and Paleoceanography During the Late Pleistocene and Holocene (SAMBA) - Cruise No. M125 - March 21 - April 15, 2016 - Rio De Janeiro (Brazil) - Fortaleza (Brazil)* (Bremen: DFG-Senatskommission für Ozeanographie). doi: 10.2312/cr_m125

Baker, P. A., Rigsby, C. A., Seltzer, G. O., Fritz, S. C., Lowenstein, T. K., Bacher, N. P., et al. (2001). Tropical Climate Changes at Millennial and Orbital Timescales on the Bolivian Altiplano. *Nature* 409, 698–701. doi: 10.1038/35055524

Barker, S., and Diz, P. (2014). Timing of the Descent Into the Last Ice Age Determined by the Bipolar Seesaw. *Paleoceanography* 29, 489–507. doi: 10.1002/2014PA002623

Barker, S., Diz, P., Vautravers, M. J., Pike, J., Knorr, G., Hall, I. R., et al. (2009). Interhemispheric Atlantic Seesaw Response During the Last Deglaciation. *Nature* 457, 1097–1102. doi: 10.1038/nature07770

Behling, H. (1997). Late Quaternary Vegetation, Climate and Fire History From the Tropical Mountain Region of Morro De Itapeva, SE Brazil. *Palaeogeogr. Palaeoclimatol. Palaeoecol.* 129, 407–422. doi: 10.1016/S0031-0182(97)88177-1

Behling, H. (2002). South and Southeast Brazilian Grasslands During Late Quaternary Times: A Synthesis. *Palaeogeogr. Palaeoclimatol. Palaeoecol.* 177, 19–27. doi: 10.1016/S0031-0182(01)00349-2

Bernal, J. P., Cruz, F. W., Stríkis, N. M., Wang, X., Deininger, M., Catunda, M. C. A., et al. (2016). High-Resolution Holocene South American Monsoon History Recorded by a Speleothem From Botuverá Cave, Brazil. *Earth Planet. Sci. Lett.* 450, 186–196. doi: 10.1016/j.epsl.2016.06.008

Biscaye, P. E. (1965). Mineralogy and Sedimentation of Recent Deep-Sea Clay in the Atlantic Ocean and Adjacent Seas and Oceans. *Geol. Soc. America Bull.* 76, 803. doi: 10.1130/0016-7606(1965)76[803:MASORD]2.0.CO;2

Blaauw, M., and Christen, J. A. (2011). Flexible Paleoclimate Age-Depth Models Using an Autoregressive Gamma Process. *Bayes. Anal.* 6, 457–474. doi: 10.1214/11-BA618

Blunier, T., Schwander, J., Stauffer, B., Stocker, T., Dällenbach, A., Indermühle, A., et al. (1997). Timing of the Antarctic Cold Reversal and the Atmospheric CO2 Increase With Respect to the Younger Dryas Event. *Geophys. Res. Lett.* 24, 2683–2686. doi: 10.1029/97GL02658

Boers, N., Rheinwalt, A., Bookhagen, B., Barbosa, H. M. J., Marwan, N., Marengo, J., et al. (2014). The South American Rainfall Dipole: A Complex Network Analysis of Extreme Events. *Geophys. Res. Lett.* 41, 7397–7405. doi: 10.1002/2014GL061829

Böhm, E., Lippold, J., Gutjahr, M., Frank, M., Blaser, P., Antz, B., et al. (2015). Strong and Deep Atlantic Meridional Overturning Circulation During the Last Glacial Cycle. *Nature* 517, 73–76. doi: 10.1038/nature14059

Bonatti, E., and Gartner, S. (1973). Caribbean Climate During Pleistocene Ice Ages. *Nature* 244, 563–565. doi: 10.1038/244563a0

Brendryen, J., Haflidason, H., Yokoyama, Y., Haaga, K. A., and Hannisdal, B. (2020). Eurasian Ice Sheet Collapse was a Major Source of Meltwater Pulse 1A 14,600 Years Ago. *Nat. Geosci.* 13, 363–368. doi: 10.1038/s41561-020-0567-4

Broecker, W. S. (1998). Paleocean Circulation During the Last Deglaciation: A Bipolar Seesaw? *Paleoceanography* 13, 119–121. doi: 10.1029/97PA03707

Burnett, A. P., Soreghan, M. J., Scholz, C. A., and Brown, E. T. (2011). Tropical East African Climate Change and its Relation to Global Climate: A Record From Lake Tanganyika, Tropical East Africa, Over the Past 90+Kyr.

Palaeogeogr. Palaeoclimatol. Palaeoecol. 303, 155–167. doi: 10.1016/j.palaeo.2010.02.011

Campos, M. C., Chiessi, C. M., Prange, M., Mulitza, S., Kuhnert, H., Paul, A., et al. (2019). A New Mechanism for Millennial Scale Positive Precipitation Anomalies Over Tropical South America. *Quaternary. Sci. Rev.* 225, 105990. doi: 10.1016/j.quascirev.2019.105990

Carvalho, L. M. V., Jones, C., and Liebmann, B. (2004). The South Atlantic Convergence Zone: Intensity, Form, Persistence, and Relationships With Intraseasonal to Interannual Activity and Extreme Rainfall. *J. Climate* 17, 88–108. doi: 10.1175/1520-0442(2004)017<0088:TSACZI>2.0.CO;2

Ceppi, P., Hwang, Y.-T., Liu, X., Frierson, D. M. W., and Hartmann, D. L. (2013). The Relationship Between the ITCZ and the Southern Hemispheric Eddy-Driven Jet. *J. Geophys. Res.: Atmosph.* 118, 5136–5146. doi: 10.1002/jgrd.50461

Chaves, R. R., and Nobre, P. (2004). Interactions Between Sea Surface Temperature Over the South Atlantic Ocean and the South Atlantic Convergence Zone. *Geophys. Res. Lett.* 31. doi: 10.1029/2003GL018647

Chiessi, C. M., Mulitza, S., Mollenhauer, G., Silva, J. B., Groeneveld, J., and Prange, M. (2015). Thermal Evolution of the Western South Atlantic and the Adjacent Continent During Termination 1. *Climate Past.* 11, 915–929. doi: 10.5194/cp-11-915-2015

Chiessi, C. M., Mulitza, S., Pätzold, J., and Wefer, G. (2010). How Different Proxies Record Precipitation Variability Over Southeastern South America. *IOP. Conf. Ser.: Earth Environ. Sci.* 9, 12007. doi: 10.1088/1755-1315/9/1/012007

Chiessi, C. M., Mulitza, S., Paul, A., Pätzold, J., Groeneveld, J., and Wefer, G. (2008). South Atlantic Interocean Exchange as the Trigger for the Bølling Warm Event. *Geology* 36, 919. doi: 10.1130/G24979A.1

Chiessi, C. M., Ulrich, S., Mulitza, S., Pätzold, J., and Wefer, G. (2007). Signature of the Brazil-Malvinas Confluence (Argentine Basin) in the Isotopic Composition of Planktonic Foraminifera From Surface Sediments. *Mar. Micropaleontol.* 64, 52–66. doi: 10.1016/j.marmicro.2007.02.002

Christen, J. A., and Pérez, S. (2009). A New Robust Statistical Model for Radiocarbon Data. *Radiocarbon* 51, 1047–1059. doi: 10.1017/S003382220003410X

Clift, P. D., Wan, S., and Blusztajn, J. (2014). Reconstructing Chemical Weathering, Physical Erosion and Monsoon Intensity Since 25Ma in the Northern South China Sea: A Review of Competing Proxies. *Earth-Sci. Rev.* 130, 86–102. doi: 10.1016/j.earscirev.2014.01.002

Coelho, C. A. S., de Oliveira, C. P., Ambrizzi, T., Reboita, M. S., Carpenedo, C. B., Campos, J. L. P. S., et al. (2016). The 2014 Southeast Brazil Austral Summer Drought: Regional Scale Mechanisms and Teleconnections. *Clim. Dyn.* 46, 3737–3752. doi: 10.1007/s00382-015-2800-1

Coumou, D., Lehmann, J., and Beckmann, J. (2015). The Weakening Summer Circulation in the Northern Hemisphere Mid-Latitudes. *Science* 348, 324–327. doi: 10.1126/science.1261768

Coumou, D., Petoukhov, V., Rahmstorf, S., Petri, S., and Schellnhuber, H. J. (2014). Quasi-Resonant Circulation Regimes and Hemispheric Synchronization of Extreme Weather in Boreal Summer. *Proc. Natl. Acad. Sci.* 111, 12331–12336. doi: 10.1073/pnas.1412797111

I. W. Croudace and R. G. Rothwell (Eds.) (2015). "Micro-XRF Studies of Sediment Cores," in *Applications of a non-Destructive Tool for the Environmental Sciences* (Dordrecht: Springer Netherlands). doi: 10.1007/978-94-017-9849-5

Cruz, F. W., Burns, S. J., Jercinovic, M., Karmann, I., Sharp, W. D., and Vuille, M. (2007). Evidence of Rainfall Variations in Southern Brazil From Trace Element Ratios (Mg/Ca and Sr/Ca) in a Late Pleistocene Stalagmite. *Geochim. Cosmochim. Acta* 71, 2250–2263. doi: 10.1016/j.gca.2007.02.005

Cruz, F. W., Burns, S. J., Karmann, I., Sharp, W. D., and Vuille, M. (2006). Reconstruction of Regional Atmospheric Circulation Features During the Late Pleistocene in Subtropical Brazil From Oxygen Isotope Composition of Speleothems. *Earth Planet. Sci. Lett.* 248, 495–507. doi: 10.1016/j.epsl.2006.06.019

Cruz, F. W., Burns, S. J., Karmann, I., Sharp, W. D., Vuille, M., Cardoso, A. O., et al. (2005). Insolation-Driven Changes in Atmospheric Circulation Over the Past 116,000 Years in Subtropical Brazil. *Nature* 434, 63–66. doi: 10.1038/nature03365

Deplazes, G., Lückge, A., Peterson, L. C., Timmermann, A., Hamann, Y., Hughen, K. A., et al. (2013). Links Between Tropical Rainfall and North Atlantic Climate During the Last Glacial Period. *Nat. Geosci.* 6, 213–217. doi: 10.1038/ngeo1712

Díaz, A., and Aceituno, P. (2003). Atmospheric Circulation Anomalies During Episodes of Enhanced and Reduced Convective Cloudiness Over Uruguay. *J. Climate* 16, 3171–3185. doi: 10.1175/1520-0442(2003)016<3171:ACADEO>2.0.CO;2

Donohoe, A., Marshall, J., Ferreira, D., and Mcgee, D. (2012). The Relationship Between ITCZ Location and Cross-Equatorial Atmospheric Heat Transport: From the Seasonal Cycle to the Last Glacial Maximum. *J. Climate* 26, 3597–3618. doi: 10.1175/JCLI-D-12-00467.1

Doyle, M. E., and Barros, V. R. (2002). Midsummer Low-Level Circulation and Precipitation in Subtropical South America and Related Sea Surface Temperature Anomalies in the South Atlantic. *J. Climate* 15, 3394–3410. doi: 10.1175/1520-0442(2002)015<3394:MLLCAP>2.0.CO;2

Elderfield, H., Vautravers, M., and Cooper, M. (2002). The Relationship Between Shell Size and Mg/Ca, Sr/Ca, δ18o, and δ13c of Species of Planktonic Foraminifera. *Geochem. Geophys. Geosyst.* 3, 1–13. doi: 10.1029/2001GC000194

Fleitmann, D., Treble, P., Cruz, F.Jr., Cole, J., and Cobb, K. (2008). "White Paper on "Speleothem-Based Climate Proxy Records"," in *PAGES/CLIVAR Paleoclimate Uncertainties Workshop Report (Citeseer)*. (International Center for Theoretical Physics, Trieste, Italy: PAGES/CLIVAR Paleoclimate Uncertainties Workshop) Available at: https://pastglobalchanges.org/sites/default/files/download/docs/meeting-products/other/2008-trieste-ws-whitepaper-speleothems.pdf (accessed on 13 June 2022).

Freeman, K. H., and Colarusso, L. A. (2001). Molecular and Isotopic Records of C4 Grassland Expansion in the Late Miocene. *Geochim. Cosmochim. Acta* 65, 1439–1454. doi: 10.1016/S0016-7037(00)00573-1

Freeman, K. H., and Pancost, R. D. (2014). ""12.15 - Biomarkers for Terrestrial Plants and Climate,"," in *Treatise on Geochemistry, 2nd ed.* Eds. H. D. Holland and K. K. Turekian (Oxford: Elsevier), 395–416. doi: 10.1016/B978-0-08-095975-7.01028-7

Friedrich, O., Schiebel, R., Wilson, P. A., Weldeab, S., Beer, C. J., Cooper, M. J., et al. (2012). Influence of Test Size, Water Depth, and Ecology on Mg/Ca, Sr/Ca, δ18o and δ13c in Nine Modern Species of Planktic Foraminifers. *Earth Planet. Sci. Lett.* 319–320, 133–145. doi: 10.1016/j.epsl.2011.12.002

Gan, M. A., Kousky, V. E., and Ropelewski, C. F. (2004). The South America Monsoon Circulation and Its Relationship to Rainfall Over West-Central Brazil. *J. Climate* 17, 47–66. doi: 10.1175/1520-0442(2004)017<0047:TSAMCA>2.0.CO;2

Gan, M. A., and Rao, V. B. (1991). Surface Cyclogenesis Over South America. *Month. Weath. Rev.* 119, 1293–1302. doi: 10.1175/1520-0493(1991)119<1293:SCOSA>2.0.CO;2

Garreaud, R. D., Vuille, M., Compagnucci, R., and Marengo, J. (2009). Present-Day South American Climate. *Palaeogeogr. Palaeoclimatol. Palaeoecol.* 281, 180–195. doi: 10.1016/j.palaeo.2007.10.032

Gelbrecht, M., Boers, N., and Kurths, J. (2018). Phase Coherence Between Precipitation in South America and Rossby Waves. *Sci. Adv.* 4, eaau3191. doi: 10.1126/sciadv.aau3191

Gonzalez, P. L. M., Goddard, L., and Greene, A. M. (2013). Twentieth-Century Summer Precipitation in South Eastern South America: Comparison of Gridded and Station Data. *Int. J. Climatol.* 33, 2923–2928. doi: 10.1002/joc.3633

Govin, A., Holzwarth, U., Heslop, D., Keeling, L. F., Zabel, M., Mulitza, S., et al. (2012). Distribution of Major Elements in Atlantic Surface Sediments (36°N–49°S): Imprint of Terrigenous Input and Continental Weathering. *Geochem. Geophys. Geosyst.* 13. doi: 10.1029/2011GC003785

Grimm, A. M. (2011). Interannual Climate Variability in South America: Impacts on Seasonal Precipitation, Extreme Events, and Possible Effects of Climate Change. *Stoch. Environ. Res. Risk Assess.* 25, 537–554. doi: 10.1007/s00477-010-0420-1

Grimm, A. M., and Ambrizzi, T. (2009). "Teleconnections Into South America From the Tropics and Extratropics on Interannual and Intraseasonal Timescales in Past Climate Variability in South America and Surrounding Regions," in *From the Last Glacial Maximum to the Holocene Developments in Paleoenvironmental Research*. Eds. F. Vimeux, F. Sylvestre and M. Khodri (Dordrecht: Springer Netherlands), 159–191. doi: 10.1007/978-90-481-2672-9_7

Grimm, A. M., and Saboia, J. P. J. (2015). Interdecadal Variability of the South American Precipitation in the Monsoon Season. *J. Climate* 28, 755–775. doi: 10.1175/JCLI-D-14-00046.1

Gu, F., Chiessi, C. M., Zonneveld, K. A. F., and Behling, H. (2018). Late Quaternary Environmental Dynamics Inferred From Marine Sediment Core GeoB6211-2 Off Southern Brazil. *Palaeogeogr. Palaeoclimatol. Palaeoecol.* 496, 48–61. doi: 10.1016/j.palaeo.2018.01.015

Gu, F., Pätzold, J., and Behling, H. (2020). Evidence of Cooling in the Tropical South Atlantic Off Southeastern Brazil During the Last 50 Kyr. *Rev. Palaeobot. Palynol.* 272, 104128. doi: 10.1016/j.revpalbo.2019.104128

Gu, F., Zonneveld, K. A. F., Chiessi, C. M., Arz, H. W., Pätzold, J., and Behling, H. (2017). Long-Term Vegetation, Climate and Ocean Dynamics Inferred From a 73,500 Years Old Marine Sediment Core (GeoB2107-3) Off Southern Brazil. *Quaternary. Sci. Rev.* 172, 55–71. doi: 10.1016/j.quascirev.2017.06.028

Heaton, T. J., Köhler, P., Butzin, M., Bard, E., Reimer, R. W., Austin, W. E. N., et al. (2020). Marine20—The Marine Radiocarbon Age Calibration Curve (0–55,000 Cal BP). *Radiocarbon* 62, 779–820. doi: 10.1017/RDC.2020.68

Herbert, T. D. (2014). "Alkenone Paleotemperature Determinations," in *Treatise on Geochemistry* (Oxford: Elsevier), 399–433. doi: 10.1016/B978-0-08-095975-7.00615-X

Hopmans, E. C., Schouten, S., and Sinninghe Damsté, J. S. (2016). The Effect of Improved Chromatography on GDGT-Based Palaeoproxies. *Org. Geochem.* 93, 1–6. doi: 10.1016/j.orggeochem.2015.12.006

Hopmans, E. C., Weijers, J. W. H., Schefuß, E., Herfort, L., Sinninghe Damsté, J. S., and Schouten, S. (2004). A Novel Proxy for Terrestrial Organic Matter in Sediments Based on Branched and Isoprenoid Tetraether Lipids. *Earth Planet. Sci. Lett.* 224, 107–116. doi: 10.1016/j.epsl.2004.05.012

Hou, A., Bahr, A., Raddatz, J., Voigt, S., Greule, M., Albuquerque, A. L., et al. (2020). Insolation and Greenhouse Gas Forcing of the South American Monsoon System Across Three Glacial-Interglacial Cycles. *Geophys. Res. Lett.* 47, e2020GL087948. doi: 10.1029/2020GL087948

Huang, Y., Bol, R., Harkness, D. D., Ineson, P., and Eglinton, G. (1996). Post-Glacial Variations in Distributions, 13C and 14C Contents of Aliphatic Hydrocarbons and Bulk Organic Matter in Three Types of British Acid Upland Soils. *Org. Geochem.* 24, 273–287. doi: 10.1016/0146-6380(96)00039-3

Huguet, C., Hopmans, E. C., Febo-Ayala, W., Thompson, D. H., Sinninghe Damsté, J. S., and Schouten, S. (2006). An Improved Method to Determine the Absolute Abundance of Glycerol Dibiphytanyl Glycerol Tetraether Lipids. *Org. Geochem.* 37, 1036–1041. doi: 10.1016/j.orggeochem.2006.05.008

Huguet, C., Smittenberg, R. H., Boer, W., Sinninghe Damsté, J. S., and Schouten, S. (2007). Twentieth Century Proxy Records of Temperature and Soil Organic Matter Input in the Drammensfjord, Southern Norway. *Org. Geochem.* 38, 1838–1849. doi: 10.1016/j.orggeochem.2007.06.015

Jaeschke, A., Wengler, M., Hefter, J., Ronge, T. A., Geibert, W., Mollenhauer, G., et al. (2017). A Biomarker Perspective on Dust, Productivity, and Sea Surface Temperature in the Pacific Sector of the Southern Ocean. *Geochim. Cosmochim. Acta* 204, 120–139. doi: 10.1016/j.gca.2017.01.045

Jones, C., and Carvalho, L. M. V. (2018). The Influence of the Atlantic Multidecadal Oscillation on the Eastern Andes Low-Level Jet and Precipitation in South America. *NPJ Clim. Atmos. Sci.* 1, 1–7. doi: 10.1038/s41612-018-0050-8

Junquas, C., Vera, C. S., Li, L., and Le Treut, H. (2013). Impact of Projected SST Changes on Summer Rainfall in Southeastern South America. *Clim. Dyn.* 40, 1569–1589. doi: 10.1007/s00382-013-1695-y

Kanner, L. C., Burns, S. J., Cheng, H., and Edwards, R. L. (2012). High-Latitude Forcing of the South American Summer Monsoon During the Last Glacial. *Science* 335, 570–573. doi: 10.1126/science.1213397

Karner, M. B., DeLong, E. F., and Karl, D. M. (2001). Archaeal Dominance in the Mesopelagic Zone of the Pacific Ocean. *Nature* 409, 507–510. doi: 10.1038/35054051

Kirst, G. J., Schneider, R. R., Müller, P. J., von Storch, I., and Wefer, G. (1999). Late Quaternary Temperature Variability in the Benguela Current System Derived From Alkenones. *Quaternary. Res.* 52, 92–103. doi: 10.1006/qres.1999.2040

Lantzsch, H., Hanebuth, T. J. J., Chiessi, C. M., Schwenk, T., and Violante, R. A. (2014). The High-Supply, Current-Dominated Continental Margin of Southeastern South America During the Late Quaternary. *Quaternary. Res.* 81, 339–354. doi: 10.1016/j.yqres.2014.01.003

Lee, S.-Y., Chiang, J. C. H., Matsumoto, K., and Tokos, K. S. (2011). Southern Ocean Wind Response to North Atlantic Cooling and the Rise in Atmospheric CO2: Modeling Perspective and Paleoceanographic Implications. *Paleoceanography* 26. doi: 10.1029/2010PA002004

Liebmann, B., Kiladis, G. N., Marengo, J., Ambrizzi, T., and Glick, J. D. (1999). Submonthly Convective Variability Over South America and the South Atlantic Convergence Zone. *J. Climate* 12, 1877–1891. doi: 10.1175/1520-0442(1999)012<1877:SCVOSA>2.0.CO;2

Liebmann, B., Kiladis, G. N., Vera, C. S., Saulo, A. C., and Carvalho, L. M. V. (2004). Subseasonal Variations of Rainfall in South America in the Vicinity of the Low-Level Jet East of the Andes and Comparison to Those in the South Atlantic Convergence Zone. *J. Climate* 17, 3829–3842. doi: 10.1175/1520-0442(2004)017<3829:SVORIS>2.0.CO;2

Lippold, J., Pöppelmeier, F., Süfke, F., Gutjahr, M., Goepfert, T. J., Blaser, P., et al. (2019). Constraining the Variability of the Atlantic Meridional Overturning Circulation During the Holocene. *Geophys. Res. Lett.* 46, 11338–11346. doi: 10.1029/2019GL084988

Liu, J., Milne, G. A., Kopp, R. E., Clark, P. U., and Shennan, I. (2016). Sea-Level Constraints on the Amplitude and Source Distribution of Meltwater Pulse 1a. *Nat. Geosci.* 9, 130–134. doi: 10.1038/ngeo2616

Maksic, J., Venancio, I. M., Shimizu, M. H., Chiessi, C. M., Piacsek, P., Sampaio, G., et al. (2022). Brazilian Biomes Distribution: Past and Future. *Palaeogeogr. Palaeoclimatol. Palaeoecol.* 585, 110717. doi: 10.1016/j.palaeo.2021.110717

Mann, M. E., Rahmstorf, S., Kornhuber, K., Steinman, B. A., Miller, S. K., and Coumou, D. (2017). Influence of Anthropogenic Climate Change on Planetary Wave Resonance and Extreme Weather Events. *Sci. Rep.* 7, 45242. doi: 10.1038/srep45242

Marengo, J. A., Soares, W. R., Saulo, C., and Nicolini, M. (2004). Climatology of the Low-Level Jet East of the Andes as Derived From the NCEP–NCAR Reanalyses: Characteristics and Temporal Variability. *J. Climate* 17, 2261–2280. doi: 10.1175/1520-0442(2004)017<2261:COTLJE>2.0.CO;2

Marengo, J. A., Torres, R. R., and Alves, L. M. (2017). Drought in Northeast Brazil—past, Present, and Future. *Theor. Appl. Climatol.* 129, 1189–1200. doi: 10.1007/s00704-016-1840-8

Masson-Delmotte, V., Zhai, P., Pirani, A., Connors, S. L., Péan, C., Berger, S., et al. (2021). "Ipc: Climate Change 2021: The Physical Science Basis," in *Contribution of Working Group I to the Sixth Assessment Report of the Intergovernmental Panel on Climate Change* (Cambridge, United Kingdom and New York, NY, USA: Cambridge University Press).

Mathias, G. L., Roud, S. C., Chiessi, C. M., Campos, M. C., Dias, B. B., Santos, T. P., et al. (2021). A Multi-Proxy Approach to Unravel Late Pleistocene Sediment Flux and Bottom Water Conditions in the Western South Atlantic Ocean. *Paleoceanogr. Paleoclimatol.* 36, e2020PA004058. doi: 10.1029/2020PA004058

McGee, D., Donohoe, A., Marshall, J., and Ferreira, D. (2014). Changes in ITCZ Location and Cross-Equatorial Heat Transport at the Last Glacial Maximum, Heinrich Stadial 1, and the Mid-Holocene. *Earth Planet. Sci. Lett.* 390, 69–79. doi: 10.1016/j.epsl.2013.12.043

McManus, J. F., Francois, R., Gherardi, J.-M., Keigwin, L. D., and Brown-Leger, S. (2004). Collapse and Rapid Resumption of Atlantic Meridional Circulation Linked to Deglacial Climate Changes. *Nature* 428, 834–837. doi: 10.1038/nature02494

Meier, K. J. F., Bahr, A., Chiessi, C. M., Albuquerque, A. L., Raddatz, J., and Friedrich, O. (2021). Role of the Tropical Atlantic for the Interhemispheric Heat Transport During the Last Deglaciation. *Paleoceanogr. Paleoclimatol.* 36, e2020PA004107. doi: 10.1029/2020PA004107

Moura, A. D., and Shukla, J. (1981). On the Dynamics of Droughts in Northeast Brazil: Observations, Theory and Numerical Experiments With a General Circulation Model. *J. Atmosph. Sci.* 38, 2653–2675. doi: 10.1175/1520-0469(1981)038<2653:OTDODI>2.0.CO;2

Mulitza, S., Chiessi, C. M., Schefuß, E., Lippold, J., Wichmann, D., Antz, B., et al. (2017). Synchronous and Proportional Deglacial Changes in Atlantic Meridional Overturning and Northeast Brazilian Precipitation: AMOC and Precipitation Over NE Brazil. *Paleoceanography* 32, 622–633. doi: 10.1002/2017PA003084

Nogués-Paegle, J., and Mo, K. C. (1997). Alternating Wet and Dry Conditions Over South America During Summer. *Month. Weath. Rev.* 125, 279–291. doi: 10.1175/1520-0493(1997)125<0279:AWADCO>2.0.CO;2

Novello, V. F., Cruz, F. W., McGlue, M. M., Wong, C. I., Ward, B. M., Vuille, M., et al. (2019). Vegetation and Environmental Changes in Tropical South America From the Last Glacial to the Holocene Documented by Multiple Cave Sediment Proxies. *Earth Planet. Sci. Lett.* 524, 115717. doi: 10.1016/j.epsl.2019.115717

Novello, V. F., Cruz, F. W., Vuille, M., Stríkis, N. M., Edwards, R. L., Cheng, H., et al. (2017). A High-Resolution History of the South American Monsoon From Last Glacial Maximum to the Holocene. *Sci. Rep.* 7, 44267. doi: 10.1038/srep44267

Pedro, J. B., Bostock, H. C., Bitz, C. M., He, F., Vandergoes, M. J., Steig, E. J., et al. (2016). The Spatial Extent and Dynamics of the Antarctic Cold Reversal. *Nat. Geosci.* 9, 51–55. doi: 10.1038/ngeo2580

Pedro, J. B., van Ommen, T. D., Rasmussen, S. O., Morgan, V. I., Chappellaz, J., Moy, A. D., et al. (2011). The Last Deglaciation: Timing the Bipolar Seesaw. *Climate Past.* 7, 671–683. doi: 10.5194/cp-7-671-2011

Peterson, R. G., and Stramma, L. (1991). Upper-Level Circulation in the South Atlantic Ocean. *Prog. Oceanogr.* 26, 1–73. doi: 10.1016/0079-6611(91)90006-8

Portilho-Ramos, R. C., Chiessi, C. M., Zhang, Y., Mulitza, S., Kucera, M., Siccha, M., et al. (2017). Coupling of Equatorial Atlantic Surface Stratification to Glacial Shifts in the Tropical Rainbelt. *Sci. Rep.* 7, 1561. doi: 10.1038/s41598-017-01629-z

Prahl, F. G., Collier, R. B., Dymond, J., Lyle, M., and Sparrow, M. A. (1993). A Biomarker Perspective on Prymnesiophyte Productivity in the Northeast Pacific Ocean. *Deep. Sea. Res. Part I.: Oceanogr. Res. Pap.* 40, 2061–2076. doi: 10.1016/0967-0637(93)90045-5

Ramos, A. M., Blamey, R. C., Algarra, I., Nieto, R., Gimeno, L., Tomé, R., et al. (2019). From Amazonia to Southern Africa: Atmospheric Moisture Transport Through Low-Level Jets and Atmospheric Rivers. *Ann. New York. Acad. Sci.* 1436, 217–230. doi: 10.1111/nyas.13960

Rao, V. B., de Lima, M. C., and Franchito, S. H. (1993). Seasonal and Interannual Variations of Rainfall Over Eastern Northeast Brazil. *J. Climate* 6, 1754–1763. doi: 10.1175/1520-0442(1993)006<1754:SAIVOR>2.0.CO;2

Ravelo, A. C., and Hillaire-Marcel, C. (2007). ""Chapter Eighteen The Use of Oxygen and Carbon Isotopes of Foraminifera in Paleoceanography,"," in *Developments in Marine Geology* (Amsterdam: Elsevier), 735–764. doi: 10.1016/S1572-5480(07)01023-8

Riedinger, N., Pfeifer, K., Kasten, S., Garming, J. F. L., Vogt, C., and Hensen, C. (2005). Diagenetic Alteration of Magnetic Signals by Anaerobic Oxidation of Methane Related to a Change in Sedimentation Rate. *Geochim. Cosmochim. Acta* 69, 4117–4126. doi: 10.1016/j.gca.2005.02.004

Rippert, N., Nürnberg, D., Raddatz, J., Maier, E., Hathorne, E., Bijma, J., et al. (2016). Constraining Foraminiferal Calcification Depths in the Western Pacific Warm Pool. *Mar. Micropaleontol.* 128, 14–27. doi: 10.1016/j.marmicro.2016.08.004

Robertson, A. W., and Mechoso, C. R. (2000). Interannual and Interdecadal Variability of the South Atlantic Convergence Zone. *Month. Weath. Rev.* 128, 2947–2957. doi: 10.1175/1520-0493(2000)128<2947:IAIVOT>2.0.CO;2

Rostek, F., Bard, E., Beaufort, L., Sonzogni, C., and Ganssen, G. (1997). Sea Surface Temperature and Productivity Records for the Past 240 Kyr in the Arabian Sea. *Deep. Sea. Res. Part II.: Top. Stud. Oceanogr.* 44, 1461–1480. doi: 10.1016/S0967-0645(97)00008-8

Salio, P., and Nicolini, M. (2006). "Seasonal Characterization on the Diurnal Cycle of Convection Frequency Over Southeastern South America Under Different Low-Jet Conditions," in *Proceedings of the 8th International Conference on Southern Hemisphere Meteorology and Oceanography.* (Foz do Iguacu, Brazil: 8th International Conference on Southern Hemisphere Meteorology and Oceanography (8ICSHMO)) 1157–1162.

Salio, P., Nicolini, M., and Saulo, A. C. (2002). Chaco Low-Level Jet Events Characterization During the Austral Summer Season. *J. Geophys. Res.: Atmosph.* 107, ACL 32–1-ACL 32-17. doi: 10.1029/2001JD001315

Saulo, A. C., Nicolini, M., and Chou, S. C. (2000). Model Characterization of the South American Low-Level Flow During the 1997–1998 Spring–Summer Season. *Climate Dyn.* 16, 867–881. doi: 10.1007/s003820000085

Saulo, A. C., Seluchi, M. E., and Nicolini, M. (2004). A Case Study of a Chaco Low-Level Jet Event. *Month. Weath. Rev.* 132, 2669–2683. doi: 10.1175/MWR2815.1

Saurral, R. I., Camilloni, I. A., and Barros, V. R. (2017). Low-Frequency Variability and Trends in Centennial Precipitation Stations in Southern South America. *Int. J. Climatol.* 37, 1774–1793. doi: 10.1002/joc.4810

Schneider, T., Bischoff, T., and Haug, G. H. (2014). Migrations and Dynamics of the Intertropical Convergence Zone. *Nature* 513, 45–53. doi: 10.1038/nature13636

Schouten, S., Hopmans, E. C., Pancost, R. D., and Damste, J. S. (2000). Widespread Occurrence of Structurally Diverse Tetraether Membrane Lipids: Evidence for the Ubiquitous Presence of Low-Temperature Relatives of Hyperthermophiles. *Proc. Natl. Acad. Sci.* 97, 14421–14426. doi: 10.1073/pnas.97.26.14421

Silva, V. B. S., and Berbery, E. H. (2006). Intense Rainfall Events Affecting the La Plata Basin. *J. Hydrometeorol.* 7, 769–787. doi: 10.1175/JHM520.1

Sinninghe Damsté, J. S., Rijpstra, W. I. C., Hopmans, E. C., Prahl, F. G., Wakeham, S. G., and Schouten, S. (2002a). Distribution of Membrane Lipids of Planktonic Crenarchaeota in the Arabian Sea. *Appl. Environ. Microbiol.* 68, 2997–3002. doi: 10.1128/AEM.68.6.2997-3002.2002

Sinninghe Damsté, J. S. S., Schouten, S., Hopmans, E. C., van Duin, A. C. T., and Geenevasen, J. A. J. (2002b). Crenarchaeol. *J. Lipid Res.* 43, 1641–1651. doi: 10.1194/jlr.M200148-JLR200

Stocker, T. F. (1998). The Seesaw Effect. *Science* 282, 61–62. doi: 10.1126/science.282.5386.61

Stramma, L., and England, M. (1999). On the Water Masses and Mean Circulation of the South Atlantic Ocean. *J. Geophys. Res.: Ocean.* 104, 20863–20883. doi: 10.1029/1999JC900139

Stríkis, N. M., Chiessi, C. M., Cruz, F. W., Vuille, M., Cheng, H., Barreto, E. A., et al. (2015). Timing and Structure of Mega-SACZ Events During Heinrich Stadial 1. *Geophys. Res. Lett.* 42, 5477–5484A. doi: 10.1002/2015GL064048

Stríkis, N. M., Cruz, F. W., Barreto, E. A. S., Naughton, F., Vuille, M., Cheng, H., et al. (2018). South American Monsoon Response to Iceberg Discharge in the North Atlantic. *Proc. Natl. Acad. Sci.* 115, 3788–3793. doi: 10.1073/pnas.1717784115

Tintelnot, M. (1995). *Transport and Deposition of Fine-Grained Sediments on the Brazilian Continental Shelf as Revealed by Clay Mineral Distribution* (Heidelberg: Univ., Diss.).

Venancio, I. M., Belem, A. L., Santos, T. P., Lessa, D. O., Albuquerque, A. L. S., Mulitza, S., et al. (2017). Calcification Depths of Planktonic Foraminifera From the Southwestern Atlantic Derived From Oxygen Isotope Analyses of Sediment Trap Material. *Mar. Micropaleontol.* 136, 37–50. doi: 10.1016/j.marmicro.2017.08.006

Venancio, I. M., Shimizu, M. H., Santos, T. P., Lessa, D. O., Portilho-Ramos, R. C., Chiessi, C. M., et al. (2020). Changes in Surface Hydrography at the Western Tropical Atlantic During the Younger Dryas. *Global Planet. Change* 184, 103047. doi: 10.1016/j.gloplacha.2019.103047

Venegas, S. A., Mysak, L. A., and Straub, D. N. (1997). Atmosphere–Ocean Coupled Variability in the South Atlantic. *J. Climate* 10, 2904–2920. doi: 10.1175/1520-0442(1997)010<2904:AOCVIT>2.0.CO;2

Vera, C., Baez, J., Douglas, M., Emmanuel, C. B., Marengo, J., Meitin, J., et al. (2006). The South American Low-Level Jet Experiment. *Bull. Am. Meteorol. Soc.* 87, 63–78. doi: 10.1175/BAMS-87-1-63

Vera, C. S., and Díaz, L. (2015). Anthropogenic Influence on Summer Precipitation Trends Over South America in CMIP5 Models. *Int. J. Climatol.* 35, 3172–3177. doi: 10.1002/joc.4153

Vera, C. S., Vigliarolo, P. K., and Berbery, E. H. (2002). Cold Season Synoptic-Scale Waves Over Subtropical South America. *Month. Weath. Rev.* 130, 684–699. doi: 10.1175/1520-0493(2002)130<0684:CSSSWO>2.0.CO;2

Wang, X., Auler, A. S., Edwards, R. L., Cheng, H., Ito, E., Wang, Y., et al. (2007). Millennial-Scale Precipitation Changes in Southern Brazil Over the Past 90,000 Years. *Geophys. Res. Lett.* 34. doi: 10.1029/2007GL031149

Warratz, G., Henrich, R., Voigt, I., Chiessi, C. M., Kuhn, G., and Lantzsch, H. (2017). Deglacial Changes in the Strength of Deep Southern Component Water and Sediment Supply at the Argentine Continental Margin. *Paleoceanography* 32, 796–812. doi: 10.1002/2016PA003079

Weaver, A. J., Saenko, O. A., Clark, P. U., and Mitrovica, J. X. (2003). Meltwater Pulse 1A From Antarctica as a Trigger of the Bølling-Allerød Warm Interval. *Science* 299, 1709–1713. doi: 10.1126/science.1081002

Weijers, J. W. H., Schouten, S., Hopmans, E. C., Geenevasen, J. A. J., David, O. R. P., Coleman, J. M., et al. (2006). Membrane Lipids of Mesophilic Anaerobic Bacteria Thriving in Peats Have Typical Archaeal Traits. *Environ. Microbiol.* 8, 648–657. doi: 10.1111/j.1462-2920.2005.00941.x

Wolf, G., Brayshaw, D. J., Klingaman, N. P., and Czaja, A. (2018). Quasi-Stationary Waves and Their Impact on European Weather and Extreme Events. *Q. J. R. Meteorol. Soc.* 144, 2431–2448. doi: 10.1002/qj.3310

Yarincik, K. M., Murray, R. W., and Peterson, L. C. (2000). Climatically Sensitive Eolian and Hemipelagic Deposition in the Cariaco Basin, Venezuela, Over the

Past 578,000 Years: Results From Al/Ti and K/Al. *Paleoceanography* 15, 210–228. doi: 10.1029/1999PA900048

Zabel, M., Schneider, R. R., Wagner, T., Adegbie, A. T., de Vries, U., and Kolonic, S. (2001). Late Quaternary Climate Changes in Central Africa as Inferred From Terrigenous Input to the Niger Fan. *Quaternary. Res.* 56, 207–217. doi: 10.1006/qres.2001.2261

Zanin, P. R., and Satyamurty, P. (2020). Hydrological Processes Interconnecting the Two Largest Watersheds of South America From Multi-Decadal to Inter-Annual Time Scales: A Critical Review. *Int. J. Climatol.* 40, 4006–4038. doi: 10.1002/joc.6442

Zhang, Y., Chiessi, C. M., Mulitza, S., Sawakuchi, A. O., Häggi, C., Zabel, M., et al. (2017). Different Precipitation Patterns Across Tropical South America During Heinrich and Dansgaard-Oeschger Stadials. *Quaternary. Sci. Rev.* 177, 1–9. doi: 10.1016/j.quascirev.2017.10.012

Zhang, R., and Delworth, T. L. (2005). Simulated Tropical Response to a Substantial Weakening of the Atlantic Thermohaline Circulation. *J. Climate* 18, 1853–1860. doi: 10.1175/JCLI3460.1

Conflict of Interest: The authors declare that the research was conducted in the absence of any commercial or financial relationships that could be construed as a potential conflict of interest.

frontiers | Frontiers in Earth Science

ORIGINAL RESEARCH
published: 15 July 2022
doi: 10.3389/feart.2022.846245

Marine Paleoproductivity From the Last Glacial Maximum to the Holocene in the Southwestern Atlantic: A Coccolithophore Assemblage and Geochemical Proxy Perspective

Guilherme A. Pedrão[1], Marcus V. Hirama[1], Mariana O. Tomazella[1], Ana Luiza S. Albuquerque[2], Cristiano M. Chiessi[3], Karen B. Costa[1] and Felipe A. L. Toledo[1]*

[1]Instituto Oceanográfico, Universidade de São Paulo, São Paulo, Brazil, [2]Programa de Geociências (Geoquímica), Universidade Federal Fluminense, Niterói, Brazil, [3]Escola de Artes e Ciências Humanas, Universidade de São Paulo, São Paulo, Brazil

OPEN ACCESS

Edited by:
Michaël Hermoso, UMR8187 Laboratoire d'océanologie et de géosciences (LOG), France

Reviewed by:
Hongrui Zhang, ETH Zürich, Switzerland
Xinquan Zhou, Tongji University, China

***Correspondence:**
Guilherme A. Pedrão
guilherme.pedrao@usp.br

Specialty section:
This article was submitted to Quaternary Science, Geomorphology and Paleoenvironment, a section of the journal Frontiers in Earth Science

Received: *30 December 2021*
Accepted: *13 June 2022*
Published: *15 July 2022*

Citation:
Pedrão GA, Hirama MV, Tomazella MO, Albuquerque ALS, Chiessi CM, Costa KB and Toledo FAL (2022) Marine Paleoproductivity From the Last Glacial Maximum to the Holocene in the Southwestern Atlantic: A Coccolithophore Assemblage and Geochemical Proxy Perspective. Front. Earth Sci. 10:846245. doi: 10.3389/feart.2022.846245

In this study, we associated the variations in coccolithophore assemblages with the variability in major elements (Fe, Ca, and Ti) from the continental slope of the western South Atlantic by investigating two marine sediment cores (GL-824 and GL-1109) to reconstruct paleoceanographic and paleoproductivity changes from the Last Glacial Maximum (LGM) to the present. Terrigenous-supply proxies (Fe/Ca and Ti/Ca) showed a very similar pattern compared with the fine-fraction sediments, higher values throughout the LGM and lower values during the Holocene. The dominant species in the coccolithophore assemblages were *Emiliania huxleyi*, *Gephyrocapsa* spp., and *Florisphaera profunda*, with these species together representing between 82 and 99% of the total assemblage. Additionally, we used three other subordinate species (*Umbellosphaera* ssp., *Rhabdosphaera* spp., and *Syracosphaera* spp.) for paleoproductivity reconstruction. The estimates of primary production using *F. profunda* and *Gephyrocapsa* spp. exhibited a similar trend, with higher productivity values during the LGM. Paleoproductivity decreased toward the Late Holocene. Analyzing these results, we observed that the oscillation of relative sea level was the process that controlled paleoproductivity, primarily by changing the position of the main flow of the Brazil Current (BC). During periods of high sea level (low Fe/Ca and Ti/Ca), the BC transported warm and oligotrophic water to the upper slope, preventing any nutrient transport from deeper layers or coastal water. In contrast, during low sea-level periods (high Fe/Ca and Ti/Ca), the offshore displacement of the BC allowed the presence of coastal water (more nutrient-rich than tropical water) and the erosion of the exposed shelf that along with a more enhanced fluvial input provided more nutrients to the photic zone, thus enhancing primary productivity.

Keywords: paleoproductivity, X-ray fluorescence, Fe/Ca, Ti/Ca, Brazil Current

1 INTRODUCTION

Studying the variations in oceanic parameters over time is extremely important to understand their influence on climate because the ocean is one of the largest carbon reservoirs on the planet. In addition, marine phytoplankton uses carbon dioxide and ocean surface sunlight to generate organic matter through photosynthesis. Therefore, oceanic productivity plays a unique role in this system because changes in the strength of the biological pump might be one of the processes controlling the CO_2 variations in glacial/interglacial time scales. In this context, the Last Glacial Maximum (LGM) is a significant contrasting period compared with the actual warming trend. During the LGM, the CO_2 concentration was about 50% lower than the present values, atmospheric temperatures were cooler, and the ice sheets cover was at its maximum, leaving the sea level at its minimum. Thus, studying this steady state of the glacial word is essential, even for assisting model studies in boundary conditions.

Marine sediments record climate and oceanographic variations by means of chemical element variations during a specific period. In this study, we employ the relative concentrations of chemical elements, titanium (Ti), iron (Fe), and calcium (Ca), to infer terrigenous sediment contributions. Ca mainly reflects marine carbonate content; Ti and Fe, on the other hand, are related to siliciclastic content (Arz et al., 1998; Jansen et al., 1998; Govin et al., 2012a). Therefore, the variations in these elements allow us to obtain paleoclimatic and paleoceanographic information about the study area. Several authors have applied Fe/Ca and Ti/Ca ratios to trace-element changes in terrigenous input of mainly fluvial origin, particularly offshore northeastern Brazil (Arz et al., 1998; Arz et al., 1999; Jaeschke et al., 2007).

The Brazilian margin is an important region to study climate changes because the Brazil Current directly influences it. This western boundary current transports warm oligotrophic water from the tropics to subtropics, affecting the local environment and productivity. Thus, marine paleoproductivity reconstructions associating changes in these processes, especially in the continental slope and shelf transition, are crucial to understanding the interplay between the continental and marine environments.

Paleoproductivity along the southeastern Brazilian upper slope has been correlated with hydrodynamic changes driven by sea-level fluctuations that during glacial periods would promote the offshore displacement of the Brazil Current leading to higher marine productivity in the continental shelf and upper slope (Mahiques et al., 2007; Nagai et al., 2010; Nagai et al., 2014; Lourenço et al., 2016; Pereira et al., 2018). Previous paleoproductivity studies for the region were based on the variation in foraminiferal assemblages (Nagai et al., 2010; Pereira et al., 2018), the evaluation of sedimentary changes (Mahiques et al., 2007), and the use of organic biomarkers (Lourenço et al., 2016). A multiproxy approach combining all these indicators is a more reliable perspective since any given proxy has limitations. For instance, the benthic foraminiferal accumulation rate (Nagai et al., 2010) and total organic carbon accumulation might be influenced by changes in preservation and sedimentation rates (Rühlemann et al., 1999; Lourenço et al., 2016). Benthic (Nagai et al., 2010) and planktonic foraminiferal assemblage analyses (Pereira et al., 2018) are excellent paleoproductivity proxies. However, they provide an indirect paleoproductivity perspective because planktonic foraminifera are mainly heterotrophic, feeding on smaller organisms, organic matter, and phytodetritus. Furthermore, coccolithophores offer us a unique and more direct vision of productivity.

Coccolithophores are unicellular microalgae belonging to the Haptophyte division and they have an inorganic envelope of calcium carbonate ($CaCO_3$) composed mainly of calcite, known as the coccosphere, formed by a series of small plates called coccoliths. Coccolithophores are among the most significant components of calcium carbonate in seafloor sediments and they are the major carbonate-shelled primary producer group with extensive geographic fossil preservation during the Quaternary (Stoll and Ziveri, 2002). As primary producers, environmental parameters control coccolithophore distribution and include nutrient availability, light, and temperature (Winter et al., 1994). These factors make this fossil group a valuable tool in paleoceanographic and paleoproductivity reconstructions (Flores et al., 1999, 2000; Toledo et al., 2007; Saavedra-Pellitero et al., 2011; Leonhardt et al., 2013; Cabarcos et al., 2014; Costa et al., 2016). Therefore, combining coccolithophore records with geochemical sedimentary proxies is ideal for understanding how climate change in past environments affected these organisms, especially in regard to paleoproductivity (Zhou et al., 2020).

The main goal of this study is to acquire information about the paleoproductivity record based on coccolithophore assemblage variations and the contribution of terrigenous supply in the marine sedimentary record. Then, we analyzed the observed variations to infer paleoenvironmental changes connected to processes that could modify the paleoclimate and paleoceanography of southeastern Brazil.

2 REGIONAL SETTING

The Brazil Current (BC) dominates surface circulation in this region (**Figure 1**). This current originates from the southern branch of the South Equatorial Current (SEC) bifurcation around 10° S latitude. The BC flows southward, carrying mainly warm and saline water flowing along the shelf-break isobaths, with possible meandering occurring close to the shelf. This current is usually 100 km wide, with its extension flowing in the upper 500 m (Silveira et al., 2000). The BC has a so-called "floor polisher effect" that regularly does not allow the deposition of thinner sediments, leading to a marine bottom composed mainly of coarse sand and carbonate gravel (Mahiques et al., 2002).

The major water masses that compose the upper water column are Coastal Water (CW), Tropical Water (TW), and South Atlantic Central Water (SACW). CW is located on the continental shelf, containing a mix of oceanic water with water from continental drainage (Campos et al., 1999). In offshore regions, the BC transports, at the surface, warm and saline water of the TW and, at the pycnocline, the colder and

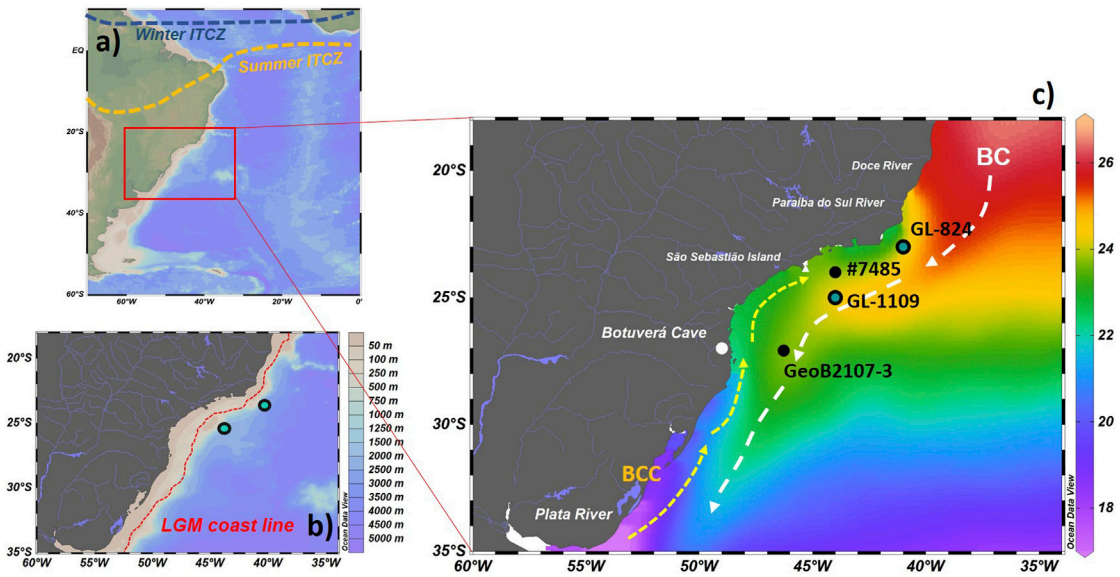

FIGURE 1 | (A) Location of the southwestern Atlantic margin. The dashed lines represent the position of the ITCZ during winter (blue) and summer (yellow). **(B)** Magnified view of the bathymetry of the study area with the approximate coastline during the LGM. **(C)** The annual mean sea surface temperature is represented °C (Locarnini et al., 2018). Blue dots mark the cores used in the present study (GL-824 and GL-1109). Cores #7485 (Lourenço et al., 2016) and GeoB2107-3 (Pereira et al., 2018) with data shown in the discussion are represented by black dots. The white dots represent the central geographic locations cited in this work. The dashed white arrows represent the main flow of the Brazil Current, while the yellow arrows show the main flow of the Brazilian Coastal Current.

nutrient-rich SACW (Silveira et al., 2000). In the deeper portions of the water column, there are movements of two relevant deep water masses: the Deep Western Boundary Current transports the North Atlantic Deep Water (NADW), which flows southward, and the Antarctic Bottom Water (AABW), which flows northward as a sluggish flow above the ocean floor (Stramma and England, 1999; Silveira et al., 2020). According to Vianna et al. (1998), changes in relative sea level (RSL) are the primary cause of oceanic circulation variations during the Quaternary.

The main controlling forces of modern sedimentary processes on the southeastern Brazilian margin are the BC system flow variations and the dynamics between the continental shelf and oceanic water masses (Mahiques et al., 2004). There is a division in sedimentation on the continental shelf into two distinct zones separated by São Sebastião Island. In the north, meandering of the BC, which promotes mixing between terrigenous and pelagic sedimentary fractions, is the primary control of sedimentation. On the other hand, the southern sector is characterized mainly by marine sedimentation. Infiltration of the Plata River plume directly influences this region because there is a lack of a local fluvial supply (Mahiques et al., 2004). This process transports more terrigenous sediments and nutrients to the surface water, increasing oceanic productivity (Ciotti et al., 1995; Pivel et al., 2011; Nagai et al., 2014; Bícego et al., 2021). The fluvial supply is a vital sediment source in the northern section of the study area. The main rivers that conduct terrigenous sediments in this area are the Doce River and Paraíba do Sul River (Behling et al., 2002). At glacial and interglacial scales, sea level variations and climate conditions on the adjacent continent, particularly precipitation, are factors that may influence the terrigenous sediment supply to the continental slope (Mahiques et al., 2004; Nagai et al., 2014; Razik et al., 2015; Zhou et al., 2020).

The southwestern Atlantic is an oligotrophic zone (Rühlemann et al., 1999) where nutrient concentration is the key factor limiting primary productivity. Local fluvial discharge (Brandini et al., 2014) and upwelling associated with cyclonic meanders of the BC occur throughout the entire year (Campos et al., 1995; Campos et al., 2000), increasing photic-zone nutrient concentration. In a seasonal pattern, wind-driven coastal upwelling peaks during austral summer and enhances shelf-break upwelling that occurs due to the meanders of the BC, causing higher rates of primary productivity (Campos et al., 2000; Brandini et al., 2014). During winter, the Plata River plume transports more nutrients to the study area under favorable wind conditions (Campos et al., 1999; Piola et al., 2005; Pivel et al., 2011). Therefore, the interplay between the dynamics of the BC and the continental source nutrients characterizes the primary productivity of the region.

The South American Summer Monsoon (SASM) controls precipitation in the study region (Vera et al., 2006), which varies according to its intensity and expansion. Therefore, precipitation has a strong seasonal pattern, with most precipitation occurring during summer. In this period, SASM circulation transports moisture from the Atlantic Ocean to the Amazon Basin, feeding the low-level jets of the Andes and transporting this moisture to southeastern Brazil (Cheng et al., 2013), entering the South Atlantic Convergence Zone (SACZ). Throughout Quaternary glacial–interglacial climate change, during glacial periods, in contrast to interglacial periods, there was a reinforcement of the SASM, especially during the Last Glacial Maximum (LGM), transporting more humidity to

TABLE 1 | Radiocarbon ages based on planktonic foraminifera from the GL-824 core. Both white (w) and pink (p) *G. ruber* morphotypes were used.

Depth (cm)	Foraminifera species	Age ^{14}C (years BP)
0	*G. ruber*	200 ± 50
205	*G. ruber*	1960 ± 30
400	*G. ruber*	3,750 ± 35
620	*G. ruber*	6,080 ± 45
820	*G. ruber*	8,140 ± 50
947	*G. ruber*	9,780 ± 60
1,020	*G. ruber*	10,400 ± 60
1,220	*G. ruber*	13,050 ± 85
1,420	*G. ruber* and *G. sacculifer*	13,100 ± 70
1,620	*G. ruber* and *G. sacculifer*	15,650 ± 110

southern Brazil (Sylvestre, 2009). The SACZ is a zone oriented in a northwest-southeast direction characterized by converging winds, considerable cloud cover, and heavy precipitation (Liebmann et al., 2004; Carvalho et al., 2002, 2004), with most extreme events of precipitation over southeastern Brazil occurring during summer being associated with intensification of the SACZ (Carvalho et al., 2002).

The position of the Intertropical Convergence Zone (ITCZ) directly influences the intensity of the SACZ and is the zone near the equator where the northeast and southeast trade winds converge, forming a band of clouds. The position of the ITCZ has a seasonal variation. It migrates toward the hemisphere that is warmer relative to the other (Deplazes et al., 2013; Schneider et al., 2014). During austral summer, the ITCZ is in its southernmost position, and in winter, it migrates to its northerly position (**Figure 1**).

3 MATERIALS AND METHODS

3.1 Sediment Core Recovery

Two marine sediment cores, GL-824 and GL-1109, were collected on the Brazilian continental margin; more precisely, on the continental slope, GL-824 core was collected at a water depth of 532 m at 23°29′17,87″ S and 41°08′02,99″ W, while GL-1109 was located at a water depth of 848 m at 25°11′00″ S and 44°43′30″ W (**Figure 1**). Sediment core GL-824 was collected during an expedition with the Fugro Explorer Vessel. A piston corer was used to recover 2004 cm of sediment. This work analyzes 100 samples at an average 20 cm resolution. According to the lithology, the first 1,500 cm is composed of olive-gray carbonate-rich mud (18–30% $CaCO_3$), and from 1,550 to 2004 cm, the sediment is composed of dark gray carbonate-poor mud (5–18% $CaCO_3$). GL-1109 had a total recovery of 1,367 cm of marine sediment. This work analyzes the section from 515 cm to the top of the core, sampling approximately every 5 cm, with 95 samples investigated. According to the lithology, the core comprises dark gray carbonate-poor mud (5–18% $CaCO_3$).

3.2 Age Model

The age model of both cores was constructed based on radiocarbon dating conducted mainly on the planktonic foraminifer *Globigerinoides ruber* (white and pink morphotypes). In the absence of *G. ruber*, we collected other species, such as *Globigerinoides sacculifer* (>150 μm size) and *Globigerina bulloides* (**Table 1**), with all of these species exhibiting a good preservation state and no overgrowth or dissolution effects. For the GL-824 core, 11 samples were selected and analyzed at the National Ocean Science Accelerator Mass Spectrometer Facility (NOSAMS), Woods Hole Oceanographic Institution (WHOI) (**Table 1**). For GL-1109, 19 samples were analyzed at the Beta Analytic Radiocarbon Dating Laboratory, Miami, United States (**Table 2**).

To transform the radiocarbon ages into calibrated ages, we used the calibration curve Marine13 (Reimer et al., 2013) and a marine reservoir age of 370 ± 19 years (Alves et al., 2015) with Bacon 2.2 software (Blaauw and Christen, 2011). This software constructs the age model using Bayesian statistics and estimates mean ages and 95% error margins based on 10,000 downcore age-depth realizations at a 1 cm resolution. To establish the ages, we applied the default parameters, except for the calibration curve, in which we selected Marine13 and acc. shape (set to 0.5).

3.3 Sample Preparation and Fine Fraction Quantification

The bulk samples were wet sieved through a 63 μm mesh. The coarse fraction (>63 μm) was dried on the mesh in an oven at 50°C and allowed to cool before weighing. The fine fraction (<63 μm) was collected in beakers where it was allowed to settle. The water was removed, and the samples were dried in an oven at 50°C and allowed to cool before weighing. To calculate the fine fraction (FF) percentage in every sample, we used the difference in weight between the coarse fraction and the total dried weight of the sample. The FF was used for all the procedures and analysis described below, except for GL-1109 elementary composition measurements.

3.4 Calcium Carbonate

The carbonate content was measured by the difference in weight before and after acidification with HCl. Approximately 1.0 g of dry sediment was weighed and acidified with 10% HCl. The sample was kept overnight, and the supernatant was discarded. Then, distilled water was added (3 times) to the sample for acid removal. Finally, the precipitated sample was kept at 60°C in an oven overnight and weighed again. The difference in weight before (Weight 1) and after reaction with HCl (Weight 2) provides an approximate estimate of the carbonate content %: $CaCO_3$ = [(Weight 1 − Weight 2) × 100)/Weight 1].

3.5 X-Ray Fluorescence

The samples were powdered and homogenized with an agate mortar to calculate the elementary ratios in GL-824 core. Then, metals (Ti, Fe, and Ca) were analyzed in a bench equipment model BTX-II to perform X-ray fluorescence measurements in the Laboratory of Geoprocessing (LabGEO-USP), following the technique described in Pedrão et al. (2021). Briefly, the technique consists of analyzing the metals in approximately 1 cm^3 of sediment (<63 μm) per sample that was previously hand-

TABLE 2 | Radiocarbon ages based on planktonic foraminifera from the GL-1109 core. Both white (w) and pink (p) *G. ruber* morphotypes were used.

Depth (cm)	Foraminifera species	Age ^{14}C (years BP)	
1	*G. ruber* (w)	120 ± 30	
17	*G. ruber* (w)	970 ± 30	
31	*G. ruber* (w)	2,360 ± 30	
53	*G. ruber* (w)	3,980 ± 30	
75	*G. ruber* (w)	6,200 ± 30	
101	*G. ruber* (w)	8,790 ± 30	
143	*G. ruber* (w+p), *G. sacculifer,* and *G. bulloides*	12,840 ± 50	
291	*G. ruber* (w+p), *G. sacculifer,* and *G. bulloides*	16,170 ± 60	
331	*G. ruber* (w+p), *G. sacculifer,* and *G. bulloides*	16,310 ± 60	
365	*G. ruber* (w+p)	16,690 ± 50	
463	*G. ruber* (w+p), *G. sacculifer,* and *G. bulloides*	17,810 ± 80	
507	*G. ruber* (w+p), *G. sacculifer,* and *G. bulloides*	19,420 ± 70	Age reversal
563	*G. ruber* (w+p), *G. sacculifer,* and *G. bulloides*	18,820 ± 60	
597	*G. ruber* (w+p), *G. sacculifer,* and *G. bulloides*	20,470 ± 80	
663	*G. ruber* (w+p), *G. sacculifer,* and *G. bulloides*	22,350 ± 80	
793	*G. ruber* (w)	28,300 ± 140	
825	*G. ruber* (w)	28,970 ± 150	
857	*G. ruber* (w)	31,280 ± 190	
938	*G. ruber* (w)	36,950 ± 330	
967	*G. ruber* (w)	40,730 ± 500	

ground in a jade mortar to be used in the XRF analysis. We selected this size fraction due to the more negligible interference in the intensity values measured by the device. In GL-1109 core, we analyzed the elementary composition of the sediments by conducting an XRF analysis using an XRF Core–Scanner II (AVAATECH Serial No. 2) at MARUM, University of Bremen, to estimate the elementary ratios throughout the core.

The geochemical data were presented in the logarithmic form of elemental ratios since ratios are insensitive to dilution effects (Wetje and Tjallingii, 2008; Govin et al., 2012b), and the logarithmic form accounts for the lack of symmetry between ratios (Govin et al., 2012b).

3.6 Coccolithophore Assemblages

The qualitative technique described by Antunes (1997) and Toledo (2000) was utilized to prepare samples to identify and quantify the coccolithophore assemblages in terms of percentages. Counts were made under a polarized light microscope at a 1,000X magnification. A minimum of 300 coccoliths, in addition to *Florisphaera profunda* coccoliths, were counted in each sample, assuring that all species with relative abundances greater than 3% were well represented (Dennison and Hay, 1967; Roth, 1994; Fatela and Taborda, 2002). *Florisphaera profunda* was excluded from the 300 coccoliths minimum counts because it may dominate the assemblages and mask the signal of other species. However, the total number of coccolithophore species, including *F. profunda*, was used for calculating the relative abundances of coccoliths.

Variations between the relative abundance of the main species in the upper photic zone (*Emiliania huxleyi* and *Gephyrocapsa* spp.) and the lower photic zone (*F. profunda*) can be used as indicators of primary productivity (e.g., Beaufort et al., 1997, 2001; Flores et al., 2000). *Florisphaera profunda* is an habitant in the lower photic zone (LPZ) (Okada and Honjo, 1973) and is commonly used as a paleoproductivity proxy (Beaufort et al., 2001; Hernandez-Almeida et al., 2019), mainly because this species is an indicator of the thermocline/nutricline position (Molfino and McIntyre, 1990; Flores et al., 2000). When more nutrients are available in the upper photic zone (UPZ), opportunistic species such as *Gephyrocapsa* spp. and *E. huxleyi* increase in abundance, while *F. profunda* decreases in relative abundance. In contrast, when the nutricline is greater, more nutrients are available for species in the LPZ, such as *F. profunda*, raising their relative abundance compared to the UPZ dwellers. Therefore, Beaufort et al. (1997) established an equation to estimate primary productivity (EPP, grams of carbon ((gC) m^{-2} $year^{-1}$)) based on the relative abundance of *F. profunda* (Fp, %) [EPP = 617 − (279 log(Fp + 3))].

To evaluate the effect of dissolution in our record, we applied the CEX' index (Boeckel and Baumann, 2004), which compares the relative abundances of the small and more sensitive species, *Gephyrocapsa* spp. and *E. huxleyi*, to the more resistant large species, such as *Calcidiscus leptoporus*. The index varies between 1 and 0, with values close to 1 indicating no dissolution and values below 0.6 indicating a more substantial dissolution influence.

We applied the Pearson linear correlation index (r) using Past 3.05 software (Hammer et al., 2001) in both cores separately to investigate the associations among sedimentology and geochemical and micropaleontological proxies.

4 RESULTS

4.1 Age Model

The results of 11 radiocarbon ages for GL-824 show continuous sedimentation (**Figure 2A**), which indicates that no hiatus occurred in the core. The core covers an age range of approximately 22 kyrs BP with an average accumulation rate of approximately 97 cm/kyrs (**Figure 2A**), with the lowest sedimentation rate occurring in the Early Holocene (~70 cm/

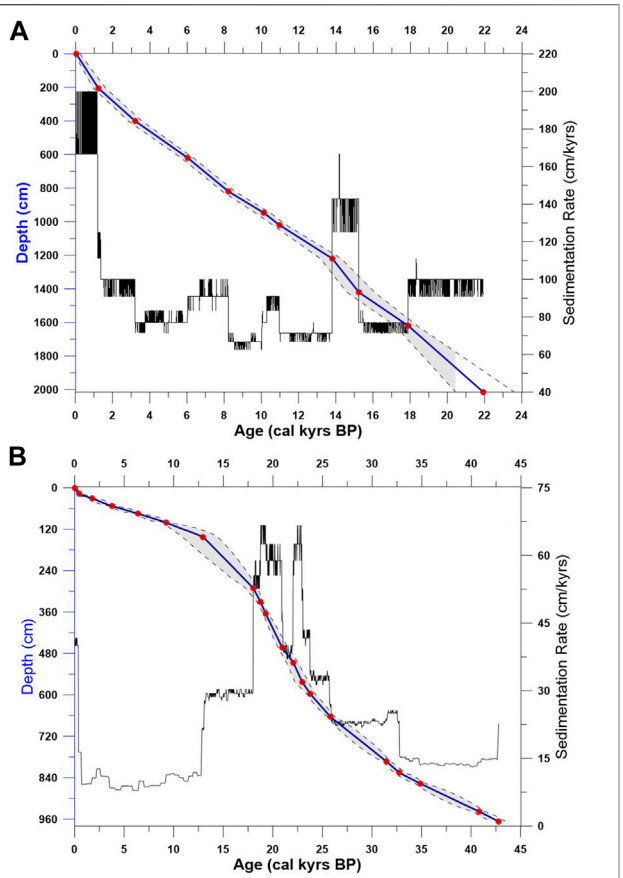

FIGURE 2 | Age model (solid line) and sedimentation rates for the **(A)** GL-824 and **(B)** GL-1109 cores. The red dots represent the calibrated radiocarbon ages, while the dashed lines are the upper and lower confidence intervals. We applied Bacon 2.2 software (Blaauw and Christen, 2011) to build this age model.

kyrs) and the highest occurring at its top (~180 cm/kyrs) and between 14 and 15 kyrs BP (~150 cm/kyrs).

Even though we observed an age reversion in GL-1109 core (**Table 2**), using Bacon 2.2, we constructed an age model that represents continuous sedimentation with no hiatus (**Figure 2B**). The core comprises the last 45 kyrs BP. However, this study only analyzed the top 550 cm of the core at a resolution of 2–5 cm between samples, comprising the last 23 kyrs BP. This section had a medium sedimentation rate of 38 cm/kyrs, with significant sedimentation occurring in the LGM period between 25 kyrs BP and 19 kyrs BP (65 cm/kyrs). The sedimentation rate then decreased until 12 kyrs BP, reaching the lowest value, 8 cm/kyrs (**Figure 2B**).

4.2 Sedimentary Record

The proxies for terrigenous sediment supply in both cores show a similar distribution to the FF content (**Figures 3A–F**). Higher values of terrigenous supply and FF percentage were recorded at the bottom of the cores during the glacial period, with almost all samples having 100% FF and top metal content. In Core GL-824, a marked decrease was recorded at approximately 15 kyrs BP,

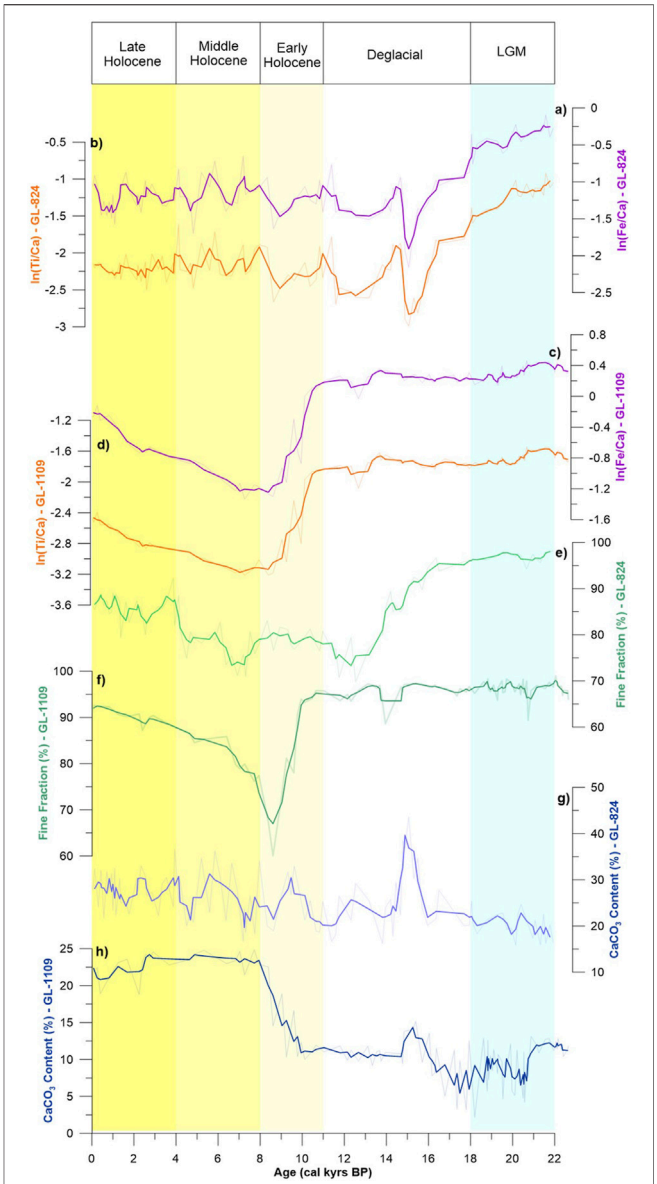

FIGURE 3 | Results of the sedimentary record from GL-824 and GL-1109 cores. Thick lines represent a weighted average of 3 points, and the background lines are the original data. **(A)** ln (Fe/Ca) and **(B)** ln (Ti/Ca) results for GL-824. **(C)** ln (Fe/Ca) and **(D)** ln (Ti/Ca) results for GL-1109. **(E)** Percentage of fine fraction present in the GL-824 core. **(F)** Percentage of fine fraction present in the GL-1109 core. **(G)** Calcium carbonate content throughout the GL-824 core. **(H)** Calcium carbonate content throughout the GL-1109 core.

with the proxies reaching their minimum values. However, in GL-1109 core, it occurred at the beginning of the Holocene (~11 kyrs BP).

The $CaCO_3$ content was the most divergent parameter between the cores, with higher mean values in GL-824 (25%) than in GL-1109 (13%). The $CaCO_3$ content presented the same general trend between the cores, with lower values in the late glacial period and a rapid rise during the transition between the deglacial period and the early Holocene (16–8 kyrs BP), reaching

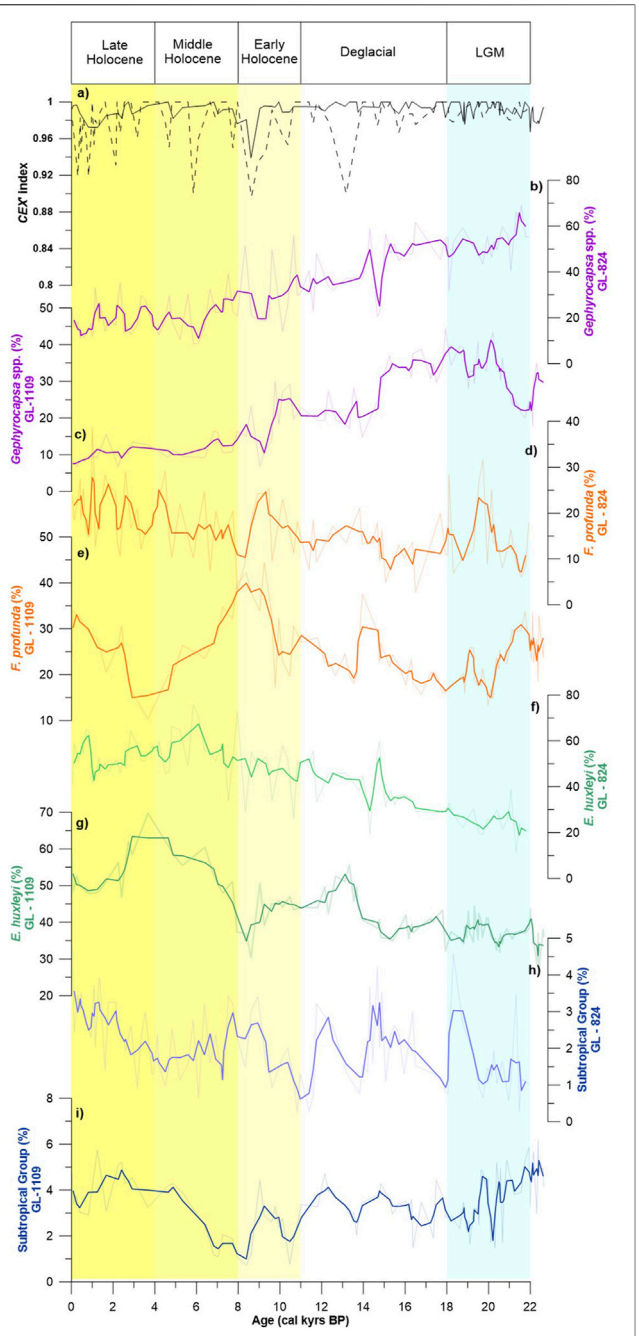

FIGURE 4 | Results of the coccolithophore assemblages from GL-824 and GL-1109 cores. Thick lines represent a weighted average of 3 points, and the background lines are the original data. **(A)** CEX′ index for both cores. The solid line represents GL-824 core, and the dashed line represents GL-1109 core. **(B)** Relative abundance of *Gephyrocapsa* spp. in the GL-824 core. **(C)** Relative abundance of *Gephyrocapsa* spp. in the GL-1109 core. **(D)** Relative abundance of *F. profunda* in the GL-824 core. **(E)** Relative abundance of *F. profunda* in the GL-1109 core. **(F)** Relative abundance of *E. huxleyi* in the GL-824 core. **(G)** Relative abundance of *E. huxleyi* in the GL-1109 core. **(H)** Relative abundance of the subtropical group in the GL-824 core. **(I)** Relative abundance of the subtropical group in the GL-1109 core.

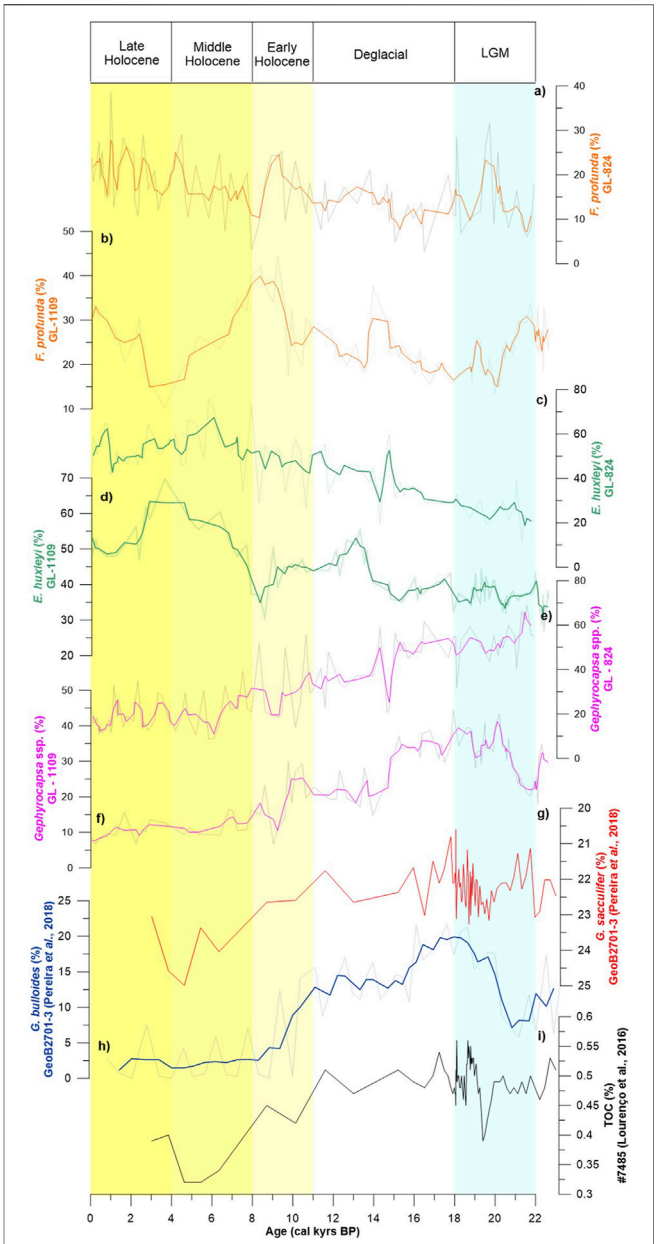

FIGURE 5 | Paleoproductivity proxy results. Thick lines represent a weighted average of 3 points, and the background lines are the original data. **(A)** *F. profunda* relative abundance for the GL-824 core. **(B)** *F. profunda* relative abundance for the GL-1109 core. **(C)** Relative abundance of *E. huxleyi* in the GL-824 core. **(D)** Relative abundance of *E. huxleyi* in the GL-1109 core. **(E)** *Gephyrocapsa* spp. relative abundance for the GL-824 core. **(F)** *Gephyrocapsa* spp. relative abundance for the GL-1109 core. **(G)** Relative abundance of the oligotrophic planktonic foraminifera *G. sacculifer* (Pereira et al., 2018). **(H)** Relative abundance of *G. bulloides*, an upwelling proxy (Pereira et al., 2018). **(I)** TOC content (Lourenço et al., 2016).

higher values toward the mid-Holocene (**Figures 3G,H**). This trend was opposite to the distribution observed in the elementary ratios and FF (**Figures 3E–H**).

4.3 Coccolithophore Assemblages

Coccolithophore assemblage variations (**Figure 4**) had the same general variations in both cores. The dominant species were *E. huxley*, *Gephyrocapsa* spp., and *F. profunda*, representing 82–99% of the total assemblage in GL-824 and 85–97% in GL-1109. The mean relative abundances for the dominant species were 43–42% for *E. huxleyi*, 33–25% for *Gephyrocapsa* spp., and 16–24% for *F. profunda* (first valor for GL-824 and second for GL-1109). *Gephyrocapsa oceanica* (mean relative abundance = 15%) was the most common species in *Gephyrocapsa* (**Figures 4B,C**). The CEX' index had high values in the entire core (**Figure 4A**), indicating that dissolution was not a problem in regard to paleoenvironmental interpretations. The relative abundances of *F. profunda* and *E. huxleyi* had a similar trend. The lowest values occurred during the glacial period, with a gradual increase toward the deglacial period, reaching higher values during the Holocene (**Figures 4D–G**). In contrast, *Gephyrocapsa* spp. had an opposite distribution, with higher values during the glacial period and lower values in the Holocene (**Figures 4B,C**).

Discosphaera tubifera, *Rhabdosphaera* spp., *Syracosphaera* spp., and *Umbellosphaera* spp. composed a subtropical group with a tendency toward warmer and oligotrophic water conditions, as suggested by Boeckel et al. (2006). The relative abundance of this group showed a similar trend as that of *F. profunda* (**Figures 4H, 1**). However, low relative abundances appeared, with a mean value of 2% in GL-824 and 3.5% in GL-1109.

The N ratio proposed by Flores et al. (2000) compares the relative abundances of LPZ species (*F. profunda*) with those of the UPZ (*Gephyrocapsa* spp. and *E. huxleyi*); thus, this ratio can be used as an indicator of the nutricline position and, therefore, of primary productivity. The N ratio and EPP presented a similar general pattern in the cores (**Supplementary Figure S1**), with higher paleoproductivity values at the bottom of the core during the glacial period. The values rapidly decreased at approximately 15 kyrs BP until these proxies reached their minimum values at ~ 9 kyrs BP. However, a maximum value at approximately 4 kyrs BP, which was the transition between the Middle and Late Holocene, was observed in Core GL-1109 , in which *E. huxleyi* was the dominant species, accounting for approximately 70% of the total assemblage (**Figure 4G**).

Comparing these proxies with previous studies (**Figure 5**), we can observe that variation in the *F. profunda* percentage showed a similar trend to that for *G. sacculifer,* an oligotrophic foraminiferal species (Pereira et al., 2018), and an opposite distribution pattern to *G. bulloides* relative abundance (Pereira et al., 2018) and TOC content (Lourenço et al., 2016), demonstrating similar observations between the studies.

5 DISCUSSION

5.1 Sedimentary Processes as a Function of Sea-Level Variations

5.1.1 Similarity Among XRF, $CaCO_3$, and FF

According to the sedimentary record, it is possible to distinguish three different periods in both cores: the glacial period with a higher terrigenous supply, a brief transition period, and the Holocene with a lower terrigenous supply.

The FF positively correlated with the terrigenous sediment supply proxies (**Figures 3A–F**; **Tables 3**, **4**). The highest percentage of the FF occurred when sea level dropped. In contrast, the carbonate content had an opposite correlation and distribution with the FF (**Figures 3E–H**; **Tables 3**, **4**). Through these distributions, we can infer that the abundance of coccoliths did not cause changes in the FF. The primary process involved in these changes in the FF was the contribution of external silt–clay minerals associated with terrigenous supply, as observed by Costa et al. (2016).

The elementary ratio data show that the terrigenous sediment supply was maximal during the LGM (**Figures 3A–D**). This more significant terrigenous sediment supply possibly caused a dilution in the carbonate content values because they were minimal despite the higher paleoproductivity (**Figures 6C–H**), which was also observed by Arz et al. (1998) and Mahiques et al. (2007). After the end of the LGM, at approximately 19 kyrs BP, the terrigenous supply started to decline in the same proportion as the FF. An increase in the coarse fraction could indicate more marine influence ($CaCO_3$) or an increase in primary productivity because foraminiferal tests were the main component of this fraction. Both processes were observed in this period (**Figures 3C–H**), suggesting that deglaciation was a transition period of abrupt changes in the environment and deposition of sediments.

During the Holocene, the variability in terrigenous supply was stable compared to the differences between glacial and interglacial periods (**Figures 3A–D**). The stability tendency of carbonate variation (**Figures 3G,H**), even with variable biological productivity (**Figures 6E–H**), particularly in CoreGL-1109, also indicates that terrigenous sediments diluted the carbonate content.

The processes behind these observations may have been the variations in sea level and/or precipitation rates, which would have interfered with the riverine input and consequently in terrigenous supply and primary productivity, allowing a higher concentration of coarse fraction organisms. Analyzing the paleoproductivity record, we observed less productivity during this period (**Figures 6E–H**); therefore, we infer that a combined effect of sea level and precipitation was probably the main reason for changes in terrigenous input, FF and $CaCO_3$ content.

5.1.2 Main Sedimentary Process Drivers

The proxies for terrigenous sediment supply may vary mainly due to three processes. The first is relative sea-level variation. Its rise would make the transport of sediments to the upper continental slope more complicated since it would increase the distance between the core area and the sediment source, covering the shelf (Mahiques et al., 2004; Nagai et al., 2010). The second might be variation in fluvial discharge. In other words, with more precipitation, a higher terrigenous sediment supply would lead to higher values of these proxies during humid periods (Behling et al., 2000; Costa et al., 2016). The third might be percentage dilution of the continental material due to mixing with biogenic marine particles/material.

TABLE 3 | Correlation matrix (Pearson linear correlation coefficient, r) between all variables estimated in this study for the GL-824 core. Bold values correspond to a significant correlation at the 0.05 level.

	ln Ti/Ca	ln Fe/Ca	% $CaCO_3$	% FF	*E. huxleyi*	*F. profunda*	*Gephyrocapsa* spp.	Subtropical	N ratio	EPP
ln Ti/Ca	—	0.942	**-0.477**	**0.627**	**–0.522**	–0.133	**0.486**	**–0.266**	0.132	0.160
ln Fe/Ca	**0.942**	—	**-0.503**	**0.548**	**–0.484**	–0.126	**0.459**	**–0.277**	0.128	0.141
% $CaCO_3$	**–0.477**	**–0.503**	—	–0.172	**0.430**	–0.053	**-0.357**	**0.210**	0.043	0.077
% FF	**0.627**	**0.548**	**–0.172**	—	**-0.632**	–0.129	**0.551**	–0.085	0.114	0.166
E. huxleyi	**–0.522**	**–0.484**	**0.430**	**–0.632**	—	**0.217**	**-0.898**	0.152	**–0.203**	**–0.252**
F. profunda	–0.133	–0.126	–0.053	–0.129	0.217	—	**-0.601**	0.152	**–0.998**	**–0.971**
Gephyrocapsa spp.	**0.486**	**0.459**	**–0.357**	**0.551**	**–0.898**	**–0.601**	—	**–0.274**	**0.597**	**0.615**
Subtropical	**–0.266**	**–0.277**	**0.210**	–0.085	0.152	0.152	–0.274	—	**–0.188**	–0.158
N ratio	0.132	0.128	0.043	0.114	**–0.203**	**–0.998**	**0.597**	–0.188	—	**0.966**
EPP	0.160	0.141	0.077	0.166	–0.252	**–0.971**	**0.615**	–0.158	**0.966**	—

TABLE 4 | Correlation matrix (Pearson linear correlation coefficient, r) between all variables estimated in this study for the GL-1109 core. Bold values correspond to a significant correlation at the 0.05 level.

	ln Ti/Ca	ln Fe/Ca	% $CaCO_3$	% FF	*E. huxleyi*	*F. profunda*	*Gephyrocapsa* spp.	Subtropical	N ratio	EPP
ln Ti/Ca	—	**0.985**	**–0.798**	**0.809**	**–0.571**	**–0.359**	**0.708**	**0.183**	**0.359**	**0.313**
ln Fe/Ca	**0.985**	—	**–0.738**	**0.842**	**–0.519**	**–0.377**	**0.665**	**0.229**	**0.372**	**0.328**
% $CaCO_3$	**–0.798**	**–0.738**	—	**–0.564**	**0.551**	**0.307**	**–0.701**	–0.009	**–0.328**	**–0.295**
% FF	**0.809**	**0.842**	**–0.564**	—	**–0.308**	**–0.504**	**0.573**	0.255	**0.498**	**0.448**
E. huxleyi	**–0.571**	**–0.519**	**0.551**	**–0.308**	—	–0.137	**–0.736**	0.052	0.130	0.147
F. profunda	**–0.359**	**–0.377**	**0.307**	**–0.504**	–0.137	—	**–0.534**	–0.136	**–0.996**	**–0.989**
Gephyrocapsa spp.	**0.708**	**0.665**	**–0.701**	**0.573**	**–0.736**	**–0.534**	—	–0.094	**0.557**	**0.523**
Subtropical	**0.183**	**0.229**	–0.009	0.255	0.052	–0.136	–0.094	—	0.076	0.114
N ratio	**0.359**	**0.372**	**–0.328**	**0.498**	0.130	**–0.996**	**0.557**	0.076	—	**0.987**
EPP	**0.313**	**0.328**	**–0.295**	**0.448**	0.147	**–0.989**	**0.523**	0.114	**0.987**	—

The terrigenous supply had maximum values during the LGM when sea level reached its lowest position (**Figures 6C,D,I**). This indicates that a major continental shelf area was exposed, resulting in a more extensive area for weathering and a smaller distance between the sediment source and the study sites. Therefore, the continental slope was more likely to receive terrigenous sediments. Thus, the lower relative sea level contributed to more intense deposition of terrigenous and FF sediments (**Figures 3E,F** and **Figure 6I**). This could also have been connected to the offshore displacement of the BC to deeper regions during the LGM (Viana et al., 1998; Mahiques et al., 2007; Kowsmann et al., 2015), which would have lowered the local hydrodynamics and allowed or enhanced the deposition of FF sediments.

There was a stable sea level during the Holocene. Nevertheless, the input of terrigenous sediments showed a slight increase. This was linked to an increase in rainfall that occurred during this period (**Figures 6C,D,I,J**), suggesting that precipitation was directly responsible for these oscillations during this specific period.

Wang et al. (2007) analyzed precipitation during the study period based on $\delta^{18}O$ data from speleothems. These data showed variability similar to the variation in the FF (**Figures 3E,F** and **Figure 6J**), especially in GL-824 core, probably because the primary source of fine sediments was fluvial runoff, which was higher when precipitation rates were higher. According to Behling et al. (2000), when there are periods with more precipitation, there are increases in the Fe/Ca and Ti/Ca ratio values. This was also observed in our study (**Figures 6C,D,J**). In other words, precipitation can be a controlling factor in the terrigenous supply. During the LGM, humidity was higher in South America than during the Holocene (Cruz et al., 2005; Wang et al., 2007; Sylvestre, 2009); therefore, fluvial runoff would have been higher thus transporting more terrigenous sediments to the continental slope. According to Jennerjahn et al. (2004) and Jaeschke et al. (2007), this increase in precipitation was related to the displacement of the ITCZ to the south and an increase in the intensity of winds from the southeast during colder periods, also increasing the humidity on the continent.

Comparing the precipitation oscillation to the paleoproductivity and terrigenous supply proxies, we observed that the general trend was similar between these indicators (**Figures 6C–J**). However, when precipitation had higher peaks without substantial sea-level variation, we did not observe significant changes in any other proxies, highlighting that rainfall may have influenced terrigenous supply and FF records, but on a smaller scale. The moisture source can also influence the $\delta^{18}O$ speleothems record and not only the precipitation intensity (Lee et al., 2009). Furthermore, there are differences between LGM rainfall reconstructed by nonisotope proxies and interpretations of speleothem records

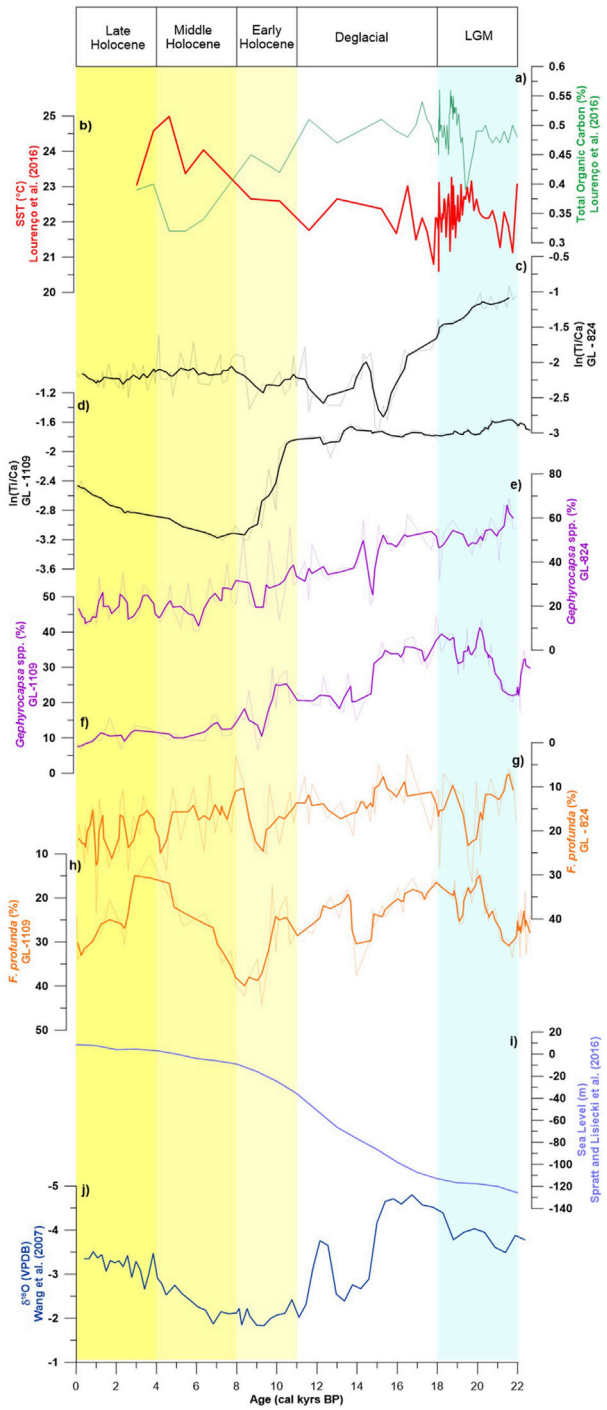

FIGURE 6 | Comparison of the results obtained in GL-824 and GL-1109 with those of other studies. Thick lines represent a weighted average of 3 points, and the background lines are the original data. **(A)** Total organic carbon and **(B)** sea surface temperature calculated based on alkenones (Lourenço et al., 2016). Measured ln (Ti/Ca) for **(C)** GL-824 and **(D)** GL-1109. The relative abundance of eutrophic *Gephyrocapsa* spp. for **(E)** GL-824 and **(F)** GL-1109. Relative abundance of the oligotrophic proxy *F. profunda* for **(G)** GL-824 and **(H)** GL-1109. **(I)** Sea-level reconstruction (Spratt and Lisiecki, 2016). **(H)** Oxygen isotope composition of speleothems in the Botuverá cave (Wang et al., 2007).

(Sylvestre, 2009; Berman et al., 2016). Thus, we interpreted the maximum terrigenous supply to the upper slope during the glacial period to have been primarily due to the effects of lower sea level. Besides, the possible rise in precipitation could also be improving the terrigenous supply.

Several researchers have previously observed the influence of Heinrich events in the Southern Hemisphere in the tropical region of the South Atlantic (Arz et al., 1999; Vidal et al., 1999; Jennerjahn et al., 2004; Jaeschke et al., 2007), yet in our study, we did not observe a significant influence of Heinrich events or even of the Younger Dryas (**Figures 6C,D**). These events could have led to the movements of the ITCZ, causing anomalously higher precipitation rates in southeastern Brazil (Cruz et al., 2006; Wang et al., 2007). This should have raised fluvial runoff, transporting more terrigenous sediments and nutrients to the core region. Nevertheless, we did not observe such changes in either of these records, indicating that the main driver of most changes in the deposition of terrigenous sediments was probably relative sea-level variation (**Figure 7**).

Changes in sedimentary proxies can also indicate changes in the hydrodynamics of the region. A low-energy environment would allow more deposition of silt–clay minerals than a high-energy environment. This process has already been correlated with the displacement of the BC toward the coast, which resulted from the higher relative sea-level conditions and the covering of the continental shelf, as has also been described by other authors (Viana et al., 1998; Mahiques et al., 2007; Kowsmann 2015). The offshore displacement of the BC system can lead to more fine sediments depositing on the upper slope (Viana et al., 1998; Mahiques et al., 2007; Nagai et al., 2010; Kowsmann et al., 2015). This displacement would diminish the local hydrodynamics and promote the deposition of the FF. Furthermore, the "floor polisher" effect on the seabed described by Mahiques et al. (2004) would prevent mud deposition on the shelf break and upper slope depths in the periods where the BC moved toward the coast.

The XRF and FF records of the two cores have different trends. GL-824 shows a decrease over the last deglaciation, while GL-1109 remains constant. The decreasing trend in GL-1109 is observed during the early Holocene. Additionally, in GL-824 core, there was a more significant amount of FF and terrigenous sediments and lower percentages of $CaCO_3$ than in GL-1109 core (**Figures 3E–H**), highlighting differences in sedimentary processes between the two cores. This is primarily associated with their different water depths (**Figure 1B**). GL-824 location is more susceptible to sea-level variations because this core is located on the upper slope, an environment that during the LGM would be analog to the continental shelf. Consequently, the coastal processes influence more the GL-824 than the GL-1109. Thus, its elements and granulometry change as soon as the sea level rises. On the other hand, in the GL-1109, the trends of the terrigenous supply and FF occur later when the sea level is nearly at its maximum. GL-824 core would also have been less affected by the action of the BC compared with GL- 1109. Moreover, GL-824 core is farther north than GL-

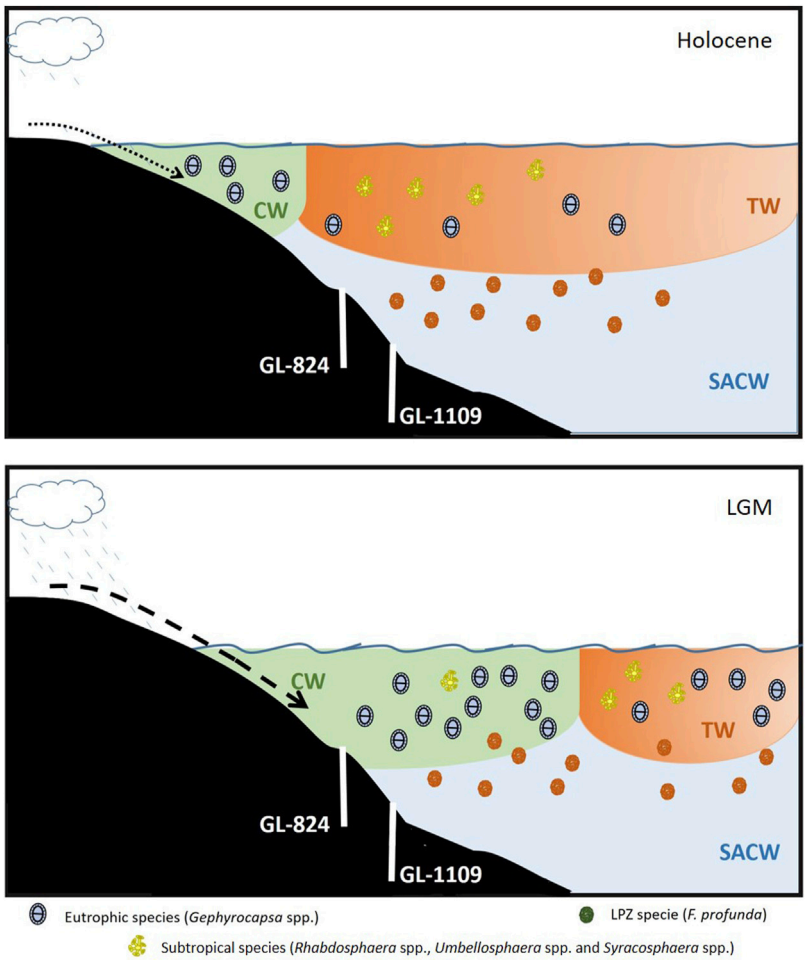

FIGURE 7 | Conceptual model of the main processes controlling the terrigenous supply and paleoproductivity in the southwestern Atlantic. The model shows high (low) productivity during the LGM (Holocene) period on the upper slope associated with variations in sea level and precipitation, promoting more input of nutrients due to enhanced terrigenous supply caused by a combination of lower sea level and higher rainfall. At the same time, the offshore displacement of the BC occurred, increasing the influence of the more eutrophic CW in the core area during the LGM.

1109 core, placing it closer to sediment sources such as Rio Doce and Rio Paraíba do Sul.

5.2 Coccolithophore Response to Paleoproductivity Variations in the Southwestern Atlantic Ocean

5.2.1 Coccolithophore Assemblage Response

The relative abundance of *F. profunda* was opposite to the total organic carbon (TOC) content (Lourenço et al., 2016) and the *G. bulloides* percentage (Pereira et al., 2018). Additionally, it was similar to higher SSTs (Lourenço et al., 2016) and the relative abundance of the oligotrophic *G. sacculifer* (**Figures 5A–I**, Pereira, et al., 2018). Therefore, we used this species to indicate oligotrophic conditions, which has also been corroborated by other studies (Beaufort et al., 2001; Hernandez-Almeida et al., 2019).

Emiliania huxleyi and *F. profunda* showed a similar general fluctuation (**Figures 5A–D**). *E. huxleyi* is known to tolerate a wide range of ecological conditions (Okada and Honjo, 1973; Okada and McIntyre, 1979; Boeckel and Baumann, 2008) and can dominate in both oligotrophic (Okada and Honjo, 1975; Kleijne, 1993; Haidar and Thierstein, 2001; Tyrrell and Merico, 2004) and eutrophic environments (Brand, 1994; Young, 1994; Boeckel et al., 2006). In contrast, *Gephyrocapsa* spp. exhibits an inverse distribution compared to *F. profunda* (**Figures 5A–F**; **Tables 3**, **4**), indicating the different environmental preferences of these species. In the Iberian margin upwelling region, *E. huxleyi* and *Gephyrocapsa* spp (mainly small *Gephyrocapsa* and *G. oceanica*) were both indicators of upwelling periods (Ausín et al., 2018). However, they were separated into distinct ecological preferences, with *E. huxleyi* related to a more stable, warmer, and nutrient-poor water column associated with the upwelling relaxation stage and *Gephyrocapsa* spp. to colder water and higher nutrient availability associated with the early stages of the upwelling event (Ausín et al., 2018; Jin et al. (2019) in the South China Sea also found that *Gephyrocapsa* spp. were dominant in coastal water associated with

higher diatom production and increased silicon content, while *E. huxleyi* was associated with a regular nutrient regime with lower amounts of silicon.

Comparing our record to SSTs estimated by Lourenço et al. (2016), we analyzed the same process described by Jin et al. (2019), with *E. huxleyi* dominating the period with warm and stable water and *Gephyrocapsa* spp. with colder nutrient-rich (silicon) water of the CW (**Figures 5C–F** and **Figures 6B–F**). Additionally, *E. huxleyi* had higher abundances in the periods with lower riverine influence, more negligible rainfall, and higher sea level, interpreted here as a low nutrient period, which was similar to *F. profunda* and the subtropical species that are associated with high temperature and oligotrophic environments (Boeckel et al., 2006). In this work, we interpreted the variations in *E. huxleyi* with a possible relation to more oligotrophic environments and as a response to evolutionary factors. This species first appeared and rapidly grew in the late/middle Quaternary, replacing the former more abundant *Gephyrocapsa* spp. (Toledo et al., 2016), making it a species with a signal that is difficult to deduce. Furthermore, as a cosmopolitan species, it may not indicate upwelling processes but is more typical of a stable regime, as observed in other studies (Andruleit and Rogalla, 2002; Jin et al., 2019).

Since *Gephyrocapsa* spp. and *E. huxleyi* seem to represent different ecological aspects, the N ratio (Flores et al., 2000) is not the best proxy to estimate paleoproductivity in this region. Therefore, the leading proxy used in this study to infer changes in primary productivity in surface water was the contrast between eutrophic *Gephyrocapsa* spp. and *F. profunda*, which represents low nutrients in surface water.

Variations in the relative abundances of *F. profunda* and *Gephyrocapsa* spp., particularly in GL-1109, were very similar to TOC content and *G. bulloides* relative abundance (**Figures 5A–H**), showing higher nutrients/productivity during the glacial period and lower nutrients/productivity during the Holocene, with a transition period of ~19 kyrs BP to ~14 kyrs BP. These observed variations likely reflect the opposite trend in the relative abundances of *F. profunda* and *Gephyrocapsa* spp., which reveals a change in the upper water column during these periods, with the LGM period characterized by a shallower nutricline and high productivity and the interglacial period characterized by a deeper nutricline and lower productivity. This is also supported by the UPZ species in the subtropical group, an indicator of oligotrophic surface environments, being more abundant in the Holocene than in the LGM, suggesting a warmer and poor-nutrient surface ocean during the Holocene. Nagai et al. (2010), mainly applying benthic foraminifera, and Mahiques et al. (2007), using sedimentary data, also inferred high productivity during the LGM on the southeastern Brazilian upper slope. Toledo et al. (2008) reported evidence of decreased productivity over the Holocene compared to the LGM along the Brazilian continental margin, which is consistent with our observations.

The terrigenous supply and FF content oscillated similarly to the *Gephyrocapsa* spp. record, in contrast to the subtropical group (**Tables 3**, **4**). Three processes could lead to this configuration, or a combination of all of them: 1) there was high availability of nutrients in the UPZ during the low stands of sea level, caused by a higher riverine input transporting more nutrients along with terrigenous material. 2) Higher influence of coastal nutrient-rich water due to the offshore displacement of the BC during low stands of sea level, leading to withdrawal of the surface warm oligotrophic TW (**Figure 7**). 3) High turbidity in the UPZ due to higher FF content and terrigenous sediments in the water column decreasing the light availability to the LPZ, limiting the growth of *F. profunda*.

5.2.2 Productivity Driving Factors in the Southwestern Atlantic

Gephyrocapsa spp. and EPP indicators reflect the same three distinct periods noted in the geochemical and sedimentary record. This suggests that a more substantial continental influence or the BC offshore displacement during the glacial period would have enhanced nutrient availability in surface water. In the same way, during the LGM, a weaker BC would have had more eddies and meanders because stronger currents were closer to linear fluxes. These meanders could have transported more nutrients to the photic zone from greater depths if they were anticyclones or by mixing ocean water with shelf water, which contains higher nutrient concentrations. The Plata River plume could also have reached the study area more frequently during winter-like conditions, promoting higher nutrients and terrigenous input.

Guerreiro et al. (2013) observed a more significant presence of *G. oceanica* in the water column associated with higher productivity related to fluvial discharge on the central Portuguese margin. Mahiques et al. (2007) and Nagai et al. (2010) suggested an increase in water column temperature and more intense action of the BC during periods of higher sea level, indicating a displacement of the warm water of the Brazil Current toward the coast, which would have prevented any increase in water productivity or the deposition of organic matter.

The correlation between the terrigenous supply, productivity, and nutrient content in surface water, represented by *Gephyrocapsa* spp. (**Table 2**), can be explained by two factors: 1) there was probably high nutrient content in the water column transported by enhanced continental runoff during lowstands of sea level and more winter-like conditions increasing the influence of the Plata River plume (Portilho-Ramos et al., 2019); and 2) the displacement of the BC toward the coast during higher sea level enhanced the influence of the TW, transporting more oligotrophic water, deepening the nutricline and preventing any increase in nutrient content (**Figure 7**). This shows that in the study region, *Gephyrocapsa* spp. is a more opportunistic species than *E. huxleyi*, especially when there is a more substantial influence of coastal water because *G. oceanica* tends to dominate such regions (Guerreiro et al., 2013; Ausín et al., 2018). Furthermore, all processes could act simultaneously, increasing continental runoff related to enhanced rainfall (Wang et al., 2007) and favorable conditions for the northward penetration of the Plata River plume, as also suggested by Portilho-Ramos et al. (2019).

During periods of lower sea level, the input of nutrients and terrigenous materials favored the productivity and deposition of organic carbon (**Figures 6A–I**), which was observed by Lourenço et al. (2016). Lower $CaCO_3$ content corresponded to the period of higher SSTs, productivity, and terrigenous supply (**Figures 3G,H** and **Figures 6A–H**), which demonstrates an inverse correlation

between the productivity record and carbonate content (**Tables 3**, **4**), suggesting a possible dilution effect of the carbonate content by terrigenous input. Along with this dilution during periods of higher terrigenous input, there was an increase in FF content, increasing turbidity and lowering light penetration in the LPZ, limiting the growth of *F. profunda* and enhancing the relative abundance of the UPZ dweller *Gephyrocapsa* spp.

The deglacial transitional period was characterized by a decrease in paleoproductivity and terrigenous supply (**Figures 6C–H**). This was probably related to the processes discussed above (i.e., sea level rise and diminished precipitation), both limiting the nutrient input to the study area from both sources: continental input (regional input or lower Plata River plume influence) and the closer BC system increasing the oligotrophic TW influence. In addition, sea level rise may have modified the region's geomorphology, limiting shelf-break upwelling to areas closer to the coast.

As stated before, the Holocene was a period with the lowest productivity. However, the transition between the Middle to Late Holocene had low percentages of *F. profunda* (EPP, **Supplementary Material**) in the GL-1109 core (**Figure 6H**). This was not related to precipitation or sea-level oscillation because these parameters were relatively stable during this period. The low *F. profunda* relative abundance was caused by the higher relative abundances of *E. huxleyi*, representing approximately 70% of the assemblage during this period (**Figure 5D**). Most likely, related to changes in sea surface nutrients, also in the same interval, we observed high percentages of the eutrophic indicator *Helicosphaera* spp. (Boeckel et al., 2006) and lower rates of oligotrophic *Umbellosphaera* spp. (Boeckel et al., 2006; Saavedra-Pelitero et al., 2011) and subtropical groups (**Supplementary Figure S2**). Austral summer-like conditions observed in the Middle-Late Holocene could have promoted increased shelf-break upwelling, which would have been enhanced due to higher BC meander-driven upwelling, causing higher rates of primary productivity in more offshore positions affecting the GL-1109 region, but not the shallower GL-824 core, which would have been influenced by colder coastal water and did not show such peaks in *E. huxleyi* relative abundance.

6 CONCLUSION

The distribution of terrigenous proxies, together with the fine fraction and carbonate contents, represented good indicators of the transport of sediments to the upper continental slope.

The terrigenous supply varied between the LGM and the Holocene, with the relative sea-level being the central controller and precipitation possibly enhancing this supply. Sea-level fluctuations were responsible for determining the distance between the sediment source and the core area and modulating how the BC displacement influenced sediment deposition. Therefore, the terrigenous supply was higher during the LGM, when sea level was lower and precipitation rates were higher. The BC dislocated offshore also led to a less energetic environment promoting the deposition of the fine fraction and terrigenous sediments.

The paleoproductivity of the upper slope was controlled mainly by the position of the BC main flow, which was associated with relative sea level. In the Holocene, a period of high sea level, the BC transports warm water of the TW to the upper slope, preventing any nutrient arrival, which was opposite to that during the LGM, an interval with lower sea level in which offshore displacement of the BC allowed the transport of more nutrients, enhancing primary productivity. Similar associations of this process have been made based on different proxies (Mahiques et al., 2007; Nagai et al., 2010; Lourenço et al., 2016), but this is the first study based on coccolithophores from the LGM-Holocene transition in the southwestern Atlantic.

DATA AVAILABILITY STATEMENT

The original contributions presented in the study are included in the article/**Supplementary Materials**; further inquiries can be directed to the corresponding author.

AUTHOR CONTRIBUTIONS

GP: writing—original draft, and geochemical analysis. MH: coccolithophore assemblages and review and editing. MT: conceptualization, investigation, and writing—review and editing. AA: conceptualization and writing—review and editing. CC: conceptualization and writing—review and editing. KC: supervision, project administration, and writing—review and editing. FT: supervision, project administration, funding acquisition, and writing—review and editing.

FUNDING

This study was supported by the CAPES-ASPECTO project (grant no. 88887.091731/2014-01). GAP acknowledges the financial support from CNPq (grant 167794/2018-3). MOT appreciates financial support from Capes (grant 88887.388307/2019-00). ALSA is a senior scholar CNPq (grant 302521/2017-8). CMC acknowledges the financial support from FAPESP (grants 2018/15123-4 and 2019/24349-9) and CNPq (grant 312458/2020-7). KBC acknowledges the financial support from CNPq (grant 310909/2019-8). FALT appreciates financial support from CNPq (310843/2019-7).

ACKNOWLEDGMENTS

The authors wish to express their thanks to R. Kowsman (CENPES/Petrobras) and the Petrobras Core Repository staff (Macaé/Petrobras) for providing the sediment core used in this research. Acknowledgments are also due to the reviewers for their insightful suggestions.

SUPPLEMENTARY MATERIAL

The Supplementary Material for this article can be found online at: https://www.frontiersin.org/articles/10.3389/feart.2022.846245/full#supplementary-material

REFERENCES

Alves, E., Macario, K., Souza, R., Pimenta, A., Douka, K., Oliveira, F., et al. (2015). Radiocarbon Reservoir Corrections on the Brazilian Coast from Pre-bomb Marine Shells. *Quat. Geochronol.* 29, 30–35. doi:10.1016/j.quageo.2015.05.006

Andruleit, H., and Rogalla, U. (2002). Coccolithophores in Surface Sediments of the Arabian Sea in Relation to Environmental Gradients in Surface Waters. *Mar. Geol.* 186 (3-4), 505–526. doi:10.1016/S0025-3227(02)00312-2

Antunes, R. L. (1997). *Introdução Ao Estudo Dos Nanofósseis Calcários*. Rio de Janeiro: Instituto de Geociências-Universidade Federal do Rio de Janeiro.115

Arz, H. W., Pätzold, J., and Wefer, G. (1999). Climatic Changes during the Last Deglaciation Recorded in Sediment Cores from the Northeastern Brazilian Continental Margin. *Geo-Marine Lett.* 19 (3), 209–218. doi:10.1007/s003670050111

Arz, H. W., Pätzold, J., and Wefer, G. (1998). Correlated Millennial-Scale Changes in Surface Hydrography and Terrigenous Sediment Yield Inferred from Last-Glacial Marine Deposits off Northeastern Brazil. *Quat. Res.* 50 (2), 157–166. doi:10.1006/qres.1998.1992

Ausín, B., Zúñiga, D., Flores, J. A., Cavaleiro, C., Froján, M., Villacieros-Robineau, N., et al. (2018). Spatial and Temporal Variability in Coccolithophore Abundance and Distribution in the NW Iberian Coastal Upwelling System. *Biogeosciences* 15 (1), 245–262. doi:10.5194/bg-15-245-2018

Beaufort, L., de Garidel-Thoron, T., Mix, A. C., and Pisias, N. G. (2001). ENSO-like Forcing on Oceanic Primary Production during the Late Pleistocene. *Science* 293 (5539), 2440–2444. doi:10.1126/science.293.5539.2440

Beaufort, L., Lancelot, Y., Camberlin, P., Cayre, O., Vincent, E., Bassinot, F., et al. (1997). Insolation Cycles as a Major Control of Equatorial Indian Ocean Primary Production. *Science* 278 (5342), 1451–1454. doi:10.1126/science.278.5342.1451

Behling, H. (2002). South and Southeast Brazilian Grasslands during Late Quaternary Times: a Synthesis. *Palaeogeogr. Palaeoclimatol. Palaeoecol.* 177 (1-2), 19–27. doi:10.1016/S0031-0182(01)00349-2

Behling, H., W. Arz, H., Pätzold, J., and Wefer, G. (2000). Late Quaternary Vegetational and Climate Dynamics in Northeastern Brazil, Inferences from Marine Core GeoB 3104-1. *Quat. Sci. Rev.* 19 (10), 981–994. doi:10.1016/S0277-3791(99)00046-3

Berman, A. L., Silvestri, G. E., and Tonello, M. S. (2016). Differences between Last Glacial Maximum and Present-Day Temperature and Precipitation in Southern South America. *Quat. Sci. Rev.* 150, 221–233. doi:10.1016/j.quascirev.2016.08.025

Bícego, M. C., Santos, F. R., de Aandrade Furlan, P. C., Lourenço, R. A., Taniguchi, S., de Mello e Sousa, S. H., Nagai, R. H., Cavalcante, A. B. L., Figueira, R. C. L., Wainer, I. K. C., and de Mahiques, M. M. (2021). Mid- to Late-Holocene Analysis of the Influence of the La Plata River Plume on the Southwestern Atlantic Shelf: A Paleoenvironmental Reconstruction Based on Lipid Biomarkers and Benthic Foraminifera. *Holocene* 095968362110417. doi:10.1177/09596836211041727

Blaauw, M., and Christen, J. A. (2011). Flexible Paleoclimate Age-Depth Models Using an Autoregressive Gamma Process. *Bayesian Anal.* 6, 457–474. doi:10.1214/11-BA61810.1214/ba/1339616472

Boeckel, B., and Baumann, K.-H. (2004). Distribution of Coccoliths in Surface Sediments of the South-Eastern South Atlantic Ocean: Ecology, Preservation and Carbonate Contribution. *Mar. Micropaleontol.* 51 (3-4), 301–320. doi:10.1016/j.marmicro.2004.01.001

Boeckel, B., Baumann, K.-H., Henrich, R., and Kinkel, H. (2006). Coccolith Distribution Patterns in South Atlantic and Southern Ocean Surface Sediments in Relation to Environmental Gradients. *Deep Sea Res. Part I Oceanogr. Res. Pap.* 53 (6), 1073–1099. doi:10.1016/j.dsr.2005.11.006

Boeckel, B., and Baumann, K.-H. (2008). Vertical and Lateral Variations in Coccolithophore Community Structure across the Subtropical Frontal Zone in the South Atlantic Ocean. *Mar. Micropaleontol.* 67 (3-4), 255–273. doi:10.1016/j.marmicro.2008.01.014

Bradley, R. S. (2000). Past Global Changes and Their Significance for the Future. *Quat. Sci. Rev.* 19 (1-5), 391–402. doi:10.1016/S0277-3791(99)00071-2

Brand, L. E. (1994). "Physiological Ecology of Marine Coccolithophores," in *Coccolithophores*. Editors A. Winter and W. G. Siesser (Cambridge: Cambridge University Press), 39

Cabarcos, E., Flores, J.-A., and Sierro, F. J. (2014). High-resolution Productivity Record and Reconstruction of ENSO Dynamics during the Holocene in the Eastern Equatorial Pacific Using Coccolithophores. *Holocene* 24 (2), 176–187. doi:10.1177/0959683613516818

Campos, E. J. D., Gonçalves, J. E., and Ikeda, Y. (1995). Water Mass Characteristics and Geostrophic Circulation in the South Brazil Bight: Summer of 1991. *J. Geophys. Res. Oceans* 100 (C9), 18537–18550. doi:10.1029/95JC01724

Campos, E. J. D., Lentini, C. A. D., Miller, J. L., and Piola, A. R. (1999). Interannual Variability of the Sea Surface Temperature in the South Brazil Bight. *Geophys. Res. Lett.* 26 (14), 2061–2064. doi:10.1029/1999GL900297

Campos, E. J. D., Velhote, D., and da Silveira, I. C. A. (2000). Shelf Break Upwelling Driven by Brazil Current Cyclonic Meanders. *Geophys. Res. Lett.* 27 (6), 751–754. doi:10.1029/1999GL010502

Carvalho, L. M. V., Jones, C., and Liebmann, B. (2002). Extreme Precipitation Events in Southeastern South America and Large-Scale Convective Patterns in the South Atlantic Convergence Zone. *J. Clim.* 15 (17), 2377–2394. doi:10.1175/1520-0442(2002)015<2377:epeiss>2.0.co;2

Carvalho, L. M. V., Jones, C., and Liebmann, B. (2004). The South Atlantic Convergence Zone: Intensity, Form, Persistence, and Relationships with Intraseasonal to Interannual Activity and Extreme Rainfall. *J. Clim.* 17 (1), 88–108. doi:10.1175/1520-0442(2004)017<0088:tsaczi>2.0.co;2

Cheng, H., Sinha, A., Cruz, F. W., Wang, X., Edwards, R. L., d'Horta, F. M., et al. (2013). Climate Change Patterns in Amazonia and Biodiversity. *Nat. Commun.* 4, 1411. doi:10.1038/ncomms2415

Ciotti, Á. M., Odebrecht, C., Fillmann, G., and Moller, O. O., Jr (1995). Freshwater Outflow and Subtropical Convergence Influence on Phytoplankton Biomass on the Southern Brazilian Continental Shelf. *Cont. shelf Res.* 15 (14), 1737–1756. doi:10.1016/0278-4343(94)00091-Z

Costa, K. B., Cabarcos, E., Santarosa, A. C. A., Battaglin, B. B. F., and Toledo, F. A. L. (2016). A Multiproxy Approach to the Climate and Marine Productivity Variations along MIS 5 in SE Brazil: A Comparison between Major Components of Calcareous Nannofossil Assemblages and Geochemical Records. *Palaeogeogr. Palaeoclimatol. Palaeoecol.* 449, 275–288. doi:10.1016/j.palaeo.2016.02.032

Cremer, M., Gonthier, E., Duprat, J., Faugères, J.-C., and Courp, T. (2007). Late Quaternary Variability of the Sedimentary Record in the Sao Tome Deep-Sea System (South Brazilian Basin). *Mar. Geol.* 236 (3-4), 223–245. doi:10.1016/j.margeo.2006.10.032

Cruz, F. W., Burns, S. J., Karmann, I., Sharp, W. D., Vuille, M., Cardoso, A. O., et al. (2005). Insolation-driven Changes in Atmospheric Circulation over the Past 116,000 Years in Subtropical Brazil. *Nature* 434 (7029), 63–66. doi:10.1038/nature03365

Cruz, F. W., Jr, Burns, S. J., Karmann, I., Sharp, W. D., and Vuille, M. (2006). Reconstruction of Regional Atmospheric Circulation Features during the Late Pleistocene in Subtropical Brazil from Oxygen Isotope Composition of Speleothems. *Earth Planet. Sci. Lett.* 248 (1-2), 495–507. doi:10.1016/j.epsl.2006.06.019

da Silveira, I. C. A., Napolitano, D. C., and Farias, I. U. (2020). "Water Masses and Oceanic Circulation of the Brazilian Continental Margin and Adjacent Abyssal Plain," in *Brazilian Deep-Sea Biodiversity*. Editors P. Y. G. Sumida, A. F. Bernardino, and F. C. D. Léo (Cham): Springer), 7–36. doi:10.1007/978-3-030-53222-2_2

de Mahiques, M. M., Tessler, M. G., Maria Ciotti, A., da Silveira, I. C. A., e Sousa, S. H. d. M., Figueira, R. C. L., et al. (2004). Hydrodynamically Driven Patterns of Recent Sedimentation in the Shelf and Upper Slope off Southeast Brazil. *Cont. Shelf Res.* 24 (15), 1685–1697. doi:10.1016/j.csr.2004.05.013

Dennison, J. M., and Hay, W. W. (1967). Estimating the Needed Sampling Area for Subaquatic Ecological Studies. *J. Paleontol.* 41 (3), 706

Deplazes, G., Lückge, A., Peterson, L. C., Timmermann, A., Hamann, Y., Hughen, K. A., et al. (2013). Links between Tropical Rainfall and North Atlantic Climate during the Last Glacial Period. *Nat. Geosci.* 6 (3), 213–217. doi:10.1038/ngeo1712

Fatela, F., and Taborda, R. (2002). Confidence Limits of Species Proportions in Microfossil Assemblages. *Mar. Micropaleontol.* 45, 169–174. doi:10.1016/s0377-8398(02)00021-x

Flores, J.-A., Gersonde, R., and Sierro, F. J. (1999). Pleistocene Fluctuations in the Agulhas Current Retroflection Based on the Calcareous Plankton Record. *Mar. Micropaleontol.* 37 (1), 1–22. doi:10.1016/S0377-8398(99)00012-2

Flores, J. A., Bárcena, M. A., and Sierro, F. J. (2000). Ocean-surface and Wind Dynamics in the Atlantic Ocean off Northwest Africa during the Last 140 000 Years. *Palaeogeogr. Palaeoclimatol. Palaeoecol.* 161 (3-4), 459–478. doi:10.1016/S0031-0182(00)00099-7

Govin, A., Braconnot, P., Capron, E., Cortijo, E., Duplessy, J.-C., Jansen, E., et al. (2012a). Persistent Influence of Ice Sheet Melting on High Northern Latitude Climate during the Early Last Interglacial. *Clim. Past.* 8, 483–507. doi:10.5194/cp-8-483-2012

Govin, A., Holzwarth, U., Heslop, D., Ford Keeling, L., Zabel, M., Mulitza, S., et al. (2012b). Distribution of Major Elements in Atlantic Surface Sediments (36°N-49°S): Imprint of Terrigenous Input and Continental Weathering. *Geochem. Geophys. Geosyst.* 13 (1), a–n. doi:10.1029/2011GC003785

Guerreiro, C., Oliveira, A., De Stigter, H., Cachão, M., Sá, C., Borges, C., et al. (2013). Late Winter Coccolithophore Bloom off Central Portugal in Response to River Discharge and Upwelling. *Cont. Shelf Res.* 59, 65–83. doi:10.1016/j.csr.2013.04.016

Haidar, A. T., and Thierstein, H. R. (2001). Coccolithophore Dynamics off Bermuda (N. Atlantic). *Deep Sea Res. Part II Top. Stud. Oceanogr.* 48 (8-9), 1925–1956. doi:10.1016/S0967-0645(00)00169-7

Hammer, O., Harper, D. A. T., and Ryan, P. D. (2001). Past: Paleontological Statistics Software Package for Education and Data Analysis. *Palaeontol. Electron* 4 (1), 1–9. http://palaeoelectronica.org/2001_1/past/issue1_01.htm.

Hernández-Almeida, I., Ausín, B., Saavedra-Pellitero, M., Baumann, K.-H., and Stoll, H. M. (2019). Quantitative Reconstruction of Primary Productivity in Low Latitudes during the Last Glacial Maximum and the Mid-to-late Holocene from a Global *Florisphaera Profunda* Calibration Dataset. *Quat. Sci. Rev.* 205, 166–181. doi:10.1016/j.quascirev.2018.12.016

Jaeschke, A., Rühlemann, C., Arz, H., Heil, G., and Lohmann, G. (2007). Coupling of Millennial-Scale Changes in Sea Surface Temperature and Precipitation off Northeastern Brazil with High-Latitude Climate Shifts during the Last Glacial Period. *Paleoceanography* 22, 4, a–n. doi:10.1029/2006PA001391

Jansen, J. H., van der Gaast, S. J., Koster, B., and Vaars, A. J. (1998). CORTEX, a Shipboard XRF Scanner for Element Analyses in Split Sediment Cores. *Mar. Geol.* 151 (1), 143–153. doi:10.1016/S0025-3227(98)00074-7

Jennerjahn, T. C., Ittekkot, V., Arz, H. W., Behling, H., Pätzold, J., and Wefer, G. (2004). Asynchronous Terrestrial and Marine Signals of Climate Change during Heinrich Events. *Science* 306 (5705), 2236–2239. doi:10.1126/science.1102490

Jin, X. B., Liu, C. L., Zhao, Y. L., Zhang, Y. W., Wen, K., Lin, S., et al. (2019). Two Production Stages of Coccolithophores in Winter as Revealed by Sediment Traps in the Northern South China Sea. *J. Geophys. Res. Biogeosci.* 124 (7), 2335–2350. doi:10.1029/2019JG005070

Kleijne, A. (1993). "*Morphology, Taxonomy and Distribution of Extant Coccolithophorids (Calcareous Nannoplankton)*. Amsterdam: Free University of Amsterdam). thesis.

Kowsmann, R. O., de Lima, A. C., and Vicalvi, M. A. (2015). "Feições Indicadoras De Instabilidade Geológica No Talude Continental E No Platô De São Paulo," in *Geologia e Geomorfologia* (Campus, 71–97. doi:10.1016/B978-85-352-6937-6.50012-4

Lee, J.-E., Johnson, K., and Fung, I. (2009). Precipitation over South America during the Last Glacial Maximum: An Analysis of the "amount Effect" with a Water Isotope-Enabled General Circulation Model. *Geophys. Res. Lett.* 36, L19701. doi:10.1029/2009GL039265

Leonhardt, A., Toledo, F. A. L., and Coimbra, J. C. (2013). The Productivity History in the Southwestern Atlantic as Inferred from Coccolithophore Record for the Last 130 Kyr. *Rev. Bras. Paleontol.* 16 (3), 361–375. doi:10.4072/rbp.2013.3.02

Liebmann, B., Vera, C. S., Carvalho, L. M. V., Camilloni, I. A., Hoerling, M. P., Allured, D., et al. (2004). An Observed Trend in Central South American Precipitation. *J. Clim.* 17 (22), 4357–4367. doi:10.1175/3205.1

Locarnini, M. M., Mishonov, A. V., Baranova, O. K., Boyer, T. P., Zweng, M. M., Garcia, H. E., et al. (2018). World Ocean Atlas 2018. *Temperature* 1, 52.

Lourenço, R. A., de Mahiques, M. M., Wainer, I. E. K. C., Rosell-Melé, A., and Bícego, M. C. (2016). Organic Biomarker Records Spanning the Last 34,800 Years from the Southeastern Brazilian Upper Slope: Links between Sea Surface Temperature, Displacement of the Brazil Current, and Marine Productivity. *Geo-Mar Lett.* 36 (5), 361–369. doi:10.1007/s00367-016-0453-7

Mahiques, M. M., Fukumoto, M. M., Silveira, I. C. A., Figueira, R. C. L., Bícego, M. C., Lourenço, R. A., et al. (2007). Sedimentary Changes on the Southeastern Brazilian Upper Slope during the Last 35,000 Years. *An. Acad. Bras. Ciênc.* 79, 171–181. doi:10.1590/S0001-37652007000100018

Michaelovitch de Mahiques, M., Almeida da Silveira, I. C., de Mello e Sousa, S. H., and Rodrigues, M. (2002). Post-LGM Sedimentation on the Outer Shelf-Upper Slope of the Northernmost Part of the São Paulo Bight, Southeastern Brazil. *Mar. Geol.* 181 (4), 387–400. doi:10.1016/S0025-3227(01)00225-0

Molfino, B., and McIntyre, A. (1990). Precessional Forcing of Nutricline Dynamics in the Equatorial Atlantic. *Science* 249 (4970), 766–769. doi:10.1126/science.249.4970.766

Nagai, R. H., Ferreira, P. A. L., Mulkherjee, S., Martins, M. V., Figueira, R. C. L., Sousa, S. H. M., et al. (2014). Hydrodynamic Controls on the Distribution of Surface Sediments from the Southeast South American Continental Shelf between 23°S and 38°S. *Cont. shelf Res.* 89, 51–60. doi:10.1016/j.csr.2013.09.016

Nagai, R. H., Sousa, S. H. D. M., Lourenço, R. A., Bícego, M. C., and Mahiques, M. M. D. (2010). Paleoproductivity Changes during the Late Quaternary in the Southeastern Brazilian Upper Continental Margin of the Southwestern Atlantic. *Braz. J. Oceanogr.* 58, 31–41. doi:10.1590/S1679-87592010000500004

Okada, H., and Honjo, S. (1975). Distribution of Coccolithophores in Marginal Seas along the Western Pacific Ocean and in the Red Sea. *Mar. Biol.* 31 (3), 271–285. doi:10.1007/BF00387154

Okada, H., and Honjo, S. (1973). The Distribution of Oceanic Coccolithophorids in the Pacific. *Deep Sea Res. Oceanogr. Abstr.* 20 (4), 355–374. doi:10.1016/0011-7471(73)90059-4

Okada, H., and McIntyre, A. (1979). Seasonal Distribution of Modern Coccolithophores in the Western North Atlantic Ocean. *Mar. Biol.* 54 (4), 319–328. doi:10.1007/BF00395438

Pedrão, G. A., Costa, K. B., Toledo, F. A. L., Tomazella, M. O., and Jovane, L. (2021). Semi-Quantitative Analysis of Major Elements and Minerals: Clues from a Late Pleistocene Core from Campos Basin. *Appl. Sci.* 11 (13), 6206. doi:10.3390/app11136206

Pereira Brandini, F., Nogueira, M., Jr, Simião, M., Carlos Ugaz Codina, J., and Almeida Noernberg, M. (2014). Deep Chlorophyll Maximum and Plankton Community Response to Oceanic Bottom Intrusions on the Continental Shelf in the South Brazilian Bight. *Cont. Shelf Res.* 89, 61–75. doi:10.1016/j.csr.2013.08.002

Pereira, L. S., Arz, H. W., Pätzold, J., and Portilho-Ramos, R. C. (2018). Productivity Evolution in the South Brazilian Bight during the Last 40,000 Years. *Paleoceanogr. Paleoclimatology* 33 (12), 1339–1356. doi:10.1029/2018PA003406

Piola, A. R., Matano, R. P., Palma, E. D., Möller, O. O., Jr, and Campos, E. J. (2005). The Influence of the Plata River Discharge on the Western South Atlantic Shelf. *Geophys. Res. Lett.* 32, 1. doi:10.1029/2004GL021638

Pivel, M. A. G., Santarosa, A. C. A., Bariani, L., Costa, K. B., and Toledo, F. A. L. (2011). Paleoprodutividade na Bacia de Santos nos últimos 15 mil anos. *Paleontol. Cenários Vida* 3, 333

Portilho-Ramos, R. D. C., Pinho, T. M. L., Chiessi, C. M., and Barbosa, C. F. (2019). Understanding the Mechanisms behind High Glacial Productivity in the Southern Brazilian Margin. *Clim. Past.* 15 (3), 943–955. doi:10.5194/cp-15-943-2019

Razik, S., Govin, A., Chiessi, C. M., and von Dobeneck, T. (2015). Depositional Provinces, Dispersal, and Origin of Terrigenous Sediments along the SE South American Continental Margin. *Mar. Geol.*, 363, 261–272. doi:10.1016/j.margeo.2015.03.001

Reimer, P. J., Bard, E., Bayliss, A., Beck, J. W., Blackwell, P. G., Ramsey, C. B., et al. (2013). IntCal13 and Marine13 Radiocarbon Age Calibration Curves 0-50,000 Years Cal BP. *Radiocarbon* 55 (4), 1869–1887. doi:10.2458/azu_js_rc.55.16947

Roth, P. H. (1994). "Distribution of Coccoliths in Oceanic Sediments," in *Coccolithophores*. Editors A. Winter and W. G. Siesser (Cambridge, U.K): Cambridge University Press), 178

Rühlemann, C., Mulitza, S., Müller, P. J., Wefer, G., and Zahn, R. (1999). Warming of the Tropical Atlantic Ocean and Slowdown of Thermohaline Circulation during the Last Deglaciation. *Nature* 402 (6761), 511–514. doi:10.1038/990069

Saavedra-Pellitero, M., Flores, J. A., Lamy, F., Sierro, F. J., and Cortina, A. (2011). Coccolithophore Estimates of Paleotemperature and Paleoproductivity Changes in the Southeast Pacific over the Past ~27 Kyr. *Paleoceanography* 26, 1. doi:10.1029/2009PA001824

Schneider, T., Bischoff, T., and Haug, G. H. (2014). Migrations and Dynamics of the Intertropical Convergence Zone. *Nature* 513 (7516), 45–53. doi:10.1038/nature13636

Silveira, I. C. A. d., Schmidt, A. C. K., Campos, E. J. D., Godoi, S. S. d., and Ikeda, Y. (2000). A corrente Do Brasil ao largo da costa leste brasileira. *Rev. Bras. Oceanogr.* 48 (2), 171–183. doi:10.1590/S1413-77392000000200008

Spratt, R. M., and Lisiecki, L. E. (2016). A Late Pleistocene Sea Level Stack. *Clim. Past.* 12 (4), 1079–1092. doi:10.5194/cp-12-1079-2016

Stoll, H. M., and Ziveri, P. (2002). Separation of Monospecific and Restricted Coccolith Assemblages from Sediments Using Differential Settling Velocity. *Mar. Micropaleontol.* 46 (1-2), 209–221. doi:10.1016/S0377-8398(02)00040-3

Stramma, L., and England, M. (1999). On the Water Masses and Mean Circulation of the South Atlantic Ocean. *J. Geophys. Res.* 104 (C9), 20863–20883. doi:10.1029/1999JC900139

Sylvestre, F. (2009). "Moisture Pattern during the Last Glacial Maximum in South America," in *Past Climate Variability in South America and Surrounding Regions*. Editors F. Vimeux, F. Sylvestre, and M. Khodri (Dordrecht): Springer), 3–27. doi:10.1007/978-90-481-2672-9_1

Toledo, F. A. L., Cachão, M., Costa, K. B., and Pivel, M. A. G. (2007). Planktonic Foraminifera, Calcareous Nannoplankton and Ascidian Variations during the Last 25 Kyr in the Southwestern Atlantic: A Paleoproductivity Signature? *Mar. Micropaleontol.* 64 (1-2), 67–79. doi:10.1016/j.marmicro.2007.03.001

Toledo, F. A. L., Quadros, J. P., Camillo, E., Jr, Santarosa, A. C. A., Flores, J.-A., and Costa, K. B. (2016). Plankton Biochronology for the Last 772,000 Years from the Western South Atlantic Ocean. *Mar. Micropaleontol.* 127, 50–62. doi:10.1016/j.marmicro.2016.07.002

Toledo, F. A. L. (2000). "*Variações Paleoceanográficas nos últimos 30.000 anos no oeste Do Atlântico Sul: Isótopos de oxigênio, assembléias de foraminíferos planctônicos e nanofósseis calcários*," (Brazil: [Geoscience Institute]: Federal Univ. Rio Grande do Sul). PhD Thesis.

Toledo, F., Costa, K. B., Pivel, M. A., and Campos, E. J. (2008). Tracing Past Circulation Changes in the Western South Atlantic Based on Planktonic Foraminifera. *Rev. Bras. Paleontol.* 11 (3), 169–178. doi:10.4072/rbp.2008.3.03

Tyrrell, T., and Merico, A. (2004). "*Emiliania Huxleyi*: Bloom Observations and the Conditions that Induce Them," in *Coccolithophores* (Berlin, Heidelberg: Springer), 75–97. doi:10.1007/978-3-662-06278-4_4

Vera, C., Silvestri, G., Liebmann, B., and González, P. (2006). Climate Change Scenarios for Seasonal Precipitation in South America from IPCC-AR4 Models. *Geophys. Res. Lett.* 33 (13), 13707–13711. doi:10.1029/2006GL025759

Viana, A. R., Faugères, J. C., Kowsmann, R. O., Lima, J. A. M., Caddah, L. F. G., and Rizzo, J. G. (1998). Hydrology, Morphology and Sedimentology of the Campos Continental Margin, Offshore Brazil. *Sediment. Geol.* 115 (1-4), 133–157. doi:10.1016/S0037-0738(97)00090-0

Vidal, L., Schneider, R. R., Marchal, O., Bickert, T., Stocker, T. F., and Wefer, G. (1999). Link between the North and South Atlantic during the Heinrich Events of the Last Glacial Period. *Clim. Dyn.* 15 (12), 909–919. doi:10.1007/s003820050321

Wang, X., Auler, A. S., Edwards, R. L., Cheng, H., Ito, E., Wang, Y., et al. (2007). Millennial-scale Precipitation Changes in Southern Brazil over the Past 90,000 Years. *Geophys. Res. Lett.* 34 (23), n/a–n/a. doi:10.1029/2007gl031149

Weltje, G. J., and Tjallingii, R. (2008). Calibration of XRF Core Scanners for Quantitative Geochemical Logging of Sediment Cores: Theory and Application. *Earth Planet. Sci. Lett.* 274, 423–438. doi:10.1016/j.epsl.2008.07.054

Winter, A., Jordan, R. W., and Roth, P. H. (1994). "Biogeography of Living Coccolithophores in Ocean Waters," in *Coccolithophores*. Editors A. Winter and W. G. Siesser (CambridgeCambridge, U.K): Cambridge University Press), 161

Young, J. R. (1994). "Functions of Coccoliths," in *Coccolithophores*. Editors A. Winter and W. G. Siesser (Cambridge, U.K: Cambridge University Press), 63

Zhou, X., Duchamp-Alphonse, S., Kageyama, M., Bassinot, F., Beaufort, L., and Colin, C. (2020). Dynamics of Primary Productivity in the Northeastern Bay of Bengal over the Last 26 000 Years. *Clim. Past.* 16 (5), 1969–1986. doi:10.5194/cp-16-1969-2020

Conflict of Interest: The authors declare that the research was conducted in the absence of any commercial or financial relationships that could be construed as a potential conflict of interest.

frontiers | Frontiers in Marine Science

ORIGINAL RESEARCH
published: 20 July 2022
doi: 10.3389/fmars.2022.901224

Controlling Parameters of Benthic Deep-Sea Foraminiferal Biogeography at the Brazilian Continental Margin (11-22°S)

Anna Saupe[1], Johanna Schmidt[1], Jassin Petersen[1], André Bahr[2], Bruna Borba Dias[3], Ana Luiza Spadano Albuquerque[4], Rut Amelia Díaz Ramos[4] and Patrick Grunert[1]*

[1] Institute of Geology and Mineralogy, University of Cologne, Cologne, Germany, [2] Institute of Earth Sciences, Heidelberg University, Heidelberg, Germany, [3] School of Arts, Sciences and Humanities, University of São Paulo, São Paulo, Brazil, [4] Departamento de Geoquímica, University Federal Fluminense, Niterói, Brazil

OPEN ACCESS

Edited by:
Jeroen Ingels,
Florida State University, United States

Reviewed by:
Andrew John Gooday,
National Oceanography Centre, Southampton, United Kingdom
Michael Martínez-Colón,
Florida Agricultural and Mechanical University, United States
Bryan O'Malley,
Eckerd College, United States

***Correspondence:**
Anna Saupe
anna.saupe@uni-koeln.de

Specialty section:
This article was submitted to Coastal Ocean Processes, a section of the journal Frontiers in Marine Science

Received: 21 March 2022
Accepted: 01 June 2022
Published: 20 July 2022

Citation:
Saupe A, Schmidt J, Petersen J, Bahr A, Dias BB, Albuquerque ALS, Díaz Ramos RA and Grunert P (2022) Controlling Parameters of Benthic Deep-Sea Foraminiferal Biogeography at the Brazilian Continental Margin (11-22°S). Front. Mar. Sci. 9:901224. doi: 10.3389/fmars.2022.901224

This study presents new quantitative data on benthic foraminifera from three bathymetric transects of the Brazil (11-14°S, 420-1900 m) and Campos (22°S, 430-2000 m) basins. The quantity and quality of organic matter flux as well as substrate properties and hydrodynamic conditions at the sediment-water interface are identified as key parameters controlling assemblage distribution. Based on the total (stained and unstained) fauna, a distinct biogeographic divide between a *Globocassidulina subglobosa/crassa* assemblage in the Campos Basin and a rosalinid/bolivinid assemblage in the Brazil Basin occurs across the bifurcation of the South Atlantic Central Water into its southward subtropical and northward tropical branches. In the Campos Basin, coarser sediments, increased bottom current activity, and variable nutrient supply favor an assemblage of *Globocassidulina subglobosa/crassa*, *Nuttalides umbonifer* and *Alabaminella weddellensis*. Occurrences of cold-water coral mounds in 870 m provide an ecological niche favoring species such as *Alabaminella weddellensis* which benefit from trapped nutrients. The Brazil Basin is characterized by increased abundances of *Rosalina* and *Bolivina*, while *Globocassidulina subglobosa/crassa* is comparatively less frequent. Assemblages with *G. subglobosa/crassa*, *Rosalina* spp., *Bolivina variabilis* and *Bolivina subreticulata* are favored by a relatively high nutrient input at 14°S. Further north, assemblages with *Bolivina subreticulata*, *Bolivina variabilis*, *Epistominella exigua*, *G. subglobosa/crassa* are located beneath the velocity core of the North Brazil Undercurrent (NBUC), coinciding with more clayey sediments rich in TOC. Occurrences of delicate branching forms such as *Saccorhiza ramosa* indicate a more stable setting, distal to the main current. Rose Bengal stained (living) specimens are scarce in all three regions, as is typical for deep-sea foraminiferal faunas. Their patterns of species distribution largely reflect those observed for the total fauna.

Keywords: benthic foraminifera, Brazilian margin, continental slope, deep-sea, South Atlantic

1 INTRODUCTION

Benthic deep-sea foraminifera are a diverse group of shell-bearing unicellular eukaryotes adapted to a wide range of marine microhabitats (e.g., Sen Gupta, 2002). Their distribution is largely determined by the interplay of organic carbon influx, physical and chemical properties of major water masses, and the hydrodynamic regime at the sediment-water interface (Mackensen et al., 1995; Schmiedl et al., 1997; Gooday and Jorissen, 2012). At the extensive Brazilian continental margin, the impact of such environmental factors on the benthic foraminiferal fauna is poorly understood as previous studies have mainly focused on shelf areas south of 20°S (Oliveira-Silva et al., 2005; de Mello e Sousa et al., 2006; Eichler et al., 2008; Burone et al., 2011; Eichler et al., 2012; Vieira et al., 2015; Yamashita et al., 2018; Yamashita et al., 2020). Studies on benthic foraminiferal assemblages on the continental slope are particularly rare and limited to the Campos Basin (~ 22°S; de Mello e Sousa et al., 2006; Yamashita et al., 2018; de Almeida et al., 2022). Analyses of modern deep-sea foraminifera from the continental shelf and slope north of 20°S off Eastern Brazil are lacking (Murray, 2006). Environmental conditions vary greatly along the Brazilian continental slope due to a complex water mass system and varied local seafloor topographies. Diverse microhabitats occupied by a wide range of different foraminiferal associations are thus to be expected to the North of the Campos Basin. Filling this gap in biogeographic documentation is essential to fully understand the controls on foraminiferal distribution off Brazil.

During R/V METEOR expedition M125, the Brazilian continental shelf and slope were sampled between 10°S and 23°S (Bahr et al., 2016), offering a unique opportunity to document benthic foraminiferal distribution patterns north of 20°S. Here we investigate recent benthic foraminiferal assemblages from three bathymetric transects in the Brazil (11°S, 14°S) and Campos (22°S) basins. Through integration of the observed faunal patterns with environmental parameters we gain new insights into the drivers of diversity and biogeographic patterns of deep-sea benthic foraminifera along the Brazilian continental margin. This study will serve as a baseline for future biogeographic and palaeoceanographic investigations on benthic foraminiferal faunas in the area.

2 STUDY AREA

The Brazilian margin, with a length of 7400 km, can be divided into different physiographical provinces (Martins and Coutinho, 1981). The north-eastern part stretches from Cabo Sao Roque to Belmonte and includes the Brazil Basin (5-16°S; **Figure 1**; Martins and Coutinho, 1981; da Silveira et al., 2020). Reduced continental erosion and low marine sedimentation rates result in a very narrow continental shelf (**Figures 2A, B**) less than 10 km in width (Summerhayes et al., 1976; Knoppers et al., 1999; Bahr et al., 2016). Extensive canyon systems are common and determine seafloor topography along the continental slope (Bahr et al., 2016). Further south (16-23°S), the east coast extends to Cabo Frio including the Campos Basin. The shelf area

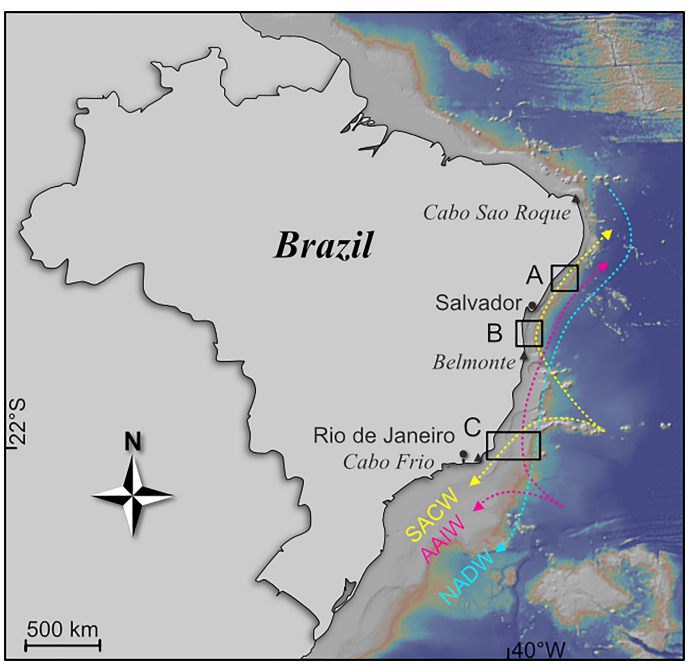

FIGURE 1 | General map of the study area along the Brazilian continental margin. A, B, and C indicate the three investigated areas at 11°S, 14°S, and 22°S, respectively. South Atlantic Central Water (SACW), Antarctic Intermediate Water (AAIW) and North Atlantic Deep Water (NADW) are the major water masses. The map was created with GeoMapApp (www.geomapapp.org), using the base map of Ryan et al. (2009).

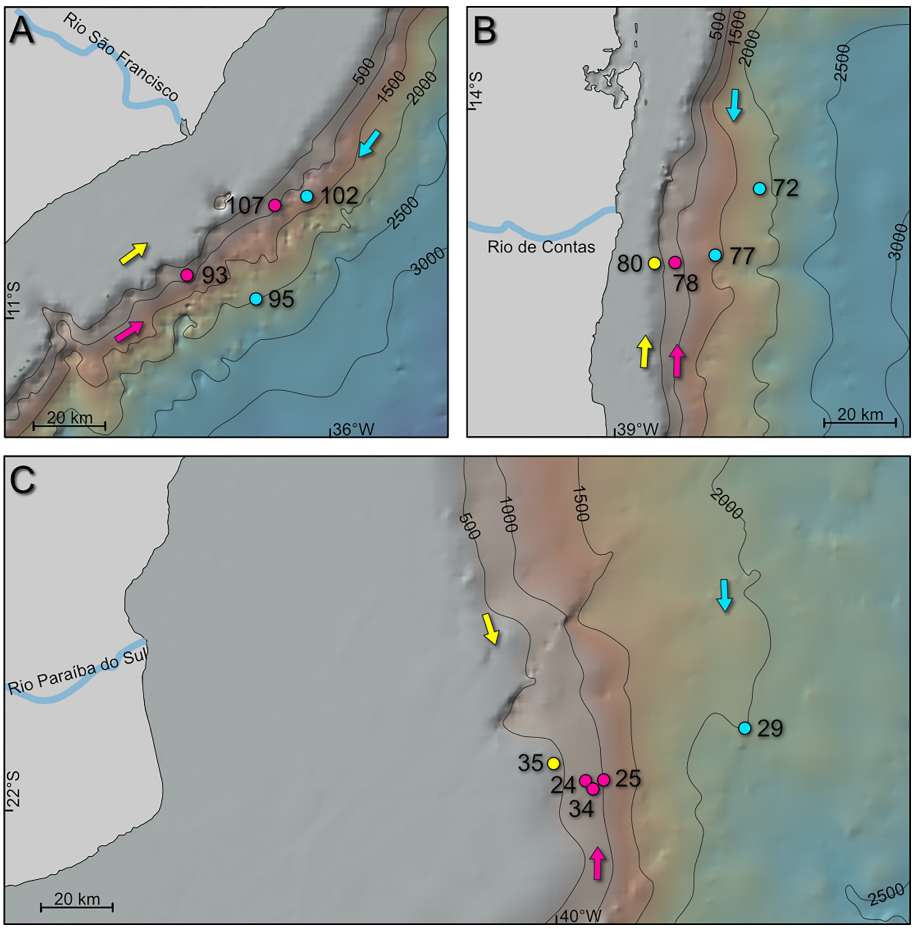

FIGURE 2 | Sample sites of the studied transects of R/V *Meteor* cruise M125: **(A)** Transect 7 off Rio Sao Francisco at 11°S; **(B)** Transect 6 off Rio de Contas at 14°S; **(C)** Transect 2 off Rio Paraíba do Sul at 22°S. Arrows indicate direction of South Atlantic Central Water (SACW; yellow), Antarctic Intermediate Water (AAIW; pink), and North Atlantic Deep Water (NADW; blue), respectively. Maps were created with GeoMapApp (www.geomapapp.org), using the base map of Ryan et al. (2009).

is considerably wider compared to the north and may reach a width of up to 90 km (**Figure 2C**; Martins and Coutinho, 1981; Knoppers et al., 1999). The upper slope is characterized by bottom current-induced and contour-parallel erosional ridges (Viana et al., 2002; Bahr et al., 2016). Contouritic deposits shaped by bottom currents characterize the middle and lower slope of the Campos Basin (Viana, 2001).

Four major water masses strongly affect the Brazilian continental margin to a water depth of 3500 m: the Tropical Water (TW), the South Atlantic Central Water (SACW), the Antarctic Intermediate Water (AAIW) and the North Atlantic Deep Water (NADW; **Figure 1**; Stramma and England, 1999; da Silveira et al., 2020). The warm and saline TW represents the uppermost layer and extends to a depth of 150 m. Beneath the TW, the nutrient-rich SACW with salinities around 35.8 prevails to a depth of 500 m. Sediments transported from the shelf, facilitated by the complex channel system, are considered a major source of organic matter input to the continental margin and contribute to an enhanced nutrient availability within the SACW (Braga et al., 2008). SACW is generated in the South Atlantic at about 40°S by the Brazil- and Falkland Currents (Stramma and England, 1999). It circulates as subtropical SACW within the Southern Subtropical Gyre and is largely driven by the Brazil Current (BC) (Peterson and Stramma, 1991; Stramma and England, 1999). The BC reaches current velocities between 50-80 cm s^{-1} in the subtropical SACW at the Campos Basin (de Mello e Sousa et al., 2006). At about 20°S, part of the SACW is deflected northwards (Stramma and England, 1999; da Silveira et al., 2020). Slightly lower salinities distinguish it from the subtropical SACW (Stramma and England, 1999). The tropical branch of the SACW, as well as the underlying AAIW, are controlled by the North Brazil Undercurrent (NBUC), which is formed mainly in the northern Drake Passage and the Falkland Current Loop at about 40°S and flows towards the north along the eastern continental margin of South America (Stramma and England, 1999). The AAIW, present at water depths between 500 and 1100 m, is distinguishable from SACW by lower salinities of about 34.2 (Mémery et al., 2000; da Silveira et al., 2020; Raddatz et al., 2020). The equatorward flowing NBUC reaches current velocities of up to 80 cm s^{-1} in the tropical SACW (da Silveira et al., 2020) and up to 30 cm s^{-1} in the underlying AAIW (Viana, 2001). The layer of the AAIW at the Brazilian continental slope provides an ideal habitat for cold water coral (CWC) mounds

which are mainly known from the Campos Basin at depths of 800-900 m (Viana et al., 1998; Bahr et al., 2016; Raddatz et al., 2020). Below the AAIW lies the upper North Atlantic Deep Water (UNADW), which is carried by the Deep Western Boundary Current (DWBC) from the Northern Hemisphere into the South Atlantic (Stramma and England, 1999; da Silveira et al., 2020). It achieves current speeds up to 20 cm s^{-1} in the study area (De Madron and Weatherly, 1994) and is characterized by lower nutrient levels compared to its overlying water mass layers (da Silveira et al., 2020; Raddatz et al., 2020).

3 MATERIAL & METHODS

3.1 Stations and Sample Material

All samples used in this study were obtained during R/V METEOR expedition M125 'SAMBA' along the Brazilian Margin (Bahr et al., 2016). They were taken as multicores or box cores, from which the upper 0.5 cm or 1 cm of sediment were used for foraminiferal analysis, respectively. The internal diameter of the multicore tubes was 10 cm. For the box corer samples, ~78.5 cm^3 of surface sediment (1cm depth) was removed using the MUC tube. Samples were partitioned for the measurement of various parameters (e.g., benthic foraminifera, grain size, bulk geochemistry). For calculating the benthic foraminiferal density, the analyzed 'real' sediment volume was calculated based on sediment density and analyzed dry weight. A total of 13 surface samples, stained with Rose Bengal, were selected from bathymetric transects 2, 6 and 7 of the cruise. They range from the upper to lower slope between 400 and 2000 m water depth. Transect 2 represents the southernmost transect at approximately 22°S, consisting of 5 stations (24, 25, 29, 34, 35) in water depths ranging from 430 to 2019 m. Transects 6 and 7 are located about 800 km and 1100 km further north, respectively. At 14°S, transect 6 spans four stations (72, 77, 78, 80) at water depths between 420 and 1738 m. Four stations from transect 7 (93, 95, 102, 107) are located at 11°S between 924 and 1900 m (**Table 1**).

3.2 Sedimentological Parameters

Grain size analysis (**Table 2; Figure 3**) was performed with a particle analyzer *via* laser diffraction (CILAS 1064) at the Institute of Chemistry, Department of Geochemistry, Universidade Federal Fluminense (UFF), Brazil. The analysis was conducted with decarbonized samples free of organic matter by adding 1M HCl and 30% hydrogen peroxide. For particle dispersion sodium hexametaphosphate solution (4%) was added before the laser analysis.

Total organic carbon (TOC) and total nitrogen (TN) contents, and their stable carbon ($\delta^{13}C_{org}$) and nitrogen ($\delta^{15}N$) isotopes were measured in approximately 60 mg of decarbonized, macerated sediment samples. They were analyzed in the PDZ Europa ANCA-GSL elemental analyzer at the UFF, coupled to a 20-20 PDZ Europa isotope ratio mass spectrometer (SERCON Ltd. Cheshire UK). Isotope ratios were reported relative to the Vienna Pee Dee Belemnite (V-PDB) international standard for carbon and atmospheric N_2 for nitrogen. The analytical precision for standards was within ±0.14‰ for $\delta^{13}C_{org}$ and ±0.13‰ for $\delta^{15}N$.

3.3 Benthic Foraminifera

All samples were stored between April 2016 to March 2017 in buffered 4% formaldehyde solution to which had been added Rose Bengal with a concentration of 1g/L. The samples were wet sieved with water over a 63 μm sieve and then dried at 30°C. A dry splitter was used for sample partitioning. All benthic foraminiferal tests > 63 μm of the whole sample or split were counted, yielding at least 400 individuals per sample. Stained (Rose Bengal) and unstained specimens were counted separately, allowing to differentiate the living and dead assemblages in the total faunas (see Bernhard, 2000 for review). Only brightly stained specimens were counted as living. For porcelaneous tests, pale pink stained specimens were distinguished from white ones. Due to very low amounts of stained foraminifera, their evaluation is approached with caution.

TABLE 1 | Position and hydrological parameters of the selected transects and sample sites of Meteor cruise M125.

Station ID	Sample #	Lat. S°	Long. W°	Watermass	Water depth (mbsl)	Temp. (C°)	Salinity	O_2 (ml/l)	Density kg/m^3
Transect 2									
M125-24-2	24	21° 55,924'	39° 54,122'	AAIW	872	4.66	34.36	4.55	1027.206
M125-25-2	25	21° 55,924'	39° 51,508'	AAIW	960	4.15	34.35	4.53	1027.254
M125-29-9	29	21° 48,732'	39° 32,031'	NADW	2019	3.49	34.95	5.42	1027.799
M125-34-1	34	21° 56,960'	39° 53,112'	AAIW	876	4.65	34.35	4.56	1027.202
M125-35-2	35	21° 53,607'	40° 00,282'	SACW	430	12.53	35.14	4.56	1026.596
Transect 6									
M125-72-2	72	14° 12,774'	38° 36,528'	NADW	1738	4.15	34.95	5.06	1027.727
M125-77-2	77	14° 23,200'	38° 43,551'	NADW	1394	4.18	34.73	4.04	1027.551
M125-78-2	78	14° 24,356'	38° 50,070'	AAIW	845	5.31	34.40	4.29	1027.166
M125-80-3	80	14° 24,559'	38° 53,307'	SACW	422	11.22	34.97	4.24	1026.713
Transect 7									
M125-93-2	93	10° 24,285'	36° 23,840'	AAIW	955	4.04	34.44	4.05	1027.337
M125-95-2	95	10° 56,728'	36° 12,348'	NADW	1901	3.92	34.96	5.31	1027.763
M125-102-2	102	10° 40,032'	36° 03,953'	NADW	1256	4.14	34.71	4.06	1027.539
M125-107-1	107	10° 41,489'	36° 09,142'	AAIW	924	4.00	34.40	4.00	1027.309

AAIW, Antarctic Intermediate Water; NADW, North Atlantic Deep Water; SACW, South Atlantic Central Water.

TABLE 2 | Sediment analyses of surface samples.

Sample #	Device	Interval	TOC wt.%	TN wt.%	C:N (bulk)	δ15N bulk (per mil)	δ13C bulk (per mil VPDB)	clay %	silt %	sand %	mean grain size (μm)	median grain size (μm)
Transect 2												
24	BC/VV	0-1	0.64	0.08	8.0	6.39	-22.24	11.7	88.3	–	8.6	7.4
25	MUC	0-0.5	0.40	0.04	10.0	6.25	-22.42	22.0	78.0	–	6.3	4.8
29	MUC	0-1	1.69	0.21	8.0	7.06	-21.01	36.4	63.7	–	4.3	3.2
34	BC/VV	0-1	0.49	0.06	8.2	7.29	-21.64	12.0	75.5	12.5	19.5	10.8
35	MUC	0-0.5	0.23	0.03	7.7	4.65	-22.19	33.9	66.1	–	4.4	3.5
Transect 6												
72	MUC	0-0.5	2.96	0.25	11.8	6.26	-21.56	23.8	76.2	–	6.5	5.3
77	MUC	0-0.5	1.86	0.23	8.1	6.73	-20.71	23.2	76.8	–	7.5	5.9
78	MUC	0-0.5	1.46	0.19	7.7	4.82	-20.73	14.9	73.6	11.5	21.0	11.5
80	MUC	0-0.5	1.28	0.13	9.8	4.94	-22.07	13.8	56.3	29.9	30.5	14.4
Transect 7												
93	MUC	0-0.5	1.40	0.18	7.8	4.80	-21.04	37.4	62.7	–	3.8	2.9
95	MUC	0-0.5	1.42	0.16	8.9	5.41	-22.23	33.7	66.3	–	4.2	3.0
102	MUC	0-0.5	1.00	0.13	7.7	5.40	-20.86	28.4	71.6	–	5.1	3.7
107	BC	0-0.5	1.15	0.16	7.2	5.56	-20.79	26.3	73.7	–	7.0	5.2

BC, Boxcorer; VV, Van Veen Grab; MUC for Multicorer.

Epi- and infaunal microhabitats were assigned according to Schönfeld (1997); Sen Gupta (2002); Murray (2006); Jorissen et al. (2007) and Rasmussen and Thomsen (2017).

The assessment of tubular agglutinated species is challenging as almost all tests are fragmented. Tubular fragments were thus counted individually, but excluded from the total species dataset to avoid over-representation (Goineau and Gooday, 2017). Tubular fragments comprise the species *Rhabdammina abyssorum*, *Rhabdamminella cylindrica*, *Rhizammina algaeformis* and *Saccorhiza ramosa*. Likewise, species that were not deposited autochthonously but had clearly been transported were removed, including *Cribroelphidium* spp. and *Discorbis williamsoni* (see also **Appendix 2**). To document and assess the role of these excluded taxa, they are presented in **Table 3**, referred to an expanded matrix that includes tubular fragments and transported specimens.

The species *Globocassidulina subglobosa* and *G. crassa* were often not distinguishable from each other. We therefore combined them under the name *G. subglobosa/crassa*.

For diversity analysis, Fisher's α and Shannon *H* indices were calculated (Fisher et al., 1943; Shannon and Weaver, 1949). Due to the very low numbers of stained foraminiferal tests, these calculations were limited to the total assemblages. The dimensionless Fisher's α, based on logarithmic series, facilitates the comparison of species richness between different habitats as well as samples of different size (Peet, 1974; Murray, 2006). Species diversity, expressed *via* Shannon *H*, incorporates rare species that make a smaller contribution (Peet, 1974; Murray, 2006). To estimate foraminiferal densities, the total absolute number of foraminifera for each sample was normalized to 10 cubic centimeter (ccm).

3.4 Multivariate Statistical Analysis

The software package Past 4.02 (Hammer et al., 2001) was used for multivariate statistical analysis. Since abundances of living specimens were very low, statistical analyses were limited to the total fauna (live + dead specimens), as previously implemented by e.g., de Mello e Sousa et al. (2006) for the Campos Basin.

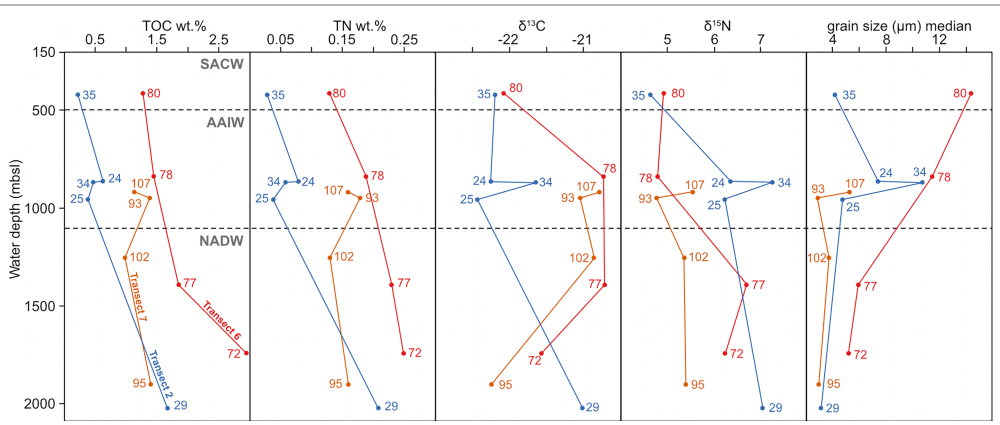

FIGURE 3 | Main sedimentological properties of transects 2, 6 and 7 plotted with increasing water depth. The numbers refer to the samples of the respective transect. Transect 2 is shown in blue, transect 6 in red and transect 7 in orange.

TABLE 3 | Diversity of benthic foraminifera > 63 µm concerning the total, living and dead fauna.

Sample #		t	s	s/10 ccm	% of total	hya. %	agg. %	porc. %	epifaunal %	infaunal %	epi- to infaunal %	*transp. s. %	tub. fragm. %	*H*	Fisher's α
Transect 2															
24	**total**	**130**	**2576**	**82,106**		**86.9**	**10.6**	**2.5**	**32.3**	**54.8**	**3.3**	**1.3**	**0.1**	**2.78**	**12.2**
AAIW	living	21	46	914	1.1	49.7	49.8	0.5	66.6	0.4	33.0				
	dead	130	2530	81,192	98.9	87.3	10.2	2.5	31.9	55.4	3.0				
25	**total**	**97**	**604**	**43,587**		**86.0**	**12.6**	**1.4**	**28.6**	**61.8**	**1.9**	**1.8**	**0.4**	**2.91**	**11.7**
AAIW	living	41	108	2,461	5.6	72.9	26.7	0.4	74.6	15.8	4.8				
	dead	86	496	41,126	94.4	86.8	11.7	1.4	25.8	64.6	1.7				
29	**total**	**89**	**626**	**57,454**		**77.7**	**15.8**	**6.5**	**39.4**	**49.3**	**4.5**	**3.7**	**1.0**	**3.07**	**8.3**
NADW	living	26	40	2,741	4.8	41.1	52.7	6.2	64.9	29.1	6.0				
	dead	87	586	54,713	95.2	79.5	14.0	6.5	38.2	50.3	4.5				
34	**total**	**117**	**1123**	**165,232**		**87.4**	**10.5**	**2.1**	**34.5**	**49.2**	**1.4**	**3.8**	**0**	**2.65**	**10.6**
AAIW	living	12	22	502	0.3	0.7	93.1	6.1	98.6	1.4	0				
	dead	113	1101	164,730	99.7	87.7	10.3	2.1	34.3	49.3	1.4				
35	**total**	**67**	**621**	**320,694**		**86.5**	**5.7**	**7.8**	**31.9**	**55.6**	**0.2**	**1.8**	**0**	**2.59**	**6.0**
subtr. SACW	living	22	58	7,242	2.3	72.6	27.4	0.0	36.6	63.4	0				
	dead	65	563	313,452	97.7	86.8	5.2	7.9	31.8	55.4	0.2				
Transect 6															
72	**total**	**86**	**530**	**54,496**		**75.5**	**14.3**	**10.2**	**37.5**	**45.6**	**3.2**	**5.0**	**0**	**3.17**	**10.2**
NADW	living	32	57	3,184	5.8	81.1	18.6	0.3	63.6	36.0	0.4				
	dead	83	473	51,312	94.2	75.2	14.0	10.8	35.9	46.2	3.4				
77	**total**	**81**	**429**	**98,955**		**87.8**	**5.5**	**6.7**	**32.9**	**52.8**	**0.5**	**4.4**	**0.4**	**2.79**	**7.9**
NADW	living	22	45	2,938	3.0	99.1	0.5	0.3	70.9	28.7	0.4				
	dead	73	384	96,017	97.0	87.5	5.6	6.9	31.8	53.6	0.5				
78	**total**	**99**	**692**	**358,733**		**83.7**	**6.0**	**10.3**	**40.6**	**45.7**	**2.2**	**4.4**	**0**	**3.08**	**9.5**
AAIW	living	28	37	11,174	3.1	79.7	20.1	0.2	20.5	59.6	0.1				
	dead	92	655	347,559	96.9	83.9	5.5	10.6	41.2	45.3	2.2				
80	**total**	**108**	**1067**	**798,547**		**80.0**	**11.9**	**8.1**	**29.4**	**52.9**	**2.3**	**4.8**	**0**	**3.18**	**9.3**
tropical SACW	living	31	52	4,918	0.6	65.2	33.5	1.2	3.4	64.1	31.3				
	dead	101	1015	793,629	99.4	80.1	11.7	8.2	29.6	52.9	2.2				
Transect 7															
93	**total**	**144**	**2363**	**13,394**		**68.2**	**18.7**	**13.0**	**27.8**	**42.4**	**1.6**	**2.6**	**2.1**	**4.02**	**23.3**
AAIW	living	48	128	795	5.9	83.3	10.4	6.3	39.7	50.9	3.0				
	dead	141	2235	12,599	94.1	67.3	19.3	13.5	27.0	41.9	1.6				
95	**total**	**98**	**714**	**5,496**		**65.4**	**27.7**	**6.9**	**23.5**	**57.2**	**3.8**	**1.8**	**8.8**	**3.53**	**18.1**
NADW	living	28	53	269	4.9	71.0	19.2	9.8	21.8	45.1	2.1				
	dead	93	661	5,227	95.1	65.1	28.1	6.8	23.6	57.9	3.9				
102	**total**	**107**	**996**	**7,096**		**76.8**	**16.7**	**6.5**	**22.6**	**56.2**	**3.1**	**1.8**	**9.0**	**3.51**	**16.1**
NADW	living	40	114	810	11.4	86.5	10.3	3.2	39.4	48.0	11.4				
	dead	102	882	6,286	88.6	75.6	17.5	6.9	20.5	57.2	2.0				
107	**total**	**92**	**824**	**5,008**		**66.8**	**22.4**	**10.8**	**27.9**	**51.5**	**1.0**	**2.8**	**4.0**	**3.68**	**13.2**
AAIW	living	17	29	196	3.9	78.4	17.6	4.1	24.3	68.9	0				
	dead	89	795	4,812	96.1	66.3	22.6	11.0	28.0	50.8	1.0				

Values in bold refer to the total fauna used for the analyses. Presented are the absolute number of taxa (t), and analyzed specimens (s); specimens per 10 cubic centimeters (s/10 ccm); proportions of living and dead specimens within the total fauna (% of total); proportions of different test types agglutinated, calcareous hyaline and porcelaneous; epi- and infaunal proportions. Asterisks indicate that the values of transported specimens and tubular fragments have been calculated with reference to the whole assemblages. Diversity indices are Shannon H and Fisher's alpha (α).

A hierarchical Q-mode cluster analysis (HCA; UPGMA algorithm, Bray-Curtis similarity index) was performed to identify groups of samples based on their similarity and dissimilarity. Based on a similarity percentage analysis (=SIMPER analysis, Bray-Curtis similarity index), the contribution of each species to the dissimilarity of each cluster is obtained for the total fauna (**Table 4**).

To contextualize foraminiferal data and environmental parameters, a canonical correspondence analysis (CCA) was conducted. A CCA is based on unimodal relationships between species abundances and site-specific environmental variables *via* synthetic ordination axes (ter Braak and Verdonschot, 1995; Ramette, 2007; Paliy and Shankar, 2016). Hydrographic properties such as salinity and oxygen are excluded as limiting factors as the faunal composition is unlikely to be affected by the rather uniform and stable values for salinity and relatively high oxygen concentrations (**Table 1**; de Mello e Sousa et al., 2006). However, parameters reflecting export productivity and sedimentation show considerably greater variability. We therefore included six parameters in the CCA that exhibit the greatest impact on the benthic fauna (TOC, TN, $\delta^{13}C_{org}$, $\delta^{15}N$, proportion of silt and clay; **Table 2**).

Since rare species tend to be overestimated in a CCA (Legendre and Legendre, 1998; Ramette, 2007), only species that occur to >

TABLE 4 | Composition of the total benthic foraminiferal community *via* a SIMPER analysis based on clusters, see **Figure 4**.

Taxon	Av. dissim	Contrib. %	Cumulative %	CB Tr. 2	BB Tr. 6	BB Tr. 7
Globocassidulina subglobosa/crassa	10.1	15.8	15.8	**32.4**	14.9	6.4
Rosalina spp.	4.9	7.6	23.4	3.3	**14.6**	1.1
Bolivina variabilis	4.8	7.5	30.9	0.9	**11.5**	9.0
Bolivina subreticulata	4.2	6.5	37.4	0.8	6.3	**11.3**
Nuttallides umbonifer	3.2	4.9	42.3	**8.0**	0.6	0.1
Alabaminella weddellensis	2.8	4.4	46.7	**7.2**	2.0	
Epistominella exigua	2.5	4.0	50.7	2.9	5.1	**7.4**
Bolivina striatula	1.5	2.4	53.0	**4.8**	1.7	1.7
Bolivina albatrossi	1.0	1.6	54.6	0.6	0.5	**2.7**
Sigmavirgulina tortuosa	0.9	1.4	56.0	0.1	0.8	**2.4**
Pyrgoella irregularis	0.9	1.4	57.4	**1.7**	1.6	0.4
Cassidulina laevigata	0.8	1.3	58.7	1.1	**2.4**	0.6
Trochammina advena	0.8	1.3	59.9	**2.1**	0.8	0.7
Miliolinella subrotunda	0.8	1.2	61.2	0.6	**2.4**	0.7
Nonionella spp.	0.8	1.2	62.4	1.9	**2.5**	1.0
Bolivina spathulata	0.7	1.1	63.5	1.3	**1.4**	0.6
Sigmoilopsis schlumbergeri	0.7	1.0	64.6			**1.8**
Gyroidinoides soldanii	0.6	0.9	65.5	**1.4**	0.9	0.3
Neoconorbina terquemi	0.6	0.9	66.4	**1.4**		0.1
Cassidulinoides bradyi	0.6	0.9	67.3	**1.5**	0.2	
Gavelinopsis praegeri	0.6	0.9	68.2	0.4	0.7	**1.4**
Glomospira gordialis	0.6	0.9	69.1	0.4	0.7	**1.3**
Cibicidoides pachyderma	0.5	0.9	69.9	0.3	0.2	**1.6**
Cibicides/Cibicidoides sp. juv.	0.5	0.8	70.7	1.1	**1.6**	0.3
Uvigerina peregrina	0.5	0.8	71.5	0.3	0.2	**1.3**
Trochammina squamata	0.5	0.7	72.2	**1.1**	0.6	0.2
Cibicidoides wuellerstorfi	0.5	0.7	73.0	0.3		**1.2**
Valvulineria minuta	0.5	0.7	73.7	**0.9**	0.3	0.5
Ioanella tumidula	0.4	0.7	74.4	0.1	**1.2**	
Paratrochammina challengeri	0.4	0.7	75.0	0.1	0.6	**0.8**

CB, Campos Basin; and BB, Brazil Basin; Av. dissim= Average dissimilarity. Shown are the first cumulative 75% of all taxa. The Bray-Curtis index was used; the average overall dissimilarity is 64.1. The highest value of a species between the clusters/transects is marked in bold.

3% in at least one sample were included; indeterminate taxa were removed, tubular fragments and transported specimens were excluded.

4 RESULTS

4.1 Environmental Characteristics

4.1.1 Grain Size Distribution

In the Campos Basin at transect 2 (22°S), mean grain sizes between 4.3 and 19.5 µm were recorded. A wider range of 6.5 to 30.5 µm is observed in the samples of transect 6 in the Brazil Basin (14°S). Finer sediment was encountered in transect 7 (11°S) with mean grain sizes between 3.8 and 7 µm. Sand contents were only recorded in sample 34 from transect 2 (12.5%, AAIW in 876 m) as well as samples 78 (11.5%, AAIW in 845 m) and 80 (29.9%, SACW in 422 m) from transect 6, while the remainder consist of silt and clay only (**Table 2**).

In the Campos Basin, sample 34 was taken within a cold-water coral (CWC) mound sequence, and sample 24 was retrieved from the marginal mound facies, covered with corals only at the surface (Bahr et al., 2016). Both samples contain the highest mean grain sizes within transect 2 of 19.5 µm (sample 34) and 8.6 µm (sample 24), as well as the highest silt contents ranging from 76 to 88%, and lowest clay contents at about 12% in each case (**Table 2**). Coarsest mean grain sizes within transect 6 are present in SACW sample 80 (422 m) with 30.5 µm and AAIW sample 78 (845 m) with 21 µm on average (**Table 2**). In transect 7, mean grain sizes reach their maximum in AAIW sample 107 (924 m) with only 7 µm. Clay contents are highest in this transect and vary between 26 and 37% (**Table 2**).

4.1.2 Total Organic Carbon, Total Nitrogen Contents and Their Stable Isotopes $\delta^{13}C_{org}$ and $\delta^{15}N$

The range of total organic carbon within the sediment is 0.2-3.0 wt.% with the maximum being measured in sample 72 (transect 6, NADW, 1738 m). Total nitrogen contents also reach their maximum of 0.3 wt. % in sample 72. In the Campos Basin (22°S) TN levels are 0.03-0.2, whereas they are 0.1-0.3 wt. % in the Brazil Basin transects (11-14°S). The C:N ratios range from 7 to 12 for the entire data set, with only sample 72 yielding a value exceeding 10 (**Table 2**).

The stable carbon isotope $\delta^{13}C_{org}$ within the bulk organic matter spans values between -22.4 and -20.7 ‰ for the entire data set. $\delta^{15}N$ content ranges from 4.7 to 7.3 ‰ of the bulk sediment (**Table 2**).

4.2 Benthic Foraminifera

4.2.1 Total Assemblage Composition

A total of 278 species was identified, of which 139 have hyaline tests, 104 are agglutinated, and 35 have a porcelaneous test.

Densities of benthic foraminifera per 10 ccm are higher in transect 2 and 6 (44 000-800 000 specimens/10 ccm) than in transect 7 (5 000-13 000 specimens/10 ccm). The highest density in transect 2 in the Campos Basin was observed in sample 35 associated with subtropical SACW (321 000 specimens/10 ccm). Population density is even higher in sample 80 associated with tropical SACW in the Brazil Basin (799 000 specimens/10 ccm; **Table 3**). A comparison of samples associated with AAIW and NADW reveals that transect 7, with a maximum of 13 000 specimens/10 ccm, has generally reduced population densities than transect 2 (max. 165 000 s/10 ccm for AAIW and NADW) and 6 (max. 359 000 s/10 ccm for AAIW and NADW; **Table 3**). However, species richness, indicated by Fisher's α, is lower in transects 2 and 6 (α=6-12) than in the northern transect 7 (α=13-23; **Table 3**). This is also reflected by the Shannon *H* index, where rare species contribute less (Murray, 2006). Smaller values were calculated for transect 2 (*H*=2.6-3.1), they increased slightly in transect 6 (*H*=2.8-3.2) and highest in transect 7 (*H*=3.5-4.0; **Table 3**; see also **Appendix 1**).

Calcareous-hyaline species predominate all investigated transects, with the highest abundances of > 86% recorded in transect 2 (samples 24, 25, 34, 35) and transect 6 (sample 77; **Table 3**). *Globocassidulina subglobosa/crassa* is abundant across all studied transects. However, it is more frequent along the Campos Basin (32%) than along the Brazil Basin transects (6-15%; result of the SIMPER analysis see **Table 4**). Important hyaline taxa that further define the dataset are *Rosalina* spp., *Bolivina variabilis* and *B. subreticulata*, which are more abundant in the Brazil Basin (each taxon occurs at > 11% in transect 6 or 7) than in the Campos Basin (each taxon occurs < 4%; according to the SIMPER analysis in **Table 4**). Agglutinated tests are more frequent in transect 7 (17-28%) than in transects 2 and 6 (6-16%; **Table 3**), with a broad range of taxa being responsible (e.g., cribrostomoidids, trochamminids; see **Appendix 2**). Additionally, the proportion of tubular fragments is increased in transect 7 (2-9%) compared to the southern sample sites (0-1%), with *Saccorhiza ramosa* fragments being most abundant (**Table 3** and **Figure 5**). Frequently occurring porcelaneous taxa include *Pyrgoella irregularis* and *Miliolinella subrotunda* in all transects (**Tables 3**, **4**).

Infaunal species dominate the data set. In the Campos Basin they make up 49-62% of the total fauna, while they range between 42 and 57% in the Brazil Basin (**Table 3**).

4.2.2 Total (Live + Dead) Assemblage Distributions

According to the hierarchical cluster analysis (HCA; cophenetic correlation coefficient: 0.88), the data set of the total assemblage can be divided into two major clusters representing the Campos Basin (cluster 'CB') and the Brazil Basin (cluster 'BB'), respectively. Cluster 'CB' comprises all transect 2 samples, while Cluster 'BB' is internally subdivided into two groups of samples corresponding to transects 6 and 7 (**Figure 4**). SIMPER analysis reveals that 30 taxa determine 75% of the cumulative dissimilarity between clusters and groups (**Table 4**). Cluster 'CB' is distinguished by increased abundances of *Globocassidulina subglobosa/crassa* associated with *Nuttallides umbonifer* and *Alabaminella weddellensis*. In contrast, Cluster 'BB' is mainly determined by an assemblage comprising various bolivinids and *Rosalina* species (**Table 4**).

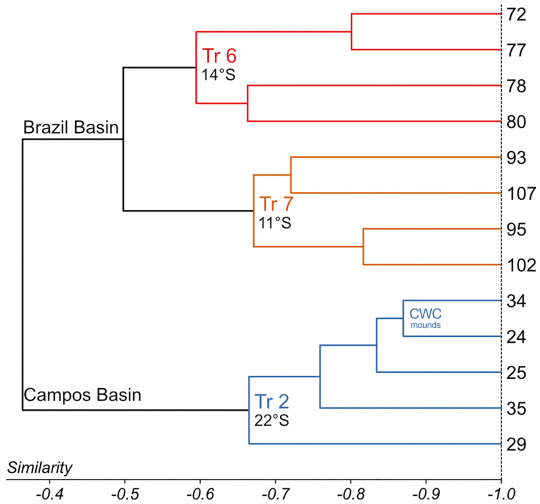

FIGURE 4 | Cluster analysis of the total assemblages of benthic foraminifera > 63 µm. The UPGMA algorithm and Bray-Curtis dissimilarity were used, cophenetic correlation is 0.88. Three clusters could be distinguished, reflecting the surveyed transects (Tr. 2, Tr. 6, and Tr. 7).

A *Globocassidulina subglobosa/crassa* assemblage prevails in the Campos Basin. According to the SIMPER analysis the transect is characterized by *G. subglobosa/crassa* (32%), *Nuttallides umbonifer* (8%), *Alabaminella weddellensis* (7%), *Bolivina striatula* (5%) and *Rosalina* spp. (3%; **Table 4**). *Globocassidulina subglobosa/crassa* and *N. umbonifer* decrease slightly with increasing depth, while *A. weddellensis* increases in the AAIW and NADW samples 24, 25, 29, 34 (**Figure 5**). *Epistominella exigua*, *Rosalina* spp. and *Pyrgoella irregularis* are associated taxa in the deeper sample 29 within the NADW (**Figure 5**). Within the 'CB' cluster, both CWC mound samples 24 and 34 form a distinct subgroup, plotting closest to cluster 'BB'.

The total assemblage of transect 6 at 14°S is mainly determined by *G. subglobosa/crassa* (15%), *Rosalina* spp. (15%), *Bolivina variabilis* (12%), *Bolivina subreticulata* (6%) and *Epistominella exigua* (5%; **Table 4**). Occurrences of *G. subglobosa/crassa* are mainly concentrated on the upper slope within SACW (sample 80) and abundances are substantially reduced when compared to the Campos Basin (**Figure 5**). With increasing depth, assemblages with various species of *Rosalina* determine the benthic fauna of transect 6. In samples 72 and 77, which are associated with NADW, bolivinids become predominant, with *Bolivina variabilis* being most abundant (**Figure 5**).

In transect 7 at 11°S, a *Bolivina* assemblage characterizes the benthic foraminiferal association. The SACW layer was not investigated in this area, so the association only reflects AAIW and NADW samples. The assemblage is composed of *Bolivina*

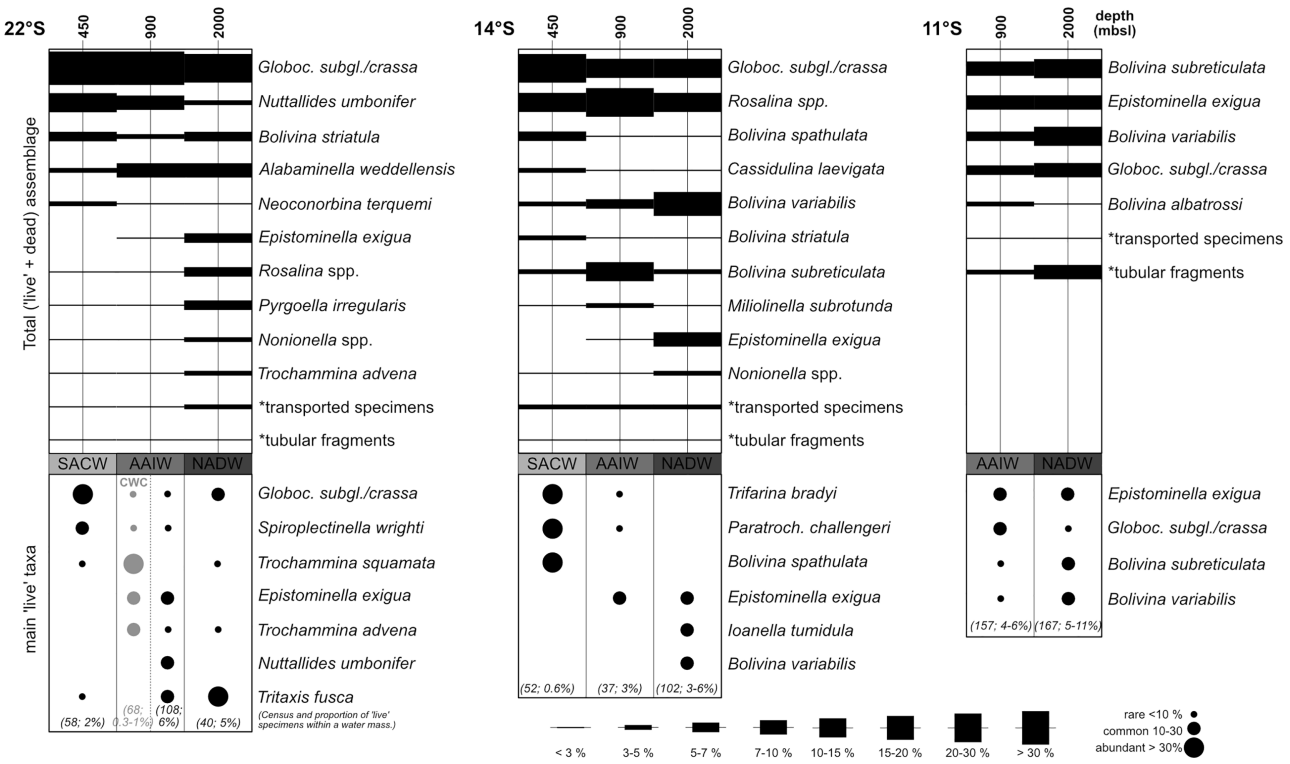

FIGURE 5 | Abundances of benthic foraminiferal taxa > 63 µm in the studied areas at 22°S, 14°S and 11°S relative to water masses. Proportions of transported specimens and tubular fragments indicated by asterisks have been calculated with reference to the whole assemblages (**Table 3**). All taxa that occur with at least 3% in one water mass are plotted. Bars indicate abundances based on the total (live+dead) assemblage. Stained (living) specimens are indicated by circles and given as rare (< 10 %), common (10-30 %), and abundant (> 30 %). The values in parentheses indicate the absolute analyzed census counts and proportions of living specimens.

subreticulata (11%), *Bolivina variabilis* (9%), *Epistominella exigua* (7%) and *Globocassidulina subglobosa/crassa* (6%; **Table 4**). Tubular fragments are common in transect 7 and increase with depth (**Table 3**; **Figure 5**). Bolivinids are slightly more common in deeper NADW samples 95 and 102 than in AAIW samples 93 and 107, where they are accompanied by increased occurrences of *Saccorhiza ramosa* fragments. Associated *Epistominella exigua* occurs equally in both water masses (**Figure 5**). Thus, the assemblages in the Brazil Basin are strongly determined by rosalinids and bolivinids, contrasting a *Globocassidulina* assemblage in the Campos Basin.

4.2.3 Key Environmental Factors and Total Assemblage Distribution

A canonical correspondence analysis (CCA) based on scale type 1 after Legendre and Legendre (1998) explains the relationship between foraminiferal species, environmental variables and sample sites (**Figure 6**). As a function of distance between the variables TOC, TN, $\delta^{13}C_{org}$, $\delta^{15}N$, silt and clay, the canonical axes CCA1 (eigenvalue = 0.28, variance = 58.4%) and CCA2 (eigenvalue = 0.09, variance = 18.1%) explain > 75% of the entire data set.

The sample sites are separated along the axes in terms of their assignment to the 'CB' and 'BB' clusters. Cluster 'CB' (transect 2) plots on negative CCA1 together with the $\delta^{15}N$ and silt vectors. Sample 35 from the upper slope (SACW) and deepest sample 29 (NADW) plot in the positive range of CCA2, more strongly associated with silt. All AAIW samples (24, 25, 34) plot in the negative range and are more strongly associated with $\delta^{15}N$. All caluster 'BB' samples (transects 6 and 7) plot on positive CCA1 in the range of TOC, TN, $\delta^{13}C_{org}$ and clay vectors. Within cluster 'BB', all transect 6 samples plot on negative CCA2, where they are associated with TOC. The samples of transect 7 fall in the positive range of CCA2, within the quadrant of TN, clay and $\delta^{13}C_{org}$ vectors (**Figure 6**).

The *Globocassidulina subglobosa/crassa* assemblage of the Campos Basin falls within the negative range of CCA1. *Globocassidulina subglobosa/crassa*, and *Alabaminella weddellensis* occur rather close to $\delta^{15}N$, while *Trochammina advena* and *Bolivina striatula* plot between the silt and clay vectors (**Figure 6**). *Bolivina spathulata* is the only bolivinid species that contrasts with the clay vector, as it is slightly enhanced in the samples close to the CWC mounds (24, 25). The CCA illustrates that the *G. subglobosa/crassa* assemblage is mainly associated with *Nuttalides umbonifer* at the upper slope (sample 35), while *Alabaminella weddellensis* is predominant in the deeper areas (samples 24, 25, 34; **Figures 5**, **6**).

The *Rosalina* assemblage of transect 6 plots on positive CCA1 and negative CCA2. *Rosalina* spp., *Miliolinella subrotunda* and *Cassidulina laevigata* are associated with relatively higher organic carbon levels (**Figure 6**).

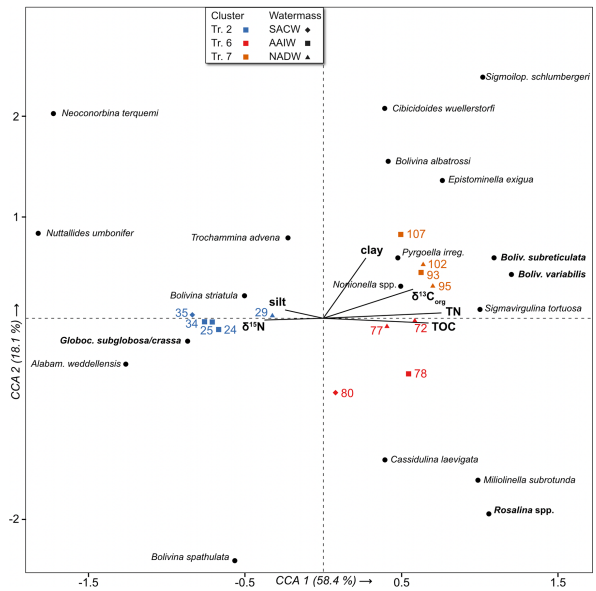

FIGURE 6 | Canonical correspondence analysis, scale type 1, with environmental parameters $\delta^{15}N$, $\delta^{13}C_{org}$, clay and silt contents, total organic carbon (TOC) and total nitrogen (TN). Taxa with abundances > 3% in at least one sample are shown. Colour coding represents affiliation to a cluster; symbols indicate the water mass of a sample.

The CCA shows that various infaunal species of the *Bolivina* assemblage, such as *Bolivina subreticulata*, *Sigmavirgulina tortuosa*, *Bolivina albatrossi* and *Sigmoilopsis schlumbergeri* occur preferentially in the clay-rich samples of transect 7, all plotting in the positive range of CCA1 and CCA2. The associated species *Epistominella exigua*, *Pyrgoella irregularis* and *Nonionella* spp. also show good concordance with higher clay contents.

4.2.4 Stained (Living) Assemblage Composition

Between 22 to 128 stained specimens were picked per sample, exceeding 100 specimens in only three samples (25, 93, 102). The contribution of living individuals to the total assemblage ranges from 0.3% to 11%, being highest in transect 7 (**Table 3**). Similar to the total assemblages, the number of living foraminifera per 10 ccm is the lowest in transect 7 (200-800 specimens/10 ccm); it is slightly increased at transect 2 in the Campos Basin (500-7000 specimens/10 ccm) and highest in transect 6 in the Brazil Basin (3000-11 000 specimens/10 ccm; **Table 3**).

Stained specimens belong to 147 species (63 hyaline, 61 agglutinated, 23 porcelaneous) all of which are represented among dead tests. The biocoenosis of transect 2 from the Campos Basin consists primarily of *G. subglobosa/crassa, Trochammina squamata*, and *Tritaxis fusca*. Stained specimens of *G. subglobosa/crassa* are abundant on the upper slope within the SACW in sample 35, associated with common occurrences of *Spiroplectinella wrighti* (**Figure 5**). AAIW samples 34 and 24, which were retrieved directly from, or very close to, a cold-water coral mound, contain mainly stained *Trochammina squamata* with *Epistominella exigua* and *Trochammina advena* (**Figure 5**). In adjacent AAIW sample 25, located distal to the coral mounds, *E. exigua, Nuttallides umbonifer* and *Tritaxis fusca* occur commonly within the biocoenosis. In sample 29, associated with NADW, *Tritaxis fusca* was the most common species in the live assemblage (**Figure 5**).

In the Brazil Basin at transect 6, the living assemblage within SACW (sample 80) consists of abundant *Trifarina bradyi*, *Paratrochammina challengeri* and *Bolivina spathulata*. Stained specimens of *Epistominella exigua* are common in sample 78 associated with AAIW. With increasing depth, live individuals of *E. exigua* are associated with live *Ioanella tumidula* and *Bolivina variabilis* in the NADW (**Figure 5**). The biocoenosis of transect 7 is mainly determined by *E. exigua, G. subglobosa/crassa, Bolivina subreticulata* and *B. variabilis* and shows the highest resemblance to the total assemblage (**Figure 5**; see also **Appendix 2**).

5 DISCUSSION

5.1 Patterns of Foraminiferal Diversity, Density, and Distribution

Diversity analyses indicate that the benthic foraminiferal faunas correspond to typical assemblages from well-oxygenated deep-sea environments (Gooday, 2003; Murray, 2006). Calculated Fisher's α and Shannon *H* indices are comparable to the species diversity for the South Atlantic (Murray, 2006). Lower diversity indices in transect 2 (α=6-12; H=2.6-3.1), slightly increased indices in transect 6 (α=8-10; H=2.8-3.2), followed by higher indices in transect 7 (α=13-23; H=3.5-4.0) may reflect a general increase in foraminiferal diversity along the Brazilian Margin from South to North (**Table 3**; **Appendix 1**). Clearly, more studies with a higher spatial resolution are needed to test the robustness of this pattern.

No direct relation is observed between benthic foraminiferal diversity and density. The latter is substantially lower in transect 7 (5 000-13 000 specimens/10 ccm) than in transects 2 and 6 (44 000-800 000 specimens/10 ccm; **Table 3**) for both total and living faunas. Thus, the population density of transect 7 is more similar to the eastern South Atlantic (cf. Schmiedl et al., 1997). The densities of transect 2 agree well with those measured in the Campos Basin by de Mello e Sousa et al. (2006), while transect 6 even exceeds these values.

Lower numbers of foraminiferal tests per 10 cubic centimeter in transect 7 do not result in a lower diversity, as might be expected from other faunal studies, e.g., Jorissen et al. (1995) and Fontanier et al. (2002). A low number of specimens per 10 ccm coupled with a high species heterogeneity could be linked to increased inputs of phytodetritus (Lambshead and Gooday, 1990; Gooday and Rathburn, 1999). This is supported by occurrences of species sometimes associated with phytodetritus such as *Pyrgoella irregularis* in transect 7 (**Figure 6** and **Appendix 2**; Gooday, 1988). A higher sampling resolution would be necessary to gain more detailed insight into the observed patterns of species density and diversity.

Percentages of stained specimens in all transects (0.3-11%; **Table 3**) are consistent with the observations of de Mello e Sousa et al. (2006), who describe similarly low values from the Campos Basin. It is a common observation in deep-sea samples that only

a small proportion of benthic foraminiferal specimens consists of living individuals (Murray, 2006). Great variation in the volume of protoplasm (e.g., during periods of low food influx) in certain species further complicates the recognition of stained tests and thus limits the application of Rose Bengal (Linke and Lutze, 1993; Murray, 2006).

Regarding the distribution of different test types, a northward trend can be observed. Agglutinated tests are relatively more abundant in transect 7 (17-28%) compared to both southern transects (6-16%; tab. 3). This is further underlined when comparing the proportions of tubular fragments between transect 7 (2-9%) and transects 2 and 6 (0-1%; **Table 3**). In transect 7, tubular fragments mainly include *Saccorhiza ramosa* (**Figure 7**), which prefers areas with less pronounced bottom current activity (Altenbach et al., 1988; Gooday, 2003). Individual species of each test type will be examined in more detail in the following chapters.

5.2 Controlling Factors of Faunistic Differences Between the Campos and Brazil Basins

Multivariate statistical analyses of the total assemblages suggest that the observed patterns of benthic foraminiferal distribution are explained by the quantity and quality of organic matter exported to the seafloor, properties of the substrate and the hydrodynamic regime at the sediment/water interface. $\delta^{15}N$ values in the range of 4.7-7.3 ‰, together with $\delta^{13}C_{org}$ between

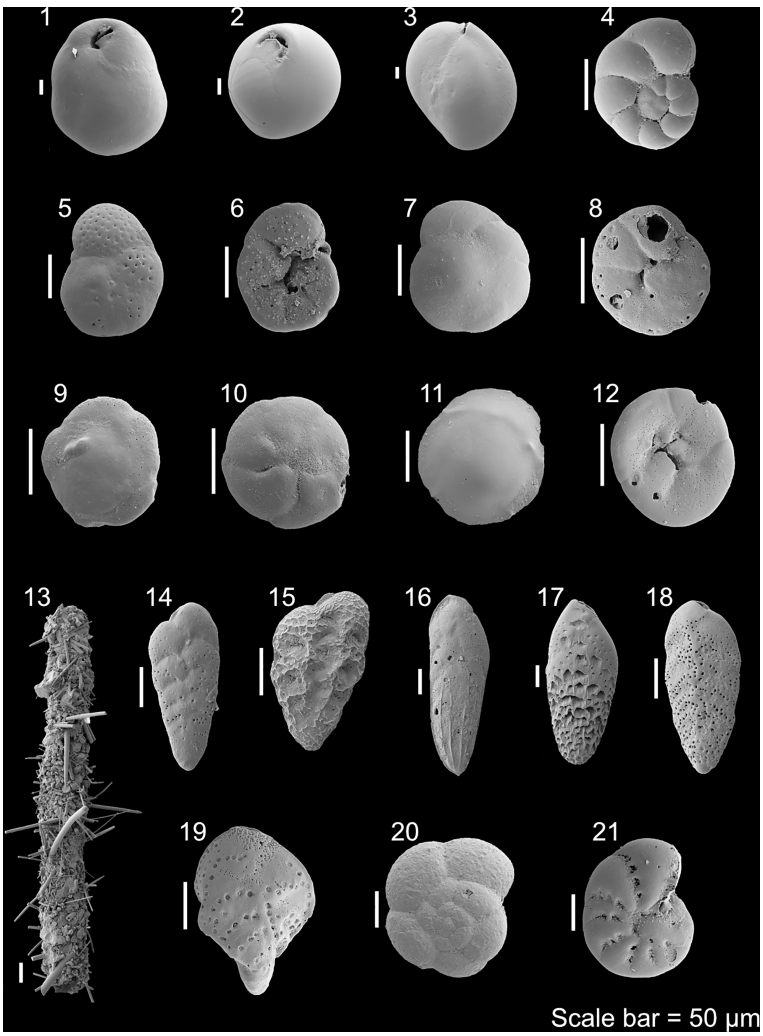

FIGURE 7 | The main taxa of the Brasil and Campos basin records: 1 *Globocassidulina subglobosa* (Brady, 1881); 2 *Pyrgoella irregularis* (d'Orbigny, 1839); 3 *Miliolinella subrotunda* (Montagu, 1803); 4 *Nonionella* sp.; 5 *Rosalina globularis* (d'Orbigny, 1826), spiral side; 6 *R. globularis* (d'Orbigny, 1826), umbilical side; 7 *Nuttallides umbonifer* (Cushman, 1933), spiral side; 8 N. *umbonifer* (Cushman, 1933), umbilical side; 9 *Alabaminella weddellensis* (Earland, 1936), spiral side; 10 A. *weddellensis* (Earland, 1936), umbilical side; 11 *Discorbis williamsoni* (Chapman & Parr, 1932), spiral side; 12 *D. williamsoni* (Chapman & Parr, 1932), umbilical side; 13 Fragment of *Saccorhiza ramosa* (Brady, 1879); 14 *Bolivina variabilis* (Williamson, 1858); 15 *Bolivina subreticulata* (Parr, 1932) 16 *Bolivina striatula* (Cushman, 1922) 17 *Bolivina albatrossi* (Cushman, 1922) 18 *Bolivina spathulata* (Williamson, 1858); 19 *Sigmavirgulina tortuosa* (Brady, 1881); 20 *Trochammina advena* Cushman, 1922, spiral side; 21 *Cribroelphidium incertum* (Williamson, 1858), side view.

-20 to -22 ‰ indicate a marine origin of the organic matter deposited along the investigated transects in the Campos and Brazil Basins (Nagel et al., 2009; Rumolo et al., 2011; Gaye et al., 2018). This interpretation is further validated by C:N ratios between 4 and 10, indicating that nitrogen is remineralized and nutrients are released (**Table 2**; Anderson, 1992; Rumolo et al., 2011). The main food source on the continental slope in the Campos Basin was previously reported to be autochthonous organic material derived from primary production (Carreira et al., 2010; Yamashita et al., 2018). Despite the exceedingly narrow shelf at the Rio de Contas and the Rio Sao Francisco (11-14°S), the southward drift of sediments delivered by these rivers prevents their transport to the continental slope (Rebouças et al., 2011; Cavalcante et al., 2020). Terrestrial organic material thus seems to play a minor role in the sediments despite nearby river discharges, implying a predominance of marine organic material (Cordeiro et al., 2018). In addition to primary production, along- and downslope transport due to major current systems and local canyons and channel networks delivers more refractory organic matter to all three study areas (Bahr et al., 2016; da Silveira et al., 2020). The Campos Basin in particular is characterized by contourite deposition and coarser sediments indicating increased bottom currents in this area (Viana, 2001; de Mello e Sousa et al., 2006). Constant bottom flow velocities reflected in increased silt proportions (**Table 2**) as well as reworked sediments result in relatively reduced organic matter concentrations in the surface substrates (de Mello e Sousa et al., 2006; Gaye et al., 2018). Towards the north, where the subtropical gyre becomes less vigorous, calmer settings and more clayey sediments predominate (**Table 2**; Stramma and England, 1999; Mémery et al., 2000; da Silveira et al., 2020).

5.2.1 Campos Basin

High abundances of *Globocassidulina subglobosa/crassa* are typical for the shelf and upper slope of the Campos Basin (Lohmann, 1978; de Mello e Sousa et al., 2006; Eichler et al., 2008; Burone et al., 2011; Dias et al., 2018). Their high abundances coincide with increased grain sizes (**Figure 6**), suggesting they prefer constant bottom flow velocities, as already suggested in previous studies (e.g., Schmiedl et al., 1997; de Mello e Sousa et al., 2006). Local occurrences of upper slope contourites as well as CWC mounds in the Campos Basin document an increased bottom current activity in this area as well (Viana, 2001; Viana et al., 2002; Bahr et al., 2020; Raddatz et al., 2020). On the upper slope in the subtropical part of the SACW at 430 m (sample 35) a *G. subglobosa/crassa-Nuttalides umbonifer* assemblage is adapted to lower nitrogen levels and reduced primary productivity, highlighted in the CCA by TN plotting contrary to it (**Figure 6**; Gooday, 1994; Gooday, 2003; Margreth et al., 2009; De and Gupta, 2010). The assemblage is complemented by *Alabaminella weddellensis* with increasing depth beyond 850 m in the AAIW. Similar to *G. subglobosa/crassa*, *A. weddellensis* can be considered as an r-strategist that responds opportunistically to the input of organic material (e.g., Gooday, 1988; Gooday, 1993; Dias et al., 2018). Bolivinids contribute less to the Campos Basin than to the Brazil Basin samples, with *Bolivina striatula* and *B. spathulata* being the most prevalent species (**Table 4** and **Figure 6**). *Bolivina striatula* is mainly recorded from the upper slope (450 m, SACW sample 35; **Figure 5**). However, it is well known from the continental shelf down to a depth of 200 m and can serve as an indicator for freshwater input in estuarine areas (Boltovskoy et al., 1980; Eichler et al., 2008; Mendes et al., 2012). Since no stained *B. striatula* were found in sample 35, downslope transport from the shelf, favored by the pronounced canyon system on the slope of the Campos Basin (Bahr et al., 2016), might explain the occurrences of *B. striatula* at greater water depths. Support for downslope transport comes from occurrences of shelf-dwelling *Discorbis williamsoni* as well as some occurrences of elphidiids, mainly represented by *Cribroelphidium incertum* (**Figure 7**; Boltovskoy et al., 1980; Murray, 2006).

The surveyed transect in the Campos Basin (430-2000 m, 22°S) agrees well in its faunal composition with the former study by de Mello e Sousa et al. (2006; 750-2000 m, 22-23°S) near the Sao Tomé and Itapemirim Canyons. The authors describe a *Globocassidulina subglobosa* assemblage, inhabiting sandier sediments and being adapted to oligotrophic conditions and increased bottom currents (de Mello e Sousa et al., 2006). Opportunistic species such as *G. subglobosa*, *Nuttalides umbonifer* and *Alabaminella weddellensis* thrive in more unstable substrates due to local bottom currents and cope with high fluctuations in food availability (Schmiedl et al., 1997; de Mello e Sousa et al., 2006; Fentimen et al., 2018; Fentimen et al., 2020). These species decline northwards and are clearly under-represented in the northern study areas.

The CWC mounds of the Campos Basin represent a distinct facies not addressed in previous studies and yielding a slightly divergent foraminiferal association. The high abundances of *A. weddellensis* in the AAIW are mainly linked to the CWC mound samples (**Figure 6**; **Appendix 2**). As coral scaffolds capture phytodetritus, increased *A. weddellensis* occurrences seem to be favored here (Fentimen et al., 2018). Attached species such as *Trochammina advena* use the constant near-bottom current for suspension feeding (Schönfeld, 2002a). It was also noticeable that particularly large specimens of *Cibicidoides wuellerstorfi* occur exclusively in CWC mounds (they occur in samples 24 and 34 almost exclusively in the > 250 µm fraction). Although *C. wuellerstorfi* appears to be more numerous in the samples from the Brazil Basin (**Figure 6**), the examined specimens were clearly smaller there. Probably *C. wuellerstorfi* benefits from a better nutrient supply in the increased current regime within the CWC mounds, which is reflected in its size. The increased proportion of attached *Trochammina squamata* in the living stock of the CWC samples, coinciding with the lack of stained globocassidulinids, demonstrates that attached suspension feeders use the elevated substrates of coral reefs as a niche to benefit from trapped suspended nutrients (Lutze and Thiel, 1989; Linke and Lutze, 1993; Schönfeld, 1997). Occurrences of *B. spathulata* close to the CWC mounds (samples 24, 25) imply that this particular bolivinid species prefers to live in silty environments near a coral facies, which has already been shown by Fentimen et al. (2018); Fentimen et al., 2020) for the CWC mounds of the Porcupine Seabight in the northeast Atlantic Ocean. The preference of *B. spathulata* for silty substrates is further reflected in its occurrences within the SACW (sample 35 in transect 2 and

sample 80 in transect 6; **Table 2** and **Figure 6**), which exhibits relatively higher current velocities (de Mello e Sousa et al., 2006; da Silveira et al., 2020).

5.2.2 Brazil Basin

The bolivinid-dominated assemblages of transects 6 and 7 coincide with comparably higher total nitrogen and organic carbon contents, as implied in the CCA (**Figure 6**). This association suggests an increased nutrient input and thus slightly higher food availability in these areas (Corliss, 1985; Schmiedl et al., 1997; de Mello e Sousa et al., 2006). The consistent presence of *Epistominella exigua* in all samples > 900 m depth (**Figure 5**) further indicates increased primary production, as this species is often associated with phytodetrital input (Gooday, 1988; Gooday, 1993; Mackensen et al., 1995; Gooday, 1996; Kurbjeweit et al., 2000; De and Gupta, 2010). Seasonal variability of the NBUC at about 10°S (Stramma et al., 1995) seems to be associated with increased *E. exigua* occurrences, as this species prefers seasonal inputs of phytodetritus (Gooday, 1988; Mackensen et al., 1990; Schmiedl et al., 1997).

In transect 6 increased occurrences of *Cassidulina laevigata*, generally linked to enhanced influx of organic matter (Schmiedl et al., 1997; de Mello e Sousa et al., 2006; De and Gupta, 2010), are mainly observed in SACW sample 80, where it coincides within the same quadrant as the TOC vector in the CCA (**Figure 5**). Downslope transport in this region is indicated by occurrences of elphidiids which are present in the total assemblage in all samples of transect 6, extending into the areas of NADW (sample 72, 1700 m; represented as 'transported species' in **Figure 5**). The steep slope with deeply incised canyons characterized by a network of meandering and straight channels, together with a very narrow continental shelf, facilitates downslope transport of entrained material (Bahr et al., 2016). Rich *Rosalina* spp. occurrences are mainly documented from the middle slope (**Figure 5**). *Rosalina* species favor more distal settings in terms of increased bottom current activity and prefer to inhabit slightly elevated substrates that are exposed to light currents (Corliss, 1985; Schönfeld, 2002b). They can move from their clinging position to a motile situation when food is scarce (DeLaca and Lipps, 1972). *Rosalina* species are thus able to search for areas with an increased nutrient supply, where they can stretch out their pseudopodia to ingest food (DeLaca and Lipps, 1972). A high *Rosalina* density in transect 6 is likely linked to sufficient food availability, as suggested by the correspondence with TOC and TN contents (depicted in the CCA, **Figure 6**). Slightly increased occurrences of *Miliolinella subrotunda* within the AAIW (sample 78) coincide with the highest occurrences of rosalinids within transect 6 (**Figure 5**). Suspension-feeding *M. subrotunda* also prefers rather gentle currents as this protist uses flexible agglutinated tubes to support its pseudopodial system that it deploys into the water to feed. These tubes may be distorted or damaged by bottom flow speeds that were too high (Altenbach et al., 1993). Along the slope in NADW samples 72 and 77, the *Rosalina* assemblage is complemented by occurrences of various *Nonionella* species (*N. turgida*, *N. iridea*, *Nonionella* spp. juv.; **Figure 5**). *Nonionella* is associated in several studies with the input of fresh organic matter and phytodetritus (Mackensen et al., 1990; Gooday and Hughes, 2002; Duffield et al., 2015; Alve et al., 2016). Transect 6 is thus characterized by a comparably higher nutrient input, corroborated by the positive association with TOC and TN contents in the CCA (**Figure 6**; Gooday, 2003; Alve et al., 2016).

Substrates sampled on the slope along transect 7 at 11°S are much finer compared to the study sites at 22°S and 14°S (**Figure 6** and **Table 2**). The fauna defined by various *Bolivina* species is complemented by occurrences of *Pyrgoella irregularis*, which is sometimes associated with phytodetritus and inhabits more clayey areas (Gooday, 1988; Gooday, 1993). *Saccorhiza ramosa* colonizes the NADW samples 95 and 102 on transect 7 (shown as 'tubular fragments' in **Figure 5**), each of which was collected at elevated positions within the canyon system and thus located distal to the main downslope transport (**Figure 5**; Bahr et al., 2016). This tubular and fragile suspension feeder requires stable substrates to dwell upright in the sediment and indicates moderate to low current intensities and poor reworking by detritus feeders (Altenbach et al., 1987; Mackensen, 1987; Linke and Lutze, 1993). Occurrences of *S. ramosa* are already known from similar settings in the Gulf of Cadiz where they live distal to the main current of the Mediterranean outflow water (Schönfeld, 1997; Schönfeld, 2002a; Schönfeld 2002b). The coincidence of enhanced silt contents with all samples from transect 7 in the CCA emphasizes a generally calmer setting in this study area (**Figure 6**). The current velocity of the northward flowing North Brazilian Undercurrent (NBUC) appears to be weaker at 11°S compared to the southern study areas (Stramma et al., 1995). This can be explained by the sampling depth far below the velocity core of the NBUC, which is located at the pycnocline between BC and SACW in this area (150-200 m; Stramma et al., 1995; da Silveira et al., 2020).

De Mello e Sousa et al. (2006) describe a *Bolivina* assemblage with reduced *G. subglobosa* abundances, from the deeper and muddier areas of the Campos Basin, where more stable substrates and reduced bottom currents prevail. In some respects, their *Bolivina* assemblage resembles that found between 11 and 14°S in the present study. However, the abundance of *G. subglobosa/crassa* on transects 6 and 7 is even lower than reported by de Mello e Sousa et al. (2006). The faunal data from 11-14°S suggests that the northward directed branch of tropical SACW, strongly controlled by the NBUC, favors an assemblage that prefers high organic matter fluxes and finer sediments (Stramma and England, 1999; Gooday, 2003; da Silveira et al., 2020). In transect 6, *G. subglobosa/crassa* is still the most common taxon, but accompanied by a rich *Rosalina* association, which is missing at the Campos Basin (de Mello e Sousa et al., 2006). *Globocassidulina subglobosa/crassa* plays a very minor role at 11°S in transect 7 (**Table 4**). *Alabaminella weddellensis* is much less abundant in the northern sample sites compared to the Campos Basin; in transect 7 it is not recorded at all (**Table 4**). This could be due to the lack of CWC mounds in the Brazil Basin as well as finer sediments in transect 7 (Fentimen et al., 2018; Fentimen et al., 2020). High organic matter fluxes considerably influence the bolivinid-determined assemblage in these areas (Gooday, 2003). The additional occurrence of the opportunistic species *Epistominella exigua* further distinguishes the northern

assemblage from the deeper Campos Basin, where this species is under-represented (de Mello e Sousa et al., 2006).

Regarding the sparse living assemblage, stained specimens such as attached *Tritaxis fusca* and *Trochammina squamata* in transect 2 contrast with the few living foraminifera at transects 6 and 7, some of which are infaunal bolivinids (transect 6) and vulnerable tube-shaped tests of *Saccorhiza ramosa* (transect 7). *Tritaxis fusca* and *Trochammina squamata* have already been mentioned in relation to increased bottom currents, confirming an increased hydrodynamic energy level in the Campos Basin (e.g., Schönfeld, 1997; Schönfeld and Zahn, 2000; Schönfeld 2002a), whereas the biocenosis of the Brazil Basin transects well reflects calmer environments (**Figure 5**).

6 CONCLUSIONS AND FUTURE DIRECTIONS

New microfaunal and sedimentological data indicate that the benthic foraminiferal fauna at the Brazilian continental margin between 11 and 22°S is controlled by the quantity and quality of organic matter fluxes as well as substrate properties and hydrodynamic conditions at the sediment water interface. This study reveals that a *Globocassidulina subglobosa*/*crassa* assemblage in the Campos Basin is contrasted by a rosalinid/bolivinid assemblage in the Brazil Basin. This biogeographic divide occurs across the bifurcation of the SACW into its southward subtropical and northward tropical branches. The subtropical transect at 22°S reveals slightly lower diversity indices but increased population densities compared to the tropical study areas (11-14°S). The proportion of stained (living) specimens is somewhat lower at 22°S compared to 11-14°S. However, typically for deep-sea samples, their proportion is rather small for all three sample areas.

The Campos Basin is characterized by a *Globocassidulina subglobosa/crassa* assemblage, further defined by *Nuttalides umbonifer* and *Alabaminella weddellensis*. This assemblage reflects a variable nutrient supply and coarser substrates due to increased bottom current activity. *Alabaminella weddellensis* occupies an ecological niche in CWC mounds to benefit from trapped phytodetritus. Occurrences of elphidiids and *Bolivina striatula* indicate downslope transport due to the large canyon network on the continental slope of the Campos Basin.

A *Rosalina-Bolivina* assemblage characterizes the continental slope in the Brazil Basin. At 14°S, the assemblage composition is defined by *G. subglobosa/crassa*, *Rosalina* spp., *Bolivina variabilis* and *Bolivina subreticulata*, with a lower proportion of *G. subglobosa* compared to the Campos Basin. Enhanced abundances of *Rosalina* spp. are associated with increased TOC and TN levels. In transect 7, a faunal association of *Bolivina subreticulata*, *Bolivina variabilis*, *Epistominella exigua*, *G. subglobosa*/*crassa* characterises the upper to lower continental slope, coinciding with more clayey sediments. The bolivinid dominated assemblage is associated with an increased nutrient supply, as reflected by its coincidence with relatively higher TOC values in the CCA. Occurrences of *Saccorhiza ramosa*, especially at the lower slope, are linked to more stable substrates.

The new data set implies distinct contrasts in foraminiferal densities, diversities and assemblage composition between the Campos and Brazil basins. The quantity, quality, and seasonality of organic matter influx together with substrate properties and hydrodynamic conditions are identified as the main drivers of the observed patterns. However, the present study, while presenting the first quantitative data for the Brazilian continental margin 11-14°S, is limited in its ability to predict large-scale biogeographic patterns due to its coarse spatial resolution. It should thus be considered a base line and starting point for further faunistic studies along the Brazilian continental margin in the future. Only a significantly higher spatial resolution will allow a fuller understanding of patterns of foraminiferal densities, diversity, and biogeography in this vast area. Investigations of faunal distributions across the potentially critical water mass divide of the northern and southern SACW branches might prove particularly informative in this endeavor.

DATA AVAILABILITY STATEMENT

The original contributions presented in the study are included in the article/**Supplementary Material**. Further inquiries can be directed to the corresponding author.

AUTHOR CONTRIBUTIONS

AS performed the statistical analyses and wrote the manuscript. AS, JP and PG drafted the concept of the study and contributed to the evaluation of the statistical analyses. AS and JS conducted the taxonomic evaluation. AB and BD contributed to the collection of samples and interpretation of sedimentological parameters. BD, AA and RD performed the chemical analyses on the sediment samples. All authors contributed to the article and approved the submitted version.

FUNDING

This study was financially supported and enabled by the Deutsche Forschungsgemeinschaft (DFG, German Research Foundation) through project GR52851/1-1.

ACKNOWLEDGMENTS

We acknowledge Hanna Cieszynski (University of Cologne) for her support with the SEM. Marie Scheel (University of Cologne) is thanked for her assistance in washing and picking the samples. We thank Tobias Walla who contributed to the sample preparation. BD acknowledges the financial support from FAPESP (grants 2020/11452-3, 2019/24349-9, and 2018/15123-4). We further thank the three reviewers Andrew John Gooday, Michael Martínez-Colón, and Bryan O'Malley for their helpful comments.

SUPPLEMENTARY MATERIAL

The Supplementary Material for this article can be found online at: https://www.frontiersin.org/articles/10.3389/fmars.2022.901224/full#supplementary-material

REFERENCES

Altenbach, A. V., Heeger, T., Linke, P., Spindler, M. and Thies, A. (1993). *Miliolinella Subrotunda* (Montagu), a Miliolid Foraminifer Building Large Detritic Tubes for a Temporary Epibenthic Lifestyle. *Mar. Micropaleontol.* 20, 293–301. doi: 10.1016/0377-8398(93)90038-Y

Altenbach, A. V., Lutze, G. F. and Weinholz, P. (1987). Beobachtungen an Benthos-Foraminiferen (Teilprojekt A3). *Berichte. aus. dem. Sonderforschungsbereich.* 313 (6), 86.

Altenbach, A. V., Unsöld, G. and Walger, E. (1988). The Hydrodynamic Environment of *Saccorhiza Ramosa* (BRADY). *Meyniana* 40, 119–132.

Alve, E., Korsun, S., Schönfeld, J., Dijkstra, N., Golikova, E., Hess, S., et al. (2016). Foram-AMBI: A Sensitivity Index Based on Benthic Foraminiferal Faunas From North-East Atlantic and Arctic Fjords, Continental Shelves and Slopes. *Mar. Micropaleontol.* 122, 1–12. doi: 10.1016/j.marmicro.2015.11.001

Anderson, T. R. (1992). Modelling the Influence of Food C:N Ratio, and Respiration on Growth and Nitrogen Excretion in Marine Zooplankton and Bacteria. *J. Plankton Res.* 14, 1645–1671. doi: 10.1093/plankt/14.12.1645

Bahr, A., Doubrawa, M., Titschack, J., Austermann, G., Koutsodendris, A., Nürnberg, D., et al. (2020). Monsoonal Forcing of Cold-Water Coral Growth Off Southeastern Brazil During the Past 160 Kyr. *Biogeosciences* 17, 5883–5908. doi: 10.5194/bg-17-5883-2020

Bahr, A., Spadano Albuquerque, A. L., Ardenghi, N., Batenburg, S. J., Bayer, M., Catunda, M. C., et al. (2016). *METEOR-Berichte: South American Hydrological Balance and Paleoceanography During the Late Pleistocene and Holocene (SAMBA) - Cruise No. M125*. (Bremen, Germany: MARUM – Zentrum für Marine Umweltwissenschaften der Universität Bremen) doi: 10.2312/cr_m125

Bernhard, J. M. (2000). Distinguishing Live From Dead Foraminifera: Methods Review and Proper Applications. *Micropaleontology* 46, 38–46.

Boltovskoy, E., Giussani, G., Watanabe, S. and Wright, R. C. (1980). *Atlas of Benthic Shelf Foraminifera of the Southwest Atlantic*. 1st ed. Ed. Junk, W. (The Netherlands: bv. publishers, The Hague). doi: 10.1016/0377-8398(81)90028-1

Brady, H. B., (1879). Notes on some of the Reticularian Rhizopoda of the "Challenger" Expedition; Part I. On New or Little Known Arenaceous Types. *Quarterly Journal of Microscopical Sciences* 19, 20–67.

Brady, H. B., (1881). Notes on some of the Reticularian Rhizopoda of the "Challenger" Expedition. Part III. *Quarterly Journal of Microscopical Science* 21, 31–71.

Braga, E. S., Chiozzini, V. C., Berbel, G. B. B., Maluf, J. C. C., Aguiar, V. M. C., Charo, M., et al. (2008). Nutrient Distributions Over the Southwestern South Atlantic Continental Shelf From Mar Del Plata (Argentina) to Itajaí (Brazil): Winter-Summer Aspects. *Cont. Shelf Res.* 28, 1649–1661. doi: 10.1016/j.csr.2007.06.018

Burone, L., de e Sousa, S. H. M., de Mahiques, M. M., Valente, P., Ciotti, A. and Yamashita, C. (2011). Benthic Foraminiferal Distribution on the Southeastern Brazilian Shelf and Upper Slope. *Mar. Biol.* 158, 159–179. doi: 10.1007/s00227-010-1549-7

Carreira, R. S., Araújo, M. P., Costa, T. L. F., Ansari, N. R. and Pires, L. C. M. (2010). Lipid Biomarkers in Deep Sea Sediments From the Campos Basin, SE Brazilian Continental Margin. *Org. Geochem.* 41, 879–884. doi: 10.1016/j.orggeochem.2010.04.017

Cavalcante, G., Vieira, F., Campos, E., Brandini, N. and Medeiros, P. R. P. (2020). Temporal Streamflow Reduction and Impact on the Salt Dynamics of the São Francisco River Estuary and Adjacent Coastal Zone (NE/Brazil). *Reg. Stud. Mar. Sci.* 38, 101363. doi: 10.1016/j.rsma.2020.101363

Chapman, F., Parr, W. J. (1932). Victorian and South Australian Shallow-Water Foraminifera. Part II. *Proceedings of the Royal Society of Victoria* 44, 218–234.

Cordeiro, L. G. M. S., Wagener, A. L. R. and Carreira, R. S. (2018). Organic Matter in Sediments of a Tropical and Upwelling Influenced Region of the Brazilian Continental Margin (Campos Basin, Rio De Janeiro). *Org. Geochem.* 120, 86–98. doi: 10.1016/j.orggeochem.2018.01.005

Corliss, B. H. (1985). Microhabitats of Benthic Foraminifera Within Deep-Sea Sediments. *Nature* 314, 435–438. doi: 10.1038/314435a0

Cushman, J. A. (1922). Shallow-Water Foraminifera of the Tortugas Region. Publications of the Carnegie Institution of Washington 311. *Department of Marine Biology of the Carnegie Institution of Washington* 17, 1–85.

Cushman, J. A., (1933). Some New Recent Foraminifera from the Tropical Pacific. *Contributions from the Cushman Laboratory for Foraminiferal Research* 9 (4), 77–95.

da Silveira, I. C. A., Napolitano, D. C. and Farias, I. U. (2020). Water Masses and Oceanic Circulation of the Brazilian Continental Margin and Adjacent Abyssal Plain . In: Sumida, P.Y.G., Bernardino, A.F., De Léo, F.C. (eds) *Brazilian Deep-Sea Biodiversity. Brazilian Marine Biodiversity.* Springer, Cham. 7–36. doi: 10.1007/978-3-030-53222-2_2

de Almeida, F. K., de Mello, R. M., Rodrigues, A. R. and Bastos, A. C. (2022). Bathymetric and Regional Benthic Foraminiferal Distribution on the Espírito Santo Basin Slope, Brazil (SW Atlantic). *Deep. Res. Part I Oceanogr. Res. Pap.* 181, 103688. doi: 10.1016/j.dsr.2022.103688

De, S. and Gupta, A. K. (2010). Deep-Sea Faunal Provinces and Their Inferred Environments in the Indian Ocean Based on Distribution of Recent Benthic Foraminifera. *Palaeogeogr. Palaeoclimatol. Palaeoecol.* 291, 429–442. doi: 10.1016/j.palaeo.2010.03.012

DeLaca, T. E. and Lipps, J. H. (1972). The Mechanism and Adaptive Significance of Attachment and Substrate Pitting in the Foraminiferan *Rosalina Globularis* d'Orbigny. *J. Foraminifer. Res.* 2, 68–72. doi: 10.2113/gsjfr.2.2.68

De Madron, X. D. and Weatherly, G. (1994). Circulation, Transport and Bottom Boundary Layers of the Deep Currents in the Brazil Basin. *J. Mar. Res.* 52, 583–638. doi: 10.1357/0022240943076975

de Mello e Sousa, S. H., Passos, R. F., Fukumoto, M., da Silveira, I. C. A., Figueira, R. C. L., Koutsoukos, E. A. M., et al. (2006). Mid-Lower Bathyal Benthic Foraminifera of the Campos Basin, Southeastern Brazilian Margin: Biotopes and Controlling Ecological Factors. *Mar. Micropaleontol.* 61, 40–57. doi: 10.1016/j.marmicro.2006.05.003

Dias, B. B., Barbosa, C. F., Faria, G. R., Seoane, J. C. S. and Albuquerque, A. L. S. (2018). The Effects of Multidecadal-Scale Phytodetritus Disturbances on the Benthic Foraminiferal Community of a Western Boundary Upwelling System, Brazil. *Mar. Micropaleontol.* 139, 102–112. doi: 10.1016/j.marmicro.2017.12.003

d'Orbigny, A.D., (1826). Tableau méthodique de la classe des Céphalopodes. *Annales des Sciences Naturelles* 7, 245–314.

d'Orbigny, A. D., (1839). Voyage dans l'Amérique méridionale. Foraminifères. *Pitoit-Levrault*, Paris. 1–86. doi.org/10.5962/bhl.title.110540

Duffield, C. J., Hess, S., Norling, K. and Alve, E. (2015). The Response of Nonionella Iridea and Other Benthic Foraminifera to "Fresh" Organic Matter Enrichment and Physical Disturbance. *Mar. Micropaleontol.* 120, 20–30. doi: 10.1016/j.marmicro.2015.08.002

Earland, A., (1936). Foraminifera, Part IV. Additional Records from the Weddell Sea Sector from Material obtained by the S.Y 'Scotia'. *Discovery Reports* 13. 1–76.

Eichler, P. P. B., Rodrigues, A. R., Eichler, B. B., Braga, E. S. and Campos, E. J. D. (2012). Tracing Latitudinal Gradient, River Discharge and Water Masses Along the Subtropical South American Coast Using Benthic Foraminifera Assemblages. *Braz. J. Biol.* 72, 723–759. doi: 10.1590/s1519-69842012000400010

Eichler, P. P. B., Sen Gupta, B. K., Eichler, B. B., Braga, E. S. and Campos, E. J. (2008). Benthic Foraminiferal Assemblages of the South Brazil: Relationship to Water Masses and Nutrient Distributions. *Cont. Shelf Res.* 28, 1674–1686. doi: 10.1016/j.csr.2007.10.012

Fentimen, R., Lim, A., Rüggeberg, A., Wheeler, A. J. and Van Rooij, D. (2020). Impact of Bottom Water Currents on Benthic Foraminiferal Assemblages in a Cold-Water Coral Environment: The Moira Mounds (NE Atlantic). *Mar. Micropaleontol.* 154, 1–14. doi: 10.1016/j.marmicro.2019.101799

Fentimen, R., Rüggeberg, A., Lim, A., Kateb, A., Foubert, A., Wheeler, A. J., et al. (2018). Benthic Foraminifera in a Deep-Sea High-Energy Environment: The Moira Mounds (Porcupine Seabight, SW of Ireland). *Swiss. J. Geosci.* 111, 533–544. doi: 10.1007/s00015-018-0317-4

Fisher, R. A., Corbet, A. S. and Williams, C. B. (1943). The Relation Between the Number of Species and the Number of Individuals in a Random Sample of an Animal Population. *J. Anim. Ecol.* 12, 42. doi: 10.2307/1411

Fontanier, C., Jorissen, F. J., Licari, L., Alexandre, A., Anschutz, P. and Carbonel, P. (2002). Live Benthic Foraminiferal Faunas From the Bay of Biscay: Faunal Density, Composition, and Microhabitats. *Deep. Res. Part I Oceanogr. Res. Pap.* 49, 751–785. doi: 10.1016/S0967-0637(01)00078-4

Gaye, B., Böll, A., Segschneider, J., Burdanowitz, N., Emeis, K. C., Ramaswamy, V., et al. (2018). Glacial-Interglacial Changes and Holocene Variations in Arabian Sea Denitrification. *Biogeosciences* 15, 507–527. doi: 10.5194/bg-15-507-2018

Goineau, A. and Gooday, A. J. (2017). Novel Benthic Foraminifera are Abundant and Diverse in an Area of the Abyssal Equatorial Pacific Licensed for Polymetallic Nodule Exploration. *Sci. Rep.* 7, 1–15. doi: 10.1038/srep45288

Gooday, A. J. (1988). A Response by Benthic Foraminifera to the Deposition of Phytodetritus in the Deep Sea. *Nature* 332, 70–73. doi: 10.1038/332070a0

Gooday, A. J. (1993). Deep-Sea Benthic Foraminiferal Species Which Exploit Phytodetritus: Characteristic Features and Controls on Distribution. *Mar. Micropaleontol.* 22, 187–205. doi: 10.1016/0377-8398(93)90043-W

Gooday, A. J. (1994). The Biology of Deep-Sea Foraminifera: A Review of Some Advances and Their Applications in Paleoceanography. *PALAIOS* 9, 14–31. doi: 10.2307/3515075

Gooday, A. J. (1996). Epifaunal and Shallow Infaunal Foraminiferal Communities at Three Abyssal NE Atlantic Sites Subject to Differing Phytodetritus Input Regimes. *Deep. Res. Part I Oceanogr. Res. Pap.* 43, 1395–1421. doi: 10.1016/S0967-0637(96)00072-6

Gooday, A. J. (2003). Benthic Foraminifera (Protista) as Tools in Deep-Water Palaeoceanography: Environmental Influences on Faunal Characteristics. *Adv. Mar. Biol.* 46, 1–90. doi: 10.1016/S0065-2881(03)46002-1

Gooday, A. J. and Hughes, J. A. (2002). Foraminifera Associated With Phytodetritus Deposits at a Bathyal Site in the Northern Rockall Trough (NE Atlantic): Seasonal Contrasts and a Comparison of Stained and Dead Assemblages. *Mar. Micropaleontol.* 46, 83–110. doi: 10.1016/S0377-8398(02)00050-6

Gooday, A. J. and Jorissen, F. J. (2012). Benthic Foraminiferal Biogeography: Controls on Global Distribution Patterns in Deep-Water Settings. *Ann. Rev. Mar. Sci.* 4, 237–262. doi: 10.1146/annurev-marine-120709-142737

Gooday, A. J. and Rathburn, A. E. (1999). Temporal Variability in Living Deep-Sea Benthic Foraminifera: A Review. *Earth Sci. Rev.* 46, 187–212. doi: 10.1016/S0012-8252(99)00010-0

Hammer, Ø., Harper, D. A. T. and Ryan, P. D. (2001). Past: Paleontological Statistics Software Package for Education and Data Analysis. *Palaeontol. Electron.* 4, 9.

Jorissen, F. J., de Stigter, H. C. and Widmark, J. G. V. (1995). A Conceptual Model Explaining Benthic Foraminiferal Microhabitats. *Mar. Micropaleontol.* 26, 3–15. doi: 10.1016/0377-8398(95)00047-X

Jorissen, F. J., Fontanier, C. and Thomas, E. (2007). "Paleoceanographical Proxies Based on Deep-Sea Benthic Foraminiferal Assemblage Characteristics," in *Proxies in Late Cenozoic Paleoceanography: Pt. 2: Biological Tracers and Biomarkers*. Eds. Hillaire-Marcel, C. and de Vernal, A., (Amsterdam, The Netherlands: Elsevier) 263–325. doi: 10.1016/S1572-5480(07)01012-3

Knoppers, B., Ekau, W. and Figueiredo, A. G. (1999). The Coast and Shelf of East and Northeast Brazil and Material Transport. *Geo-Marine. Lett.* 19, 171–178. doi: 10.1007/s003670050106

Kurbjeweit, F., Schmiedl, G., Schiebel, R., Hemleben, C., Pfannkuche, O., Wallmann, K., et al. (2000). Distribution, Biomass and Diversity of Benthic Foraminifera in Relation to Sediment Geochemistry in the Arabian Sea. *Deep. Res. Part II Top. Stud. Oceanogr.* 47, 2913–2955. doi: 10.1016/S0967-0645(00)00053-9

Lambshead, P. J. D. and Gooday, A. J. (1990). The Impact of Seasonally Deposited Phytodetritus on Epifaunal and Shallow Infaunal Benthic Foraminiferal Populations in the Bathyal Northeast Atlantic: The Assemblage Response. *Deep Sea Res. Part A Oceanogr. Res. Pap.* 37:1263-1283. doi: 10.1016/0198-0149(90)90042-T

Legendre, L. and Legendre, P. (1998). *Numerical Ecology*. 2nd ed Vol. Volume 24 (Amsterdam, The Netherlands: Elsevier Science).

Linke, P. and Lutze, G. F. (1993). Microhabitat Preferences of Benthic Foraminifera – a Static Concept or a Dynamic Adaptation to Optimize Food Acquisition? *Mar. Micropaleontol.* 20, 215–234. doi: 10.1016/0377-8398(93)90034-U

Lohmann, G. P. (1978). Abyssal Benthonic Foraminifera as Hydrographic Indicators in the Western South Atlantic Ocean. *J. Foraminifer. Res.* 8, 6–34. doi: 10.2113/gsjfr.8.1.6

Lutze, G. F. and Thiel, H. (1989). Epibenthic Foraminifera From Elevated Microhabitats; Cibicidoides Wuellerstorfi and Planulina Ariminensis. *J. Foraminifer. Res.* 19, 153–158. doi: 10.2113/gsjfr.19.2.153

Mackensen, A. (1987). Benthische Foraminiferen Auf Dem Island-Schottland Rücken: Umwelt-Anzeiger an Der Grenze Zweier Ozeanischer Räume. *Paläontologische. Z.* 61, 149–179. doi: 10.1007/BF02985902

Mackensen, A., Grobe, H., Kuhn, G. and Fütterer, D. K. (1990). Benthic Foraminiferal Assemblages From the Eastern Weddell Sea Between 68 and 73°S: Distribution, Ecology and Fossilization Potential. *Mar. Micropaleontol.* 16, 241–283. doi: 10.1016/0377-8398(90)90006-8

Mackensen, A., Schmiedl, G., Harloff, J. and Giese, M. (1995). Deep-Sea Foraminifera in the South Atlantic Ocean: Ecology and Assemblage Generation. *Micropaleontology* 41, 342–358. doi: 10.2307/1485808

Margreth, S., Rüggeberg, A. and Spezzaferri, S. (2009). Benthic Foraminifera as Bioindicator for Cold-Water Coral Reef Ecosystems Along the Irish Margin. *Deep. Res. Part I Oceanogr. Res. Pap.* 56, 2216–2234. doi: 10.1016/j.dsr.2009.07.009

Martins, L. R. and Coutinho, P. N. (1981). The Brazilian Continental Margin. *Earth Sci. Rev.* 17, 87–107. doi: 10.1016/0012-8252(81)90007-6

Mémery, L., Arhan, M., Alvarez-Salgado, X. A., Messias, M. J., Mercier, H., Castro, C. G., et al. (2000). The Water Masses Along the Western Boundary of the South and Equatorial Atlantic. *Prog. Oceanogr.* 47, 69–98. doi: 10.1016/S0079-6611(00)00032-X

Mendes, I., Dias, J. A., Schönfeld, J. and Ferreira, O. (2012). Distribution of Living Benthic Foraminifera on the Northern Gulf of Cadiz Continental Shelf. *J. Foraminifer. Res.* 42, 18–38. doi: 10.2113/gsjfr.42.1.18

Montagu, G., (1803). Testacea Britannica, or Natural History of British Shells, Marine, Land and Fresh Water, Including the Most Minute: Systematically Arranged and Embellished with Figures. *J. White*, London, England, 606 pp. doi.org/10.5962/bhl.title.33927

Murray, J. W. (2006). Ecology and Applications of Benthic Foraminifera. Cambridge University Press, Cambridge. 426 pp.

Nagel, B., Gaye, B., Kodina, L. A. and Lahajnar, N. (2009). Stable Carbon and Nitrogen Isotopes as Indicators for Organic Matter Sources in the Kara Sea. *Mar. Geol.* 266, 42–51. doi: 10.1016/j.margeo.2009.07.010

Oliveira-Silva, P., Fernandes Barbosa, C. and Soares-Gomes, A. (2005). Distribution of Macrobenthic Foraminifera on Brazilian Continental Margin Between 18°S – 23°S. *Rev. Bras. Geociências.* 35, 209–216. doi: 10.25249/0375-7536.2005352209216

Paliy, O. and Shankar, V. (2016). Application of Multivariate Statistical Techniques in Microbial Ecology. *Mol. Ecol.* 25, 1032–1057. doi: 10.1111/mec.13536

Parr, W. J. (1932). Victorian and South Australian Shallow-Water Foraminifera. Part I. *Proceedings of the Royal Society of Victoria* 44, 1−14.

Peet, R. K. (1974). The Measurement of Species Diversity. *Annu. Rev. Ecol. Syst.* 5, 285–307. doi: 10.2110/scn.79.06.0003

Peterson, R. G. and Stramma, L. (1991). Upper-Level Circulation in the South Atlantic Ocean. *Prog. Oceanogr.* 26, 1–73. doi: 10.1016/0079-6611(91)90006-8

Raddatz, J., Titschack, J., Frank, N., Freiwald, A., Conforti, A., Osborne, A., et al. (2020). Solenosmilia Variabilis-Bearing Cold-Water Coral Mounds Off Brazil. *Coral. Reefs* 39, 69–83. doi: 10.1007/s00338-019-01882-w

Ramette, A. (2007). Multivariate Analyses in Microbial Ecology. *FEMS Microbiol. Ecol.* 62, 142–160. doi: 10.1111/j.1574-6941.2007.00375.x

Rasmussen, T. L. and Thomsen, E. (2017). Ecology of Deep-Sea Benthic Foraminifera in the North Atlantic During the Last Glaciation: Food or Temperature Control. *Palaeogeogr. Palaeoclimatol. Palaeoecol.* 472, 15–32. doi: 10.1016/j.palaeo.2017.02.012

Rebouças, R. C., Dominguez, J. M. L. and da Silva Pinto Bittencourt, A. C. (2011). Provenance, Transport and Composition of Dendê Coast Beach Sands in Bahia, Central Coast of Brazil. *Braz. J. Oceanogr.* 59, 339–347. doi: 10.1590/S1679-87592011000400004

Rumolo, P., Barra, M., Gherardi, S., Marsella, E. and Sprovieri, M. (2011). Stable Isotopes and C/N Ratios in Marine Sediments as a Tool for Discriminating Anthropogenic Impact. *J. Environ. Monit.* 13, 3399–3408. doi: 10.1039/c1em10568j

Ryan, W.B.F., Carbotte, S.M., Coplan, J.O., O'Hara, S., Melkonian, A. and Arko, R., et al. (2009). Global Multi-Resolution Topography Synthesis. Geochemistry, *Geophys. Geosystems* 10, 1-9. doi:10.1029/2008GC002332

Schmiedl, G., Mackensen, A. and Müller, P. J. (1997). Recent Benthic Foraminifera From the Eastern South Atlantic Ocean: Dependence on Food Supply and Water Masses. *Mar. Micropaleontol.* 32, 249–287. doi: 10.1016/S0377-8398(97)00023-6

Schönfeld, J. (1997). The Impact of the Mediterranean Outflow Water (MOW) on Benthic Foraminiferal Assemblages and Surface Sediments at the Southern Portuguese Continental Margin. *Mar. Micropaleontol.* 29, 21–236. doi: 10.1016/S0377-8398(96)00050-3

Schönfeld, J. (2002a). Recent Benthic Foraminiferal Assemblages in Deep High-Energy Environments From the Gulf of Cadiz (Spain). *Mar. Micropaleontol.* 44, 141–162. doi: 10.1016/S0377-8398(01)00039-1

Schönfeld, J. (2002b). A New Benthic Foraminiferal Proxy for Near-Bottom Current Velocities in the Gulf of Cadiz, Northeastern Atlantic Ocean. *Deep. Res. I* 49, 1853–1875. doi: 10.1016/S0967-0637(02)00088-2

Schönfeld, J. and Zahn, R. (2000). Late Glacial to Holocene History of the Mediterranean Outflow. Evidence From Benthic Foraminiferal Assemblages and Stable Isotopes at the Portuguese Margin. *Palaeogeogr. Palaeoclimatol. Palaeoecol.* 159, 85–111. doi: 10.1016/S0031-0182(00)00035-3

Sen Gupta, B. K. (Ed.) (2002). *Modern Foraminifera* (Dordrecht, The Netherlands: Kluwer Academic Publishers), 384.

Shannon, C. E., Weaver, W., (1949). *The Mathematical Theory of Communication*. University of Illinois Press, Urbana, pp. 144.

Stramma, L. and England, M. (1999). On the Water Masses and Mean Circulation of the South Atlantic Ocean. *Geophys. Res.* 104, 20,863–20,883. doi: 10.1029/1999JC900139

Stramma, L., Fischer, J. and Reppin, J. (1995). The North Brazil Undercurrent. *Deep. Res. Part I* 42, 773–795. doi: 10.1016/0967-0637(95)00014-W

Summerhayes, C. P., Fainstein, R. and Ellis, J. P. (1976). Continental Margin Off Sergipe and Alagoas, Northeastern Brazil: A Reconnaissance Geophysical Study of Morphology and Structure. *Mar. Geol.* 20, 345–361. doi: 10.1016/0025-3227(76)90112-2

ter Braak, C. J. F. and Verdonschot, P. F. M. (1995). Canonical Correspondence Analysis and Related Multivariate Methods in Aquatic Ecology. *Aquat. Sci.* 57, 255–289. doi: 10.1007/BF00877430

Viana, A. R. (2001). Seismic Expression of Shallow- to Deep-Water Contourites Along the South-Eastern Brazilian Margin. *Mar. Geophys. Res.* 22, 509–521. doi: 10.1023/A:1016307918182

Viana, A. R., Almeida, W., Jr. and Almeida, C. W. (2002). Upper Slope Sands: Late Quaternary Shallow-Water Sandy Contourites of Campos Basin, SW Atlantic Margin. *Geol. Soc London. Mem.* 22, 261–270. doi: 10.1144/GSL.MEM.2002.022.01.19

Viana, A. R., Faugères, J. C., Kowsmann, R. O., Lima, J. A. M., Caddah, L. F. G. and Rizzo, J. G. (1998). Hydrology, Morphology and Sedimentology of the Campos Continental Margin, Offshore Brazil. *Sediment. Geol.* 115, 133–157. doi: 10.1016/S0037-0738(97)00090-0

Vieira, F. S., Koutsoukos, E. A. M., Machado, A. J. and Dantas, M. A. T. (2015). Biofaciological Zonation of Benthic Foraminifera of the Continental Shelf of Campos Basin, SE Brazil. *Quat. Int.* 377, 18–27. doi: 10.1016/j.quaint.2014.12.020

Williamson, W.C., (1858). On the Recent Foraminifera of Great Britain. *The Ray Society*, London. 1–107.

Yamashita, C., Mello e Sousa, S. H., Vicente, T. M., Martins, M. V., Nagai, R. H., Frontalini, F., et al. (2018). Environmental Controls on the Distribution of Living (Stained) Benthic Foraminifera on the Continental Slope in the Campos Basin Area (SW Atlantic). *J. Mar. Syst.* 181, 37–52. doi: 10.1016/j.jmarsys.2018.01.010

Yamashita, C., Omachi, C., Santarosa, A. C. A., Iwai, F. S., Araujo, B. D., Disaró, S. T., et al. (2020). Living Benthic Foraminifera of Santos Continental Shelf, Southeastern Brazilian Continental Margin (SW Atlantic): Chlorophyll-a and Particulate Organic Matter Approach. *J. Sediment. Environ.* 5, 17–34. doi: 10.1007/s43217-019-00001-7

Conflict of Interest: The authors declare that the research was conducted in the absence of any commercial or financial relationships that could be construed as a potential conflict of interest.

Publisher's Note: All claims expressed in this article are solely those of the authors and do not necessarily represent those of their affiliated organizations, or those of the publisher, the editors and the reviewers. Any product that may be evaluated in this article, or claim that may be made by its manufacturer, is not guaranteed or endorsed by the publisher.

frontiers | Frontiers in Marine Science

TYPE Original Research
PUBLISHED 02 August 2022
DOI 10.3389/fmars.2022.909407

OPEN ACCESS

EDITED BY
Ravi Bhushan,
Physical Research Laboratory, India

REVIEWED BY
Li Lo,
National Taiwan University, Taiwan
Selvaraj Kandasamy,
Xiamen University, China

*CORRESPONDENCE
S. Endress
serafina.endress@gmail.com

SPECIALTY SECTION
This article was submitted to Marine Biogeochemistry, a section of the journal Frontiers in Marine Science

RECEIVED 31 March 2022
ACCEPTED 04 July 2022
PUBLISHED 02 August 2022

CITATION
Endress S, Schleinkofer N, Schmidt A, Tracey D, Frank N and Raddatz J (2022) The cold-water coral *Solenosmilia variabilis* as a paleoceanographic archive for the reconstruction of intermediate water mass temperature variability on the Brazilian continental margin. *Front. Mar. Sci.* 9:909407. doi: 10.3389/fmars.2022.909407

The cold-water coral *Solenosmilia variabilis* as a paleoceanographic archive for the reconstruction of intermediate water mass temperature variability on the Brazilian continental margin

S. Endress[1,2]*, N. Schleinkofer[1,2], A. Schmidt[1,2], D. Tracey[3], N. Frank[4] and J. Raddatz[1,2]

[1]Institute of Geosciences, Goethe University Frankfurt, Frankfurt am Main, Germany, [2]Frankfurt Isotope and Element Research Center (FIERCE), Goethe University Frankfurt, Frankfurt am Main, Germany, [3]National Institute of Water & Atmospheric Research, Wellington, New Zealand, [4]Institute for Environmental Physics, University of Heidelberg, Heidelberg, Germany

Recent oceanographic observations have identified significant changes of intermediate water masses characterized by increased temperatures, lowered pH and deoxygenation. In order to improve our understanding as to how these changes may impact deep-sea ecosystems one important strategy is to reconstruct past oceanic conditions. Here we examine the applicability of the scleractinian cold-water coral *Solenosmilia variabilis* as a marine archive for the reconstructions of past intermediate water mass temperatures by using Lithium (Li)/Magnesium (Mg) ratios. In particular, our study addresses 1) the calibration of Li/Mg ratios against *in-situ* temperature data, 2) the reconstruction of past intermediate water mass temperatures using scleractinian coral fossil samples from the Brazilian continental margin and 3) the identification of intraspecies variability within the coral microstructure. Results showed that Li/Mg ratios measured in the skeletons of *S. variabilis* fit into existing Li/Mg-T calibrations of other cold-water scleractinian. Furthermore, the coral microstructure exhibits interspecies variability of Li/Ca and Mg/Ca ratios were also similar to what has been observed in other cold-water scleractinian corals, suggesting a similar biomineralization control on the incorporation of Li and Mg into the skeleton. However, the Li/Mg based temperature reconstruction using fossil samples resulted in unexpectedly high variations >10°C, which might not be solely related to temperature variations of the intermediate water mass over the last 160 ka on the Brazilian continental margin. We speculate that such temperature variability may be caused by vertical movements of the aragonite saturation horizon and the associated seawater pH changes, which in turn influence the incorporation of Li and Mg into the coral skeleton. Based on these results it is recommended

that future studies investigating past oceanic conditions need to consider the carbonate system parameters and how they might impact the mechanisms of Li and Mg being incorporated into skeletons of cold-water coral species such as *S. variabilis*.

KEYWORDS

cold water coral (CWC), south atlantic, *solenosmilia variabilis*, Li/Mg, intermediate water mass

1 Introduction

The reconstruction of past oceanic and environmental conditions is one important application to help predict the impact of the current climate change on ocean circulation, ocean chemistry and deep-sea ecosystems. Seawater temperature is a particularly important parameter to assess as temperature influences various physical and chemical processes within the oceanic system (Weyl, 1959). For decades, the Antarctic Intermediate water (AAIW) has experienced warming off the coast off Brazil. From 1958 to 2009, the temperature has increased to about 0.23°C (McCarthy et al., 2011).

To accurately predict how anthropogenic climate change will affect the mid-depth of the South Atlantic, it is crucial to study the sensitivity of physiochemical properties in marine systems to changes in atmospheric greenhouse gases such as CO_2, as well as rising atmospheric temperatures. Already, it is known how much deep ocean waters in certain regions have changed in terms of temperature. During the last ice age and the deglacial period (about 20,000-10,000 years ago), high-resolution records from ice cores from polar regions showed rapid (centennial to decadal) changes in ocean climate (Barnola et al., 1987; Indermühle et al., 1999; Petit et al., 1999; Augustin et al., 2004). Conventional paleoceanographic reconstructions are often made from marine sediment cores (e.g. Charles et al., 1996; Raddatz et al., 2017) but these have the disadvantage of being intermixed with marine organisms, thus blurring rapid signals (e.g. Leuschner et al., 2002). In addition, the timing of deposition is difficult to determine from the sediment cores, leading to inaccurate age models. As such, there is an urgent need to combine both atmospheric and oceanic records to understand the various coupling mechanisms involved during times of rapid climate change.

In this study cold-water scleractinian stony corals present a promising new tool to reconstruct past ocean properties. In comparison to other marine proxy archives in use, this group have the advantage that they, 1) commonly occur in almost all oceans, 2) are located in great depths, living far from sunlight inn well over 1000 m depth, 3) incorporate the isotopic and element composition of the surrounding seawater in equilibrium with various ocean parameters such as temperature and pH, 4) can live for decades to millennia, and lastly 5) their skeletons can be accurately dated using radioactive isotope decay methods (Cheng et al., 2000; Houlbrèque et al., 2010; Frank et al., 2011; Montagna et al., 2014; Raddatz et al., 2014a; Robinson et al., 2014; Wefing et al., 2017; Freiwald et al., 2021).

For instance, U/Ca and boron isotope systematics are commonly used for reconstruction of parameters of the carbonate system (Sinclair et al., 2006; Blamart et al., 2007; Anagnostou et al., 2011; Anagnostou et al., 2012; McCulloch et al., 2012; Raddatz et al., 2014a; Raddatz et al., 2014b; Raddatz et al., 2016). Element ratios such as P/Ca, B/Ca and Cd/Ca in scleractinian corals are known for the nutrient concentration (Adkins et al., 1998; Montagna et al., 2006; Mangini et al., 2010; Anagnostou et al., 2011; Hemsing et al., 2018; Spooner et al., 2018). Biological processes however, need to be considered in the development of proxies in coral skeletons, as the incorporation of the elements can be affected by different pathways. The most pronounced geochemical and mineralogical variations occur in corals between the center of calcification (COC) and the theca wall (e.g. Gladfeiter, 1982; Cohen et al., 2006; Meibom et al., 2006; Sinclair et al., 2006; Gladfelter, 2007; Meibom et al., 2008; Rollion-Bard et al., 2010; Raddatz et al., 2013; Schleinkofer et al., 2019). The COC is composed of small granular crystals and the fibrous aragonite of organic mineral compounds forming long aragonite needles (Gladfeiter, 1982; Constantz, 1989; Gladfelter, 2007). Various vital effects influence geochemical properties within the calcification process, both on the pathway itself as well as in the formation of the skeletal structure (Adkins et al., 2003; Gagnon et al., 2007). It is postulated that there are several ways that the elements enter the calcifying fluid. According to Holcomb et al. (2009) and Gagnon et al. (2007) the increase of the pH in the extracellular calcifying fluid causes a higher saturation of the Element/Ca (E/Ca) ratio in the COC than in the fibrous aragonite. In contrast Rollion-Bard et al. (2010) assumes the fibrous aragonite and COC to be formed independently and therefore have different E/Ca composition.

Other changes that may cause a difference in the coral chemistry and calcification process are Rayleigh fractionation and kinetic effects (Cohen et al., 2006; Montagna et al., 2006; Sinclair et al., 2006; Gagnon et al., 2007).

Recent studies developed a method to overcome such "vital effects", by implementing Li/Mg ratio of aragonitic marine carbonates (Bryan and Marchitto, 2008; Case et al., 2010; Hathorne et al., 2013; Raddatz et al., 2013). A positive correlation between Li/Ca and Mg/Ca suggest that the uptake mechanism and the biological and physicochemical factors are in fact the same for both E/Ca (Case et al., 2010; Raddatz et al., 2013; Montagna et al., 2014). By combining Li/Ca and Mg/Ca ratios the effect of the biological processes is reduced, resulting in temperature being the primary factor to influence the coral's Li/Mg composition. Hence, the Li/Mg ratios exhibits a strong inverse exponential relationship with temperature across both warm and cold-water corals of 0-30°C (Case et al., 2010; Hathorne et al., 2013; Raddatz et al., 2013; Montagna et al., 2014). This is also seen in benthic foraminifera (Stewart et al., 2020). Very few studies to date have applied this proxy for the reconstruction of past seawater temperatures (e.g. Montero-Serrano et al., 2013; Raddatz et al., 2014b; Fowell et al., 2016; Raddatz et al., 2016; Cuny-Guirriec et al., 2019).

The cold-water coral (CWC) *Solenosmilia variabilis* is one of the six most important reef building corals located in the deep sea but thus far, this group has not been the focus of paleoceanographic studies. *S. variabilis* occurs primarily in depths of 220-2.165 m and is often found below the dominat depths of the cold-water corals *Desmophyllum pertusum* (also known as *Lophelia pertusa*) and *Madrepora oculata*. The distribution of *S. variabilis* extends over mostly all oceans of the world however no occurrences have been recorded from the Antarctic Ocean nor in the North and East Pacific regions (Cairns, 1995; Freiwald et al., 2004; Davies and Guinotte, 2011). A possible reason for this distribution pattern is the appearance of *S. variabilis* in the aragonite undersaturated zones or close to the aragonite saturation horizon (Davies and Guinotte, 2011; Bostock et al., 2015), which in the North Pacific is in > 2000 m at greater depths than in the Northeast Atlantic (50-600 m) (Guinotte et al., 2006). Suitable growth areas are predicted in the Atlantic at continental slopes and the Mid ocean ridge (Davies and Guinotte, 2011). Today live and dead *S. variabilis* colonies are located primarily on underwater features such as seamounts in the New Zealand (NZ) region (Tracey et al., 2011) as well as in the Drake passage in the southwestern part of the Atlantic Ocean, southeastern Pacific Ocean. While the reef-like colonies in NZ do survive in waters that are deeper than 2000 m, they thrive in depths from ~800 to 1000 m (Davies and Guinotte, 2011; Tracey et al., 2011; Bostock et al., 2015; Freiwald et al., 2021).

Here we study the applicability of the scleractinian cold-water coral *S. variabilis* as a geochemical proxy archive for the reconstructions of past intermediate water masses in the Brazilian Continental margin, South Atlantic and in the South Pacific region. In particular, we address 1) the calibration of Li/Mg ratios against *in-situ* temperature, 2) the reconstruction of past intermediate water mass temperature using fossil samples and 3) discuss the intraspecies variability of Li/Mg ratios.

1.1 Study area

1.1.1 SW Pacific

Live collected *S. variabilis* were provided from the National Institute for Water and Atmosphere (NIWA), Wellington, New Zealand. The sampling area is restricted to offshore deep waters the NZ Exclusive Economic Zone in the Southwest Pacific (Figure 1A; Table 1). Two samples were collected from a ridge-like feature on, the Chatham Rise, an area that stretches about 1400 km to the east of New Zealand (Clark and Rowden, 2009) and one sample was gathered north of New Zealand, in the southern area of the Kermadec Ridge. All samples were located in the Antarctic intermediate water (AAIW) at a water depth of 1000-1300 m and a temperature range of 3.7-5.4°C (Locarnini

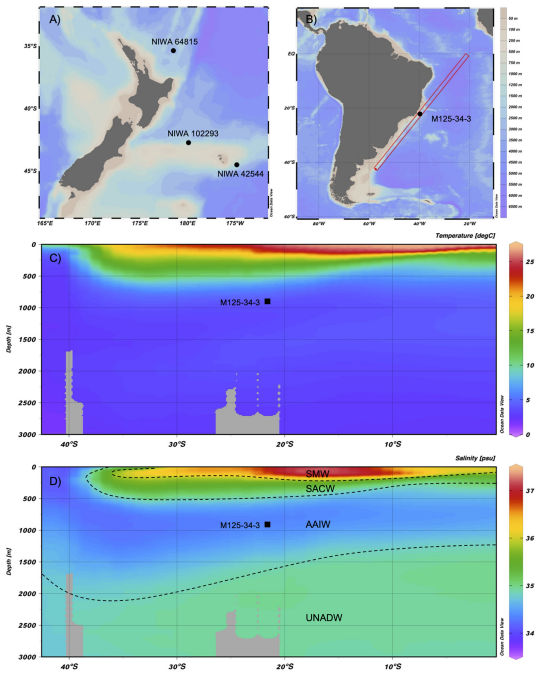

FIGURE 1
Map of the sampling locations: **(A)** live samples locations off New Zealand and **(B)** the location of the sediment core M125-34-3 off the coast of Brazil. **(C)** Temperature profile and **(D)** salinity profile of marked area in B, the black squares mark the position of the Bowie Mound (Schlitzer, 2021). The dashed lines show the boundary of the water masses from shallow to deep. These are: the salinity maximum waters (SMW), South Atlantic Central waters (SACW), Antarctic intermediate waters (AAIW) and Upper North Atlantic deep waters (UNADW).

TABLE 1 Coordinates of the analyzed samples in the Pacific (NIWA 102293; NIWA 42544; NIWA 64815) and the gravity core (M125-34-2) in the South Atlantic.

	NIWA 102293	NIWA 42544	NIWA 64815	M125-34-2
Latitude	42°43.62'S	44°29,88'S	35°21.18'S	21°56, 957'S
Longitude	179°53'49'W	174°49,02'W	178°30.66'E	39°35,117'W
Depth [m]	1020	1386	1382	866
Temp. [°C]	5.4 ± 0.2	3.8 ± 0.1	3.7 ± 0.2	4.3

et al., 2009). The samples are all located in the lower part of the AAIW, characterized by a low salinity of 34.4 g/kg (Antonov et al., 2009).

1.1.2 South Atlantic

The modern hydrography around the Bowie Mound, in the South Atlantic, to the east of Brazil is shown in Figure 1. The top water mass is the Salinity maximum water and reaches depth of up to 200 m (Mémery et al., 2000). In deeper waters, the north flowing South Atlantic Central Water (SACW) is characterized by lower temperatures and salinities. At the depth of the Bowie Mound (866 m) the AAIW follows with a transport direction to the north and low salinity (< 34.4 g/kg). At 900 m the Ω_{Ar} is ~1.2, the pH of the seawater ~7.97, the CO_3^2 concentration 79 µmol/kg and temperatures are about 4.3°C (Raddatz et al., 2020). Beneath AAIW the Upper North Atlantic Deep Water (UNADW) flows in the southward direction with higher salinity (Antonov et al., 2009).

2 Material and methods

Three live collected samples of *S. variabilis* came from various research surveys in New Zealand waters, Southwest Pacific region. Sample depth and temperature details are as follows: NIWA 102293 was collected at a depth of 1020 m in 5.4 ± 0.2°C; NIWA 42544 in 1386 m at 3.8 ± 0.1°C; and NIWA 64815 in a depth of 1382 m at 3.7 ± 0.2°C (Figures 1A, 2A; Table 1).

Fossil *S. variabilis* (Figure 2B) samples were retrieved during cruise M125 with the German research vessel METEOR and originate from the Bowie Mound, east of Brazil in a depth of 866 m and in 4.3°C (Figure 1; Table 1; Bahr et al., 2016).

The 5.86 m gravity core retrieved from Bowie Mound covered 160 ka and was characterized by non-coral-bearing and coral-bearing intervals. The coral-bearing intervals mainly comprised fossil forms of *S. variabilis* cold-water corals (Raddatz et al., 2020), and these were bedded in silty clay and clay-like

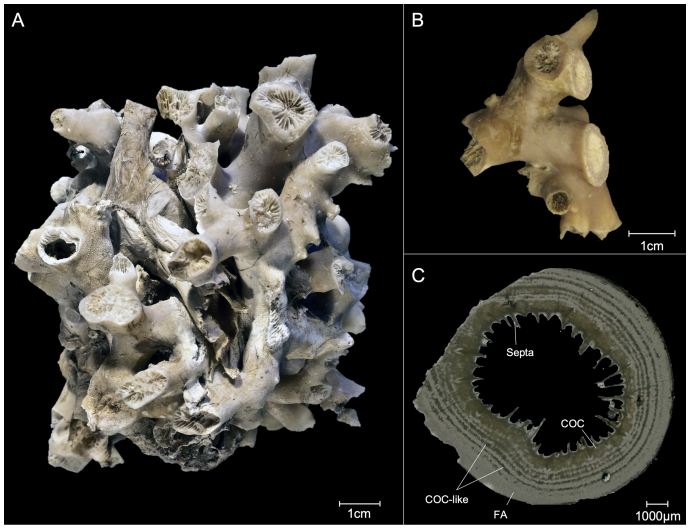

FIGURE 2
Different representations of the coral samples of S. variabilis: **(A)** Live picked sample in the Pacific near New Zealand. **(B)** Fossil sample of the Bowie Mound in AAIW and **(C)** cross section of a fossil sample; COC, center of Calcification; FA, Fibrous aragonite.

sand sediment (Bahr et al., 2020), providing very good preservation of the coral fragments.

The coral fragments were dated by using the ^{230}Th/U method (seen in Raddatz et al., 2020). Further information on the structure of the sediment core can be obtained from the studies by Raddatz et al. (2020) and Bahr et al. (2020). For this study a total of 27 samples were analyzed.

2.1 Element/Ca measurements

About 1 mg of calcium-carbonate was taken from the uppermost calices extracted with a Proxxon IBS/E dremel tool out of the theca wall. Samples have been drilled by avoiding visible lines of calcification (COC), as they display different element compositions compared to the surrounding theca wall (Gagnon et al., 2007; Montagna et al., 2014). Subsequently, samples were cleaned by weak acid leach in 5 % HNO_3 for 5 sec. Samples for the heterogeneity profiles (Figure 2C; N = 5-6) did not avoid COCs and were extracted using a Micromill.

Elemental ratios of CWCs were measured with an Inductively-Coupled-Plasma-Mass-Spectrometer (ICP-MS) ThermoScientific Element 2 at Fierce, Institute of Geoscience, Goethe University Frankfurt. Approximately 150 µg of homogenized carbonate powder was dissolved in 1.8 ml 2% HNO_3 containing 1.2 ppm Yttrium (Y) used as an internal standard. The measured intensities were background subtracted and standardized internally to Y and normalized to Ca. External standards were made from single-element solutions to match typical element compositions of cold-water scleractinian corals (Rosenthal. 1999). The coral standard JCp- 1 was measured after every fifth sample in order to allow for any drift corrections. The measured JCp-1 (N = 15) are consistent with the recommended values by Hathorne et al. (2013): Li/Ca 6.185 ± 0.107 µmol/mol, Mg/Ca 4.199 ± 0.065 mmol/mol and this study Li/Ca 6.036 ± 0.701 µmol/mol (97.6 %), Mg/Ca 4.153 ± 0.374 mmol/mol (98.9 %).

3 Results and discussion

3.1 *S. variabilis* as a geochemical archive for Li/Mg based temperature reconstructions

3.1.1 Adding *S. variabilis* to the Li/Mg-T calibration

In previous studies, elemental ratios (e.g. Li/Ca, Sr/Ca, Mg/Li) have been identified to be temperature depended in scleractinian cold-water corals (Case et al., 2010; Raddatz et al., 2013; Raddatz et al., 2014a). The most robust temperature proxy, including aragonitic zooxanthellate (shallow) and azooxanthellate (deep) scleractinian, appears to be Li/Mg ratio (Case et al., 2010; Montagna et al., 2014; Cuny-Guirriec et al., 2019; Stewart et al., 2020).

To test the cold-water coral *S. variabilis* as a suitable archive for reconstructions of intermediate water temperatures, the Li/Mg-temperature calibration by Montagna et al. (2014), was applied:

$$\mathrm{Li/Mg\,(mmol/mol)} = 5.41 \exp(-0.049 \pm 0.002 \times T\,(^{\circ}C)), R^2 = 0.975. \quad (1)$$

This calibration includes a temperature range of 0-30°C for cold- temperate- and warm-water scleractinian corals. In addition, the study by Stewart et al. (2020) extended this calibration to cover other aragonitic corals, including stylasterid hydrocorals, scleractinian (including Zooxanthellate) corals, as well as foraminifera:

$$\mathrm{Li/Mg\,(mmol/mol)} = 5.42 \pm 0.04 \exp(-0.050 \pm 0.0004 \times T\,(^{\circ}C)), R^2 = 0.97 \quad (2)$$

within uncertainty similar to the original calibration by Montagna et al. (2014).

Using the *in-situ* temperature data, extracted from World Ocean Atlas 2009 (Locarnini et al., 2009), the live collected samples from the SW Pacific produced expected Li/Mg ratios of 2.74 ± 0.14 mmol/mol (2SD) at 5.4 ± 0.5°C, 4.52 ± 0.78 mmol/mol at 3.8 ± 0.1°C and 3.74 ± 0.61 mmol/mol at 3.7 ± 0.2°C (Figure 3). Combining these data with published data from Case et al. (2010) and Montagna et al. (2014) results in the following empirical Li/Mg-T calibration:

$$\mathrm{Li/Mg\,(mmol/mol)} = 5.23 \exp(-0.46 \times T\,(^{\circ}C)), R^2 = 0.94. \quad (3)$$

The new samples and calibration are consistent with the original exponential function by Montagna et al. (2014), considering the confidence interval (Figure 3).

3.2 Li/Mg based temperatures using fossil *S. variabilis* from Bowie Mound, off Brazil

The Li/Mg measurements obtained from the Bowie Mound samples produced a variability of 2.55-5.55 ± 0.11 mmol/mol (Figure 4), resulting in a large temperature range of - 0.53 to 15.34 ± 1.55°C, when applying the Li/Mg-Temperature calibration by Montagna et al. (2014). In particular, four samples plot outside the expected temperature range of 4-15.2°C (Mienis et al., 2014; Raddatz and Rüggeberg, 2021). AAIW temperatures of up to 15°C appear very high considering the water depth of almost 900 m (Figure 5). However, Mg/Ca data based temperature reconstruction using the endobenthic foraminiferal species *Uvigerina* spp. also show reconstructed temperature variations of 8-9°C (± 1°C 2σ) in the intermediate water (IW) (852 m water

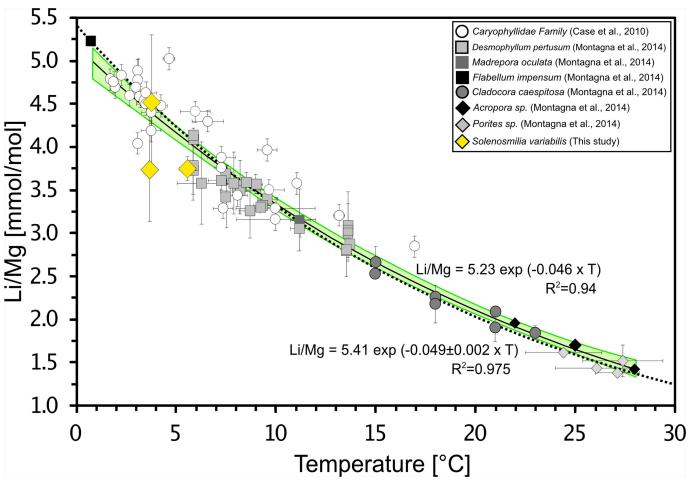

FIGURE 3
Li/Mg. ratio vs. seawater temperature for the published data Case et al. (2010); Montagna et al. (2014) and new data from current study (yellow diamond). The temperature range of cold-water, temperate, and warm-water corals is 0-30°C with a range of the Li/Mg of 1-5.5 mmol/mol measured by laser and solution ICP-MS. The additional measurements are 2.74 ± 0.14 mmol/mol (2SD) at 5.4 ± 0.2°C, 4.52 ± 0.78 mmol/mol at 3.8 ± 0.1°C and 3.74 ± 0.61 mmol/mol at 3.7 ± 0.2°C. The calibration of Montagna et al. (2014) is shown as black dashed line (R2 = 0.975). The black solid line indicates the new function with additional data of this study (R2 = 0.94). Light green shaded band show the 95% confidence interval.

depth) in the SW Atlantic (M78/1-235-1; 11°36.53'N, 60°57.86'W) over the last 24 ka (Poggemann et al., 2018).

The Bowie Mound represent five distinct coral growth periods (C_1-C_5) according to their occurrence between 0-160 ka (Raddatz et al., 2020) (Table 2). The calculated average Li/Mg temperature are with 7.71°C (± 1.55°C, 2SD), by 3.4°C higher than the present day ambient AAIW (Raddatz et al., 2020).

At about 16.5 ka, Poggemann et al. (2018) recorded an IW temperature of 4.4°C based on the Mg/Ca ratios of benthic foraminifera, which is consistent with the average temperature of 3.2°C in this study in C_1 (Table 2). The cold temperatures of < 4°C retrieved from one of the two coral fragments in C_1 and the one sample from C_2 cannot be treated as outliers, since Roberts et al. (2016) also reconstructed temperatures below 0°C in the IW at a depth of 598 m 2-20 ka BP. Accordingly, we assume here that the cold temperatures are part of the ecological niche of *S. variabilis*, as they live in the South Pacific Region of New Zealand at 2-3°C (Davies and Guinotte, 2011).

Compared to average temperature of the last 160 ka, *S. variabilis* occurred in colder temperature periods (Figure 5A), in times when both, global sea level and atmospheric CO_2 concentration were lower than they are today (Figures 5B, F; Petit et al., 1999; Grant et al., 2012). The occurrence of *S. variabilis* during these periods correlates with the cold events in the northern hemisphere, in particular the Heinrich stadial (HS) 1 before 14.6-18 ka, the HS4 before approx. 40 ka and the HS6 before 60 ka, as reported in the study by (Raddatz et al., 2020). During HS's large amounts of ice collapsed from the northern ice sheets (Toggweiler and Lea, 2010), thereby reduced the temperature gradient between the two hemispheres (Toggweiler and Lea, 2010). There is an ongoing discussion as to whether the Atlantic meridional overturning circulation (AMOC) was significantly weakened during such periods or possibly completely ceased and therefore inhibited North Atlantic deep-water formation (NADW) (Böhm et al., 2014; Lund et al., 2015; Lynch-Stieglitz 2017; Poggemann et al., 2017). The conditions for a collapse scenario could only have been fulfilled in HS1, HS2 and HS11; HS3 to HS10 resulted only to a weakening of NADW formation (Böhm et al., 2015). Poggemann et al. (2018) postulated three possible explanations for the heating of IW in HS1: (1) the exchange of the AAIW with warm water, (2) a heating of the surface water, which is transferred to the intermediate water, or (3) a warming of the AAIW itself. In the first scenario, warmer water masses from the north would have had to replace the IW or at least be involved in their warming (Poggemann et al., 2018). However, the influence of overlying or northerly water masses could not be detected by using different proxies (Poggemann et al., 2018). The second scenario can be excluded here as the SST in the South Atlantic (Figures 5D, E; Santos et al., 2017; Hou et al., 2020) was quite constant and do not correlate with the temperature at *S. variabilis* locations in the IW. Therefore, the present data set supports the hypothesis of the third scenario, in which the AAIW warmed by itself. Poggemann et al. (2018) demonstrated a warming of the IW in HS1 of about 1.6-10.9°C, which is consistent with the temperature ranges of 1.4-3.3°C obtained in this study. The apparently weakened or even ceased southward flowing NADW no longer influenced the

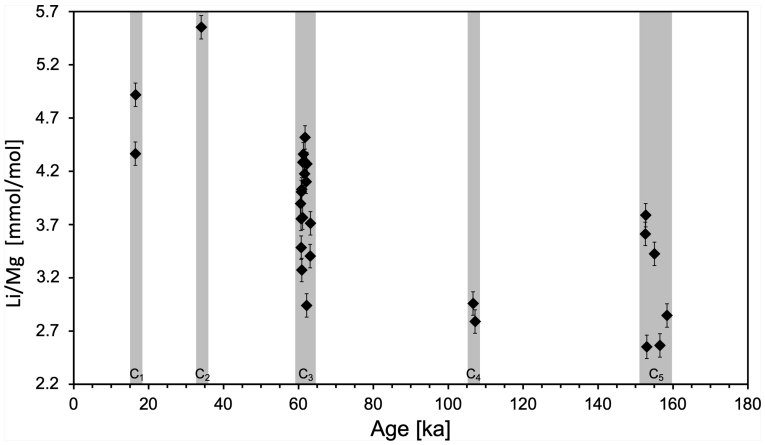

FIGURE 4
Li/Mg [mmol/mol] (± 0.11 2SD) measurements of fossil S. variabilis of the past 180 ka, subdivided in intervals C1-C5.

formation of the AAIW in the HS1 (Böhm et al., 2015; Poggemann et al., 2017). Additionally, this contributed to an intense upwelling and release of CO_2 from the Circumpolar Deepwater (CPDW) in the SO (e.g. Broecker, 1998; Burke and Robinson, 2012; Poggemann et al., 2017). The resulting increase in nutrient concentration in the SO could not be metabolized due to an insufficient iron content (e.g. Martínez-García et al., 2014). Subsequently, these excessive nutrients were transported northwards *via* AAIW to the tropical West Atlantic (Poggemann et al., 2017). This may have increased primary production and enhanced the biological pump, leading to a deglacial CO_2 plateau in the atmosphere and an elevated export of organic matter to the deep sea (Archer et al., 2000; Sigman and Boyle, 2000; Marcott et al., 2014). The resulting higher respiration outputs of CO_2 in the AAIW has the potential to lower seawater pH and drive aragonite dissolution, thereby shift the aragonite compensation depth. The study by Allen et al. (2015) presents such an effect of CO_3^{2-}. decrease in the deep water and a lowering in atmospheric CO_2 in the southwest Pacific during the onset of HS1 (18-20 ka). In contrast Lynch-Stieglitz et al. (2019) suggests that the high nutrient content in the water masses is not the source of the high CO_2 content in the deglacial. The study assumes a direct atmosphere CO_2 uptake direct by the surface and intermediate water masses in the Southern and North Atlantic.

It is typical for *S. variabilis* to grow in a temperature range of 3-4°C, which differs by 3°C from *D. pertusum* (Fallon et al., 2014; Flögel et al., 2014; Gammon et al., 2018). As *D. pertusum* exhibits temperature fluctuations of more than 6°C in Tisler Reef (Guihen et al., 2012), we also suggest a large tolerance range of temperature (> 8°C) and possibly other environmental parameters for *S. variabilis*. While *D. pertusum* occurs primarily in interglacial periods at higher latitudes at shallower depths, *S. variabilis* has already been documented to prefer more extreme environmental conditions at lower latitudes, greater depths and thus less aragonite-saturated water masses (Schröder-Ritzrau et al., 2005; Thresher et al., 2011; Flögel et al., 2014; Bostock et al., 2015; Gammon et al., 2018).

Considering the high temperature tolerance, we assume, that a secondary factor influences the incorporation of Li and Mg into the coral skeleton. Regarding the lower aragonite saturation within the occurrence of *S. variabilis*, we propose the aragonite saturation here as a secondary controller of Li/Mg. At a aragonite saturation($\Omega_{Ar} = ([Ca^{2+}] \times [CO_3^{2-}])/K_{sp}$; K_{sp} is the solubility product of aragonite) $\Omega_{Ar} > 1$ precipitation is induced, whereas at $\Omega_{Ar} < 1$ dissolution of aragonite is preferred (Mucci, 1983; Doney et al., 2009).

Aragonite dissolution in the late Pleistocene South Atlantic has been reconstructed using the pteropod *Limacina inflata* dissolution index (LDX) (Gerhardt et al., 2000; Gerhardt and Henrich, 2001). In particular, in the western South Atlantic, LDX traced undersaturated AAIW and Upper Circumpolar Deep Water (UCDW; Henrich et al., 2003). The coral periods (C_1-C_4) mostly occur during such phases of low aragonite saturation (Henrich et al., 2003). Since aragonite saturation influences the calcification rate, this could also have an impact on the elemental composition of the Li/Mg. Such an effect has been demonstrated in foraminifera on Mg/Ca-temperature proxy (Gray et al., 2018; Gray and Evans, 2019). Several pathways of element incorporation into foraminifera shells have been postulated as well as vital effects that control the incorporation of Mg during calcification (Bentov and Erez, 2006). Furthermore it has been shown that also salinity and pH influence the Mg/Ca the shell composition (Gray and Evans, 2019). In addition to the temperature sensitivity, the study conducted by Gray and Evans (2019) on foraminifera revealed

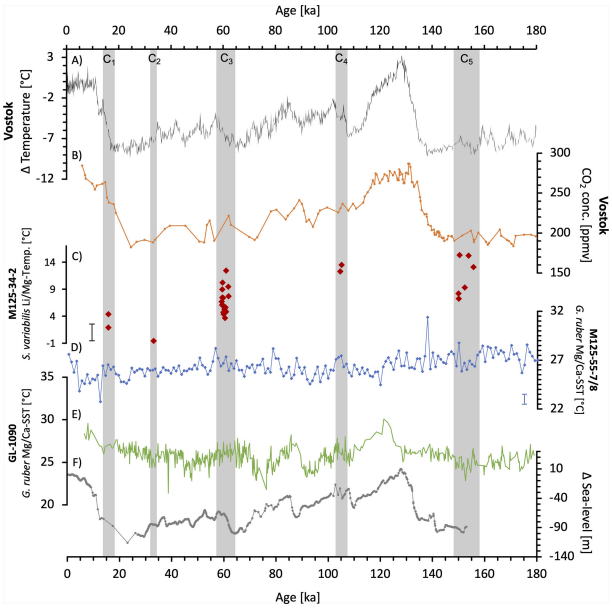

FIGURE 5
Evolution of enviromental parameters over the last 180 ka before present. **(A)** The temperaturefluctuations, averaged over the last 1,000 years, from the Vostok ice core (Petit et al., 1999). **(B)** CO2 concentration in ppmv reconstructed from the Vostok ice core (Petit et al., 1999). **(C)** Temperature reconstruction of the SAIW from sediment core M125-34-2, using the Li/Mg in the CWC S. variabilis (this study). With a 2SD of 1.55°C calculated from the JCp-1 measurements. **(D)** Temperature reconstruction of surface water from the southwestern tropical Atlantic (M125-55-7/8) based on the Mg/Ca of Globigerinoides ruber (G. ruber) (pink). The standard deviation is ±0.5°C (Hou et al., 2020). **(E)** Surface water temperatures of the subtropical western South Atlantic reconstructed from sediment core GL-1090 of the Mg/Ca of G. ruber (Santos et al., 2017). **(F)** Global sea level variations referenced to present-day sea level (Grant et al., 2012). The gray bars mark the intervals (C_{1-5}) of S. variabilis.

a salinity sensitivity of 3.6 ± 0.01 % (2SD) per g/kg and a carbonate chemistry sensitivity of -5 to -9 % per 0.1 pH unit. This may also be valid for Li/Mg with respect to aragonite saturation. To follow this up, further studies should investigate the dependence of Li/Mg on aragonite saturation using boron isotopes and U/Ca (Anagnostou et al., 2011; Anagnostou et al., 2012; McCulloch et al., 2012).

3.3 Heterogeneity profiles of Li/Ca and Mg/Ca in *S. variabilis*

Different fluctuations on the cross-sectional axis, with almost uniform changes are reflected in the elemental ratios of the coral skeleton (Figure 6). Here the change of E/Ca ratios are prominent in the COC and fibrous aragonite (theca wall) (Figure 2). In three of four samples, the Mg/Ca and Li/Ca ratios exhibits a decreasing trend following the direction of the COC structure to the theca-wall (Figures 6A–C), at the fourth sample (Figure 6D) the Li/Ca and Mg/Ca increase. The Mg/Ca shows a range of 0.75-4.71 ± 0.25 mmol/mol (2SD). Within the coral structure the variability is about 0.75-2.27 mmol/mol, with an average variation factor of 1.5. The Li/Ca varies between 8.48 and 19.31 ± 0.77 µmol/mol (2SD), with an internal fluctuation of ~5 µmol/mol and an average variation factor of 1.5. The corresponding Li/Mg ratios indicate an increase in the direction of the theca-wall in three samples, in the fourth sample the trend is opposite. The measured range is 2.93-5.15 ± 0.11 mmol/mol (2SD).

Previous studies also indicated internal fluctuations of Mg/Ca and Li/Ca up to a variation factor of 3 (e.g. Case et al., 2010; Raddatz et al., 2013; Montagna et al., 2014). Here we compare the *S. variabilis* measurements with the additional scleractinian cold-water corals: *D. pertusum*, *Balanophyllia* sp., *Desmophyllum cristagalli (D. cristagalli)* and *Desmophyllum dianthus (D. dianthus)* (Figure 7). *D. pertusum* exhibits a Mg/Ca range of 1.5-4.6 mmol/mol and Li/Ca about 8.0-25.3 µmol/mol with a variation factor of 1.48-2.4 and 1.68-1.8 (Raddatz et al., 2013; Rollion-Bard and Blamart, 2015 and Schleinkofer et al., 2019). *Balanophyllia* reveals Mg/Ca variations of 1.2-2.8 mmol/mol and 6.0-13.5 µmol/mol Li/Ca, with a variation factor over 2 on both E/Ca (Case et al., 2010). The Mg/Ca is about 2.0-3.7 mmol/mol and Li/Ca is 7.7-13.8 µmol/mol in the internal coral structure of *D. cristagalli*, the variation factor for both ratios is 1.8 (Rollion-Bard and Blamart, 2015). Recorded Mg/Ca in *D. dianthus* indicate a range of 0.9-4.0 mmol/mol and Li/Ca of 6.0-15.0 µmol/mol, with a variation factor of 2-3 and 2 (Gagnon et al., 2007; Case et al., 2010), which is higher than in *S. variabilis*.

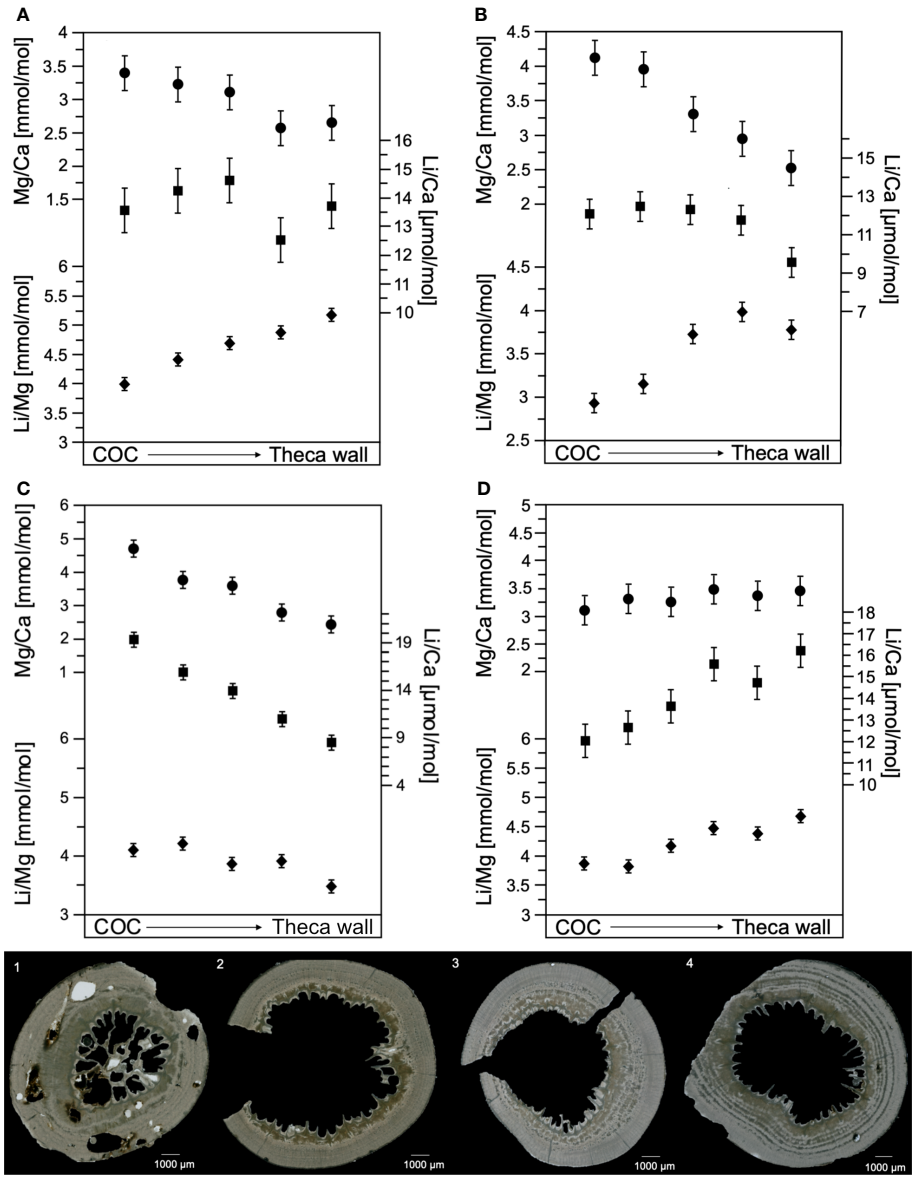

FIGURE 6
Elemental ratios Mg/Ca [mmol/mol], Li/Ca [µmol/mol], and Li/Mg [mmol/mol], of four samples from the South Atlantic. The doubled standard variation for Mg/Ca ±0.25 mmol/mol, Li/Ca ±0.77 µmol/mol and Li/Mg ±0.11 mmol/mol was determined by JCp-1 measurements. Figures 1–**4** below, show the cross-section of the analyzed sample with an allocation of **1-A, 2-B, 3-C** and **4-D**. Samples were collected by micromill starting at the COC structure ongoing until the theca wall.

TABLE 2 Coral periods C_1-C_5, their time range, temperature range and average temperature.

Coral periods	C_1	C_2	C_3	C_4	C_5
Time range [ka]	16.443-16.476	34.03	60.53-63.19	106.62-107.14	152.61-158.40
Temp. range [°C]	1.9-4.3	-0.5	3.6-12.4	12.3-13.5	7.2-15.3
Average Temp. [°C]	3.2	-0.5	6.81	12.9	11.4

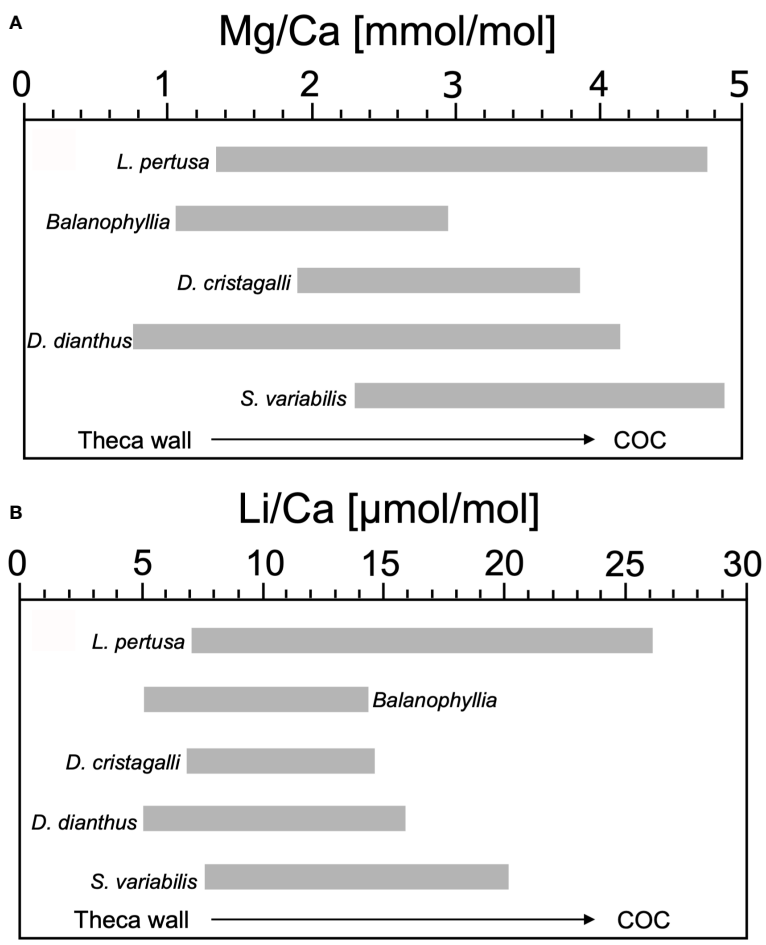

FIGURE 7
Comparison of the Mg/Ca [mmol/mol] and Li/Ca [µmol/mol] in the internal skeleton structure of different CWC's: L. pertusa, Balanophyllia, D. cristagalli, D. dianthus and S. variabilis. **(A)** In L. pertusa, Mg/Ca vary in a range of 1.5-4.6 mmol/mol (Raddatz et al., 2013; Rollion-Bard and Blamart, 2015; Schleinkofer et al., 2019), in Balanophyllia 1.2-2.8 mmol/mol (Case et al., 2010), in D. cristagalli 2.0-3.7 mmol/mol (Rollion-Bard and Blamart, 2015), in D. dianthus the range of values extends of 0.9-4.0 mmol/mol (Gagnon et al., 2007; Case et al., 2010), and in S. variabilis between 2.4-4.7mmol/mol (this study). **(B)** Li/Ca range from 8.0-25.3 µmol/mol in L. pertusa (Raddatz et al., 2013; Rollion-Bard and Blamart, 2015), 6.0-13.5 µmol/mol in Balanophyllia (Case et al., 2010), in D. cristagalli 7.7-13.8 µmol/mol (Rollion-Bard and Blamart, 2015), in D. dianthus 6.0-15.0 µmol/mol (Case et al., 2010), and in S. variabilis 8.5-19.3 µmol/mol (this study).

The internal correlation of the Mg/Ca and Li/Ca ratios is apparent in all measurements, especially in sample D (Figure 6D). These internal variations are suspected to be induced by another factor than temperature. Based on the positive correlation between Mg/Ca and Li/Ca (Figure 8) (R^2 = 0.48; P =1.66*10^{-8}), it is most likely that both ratios are controlled by similar mechanism (Case et al., 2010; Raddatz et al., 2013) and diagenetic overprints appear to be unlikely. The increase in element ratios from the COC to the outer part of theca wall in sample D (Figure 6) can be explained by the occurrence of several COC-like structures within the fibrous aragonite (shown in Figure 2C). Hence, the internal fluctuations in the remaining samples can also be explained by the presence of COC-like structures.

Finally, *S. variabilis* exhibits the same fluctuation in E/Ca ratios as other scleractinian corals that are likely induced by vital effects. We assume here that Li/Ca and Mg/Ca in *S. variabilis* also mainly follows the Rayleigh-fractionation model, as this is the primary model in warm, temperate and cold-water corals (Montagna et al., 2014). However, the variation factor is still smaller compared to other CWC's, possibly due to the slow growth rate of *S. variabilis* (Fallon et al., 2014; Gammon et al., 2018). The E/Ca ratios of *S. variabilis* are most consistent with measured E/Ca ratios of *D. pertusum* in the North Atlantic, Mediteranean Sea and Red Sea (Figure 8; Raddatz et al., 2013; Rollion-Bard and Blamart, 2015; Schleinkofer et al., 2019). *S. variabilis* growth rate is about 0.8-1.25 mm/yr in natural habitats (Fallon et al., 2014) and in cultivation experiments

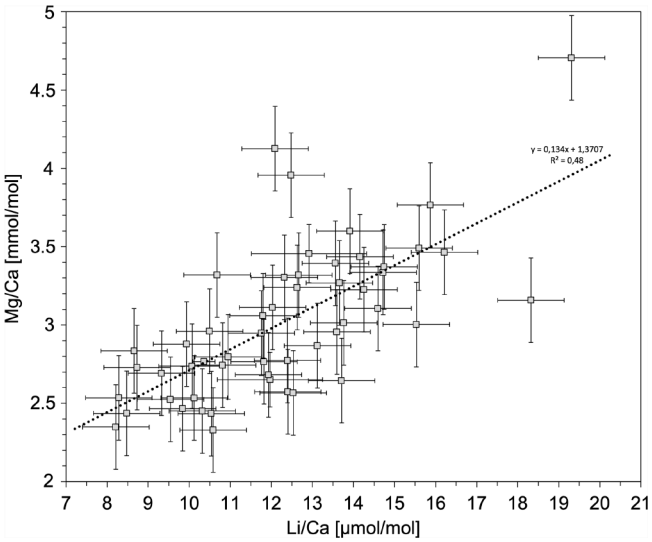

FIGURE 8
All samples exhibit a correlation of Mg/Ca and Li/Ca in S. variabilis, which is shown by the dotted line. Uncertainties are indicated in 2SD.

about 0.5-3.968 mm/yr (Gammon et al., 2018) with a similar growth rate as *D. pertusum* about 2.44-3.77 mm/yr in the Gulf of Mexico (Brooke and Young 2009). The gradual growth rate of *S. variabilis* could result in an increased variability of the element concentrations and formation of COC-like structures due to the reflection of longer time scales of elemental incorporation.

The large internal fluctuation within the coral structure represents an inaccuracy in the proxy application. Here we used bulk samples for solution-based chemistry, which might contain COC-like structures and could affect the resulting Li/Mg. However, Mg/Ca and Li/Ca show larger fluctuations, which are already reduced by using Li/Mg. To avoid a possible bias, alternative sampling strategies can be applied. Since COC-like structures can be visually identified in the skeleton of the coral, they could be excluded if sampled by a micromill. Another approach are *in situ* techniques using laser ICP-MS, EPMA (electron probe microanalyzer) or NanoSIMS (secondary ion mass spectrometry) to directly detect and reject variations induced by the COC or COC-like structures. High Mg/Ca ratios could be caused by high organic material content in the COC/COC-like structures as shown in other scleractinian corals (Cuif et al., 2003, Stolarski 2003).

4 Conclusion

This study provides the first application of using *S. variabilis* as a geochemical archive using the Li/Mg-T paleothermometer. Our analysis of live collected samples from the South Pacific Region of New Zealand fit in the existing Li/Mg-Temperature calibrations, indicating that a species-specific calibration is not needed.

However, the reconstructed Li/Mg bases paleotemperatures of intermediate water masses from the fossil *S. variabilis* coral from sediment cores exhibit relatively large temperature fluctuations of up to 15°C in the AAIW off Brazil. We propose that such high temperature fluctuations can be, to a certain degree, related to intermediate water mass warming during Heinrich Stadials, but are possibly also related to change in the aragonite saturation state.

Nevertheless, the internal variation of Li/Ca and Mg/Ca in the coral microstructure is consistent with previous studies of e.g. Case et al. (2010); Raddatz et al. (2013) and Schleinkofer et al. (2019). Compared to other scleractinian CWCs, the variation factor is assumed to be related to the slow growth rate.

For more accurate reconstructions of temperature future studied should investigate other secondary factors, such as pH, aragonite saturation and salinity that might influence the Li and Mg incorporation in *S. variabilis*. We encourage further investigation on cold-water corals for their suitability as archives for their use in multiproxy studies. Especially with regard to studies on climate change, it is important to understand and recognize to which environmental conditions different species can adapt to and which future changes in their marine environment they can cope with.

Data availability statement

The raw data supporting the conclusions of this article will be made available by the authors, without undue reservation.

Author contributions

ES, SN and RJ contributed to conception and design of the study. ES, SA and RJ organized the database. ES wrote the first draft of the manuscript. SN, RJ, TD, FN wrote sections of the manuscript. RJ cruise participation. All authors contributed to manuscript revision, read, and approved the submitted version.

Acknowledgments

We thank the captain, crew and the scientific part of R/V Meteor cruise M125. The *S. variabilis* specimens off New Zealand were collected by NIWA staff as part of their various Ministry of Business, Innovation and Employment funded research programmes on R/V *Tangaroa* and by Fisheries New Zealand Observers. JR acknowledges funding from the Focus Track A/B programme by the Goethe University Frankfurt. This is FIERCE contribution No. 101.

Conflict of interest

The authors declare that the research was conducted in the absence of any commercial or financial relationships that could be construed as a potential conflict of interest.

Publisher's note

All claims expressed in this article are solely those of the authors and do not necessarily represent those of their affiliated organizations, or those of the publisher, the editors and the reviewers. Any product that may be evaluated in this article, or claim that may be made by its manufacturer, is not guaranteed or endorsed by the publisher.

References

Adkins, J. F., Boyle, E. A., Curry, W. B., and Lutringer, A. (2003). Stable isotopes in deep-sea corals and a new mechanism for "vital effects". *In: Geochimica Cosmochimica Acta* 67 (6), 1129–1143. doi: 10.1016/S0016-7037(02)01203-6

Adkins, J. F., Cheng, H., Boyle, E. A., Druffel, E. R. M., and Edwards, R. L. (1998). Deep-Sea coral evidence for rapid change in ventilation of the deep north atlantic 15,400 years ago. *Sci. (New York N.Y.)* 280 (5364), 725–728. doi: 10.1126/science.280.5364.725

Allen, K. A., Sikes, E. L., Hönisch, B., Elmore, A. C., Guilderson, T. P., Rosenthal, Y., et al. (2015). Southwest pacific deep water carbonate chemistry linked to high southern latitude climate and atmospheric CO2 during the last glacial termination. *Quaternary Sci. Rev.* 122, 180–191. doi: 10.1016/j.quascirev.2015.05.007

Anagnostou, E., Huang, K.-F., You, C.-F., Sikes, E. L., and Sherrell, R. M. (2012). Evaluation of boron isotope ratio as a pH proxy in the deep sea coral desmophyllum dianthus: Evidence of physiological pH adjustment. in. *Earth Planetary Sci. Lett.* 349-350, 251–260. doi: 10.1016/j.epsl.2012.07.006

Anagnostou, E., Sherrell, R. M., Gagnon, A., LaVigne, M., Field, M.P., and McDonough, W. F. (2011). Seawater nutrient and carbonate ion concentrations recorded as P/Ca, Ba/Ca, and U/Ca in the deep-sea coral desmophyllum dianthus. *Geochimica Cosmochimica Acta* 75 (9), 2529–2543. doi: 10.1016/j.gca.2011.02.019

Antonov, J. I., Seidov, D., Boyer, T. P., Locarnini, R. A., Mishonov, A. V., Garcia, H. E., et al. (2009). *World ocean atlas 2009,* Vol. Volume 2. 184 pp.

Archer, D., Winguth, A., Lea, D., and Mahowald, N (2000). What caused the glacial/interglacial atmospheric pCO2 cycles? *Reviews of Geophysics* 38 (2), 159–89. doi: 10.1029/1999RG000066

Augustin, L., Barbante, C., Barnes, P. R.F., Barnola, J. M., Bigler, M., Castellano, E., et al. (2004). Eight glacial cycles from an Antarctic ice core. *Nature* 429 (6992), 623–628. doi: 10.1038/nature02599

Bahr, A., Spadano Albuquerque, A. L., Ardenghi, N., Batenburg, S., Bayer, M., et al. (2016). *South American hydrological balance and paleoceanography during the late pleistocene and Holocene (SAMBA) - cruise no. M125 - march 21 - April 15, 2016 - Rio de Janeiro (Brazil) - fortaleza (Brazil)* (Unter Mitarbeit von TIB - Technische Informationsbibliothek Universitätsbibliothek Hannover and Alfred-Wegener-Institut für Polar- und Meeresforschung).

Bahr, A., Doubrawa, M., Titschack, J., Austermann, G., Koutsodendris, A., Nürnberg, D, et al (2020). Monsoonal forcing of cold-water coral growth off southeastern Brazil during the past 160 kyr. *Biogeosciences* 17 (23), 5883–5908. doi: 10.5194/bg-17-5883-2020

Barnola, J. M., Raynaud, D., Korotkevich, Y. S., and Lorius, C. (1987). Vostok ice core provides 160,000-year record of atmospheric CO2. *Nature* 329 (6138), 408–414. doi: 10.1038/329408a0

Bentov, S., and Erez, J. (2006). Impact of biomineralization processes on the mg content of foraminiferal shells: A biological perspective. *Geochem. Geophys. Geosyst.* 7 (1). doi: 10.1029/2005GC001015

Blamart, D., Rollion-Bard, C., Meibom, A., Cuif, J.-P., Juillet-Leclerc, A., and Dauphin, Y. (2007). Correlation of boron isotopic composition with ultrastructure in the deep-sea coral lophelia pertusa: Implications for biomineralization and paleo-pH. *Geochem. Geophys. Geosyst.* 8 (12). doi: 10.1029/2007GC001686

Böhm, E., Lippold, J., Gutjahr, M., Frank, M., Blaser, P., Antz, B., et al. (2015). Strong and deep Atlantic meridional overturning circulation during the last glacial cycle. *Nature* 517 (7532), 73–76. doi: 10.1038/nature14059

Bostock, H. C., Tracey, D. M., Currie, K. I., Dunbar, G. B., Handler, M. R., Mikaloff Fletcher, S. E., et al. (2015). : The carbonate mineralogy and distribution of habitat-forming deep-sea corals in the southwest pacific region. *Deep Sea Res. Part I: Oceanogr. Res. Papers* 100, 88–104. doi: 10.1016/j.dsr.2015.02.008

Broecker, W. S. (1998). Paleocean circulation during the last deglaciation: A bipolar seesaw? *Paleoceanography.* 13(2), 119–121. doi: 10.1029/97pa03707

Brooke, S., and Young, C.M (2009). In situ measurement of survival and growth of Lophelia pertusa in the northern Gulf of Mexico. *Marine Ecology Progress Series* 397, 153–61. doi: 10.3354/meps08344

Bryan, S. P., and Marchitto, T. M. (2008). Mg/Ca-temperature proxy in benthic foraminifera: New calibrations from the Florida straits and a hypothesis regarding Mg/Li. *Paleoceanography* 23 (2), n/a–n/a. doi: 10.1029/2007PA001553

Burke, A., and Robinson, L. (2012). The southern ocean's role in carbon exchange during the last deglaciation. *Science* 335, 557–561. doi: 10.1126/science.1208163

Cairns, S. D. (1995). *The marine fauna of new Zealand: Scleractinia (Cnidaria: Anthozoa) (103:139).*

Case, D. H., Robinson, L. F., Auro, M. E., and Gagnon, A. C. (2010). Environmental and biological controls on mg and Li in deep-sea scleractinian corals. *Earth Planetary Sci. Lett.* 300 (3-4), 215–225. doi: 10.1016/j.epsl.2010.09.029

Charles, C. D., Lynch-Stieglitz, J., Ninnemann, U. S., and Fairbanks, R. G. (1996). Climate connections between the hemisphere revealed by deep sea sediment core/ice core correlations. in. *Earth Planetary Sci. Lett.* 142 (1-2), 19–27. doi: 10.1016/0012-821X(96)00083-0

Cheng, H., Adkins, J., Edwards, R.L., and Boyle, E. A. (2000). U-Th Dating of deep-sea corals. *Geochimica Cosmochimica Acta* 64 (14), 2401–2416. doi: 10.1016/S0016-7037(99)00422-6

Clark, M. R., and Rowden, A. A. (2009). Effect of deepwater trawling on the macro-invertebrate assemblages of seamounts on the chatham rise, new Zealand. *Deep Sea Res. Part I: Oceanogr. Res. Papers* 56 (9), 1540–1554. doi: 10.1016/j.dsr.2009.04.015

Cohen, A. L., Gaetani, G. A., Lundälv, T., Corliss, B. H., and George, R. Y. (2006). Compositional variability in a cold-water scleractinian, lophelia pertusa: New insights into "vital effects". *Geochem. Geophys. Geosyst.* 7 (12). doi: 10.1029/2006GC001354

Constantz, B. R. (1989). "Skeletal organization in Caribbean acropora spp. (Lamarck)," in *Rex E. crick (Hg.): Origin, evolution, and modern aspects of biomineralization in plants and animals* (Boston, MA: Springer US), 175–199

Cuif, J. P., Dauphin, Y., Doucet, J., Salome, M., and Susini, J. (2003). XANES mapping of organic sulfate in three scleractinian coral skeletons. *Geochimica et Cosmochimica Acta* 67(1), 75–83. doi: 10.1016/S0016-7037(02)01041-4

Cuny-Guirriec, K., Douville, E., Reynaud, S., Allemand, D., Bordier, L., Canesi, M., et al. (2019). Coral Li/Mg thermometry: Caveats and constraints. *Chem. Geol.* 523, 162–178. doi: 10.1016/j.chemgeo.2019.03.038

Davies, A. J., and Guinotte, J. M. (2011). Global habitat suitability for framework-forming cold-water corals. *PloS One* 6 (4), e18483. doi: 10.1371/journal.pone.0018483

Doney, S. C., Fabry, V. J., Feely, R. A., and Kleypas, J. A. (2009). Ocean acidification: the other CO2 problem. *Annu. Rev. Mar. Sci.* 1, 169–192. doi: 10.1146/annurev.marine.010908.163834

Fallon, S. J., Thresher, R. E., and Adkins, J. (2014). Age and growth of the cold-water scleractinian solenosmilia variabilis and its reef on SW pacific seamounts. *Coral Reefs* 33 (1), 31–38. doi: 10.1007/s00338-013-1097-y

Flögel, S., Dullo, W.-C., Pfannkuche, O., Kiriakoulakis, K., and Rüggeberg, A. (2014). Geochemical and physical constraints for the occurrence of living cold-water corals. *Deep Sea Res. Part II: Topical Stud. Oceanogr.* 99, 19–26. doi: 10.1016/j.dsr2.2013.06.006

Fowell, S. E., Sandford, K., Stewart, J. A., Castillo, K. D., Ries, J. B., and Foster, G. L. (2016). Intrareef variations in Li/Mg and Sr/Ca sea surface temperature proxies in the Caribbean reef-building coral siderastrea siderea. *Paleoceanography* 31 (10), 1315–1329. doi: 10.1002/2016PA002968

Frank, N., Freiwald, A., Correa, M. L., Wienberg, C., Eisele, M., Hebbeln, D., et al. (2011). Northeastern Atlantic cold-water coral reefs and climate. in. *Geology* 39 (8), 743–746. doi: 10.1130/G31825.1

Freiwald, A., Fosså, J., Grehan, A., Koslow, T., and Roberts, J. (2004). *Cold-water coral reefs: Out of sight – no longer out of mind.*

Freiwald, A., Rogers, A., Hall-Spencer, J., Guinotte, J. M., Davies, A. J., Yesson, C., et al. (2021). *Global distribution of cold-water corals.*

Gagnon, A. C., Adkins, J. F., Fernandez, D. P., and Robinson, L. F. (2007). Sr/Ca and Mg/Ca vital effects correlated with skeletal architecture in a scleractinian deep-sea coral and the role of Rayleigh fractionation. *Earth Planetary Sci. Lett.* 261 (1-2), 280–295. doi: 10.1016/j.epsl.2007.07.013

Gammon, M. J., Tracey, D. M., Marriott, P. M., Cummings, V. J., and Davy, S. K. (2018). The physiological response of the deep-sea coral solenosmilia variabilis to ocean acidification. *PeerJ* 6, e5236. doi: 10.7717/peerj.5236

Gerhardt, S., Groth, H., Rühlemann, C., and Henrich, R. (2000). Aragonite preservation in late quaternary sediment cores on the Brazilian continental slope: implications for intermediate water circulation. *Int. Journ Earth Sci.* 88, 607–618. doi: 10.1007/s005310050291

Gerhardt, S., and Henrich, R. (2001). Shell preservation of *Limacina inflata* (Pteropoda) in surface sediments from the central and south Atlantic ocean: A new proxy to determine the aragonite saturation state of water masses. *Deep Sea Res. Part I: Oceanogr. Res. Papers* 48, 2051–2071. doi: 10.1016/S0967-0637(01)00005-X

Gladfeiter, E. H. (1982). Skeletal development in acropora cervicornis: I. patterns of calcium carbonate accretion in the axial corallite. *Coral Reefs* 1 (1), 45–51. doi: 10.1007/BF00286539

Gladfelter, E. H. (2007). Skeletal development in acropora palmata (Lamarck 1816): a scanning electron microscope (SEM) comparison demonstrating similar mechanisms of skeletal extension in axial versus encrusting growth. *Coral Reefs* 26 (4), 883–892. doi: 10.1007/s00338-007-0278-y

Grant, K. M., Rohling, E. J., Bar-Matthews, M., Ayalon, A., Medina-Elizalde, M., Ramsey, C.B., et al. (2012). Rapid coupling between ice volume and polar temperature over the past 150,000 years. *Nature* 491 (7426), 744–747. doi: 10.1038/nature11593

Gray, W. R., and Evans, D. (2019). Nonthermal influences on Mg/Ca in planktonic foraminifera: A review of culture studies and application to the last glacial maximum. *Paleoceanography Paleoclimatology* 34 (3), 306–315. doi: 10.1029/2018PA003517

Gray, W. R., Weldeab, S., Lea, D. W., Rosenthal, Y., Gruber, N., et al. (2018). The effects of temperature, salinity, and the carbonate system on Mg/Ca in globigerinoides ruber (white): A global sediment trap calibration. *Earth Planetary Sci. Lett.* 482, 607–620. doi: 10.1016/j.epsl.2017.11.026

Guihen, D., White, M., and Lundälv, T. (2012). Temperature shocks and ecological implications at a cold-water coral reef. *Mar. Biodivers. Rec.* 5. doi: 10.1017/S1755267212000413

Guinotte, J. M., Orr, J., Cairns, S., Freiwald, A., Morgan, L., and George, R. (2006). Will human-induced changes in seawater chemistry alter the distribution of deep-sea scleractinian corals? in. *Front. Ecol. Environ.* 4 (3), 141–146. doi: 10.1890/1540-9295(2006)004[0141:WHCISC]2.0.CO;2

Hathorne, E., Gagnon, A., Felis, T., Adkins, J., Asami, R., Boer, W., et al. (2013). Interlaboratory study for coral Sr/Ca and other element/Ca ratio measurements. *Geochem. Geophys. Geosyst.* 14 (9), 3730–3750. doi: 10.1002/ggge.20230

Hemsing, F., Hsieh, Y.-T., Bridgestock, L., Spooner, P. T., Robinson, L. F., Frank, N., et al. (2018). Barium isotopes in cold-water corals. *Earth Planetary Sci. Lett.* 491, 183–192. doi: 10.1016/j.epsl.2018.03.040

Henrich, R., Baumann, K. H., Gerhardt, S., Gröger, M., and Volbers, A. (2003). "Carbonate preservation in deep and intermediate water masses in the south Atlantic: Evaluation and geological record (a review)," in *The south Atlantic in the late quaternary*. Eds. G. Wefer, S. Mulitza and V. Ratmeyer (Berlin, Heidelberg: Springer). doi: 10.1007/978-3-642-18917-3_28

Holcomb, M., Cohen, A. L., Gabitov, R. I., and Hutter, J.L. (2009). Compositional and morphological features of aragonite precipitated experimentally from seawater and biogenically by corals. *Geochimica et Cosmochimica Acta* 73, (, 4166–79. doi: 10.1016/j.gca.2009.04.015

Hou, A., Bahr, A., Schmidt, S., Strebl, C., Albuquerque, A. L., Chiessi, C. M., et al. (2020). Forcing of western tropical south Atlantic sea surface temperature across three glacial-interglacial cycles. *Global Planetary Change* 188, 103150. doi: 10.1016/j.gloplacha.2020.103150

Houlbrèque, F., McCulloch, M., Roark, B., Guilderson, T., Meibom, A., Kimball, J., et al. (2010). Uranium-series dating and growth characteristics of the deep-sea scleractinian coral: Enallopsammia rostrata from the equatorial pacific. *Geochimica Cosmochimica Acta* 74 (8), 2380–2395. doi: 10.1016/j.gca.2010.01.017

Indermühle, A., Stocker, T. F., Joos, F., Fischer, H., Smith, H. J., Wahlen, M., et al. (1999). Holocene Carbon-cycle dynamics based on CO2 trapped in ice at Taylor dome, Antarctica. *Nature* 398 (6723), 121–126. doi: 10.1038/18158

Leuschner, D. C., Sirocko, F., Grootes, P. M., and Erlenkeuser, H. (2002). Possible influence of zoophycos bioturbation on radiocarbon dating and environmental interpretation. *Mar. Micropaleontol.* 46 (1-2), 111–126. doi: 10.1016/S0377-8398(02)00044-0

Locarnini, R. A., Mishonov, A. V., Antonov, J. I., Boyer, T. P., Garcia, H. E., Baranova, O. K., et al. (2009) *World ocean atlas 2009*. Available at: http://www.nodc.noaa.gov/OC5/indprod.html.

Lynch-Stieglitz, J. (2017). The Atlantic meridional overturning circulation and abrupt climate change. *Annu. Rev. Mar. Sci* 9 (585) 83–104. doi: 10.1146/annurev-marine-010816-060415

Lynch-Stieglitz, J., Valley, S. G., and Schmidt, M. W. (2019). Temperature-dependent ocean–atmosphere equilibration of carbon isotopes in surface and intermediate waters over the deglaciation. *Earth Planetary Sci. Lett.* 506, 466–475. doi: 10.1016/j.epsl.2018.11.024

Lund, D. C., Tessin, A. C., Hoffman, J. L., and Schmittner, A (2015). Southwest Atlantic water mass evolution during the last deglaciation. *Paleoceanography* 30 (5), 477–94. doi: 10.1002/2014PA002657

Mangini, A., Godoy, J. M., Godoy, M. L., Kowsmann, R., Santos, G. M., and Ruckelshausen, M. (2010). Deep sea corals off Brazil verify a poorly ventilated southern pacific ocean during H2, H1 and the younger dryas. *In: Earth Planetary Sci. Lett.* 293 (3-4), 269–276. doi: 10.1016/j.epsl.2010.02.041

Marcott, S., Bauska, T., Buizert, C., Steig, E. J., Rosen, J. L., Cuffey, K. M., et al. (2014). Centennial-scale changes in the global carbon cycle during the last deglaciation. *Nature* 514, 616–619. doi: 10.1038/nature13799

Martínez-García, A., Sigman, D. M., Ren, H., Anderson, R. F., Straub, M., Hodell, D. A., et al. (2014). Iron fertilization of the subantarctic ocean during the last ice age. *Sci. (New York N.Y.)* 343 (6177), 1347–1350. doi: 10.1126/science.1246848

McCarthy, G., McDonagh, E., and King, B. (2011). Decadal variability of thermocline and intermediate waters at 24°S in the south Atlantic. *J. Phys. Oceanogr.* 41 (1), 157–165. doi: 10.1175/2010JPO4467.1

McCulloch, M., Falter, J., Trotter, J., and Montagna, P. (2012). Coral resilience to ocean acidification and global warming through pH up-regulation. *Nat. Clim Change* 2 (8), 623–627. doi: 10.1038/NCLIMATE1473

Meibom, A., Cuif, J.-P., Houlbreque, F., Mostefaoui, S., Dauphin, Y., Meibom, K. L., et al. (2008). Compositional variations at ultra-structure length scales in coral

skeleton. *Geochimica Cosmochimica Acta* 72 (6), 1555–1569. doi: 10.1016/j.gca.2008.01.009

Meibom, A., Yurimoto, H., Cuif, J.-P., Domart-Coulon, I., Houlbreque, F., Constantz, B., et al. (2006). Vital effects in coral skeletal composition display strict three-dimensional control. *Geophys. Res. Lett.* 33 (11). doi: 10.1029/2006GL025968

Mémery, L., Arhan, M., Álvarez-Salgado, X. A., Messias, M. J., Mercier, H., Castro, C. G, et al. (2000). The water masses along the western boundary of the south and equatorial Atlantic. *Progress in Oceanography* 47 (1), 69–98. doi: 10.1016/S0079-6611(00)00032-X

Mienis, F., Duineveld, G. C. A., Davies, A. J., Lavaleye, M. M. S., Ross, S. W., Seim, H., et al. (2014). Cold-water coral growth under extreme environmental conditions, the cape lookout area, NW Atlantic. *Biogeosciences* 11 (9), 2543–2560. doi: 10.5194/bg-11-2543-2014

Montagna, P., McCulloch, M., Douville, E., López Correa, M., Trotter, J., Rodolfo-Metalpa, R., et al. (2014). Li/Mg systematics in scleractinian corals: Calibration of the thermometer. *Geochimica Cosmochimica Acta* 132, 288–310. doi: 10.1016/j.gca.2014.02.005

Montagna, P., McCulloch, M., Taviani, M., Mazzoli, C., and Vendrell, B. (2006). Phosphorus in cold-water corals as a proxy for seawater nutrient chemistry. *Sci. (New York N.Y.)* 312 (5781), 1788–1791. doi: 10.1126/science.1125781

Montero-Serrano, J. C., Frank, N., Tisnerat-Laborde, N., Colin, C., Wu, C. C., Lin, K, et al (2013). Decadal changes in the mid-depth water mass dynamic of the Northeastern Atlantic margin (Bay of Biscay. *Earth and Planetary Science Letters* 364), 134–44. doi: 10.1016/j.epsl.2013.01.012

Mucci, A. (1983). The solubility of calcite and aragonite in seawater at various salinities, temperatures, and one atmosphere total pressure. *Am. J. Sci.* 283 (7), 780–799. doi: 10.2475/ajs.283.7.780

Petit, J. R., Jouzel, J., Raynaud, D., Barkov, N. I., Barnola, J.-M., Basile, I., et al. (1999). Climate and atmospheric history of the past 420,000 years from the vostok ice core, Antarctica. *Nature* 399 (6735), 429–436. doi: 10.1038/20859

Poggemann, D.-W., Hathorne, E., Nürnberg, D., Frank, M., Bruhn, I., Reißig, S., et al. (2017). Rapid deglacial injection of nutrients into the tropical Atlantic *via* Antarctic intermediate water. *Earth Planetary Sci. Lett.* 463, 118–126. doi: 10.1016/j.epsl.2017.01.030

Poggemann, D.-W., Nürnberg, D., Hathorne, E. C., Frank, M., Rath, W., Reißig, S., et al. (2018). Deglacial heat uptake by the southern ocean and rapid northward redistribution *Via* Antarctic intermediate water. *Paleoceanography Paleoclimatology* 33 (11), 1292–1305. doi: 10.1029/2017PA003284

Raddatz, J., Liebetrau, V., Rüggeberg, A., Hathorne, E., Krabbenhöft, A., Eisenhauer, A., et al. (2013). Stable Sr-isotope, Sr/Ca, Mg/Ca, Li/Ca and Mg/Li ratios in the scleractinian cold-water coral lophelia pertusa. *Chem. Geol.* 352, 143–152. doi: 10.1016/j.chemgeo.2013.06.013

Raddatz, J., Liebetrau, V., Trotter, J., Rüggeberg, A., Flögel, S., Dullo, W.-C., et al. (2016). Environmental constraints on Holocene cold-water coral reef growth off Norway: Insights from a multiproxy approach. *Paleoceanography* 31 (10), 1350–1367. doi: 10.1002/2016PA002974

Raddatz, J., Nürnberg, D., Tiedemann, R., and Rippert, N. (2017). Southeastern marginal West pacific warm pool sea-surface and thermocline dynamics during the pleistocene (2.5–0.5 ma). *Palaeogeography Palaeoclimatology Palaeoecol.* 471, 144–156. doi: 10.1016/j.palaeo.2017.01.024

Raddatz, J., and Rüggeberg, A. (2021). Constraining past environmental changes of cold-water coral mounds with geochemical proxies in corals and foraminifera. *Depositional Rec* 7 (2), 200–222. doi: 10.1002/dep2.98

Raddatz, J., Rüggeberg, A., Flögel, S., Hathorne, E. C., Liebetrau, V., Eisenhauer, A., et al. (2014a). The influence of seawater pH on U / Ca ratios in the scleractinian cold-water coral lophelia pertusa. *Biogeosciences* 11 (7), 1863–1871. doi: 10.5194/bg-11-1863-2014

Raddatz, J., Rüggeberg, A., Liebetrau, V., Foubert, A., Hathorne, E., Fietzke, J., et al. (2014b). Environmental boundary conditions of cold-water coral mound growth over the last 3 million years in the porcupine seabight, northeast Atlantic. *Deep Sea Res. Part II: Topical Stud. Oceanogr.* 99, 227–236. doi: 10.1016/j.dsr2.2013.06.009

Raddatz, J., Titschack, J., Frank, N., Freiwald, A., Conforti, A., Osborne, A., et al. (2020). Solenosmilia variabilis-bearing cold-water coral mounds off Brazil. *Coral Reefs* 39 (1), 69–83. doi: 10.1007/s00338-019-01882-w

Roberts, J., Gottschalk, J., Skinner, L. C., Peck, V. L., Kender, S., Elderfield, H., et al. (2016). Evolution of south Atlantic density and chemical stratification across the last deglaciation. *Proc. Natl. Acad. Sci. United States America* 113 (3), 514–519. doi: 10.1073/pnas.1511252113

Robinson, L. F., Adkins, J. F., Frank, N., Gagnon, A. C., Prouty, N. G., Brendan Roark, E., et al. (2014). The geochemistry of deep-sea coral skeletons: A review of vital effects and applications for palaeoceanography. *Deep Sea Res. Part II: Topical Stud. Oceanogr.* 99, 184–198. doi: 10.1016/j.dsr2.2013.06.005

Rollion-Bard, C., and Blamart, D. (2015). Possible controls on Li, Na, and mg incorporation into aragonite coral skeletons. *Chem. Geol.* 396, 98–111. doi: 10.1016/j.chemgeo.2014.12.011

Rollion-Bard, C., Blamart, D., Cuif, J.-P., and Dauphin, Y. (2010). *In situ* measurements of oxygen isotopic composition in deep-sea coral, lophelia pertusa: Re-examination of the current geochemical models of biomineralization. *Geochimica Cosmochimica Acta* 74 (4), 1338–1349. doi: 10.1016/j.gca.2009.11.011

Rosenthal, Y., Field, M. P., and Sherrell, R.M. (1999). Precise determination of element/calcium ratios in calcareous samples using sector field inductively coupled plasma mass spectrometry. *Analytical chemistry* 7(15), 3248–53. doi: 10.1021/ac981410x

Santos, T. P., Lessa, D. O., Venancio, I. M., Chiessi, C. M., Mulitza, S., Kuhnert, H., et al. (2017). Prolonged warming of the Brazil current precedes deglaciations. *Earth Planetary Sci. Lett.* 463, 1–12. doi: 10.1016/j.epsl.2017.01.014

Schleinkofer, N., Raddatz, J., Freiwald, A., Evans, D., Beuck, L., Rüggeberg, A., et al. (2019). Environmental and biological controls on Na/Ca ratios in scleractinian cold-water corals. in. *Biogeosciences* 16 (18), 3565–3582. doi: 10.5194/bg-16-3565-2019

Schlitzer, R. (2021) *Ocean data view. version 2021*. Available at: http://odv.awi.de.

Schröder-Ritzrau, A., Freiwald, A., and Mangini, A. (2005). "U/Th-dating of deep-water corals from the eastern north Atlantic and the western Mediterranean Sea," in *André Freiwald and J. Murray Roberts (Hg.): Cold-Water Corals and Ecosystems. Berlin/Heidelberg: Springer-Verlag (Erlangen Earth Conference Series).* 157–172.

Sigman, D. M., and Boyle, E. A (2000). Glacial/interglacial variations in atmospheric carbon dioxide. *Nature.* 407 (6806), 859–69. doi: 10.1038/35038000

Sinclair, D. J., Williams, B., and Risk, M. (2006). A biological origin for climate signals in corals–trace element "vital effects" are ubiquitous in scleractinian coral skeletons. *Geophys. Res. Lett.* 33 (17). doi: 10.1029/2006GL027183

Spooner, P. T., Robinson, L. F., Hemsing, F., Morris, P., and Stewart, J. A. (2018). Extended calibration of cold-water coral Ba/Ca using multiple genera and co-located measurements of dissolved barium concentration. *Chem. Geol.* 499, 100–110. doi: 10.1016/j.chemgeo.2018.09.012

Stewart, J. A., Robinson, L. F., Day, R. D., Strawson, I., Burke, A., Rae, J. W, et al (2020). Refining trace metal temperature proxies in cold-water scleractinian and stylasterid corals. *Earth and Planetary Science Letters* 545, 116412. doi: 10.1016/j.epsl.2020.116412

Stolarski, J (2003). Three-dimensional micro-and nanostructural characteristics of the scleractinian coral skeleton: a biocalcification proxy. *Acta Palaeontologica Polonica* 48 (4)

Thresher, R. E., Adkins, J., Fallon, S. J., Gowlett-Holmes, K., Althaus, F., and Williams, A. (2011). Extraordinarily high biomass benthic community on southern ocean seamounts. *Sci. Rep.* 1, 119. doi: 10.1038/srep00119

Toggweiler, J. R., and Lea, D. W. (2010). Temperature differences between the hemispheres and ice age climate variability. *Paleoceanography* 25 (2). doi: 10.1029/2009PA001758

Tracey, D., Rowden, A., Mackay, K., and Compton, T. (2011). Habitat-forming cold-water corals show affinity for seamounts in the new Zealand region. *Mar. Ecol. Prog. Series* 430, 1–22. doi: 10.3354/meps09164

Wefing, A.-M., Arps, J., Blaser, P., Wienberg, C., Hebbeln, D., and Frank, N. (2017). High precision U-series dating of scleractinian cold-water corals using an automated chromatographic U and Th extraction. *Chem. Geol.* 4751, 140–148. doi: 10.1016/j.chemgeo.2017.10.036

Weyl, P. K. (1959). The change in solubility of calcium carbonate with temperature and carbon dioxide content. *Geochimica Cosmochimica Acta* 17 (3-4), 214–225. doi: 10.1016/0016-7037(59)90096-1

frontiers | Frontiers in Marine Science

TYPE Original Research
PUBLISHED 22 August 2022
DOI 10.3389/fmars.2022.924556

OPEN ACCESS

EDITED BY
Jacek Raddatz,
Goethe University Frankfurt, Germany

REVIEWED BY
André Bahr,
Institute of Earth Sciences, Heidelberg University, Germany
Tomoko Komada,
San Francisco State University, United States

*CORRESPONDENCE
Ana Lúcia Lindroth Dauner
anadauner@gmail.com
César de Castro Martins
ccmart@ufpr.br

SPECIALTY SECTION
This article was submitted to Marine Biogeochemistry, a section of the journal Frontiers in Marine Science

RECEIVED 20 April 2022
ACCEPTED 03 August 2022
PUBLISHED 22 August 2022

CITATION
Dauner ALL, Mollenhauer G, Hefter J, Bícego MC, de Mahiques MM and Martins CdC (2022) Late Pleistocene to Holocene variations in marine productivity and terrestrial material delivery to the western South Atlantic.
Front. Mar. Sci. 9:924556.
doi: 10.3389/fmars.2022.924556

Late Pleistocene to Holocene variations in marine productivity and terrestrial material delivery to the western South Atlantic

Ana Lúcia Lindroth Dauner[1,2,3]*, Gesine Mollenhauer[4,5], Jens Hefter[4], Márcia Caruso Bícego[6], Michel Michaelovitch de Mahiques[6] and César de Castro Martins[2,3]*

[1]Ecosystems and Environment Research Program, University of Helsinki, Helsinki, Finland, [2]Graduate Program in Coastal and Oceanic Systems (PGSISCO), Federal University of Paraná, Pontal do Paraná, Brazil, [3]Center for Marine Studies, Federal University of Paraná, Pontal do Paraná, Brazil, [4]Alfred Wegener Institute, Helmholtz Center for Polar and Marine Research, Bremerhaven, Germany, [5]Center for Marine Environmental Sciences (MARUM) and Department of Geosciences, University of Bremen, Bremen, Germany, [6]Oceanographic Institute, University of São Paulo, São Paulo, Brazil

Despite the increased number of paleoceanographic studies in the SW Atlantic in recent years, the mechanisms controlling marine productivity and terrestrial material delivery to the South Brazil Bight remain unresolved. Because of its wide continental shelf and abrupt change in coastline orientation, this region is under the influence of several environmental forcings, causing the region to have large variability in primary production. This study investigated terrestrial organic matter (OM) sources and marine OM sources in the South Brazil Bight, as well as the main controls on marine productivity and terrestrial OM export. We analyzed OM geochemical (bulk and molecular) proxies in sediment samples from a core (NAP 63-1) retrieved from the SW Atlantic slope (24.8°S, 44.3°W, 840-m water depth). The organic proxies were classified into "terrestrial-source" and "marine-source" groups based on a cluster analysis. The two sources presented different stratigraphical profiles, indicating distinct mechanisms governing their delivery. Bulk proxies indicate the predominance of marine OM, although terrestrial input also affected the total OM deposition. The highest marine productivity, observed between 50 and 39 ka BP, was driven by the combined effects of the South Atlantic Central Water upwelling promoted by Brazil Current eddies and fluvial nutrient inputs from the adjacent coast. After the last deglaciation, decreased phytoplankton productivity and increased archaeal productivity suggest a stronger oligotrophic tropical water presence. The highest terrestrial OM accumulation occurred between 30 and 20 ka BP, with its temporal evolution controlled mainly by continental moisture evolution. Sea level fluctuations affected the distance between the coastline and the sampling site. In contrast, continental moisture affected the phytogeography, changing from lowlands covered by grasses and

saltmarshes to a landscape dominated by mangroves and the Atlantic Forest. Our results suggest how the OM cycle in the South Brazil Bight may respond to warmer and dryer climate conditions.

KEYWORDS

continental slope, marine productivity, mass accumulation rates, organic proxies, paleoceanography, South Brazil Bight, stratigraphical zones, terrestrial matter

Introduction

Temporal changes in carbon source delivery have been frequently recorded in ocean sediments. They can explain the linkages among climate, organic matter (OM) biogeochemical cycling, and carbon sequestration over different time scales (Faux et al., 2011). The South Atlantic Ocean plays an essential role in the global climate system by forming nutrient-rich dense water masses and promoting heat transport into the Southern Ocean (Garzoli and Matano, 2011). It also receives large amounts of terrestrial OM originating from South America [e.g., Rio de la Plata (RdlP) Basin] and Africa (e.g., Congo basin) (Weijers et al., 2007; Muelbert et al., 2008). The delivery of terrestrial OM to the ocean can function as a long-term sink and, consequently, a significant CO_2 sequestration mechanism (Sarmiento and Gruber, 2006). Along with the terrestrial OM input, rivers also deliver nutrients to the adjacent ocean, promoting marine productivity (Bianchi et al., 2018).

Knowledge about variations in the terrestrial input and primary productivity is crucial for the comprehension of past climate changes in the Southern Hemisphere, especially in the southeastern (SE) part of South America. This knowledge is expected to provide insights into the natural trends of climate variability for the next millennia. Also, the South Atlantic plays a major role in the world ocean overturning circulation. Specifically, the southwest (SW) Atlantic margin is marked by a strong N–S dynamics, characterized by the southward flow of the North Atlantic Deep Water and the northward flow of the Antarctic Intermediate Water, two of the main components of the meridional circulation in the Atlantic Ocean (Mahiques et al., 2022). Several studies have reported temporal variations in OM input to the continental margin of the SW Atlantic (e.g., Costa et al., 2016; Lourenço et al., 2016; Gu et al., 2017) and put forth distinct mechanisms governing marine paleoproductivity and terrestrial OM input. Portilho-Ramos et al. (2015) and Pereira et al. (2018) related high rates of marine paleoproductivity in the SW Atlantic to upwelling of the South Atlantic Central Water (SACW) promoted by the Brazil Current (BC) eddies. Other studies associated elevated marine productivity in the South Brazil Bight (SBB) with periods of greater terrestrial inputs (Mahiques et al., 2007; Nagai et al., 2010; Lourenço et al., 2016; Gu et al., 2017). Therefore, the primary mechanism controlling marine productivity in the SBB central portion remains unresolved.

Terrestrial OM content in continental margin sediments may vary in response to the type and amount of OM produced on the continent and exported to the ocean. An additional factor is the distance of the core site to the continent, which is a function of sea level that affects the continental shelf width. Previous studies in the region (Mahiques et al., 2007; Nagai et al., 2010; Lourenço et al., 2016) focused on terrestrial OM amount but did not investigate the sources. Presently, the RdlP drains the inner portion of the southern part of South America and influences only the southern portion of the SBB (Nagai et al., 2014a; Razik et al., 2015), whereas the northern portion receives sediments carried by the southward BC (Nagai et al., 2014a). A recent study (Mahiques et al., 2017) on core top sediments (including NAP 63-1) from the continental shelf and slope in the central portion of SBB suggested that terrestrial input to the mid-slope is influenced by the northward Intermediate Western Boundary Current (IWBC) rather than by the southward BC (Figure 1).

In this study, we quantified markers in SBB mid-slope sediments [*n*-alkanes, long-chain alkenones (LCA), glycerol dialkyl glycerol tetraethers (GDGTs), *n*-alkanols, sterols, and long-chain diols] to evaluate the sources of OM delivered to the site, and how these sources varied over time, from the Late Pleistocene to the Holocene. We investigated the primary mechanism controlling marine productivity in the SBB central portion as well as the main delivery routes of the terrestrial OM to the region. Molecular organic biomarkers can provide insights into OM sources to aquatic environments and OM sequestration to sediments over decadal to geological time scales. Therefore, they help resolve the complexity in systems with multiple organic carbon sources (Yunker et al., 2005; Holland et al., 2013). Based on their temporal evolution, we associated the OM flux with oceanographic and climatological processes during the Late Pleistocene and Holocene. We compared the evolution of these organic biomarker contents with other studies from the vicinity of the study site to identify the mechanisms that

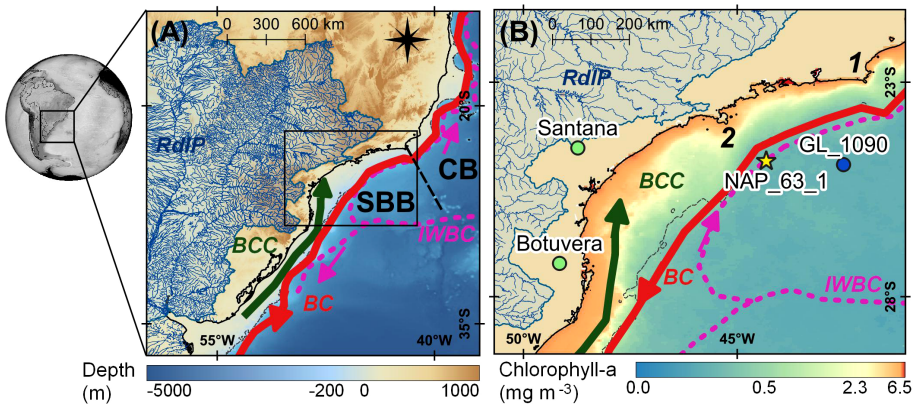

FIGURE 1
(A) Indication of the main ocean currents in the SW Atlantic as well as the location of Campos Basin (CB) and South Brazil Bight (SBB) separated by the black dashed line. The black rectangle is displayed in map B. **(B)** Map highlighting the SBB with the location of sediment core NAP 63-1 (yellow star), GL-1090 (blue circle), and the speleothem sites (green circles) used in the discussion. The gray dashed line indicates the continental shelf break. Current names, BC, Brazil Current; BCC, Brazil Coastal Current; IWBC, Intermediate Western Boundary Current. Geographical features: 1 - Cabo Frio; 2 - São Sebastião Island.

governed marine productivity and possible sources of terrestrial OM during the Last Glacial Period.

Study area

Today, circulation in the SBB (latitudes 22°S–34°S) is characterized by two western boundary currents, the BC and the IWBC (Figure 1). The BC flows southward and meanders around the 200-m isobath (Campos et al., 2000). It transports warm and oligotrophic tropical water (T > 20°C and S > 36.4) in the first 100 m of the water column, and cold and nutrient-rich SACW (T = 6°C–20°C and S = 34.5–36.4) below 100 m and down to approximately 600-m depth (Silveira et al., 2015). Below the BC, the IWBC flows northward in the SBB, carrying Antarctic Intermediate Water (T = 3°C–7°C and S = 24.6–34.4) down to approximately 1,100-m depth (Silveira et al., 2015).

The change in the coastline orientation at Cabo Frio induces a meandering pattern in the BC, which frequently becomes unstable, forming strong cyclonic and anticyclonic frontal eddies (Campos et al., 2000). These eddies represent an efficient mechanism for increasing vertical speeds, acting decisively in the upwelling of SACW. This type of meander-induced upwelling brings SACW to shallower depths and fertilizes the otherwise typically oligotrophic waters (Campos et al., 2000; Ribeiro et al., 2016).

The SBB can also be considered a convergence zone regarding OM transport, receiving material from the south through the advancement of the RdlP plume and from the north through the upwelling region of SACW (Mahiques et al., 2004). The area off São Sebastião Island (24°00′S; 45°30′W) marks a regional boundary between the two sedimentary provinces. The RdlP drains the second largest drainage basin in South America and discharges approximately 710 km^3 yr^{-1} (or 22,514 m^3 s^{-1}) of freshwater at the RdlP estuary at ~35°S (Razik et al., 2015). This material is redistributed northward up to 27°S by the Brazil Coastal Current (Nagai et al., 2014a), south of the coring site. Aside from the RdlP, the SBB region receives only small contributions of terrestrial material from the adjacent coast, especially from SE Brazil, resulting in little terrestrial input to the coring site.

The adjacent continent is characterized by a narrow (>80 km) coastal lowland (<100-m altitude), limited by the "Serra do Mar" coastal mountain range extending approximately parallel to the coast (Almeida and Carneiro, 1998). The Atlantic rainforest is the typical vegetation of the lowland and the slopes of the "Serra do Mar" mountain range (Ribeiro et al., 2009). The estuaries are mainly dominated by mangrove trees (*Rhizophora* sp., *Avicennia* sp., and *Languncularia* sp.) as far south as 28°30′S, where they are replaced by saltmarshes (formed by *Spartina alterniflora*) (Schaeffer-Novelli et al., 1990).

Material and methods

Sampling and age model

Sediment core NAP 63-1 was collected on the continental slope of the subtropical southwestern Atlantic (24°50.304′S; 44°19.124′W; 840-m water depth; 2.24-m long) (Figure 1). The distance from the coring site to the coast today is about 140 km. The sampling took place on 26 February 2013, during an RV

Alpha Crucis cruise, from the Oceanographic Institute of the University of São Paulo (IO-USP; Brazil), using a piston corer. The core was sectioned every 2 cm, yielding a total of 112 samples. The samples were stored frozen in pre-combusted aluminum trays for further analysis.

The age model for this sediment core was described by Dauner et al. (2019). Briefly, it was based on radiocarbon dating of planktonic foraminifera (AMS ^{14}C) and benthic foraminifera stable oxygen isotope ($\delta^{18}O$) tie points aligned to two reference curves (Lisiecki and Raymo, 2005; Lisiecki and Stern, 2016). The downcore ages were modeled using BACON software version 2.3.5 (Blaauw and Christen, 2011). The core material covered approximately the past 78 ka with no observed age inversion in the radiocarbon ages.

Bulk parameters

Analysis of total organic carbon (TOC) content and carbon isotope composition ($\delta^{13}C$) was performed on decarbonated dry sediment samples (acid treatment with 1 mol L^{-1} HCl solution). Determinations of total nitrogen (TN) content and the nitrogen isotope composition ($\delta^{15}N$) were performed on dry unacidified sediment. The samples were analyzed by an EA-Costech elemental analyzer coupled to a Thermo Scientific Delta V Advantage isotope ratio mass spectrometer (EA-IRMS). The analytical accuracy was verified using the USGS-40 (L-glutamic acid, United States Geological Survey) and IAEA-600 (caffeine, International Atomic Energy Agency) standards before and after each group of 40 samples. Standard deviations for calibration were within the expected range, being 0.01‰ for both ratios for USGS-40, 0.03‰ for $\delta^{13}C$, and 0.09‰ for $\delta^{15}N$ for IAEA-600. The standard used as a reference for carbon and nitrogen contents was Soil LECO (LECO Corporation, USA), whose estimated levels are 13.55% and 0.81% dry weight, respectively, and in agreement with the certified values.

Lipid extraction and purification

About 5 g of freeze-dried and homogenized samples were extracted three times using an ultrasonic bath with 25 ml of methanol:dichloromethane (1:9; v:v). Known amounts of squalene, C_{19} ketone, 5α-androstanol, and C_{46} GDGT were added as internal standards before extraction. The combined extracts were evaporated by rotary evaporation under vacuum at 40°C. The total lipid extracts were saponified for 2 h at 80°C with 1 ml of 0.1 mol L^{-1} KOH in methanol:H_2O (9:1; v:v). After saponification, neutral lipids were liquid–liquid extracted into *n*-hexane and further purified by passing them over a silica gel column (1% deactivated with water). They were eluted with 4 ml of *n*-hexane (recovery of *n*-alkanes), 4 ml of *n*-hexane:dichloromethane (1:2; v:v; recovery of ketones), and 4 ml of dichloromethane:methanol (1:1; v:v; recovery of *n*-alkanols, sterols, diols, and GDGTs) and dried using a Silli-Therm at 50°C under a stream of nitrogen.

Before capillary gas chromatography analyses, the *n*-alkane and alkenone fractions were re-dissolved in 100 µl of *n*-hexane. The dry polar fractions were weighed and adjusted to concentrations of approximately 2 mg ml^{-1} by dissolution with isopropanol:*n*-hexane (1:99; v:v). Before the analysis, the polar fractions were filtered (Thermo Scientific PTFE filter: 4 mm in diameter and 0.45 µm porosity) to retain any remaining particles. These extracts were injected into a high-performance liquid chromatograph coupled to a mass spectrometer. The remaining extracts were then dried and derivatized by adding 30 µl of *N,O*-bis(trimethylsilyltrifluoroacetamide):trimethylchlorosilane (BSTFA : TMCS; 99:1; v:v) and 30 µl of acetonitrile and heated for 60 min at approximately 60°C. After derivatization, the reagents were dried, and the fraction was re-dissolved in 50 µl of *n*-hexane before capillary gas chromatography.

Analytical methods

n-Alkanes were analyzed by injecting 2-µl sample aliquots in the split mode in an Agilent 7890A series gas chromatograph equipped with a flame ionization detector and an Agilent DB-5ms capillary fused silica column coated with 5% phenyl/dimethyl arylene siloxane (60-m length, 0.25-mm internal diameter, and 0.25-µm film thickness). Helium was used as the carrier gas with a constant flow rate of 1.5 ml min^{-1}. The initial oven temperature was 60°C, held for 1 min, increased to 150°C at a rate of 20°C min^{-1}, then raised to 320°C at a rate of 6°C min^{-1} and held for 35 min with a total run time of 69 min. The injector and detector temperatures were adjusted to 250°C and 330°C, respectively.

Alkenones were analyzed by injecting 2-µl sample aliquots in the splitless mode in an Agilent 7890A series gas chromatograph equipped with a flame ionization detector and an Agilent HP-5 capillary fused silica column coated with 5% phenyl/methylpolysiloxane (50-m length, 0.32-mm internal diameter, and 0.17-µm film thickness). Hydrogen was used as the carrier gas with a constant flow rate of 1.2 ml min^{-1}. The initial oven temperature was 40°C, increased to 60°C at a rate of 20°C min^{-1}, then raised to 320°C at a rate of 5°C min^{-1} and held for 15 min with a total run time of 68 min. The injector and detector temperatures were adjusted to 300°C and 325°C, respectively.

GDGT analyses were performed using an Agilent 1200 Series high-performance liquid chromatography system coupled with an Agilent 6120 mass spectrometer. The 20-µl aliquots were injected into an Alltech Prevail® Cyano column (2.1 × 150 mm^2, 3 µm; Grace) maintained at 30°C. GDGTs were eluted using the following gradient with solvent A (*n*-hexane:isopropanol: chloroform; 98:1:1) and solvent B (*n*-hexane:isopropanol: chloroform; 89:10:1): 100% A for 5 min, linear gradient to 10% B in 20 min, linear gradient to 100% B in 10 min, and then held for 7 min. The flow rate was 0.2 ml min^{-1}. After each analysis, the column was cleaned by back-flushing with 100% B

at 0.6 ml min^{-1} for 5 min and then held for 10 min in the initial conditions (100% A at 0.2 ml min^{-1}).

n-Alkanols, sterols, and diols were analyzed by injecting 2-µl sample aliquots in the splitless mode in an Agilent 6850A series gas chromatograph equipped with an Agilent 5975C VL MSD mass spectrometer, a Restek Rxi-1ms capillary fused silica column coated with 1% diphenyl/dimethylsiloxane (30-m length, 0.25-mm internal diameter, and 0.25-µm film thickness) and a 5-m precolumn. Helium was used as the carrier gas with a constant flow rate of 1.2 ml min^{-1}. The initial oven temperature was 100°C, held for 8 min, and subsequently increased to 300°C at a rate of 4°C min^{-1} with a total run time of 58 min. The injector temperature was set to 280°C and operated in splitless injection mode. The detector and ion source temperatures were set to 280°C and 230°C, respectively.

n-Alkanes were individually identified by matching retention times against a standard containing the homologous series from *n*-C_{14} to *n*-C_{40}. LCA were identified by matching retention times against a standard containing C_{19} ketone and $C_{37:2}$ and $C_{37:3}$ alkenones. *n*-Alkanol, sterol, and diol data were acquired using the selected ion monitoring mode, and they were identified by the ion fragments characteristic of each compound (Supplementary Tables S1–S3). GDGT data were also acquired using the selected ion monitoring mode, but they were identified by the molecular ions (Supplementary Table S4).

The following compounds were quantified and will be used in the discussion: (i) *n*-alkanes: odd-numbered *n*-C_{15} to *n*-C_{39}; (ii) LCA: $C_{37:3}$ methyl, $C_{37:2}$ methyl, $C_{38:3}$ methyl and ethyl, $C_{38:2}$ methyl and ethyl, $C_{39:3}$ ethyl, and $C_{39:2}$ ethyl; (iii) *n*-alkanols: even-numbered *n*-C_{12}-OH to *n*-C_{34}-OH; (iv) phytol; (v) sterols: $27\Delta^{5,22E}$ (dehydrocholesterol), $27\Delta^{5}$ (cholesterol), $28\Delta^{5,22E}$ (brassicasterol), $28\Delta^{5}$ (campesterol), $29\Delta^{5,22E}$ (stigmasterol), $29\Delta^{5}$ (sitosterol), and $30\Delta^{22E}$ (dinosterol); (vi) long-chain diols: C_{28}1,14 and C_{30}1,14; and (vii) GDGTs: crenarchaeol, branched GDGT-IIIa, branched GDGT-IIa, and branched GDGT-Ia. The quantification was done *via* internal standards by assuming identical response factors as the respective compounds.

Procedural blanks were analyzed for each set of 15 samples, and they showed no significant level peaks in the analyses of target compounds. Finally, four replicates of the same sediment sample were extracted and used as an internal laboratory reference. The coefficient of variation among the four replicates was lower than 25% for all the compounds.

Data processing

A cluster using SAX (Symbolic Aggregate approXimation) representation (Lin et al., 2007) in the dissimilarity measure calculation was used to group the different proxies according to their evolutions through time. SAX representation is a "structured-based" dissimilarity measure that focuses on comparing underlying dependence structures, being suitable to analyze long time series. The symbolization approach involves transformation of time series into sequences of discretized symbols, allowing dimensionality reduction but keeping the distance measures defined on the original time series (Lin et al., 2007). Thus, the cluster analysis using SAX representation in the dissimilarity measure can be used to group different proxies according to their temporal evolution, regardless of their concentration ranges. For this analysis, we used packages "TSclust" (Montero and Vilar, 2014), "vegan" (Oksanen et al., 2018), and "rioja" (Juggins, 2017) with R environment version 4.1.2 (R Core Team, 2021).

Two groups were formed based on the cluster analysis previously mentioned: the "terrestrial-source" group and the "marine-source" group (Dauner et al., 2020) (Figure 2). For all samples, contents of the organic biomarkers (in ng g^{-1} dry sediment) were converted to mass accumulation rates (MAR) using the sedimentation rates from Dauner et al. (2019). As the dry bulk density values for NAP 63-1 were not determined, we used mean dry bulk density values obtained by Müller (2004) for a nearby sediment core from the SBB (core GeoB 2107-3; 27.18°S, 46.45°W, 1,048-m water depth).

After the organic markers were separated into these two groups, a constrained cluster analysis was performed, considering the groups separately to define stratigraphical zones. For this analysis, we used accumulation rates of the following organic compounds: mid-chain odd-numbered *n*-alkanes (*n*-C_{19} – *n*-C_{23}), long-chain odd-numbered *n*-alkanes (*n*-C_{25} – *n*-C_{39}), LCA, crenarchaeol, branched GDGTs, short-chain even-numbered *n*-alkanols (*n*-C_{12}-OH – *n*-C_{18}-OH), long-chain even-numbered *n*-alkanols (*n*-C_{20}-OH – *n*-C_{34}-OH), phytol, C_{28} and C_{30} 1,14-diols, and the sterols $27\Delta^{5,22E}$, $27\Delta^{5}$, $28\Delta^{5,22E}$, $28\Delta^{5}$, $29\Delta^{5,22E}$, $29\Delta^{5}$, and $30\Delta^{22E}$. All accumulation rate data were normalized by subtracting the mean and dividing by the standard deviation.

Wavelet analyses were performed in R, using "signal" (Ligges et al., 2021) and "WaveletComp" (Roesch and Schmidbauer, 2018) packages, following the procedure described by Torrence and Compo (1998). The data were converted to equally spaced time series for wavelet analysis. We removed all periodicities above 10 ka using a moving average filter, with a window of 11 ka to eliminate all unresolved frequencies and the general trend. Cross-wavelet analyses were performed to compare the NAP 63-1 OM signal with the stable carbon isotope from thermocline-dwelling foraminifera *Globorotalia inflata* from sediment core GL-1090 (Nascimento et al., 2021) as a proxy of SACW variability. In the discussion about rainfall over the continent, the following speleothem records were used (Figure 1): Bt-2 from Botuverá cave (Cruz et al., 2005) and St-8 from Santana cave (Cruz et al., 2007).

In addition to stable carbon isotopic composition ($\delta^{13}C$) of OM, the branched and isoprenoid tetraether index (BIT; formula 1) was calculated and used as a proxy for the marine vs. terrestrial origin of OM. Since isoprenoid GDGTs (especially crenarchaeol) are found primarily in aquatic environments and

10.3389/fmars.2022.924556

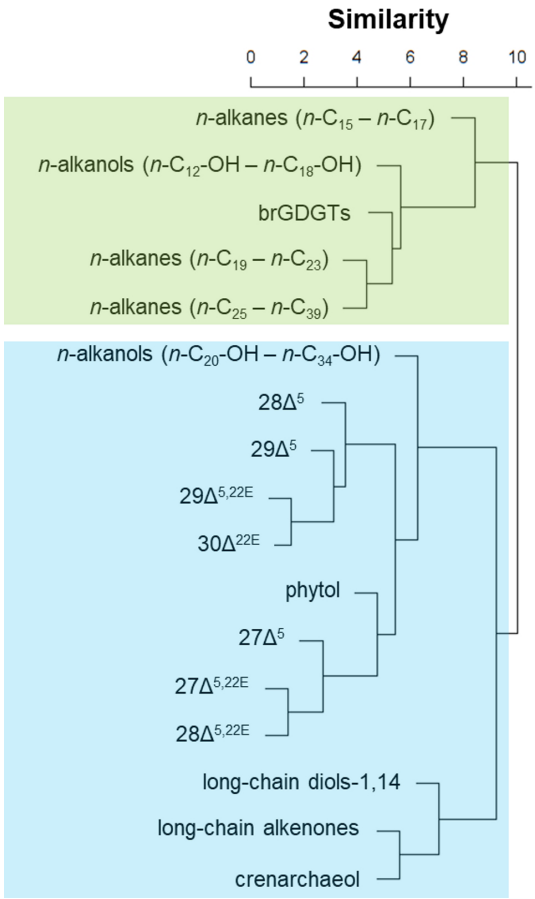

FIGURE 2
Cluster analysis based on the temporal evolution of each organic compound group, using the SAX representation as the dissimilarity measure. The green rectangle indicates the "terrestrial-source" group and the blue rectangle indicates the "marine-source" group.

branched GDGTs (brGDGTs) are mainly associated with bacteria found in soils and peat, the BIT index is used to evaluate the influence of terrigenous inputs in the aquatic environment. BIT values close to 1.0 indicate the dominance of terrestrial input, whereas values close to 0.0 indicate marine input (Hopmans et al., 2004). The average chain length (ACL) index (formula 2) was proposed to reflect woody plants/forests input relative to that from grasses (Poynter and Eglinton, 1990; Mahiques et al., 2017). Whereas woody plants contain large proportions of C_{27} and C_{29} *n*-alkanes, C_{31} and C_{33} are the major sediment *n*-alkanes in watersheds where grasses dominate (Meyers, 2003; Rommerskirchen et al., 2003).

$$BIT = \frac{([brGDGT-Ia] + [brGDGT-IIa] + [brGDGT-IIIa])}{([brGDGT-Ia] + [brGDGT-IIa] + [brGDGT-IIIa] + [crenarchaeol])} \quad (1)$$

$$ACL_{25-33} = \frac{25\star[n-C_{25}] + 27\star[n-C_{27}] + 29\star[n-C_{29}] + 31\star[n-C_{31}] + 33\star[n-C_{33}]}{[n-C_{25}] + [n-C_{27}] + [n-C_{29}] + [n-C_{31}] + [n-C_{33}]} \quad (2)$$

Results and discussion

Predominant sources

Elemental and isotopic compositions of OM have been extensively used to identify OM sources (e.g., Meyers, 1994; Mahiques et al., 2007; Nagai et al., 2010). In our core, % TOC varied between 0.17% and 0.81% (mean = 0.48% ± 0.09%) (Figure 3A), % TN ranged from 0.04% to 0.10% (mean = 0.08% ± 0.01%) (Figure 3B) and TOC/TN ratio varied between 3.67 and 10.98 (mean = 6.34 ± 1.15). The relatively low TOC content (close to 0.3%; Meyers, 1997) coupled to a low Pearson's correlation between % TOC and % TN (R = 0.48) indicates a limited applicability of the TOC/TN ratio as a proxy for OM source (Meyers, 1997; Bianchi and Canuel, 2011).

The $\delta^{13}C$ varied between −22.6‰ and −20.3‰ (mean = −21.4‰ ± 0.6) (Figure 3C) and the $\delta^{15}N$ ranged from 5.57‰ to 10.33‰ (mean = 7.87‰ ± 0.76) (Figure 3D). Values of $\delta^{13}C$ also indicated the predominance of marine OM ($\delta^{13}C$ = −22‰–−20‰; Meyers, 1994) and were in the same range as observed in SBB surface sediments ($\delta^{13}C$ = −21.0‰–−20.5‰; Mahiques et al., 2004). The $\delta^{15}N$ values varied slightly throughout the core but remained approximately 7.5‰, reinforcing the marine and/or microbial nature of the OM (Meyers, 1997) (Supplementary Figure S1). The overall low BIT values (mean = 0.22 ± 0.06) corroborate the mainly marine OM source (BIT< 0.3; Hopmans et al., 2004).

Overall, $\delta^{13}C$ and BIT values indicate a predominance of marine primary production. Specially between 80 and 40 ka BP, a decreasing BIT trend (Figure 3E) coupled to increasing $\delta^{13}C$ values (Figure 3C) suggests a reduced input from terrestrial sources, either from soil ($\delta^{13}C$ = −27‰–−23‰; Bianchi and Canuel, 2011) or vascular plants ($\delta^{13}C$ = −30‰–−26‰; Bianchi and Canuel, 2011). However, during MIS (Marine Isotope Stage) 2 (approximately 20 ka BP), BIT values exceeded the threshold of 0.3 for terrestrial input (Hopmans et al., 2004). It coincided with an excursion toward more negative $\delta^{13}C$ values, corroborating a slight increase in the contribution of terrestrial OM to the region.

During the Holocene, from 11 ka BP to the present, the TOC content increased. The increasing trend of BIT values suggests that this TOC increase was related to terrestrial rather than marine OM sources. This TOC increase could be caused by a higher terrestrial OM input in response to higher precipitation in southeast America and the expansion of the Atlantic rainforest (Ledru et al., 2009). However, it should have resulted in a decrease in $\delta^{13}C$ values

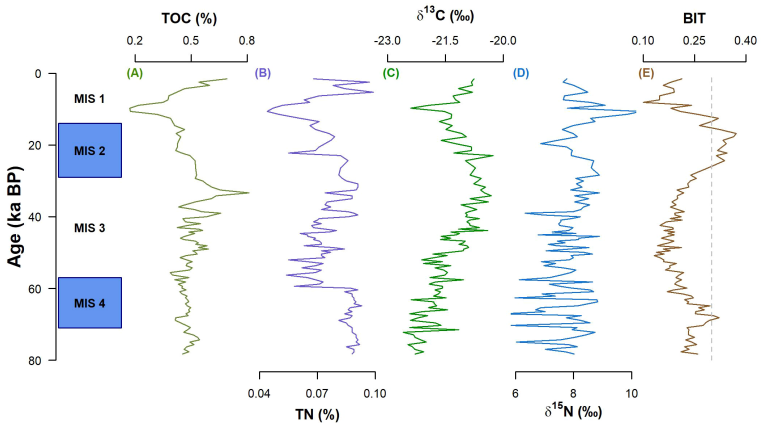

FIGURE 3
Records of the elemental **(A, B)** and isotopic **(C, D)** composition, and BIT values **(E)** for core NAP 63-1. MIS, Marine Isotope Stage.

toward more negative values ($\delta^{13}C$ from vascular plants = −30‰–−26‰; Bianchi and Canuel, 2011), which is not observed. Possible sources of terrestrial OM with less negative values include plants with C4 and CAM photosynthetic metabolism, such as grasses and plants from tropical regions (Muccio and Jackson, 2009; Chen and Blankenship, 2021). During the last 10 ka, Ledru et al. (2009) observed an expansion of Asteraceae tubuliflorae (C4 metabolism), Ericacea, and *Isoetes* (both with CAM metabolism) in SE Brazil. Their contribution could explain the relative increase in the terrestrial contribution to the OM input in the sampling region, but without decreasing $\delta^{13}C$ values.

Marine OM

According to the cluster using SAX representation, 12 compounds were assigned to have a marine source: long-chain even-numbered *n*-alkanols (*n*-C_{20}-OH – *n*-C_{34}-OH), phytol, crenarchaeol, LCA, C_{28} and C_{30} 1,14-diols, and the sterols $27\Delta^{5,22E}$, $27\Delta^{5}$, $28\Delta^{5,22E}$, $28\Delta^{5}$, $29\Delta^{5,22E}$, $29\Delta^{5}$, and $30^{\Delta 22E}$ (Dauner et al., 2020) (Figure 2). The long-chain even-numbered *n*-alkanols are also usually attributed to input from higher plant waxes, but some aquatic sources have also been suggested. Sinninghe Damsté et al. (2001) argued that the most probable marine source of long-chain *n*-alkanols in Antarctic saltwater lakes is the hydrolysis of cyanobacterial glycolipids.

The constrained cluster analysis allowed us to establish four marine zones (MZs): MZ-I: 79–50 ka BP; MZ-II: 50–39 ka BP; MZ-III: 39–29 ka BP; MZ-IV: 29–2 ka BP (Figure 4). During MZ-I, a relatively high input of $28\Delta^{5,22E}$, $30\Delta^{22E}$, and phytol was observed, especially during MIS 4 (71–57 ka BP), when compared to other MZs. The MZ-II is characterized by the highest accumulation rates of marine OM proxies (Figure 4). Several studies also observed a peak in the productivity of

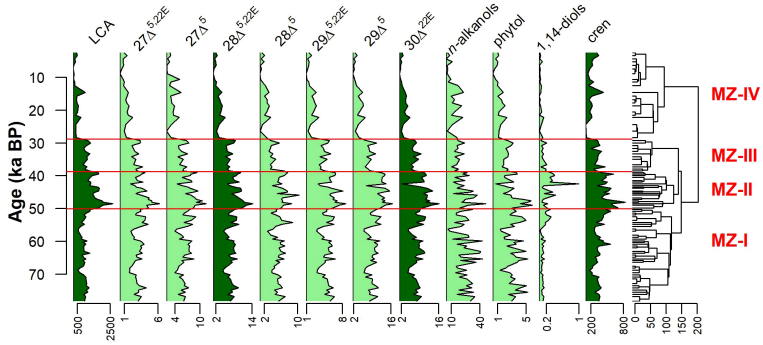

FIGURE 4
Summary diagram showing the mass accumulation rates (in ng cm^{-2} $year^{-1}$) of the organic molecular markers associated with marine organic matter, the constrained dendrogram, and the MZs for core NAP 63-1. Proxies colored with dark green will be discussed in more detail.

dinoflagellate and benthic and planktonic foraminifera in the SW Atlantic (e.g., Behling et al., 2002; Almeida et al., 2015; Portilho-Ramos et al., 2015) during this time interval. The marine productivity during MZ-III diminished slightly, returning to values similar to MZ-I, suggesting that at least one of the two fertilization processes observed during MZ-II (discussed below) diminished. The MZ-IV is characterized by the lowest accumulation rates of marine OM proxies (Figure 4).

Terrestrial OM

According to the cluster using SAX representation, four compound groups were assigned to have a terrestrial source: mid-chain odd-numbered *n*-alkanes (*n*-C_{19} – *n*-C_{23}), long-chain odd-numbered *n*-alkanes (*n*-C_{25} – *n*-C_{39}), short-chain even-numbered *n*-alkanols (*n*-C_{12}-OH – *n*-C_{18}-OH), and brGDGTs (Dauner et al., 2020) (Figure 2). The short-chain *n*-alkanols were predominant in the *n*-alkanols, especially the *n*-C_{16}-OH, which alone accounted for approximately 50% of the total *n*-alkanols. Usually, aquatic algae and bacteria have *n*-alkanol distributions dominated by C_{16} to C_{22} components (Meyers, 2003). However, Hu et al. (2009) observed a high correlation of short-chain *n*-alkanols with terrestrially derived bacterial fatty acids, indicating a bacterial source, instead of aquatic algae for the former compounds. In our samples, a high correlation between short-chain *n*-alkanols and brGDGTs ($R = 0.58$; $\alpha < 0.05$) suggests a terrestrial microbial origin for the short-chain *n*-alkanols.

The constrained cluster analysis allowed us to establish four terrestrial zones (TZ): TZ-I: 79.0–65.5 ka BP; TZ-II: 65.5–32 ka BP; TZ-III: 32.0–29 ka BP; TZ-IV: 29–2 ka BP (Figures 5D-H). During TZ-I, a relatively high input of mid-chain *n*-alkanes and brGDGTs and low MAR of long-chain *n*-alkanes were observed. The TZ-II was marked by low MAR of both mid- and long-chain *n*-alkanes, but with oscillating inputs of short-chain *n*-alkanols and brGDGTs. The short TZ-III layer was marked by a sharp increase in the *n*-alkanes MAR and continuously high *n*-alkanols and brGDGTs MAR. Lastly, TZ-IV was marked by the largest inputs of all terrestrial markers, especially approximately 20 ka BP.

Controls on OM input

OM input to the SBB may have been controlled by multiple mechanisms. Here, we consider variations in precipitation, wind patterns, ocean circulation, and the Si cycle.

Precipitation over the adjacent continent and consequent runoff have been reported to be the main processes that govern the delivery of terrestrial OM and nutrients to the SBB (Nagai et al., 2014b). Cruz et al., 2005; Cruz et al., 2007 studied rainfall variations in southern and SE Brazil through the $\delta^{18}O$ composition of speleothems in Botuverá and Santana caves, respectively (Figure 5B). Wet climate periods observed in southern and SE Brazil coincided with the high MAR of brGDGTs and *n*-alkanols in the NAP 63-1 record, especially approximately 48 and 20 ka BP. As discussed before, both proxies are associated with terrestrially derived OM. Thus, increased precipitation could have increased soil erosion, increasing the input of soil-derived OM to the SBB. Variations in sea level likely emphasized the precipitation influence. During TZ-I, sea level dropped (Miller et al., 2005; Figure 5A) and, consequently, the continental shelf shortened, reducing the distance to the coast of the core site (from about 170 km, during MIS 5e, to about 40 km, during TZ-I). The shorter distance to the coast, coupled with the wet climate, may explain

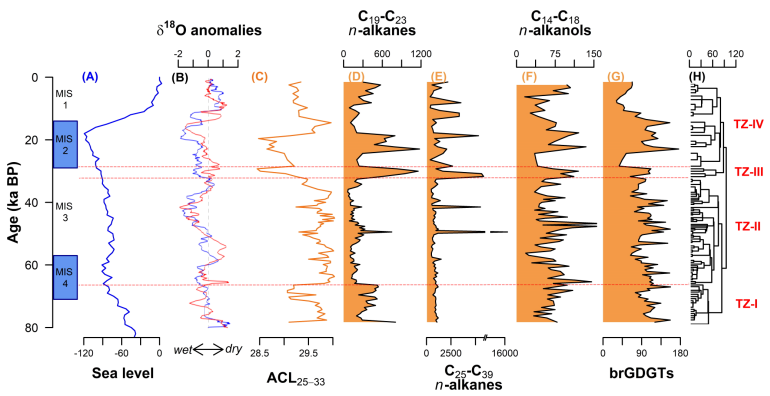

FIGURE 5
(A) Global sea level evolution (in m) (Miller et al., 2005). **(B)** Anomalies of $\delta^{18}O$ from the Botuverá (red) and Santana (blue) caves (Cruz et al., 2005; Cruz et al., 2007). **(C)** n-alkane ACL_{25-33} index from NAP 63-1 core. **(D-G)** Summary diagram showing the mass accumulation rates (in ng cm^{-2} $year^{-1}$) of the organic molecular markers associated with terrestrial organic matter, **(H)** the constrained dendrogram, and the terrestrial zones (TZ) for core NAP 63-1.

the relatively high terrestrial OM input in the SBB slope during TZ-I. Between TZ-II and TZ-III, sea level remained at approximately 85 m below the present one, without significant variation.

TZ-III was a short period marked by high MAR of all four terrestrial OM proxies. This period was marked by a slight change to more humid conditions (Figure 5B) but not so expressive that it could explain the terrestrial OM input. A possible explanation is a northward migration of the southern westerly wind belt. Razik et al. (2015) found sediments from the South America Pampas in SBB and related them with northward transport by westerly winds. Large dust flux observed in East Antarctica (Lambert et al., 2008) and high Pb isotope ratios observed in the Eastern Equatorial Pacific (Pichat et al., 2014) approximately 30 ka BP suggest a northward extension of the South Westerly wind belt. This northward migration may have enhanced the eolian transport of terrestrial material to the SBB, as also observed by Mathias et al. (2021).

At the beginning of the TZ-IV, the sea level fell to its minimum, reaching about 120 m below the present level (Miller et al., 2005; Figure 5A). During this period, the continental shelf reached its minimum length, further decreasing the distance to the coast of the core site and increasing the terrestrial input to site NAP 63-1. BIT values higher than 0.3 (Figure 3E) confirm this larger influence of terrestrial OM. During the last deglaciation (19 – 11 ka BP), rapid sea level rise caused the widening of the continental shelf (Figure 5A), which reduced the terrestrial input to the slope.

The *n*-alkanes, on the other hand, did not present a direct response to precipitation variations (Figures 5D, E). Instead, they could have been more influenced by the vegetation type in the adjacent continent. Badewien et al. (2015) studied vegetation changes of SW Africa during the last 60 ka and found a relation between the ACL values and forest pollen. During periods when forest pollen was highest, ACL values decreased. In the NAP 63-1 record (Figure 5C), the periods of relatively low $ACL_{25\text{-}33}$ occurred approximately 50 ka BP, between 30 and 20 ka BP, and in the last 10 ka BP.

The use of the ACL as a proxy for woody/forest vs. grassland vegetation is very controversial. Studying the SE Atlantic, Rommerskirchen et al. (2003) observed that marine sediments that receive material from the Congo rain forest tend to present the *n*-C_{29} as the main *n*-alkane. However, marine sediments located further south and receiving material from the savannah tend to present the *n*-C_{31} as the main *n*-alkane. Therefore, they associated the higher ACL values with plants with a C4 metabolism, like grasslands, herbs, and shrubs. More recently, some studies of the alkane composition in leaves from modern plants (Bush and McInerney, 2013; Feakins et al., 2016) did not find a direct correlation between the *n*-alkane distributions (especially the predominance of *n*-C_{29} or *n*-C_{31}) and the type of vegetation (grasses or woody plants). Bush and McInerney (2013) argued that the pattern observed in the western African coast might reflect the differences in rainforest and savanna environments, rather than in the leaf wax compositions. Nevertheless, the periods of relatively low $ACL_{25\text{-}33}$ observed in the NAP 63-1 records coincide with periods of a high percentage of arboreal pollen observed in a crater in SE Brazil, located only a few kilometers from the shoreline (Colônia crater; 23°52′S 46°42’20” W; Ledru et al., 2009). The dominance of grasslands during the rest of the period was attributed by Gu et al. (2017) to the expansion of salt marshes to the North and over the exposed continental shelf. Thus, for the SBB, it may be possible to use ACL as a proxy for the changes in the Atlantic rainforest in southern and SE Brazil, with lower ACL suggesting an expansion of the rainforest.

The influence of continental precipitation can also be seen in the marine productivity. In the southern portion of SBB, Gu et al. (2017) observed high relative abundances of eutrophic environmental dinocysts and associated them with the enhanced presence of fluvial waters during MZ-I. As shown in Figure 6A, wet climates (low $\delta^{18}O$ values) coincided with an increase in marine productivity in the central portion of the SBB during MIS 4 (approximately 65 ka BP) and during the MZ-II. These coincidences could be explained by fertilization of SBB due to increased fluvial nutrient input driven by wet climate. The spike in marine productivity approximately 16 ka BP may correspond to the wet climate during Heinrich Stadial 1 (between 18.0 and 15.6 ka BP; Campos et al., 2019). Conversely, the dryer climate during MZ-III may have decreased the fluvial input of nutrients to the SBB, causing a slight decrease in marine productivity during this period.

Marine productivity in the region is also influenced by upwelling of SACW, which in turn is affected by sea level changes. A MIS 3 high stand was reported in the southern Brazilian coast (Salvaterra et al., 2017; Dillenburg et al., 2019). This sea level rise would be responsible for the landward displacement of the whole water masses system (Mahiques et al., 2007), including the nutrient-rich SACW, seasonally upwelled into the area leading to enhanced productivity. The SACW upwelling in the SBB may also be driven by BC cyclonic meanders (Souza et al., 2020). Regardless of the mechanism that promoted the larger intrusion of SACW in the SBB, upwelling of SACW has been suggested to promote marine productivity by planktonic foraminifera in the same sediment core (NAP 63-3; Alvarenga et al., 2022), and at the slopes of the Campos Basin (GL-74 sediment core, 1279 m water column) (Portilho-Ramos et al., 2015) and the southern SBB (GeoB 2107-3 sediment core, 1,048-m water column) (Pereira et al., 2018). To assess whether SACW upwelling was indeed forcing marine productivity variations during the MZ-II and MZ-III, we computed the cross-wavelet between the stable carbon isotope from surface dwelling foraminifera (GL-1090; Nascimento et al., 2021) and the $28\Delta^{5,22E}$ accumulation rates. This analysis reveals common high energy in the range of 8 ka between 50 and 30 ka BP, with both signals in antiphase, i.e., low $\delta^{13}C$ and, consequently, more

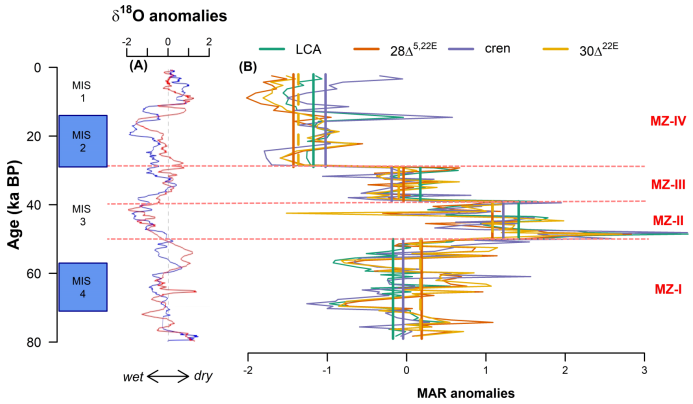

FIGURE 6
(A) Anomalies of $\delta^{18}O$ from the Botuverá and Santana caves (Cruz et al., 2005; Cruz et al., 2007) and **(B)** anomalies of the mass accumulation rates (MAR) of long-chain alkenones (LCA), $28\Delta^{5,22E}$, crenarchaeol (cren), and $30\Delta^{22E}$ from the sediment core NAP 63-1. MZ, marine zone. Bold straight lines in **(B)** refer to the average of each proxy for each MZ.

OM regeneration and nutrients coincide with increased $28\Delta^{5,22E}$ accumulation rates (Figure 7). This same relationship was observed between GL-1090 planktonic $\delta^{13}C$ and the other marine productivity proxies, such as $30\Delta^{22E}$, LCA, and crenarchaeol (not shown). This result supports the hypothesis that SACW upwelling may have fertilized the SBB, boosting marine productivity in the MZ-II and III. The difference in marine productivity observed in these two periods may be explained by the combination of precipitation and SBB upwelling. Between 50 and 40 ka BP, the combination of enhanced SACW upwelling and precipitation may have caused high marine productivity observed during MZ-II. In contrast, although the influence of the SACW was still observed between 40 and 30 ka BP, the dryer climate may have caused the decrease in the marine productivity observed in MZ-III.

From 30 ka BP onward, the relationship between subsurface temperature and other marine productivity proxies becomes variable indicating decoupling between SACW and marine OM proxies (Figure 7). Several studies from the SW Atlantic also observed a decrease in marine productivity (Almeida et al., 2015; Portilho-Ramos et al., 2015; Gu et al., 2017; Pereira et al., 2018; Alvarenga et al., 2022) during this period. The dryer climate coupled with lesser influence of SACW in the SBB, which favors the oligotrophic tropical water in the region, may have caused this substantial decline in marine productivity.

One last explanation for high marine productivity during glacial periods in tropical and subtropical regions is a mechanism related to the silicic acid leakage hypothesis (Brzezinski et al., 2002; Matsumoto et al., 2002). During glacial and dry periods, additions of Fe around Antarctica caused the uptake ratios of $Si(OH)_4$:NO_3– by diatoms to decline from 4:1 to 1:1 (Brzezinski et al., 2002). Some of the Si excess was then leaked out to lower latitudes through Sub-Antarctic Mode Water (Matsumoto et al., 2002) and may have caused diatoms to displace coccolithophores at low latitudes (Brzezinski et al., 2002). In the South Atlantic, the Sub-Antarctic Mode Water is carried northward by the Malvinas Current and, when it encounters the BC near 39°S, the water downwells, thus forming SACW (Piola and Matano, 2017). In addition to Fe input, sea-ice expansion and the weakening of the southern westerlies may have also promoted Si leakage from the Southern Ocean (Matsumoto et al., 2014). Griffiths et al. (2013) observed an increase in the opal content in the eastern equatorial Atlantic (core RC24-01; 0°33′N, 13°39′W; 3,837-m water depth) during MIS 4 and associated it with a Si-enriched Antarctic Intermediate Water. However, the silicic acid leakage hypothesis should be verified not only by an increase in the diatom productivity but also by a shift of the phytoplankton composition in favor of diatoms over calcite-secreting coccolithophores (Matsumoto et al., 2002). During MIS 4, the average MAR anomaly of $28\Delta^{5,22E}$ (proxy for diatoms; bold orange line in Figure 6B) during MZ-I is higher than the average MAR anomaly of LCA (a proxy for coccolithophores; bold green line in Figure 6B) for the same period. However, during MIS 2, the MAR anomaly of LCA is higher than the $28\Delta^{5,22E}$ MAR anomaly. This suggests that the silicic acid leakage may have influenced the marine productivity in the SBB during MIS 4 but not during MIS 2.

Composition of the marine primary producer community

Distinct primary producers characterized the MZs, and Figure 6B summarizes the variations in marine OM productivity and the relationship between these producers.

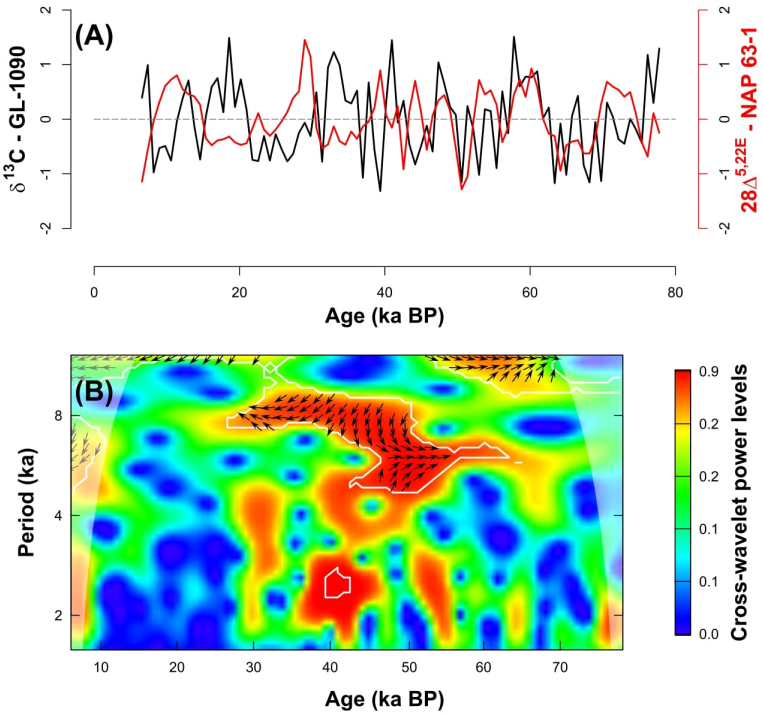

FIGURE 7
(A) Normalized time series of the stable carbon isotope from thermocline-dwelling foraminifera Globorotalia inflata from sediment core GL-1090 (black line) (Nascimento et al., 2021) and $28\Delta^{5,22E}$ accumulation rates (ng cm^{-2} $year^{-1}$; blue line) and **(B)** cross-wavelet analysis between them. The phase arrows in the cross-wavelet power spectrum rotate clockwise with a "north" origin. The vectors indicate the phase relationship, where in-phase signals point upward (N), and antiphase signals point downward (S). If X ($\delta^{13}C$) leads Y ($28\Delta^{5,22E}$), arrows point to the right (E), and if X lags Y, an arrow points to the left (W). Marked regions on the wavelet spectrum indicate significant power to a 95% confidence interval, and areas under the translucid cone of influence show where edge effects are important, and the analysis is unreliable.

Although differential degradation among different compounds during diagenesis makes it challenging to infer the abundance of living organisms from the biomarker data, their normalized MAR may reflect changes in the contribution of each specific group of organisms (Li et al., 2015). During MZ-I, there was a predominance of diatoms and dinoflagellates, indicated by the concentrations above the long-term mean of $28\Delta^{5,22E}$ and $30\Delta^{22E}$, respectively (Volkman, 1986). A similarity between $28\Delta^{5,22E}$ and $30\Delta^{22E}$ contents was also observed by Li et al. (2015), indicating that diatoms and dinoflagellates respond similarly to hydrological variability. During the MZ-II and MZ-III, a relative increase in long-chain alkenones content, biomarkers produced by coccolithophores (Epstein et al., 2001), was observed. Finally, during MZ-IV, a decrease occurred in the contents of the three microalgae proxies. This decrease of the microalgae proxies coincided with an increase in the crenarchaeol accumulation rates, a proxy for Thaumarchaeota (Sinninghe Damsté et al., 2002).

Diatoms are common in eutrophic waters, like coastal regions (Libes, 2009), whereas coccolithophores are usually associated with oligotrophic environments, such as the subtropical gyres (Perrin et al., 2016). Changes in the dominant phytoplankton group are consistent with a shift from a more eutrophic environment during MZ-I to a less nutrient-rich environment during MZ-III. During MZ-I, the surface waters enriched in terrestrially derived nutrients may have favored diatom and dinoflagellate productivity. The hydrodynamic conditions changed entering the MZ-II, and a transient SACW upwelling, driven by BC cyclonic meanders (Almeida et al., 2015), was probably responsible for the relative success of the coccolithophores. The BC cyclonic meanders may have occurred more frequently during this time interval, or the SACW may have reached shallower depths than today.

In the last 20 ka, the decrease in the phytoplankton proxies and increase of the Thaumarchaeota proxies suggest a further decrease in nutrient availability toward the present oligotrophic conditions of the BC (Portilho-Ramos et al., 2015; Lourenço et al., 2016). Thaumarchaeota are a group of chemolithotrophic ammonia-oxidizing archaea, which compete poorly with phytoplankton for nutrients but endure in particularly oligotrophic conditions (Santoro et al., 2019). They can also use organic compounds, such as urea and cyanate, as energy and nitrogen sources (Kitzinger et al., 2019). These abilities allowed the Thaumarchaeota to thrive in the Holocene, becoming an

important link in the microbial loop and trophic web of the present BC in the SBB (Moser et al., 2016). In a future warmer scenario, studies using climate and niche models indicate an expansion of oligotrophic regions and replacing larger phytoplankton with smaller organisms (Cabré et al., 2015; Šolić et al., 2018). The picoplankton will probably play an even more important role in the carbon cycle in these situations.

Summary and conclusions

This study highlighted how climate changes affected the sources of OM delivered to the central SBB from the Late Pleistocene to the Holocene. We investigated the primary mechanism controlling marine productivity in the SBB central portion as well as the main delivery routes of the terrestrial OM to the region. According to their temporal evolution, the organic geochemical proxies were classified into "terrestrial-source" and "marine-source" groups. The two OM sources presented distinct stratigraphical zones, indicating distinct mechanisms governing marine OM production and terrestrial OM production and export.

Marine organisms were the primary source of OM for the slope in the last 80 ka. Nutrient input from the adjacent coast seems to have controlled the marine productivity during MZ-I and -II (before 39 ka BP). Upwelling of SACW promoted by the BC cyclonic eddies was likely the primary mechanism controlling marine productivity during MZ-II and -III (between 50 and 29 ka BP). The synergistic effect of terrigenous input and upwelling may have caused the highest marine productivity rates in the Last Glacial Period. In the last 20 ka, a more substantial presence of the oligotrophic tropical water in the region was suggested by a decrease in the phytoplanktonic productivity and a relative increase in archaeal productivity. Due to their ability to use organic compounds and ammonia as energy and nitrogen sources, Thaumarchaeota may have become an important link in the microbial loop and trophic web of the present BC in the SBB.

Stratigraphic zones of the terrestrial OM indicated an oscillating input of soil OM and more sporadic inputs of macrophytes and vascular plants. In general, terrestrial input to the central SBB slope was likely strongly controlled by changes in the continental shelf width and in the type of vegetation over the continent, primarily controlled by sea level fluctuations and the continental moisture evolution, respectively.

Data availability statement

The raw data supporting the conclusions of this article will be made available by the authors, without undue reservation.

Author contributions

MB, MM, and CM designed the concept of the study. AD and JH processed the lipid analyses. AD and GM interpreted the data. AD performed the statistical analysis and wrote the first draft of the manuscript. All authors contributed to manuscript revision, read, and approved the submitted version.

Funding

This study was supported by FAPESP (São Paulo Science Foundation; 2010/06147-5 and 2015/21834-2 research grants) and CNPq (Brazilian National Council for Scientific and Technological Development; 300962/2018-5 and 305763/2011-3 research grants). CM also would like to thank CAPES-PrInt for financial support (88887.311742/2018-00). AD would like to thank Helsinki University Library for the financial support for open access publication fees.

Acknowledgments

AD would like to thank CAPES (Coordenação de Aperfeiçoamento de Pessoal de Ensino Superior) for the Ph.D. Scholarship and Dr. Cristiano Chiessi for the constructive comments.

Conflict of interest

The authors declare that the research was conducted in the absence of any commercial or financial relationships that could be construed as a potential conflict of interest.

Publisher's note

Supplementary material

The Supplementary Material for this article can be found online at: https://www.frontiersin.org/articles/10.3389/fmars.2022.924556/full#supplementary-material

References

Almeida, F. F. M., and Carneiro, C. D. R. (1998). Origem e evolução da Serra do Mar. *Rev. Bras. Geociências* 28, 135–150. doi: 10.5327/rbg.v28i2.617

Almeida, F. K., de Mello, R. M., Costa, K. B., and Toledo, F. A. L. (2015). The response of deep-water benthic foraminiferal assemblages to changes in paleoproductivity during the pleistocene (last 769.2 kyr), western South Atlantic ocean. *Palaeogeogr. Palaeoclimatol. Palaeoecol.* 440, 201–212. doi: 10.1016/j.palaeo.2015.09.005

Alvarenga, A., Paladino, Í.M., Gerotto, A., DeMenocal, P., Iwai, F. S., Sousa, S. H. M., et al. (2022). S/SE Brazilian continental margin sea surface temperature and productivity changes over the last 50 kyr. *Palaeogeogr. Palaeoclimatol. Palaeoecol.* 601, 111144. doi: 10.1016/j.palaeo.2022.111144

Badewien, T., Vogts, A., Dupont, L., and Rullkötter, J. (2015). Influence of late pleistocene and Holocene climate on vegetation distributions in southwest Africa elucidated from sedimentary n-alkanes - differences between 12°S and 20°S. *Quat. Sci. Rev.* 125, 160–171. doi: 10.1016/j.quascirev.2015.08.004

Behling, H., Arz, H. W., Jürgen, P., and Wefer, G. (2002). Late quaternary vegetational and climate dynamics in southeastern Brazil, inferences from marine cores GeoB 3229-2 and GeoB 3202-1. *Palaeogeogr. Palaeoclimatol. Palaeoecol.* 179, 227–243. doi: 10.1016/S0031-0182(01)00435-7

Bianchi, T. S., and Canuel, E. A. (2011). *Chemical biomarkers in aquatic ecosystems* (Woodstock, Oxfordshire: Princeton University Press).

Bianchi, T. S., Cui, X., Blair, N. E., Burdige, D. J., Eglinton, T. I., and Galy, V. (2018). Centers of organic carbon burial and oxidation at the land-ocean interface. *Org. Geochem.* 115, 138–155. doi: 10.1016/j.orggeochem.2017.09.008

Blaauw, M., and Christen, J. A. (2011). Flexible paleoclimate age-depth models using an autoregressive gamma process. *Bayesian Anal.* 6, 457–474. doi: 10.1214/11-BA618

Brzezinski, M. A., Pride, C. J., Franck, V. M., Sigman, D. M., Sarmiento, J. L., Matsumoto, K., et al. (2002). A switch from Si(OH)4 to NO3- depletion in the glacial southern ocean. *Geophys. Res. Lett.* 29, 1–4. doi: 10.1029/2001GL014349

Bush, R. T., and McInerney, F. A. (2013). Leaf wax n-alkane distributions in and across modern plants: Implications for paleoecology and chemotaxonomy. *Geochim. Cosmochim. Acta* 117, 161–179. doi: 10.1016/j.gca.2013.04.016

Cabré, A., Marinov, I., and Leung, S. (2015). Consistent global responses of marine ecosystems to future climate change across the IPCC AR5 earth system models. *Clim. Dyn.* 45, 1253–1280. doi: 10.1007/s00382-014-2374-3

Campos, M. C., Chiessi, C. M., Prange, M., Mulitza, S., Kuhnert, H., Paul, A., et al. (2019). A new mechanism for millennial scale positive precipitation anomalies over tropical south America. *Quat. Sci. Rev.* 225:1–13. doi: 10.1016/j.quascirev.2019.105990

Campos, E. J. D., Velhote, D., and Silveira, I. C. A. (2000). Shelf break upwelling driven by Brazil current cyclonic meanders. *Geophys. Res. Lett.* 27, 751–754. doi: 10.1029/1999GL010502

Chen, M., and Blankenship, R. E. (2021). ""Photosynthesis | photosynthesis,"," in *Encyclopedia of biological chemistry III*. Ed. J. Jez (Oxford: Elsevier), 150–156. doi: 10.1016/B978-0-12-819460-7.00081-5

Costa, K. B., Cabarcos, E., Santarosa, A. C. A., Battaglin, B. B. F., and Toledo, F. A. L. (2016). A multiproxy approach to the climate and marine productivity variations along MIS 5 in SE Brazil: A comparison between major components of calcareous nannofossil assemblages and geochemical records. *Palaeogeogr. Palaeoclimatol. Palaeoecol.* 449, 275–288. doi: 10.1016/j.palaeo.2016.02.032

Cruz, F. W.Jr., Burns, S. J., Jercinovic, M., Karmann, I., Sharp, W. D., and Vuille, M. (2007). Evidence of rainfall variations in southern Brazil from trace element ratios (Mg/Ca and Sr/Ca) in a late Pleistocene stalagmite. *Geochim. Cosmochim. Acta* 71, 2250–2263. doi: 10.1016/j.gca.2007.02.005

Cruz, F. W.Jr., Burns, S. J., Karmann, I., Sharp, W. D., Vuille, M., Cardoso, A. O., et al. (2005). Insolation-driven changes in atmospheric circulation over the past 116,000 years in subtropical Brazil. *Lett. Nat.* 434, 63–66. doi: 10.1029/2003JB002684

Dauner, A. L. L., Mollenhauer, G., Bícego, M. C., and Martins, C. C. (2020). Cluster analysis for time series based on organic geochemical proxies. *Org. Geochem.* 145, 104038. doi: 10.1016/j.orggeochem.2020.104038

Dauner, A. L. L., Mollenhauer, G., Bícego, M. C., Souza, M. M., Nagai, R. H., Figueira, R. C. L., et al. (2019). Multi-proxy reconstruction of sea surface and subsurface temperatures in the western south Atlantic over the last ~ 75 kyr. *Quat. Sci. Rev.* 215, 22–34. doi: 10.1016/j.quascirev.2019.04.020

Dillenburg, S. R., Barboza, E. G., Rosa, M. L. C. C., Caron, F., Cancelli, R., Santos-Fischer, C. B., et al. (2019). Sedimentary records of marine isotopic stage 3 (MIS 3) in southern Brazil. *Geo-Mar. Lett.* 40, 1099–108. doi: 10.1007/s00367-019-00574-2

Epstein, B. L., D'Hondt, S., and Hargraves, P. E. (2001). The possible metabolic role of C37 alkenones in *emiliania huxleyi*. *Org. Geochem.* 32, 867–875. doi: 10.1016/S0146-6380(01)00026-2

Faux, J. F., Belicka, L. L., and Rodger Harvey, H. (2011). Organic sources and carbon sequestration in Holocene shelf sediments from the western Arctic ocean. *Cont. Shelf. Res.* 31, 1169–1179. doi: 10.1016/j.csr.2011.04.001

Feakins, S. J., Peters, T., Wu, M. S., Shenkin, A., Salinas, N., Girardin, C. A. J., et al. (2016). Production of leaf wax n-alkanes across a tropical forest elevation transect. *Org. Geochem.* 100, 89–100. doi: 10.1016/j.orggeochem.2016.07.004

Garzoli, S. L., and Matano, R. P. (2011). The south Atlantic and the Atlantic meridional overturning circulation. *Deep. Res. Part II Top. Stud. Oceanogr.* 58, 1837–1847. doi: 10.1016/j.dsr2.2010.10.063

Griffiths, J. D., Barker, S., Hendry, K. R., Thornalley, D. J. R., Van De Flierdt, T., Hall, I. R., et al. (2013). Evidence of silicic acid leakage to the tropical Atlantic *via* Antarctic intermediate water during marine isotope stage 4. *Paleoceanography* 28, 307–318. doi: 10.1002/palo.20030

Gu, F., Zonneveld, K. A. F., Chiessi, C. M., Arz, H. W., Jürgen, P., and Behling, H. (2017). Long-term vegetation, climate and ocean dynamics inferred from a 73,500 years old marine sediment core (GeoB2107-3) off southern Brazil. *Quat. Sci. Rev.* 172, 55–71. doi: 10.1016/j.quascirev.2017.06.028

Holland, A. R., Petsch, S. T., Castañeda, I. S., Wilkie, K. M., Burns, S. J., and Brigham-Grette, J. (2013). A biomarker record of lake El'gygytgyn, far East Russian Arctic: Investigating sources of organic matter and carbon cycling during marine isotope stages 1-3. *Clim. Past* 9, 243–260. doi: 10.5194/cp-9-243-2013

Hopmans, E. C., Weijers, J. W. H., Schefuß, E., Herfort, L., Sinninghe Damsté, J. S., and Schouten, S. (2004). A novel proxy for terrestrial organic matter in sediments based on branched and isoprenoid tetraether lipids. *Earth Planet. Sci. Lett.* 224, 107–116. doi: 10.1016/j.epsl.2004.05.012

Hu, J., Peng, P., and Chivas, A. R. (2009). Molecular biomarker evidence of origins and transport of organic matter in sediments of the Pearl river estuary and adjacent South China Sea. *Appl. Geochem.* 24, 1666–1676. doi: 10.1016/j.apgeochem.2009.04.035

Juggins, S. (2017). *Rioja: Analysis of quaternary science data. r package version 0.9-15.1. 58*. Available at: https://cran.r-project.org/web/packages/rioja/index.html.

Kitzinger, K., Padilla, C. C., Marchant, H. K., Hach, P. F., Herbold, C. W., Kidane, A. T., et al. (2019). Cyanate and urea are substrates for nitrification by Thaumarchaeota in the marine environment. *Nat. Microbiol.* 4, 234–243. doi: 10.1038/s41564-018-0316-2

Lambert, F., Delmonte, B., Petit, J. R., Bigler, M., Kaufmann, P. R., Hutterli, M. A., et al. (2008). Dust - climate couplings over the past 800,000 years from the EPICA dome c ice Core. *Nature* 452, 616–619. doi: 10.1038/nature06763

Ledru, M. P., Mourguiart, P., and Riccomini, C. (2009). Related changes in biodiversity, insolation and climate in the Atlantic rainforest since the last interglacial. *Palaeogeogr. Palaeoclimatol. Palaeoecol.* 271, 140–152. doi: 10.1016/j.palaeo.2008.10.008

Libes, S. M. (2009). *Introduction to marine biogeochemistry. 2nd ed* (London: Elsevier).

Ligges, U., Short, T., Kienzle, P., Schnackenberg, S., Billinghurst, D., Borchers, H.-W., et al. (2021) *Signal: Signal processing. r package version 0.7-7*. Available at: https://cran.r-project.org/web/packages/signal/signal.pdf.

Li, L., Li, Q., He, J., Wang, H., Ruan, Y., and Li, J. (2015). Biomarker-derived phytoplankton community for summer monsoon reconstruction in the western south China Sea over the past 450ka. *Deep. Res. Part II Top. Stud. Oceanogr.* 122, 118–130. doi: 10.1016/j.dsr2.2015.11.006

Lin, J., Keogh, E., Wei, L., and Lonardi, S. (2007). Experiencing SAX: A novel symbolic representation of time series. *Data Min. Knowl. Discov* 15, 107–144. doi: 10.1007/s10618-007-0064-z

Lisiecki, L. E., and Raymo, M. E. (2005). A pliocene-pleistocene stack of 57 globally distributed benthic δ18O records. *Paleoceanography* 20, 1–17. doi: 10.1029/2004PA001071

Lisiecki, L. E., and Stern, J. V. (2016). Regional and global benthic δ18O stacks for the last glacial cycle. *Paleoceanography* 31, 1368–1394. doi: 10.1002/2016PA003002

Lourenço, R. A., Mahiques, M. M., Wainer, I. E. K. C., Rosell-Melé, A., and Bícego, M. C. (2016). Organic biomarker records spanning the last 34,800 years from the southeastern Brazilian upper slope: Links between sea surface temperature, displacement of the Brazil current, and marine productivity. *Geo-Mar. Lett.* 36, 361–369. doi: 10.1007/s00367-016-0453-7

Mahiques, M. M., Fukumoto, M. M., Silveira, I. C. A., Figueira, R. C. L., Bícego, M. C., Lourenço, R. A., et al. (2007). Sedimentary changes on the southeastern Brazilian upper slope during the last 35,000 years. *An. Acad. Bras. Cienc.* 79, 171–181. doi: 10.1590/S0001-37652007000100018

Mahiques, M. M., Hanebuth, T. J. J., Nagai, R. H., Bícego, M. C., Figueira, R. C. L., Sousa, S. H. M., et al. (2017). Inorganic and organic geochemical fingerprinting of sediment sources and ocean circulation on a complex continental margin (São Paulo bight, Brazil). *Ocean Sci.* 13, 209–222. doi: 10.5194/os-13-209-2017

Mahiques, M. M., Nagai, R. H., Dias, G. P., and Figueira, R. C. L. (2022). An 80 kyr record of intermediate-depth water flow on the western south Atlantic margin. *Sedimentology*, 1–13. doi: 10.1111/sed.13016

Mahiques, M. M., Tessler, M. G., Ciotti, A. M., Silveira, I. C. A., Sousa, S. H. M., Figueira, R. C. L., et al. (2004). Hydrodynamically driven patterns of recent sedimentation in the shelf and upper slope off southeast Brazil. *Cont. Shelf. Res.* 24, 1685–1697. doi: 10.1016/j.csr.2004.05.013

Mathias, G. L., Roud, S. C., Chiessi, C. M., Campos, M. C., Dias, B. B., Santos, T. P., et al. (2021). A multi-proxy approach to unravel late Pleistocene sediment flux and bottom water conditions in the western South Atlantic ocean. *Paleoceanogr. Paleoclimatol.* 36, 1–22. doi: 10.1029/2020PA004058

Matsumoto, K., Chase, Z., and Kohfeld, K. (2014). Different mechanisms of silicic acid leakage and their biogeochemical consequences. *Paleoceanography* 29, 238–254. doi: 10.1002/2013PA002588

Matsumoto, K., Sarmiento, J. L., and Brzezinski, M. A. (2002). Silicic acid leakage from the southern ocean: A possible explanation for glacial atmospheric pCO2. *Global Biogeochem. Cycles* 16, 5-1-5–5-123. doi: 10.1029/2001gb001442

Meyers, P. A. (1994). Preservation of elemental and isotopic source identification of sedimentary organic matter. *Chem. Geol.* 114, 289–302. doi: 10.1016/0009-2541(94)90059-0

Meyers, P. A. (1997). Organic geochemical proxies of paleoceanographic, paleolimnologic, and paleoclimatic processes. *Org. Geochem.* 27, 213–250. doi: 10.1016/S0146-6380(97)00049-1

Meyers, P. A. (2003). Applications of organic geochemistry to paleolimnological reconstructions: A summary of examples from the Laurentian great lakes. *Org. Geochem.* 34, 261–289. doi: 10.1016/S0146-6380(02)00168-7

Miller, K. G., Kominz, M. A., Browning, J. V., Wright, J. D., Mountain, G. S., Katz, M. E., et al. (2005). The Phanerozoic record of global sea-level change. *Science* 310, 1293-1298. doi: 10.1126/science.1116412

Montero, P., and Vilar, J. A. (2014). TSclust: An R package for time series clustering. *J. Stat. Software* 62, 1–43. doi: 10.18637/jss.v062.i01

Moser, G. A. O., Castro, N. O., Takanohashi, R. A., Fernandes, A. M., Pollery, R. C. G., Tenenbaum, D. R., et al. (2016). The influence of surface low-salinity waters and cold subsurface water masses on picoplankton and ultraplankton distribution in the continental shelf off Rio de Janeiro, SE Brazil. *Cont. Shelf. Res.* 120, 82–95. doi: 10.1016/j.csr.2016.02.017

Muccio, Z., and Jackson, G. P. (2009). Isotope ratio mass spectrometry. *Analyst* 134, 213–222. doi: 10.1039/B808232D

Muelbert, J. H., Acha, M., Mianzan, H., Guerrero, R., Reta, R., Braga, E. S., et al. (2008). Biological, physical and chemical properties at the subtropical shelf front zone in the SW Atlantic continental shelf. *Cont. Shelf. Res.* 28, 1662–1673. doi: 10.1016/j.csr.2007.08.011

Müller, P. J. (2004). Density and water content of sediment core GeoB2107-3. doi: 10.1594/PANGAEA.143110

Nagai, R. H., Ferreira, P. A. L., Mulkherjee, S., Martins, M. V. A., Figueira, R. C. L., Sousa, S. H. M., et al. (2014a). Hydrodynamic controls on the distribution of surface sediments from the southeast south American continental shelf between 23° S and 38° S. *Cont. Shelf. Res.* 89, 51–60. doi: 10.1016/j.csr.2013.09.016

Nagai, R. H., Sousa, S. H. M., Lourenço, R. A., Bícego, M. C., and Mahiques, M. M. (2010). Paleoproductivity changes during the late quaternary in the southeastern Brazilian upper continental margin of the southwestern Atlantic. *Braz. J. Oceanogr.* 58, 31–41. doi: 10.1590/S1679-87592010000500004

Nagai, R. H., Sousa, S. H. M., and Mahiques, M. M. (2014b). ""The southern Brazilian shelf,"," in *Continental shelves of the world: Their evolution during the last glacio-eustatic cycle*. Eds. F. L. Chiocchi and A. R. Chivas (London: Geological Society), 47–54. doi: 10.1144/M41.5

Nascimento, R. A., Santos, T. P., Venancio, I. M., Chiessi, C. M., Ballalai, J. M., Kuhnert, H., et al. (2021). Origin of δ13C minimum events in thermocline and intermediate waters of the western south Atlantic. *Quat. Sci. Rev.* 272, 107224. doi: 10.1016/j.quascirev.2021.107224

Oksanen, J., Blanchet, F. G., Friendly, M., Kindt, R., Legendre, P., McGlinn, D., et al. (2018). "Vegan: Community ecology package," in *R package version 2*, 5–3. Available at: https://cran.r-project.org/web/packages/vegan/index.html

Pereira, L. S., Arz, H. W., Pätzold, J., and Portilho-Ramos, R. C. (2018). Productivity evolution in the south Brazilian bight during the last 40,000 years. *Paleoceanogr. Paleoclimatol.* 33, 1339–1356. doi: 10.1029/2018PA003406

Perrin, L., Probert, I., Langer, G., and Aloisi, G. (2016). Growth of the coccolithophore *Emiliania huxleyi* in light- and nutrient-limited batch reactors: Relevance for the BIOSOPE deep ecological niche of coccolithophores. *Biogeosciences* 13, 5983–6001. doi: 10.5194/bg-13-5983-2016

Pichat, S., Abouchami, W., and Galer, S. J. G. (2014). Lead isotopes in the Eastern equatorial pacific record *Quaternary* migration of the south *Westerlies*. *Earth Planet. Sci. Lett.* 388, 293–305. doi: 10.1016/j.epsl.2013.11.035

Piola, A. R., and Matano, R. P. (2017). ""Ocean currents: Atlantic Western boundary - Brazil Current/Falkland (Malvinas) current,"," in *Reference module in earth systems and environmental sciences* (Elsevier). doi: 10.1016/B978-0-12-409548-9.10541-X

Portilho-Ramos, R. C., Ferreira, F., Calado, L., Frontalini, F., and Toledo, M. B. (2015). Variability of the upwelling system in the southeastern Brazilian margin for the last 110,000 years. *Glob. Planet. Change* 135, 179–189. doi: 10.1016/j.gloplacha.2015.11.003

Poynter, J., and Eglinton, G. (1990). Molecular composition of three sediments from hole 717C: The Bengal Fan in *Proceedings of the Ocean Drilling Program, Scientific Results, eds. J. R. Cochran, D. A. V. Stow, and et al.* (College Station, TX: Ocean Drilling Program), 155–161. doi: 10.2973/odp.proc.sr.116.151.1990

Razik, S., Govin, A., Chiessi, C. M., and von Dobeneck, T. (2015). Depositional provinces, dispersal, and origin of terrigenous sediments along the SE South American continental margin. *Mar. Geol.* 363, 261–272. doi: 10.1016/j.margeo.2015.03.001

R Core Team (2021) *R: A language and environment for statistical computing*. Available at: http://www.r-project.org.

Ribeiro, C. G., Lopes dos Santos, A., Marie, D., Pellizari, V. H., Brandini, F. P., and Vaulot, D. (2016). Pico and nanoplankton abundance and carbon stocks along the Brazilian bight. *PeerJ* 4, e2587. doi: 10.7717/peerj.2587

Ribeiro, M. C., Metzger, J. P., Martensen, A. C., Ponzoni, F. J., and Hirota, M. M. (2009). The Brazilian Atlantic forest: How much is left, and how is the remaining forest distributed? implications for conservation. *Biol. Conserv.* 142, 1141–1153. doi: 10.1016/j.biocon.2009.02.021

Roesch, A., and Schmidbauer, H. (2018). "WaveletComp: Computational wavelet analysis," in *R package version 1.1*, vol. 89. . Available at: https://cran.r-project.org/package=WaveletComp.

Rommerskirchen, F., Eglinton, G., Dupont, L., Güntner, U., Wenzel, C., and Rullkötter, J. (2003). A north to south transect of Holocene southeast Atlantic continental margin sediments: Relationship between aerosol transport and compound-specific δ13C land plant biomarker and pollen records. *Geochem. Geophys. Geosystems* 4:1–29. doi: 10.1029/2003GC000541

Salvaterra, A., da, S., dos, R. F., Salaroli, A. B., Figueira, R. C. L., and Mahiques, M. M. (2017). Evidence of an marine isotope stage 3 transgression at the *Baixada Santista*, south-eastern Brazilian coast. *Braz. J. Geol.* 47, 693–702. doi: 10.1590/2317-4889201720170057

Santoro, A. E., Richter, R. A., and Dupont, C. L. (2019). Planktonic marine archaea. *Ann. Rev. Mar. Sci.* 11, 131–158. doi: 10.1146/annurev-marine-121916-063141

J. L. Sarmiento and N. Gruber (Eds.) (2006). ""Remineralization and burial in the sediments,"," in *Ocean biogeochemical dynamics* (Princeton (UK: Princeton University Press), 227–269.

Schaeffer-Novelli, Y., Cintrón-Molero, G., Adaime, R. R., and Camargo, T. M. (1990). Variability of mangrove ecosystems along the Brazilian coast. *Estuaries* 13, 204–218. doi: 10.2307/1351590

Silveira, I. C. A., Foloni Neto, H., Costa, T. P., Schmidt, A. C. K., Pereira, A. F., Castro Filho, B. M., et al. (2015). ""Caracterização da oceanografia física do talude continental e região oceânica da *Bacia de Campos*,"," in *Meteorologia e oceanografia*. Eds. R. P. Martins and G. S. Grossmann-Matheson (Rio de Janeiro, RJ: Elsevier), 135–189. doi: 10.1016/b978-85-352-6208-7.50011-8

Sinninghe Damsté, J. S., Schouten, S., Hopmans, E. C., van Duin, A. C. T., and Geenevasen, J. A. J. (2002). Crenarchaeol: The characteristic core glycerol dibiphytanyl glycerol tetraether membrane lipid of cosmopolitan pelagic crenarchaeota. *J. Lipid Res.* 43, 1641–1651. doi: 10.1194/jlr.M200148-JLR200

Sinninghe Damsté, J. S., Van Dongen, B. E., Rijpstra, W. I. C., Schouten, S., Volkman, J. K., and Geenevasen, J. A. J. (2001). Novel intact glycolipids in sediments from an Antarctic lake (Ace lake). *Org. Geochem.* 32, 321–332. doi: 10.1016/S0146-6380(00)00165-0

Šolić, M., Grbec, B., Matić, F., Šantić, D., Šestanović, S., Ninčević, G. Ž., et al. (2018). Spatio-temporal reproducibility of the microbial food web structure

associated with the change in temperature: Long-term observations in the Adriatic Sea. *Prog. Oceanogr.* 161, 87–101. doi: 10.1016/j.pocean.2018.02.003

Souza, M. M., Mathis, M., Mayer, B., Noernberg, M. A., and Pohlmann, T. (2020). Possible impacts of anthropogenic climate change to the upwelling in the South Brazil bight. *Clim. Dyn.* 55, 651–664. doi: 10.1007/s00382-020-05289-0

Torrence, C., and Compo, G. P. (1998). A practical guide to wavelet analysis. *Bull. Am. Meteorol. Soc* 79, 61–78. doi: 10.1175/1520-0477(1998)079<0061:APGTWA>2.0.CO;2

Volkman, J. K. (1986). A review of sterol markers for marine and terrigenous organic matter. *Org. Geochem.* 9, 83–99. doi: 10.1016/0146-6380(86)90089-6

Weijers, J. W. H., Schefuß, E., Schouten, S., and Sinninghe Damsté, J. S. (2007). Coupled thermal and hydrological evolution of tropical Africa over the last deglaciation. *Science* 315, 1701-1704. doi: 10.1126/science.1138131

Yunker, M. B., Belicka, L. L., Harvey, H. R., and Macdonald, R. W. (2005). Tracing the inputs and fate of marine and terrigenous organic matter in Arctic ocean sediments: A multivariate analysis of lipid biomarkers. *Deep. Res. Part II Top. Stud. Oceanogr.* 52, 3478–3508. doi: 10.1016/j.dsr2.2005.09.008

Advantages of publishing in Frontiers

OPEN ACCESS
Articles are free to read for greatest visibility and readership

FAST PUBLICATION
Around 90 days from submission to decision

HIGH QUALITY PEER-REVIEW
Rigorous, collaborative, and constructive peer-review

TRANSPARENT PEER-REVIEW
Editors and reviewers acknowledged by name on published articles

Frontiers
Avenue du Tribunal-Fédéral 34
1005 Lausanne | Switzerland

Visit us: www.frontiersin.org
Contact us: frontiersin.org/about/contact

REPRODUCIBILITY OF RESEARCH
Support open data and methods to enhance research reproducibility

DIGITAL PUBLISHING
Articles designed for optimal readership across devices

FOLLOW US
@frontiersin

IMPACT METRICS
Advanced article metrics track visibility across digital media

EXTENSIVE PROMOTION
Marketing and promotion of impactful research

LOOP RESEARCH NETWORK
Our network increases your article's readership